The electrode-electrolyte interface in CO2 reduction and H2 evolution: a multiscale approach

Cecilio de Oliveira Monteiro, M

The electrode-electrolyte interface in CO_2 reduction and H_2 evolution:

a multiscale approach

—

Proefschrift

ter verkrijging van
de graad van doctor aan de Universiteit Leiden,
op gezag van rector magnificus Prof. dr. ir. H. Bijl,
volgens besluit van het college voor promoties
te verdedigen op dinsdag 15 februari 2022
klokke 15.00 uur

—

door

Mariana C. O. Monteiro

geboren te Belo Horizonte
in 1991

PROMOTIECOMMISSIE

Promotor

Prof. dr. M. T. M. Koper (Universiteit Leiden)

Co-promotor

Prof. dr. N. López (Institut Català d'Investigació Química)

Overige leden

Dr. D. G. H. Hetterscheid (Universiteit Leiden)
Prof. dr. H. S. Overkleeft (Universiteit Leiden)
Prof. dr. E. Bouwman (Universiteit Leiden)
Prof. dr. P. R. Unwin (University of Warwick)
Prof. dr. A. Cuesta Ciscar (University of Aberdeen)

The work presented in this thesis was supported by the European Commission, as part of the Marie Skłodowska Curie Innovative Training Network ELCoREL-722614.

ISBN: 978-94-6423-628-6

Cover and chapters art: Katrina Goretskaya (katrina.goretskaya@gmail.com)
Printed by ProefschriftMaken with financial support from Equilabrium

In memory of Tia Bú,

always present...

To my parents

"Science is not only a disciple of reason
but, also, one of romance and passion."

– Stephen Hawking

Table of contents

1

Introduction

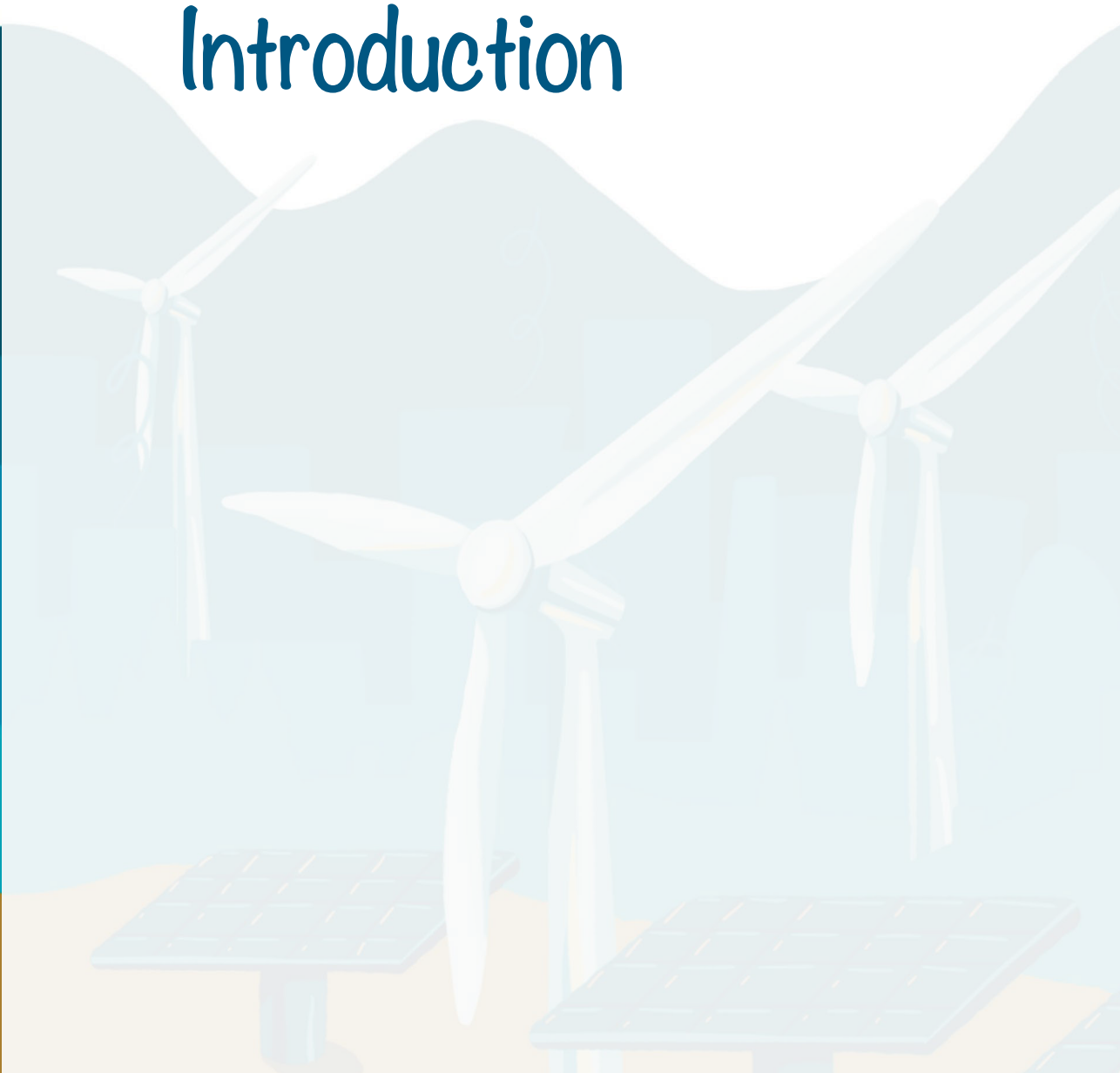

1.1 Electrochemistry and electrification

The study of the transformation of electrical energy into chemical bonds and, in the reverse process, the conversion of energy stored in chemical bonds back to electricity, defines the field of electrochemistry. While in chemical reactions electrons are transferred directly between molecules, in electrochemical reactions they are transferred through electronic or ionic media. Electrochemistry is an old science, its birth being considered to be in the 18th century, the time of the great findings of "animal electricity" by Galvani and the first battery by Volta.[1] Various devices and processes involving electrochemistry that are currently used at an industrial scale come from concepts that were developed in the 19th century. These include batteries[2] , solar cells[3], and the industrial production of chlorine from brine.[4] The field has been increasingly growing, especially since the beginning of the 21st century, due to climate change and the need for electrification, renewable energy conversion and storage technologies. The importance electrochemistry has had and will have for the future of our society is highlighted by the 2019 Nobel Prize in Chemistry, awarded to John B. Goodenough, M. Stanley Whittingham and Akira Yoshino for their contributions to the development of the rechargeable lithium-ion battery in the 1970s. The battery enabled the development of mobile phones, laptops, electric vehicles and the storage of energy generated by solar and wind power. Nevertheless, further developments in electrochemistry will still be crucial for improving the current landscape of sustainable energy production and utilization, towards a fossil fuel-free electrified society.

In the last one-and-a-half century, we have relied almost exclusively on non-renewable resources to produce things that are essential to maintain our lifestyle, such as energy, chemicals, and fuels. For example, the chemical industry is highly dependent on petroleum, both as a feedstock and energy source. In fact, roughly 6-7% of the annual oil production is consumed by this sector.[5] The combustion of these fossil resources generates greenhouse gas emissions that damage our environment and lead to climate change. To remediate that, there is growing interest in using renewable energy and sustainably produced chemicals to feed the industry and transportation sectors, as these are the main consumers of fossil resources nowadays.[6] Using clean electricity as the main source of energy is a potentially cheap and efficient way to decarbonise our economy. The costs of renewables and storage technologies are rapidly falling, making it possible to achieve the required expansion of clean power systems at low cost. Overall, with

the current existing technologies (and those under development), the replacement of greenhouse gas emitting processes and the electrification of our society can be achieved by:

- Increasing the renewable energy electricity production, supply and storage capacity;
- Replacing combustion engines by electric motors, present e.g. in battery and fuel cell powered vehicles;
- Using electricity to drive industrial processes.

A very important example of a decarbonized energy system is the use of H_2 as energy storage, fuel, and bulk chemical. Renewable electricity can be converted to H_2 through the electrolysis of water. It is cheaper to transport hydrogen than to transport electricity, which means that, for example, electrolysers can be placed on sites where the renewable electricity is cheap and delivered where it is needed, on demand. The energy stored in H_2 can in turn be used when there are shortages, or H_2 can be directly used as fuel e.g. in micro combined heat and power (CHP) fuel cells in our homes, without a carbon footprint. Although electrification is already happening in the ground transportation and electricity sectors, for some industries such as cement and steelmaking this is not yet the case, and may be more challenging to achieve. Nevertheless, there are still ways of reducing the carbon footprint of these processes using electrochemistry. For instance, renewable electricity can be used to electrochemically convert CO_2, a waste from the cement and steel industries, to a chemical building block, like CO.[7] This pure CO can, for example, be used in the industrial preparation of acetic and acrylic acid, among many other applications.[8]

Achieving global electrification will require serious breakthroughs in the different industrial sectors and, importantly, in the society. A change in mentality is necessary, to drive the initial investments that relying on electricity will require. Infrastructure will be necessary, for integrating the power grid. All this will have to come with new laws and regulations, not only regarding the electricity market but also the environment. To succeed, these have to be allied to public acceptance, and political resolve. Although promising, this may be especially challenging to achieve in developing countries, facing e.g., social inequalities. Finally, climate change and the realization that we need to shift towards more sustainable processes, calls for innovation and for re-thinking industrial approaches. In view of that, to develop new electrochemical technologies and to stop depending on non-renewable resources, bridging fundamental and applied electrochemistry, is necessary.

1.2 Heterogeneous electrocatalysis

Heterogeneous electrocatalysis is the branch of electrochemistry that studies reactions occurring at the surface of an electrode, which contains or is the catalyst. Catalysts (or electrocatalysts) are materials that enable and/or accelerate a chemical reaction, by lowering the overall potential energy landscape so that the reaction barrier decreases. Electrocatalysis uses electricity to convert molecules as for example H_2O, N_2 and CO_2 into energy carriers or important building blocks for the chemical and fuel industries as CO, H_2, ethanol, NH_3. The device that makes this electrochemical conversion possible is also known as an electrolyser (Fig. 1.1), where a direct electric current drives otherwise nonspontaneous chemical reactions. In the cathode material, electrons are provided to the reactants while at the anode material electrons enter the circuit. Fig. 1.1 exemplifies an electrolyser in which the electrocatalytic reduction of CO_2 takes place at the cathode (CO_2 reduction reaction, CO_2RR, Eq. 1.1); and the oxidation of H_2O to O_2 (Oxygen Evolution Reaction, OER, Eq. 1.2) happens at the anode. The anode and cathode are placed in an electrically conducting medium containing cations and anions, called the electrolyte. Current is passed through the electrolyte due to the movement of positively charged ions (cations) towards the cathode, and negatively charged ions (anions) towards the anode. The cathode and anode may be separated by a membrane, a material that selectively allows species to go from one electrolyte compartment to another. For instance, the membrane from Fig. 1.1, selectively allows protons to move from the anode to the cathode compartment. This may be used to avoid secondary reactions or to easily separate the products made at the two different electrodes.

$$\text{CO}_2\text{RR:}\quad x\text{CO}_2 + n\text{H}_2\text{O} + n\text{e}^- \rightarrow \textit{product} + y\text{OH}^- \qquad \text{Eq. 1.1}$$

$$\text{OER:}\quad 2\text{H}_2\text{O} \rightarrow \text{O}_2 + 4\text{H}^+ + 4\text{e}^- \qquad \text{Eq. 1.2}$$

The minimum energy input (voltage) required to drive reactions 1.1 and 1.2 (E^o_{CELL}) is the difference between the half-cell equilibrium potentials ($E^o_{CATHODE} - E^o_{ANODE}$) described by $E^o_{CELL} = -\Delta G^o/nF$, where ΔG^o is the Gibbs free energy of the overall cell reaction at 1 atm and 298 K, n is the number of moles of electrons transferred in the half-cell reaction, and F is Faraday constant (96 485 C mol^{-1}). The theoretical value of the cell potential can be calculated using the Nernst equation:

$$E_{CELL} = E^o_{CELL} - (RT/zF)\ln(Q_R) \qquad \text{Eq. 1.3}$$

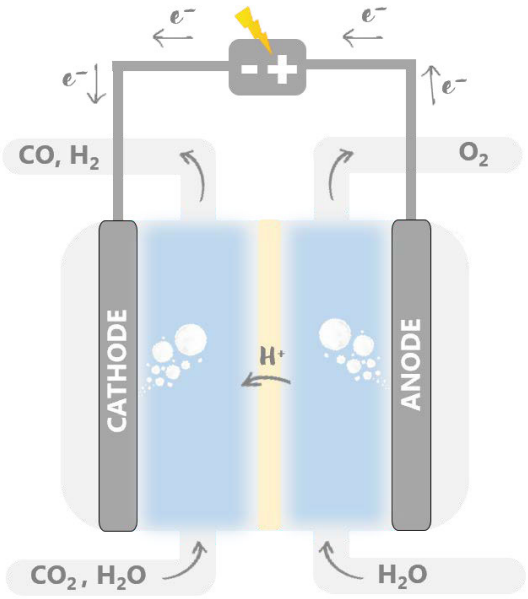

Fig. 1.1. Pictorial representation of a CO_2 to CO electrolyser, in which the cathode and anode are separated by a proton exchange membrane.

where E^o_{CELL} is the standard equilibrium cell potential, R is the universal gas constant (8.314462 J K^{-1} mol^{-1}), T is the temperature in Kelvins, z is the number of electrons transferred in the cell reaction, F is the Faraday constant and Q_R is the reaction quotient, derived from the activities of the electroactive species.

To drive sufficiently large reaction rates, an excess voltage (overpotential) must be applied to overcome the sum of several energy barriers and resistances. These include e.g. ohmic losses from the conduction of ions in the electrolyte, and the sometimes slow rates of the reactions at the cathode and anode. Studies in electrochemistry focus on minimizing the potential that must be applied for an electrocatalytic process to take place, which depends on electrode material, reactants, products, the electrode–electrolyte interface, among others. Thus, the main aim of electrocatalysis is usually to improve the reaction rate (the amount of product produced per unit of time), which can be achieved by decreasing the energy barrier of the target reaction.

1.3 The electrochemical interface

The primary role of the electrolyte is to conduct ionic charge between the electrodes. It usually consists of a solvent and a salt, that easily dissociates into cations and anions to provide a high ionic conductivity. When a metal electrode is in contact with the electrolyte, ions in the electrolyte assemble near the surface to balance the charges on the electrode. For instance, during CO_2RR, the electrode is negatively charged. Cations in the electrolyte then migrate towards the cathode surface, forming what we call the electrochemical double layer. Fig. 1.2 shows a schematic representation of the electrode-electrolyte interface according to the Gouy-Chapman-Stern theory. In this model, the double layer is composed by the Inner Helmholtz Plane (IHP), containing less solvated species and adsorbates, and the Outer Helmholtz Plane (OHP), containing fully solvated cations, which together form the Stern layer. Beyond the OHP, there are concentration gradients of the species in solution, in the region called the Gouy-Chapman diffuse layer. The charge distribution of ions as a function of distance from the metal surface, leads to a steep decrease of the electric potential extending from the electrode surface towards the bulk of the solution. The properties and composition of the electrical double layer are a function of the applied potential, the concentration and nature of the species in solution, the electrode material and reactions taking place, and can highly influence the electrocatalytic reaction.

There are different aspects of the electrode-electrolyte interface to be considered for electrocatalysis, various of which will be discussed throughout this thesis. For instance, as water participates in diverse electrochemical reactions, it is important to understand how water interacts with the surface and with the dissolved ions. Also, the degree of hydration of a cation, may dictate its concentration at the OHP, how it interacts with reaction intermediates and how it accumulates at the interface. Another important point is the dependence of the activity and selectivity of reactions on the electrolyte bulk pH. Because of that, pH gradients that may develop during a reaction that produces/consumes protons or OH^- also must be considered. All these different aspects, even though only briefly mentioned here, illustrate the complexity of the electrochemical interface. Decoupling the effects that the different electrolyte properties have on a reaction, is key towards optimizing the process and understanding underlying reaction mechanisms.

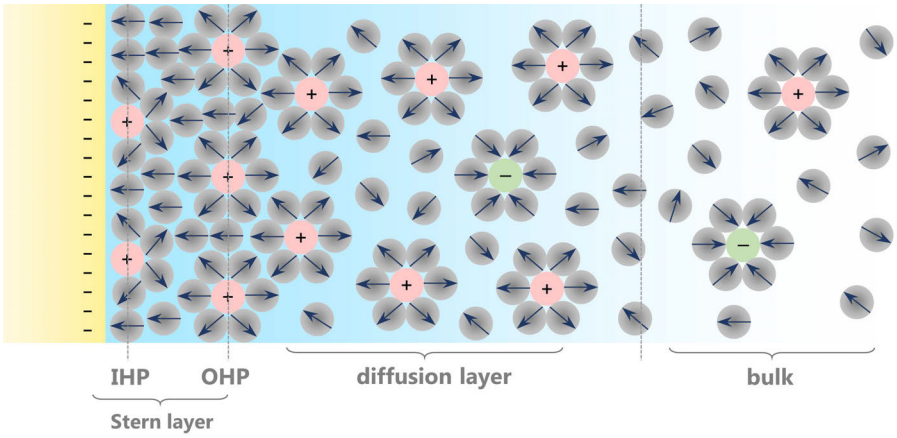

Fig. 1.2. Schematic representation of the electrode-electrolyte interface. Gray circles represent water molecules, and the arrows point towards the positive part of the dipole. Cations are represented in red and anions in green.

1.4 CO_2 electroreduction

1.4.1 Closing the carbon cycle

The first reports of the electrochemical reduction of CO_2 come from the 19th century[9], and investigations have been intensified after the pioneering works from Hori, Murata and co-workers in the 1980s.[10–12] But why to reduce CO_2? The answer is simple: because it is an abundant carbon source, processing it electrochemically does not harm the environment, and may help lowering the carbon footprint of processes. We need carbon-containing species to make fuels, chemicals, consumables, and currently we obtain this carbon mainly from processes involving fossil resources. The burning of these fossil resources produces a lot of CO_2, which is currently released into the atmosphere and contributes to climate change. In 2020, the global emissions of CO_2 reached 31.5 Gt, compared to values below 3 Gt/year before 1900.[13] Two thirds of the emitted CO_2 come from the energy sector, and the rest comes from agriculture, land use, and industries. The main goal is, of course, to stop relying on processes that emit CO_2, through electrification of the industry. Still, in cases where this is inevitable in the short term, the electrochemical CO_2RR is a way to reduce the carbon footprint of a process. In the future, CO_2RR may also help in storing excess renewable electricity in valuable products.

If instead of releasing it into the atmosphere, CO_2 is captured and utilized, it may provide the means to close the carbon cycle. Of course, at long-term, considering we will use less fossil resources and have less CO_2 waste from the energy sector, CO_2 would likely have to come from biomass processing or harvested from air, to achieve climate benefits. Also, CO_2-derived products that have a long lifetime (as building materials), offer larger emission reduction possibilities than products that ultimately involve the release of CO_2 into the atmosphere (as fuels). These, and other considerations, are of course required to access the applicability of CO_2 electroreduction, and are important for achieving a "circular economy"; a popular term nowadays which represents the idea that (carbon) waste is transformed into a fuel or building block. Such a cycle involving CO_2RR is exemplified in the schematics of Fig. 1.3. Ideally, energy from the sun and wind is converted into electricity, which powers a CO_2 electrolyser as the one showed in Fig. 1.1. The products from CO_2RR can serve as building blocks for the chemical and fuel industries, which in turn, currently emit CO_2. The CO_2 emissions can be captured and used as input to the electrolyser, leading to a net zero-emissions carbon cycle.

1.4.2 CO_2 reduction to CO

On gold, silver and zinc electrodes, CO_2RR yields mainly carbon monoxide (CO), while on Sn, Pb, Tl, Hg, In, and Cd mainly HCOOH (formic acid) is formed.[15] On copper, hydrocarbons and alcohols can be formed, such as ethylene and ethanol.[16] In this thesis, we focus on CO_2 reduction to CO on gold electrodes, as a model reaction to understand processes taking place at the electrode-electrolyte interface. The standard equilibrium potential to form most CO_2RR products, is similar to that to form H_2 from hydronium or water in aqueous electrolytes.[17] Therefore, the electrochemical reduction of CO_2 to CO (Eq. 1.4) usually competes with the hydrogen evolution reaction (HER). In acidic media, proton reduction is the main branch of HER taking place (Eq. 1.5), while in neutral to alkaline media water reduction prevails (Eq. 1.6).

$$CO_2 + H_2O + 2e^- \rightarrow CO + 2OH^- \quad \text{Eq. 1.4}$$

$$2H^+ + 2e^- \rightarrow H_2 \quad \text{Eq. 1.5}$$

$$2H_2O + 2e^- \rightarrow H_2 + 2OH^- \quad \text{Eq. 1.6}$$

Most fundamental research focuses on developing new catalysts to improve the reaction activity, selectivity and stability. Only recently, more attention has been given to optimizing the electrolyte composition[19], and to better understanding its

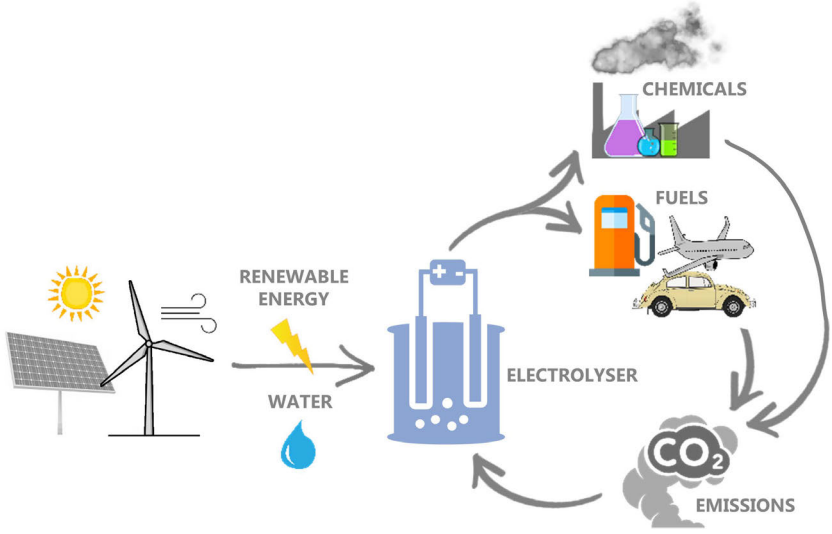

Fig. 1.3. Schematic showing the electrochemical conversion of water and CO_2 to value-added products for the chemicals and fuels industries, using energy from renewable sources. CO_2 captured from the emissions of these industries, enters the process again, closing the carbon cycle.

actual role on the reaction, which is also the focus of this thesis. Water is the most common solvent used, as it is easy to handle, safe, chemically stable, and compatible with most systems. Additionally, water can act both as proton donor and acceptor to facilitate the electrochemical reactions. Early studies on the effect of different anions and cations on the CO_2 reduction reaction, already showed that the species in the electrolyte are not mere spectators and can significantly steer the reaction activity and selectivity.[18] To date, the most reported electrolytes for CO_2 reduction are aqueous solutions of potassium bicarbonate ($KHCO_3$), due to their high buffer capacity and low price. Acidic media have usually been avoided, due to the fast kinetics of the competing proton reduction reaction (Eq. 1.4). However, we will show in this thesis that it can also be employed for efficiently running CO_2 reduction to CO. Even though CO_2 electrocatalysis is still a growing field, right now, electrolysers for the conversion of CO_2 to CO, for example, are reaching the pilot scale and are on the route towards commercialization.[20–22] This means that in the coming years, research efforts will continue to grow towards optimizing CO_2 electrolysers, and making the process more competitive.

If successfully employed at large scale, electrochemical CO_2 conversion and storage technologies have the potential to, for example, enable the sustainable production of chemicals on demand. Traditionally, CO is produced in large,

centralized plants, though e.g., gasification of coal or steam reforming. The transportation of the CO produced is expensive, as it must be pressurised and is a hazardous chemical. As of now, producing CO electrochemically at comparable scales is more expensive than e.g., via steam reforming. However, alternatively, producing CO in small decentralized electrochemical plants could allow for CO to be produced on site, according to the need. This would cut the costs of transportation and storage, make the process more competitive and improve safety.

1.5 H_2 evolution

Understanding the competing HER is relevant for improving the selectivity of the CO_2 reduction reaction. However, on its own, HER is extremely important, as the cathode reaction taking place in water electrolysers. As discussed in Section 1.1, hydrogen produced from renewable energy *via* electrolysis, has a crucial role in the global energy transition, as a clean, storable and transportable fuel.[23] There are currently three main types of low-temperature processes to make H_2 electrochemically, including alkaline electrolysis (AE), proton exchange membrane (PEM) electrolysis and anion exchange membrane (AEM) electrolysis (also known as alkaline PEM).[24] Low-temperature electrolysers are available on the market, in fact, AE have already been used for over 100 years, and account for most of the installed capacity worldwide. PEM electrolysers have been commercialized since the beginning of the 21st century, while AEM electrolysers have only recently appeared on the market. Still, the fundamental material and electrolyte properties that determine catalytic activity for the HER are not yet fully understood.[25] Fundamental research is still required in order to increase the efficiency of the electrolyser system as a whole, along with its operating life, power density and stack size, with the eventual goal of reducing costs. Mechanistic aspects of HER and further details are discussed in Chapters 9 and 10.

1.6 Multiscale approach

Throughout this thesis, we study both the fundamental and more applied aspects of electrocatalysis, or a combination thereof. On the fundamental side, electrode processes at the meso scale are mainly studied through stationary and rotating disc voltammetry. In this case, a defined portion of the working electrode area is put in contact with the electrolyte, and the current response as a function of potential is recorded. In stationary experiments, electrode reactions may face

mass transport limitations. Rotation is then used to minimize that and better control the flux of species from or towards the electrode. Going to the micro scale, investigations are carried out *in situ*, under *operando* conditions, using Scanning Electrochemical Microscopy (SECM); and *ex situ* using Scanning Electron Microscopy (SEM) coupled with Energy Dispersive X-Ray Spectroscopy (EDX). In SECM, a microelectrode is positioned a few micrometres in the proximity of a second electrode, where for instance a reaction is taking place. This microelectrode is used to monitor a variety of electrochemical signals, which in this thesis comprised of the local pH and the presence of H_2 and CO in the diffusion layer. SEM and EDX are techniques used before and after the electrochemical measurements, in which a focused electron beam interacts with the sample, allowing for assessing the topography and composition of the surface. At the nano scale, the electrode-electrolyte interface is modelled in this thesis using *Ab Initio* Molecular Dynamics (AIMD) and Density Functional Theory (DFT) through collaborations with ICIQ, the Institute of Chemical Research of Catalonia. We specifically look at the interaction of cations with the electrode surface, water molecules and reaction intermediates. On the more applied side, at the macro scale, we investigate CO_2 electrolysis using 10 cm^2 gas diffusion electrodes (GDEs). These are porous structures, that allow for CO_2 to be fed on one side of the structure, and the electrolyte on the other. All the reactants meet at the catalytic sites embedded in this porous structure, overcoming mass transport limitations that one would have using conventional flat electrodes. Finally, experiments involving the different scales are also conducted, combining for instance SECM and GDEs, in order to elucidate questions that one technique alone cannot answer.

1.7 Outline of this thesis

The main goal of this thesis is to study different aspects of processes taking place at the electrode-electrolyte interface and their consequences on the electrocatalysis of CO_2 reduction and H_2 evolution. **Chapter 2** provides an overview of methods available to measure the local pH during electrochemical processes, and highlights SECM as a powerful and versatile technique. **Chapter 3** describes the development of a new voltammetric pH sensor, that allows for measurements with high time resolution, high sensitivity, and selectivity. This is demonstrated by measuring the local pH during HER *in situ*, under *operando* conditions, using SECM. The sensor developed in Chapter 3, is used in **Chapter 4** to study the homogeneous reactions taking place in the diffusion layer during

CO_2RR, also using SECM. In **Chapter 5**, we combine measurements made with two different SECM probes, namely the voltammetric pH sensor from Chapter 3 and a Pt ultramicroelectrode, to understand the voltammetry of CO oxidation. We find a correlation between voltammetric features and the local pH, which arise from the reaction being limited by different species diffusing towards the surface. In **Chapter 6**, we carry out local pH measurements during HER under well-defined mass transport conditions. This is done by using a Rotating Ring-Disc electrode (RRDE) in which the ring is functionalized with the pH sensor from Chapter 3.

In **Chapter 7**, the effect of contamination of gold electrodes due to polishing is investigated. We show that Al^{3+} cations released from contaminating alumina polishing particles at the gold surface promote H_2O reduction. In **Chapter 8**, we elucidate the role of cations on CO_2RR using cyclic voltammetry and SECM. We show that this reaction does not take place on gold, copper and silver electrodes without a metal cation in the electrolyte. In combination with DFT and AIMD, the results explain the activity trends for CO formation as a function of alkali cation species, and allow proposing a new mechanism for CO_2RR. In **Chapter 9**, we broaden this study and investigate the effect of multivalent cations on CO_2RR and HER. Here, we describe how cation properties such as acidity and hydration energy determine the activity for the two competing reactions at low and high overpotentials. In **Chapter 10**, we look into the nature of differences in cation trends for HER on platinum and gold electrodes. On platinum, weakly hydrated cations inhibit HER in alkaline media, while on gold these species can either promote or hinder the reaction, depending on their local concentration at the reaction interface.

In **Chapter 11**, we scale up the experiments from Chapter 8, and investigate the feasibility of performing CO_2RR to CO in acidic media at more industrially relevant conditions. Using 10 cm^2 gold GDEs with different loadings, we show that up to 90% selectivity for CO can be achieved at high operating currents, and that running the reaction in acidic media leads to a 30% improvement in the energy efficiency. However, here, we cannot draw clear trends regarding the catalyst loading. Therefore, in **Chapter 12**, we use SECM to probe the effect of catalyst loading and CO_2 pressure on the local activity of gold GDEs. We find a slight increase in activity going from low to high loading, but that most CO produced comes from local hot spots, where CO_2 can easily access the catalyst particles. These hot spots are more abundant at high CO_2 pressures, given that there are enough catalyst particles accessible to form the 3-phase reaction boundary.

References

(1) Pancaldi, G. *Hist. Stud. Phys. Biol. Sci.* 1990, *21* (1), 123–160.
(2) Scrosati, B. *J. Solid State Electrochem.* 2011, *15* (7–8), 1623–1630.
(3) Goetzberger, A.; Hebling, C.; Schock, H.-W. *Mater. Sci. Eng. R.* 2003, *40* (1), 1–46.
(4) Bommaraju, T. V.; Lüke, B.; O' Brien, T. F.; Blackburn, M. C. In *Kirk-Othmer Encyclopedia of Chemical Technology*; John Wiley & Sons, Inc.: Hoboken, NJ, USA, 2002.
(5) Wirtz, C. *Publ. Off. Eur. Union* 2019 "Energy, Transport and Environment Statistics".
(6) Primary and final energy consumption in Europe. https://www.eea.europa.eu/data-and-maps/indicators/final-energy-consumption-by-sector-11/assessment (accessed Sep 1, 2021).
(7) Küngas, R. *J. Electrochem. Soc.* 2020, *167* (4), 044508.
(8) Bierhals, J. In *Ullmann' s Encyclopedia of Industrial Chemistry*; Wiley-VCH Verlag GmbH & Co. KGaA: Weinheim, Germany, 2001.
(9) Teeter, T. E.; Rysselberghe, P. van. *J. Chem. Phys.* 1954, *22* (4), 759–760.
(10) Hori, Y.; Kikuchi, K.; Murata, A.; Suzuki, S. *Chem. Lett.* 1986, *15* (6), 897–898.
(11) Hori, Y.; Murata, A.; Kikuchi, K.; Suzuki, S. *J. Chem. Soc. Chem. Commun.* 1987, *10*, 728–729.
(12) Hori, Y.; Kikuchi, K.; Suzuki, S. *Chem. Lett.* 1985, *14* (11), 1695–1698.
(13) Global Energy Review: CO_2 Emissions in 2020. https://www.iea.org/articles/global-energy-review-co2-emissions-in-2020 (accessed Sep 1, 2021).
(14) The circular economy in detail https://archive.ellenmacarthurfoundation.org/explore/the-circular-economy-in-detail (accessed Sep 1, 2021).
(15) Bagger, A.; Ju, W.; Varela, A. S.; Strasser, P.; Rossmeisl, J. *ChemPhysChem* 2017, *18* (22), 3266–3273.
(16) Nitopi, S.; Bertheussen, E.; Scott, S. B.; Liu, X.; Engstfeld, A. K.; Horch, S.; Seger, B.; Stephens, I. E. L.; Chan, K.; Hahn, C.; Nørskov, J. K.; Jaramillo, T. F.; Chorkendorff, I. *Chem. Rev.* 2019, *119* (12), 7610–7672.
(17) Zhang, W.; Hu, Y.; Ma, L.; Zhu, G.; Wang, Y.; Xue, X.; Chen, R.; Yang, S.; Jin, Z. *Adv. Sci.* 2018, *5* (1), 1700275.
(18) Murata, A.; Hori, Y. *Bull. Chem. Soc. Jpn.* 1991, *64* (1), 123–127.
(19) Moura de Salles Pupo, M.; Kortlever, R. *ChemPhysChem* 2019, *20* (22), 2926–2935.
(20) Evonik. CO_2 for a clean performance: Rheticus research project enters phase 2 https://corporate.evonik.com/en/media/press-releases/corporate/cosub2-sub-for-a-clean-performance-rheticus-research-project-enters-phase-2-118328.html (accessed Sep 1, 2021)
(21) Skyre. CO2RENEW™ https://www.skyre-inc.com/products/co2renew/ (accessed Aug 24, 2021).
(22) Dioxide Materials. CO_2 Electrolyzers https://dioxidematerials.com/technology/co2-electrolysis/ (accessed Aug 28, 2021).
(23) Jörg, G.; Weeda, M. 2018. TKI Nieuw Gas."Countouren van een Routekaart Waterstof"
(24) Adolf, J.; Balzer, C. H.; Louis, J.; Fischedick, M.; Arnold, K.; Patowski, A.; Schuwer, D. 2017 "Energy of the future?: Sustainable mobility through fuel cells and H_2; Shell hydrogen study".
(25) Dubouis, N.; Grimaud, A. *Chem. Sci.* 2019, *10* (40), 9165–9181.

2

Measuring local pH in electrochemistry

This chapter is based on: Monteiro, M. C. O., Koper, M. T. M. *Current Opinion in Electrochemistry, 25,* 100649 (2020)

Abstract

Localized pH measurements are important in various areas of electrochemistry, from corrosion to bio-electrochemistry and electrocatalysis. Different techniques are available to perform these measurements and offer numerous possibilities in terms of spatial and temporal resolution, sensitivity, and precision. In this brief review we present the recent progress made and summarize the main techniques available for localized pH measurements in electrochemistry such as scanning probe techniques (SECM, SICM, SIET), laser (confocal) fluorescence microscopy, rotating ring-disc electrode (RRDE) voltammetry, and infra-red spectroscopy, among others.

2.1 Introduction

The concept of pH as we know it today dates back to 1909 when Sørensen introduced the pH scale as a way to express the concentration of hydrogen ions.[1] In electrochemistry, the local concentration of protons in solution plays a significant role in reactions of different fields and is a function of the substrate geometry, the current density, mass transport, and the buffer capacity of the electrolyte. Corrosion via anodic oxidation is usually associated with metal dissolution and hydrolysis, thus locally producing protons.[2] Various biological processes cause intra- or extracellular pH changes and the quantification of these pH changes can help to understand the associated mechanisms.[3] Numerous electrocatalytic processes such as O_2 evolution or CO_2 reduction, that consume or produce H^+ or OH^-, generate a pH gradient between the working electrode (substrate) and the bulk of the electrolyte.[4] In all these applications, measuring the pH locally and with high sensitivity is desired to better understand the electrochemical processes involved.

Shortly after the invention of the glass pH electrode, scientists started putting efforts towards its miniaturization to perform what one could consider the first localized pH measurement ever reported: pH of arterial blood flowing through a small cannula in the cortex of a monkey.[5] It was already concluded at that time, that producing miniaturized pH probes “is quite possible, with practice”. Since then, electrochemists have invested significant efforts to develop not only new probes but also new techniques to measure pH locally with high spatial and temporal resolution. Here, we give an overview of those developments, together with a brief discussion of their advantages, drawbacks, and applicability. The techniques can be divided into direct and indirect methods to measure pH, namely techniques in which the signal monitored is the proton concentration by measuring its electrochemical potential (scanning probe microscopy, rotating ring-disc electrode) or techniques that probe species, whose signal is a function of the proton concentration (fluorescence and infrared intensities). Localized pH measurements can help to elucidate reaction mechanisms and assist in the deconvolution of pH effects from other electrolyte or structural surface effects. The rate at which the pH changes can also help understanding the stability of a certain substrate, to probe mass transport phenomena or reactivity. Spatial resolution, temporal resolution, and sensitivity will dictate which of these system properties can be captured by the different methods.

2.2 Scanning probe techniques: SECM, SICM, and SIET

Scanning probe microscopy (SPM) techniques used for pH measurements usually consist of monitoring the electrochemical signal of a miniaturized tip (ultramicroelectrode or nanoelectrode) while the tip is moved above a substrate. High spatial resolution can be achieved in three dimensions (XYZ) and is limited by the size and geometry of the tip, taking into account the radial diffusion profile towards ultramicroelectrodes (UMEs). The spatial resolution can be improved and the shielding can be minimized by miniaturizing the pH sensor and the insulating layer around it. Temporal resolution, precision, selectivity, and stability, on the other hand, are highly dependent on the nature of the pH sensor. In the next sections we discuss the main SPM techniques used to probe pH locally in electrochemistry, namely: Scanning Electrochemical Microscopy (SECM), Scanning Ion-selective Electrode Technique (SIET) and Scanning Ion Conductance Microscopy (SICM).

2.2.1 SECM

Among the different SPM techniques, SECM is the most employed to probe local pH. Normally, the tip is made of an inert or metallic material with a pH-sensitive electrochemical response, surrounded by an insulator. A schematic representation of an SECM setup is shown in Fig. 2.1a. Local pH measurements have been performed using either potentiometric or voltammetric sensors. Potentiometric pH probes consist of substrates whose open circuit potential shows a Nernstian (59 mV/pH) or super-Nernstian (> 59 mV/pH) shift as a function of pH. They are mainly based on metals, metal/metal oxides (TiO_2, RuO_2, RhO_2, Ta_2O_5, IrO_2, PtO_2, and ZrO_2)[6] or electrodeposited polymer films.[7] Among these, IrO_2 is the most popular substrate. Tefashe et al. used a Pt/IrO_2 probe to measure pH during localized corrosion of AZ31B magnesium alloy electrochemically coated with poly(3,4-ethylenedioxythiophene) (PEDOT).[8] The pH map obtained after 30 min immersion in 0.01 M NaCl can be seen in Fig. 2.1b, recorded with the pH probe positioned 10 μm from the surface. Other metal supports can also be used, as seen in the work of Santos and co-workers[9], where pH above a copper surface during nitrate reduction was measured with a Au/IrO_2 probe. Polymer films have also been used as potentiometric sensors. The most popular is polyaniline (PANI) due to its high conductivity and ease of synthesis. Recently Song et al. reported the use of a PANI coated Pt ultramicroelectrode to monitor the extracellular pH of MCF-7 cells

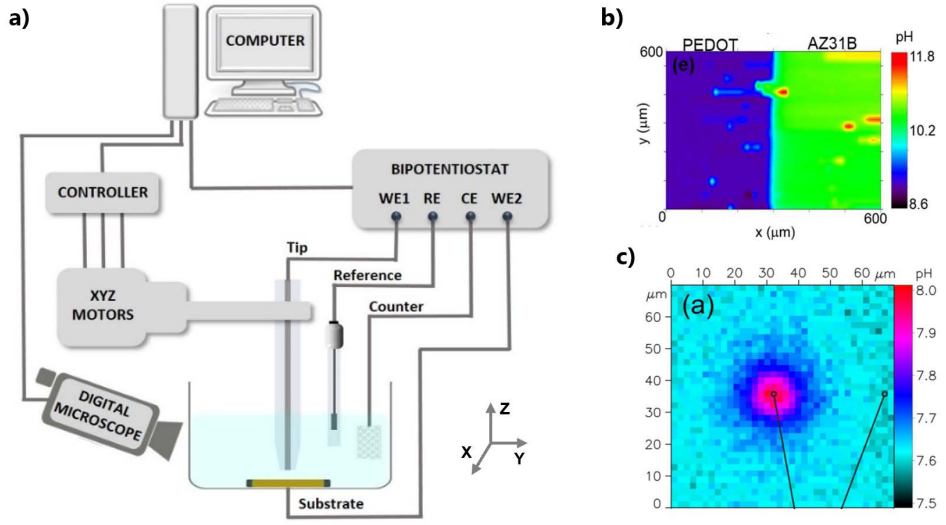

Fig. 2.1. a) Schematic representation of a scanning probe setup, **b)** pH map of uncoated and PEDOT-coated AZ31B Mg alloy after 30 min in 0.01 M NaCl, measured with a Pt/IrOx microprobe operated in constant height potentiometric mode of SECM. Adapted from Ref. 8. **c)** pH map during oxygen reduction on a 10 µm diameter Pt disc recorded with a voltammetric pH nanosensor made of a syringaldazine polymeric film. Adapted with permission from Ref. 15. Copyright (2015) American Chemical Society.

under electrical stimulation.[10] The main advantage of potentiometric pH sensors, in general, is their easy manufacturing, which facilitates their miniaturization. However, the fact that the pH response comes from the interaction of protons in solution with a solid-state film, means that potentiometric pH sensors have a relatively long response time of usually a few seconds, which can change as a function of pH.[11] The overall performance is also highly affected by the quality and thickness of the film. The synthesis of potentiometric pH sensors usually does not involve complicated steps and is often done via electrodeposition. Although there is an extensive list of synthesis protocols reported in literature[12], the success rate, even when following a well-established recipe, is known to be low. Potential drift can also prevent direct pH determination from the initial calibration curve and often requires recalibration.[13] Besides, the potential gradient across the interface being studied can potentially affect the open circuit potential recorded at the tip. The mentioned drawbacks can lead to strong deviations in the measurements (especially when pH maps are being constructed) and require a systematic data processing protocol.

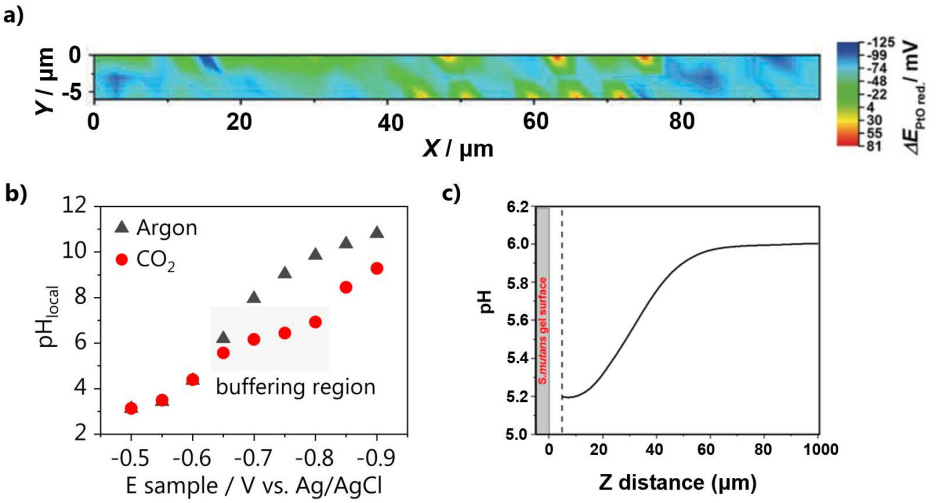

Fig. 2.2. a) Image of the shifts in the reduction peak potential of a Pt nanoelectrode during oxygen reduction at a Ag-based gas diffusion electrode. Each grid point was measured at 1 µm tip-surface distance utilizing shear force constant distance mode SECM. Adapted with permission from Ref. 14. Copyright (2018) Wiley-VCH Verlag GmbH & Co. KGaA. **b)** Buffering effect during CO_2 reduction measured with a voltammetric pH sensor based on a gold UME functionalized with a 4-NTP self-assembled monolayer (Chapter 4). **c)** Z-directional pH profile recorded with a glass capillary filled with an ion-selective cocktail, from 50 µm above the S. mutans biofilm to 1000 µm in the bulk solution after addition of 30 mM sucrose in artificial saliva (pH 6.0). Adapted with permission from Ref. 23. Copyright (2017) American Chemical Society.

Alternatively, SECM voltammetric pH sensors can be employed. They are based on the current-potential response of a certain redox reaction (upon cycling) and the pH is determined by the Nernstian shift of the reduction or oxidation midpeak potential. Voltammetric probes have the major advantage that the response time is only dependent on the time required to record a cyclic voltammogram and can easily be tuned. Michalak et al. have probed pH during ORR using a voltammetric pH nanosensor based on a syringaldazine film. The pH map obtained above a Pt-UME is shown in Fig. 2.1c.[14] The same type of sensor was also successfully applied to monitor the extracellular pH of adherently growing mammalian cells.[15] As syringaldazine is electropolymerized on a substrate, the influence of film thickness and stability on the pH response is still a concern. Botz et al. used the PtO reduction voltammetry to also successfully probe pH during oxygen reduction (ORR) over a silver gas diffusion electrode as can be seen in Fig.

2.2a.[16] Although a Pt-UME is suitable to probe the high alkalinity developed during ORR, unfortunately, it cannot be easily applied to other systems, as the Pt response is not exclusively selective to pH. We have recently presented a pH sensor that overcomes film and selectivity limitations, based on a self-assembled monolayer of 4-nitrothiophenol (4-NTP) on a Au-UME (Chapter 3 of this thesis).[17] The sensor is extremely sensitive, capturing differences as small as 0.1 pH units and is stable and selective in diverse electrolytes and under different gaseous atmospheres. This enables, for instance, pH measurements during CO_2 reduction on gold using SECM, as shown in Fig. 2.2b (Chapter 4 of this thesis).[61] We have recently also successfully employed our Au-UME/4-NTP pH sensor to better understand CO bulk electrooxidation in the CO_2 reduction reaction environment, through combined SECM measurements (Chapter 5 of this thesis).[18]

For mapping pH with high resolution above a substrate, pH sensors must be positioned accurately in solution at a controlled distance from the surface of interest. Commonly used SECM approach techniques need a mediator or a diffusion-limited reaction taking place at the tip to determine the tip-to-sample distance. However, not all pH sensors allow for diffusion-controlled feedback, as not always current can be drawn without destabilizing the tip response. The development of double-barrelled UMEs or dual probes overcomes positioning issues allowing for diffusion-controlled feedback, using the amperometric side of the tip, while carrying out pH measurements with the other side.[19,20] Other (more refined) distance control feedback systems employ shear-force[21], introduced by the group of Schuhmann, or alternating current-SECM (AC-SECM)[22]. We have also recently presented the application of a capacitive approach, performed in air, to determine the tip-to-surface distance without destabilizing the pH sensor.[17] The intricacies and applicability of commonly used distance control methods are well discussed in the book of Bard and Mirkin.[23]

2.2.2 Scanning Ion-selective Electrode (SIET)

SIET is a technique very similar to SECM, albeit employing potentiometric pH sensors that consist of a liquid ion-selective membrane enclosed in a (pulled) micro- or nanopipette. Different proton selective cocktails have been reported and many are commercially available (Fluka, Selectophore®). Joshi et al. reported the use of a H^+ selective cocktail to map the pH of the microenvironment produced by the lactate-producing S. mutans biofilm. Fig. 2.2c shows a profile in Z-direction of the pH monitored 950 µm across the diffusion layer.[24] The dynamic pH range of

these probes is usually limited so they are mostly used for measurements in the physiologically relevant pH range, or in corrosion processes where the pH changes are not too drastic.[25–27] The main drawbacks here are similar to those discussed for the potentiometric SECM probes, i.e. slow time response (limiting the scanning speed that can be used when imaging pH), fouling, and damage to the ion-selective electrode. Additionally, manufacturing requires expertise. New fabrication procedures have been reported to improve the response time by decreasing the electrode resistance. However, to date, no pH measurements have been reported with these improved probes.[28]

2.2.3 Scanning Ion Conductance Microscopy (SICM)

SICM is another powerful technique that has been used to perform pH measurements. In standard SICM, the scanning probe is a pulled nanopipette that is filled with an electrolyte containing a quasi-reference counter electrode (e.g. Ag/AgCl). Distance control is obtained by applying a potential between the tip and an external quasi-reference counter electrode placed in the bulk electrolyte which generates an ionic conductance current (feedback signal). To perform pH measurements with SICM, double-barrel SICM-SECM pipettes are used, which allow for simultaneously controlling the position of the electrode with high spatial resolution and measuring the pH locally.

A schematic representation of a SICM experimental setup is shown in Fig. 2.3a. Here, a zwitterionic label-free nanoprobe was combined with SICM in a double-barrelled nanopipette to probe the topography and pH of single living cancer cells, with 50 nm spatial resolution.[29] Fig. 2.3b shows the simultaneously obtained fluorescence image, SICM topography, and pH distribution of a group of low-buffered breast cancer MCF7 cells in an estradiol-deprived medium. Despite the remarkable results, the zwitterionic pH probe response is only linear in a narrow pH range between 5 and 8, making it mainly applicable to biological systems. Other (more robust) pH sensing substrates, on the other hand, allow for pH measurements in a wider pH range. Nadappuram et al.[30] used nanoscale double-barrelled pipettes with IrO_2 for pH measurements and a SICM barrel for distance control. The probe was used to map the topography and pH of a calcite microcrystal. The maps obtained with a 10 μm lateral resolution can be seen in Fig. 2.3c, where they are compared to an optical image of the microcrystal. Polymeric pH sensors have also been used in combination with SICM, as reported in the work of Morris et al.[31], who

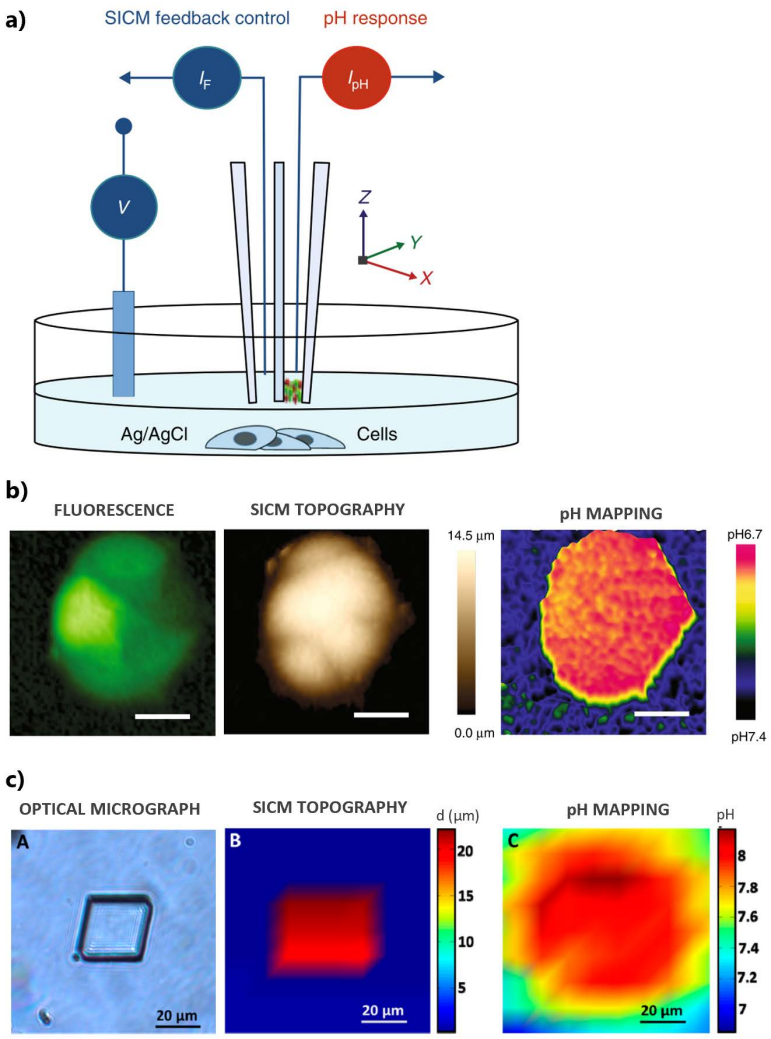

Fig. 2.3. a) Schematic representation of the operation of double-barrel nanopipettes for simultaneous SICM imaging and pH measurement and **b)** fluorescence and SICM imaging of a group of low-buffered $CD44^{GFP\text{-}high}$ breast cancer MCF7 cells in estradiol-deprived medium (−E2), together with a high resolution pH map, all simultaneously obtained from a single scan. Adapted from Ref. 28. **c)** Optical micrograph of a calcite microcrystal compared to a simultaneously recorded SICM topography image and pH map measured 100 nm from the microcrystal (bulk pH 6.85). Adapted with permission from Ref. 29. Copyright (2013) American Chemical Society.

used a Au/PANi barrel to measure pH in porous membranes. While SECM pH probes are employed with or without positional feedback (depending on the probe´s size and the nature of the substrate), positioning control is intrinsic of SICM, which makes it, combined with other techniques as SECM and fluorescence, a powerful tool for obtaining detailed information of the electrochemical interface. Similar to SIET, fabrication of the probes requires expertise.

2.3 Rotating Ring-Disc Electrode

Measuring pH under well-defined mass transport conditions using a Rotating Ring-Disc Electrode (RRDE) system was introduced by Albery and Calvo[32] and since then mainly employed to probe electrocatalytic reactions. The operation principle is similar to SECM in the sense that an electrode is used to measure pH. In the RRDE system, a shaft is connected to a rotator and the cross-section of the shaft contains two working electrodes, a disc electrode surrounded by a thin ring electrode. The ring is used to probe the flux of species coming from the disc with a certain collection (or detection, depending on the pH sensor used) efficiency that will depend on the electrode´s dimensions (radius, spacing). Initially, mainly bare Pt was used as ring material, however, that limits the number of systems that can be investigated as Pt is not a very selective H^+ sensor. In later work, the ring was modified with a potentiometric pH sensing layer, as IrO_2, which allows the use of the technique to probe a larger variety of systems, as shown in Fig. 2.4a. With the electrode shown in Fig. 2.4a, Zimer et al.[33] investigated the influence of rotation rate on the steady-state water reduction on copper. Results from Fig. 2.4b show the pH measured by the ring as a function of the rotation rate and indicate that a steady-state is achieved at rotation rates over 1200 rpm. RRDE has been employed to study other reactions as hydrogen oxidation[34], CO_2 reduction[35], oxygen reduction[36], and ethanol oxidation.[37] Additionally, it has also been used to probe electrodeposition processes, as nickel electrodeposition.[38] The main advantage of using a RRDE is that it is one of the few techniques that allows for the measurement of pH under defined mass transport conditions. On the other hand, the measurements are not spatially resolved in XY (as it probes the flux of species coming from the whole disc surface). The resolution in Z is limited and is a function of the rotation speed. It can be obtained by modelling of the system. Additionally, the time resolution to fully capture the process taking place at the disc is dependent on the time response of the pH sensor used. In Chapter 6 of this thesis, we show the application of the pH

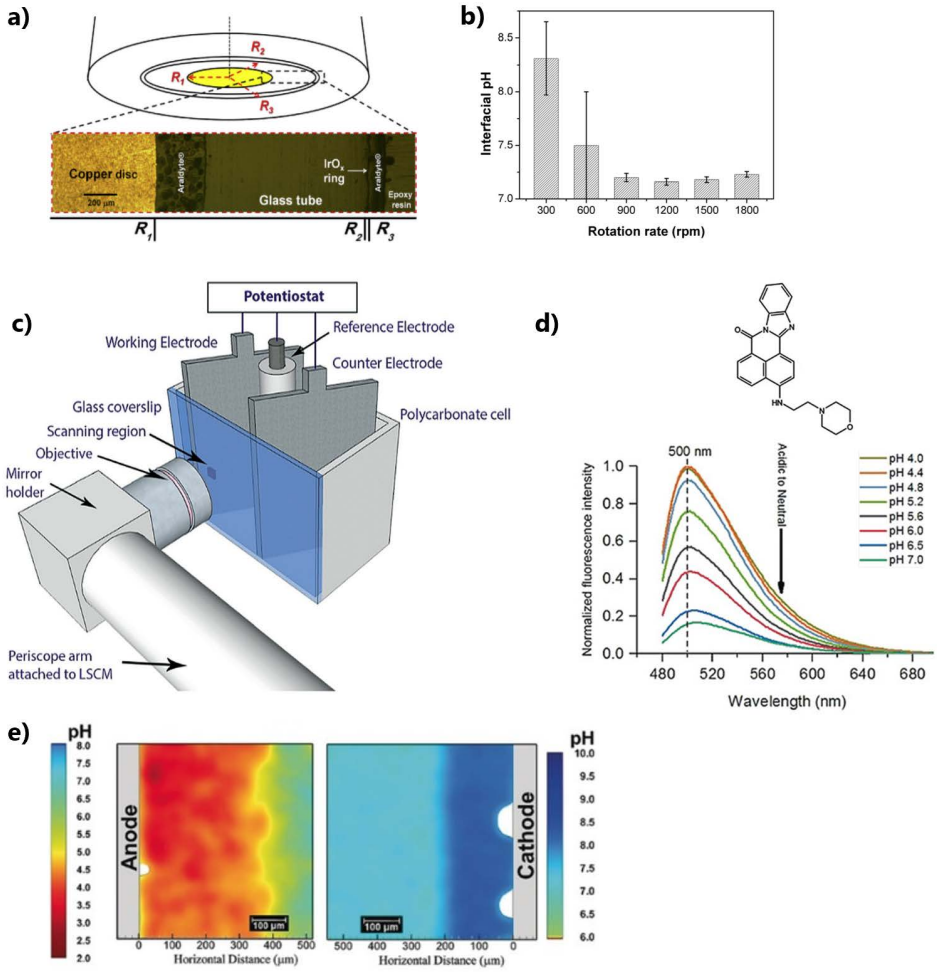

Fig. 2.4. a) Schematic representation of an RRDE pH sensor and **b)** measurements performed with it during water reduction on copper at different rotation rates. Adapted with permission from Ref. 32. Copyright (2015 Elsevier B.V. **c)** Schematic representation of a single compartment electrochemical cell coupled with a laser scanning confocal microscope, **d)** chemical structure of the LysoSensor Green DND-189 dye together with its normalized fluorescence response in phosphate buffer from pH 4 to 7, **e)** pH distribution at the anode and cathode during electrocoagulation, after a current density of 2 mA cm^{-2} is applied for 60 s. Figures c, d and e are adapted from Ref. 46. Copyright (2019) Wiley VCH Verlag GmbH & Co. KGaA.

sensor developed in Chapter 3 to RRDE, allowing for measurements with high sensitivity and temporal resolution.

2.4 Optical techniques

Various methods can be used to probe proton concentration gradients locally by using the optical properties of (electro)generated or consumed species, fluorescence being the most popular. In general, the measured optical property can be absorption or fluorescence intensity, decay time, reflectance, refractive index, light scattering, or light polarization.[39] We have selected fluorescence, infrared and Raman spectroscopy to briefly discuss here.

2.4.1 Fluorescence microscopy

Fluorescence has been widely used to indirectly measure pH in electrochemical systems. The most employed strategy is to add a pH-sensitive fluorophore to the electrolyte. The protons or OH^- produced/consumed by an electrochemical process can modulate the signal of the species in solution, which is captured using a fluorescence microscope. The workable pH range is determined by the pK_a of the fluorophores used. It is a versatile technique, that can be adapted to numerous electrochemical systems. The classic wide-field illumination setup allows for in situ mappings of pH in X- and Y-directions.[40,41] Although it has been used to record 2D pH images of different electrochemical systems, its well-known major drawback is the large signal contribution of out-of-focus light. The use of confocal laser scanning microscopy (CLSM) can overcome that by using a spatial pinhole to eliminate the out-of-focus light contribution to the image formation. It allows for mapping pH in 3D, by stacking 2D images acquired sequentially at different positions on the Z-axis. Pioneer contributions were made by the group of Unwin, demonstrating that 3D fluorescence maps can provide quantitative imaging of pH profiles during water reduction on Pt-UMEs.[42,43] CLSM has been successfully applied to measure pH in the fields of bioelectrochemistry[44,45], electrosynthesis[46], electrocatalysis[47,48], and the development of new dyes for expanding the workable pH range and stability can broaden its use even more.[49] Recently, the work of Fuladpanjeh-Hojaghan et al.[48] presented an electrochemical cell coupled with a laser scanning confocal microscope able to perform quantitative pH mapping under operando conditions during electrocoagulation (Fig. 2.4c). Two aluminium plates are used as cathode and anode and a combination of pH-sensitive fluorescent dyes with different pK_a allows for pH detection in a range from 1.5 to 8.5. An example of

the dye response upon a change in pH is shown in Fig. 2.4d for the LysoSensor Green DND-189 (LSG, pK_a 5.2). pH maps under operando conditions were obtained from the cathode and anode side and an example is shown in Fig. 2.4e, which is an image taken after 60 seconds of polarization. The anodic reaction causes aluminium dissolution and consequently aluminium cation hydrolysis, leading to acidification near the electrode surface. On the cathode side, the water reduction reaction generates a more alkaline pH near the surface. A setup for performing time-resolved CLSM pH measurements has also been recently introduced by Pande et al.[50] Fluorescein was used as a pH-sensitive fluorophore, to study the diffusion layer during ORR on platinum and the effect of sulfate buffering on the pH profiles. The results of a time-dependent numerical model give good agreement with the experimental data.

One of the main advantages of CLSM is that, differently from SPM techniques, it enables one to probe an entire macroscopic sample in real-time with high spatial resolution. Although pH maps can be obtained relatively quickly, the need of adding a fluorophore to the electrolyte is a drawback as it may affect the electrochemical process being studied. In general, the resolution limit of pH measurements using fluorescence falls into the diffraction limit of conventional light microscopes (~250 nm, considering the wavelength of green light and a numerical aperture of 1), unless a super-resolution microscopy technique is used, e.g. Stimulated Emission Depletion (STED), where pH measurements in a living cell have been performed with a resolution down to 20 nm.[51] This and other super-resolution techniques have been mainly used to probe biological substrates. Their application to other electrochemical systems is not straightforward and sometimes not possible due to the lack of stability of the pH sensing molecules.

2.4.2 Other optical techniques

pH measurements at the electrochemical interface during CO_2 reduction have recently been reported using surface-enhanced infrared absorption spectroscopy (SEIRAS).[52–54] The signal intensity of species that compose a buffer system, such as CO_2/HCO_3^- or $H_2PO_4^-/HPO_4^{2-}/PO_4^{3-}$, is monitored. Using the equilibrium equations, the average proton concentration at the interface can be indirectly derived from the ratio of the signal of these species. Valuable information can be obtained regarding the species in solution only a few nanometers from the electrode surface in the Z direction, averaged over a large portion of the surface in XY. These measurements do not provide spatial resolution and require IR active

Table 2.1. Overview of techniques discussed in this work to measure local pH in electrochemistry

Technique	pH sensor	pH range	Application	Type	Reference
SECM					
Potentiometric	IrOx/Au	2-11	Nitrate reduction	direct	9
	IrOx/Pt	1-13	Corrosion of 316L stainless steel, Corrosion of AZ31B Magnesium Alloy	direct	8,55,56
	Sb/Sb_2O_3	4-11	Corrosion of AZ63 magnesium alloy	direct	19
	Polyaniline/ Pt	4-8	extracellular pH	direct	10
	Pt	1-8	Methanol oxidation, enzymatic processes	direct	57
Voltammetric	syringaldazine	2-12	Oxygen reduction, extracellular pH	direct	15,16
	4-NTP monolayer on Au	1-12	Hydrogen evolution, CO_2 reduction on gold	direct	17 (Chapter 3), 61 (Chapter 4), 18 (Chapter 5)
SICM	zwitterion nano-membrane	4-9	Extracellular pH	direct	28
	IrOx/C	2-10	Dissolution of a calcite microcrystal	direct	29
	Polyaniline/Au	2.5-12	Nano channels of a membrane	direct	30
SIET	H^+-selective cocktail	4-10	Microbial metabolism	direct	23
	Hydrogen ionophore I - cocktail B (Selectophore™)	5-12.5	Corrosion of MA8 Mg alloy	direct	26
FLUORESCENCE	LSG + 5(6)-carboxynaphtho-fluorescein	1.5-8.5	Electrocoagulation	indirect	46
	fluorescein	5.5-7	H_2O and O_2 reduction, enzymatic O_2 reduction, coaxial flow micro-reactor	indirect	41,43,44
RRDE	Pt	5-9	H_2 evolution and oxidation	direct	33
	IrO_2	2.5-12.5	H_2O reduction	direct	32
	Pt, IrO_2	n.a.	CO_2 reduction on gold	direct	34
INFRARED	$H_2PO_4^-/HPO_4^{2-}/PO_4^{3-}$	5-13	CO_2 reduction on copper	indirect	52
	CO_2/ HCO^{3-}	n.a.	CO_2 reduction on gold	indirect	50
RAMAN	4-mercaptobenzoic acid/Au nanoparticle	2-12	Aerosol microdroplets	indirect	54

species in the electrolyte. Similarly to the dyes used in fluorescence, the pK_a of these species in equilibrium will dictate the pH range that can be measured. Raman Spectroscopy has also been used to probe pH.[55] Wei et al. developed pH nanoprobes based on plasmonic gold nanoparticles functionalized with a pH-sensitive amine or carboxylic acid. The nanoprobes were used to detect the intracellular pH of PC-3 cancer cells[56] and the pH gradients within phosphate-buffered aerosol microdroplets with a lateral resolution of 5 µm.[57] The technique is powerful to investigate micro-environments, however, can only be applied to specific systems where the addition of the signal enhancing pH-sensitive particles is feasible. Differently than in SPM, the resolution that can be achieved in pH measurements performed with optical techniques is defined by the operating system and not by the size of the pH probe.

2.5 Final considerations

Having discussed the main techniques that can be used to measure pH in electrochemistry, we have grouped a few examples in Table 2.1 to provide a general overview of the methods available, the pH range that can be measured, and the kind of systems that can be investigated with each technique. To conclude, we highlight the following:

- The main advantages of SPM for performing localized pH measurements are the high spatial resolution in X-Y-Z that can be achieved, and the versatility in terms of the sample, probes, and modes available, to be chosen according to the application. A wide pH range can be studied with a series of established potentiometric and voltammetric sensors. Voltammetric sensors are especially interesting, due to the high temporal resolution that can be achieved. The main disadvantage of SPM is shielding caused by the probe.[58] However, this can be significantly minimized by the use of nanopipettes. Additionally, these contributions can be simulated and accounted for with finite element models.
- Optical methods have the great advantage of being non-invasive techniques, and the use of a confocal laser microscope allows for achieving spatial resolutions comparable to SPM techniques. However, altering the electrolyte composition by the addition of a fluorophore is a major drawback. Additionally, the operational pH range is usually limited by the pK_a of the pH-sensitive species.

- Infrared and Raman spectroscopy can be powerful tools to probe small volumes of the electrochemical interface, although the spatial resolution in Z cannot be tuned and the XY resolution is limited by the beam size.
- Combining SPM and optical techniques can be highly effective to obtain detailed information about complex electrochemical systems, see e.g. SECM-SICM[30], SECM-fluorescence[59], SECM-infrared.[60]
- RRDE pH measurements are especially interesting for mechanistic studies as the defined mass transport control of the system allows for a more precise modeling of the reaction interface. On the other hand, the measurements are not spatially resolved and represent an average response of the whole working electrode.

There has been intensive development of methods for measuring pH in electrochemistry lately. Knowing precisely the research questions that need answers is key for defining the most suitable technique to investigate a given system. We believe the combined knowledge obtained through the different techniques discussed here, can enable a deeper understanding of complex electrochemical systems.

References

(1) Sörensen, S. P. L. *Ergebnisse der Physiol.* 1909, 21, 131–200.
(2) Jadhav, N.; Gelling, V. J. *J. Electrochem. Soc.* 2019, *166* (11), C3461–C3476.
(3) Orij, R.; Brul, S.; Smits, G. J. *Biochim. Biophys. Acta - Gen. Subj.* 2011, *1810* (10), 933–944.
(4) Ooka, H.; Figueiredo, M. C.; Koper, M. T. M. *Langmuir* 2017, *33* (37), 9307–9313.
(5) Nims, L. F. *Yale J. Biol. Med.* 1938, *10* (3), 241–246.
(6) Manjakkal, L.; Szwagierczak, D.; Dahiya, R. *Prog. Mater. Sci.* 2020, *109*, 100635.
(7) Korostynska, O.; Arshak, K.; Gill, E.; Arshak, A. *Sensors* 2007, *7* (12), 3027–3042.
(8) Tefashe, U. M.; Dauphin-Ducharme, P.; Danaie, M.; Cano, Z. P.; Kish, J. R.; Botton, G. A.; Mauzeroll, J. *J. Electrochem. Soc.* 2015, *162* (10), C536–C544.
(9) Santos, C. S.; Lima, A. S.; Battistel, D.; Daniele, S.; Bertotti, M. *Electroanalysis* 2016, *28* (7), 1441–1447.
(10) Song, R.; Xiong, Q.; Wu, T.; Ning, X.; Zhang, F.; Wang, Q.; He, P. *Anal. Bioanal. Chem.* 2020, *412* (15), 3737–3743.
(11) Zhang, X.; Ogorevc, B.; Wang, J. *Anal. Chim. Acta* 2002, *452* (1), 1–10.
(12) Jang, H.; Lee, J. *J. Energy Chem.* 2020, *46*, 152–172.
(13) Etienne, M.; Dierkes, P.; Erichsen, T.; Schuhmann, W.; Fritsch, I. *Electroanalysis* 2007, *19* (2), 318–323.
(14) Michalak, M.; Kurel, M.; Jedraszko, J.; Toczydlowska, D.; Wittstock, G.; Opallo, M.; Nogala, W. *Anal. Chem.* 2015, *87* (23), 11641–11645.
(15) Munteanu, R.-E.; Stănică, L.; Gheorghiu, M.; Gáspár, S. *Anal. Chem.* 2018, *90* (11), 6899–6905.
(16) Botz, A.; Clausmeyer, J.; Öhl, D.; Tarnev, T.; Franzen, D.; Turek, T.; Schuhmann, W. *Angew. Chemie - Int. Ed.* 2018, *57* (38), 12285–12289.
(17) Monteiro, M. C. O.; Jacobse, L.; Touzalin, T.; Koper, M. T. M. *Anal. Chem.* 2020, *92* (2), 2237–2243.
(18) Monteiro, M. C. O.; Jacobse, L.; Koper, M. T. M. *J. Phys. Chem. Lett.* 2020, *11* (22), 9708–9713.
(19) Zhu, Z.; Ye, Z.; Zhang, Q.; Zhang, J.; Cao, F. *Electrochem. commun.* 2018, *88*, 47–51.
(20) Filotás, D.; Fernández-Pérez, B. M.; Nagy, L.; Nagy, G.; Souto, R. M. *Sensors Actuators, B Chem.* 2019, *296*, 126625.
(21) Ballesteros Katemann, B.; Schulte, A.; Schuhmann, W. *Chem. - A Eur. J.* 2003, *9* (9), 2025–2033.
(22) Eckhard, K.; Schuhmann, W. *Analyst* 2008, *133* (11), 1486–1497.
(23) Bard, A. J.; Mirkin, M. V. Second.; Bard, A. J., Mirkin, M. V., Eds.; CRC Press, 2012.
(24) Joshi, V. S.; Sheet, P. S.; Cullin, N.; Kreth, J.; Koley, D. *Anal. Chem.* 2017, *89* (20), 11044–11052.
(25) Lamaka, S. V.; Taryba, M.; Montemor, M. F.; Isaacs, H. S.; Ferreira, M. G. S. *Electrochem. commun.* 2011, *13* (1), 20–23.
(26) Oltra, R. *Corros. Eng. Sci. Technol.* 2018, *53*, 2–8.
(27) Gnedenkov, A. S.; Mei, D.; Lamaka, S. V.; Sinebryukhov, S. L.; Mashtalyar, D. V.; Vyaliy, I. E.; Zheludkevich, M. L.; Gnedenkov, S. V. *Corros. Sci.* 2020, *170*, 108689.
(28) Varga, Á.; Nagy, L.; Izquierdo, J.; Bitter, I.; Souto, R. M.; Nagy, G. *Anal. Lett.* 2011, *44*

(18), 2876–2886.
(29) Zhang, Y.; Takahashi, Y.; Hong, S. P.; Liu, F.; Bednarska, J.; Goff, P. S.; Novak, P.; Shevchuk, A.; Gopal, S.; Barozzi, I.; Magnani, L.; Sakai, H.; Suguru, Y.; Fujii, T.; Erofeev, A.; Gorelkin, P.; Majouga, A.; Weiss, D. J.; Edwards, C.; Ivanov, A. P.; Klenerman, D.; Sviderskaya, E. V.; Edel, J. B.; Korchev, Y. *Nat. Commun.* 2019, *10* (1), 1–9.
(30) Nadappuram, B. P.; McKelvey, K.; Al Botros, R.; Colburn, A. W.; Unwin, P. R. *Anal. Chem.* 2013, *85* (17), 8070–8074.
(31) Morris, C. A.; Chen, C. C.; Ito, T.; Baker, L. A. *J. Electrochem. Soc.* 2013, *160* (8), H430–H435.
(32) Albery, W. J.; Calvo, E. J. *J. Chem. Soc. Faraday Trans. 1 Phys. Chem. Condens. Phases* 1983, *79* (11), 2583–2596.
(33) Zimer, A. M.; Medina da Silva, M.; Machado, E. G.; Varela, H.; Mascaro, L. H.; Pereira, E. C. *Anal. Chim. Acta* 2015, *897*, 17–23.
(34) Yokoyama, Y.; Miyazaki, K.; Miyahara, Y.; Fukutsuka, T.; Abe, T. *ChemElectroChem* 2019, 4750–4756.
(35) Zhang, F.; Co, A. C. *Angew. Chemie - Int. Ed.* 2020, *59* (4), 1674–1681.
(36) Steegstra, P.; Ahlberg, E. *J. Electroanal. Chem.* 2012, *685* , 1–7.
(37) Figueiredo, M. C.; Arán-Ais, R. M.; Climent, V.; Kallio, T.; Feliu, J. M. *ChemElectroChem* 2015, *2* (9), 1254–1258.
(38) Ji, J.; Cooper, W. C.; Dreisinger, D. B.; Peters, E. *J. Appl. Electrochem.* 1995, *25* (7).
(39) Wencel, D.; Abel, T.; McDonagh, C. *Anal. Chem.* 2014, *86* (1), 15–29.
(40) Bowyer, W. J.; Xie, J.; Engstrom, R. C. *Anal. Chem.* 1996, *68* (13), 2005–2009.
(41) O´Brien, C.; Shumaker Parry, J.; Engstrom, R. C. *Anal. Chem.* 1998, *70* (7), 1307–1308.
(42) Cannan, S.; Douglas Macklam, I.; Unwin, P. R. *Electrochem. commun.* 2002, *4* (11), 886–892.
(43) Rudd, N. C.; Cannan, S.; Bitziou, E.; Ciani, I.; Whitworth, A. L.; Unwin, P. R. *Anal. Chem.* 2005, *77* (19), 6205–6217.
(44) Hou, J. T.; Ren, W. X.; Li, K.; Seo, J.; Sharma, A.; Yu, X. Q.; Kim, J. S. *Chem. Soc. Rev.* 2017, *46* (8), 2076–2090.
(45) Tassy, B.; Dauphin, A. L.; Man, H. M.; Le Guenno, H.; Lojou, E.; Bouffier, L.; De Poulpiquet, A. *Anal. Chem.* 2020, *92* (10), 7249–7256.
(46) Abou-Hassan, A.; Dufrêchfer, J. F.; Sandre, O.; Mériguet, G.; Bernard, O.; Cabuil, V. *J. Phys. Chem. C* 2009, *113* (42), 18097–18105.
(47) Leenheer, A. J.; Atwater, H. A. *J. Electrochem. Soc.* 2012, *159* (9), H752–H757.
(48) Fuladpanjeh-Hojaghan, B.; Elsutohy, M. M.; Kabanov, V.; Heyne, B.; Trifkovic, M.; Roberts, E. P. L. *Angew. Chemie Int. Ed.* 2019, *58* (47), 16815–16819.
(49) Bigdeli, A.; Ghasemi, F.; Abbasi-Moayed, S.; Shahrajabian, M.; Fahimi-Kashani, N.; Jafarinejad, S.; Farahmand Nejad, M. A.; Hormozi-Nezhad, M. R. *Anal. Chim. Acta* 2019, *1079*, 30–58.
(50) Pande, N.; Chandrasekar, S. K.; Lohse, D.; Mul, G.; Wood, J. A.; Mei, B. T.; Krug, D. *J. Phys. Chem. Lett.* 2020, *11* (17), 7042–7048.
(51) Richardson, D. S.; Gregor, C.; Winter, F. R.; Urban, N. T.; Sahl, S. J.; Willig, K. I.; Hell, S. W. *Nat. Commun.* 2017, *8* (1), 577.
(52) Ayemoba, O.; Cuesta, A. *ACS Appl. Mater. Interfaces* 2017, *9* (33), 27377–27382.
(53) Zhou, J.; Ma, H. *Chem. Sci.* 2016, *7* (10), 6309–6315.
(54) Yang, K.; Kas, R.; Smith, W. A. *J. Am. Chem. Soc.* 2019, *141* (40), 15891–15900.
(55) Zhang, Z.; Melo, L.; Jansonius, R. P.; Habibzadeh, F.; Grant, E. R.; Berlinguette, C. P.

ACS Energy Lett. 2020, *5* (10), 3101–3107.

(56) Wei, H.; Willner, M. R.; Marr, L. C.; Vikesland, P. J. *Analyst* 2016, *141* (17), 5159–5169.

(57) Wei, H.; Vejerano, E. P.; Leng, W.; Huang, Q.; Willner, M. R.; Marr, L. C.; Vikesland, P. J. *Proc. Natl. Acad. Sci. U. S. A.* 2018, *115* (28), 7272–7277.

(58) Critelli, R. A. J.; Bertotti, M.; Torresi, R. M. *Electrochim. Acta* 2018, *292*, 511–521.

(59) Boldt, F. M.; Heinze, J.; Diez, M.; Petersen, J.; Börsch, M. *Anal. Chem.* 2004, *76* (13), 3473–3481.

(60) Wang, L.; Kowalik, J.; Mizaikoff, B.; Kranz, C. *Anal. Chem.* 2010, *82* (8), 3139–3145.

(61) Monteiro, M. C. O.; Mirabal, A.; Jacobse, L.; Doblhoff-Dier, K.; Barton, S. C.; Koper, M. T. M. *JACS Au.* 2021, 1 (11), 1915–1924.

3

Mediator-free SECM for pH measurements in the diffusion layer with functionalized gold ultramicroelectrodes

This chapter is based on Monteiro, M. C. O., Jacobse, L., Touzalin, T., Koper, M. T. M. *Anal. Chem. 92 (2)*, 2237–2243 (2020)

Abstract

Probing pH gradients during electrochemical reactions is important to better understand reaction mechanisms and to separate the influence of pH and pH gradients from intrinsic electrolyte effects. Here, we develop a pH sensor and measure pH changes in the diffusion layer during hydrogen evolution as a model system. The probe was synthesized by functionalizing a gold ultramicroelectrode with a self-assembled monolayer of 4-nitrothiophenol (4-NTP) and further converting it to form a hydroxylaminothiophenol (4-HATP)/4-nitrosothiophenol (4-NSTP) redox couple. The pH sensing is realized by recording the tip cyclic voltammetry and monitoring the Nernstian shift of the mid-peak potential. We employ a capacitive approach technique in our home-built Scanning Electrochemical Microscope (SECM) setup in which an AC potential is applied to the sample and the capacitive current generated at the tip is recorded as a function of distance. This method allows for an approach of the tip to the electrode that is electrolyte-free and consequently also mediator-free. Hydrogen evolution on gold in a neutral electrolyte was studied. The pH was measured with the probe at constant distance from the electrode (ca. 75 µm) while the electrode potential was varied in time. In the non-buffered electrolyte used (0.1 M Li_2SO_4), even at relatively low current densities, a pH difference of three units is measured between the location of the probe and the bulk electrolyte. The time scale of the diffusion layer transient is captured, due to the high time resolution that can be achieved with this probe. The sensor has high sensitivity, measuring differences of more than 8 pH units with a resolution better than 0.1 pH unit.

3.1 Introduction

The pH affects chemical reactions in a wide variety of systems and pH effects have been studied in the fields of biology[1,2], medicine[3,4], corrosion[5,6], electrocatalysis[7], among others. For example, during electrochemical reactions that consume or produce either protons or hydroxyl ions, a pH gradient is built up in the diffusion layer. The proton concentration at the electrode-electrolyte interface is known to influence the kinetics and selectivity of various electrochemical reactions such as hydrogen evolution[8], CO_2 reduction[9,10] nitrate reduction[11], and oxygen evolution.[12] Measuring the pH near the surface allows to better model these electrocatalytic processes and to understand their mechanism under different reaction conditions and in different electrolytes. In order to probe the diffusion layer, the spatial resolution of the conventional pH glass electrode and other bulk techniques using optical[13] or colorimetric[14] sensors is not high enough. Instead, local measurements of pH at the micro- and nanoscale can be achieved with Scanning Electrochemical Microscopy (SECM) where miniaturized electrodes are used to probe the local properties of an interface.[15] High spatial and temporal resolution of these measurements can be achieved, which mainly depend on the kind of probe used and the electrochemical signal monitored. Spectroscopic pH measurements at the micro scale have also been reported.[16–18] However, such measurements do not probe the local proton concentration directly, can only be used for specific electrodes and electrocatalytic reactions, and do not provide spatial resolution. Fluorescence microscopy[19–21] has also been used to map interfacial pH. Although pH maps can be obtained relatively quickly, the need of adding a fluorophore to the electrolyte is a drawback as it may affect the electrochemical process being studied. Based on the discussion presented here, SECM should be a more suitable technique to measure the interfacial pH during electrocatalytic reactions.

Different probes have been proposed for conducting local pH measurements with SECM. Various transition metal oxides show a super Nernstian open circuit potential (OCP) shift with pH and have been employed as potentiometric pH sensors. Iridium oxide (IrO_x) is the most commonly used[22] and several synthesis methods have been reported such as nanoparticles electrodeposition[23], anodic growth[24], and sol-gel synthesis.[25] The sensing response relies on the porosity of the oxide layer; dense oxide films have a slow response to pH changes, while porous layers show a fast response but with a significant OCP drift.[26] Besides drift, another

drawback of these probes comes from the adsorption of species on the sensor surface (contaminants, ions, reaction products) that can lead to a convoluted OCP response.[27] These limitations can strongly influence how precisely these IrO_x pH sensors capture the local pH gradient during electrochemical reactions. In addition, oxide dissolution can compromise the use of these probes in highly acidic or alkaline media.[28] To overcome these limitations, polymer-based potentiometric sensors[29] have been proposed, such as polyaniline-coated Au electrodes[30], and carbon electrodes modified with poly(1-naphthylamine)[31] or poly-dopamine.[32] However, many of these polymer films strongly interact with alkali metal cations which may lead to a shift in the OCP.[33] In addition, the time response is reported to strongly depend on the quality of the electropolymerization and film thickness.

Other techniques have also been used to probe the pH near the surface. Ryu et al. used the pH sensitive reaction of H_2 with cis-2-butene-1,4-diol to probe the interfacial pH during concurrent hydrogen oxidation.[34] Even though significant effects were observed as a function of buffer capacity and current density, the impact of the addition of cis-2-butene-1,4-diol to the electrolyte on the electrocatalysis cannot be determined and might limit the use of this technique to probe other reactions. Measurements of local pH have also been performed using a Rotating Ring-Disc Electrode (RRDE).[35,36] However, this method is limited in terms of the electrode materials, reactions to be analyzed and lack spatial resolution. Voltammetric pH sensors have also been proposed and are interesting due to their fast response and operation in large pH ranges.[37–40] Boltz and co-workers for instance, used the voltammetry of platinum nanoelectrodes to monitor the pH above a gas diffusion electrode during oxygen reduction.[41] However, platinum can only be used to probe reactions that do not generate species that strongly interact with the surface, affecting the voltammetry. Michalak et al. developed nano pH sensors based on the cyclic voltammetry of syringaldazine polymer films attached to carbon substrates.[42] Even though the sensor works in a large pH range, the stability of polymer films, in general, is still concerning as film detachment can hinder the pH response.

In this Chapter, we present a pH sensor based on the irreversible self-assembly of 4-nitrothiophenol on a gold ultramicroelectrode (Au-UME). After conversion, the hydroxylaminothiophenol/4-nitrosothiophenol redox couple is formed and its mid-peak potential shows a Nernstian shift of 57 mV/pH. Using hydrogen evolution as a model system, we perform pH measurements in the diffusion layer with high reproducibility. Because of the sensitivity of the

functionalized tip and to avoid possible side-effects from redox-active mediators, we also introduce an *ex situ* capacitive approach method to control the absolute tip-to-sample distance.[43] In contrast to potentiometric pH sensors, our probe provides high time resolution and stable response. In addition, the pH sensitivity is not affected by electrolyte species or reaction products, which allows for application in a wide variety of systems (electrocatalytic or not).

3.2 pH sensor synthesis

It has been previously shown how important the surface preparation and cleanliness of UMEs is for their use in electrocatalysis.[44] Au-UMEs were characterized in 0.1 M H_2SO_4 before functionalization (see Fig. A2 in Appendix A) in order to assure the glass is efficiently sealing the gold wire and that the surface is clean. Functionalization was performed by immersing the probe in a solution containing 4-nitrothiophenol (4-NTP). The molecules form a self-assembled monolayer at the gold surface, binding through the thiol anchor group. The free nitro group is then partially reduced electrochemically into a hydroxyl amino group by cycling the tip from 0.1 to –0.25 V vs. Ag/AgCl in 0.1 M H_2SO_4. The cyclic voltammogram (CV) of the conversion and a schematic representation of the species formed are shown in Fig. 3.1a and Fig. 3.1b, respectively. Hydroxylaminothiophenol (4-HATP) is formed through the transfer of four protons and four electrons and at positive potentials 4-HATP is reversibly oxidized to 4-nitrosothiophenol (4-NSTP) through the transfer of two protons and two electrons (see Fig. 3.1c). Thus, the mid-peak potential of the 4-HATP/4-NSTP redox couple is expected to show a Nernstian shift with pH.[45]

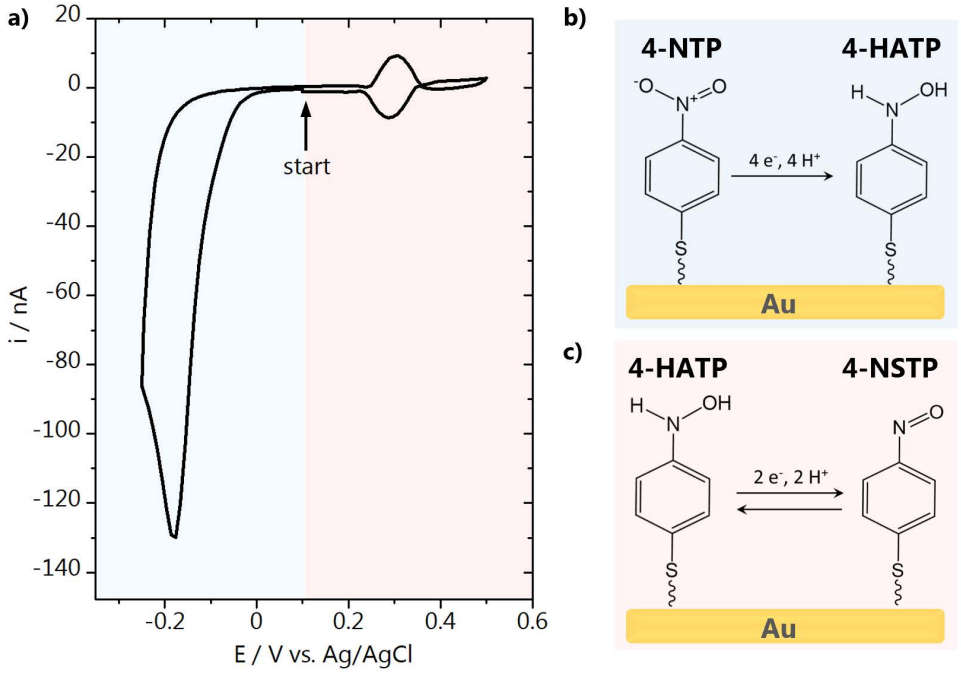

Fig. 3.1. a) Voltammetry (0.1 M H_2SO_4, 100 mV s^{-1}) and schematic representation of the conversion of **b)** 4-nitrothiophenol (4-NTP) to 4-hydroxiaminothiophenol (4-HATP), and **c)** the two proton-two electron transfer reaction of the redox couple 4-HATP/4-NSTP.

The electrochemical characterization of the reversible redox couple 4-HATP/4-NSTP in Fig. 3.2a shows that the tip voltammetry is very stable over the 30 cycles performed. It is important to point out that for successful functionalization of the Au-UME the potential of the tip must be carefully controlled. It has been previously shown by Touzalin et al.[46] that at potentials lower than –0.25 V vs. Ag/AgCl (pH = 1) 4-NTP and 4-HATP are fully irreversibly reduced to 4-aminothiophenol (4-ATP). At potentials higher than 0.6 V vs. Ag/AgCl the monolayer is destabilized, likely due to polymerization, leading to a decrease in the 4-HATP/4-NSTP signal intensity (although the exact mechanism is not yet clear).

To calibrate the pH sensor, the tip voltammetry was recorded in argon saturated solutions of various pH (see Fig. A.3a in Appendix A). The potential of the anodic peak as a function of pH was used to construct the calibration curves depicted in Fig. 3.2b. A linear fit of the data provides the following relationship: pH = $(0.341 - E_{peak})/0.057$ with an R^2 value of 0.99. The mid-peak potential shows a Nernstian behavior with a shift of 57 mV per pH unit. As the tip will be used to

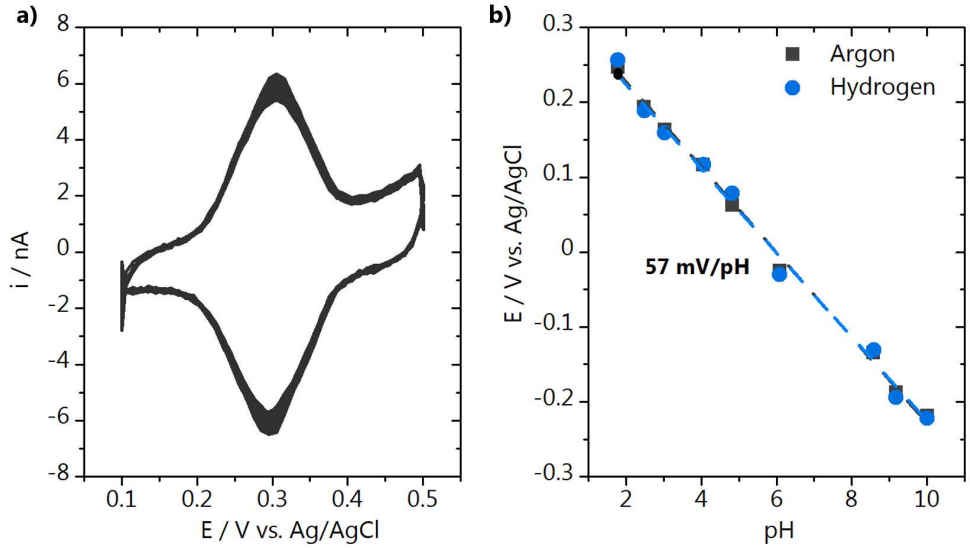

Fig. 3.2. a) Characterization of the electroactive redox couple 4-HATP/4-NATP in 0.1 M H_2SO_4 at 200 mVs^{-1} and **b)** calibration of the functionalized Au-UME in 0.1 M Li_2SO_4 solutions adjusted to different pH and saturated with argon or hydrogen.

probe pH changes during hydrogen evolution, it was also calibrated in hydrogen atmosphere. As can be seen in Fig. 3.2b, the presence of hydrogen does not affect the pH response. Even though the calibration curve shown in Fig. 3.2b does not include pH 7, other calibration curves were made where pH 7 was included and different from the work of Cobb et al.[47] on quinone-based pH electrodes, no significant deviation of the Nernstian response was found. The latter is probably related to the different interaction the quinone has with the substrate in comparison to the 4-nitrothiophenol self-assembled monolayer. In addition, 4-nitrothiophenol is only partially converted to 4-hydroxiaminothiophenol, and according to Cobb´s work the lower the coverage of the surface, the lower the deviations.

3.3 Capacitive approach

Commonly used SECM approach techniques need a mediator or a diffusion limited reaction taking place at the tip in order to determine the tip-to-sample distance.[48] However, these methods are not ideal for our experiment, because they can contaminate the electrocatalytic system and/or destabilize the self-assembled monolayer. Furthermore, it has been shown that commonly made assumptions about the exact tip geometry lead to significant errors in the calculated tip-to-sample distance.[49] In principle, the AC-SECM[50,51] approach could be employed,

although it is not known how stable the self-assembled monolayer is at high frequencies. Therefore, we have applied an electrolyte-free approach method that allows determining the absolute tip-to-surface distance without destabilizing the 4-NTP/4-HATP/4-NSTP monolayer. This *ex situ* method employs the capacitance between tip and sample and was recently introduced by De Voogd et al. as a pre-approach for Scanning Tunnelling Microscopy (STM) setups.[43]

To enable the determination of the tip-sample capacitance in air, an AC potential (10 kHz, 1.41 V_{RMS}) is applied to the sample and the resulting tip current is followed with a preamplifier. The out-of-phase (Y) component of the tip current is determined using a lock-in amplifier. Fig. 3.3a shows a schematic representation of the approach configuration. The capacitance can be calculated *via*:

$$C_{tot} = \frac{Y}{2\pi f G V} \qquad \text{Eq. 3.1}$$

where G is the preamplifier gain and f and V are the frequency and amplitude of the reference (sample) signal, respectively. At small tip-to-surface distances (smaller than ~10% of the tip radius), the tip and sample can be described as a parallel plate capacitor, of which the capacitance is:

$$C_{par} = \frac{\varepsilon_0 A}{d} \qquad \text{Eq. 3.2}$$

where ε_0 is the permittivity of air, A the area (of the tip), and d the tip-to-sample distance. In practice $d = d_0 - Z$, in which Z is the position of the stepper motor varied during the approach, and d_0 is the absolute surface position. At large tip-to-surface distances, which is the case during the approach, we find that the system is better described as a point charge in front of a plate, instead of a pure parallel plate capacitor. The capacitance is then given by Eq. 3.3, derived from Eq. 3 from Ref. 43. Here, the very end of the tip is described as a half sphere with radius R_{eff} and the term B accounts for the magnitude of the capacitance in the case where R_{eff} is assumed to remain constant as a function of d.

$$C_{point} = -2\pi R_{eff}\varepsilon_0 * \ln(d_0 - Z) + B \qquad \text{Eq. 3.3}$$

Finally, the measured capacitance as a function of the position of the stepper motor $C_{tot}(Z)$ can be fitted with Eq. 3.4. This allows to obtain the fitting parameter

d_0 which is the absolute tip-to-surface distance. The total capacitance contains also contributions that are inherent to the setup, e.g. due to the tip connection far away from the sample and the connections used.[43] These contributions are accounted for in the terms A_2 and L_{par}.

$$C_{tot}(Z) = -A_1 * \ln(d_0 - Z) + B + \left(\frac{A_2}{L_{par}+d_0-Z}\right) \quad \text{Eq. 3.4}$$

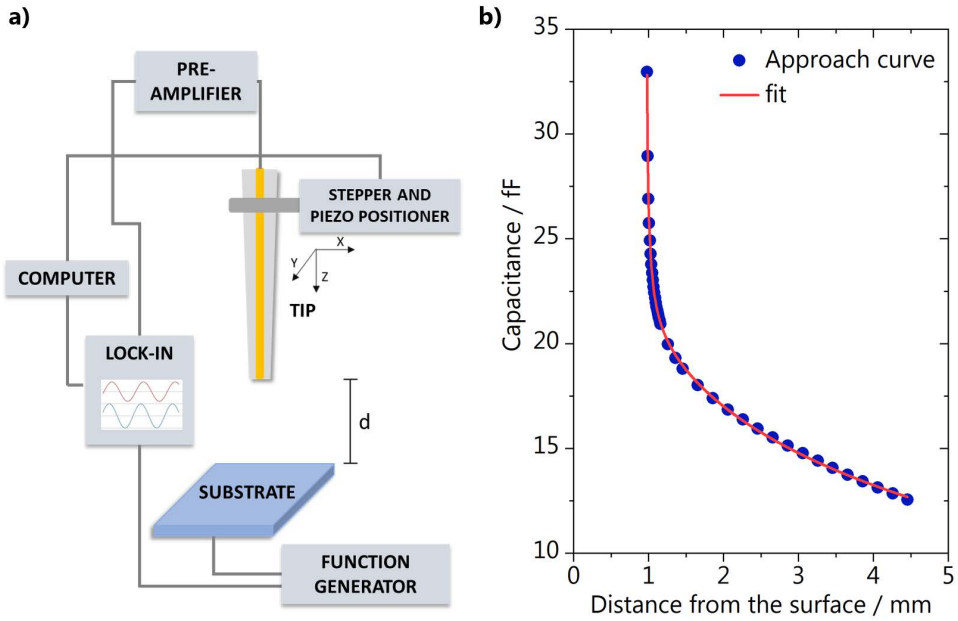

Fig. 3.3. a) Capacitive approach configuration and **b)** approach curve obtained (blue circles) with its fit using Eq. 3.4 (red line).

Fig. 3.3b shows a measured approach curve together with its fit. This enables us to approach the surface to a distance well below the tip diameter (here 10-30 µm with a 50 µm diameter tip) in a safe and reproducible way. It is important to point out that the shape of the approach curve is not affected by the probe RG (radius of the insulating layer divided by the radius of the active layer) which means that it can be employed in any SECM setup. It should be noted that, due to humidity, the measured permittivity (ε) differs from the permittivity of dry air (ε_0). In a Kelvin probe approach, this is known to significantly change the approach curve.[52] However, as seen from Eq. 3.4 it is clear that for the capacitive approach only the

absolute capacitance changes as a function of ε, while the shape of the approach curve remains the same. Finally, we have successfully tested this approach technique with electrodes of different geometries and dimensions. With the appropriate electronics, the capacitive approach can also be used for significantly smaller tips than presented here. However, one should realize that, as the shape of the approach curve does not depend on the tip diameter, without detailed tip characterization the accuracy of this method is in the range of 1-3 µm.

3.4 Local pH measurements

The functionalized gold pH sensor was used to study hydrogen evolution (HER) on gold (0.1 M Li_2SO_4, pH = 3.2) as a model system. Before the pH measurements were performed, the CV of HER was recorded at the gold substrate, which is shown in Fig. 3.4. The cathodic current observed is due to the reduction of protons ($2H^+ + 2e^- \rightarrow H_2$). The reaction rate is initially governed by kinetics and below –0.8 V vs. Ag/AgCl, the reaction becomes diffusion limited. As protons are consumed at the interface and the diffusion layer thickness increases, a pH gradient is built up. This can be observed in the CV by the decrease of the cathodic current from the first to the subsequent cycles due to proton depletion. However, quantification of the local pH is not possible based on the CV alone. At potentials more negative than –1.2 V vs. Ag/AgCl and bulk pH, mainly the reduction of water would take place ($2H_2O + 2e^- \rightarrow H_2 + 2OH^-$). The SECM pH measurements were performed in the potential range highlighted in the CV, in which in principle mostly proton reduction is taking place.

SECM pH measurements were carried out with the functionalized Au-UME placed at fixed distance, 75 ± 1 µm from the surface. Hydrogen evolution was turned “on” and “off” at the gold sample while the tip voltammetry was recorded at a scan rate of 200 mV s^{-1}. An example of the shift observed in the tip voltammetry can be found in Fig. A.6 in Appendix A. The tip CVs were fitted, and the potential of the anodic peak determined as a function of time (see Fig. A.7 in Appendix A). The calibration curve shown in Fig. 3.2b was used to convert the tip peak potentials to pH. Details on the data fitting can be found in Appendix A. Results depicted in Fig. 3.5a show the pH changes taking place when HER is turned “on” and “off” at the sample at –0.75 V vs. Ag/AgCl. Each data point corresponds to the mid-peak potential extracted from each Au-UME CV. At –0.75 V vs. Ag/AgCl, protons are being consumed at the gold working electrode and the pH has an initial fast

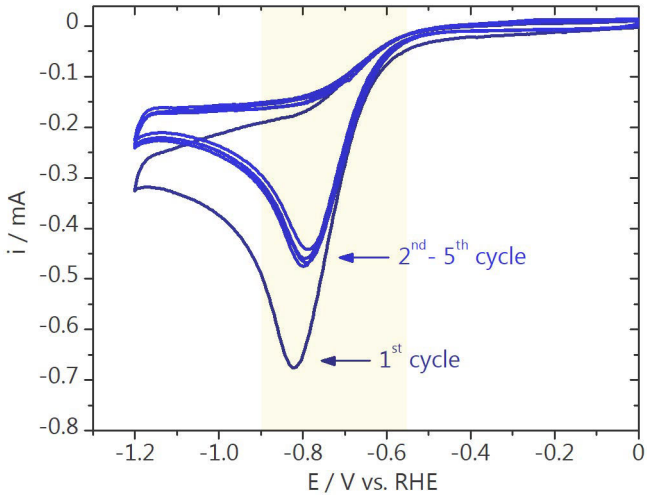

Fig. 3.4. Cyclic voltammogram of hydrogen evolution taking place at the gold sample in 0.1 M Li_2SO_4 (pH = 3.2) recorded at 100 mV s^{-1}.

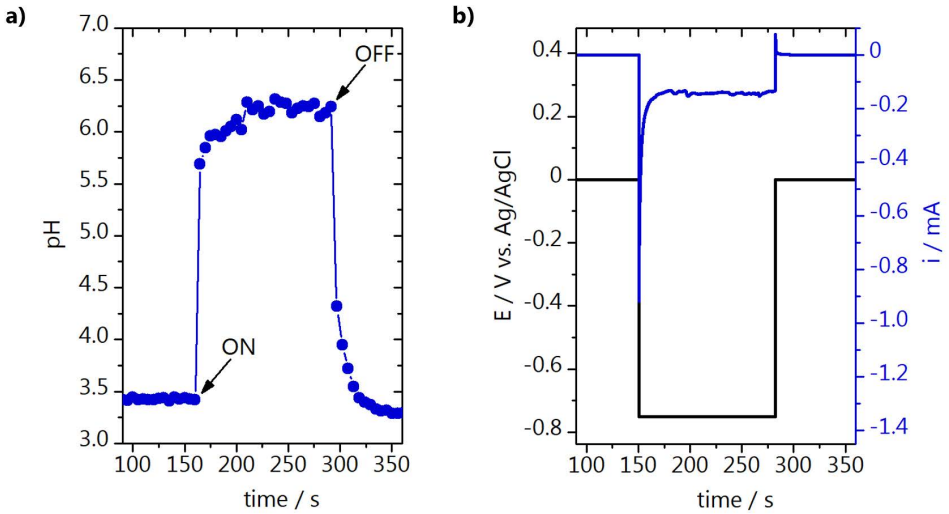

Fig. 3.5. a) pH measurement during hydrogen evolution in 0.1 M Li_2SO_4 (pH = 3.2) with the sample at -0.75 V vs. Ag/AgCl; **b)** chronoamperometry recorded at the sample.

increase of more than two units and takes 50 seconds to reach a stable value. By observing the sample chronoamperometry curve (Fig. 3.5b), this is also the time needed for the current to reach diffusion limitation due to an initially fast increase in local pH and diffusion layer thickness. At –0.75 V the maximum pH value of 6.3 was reached. This strong pH increase can be explained by the fact that the electrolyte is not buffered. After 150 seconds, HER is turned "off" and the near-surface pH returns to the bulk pH value. Similar measurements were previously performed with an IrO_x sensor.[53] Comparing our results with the data presented in Figure 8 of Ref. 54, it can be seen that our probe captures the time scale of the pH changes during HER more precisely, allowing for a larger number of data points to be obtained in time, only dependent on the scan rate at which the tip voltammetry is recorded. In addition, our pH sensor is more stable, and the response does not drift in time, which is a common drawback of potentiometric sensors such as IrO_x.

Measurements were also performed at less negative sample potentials, which due to the slower consumption of protons, should lead to lower pH values than obtained at –0.75 V vs. Ag/AgCl. As depicted in Fig. 3.6 when –0.65 V vs. Ag/AgCl is applied to the sample, the pH reaches 4.75 and when HER is carried out at –0.55 V vs. Ag/AgCl only a small increase of less than one pH unit is observed. The corresponding sample chronoamperometry can be seen in Fig. A.4 in Appendix A. To assure reproducibility of the pH response, a second measurement was performed applying the same negative potentials (black curve in Fig. 3.6). The same pH values were reached for the same potentials, which also shows how thermal drift does not compromise the measurements.

Another set of HER experiments was performed where the sample potential was changed in smaller steps, to demonstrate the sensitivity of the pH probe. The results can be seen in Fig. 3.7, where the sample potential was varied from –0.6 to –0.9 V vs. Ag/AgCl in steps of 50 mV. The electrolyte bulk pH was 3 and a gradual increase in pH can be observed as a function of sample potential, irrespective of the fact that the potentials are applied in a random order. The sample chronoamperometry recorded during the experiment can be found in Fig. A.5 in Appendix A. The inset in Fig. 3.7 shows the remarkable sensitivity of our pH probe, as differences of 0.1 and 0.35 pH unit were recorded when the sample potential was –0.6 and –0.65 V vs. Ag/AgCl, respectively. In addition, measurements at more negative sample potentials show the large pH range at which the probe can be employed. Note that the absolute pH values cannot directly be compared between this measurement and the one shown in Fig. 3.6 as different spots of the

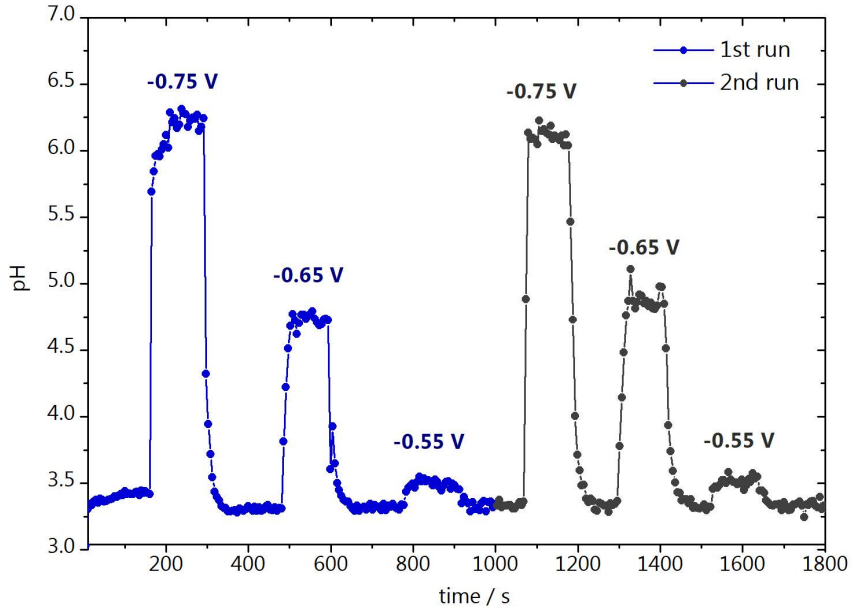

Fig. 3.6. pH measurements in the diffusion layer during hydrogen evolution in 0.1 M Li_2SO_4 (pH = 3.2) at different sample potentials. The measurement was performed in duplicate.

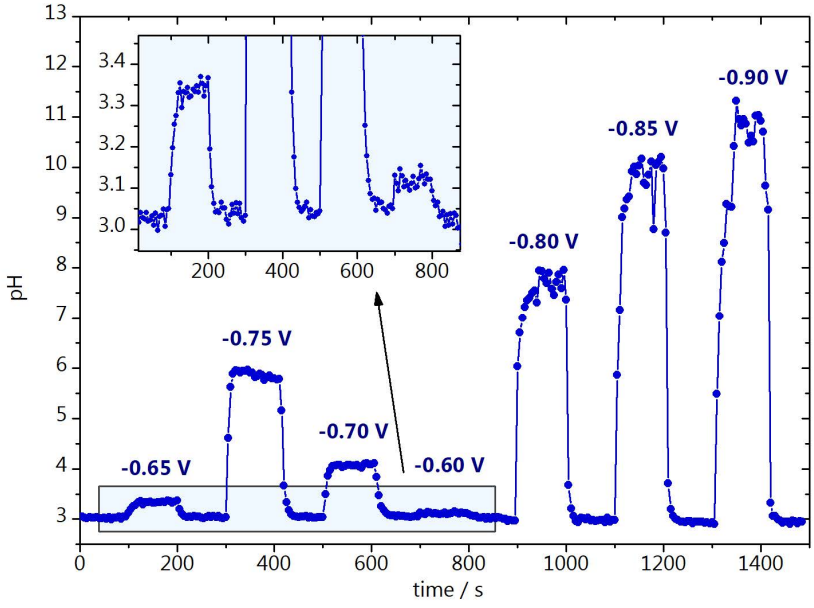

Fig. 3.7. pH measurements in the diffusion layer during hydrogen evolution in 0.1 M Li_2SO_4 (pH = 3) performed in a wider potential range. The inset shows the small pH differences recorded when the sample potential was –0.65 and –0.60 V vs. Ag/AgCl.

polycrystalline gold sample have distinct reactivities towards HER and the starting bulk pH is not the same.

It is important to point out that during the measurements, the potential window of the tip voltammetry must be adjusted due to the pH changes happening locally. Not only the 4-HATP/4-NSTP mid-peak potential shifts with pH but also the potential at which the unwanted tip reactions take place, i.e. 4-ATP formation and destabilization of the self-assembled monolayer. Therefore, the 4-HATP/4-NSTP peak intensity would decrease drastically if the potential limits were not adjusted accordingly. In addition, the time resolution of the measurement can be adjusted according to the time scale of the reaction being studied. Test CVs were recorded until up to 600 mV s^{-1} and the tip voltammetry was still stable.

3.5 Conclusions

In this work, we have successfully developed a pH sensor based on the self-assembly of 4-nitrothiphenol on gold ultramicroelectrodes. The probe voltammetry shows a Nernstian behavior with 57 mV/pH shift, which is not affected by the electrolyte composition. To assure cleanliness and avoid destabilization of the probe, we employ a mediator- and electrolyte-free capacitive approach to determine the absolute tip-to-sample distance. We have measured the pH during hydrogen evolution with the tip placed at a constant distance, 75 µm from the surface. Results show that our pH probe provides superior time resolution compared to previously reported potentiometric IrO_x pH sensors, allowing to capture the dynamics of proton diffusion during hydrogen evolution. A gold UME of 50 µm diameter was used in this work, but the functionalization with 4-NTP can also be carried out using smaller gold UMEs for further spatially resolved measurements. This would also allow for measurements with the probe positioned closer to the surface. Summarizing, we presented a highly sensitive and selective miniature pH probe that can be applied to a wide variety of systems, changing for example the gas atmosphere, electrolyte composition, and substrate. This work provides the means for more precise determination of the spatially resolved diffusion layer pH under different reactions. Consequently, it will help better understanding and modelling electrocatalytic reactions.

References

(1) Munteanu, R.-E.; Stănică, L.; Gheorghiu, M.; Gáspár, S. *Anal. Chem.* 2018, *90* (11), 6899–6905.
(2) Joshi, V. S.; Sheet, P. S.; Cullin, N.; Kreth, J.; Koley, D. *Anal. Chem.* 2017, *89* (20), 11044–11052.
(3) Choi, J.; Groisman, E. A. *Mol. Microbiol.* 2016, *101* (6), 1024–1038.
(4) Chen, Q.; Liu, X.; Chen, J.; Zeng, J.; Cheng, Z.; Liu, Z. *Adv. Mater.* 2015, *27* (43), 6820–6827.
(5) Filotás, D.; Fernández-Pérez, B. M.; Izquierdo, J.; Kiss, A.; Nagy, L.; Nagy, G.; Souto, R. M. *Corros. Sci.* 2017, *129*, 136–145.
(6) Liu, R.; Zhang, M.; Meng, Q.; Yuan, B.; Zhu, Y.; Li, L.; Wang, C. *Electrochem. commun.* 2017, *82*, 103–106.
(7) Koper, M. T. M. *Chem. Sci.* 2013, *4* (7), 2710–2723.
(8) Zheng, J.; Sheng, W.; Zhuang, Z.; Xu, B.; Yan, Y. *Sci. Adv.* 2016, *2* (3), e1501602.
(9) Ooka, H.; Figueiredo, M. C.; Koper, M. T. M. *Langmuir* 2017, *33* (37), 9307–9313.
(10) Kas, R.; Kortlever, R.; Yılmaz, H.; Koper, M. T. M.; Mul, G. *ChemElectroChem* 2015, *2* (3), 354–358.
(11) Pérez-Gallent, E.; Figueiredo, M. C.; Katsounaros, I.; Koper, M. T. M. *Electrochim. Acta* 2017, *227*, 77–84.
(12) Diaz-Morales, O.; Ferrus-Suspedra, D.; Koper, M. T. M. *Chem. Sci.* 2016, *7* (4), 2639–2645.
(13) Wencel, D.; Abel, T.; McDonagh, C. *Anal. Chem.* 2014, *86* (1), 15–29.
(14) Wang, L.; Li, M.; Li, W.; Han, Y.; Liu, Y.; Li, Z.; Zhang, B.; Pan, D. *ACS Sustain. Chem. Eng.* 2018, *6* (10), 12668–12674.
(15) Mirkin, M. V; Horrocks, B. R. *Anal. Chim. Acta* 2000, *406* (2), 119–146.
(16) Ayemoba, O.; Cuesta, A. *ACS Appl. Mater. Interfaces* 2017, *9* (33), 27377–27382.
(17) Zhou, J.; Ma, H. *Chem. Sci.* 2016, *7* (10), 6309–6315.
(18) Yang, K.; Kas, R.; Smith, W. A. *J. Am. Chem. Soc.* 2019, *141* (40), 15891–15900.
(19) Rudd, N. C.; Cannan, S.; Bitziou, E.; Ciani, I.; Whitworth, A. L.; Unwin, P. R. *Anal. Chem.* 2005, *77* (19), 6205–6217.
(20) Fuladpanjeh-Hojaghan, B.; Elsutohy, M. M.; Kabanov, V.; Heyne, B.; Trifkovic, M.; Roberts, E. P. L. *Angew. Chemie Int. Ed.* 2019, *58* (47), 16815–16819.
(21) Bowyer, W. J.; Xie, J.; Engstrom, R. C. *Anal. Chem.* 1996, *68* (13), 2005–2009.
(22) Kakooei, S.; Ismail, C.; Ari-Wahjoedi, B. *Int. J. Mater. Sci. Innov.* 2013, *1* (1), 62–72.
(23) Nadappuram, B. P.; McKelvey, K.; Al Botros, R.; Colburn, A. W.; Unwin, P. R. *Anal. Chem.* 2013, *85* (17), 8070–8074.
(24) Ouattara, L.; Fierro, S.; Frey, O.; Koudelka, M.; Comninellis, C. *J. Appl. Electrochem.* 2009, *39* (8), 1361–1367.
(25) Huang, W. D.; Cao, H.; Deb, S.; Chiao, M.; Chiao, J. C. *Sensors Actuators, A Phys.* 2011, *169* (1), 1–11.
(26) Jović, M.; Hidalgo-Acosta, J. C.; Lesch, A.; Costa Bassetto, V.; Smirnov, E.; Cortés-Salazar, F.; Girault, H. H. *J. Electroanal. Chem.* 2018, *819*, 384–390.
(27) Kiss, A.; Nagy, G. *Electroanalysis* 2015, *27* (3), 587–590.
(28) Jovanovič, P.; Hodnik, N.; Ruiz-Zepeda, F.; Arčon, I.; Jozinović, B.; Zorko, M.; Bele, M.; Šala, M.; Šelih, V. S.; Hočevar, S.; Gaberšček, M. *J. Am. Chem. Soc.* 2017, *139* (36), 12837–12846.
(29) Alam, A. U.; Qin, Y.; Nambiar, S.; Yeow, J. T. W.; Howlader, M. M. R.; Hu, N. X.; Deen,

M. J. *Prog. Mater. Sci.* 2018, *96* , 174–216.
(30) Morris, C. A.; Chen, C. C.; Ito, T.; Baker, L. A. *J. Electrochem. Soc.* 2013, *160* (8), H430–H435.
(31) Vishnu, N.; Kumar, A. S.; Pan, G. T.; Yang, T. C. K. *Sensors Actuators, B Chem.* 2018, *275*, 31–42.
(32) Zuaznabar-Gardona, J. C.; Fragoso, A. *Sensors Actuators, B Chem.* 2018, *273*, 664–671.
(33) Lindino, C. A.; Bulhões, L. O. S. *Anal. Chim. Acta* 1996, *334* (3), 317–322.
(34) Ryu, J.; Wuttig, A.; Surendranath, Y. *Angew. Chemie - Int. Ed.* 2018, *57* (30), 9300–9304.
(35) Yokoyama, Y.; Miyazaki, K.; Miyahara, Y.; Fukutsuka, T.; Abe, T. *ChemElectroChem* 2019, *6* (18), 4750–4756.
(36) Figueiredo, M. C.; Arán-Ais, R. M.; Climent, V.; Kallio, T.; Feliu, J. M. *ChemElectroChem* 2015, *2* (9), 1254–1258.
(37) Lu, M.; Compton, R. G. *Analyst* 2014, *139* (10), 2397–2403.
(38) Lu, M.; Compton, R. G. *Analyst* 2014, *139* (18), 4599–4605.
(39) Wildgoose, G. *Talanta* 2003, *60* (5), 887–893.
(40) Pöller, S.; Schuhmann, W. *Electrochim. Acta* 2014, *140*, 101–107.
(41) Botz, A.; Clausmeyer, J.; Öhl, D.; Tarnev, T.; Franzen, D.; Turek, T.; Schuhmann, W. *Angew. Chemie - Int. Ed.* 2018, *57* (38), 12285–12289.
(42) Michalak, M.; Kurel, M.; Jedraszko, J.; Toczydlowska, D.; Wittstock, G.; Opallo, M.; Nogala, W.; *Anal. Chem.* 2015, *87* (23), 11641–11645.
(43) Voogd, J. M. De; Spronsen, M. A. Van; Kalff, F. E.; Bryant, B.; Ostoji, O.; Haan, A. M. J. Den; Groot, I. M. N.; Oosterkamp, T. H.; Otte, A. F.; Rost, M. J. *Ultramicroscopy* 2017, *181*, 61–69.
(44) Jacobse, L.; Raaijman, S. J.; Koper, M. T. M. *Phys. Chem. Chem. Phys.* 2016, *18* (41), 28451–28457.
(45) Tsutsumi, H.; Furumoto, S.; Morita, M.; Matsuda, Y. *J. Colloid Interface Sci.* 1995, *171* (2), 505–511.
(46) Touzalin, T.; Joiret, S.; Maisonhaute, E.; Lucas, I. T. *Anal. Chem.* 2017, *89* (17), 8974–8980.
(47) Cobb, S. J.; Ayres, Z. J.; Newton, M. E.; Macpherson, J. V. *J. Am. Chem. Soc.* 2019, *141* (2), 1035–1044.
(48) Amphlett, J. L.; Denuault, G. *J. Phys. Chem. B* 1998, *102* (49), 9946–9951.
(49) Izquierdo, J.; Knittel, P.; Kranz, C. *Anal. Bioanal. Chem.* 2018, *410* (2), 307–324.
(50) Ballesteros Katemann, B.; Schulte, A.; Calvo, E. J.; Koudelka-Hep, M.; Schuhmann, W. *Electrochem. commun.* 2002, *4* (2), 134–138.
(51) Eckhard, K.; Schuhmann, W. *Analyst* 2008, *133* (11), 1486–1497.
(52) Maljusch, A.; Senöz, C.; Rohwerder, M.; Schuhmann, W. *Electrochim. Acta* 2012, *82*, 339–348.
(53) Critelli, R. A. J.; Bertotti, M.; Torresi, R. M. *Electrochim. Acta* 2018, *292*, 511–521.

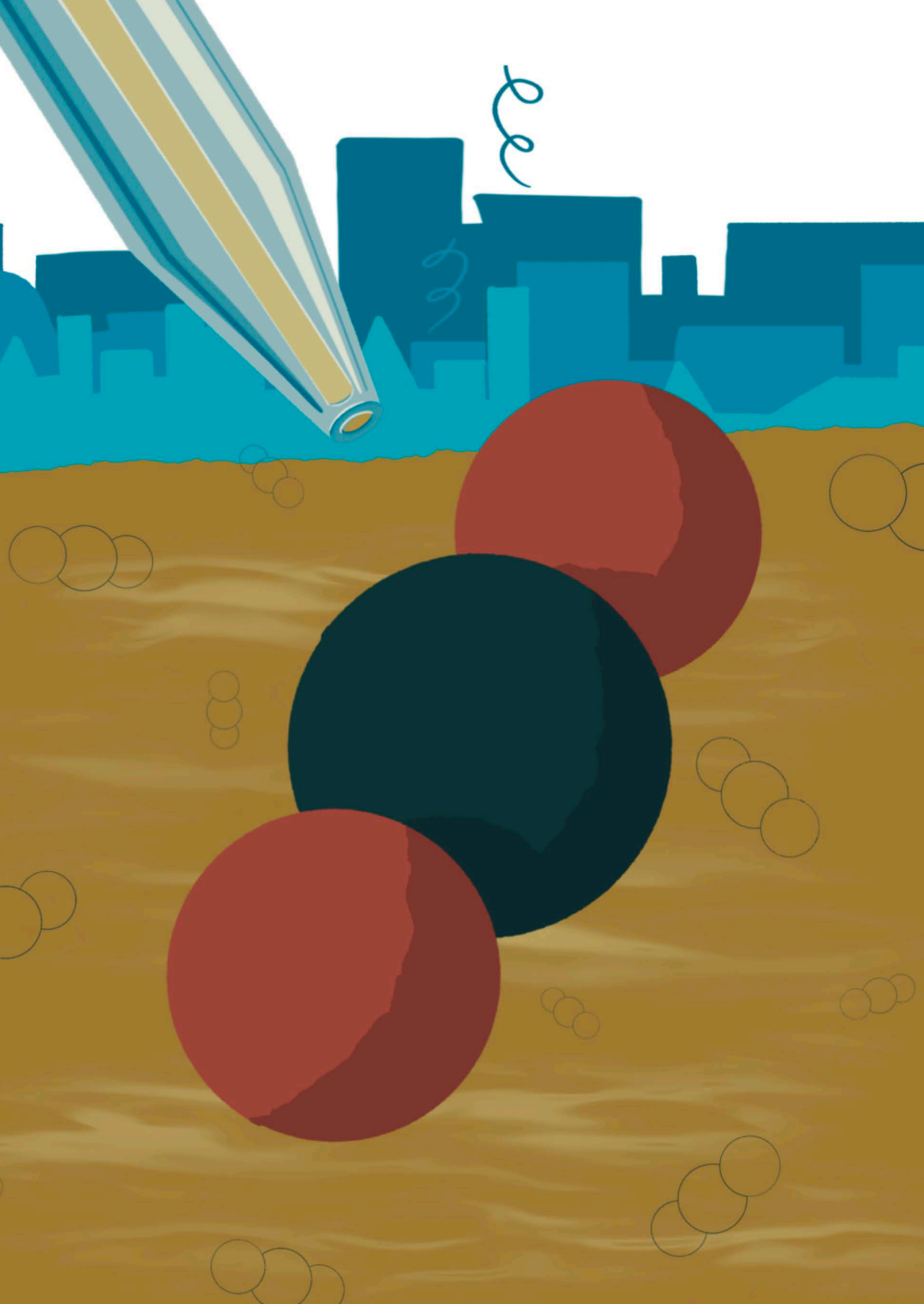

4

Time-resolved local pH measurements during CO_2 reduction using SECM: buffering and tip effects

This chapter is based on Monteiro, M. C. O., Mirabal, A., Jacobse, L., Doblhoff-Dier, K., Barton, S. C., Koper, M. T. M. *JACS Au, 1 (11),* 1915–1924 (2021)

Abstract

The electrochemical reduction of CO_2 is widely studied as a sustainable alternative to produce fuels and chemicals. The electrolyte´s bulk pH and composition play an important role in the reaction activity and selectivity, and can affect the extent of the build-up of pH gradients between the electrode surface and the bulk of the electrolyte. Quantifying the local pH and how it is affected by the solution species is desirable to gain a better understanding of the CO_2 reduction reaction. Local pH measurements can be realized using Scanning Electrochemical Microscopy (SECM), however, finding a pH probe that is stable and selective under CO_2 reduction reaction conditions is challenging. Here, we have used our recently developed voltammetric pH sensor to perform pH measurements in the diffusion layer during CO_2 reduction using SECM, with high time resolution. Using a 4-hydroxylaminothiophenol (4-HATP)/4-nitrosothiophenol (4-NSTP) functionalized gold ultramicroelectrode, we compare the local pH developed above a gold substrate in an argon atmosphere, when only hydrogen evolution is taking place, to the pH developed in a CO_2 atmosphere. The pH is monitored at a fixed distance from the surface, and the sample potential is varied in time. In argon, we observe a gradual increase of pH, while a plateau region is present in CO_2 atmosphere due to the formation of HCO_3^- buffering the reaction interface. By analysing the diffusion layer dynamics once the sample reaction is turned "off", we gain insightful information on the time scale of the homogeneous reactions happening in solution and on the time required for the diffusion layer to fully recover to the initial bulk concentration of species. To account for the effect of the presence of the SECM tip on the measured pH, we performed Finite Element Method simulations of the fluid and reaction dynamics. The results show the significant localized diffusion hindrance caused by the tip, so that in its absence the pH values are more acidic than when the tip is present. Nonetheless, through the simulation we can account for this effect and estimate the real local pH values across the diffusion layer.

4.1 Introduction

The electrochemical conversion of CO_2 to higher added value products has gained attention in the past years as a potential pathway towards replacing fossil fuels as feedstock. In aqueous media, the reduction of CO_2 (CO_2RR) competes with the hydrogen evolution reaction (HER), and activity and selectivity are key factors to make this process viable at industrially relevant scales.[1] In order to steer the selectivity and improve the overall reaction energetics, most studies focus on the catalyst material.[2,3] However, another efficient way of tuning CO_2RR is through the electrolyte composition.[4,5] By changing the electrolyte´s buffer capacity[6–8], pH[9–11], cation[12–15] or anion[16,17] one can strongly influence the rate and selectivity of the reaction. However, understanding and decoupling these electrolyte effects is necessary in order to optimize the reaction via these variables.

In many studies, the activity for CO_2 reduction is assessed without actual knowledge of the interfacial pH, which can vary drastically from the bulk depending on the current density, electrolyte buffer capacity, and diffusion coefficient of the species in solution. On gold, at low overpotentials, CO_2RR and HER yield mainly carbon monoxide (CO) and hydrogen (H_2) through the following reactions:[18]

$$CO_2 + H_2O + 2e^- \rightleftharpoons CO + 2OH^- \quad \text{Eq. 4.1}$$

$$2H^+ + 2e^- \rightleftharpoons H_2 \quad \text{Eq. 4.2}$$

$$2H_2O + 2e^- \rightleftharpoons H_2 + 2OH^- \quad \text{Eq. 4.3}$$

The interfacial pH and the overpotential will determine whether the overall HER current is dominated by proton or water reduction, displayed in Eq. 2 and 3, respectively. Because of the consumption of protons or formation of OH^- by both HER and CO_2RR, the pH near the electrode surface can drastically vary from the bulk pH. Apart from the reactions 4.1 to 4.3, various homogeneous reactions may take place in the CO_2-water system as a function of pH:[19]

$$CO_2 + H_2O \rightleftharpoons H_2CO_3 \quad \text{Eq. 4.4}$$

$$H_2CO_3 \rightleftharpoons HCO_3^- + H^+ \quad pK_a = 3.6 \quad \text{Eq. 4.5}$$

$$CO_2 + OH^- \rightleftharpoons HCO_3^- \quad pK_a = 6.4 \quad \text{Eq. 4.6}$$

$$HCO_3^- + OH^- \rightleftharpoons CO_3^{2-} \quad pK_a = 10.3 \quad \text{Eq. 4.7}$$

$$H_2O \rightleftharpoons H^+ + OH^- \quad pK_a = 14.0 \quad \text{Eq. 4.8}$$

Quantifying the pH gradients formed in the diffusion layer during CO_2RR is crucial in order to gain a better understanding of the reaction. Though various techniques are available for measuring local pH in electrochemistry[20] (Chapter 2), directly measuring the pH in the diffusion layer during CO_2 reduction is challenging. This is

due to the complex reaction environment, and the fact that, the signal and stability of the pH probe should not be affected by the reactants, products, or the electrolyte identity. To date, pH measurements during CO_2 reduction under stationary conditions have been mainly achieved using spectroscopic techniques. Yang et al.[21], for instance, used surface enhanced infrared absorption spectroscopy (SEIRAS) to determine the pH near the surface during CO_2RR on sputtered copper thin films by monitoring the change in signal intensity of the species composing the phosphate buffer used ($H_2PO_4^-$/ HPO_4^{2-}/ PO_4^{3-}). Results showed that even in strongly buffered electrolyte, the pH near the surface differs from the bulk at current densities lower than 10 mA cm^{-2}. Ayemoba et al.[22] probed the pH during CO_2RR on gold thin films using surface-enhanced infrared absorption spectroscopy in the attenuated total reflection mode (ATR-SEIRAS). In this case, the ratio between the integrated absorbance of the CO_2 and HCO_3^- bands was used to estimate the pH near the surface. Similar measurements, were recently reported in a flow cell using Raman spectroscopy.[23] Although, in general, these spectroscopic techniques can provide valuable information about the concentration of species in the first few nanometres above the surface, the signal obtained is averaged over a large surface area. Furthermore, these measurements require having infrared or Raman active species in solution, and the pH is measured indirectly, by monitoring species whose signal is a function of the proton concentration. If these species are also affected by other variables of the reaction environment, the signal might be a convolution thereof. Therefore, spectroscopic techniques can be limited in terms of electrode materials and electrolytes that can be employed. As an alternative to spectroscopy, Zhang et al.[24] have recently used the rotating ring-disc electrode technique to measure changes in pH during CO_2RR on gold under mass transport control. In this case, a correlation between potentiometric pH measurements with IrO_x and shifts in the CO oxidation peak detected with a Pt ring were used to determine the disc pH. Even though this allows for pH measurements under mass transport control, the method is limited in terms of temporal (when IrO_x is used) and spatial resolution (similarly to spectroscopic techniques). Additionally, even though the CO signal on platinum is used as pH probe, it is known that this reaction is not only affected by pH[25], but also cation identity[26] or surface structure.[27]

Scanning Electrochemical Microscopy (SECM) allows for performing pH measurements with high spatial and temporal resolution. The spatial resolution is only limited by the tip size and the temporal resolution depends on the pH probe used. SECM also offers a high versatility in terms of substrate (gas diffusion, flat,

thin film electrodes) and pH sensors (potentiometric, voltammetric) that can be used. However, finding a pH probe that is not destabilized by the CO_2 reduction reaction environment can be challenging. For example, commonly used (in both SECM and RRDE) potentiometric pH sensors such as IrO_x or Pt can strongly interact with CO. This can generate a convoluted open circuit potential response, hindering the applicability of these materials to measure pH during CO_2RR. Using gas diffusion electrodes (GDEs) operating at high current densities, Dieckenhöfer et al.[28] overcame this problem by collecting the products at the back of the GDE, so as to avoid CO getting in contact with the SECM Pt tip. Unfortunately, the pH response of the platinum nanoelectrode is only applicable in highly alkaline environments, as evident from the calibration curve reported by the authors in 1 to 16 M KOH solutions. Such a high alkalinity at the interface can only be achieved when using high turnover substrates (highly porous electrodes, GDEs) or when operating at high overpotentials. This means that this Pt sensor cannot be used to investigate CO_2RR on less porous substrates, or in neutral/acidic conditions. With that in mind, we have recently developed a highly stable, selective and sensitive SECM pH probe based on the functionalization of gold ultramicroelectrodes (Au-UMEs) with a 4-nitrothiophenol self-assembled monolayer.[29] Contrary to the commonly used IrO_x, this voltammetric pH probe can provide high temporal resolution, only dependent on the scan rate applied at the tip, showing a stable pH response in a wide pH range. Additionally, the fact that the sensor is formed by a monolayer on the tip surface, overcomes time response issues often encountered when using either a polymer or solid oxide film.

Our modified Au-UME pH sensor presented in Chapter 3, is employed in this work to perform and compare direct pH measurements during HER and CO_2RR on polycrystalline gold. We monitor the evolution of pH in time while stepping the electrode potential in either argon or CO_2 atmosphere. Our results show that the homogeneous reactions involving CO_2 in aqueous media are sufficient to buffer the reaction interface to a certain extent, in spite of using an otherwise unbuffered electrolyte. The high sensitivity and time resolution of our pH probe enables us to analyse the dynamics of the diffusion layer pH as a function of the species present in solution, which has not been previously reported for CO_2 reduction using SECM. Additionally, in this work we have accounted for the effect of the SECM tip on the diffusion layer concentration fields, and consequently on the pH measured for CO_2RR and HER, using 2D, dynamic transport and reaction simulations based on Finite Element Methods (FEM). Simulations are fitted to experimental results to

estimate kinetic parameters and enable further analysis of SECM tip effects relevant to the experimental system. This work brings pH measurements during CO_2RR one step further, by showing that it can be realized using SECM, with high time resolution and over a wide pH range. In future studies, this would allow for decoupling pH effects from other electrolyte/surface effects on the reaction.

4.2 pH sensor synthesis and calibration

The gold ultramicroelectrodes (Au-UMEs) are first characterized by blank voltammetry in 0.1 M H_2SO_4 in order to assure good sealing and surface cleanliness. A cyclic voltammogram characterizing the Au-UME (25 µm radius) used in this study can be seen in Fig. A.9 in Appendix A. To perform the SECM pH measurements, the Au-UME is functionalized with the 4-hydroxylaminothiophenol/4-nitrosothiophenol redox couple. This is done by immersion of the Au-UME in a solution containing 4-nitrothiophenol (4-NTP) which leads to the self-assembly of this organic molecule on the Au-UME surface. Next, 4-NTP is partially[30] electrochemically reduced to 4-hydroxylaminothiophenol (4-HATP) in 0.1 M H_2SO_4, as depicted in Fig. 4.1a. The cathodic potential limit must be carefully controlled in order to maximise the conversion to 4-HATP and minimise the amount of 4-aminothiophenol (4-ATP) formed. On the positive-going scan, an anodic peak can be seen in the gold double layer region between 0.2 and 0.4 V vs. Ag/AgCl due to oxidation of 4-HATP, forming 4-nitrosothiophenol (4-NSTP). This is a highly reversible reaction, demonstrated by the subsequent symmetrical cathodic current in the negative-going scan. A schematic representation of the reactions taking place at the Au-UME surface can be seen in the inset of Fig. 4.1a, which is correlated to the voltammetry of (1) the reduction of 4-NTP to 4-HATP and (2) the 4-HATP/4-NSTP redox couple.

The calibration of the functionalized Au-UME pH sensor is performed in the same electrolyte the SECM measurements are carried out, but in different gaseous atmospheres. The cyclic voltammetry (CV) of the tip is recorded in 0.1 M Li_2SO_4 solutions adjusted to different pH and saturated with either argon or CO_2. The CVs obtained in argon are shown in Fig. 4.1b and the ones recorded in CO_2 saturated electrolyte can be found in Fig. A.10 in Appendix A. The mid-peak potential of the 4-HATP/4-NSTP anodic voltammetry is obtained through a Gaussian fit (with a linear background) of the CVs, and can be used to construct the calibration curve shown in Fig. 4.1c. Due to the reversible oxidation and reduction of the 4-HATP/4-NSTP involving two protons and two electrons, a Nernstian response is obtained

with a shift of 57 mV/pH unit and an R^2 of 0.99. The calibration curves in argon and CO_2 atmosphere overlap until pH 3.45. This is expected as at higher pH values, carbonic acid is formed and the CO_2 saturated solutions equilibrate at a constant pH around 4 (see Eq. 4.4 and 4.5). We have also displayed the calibration

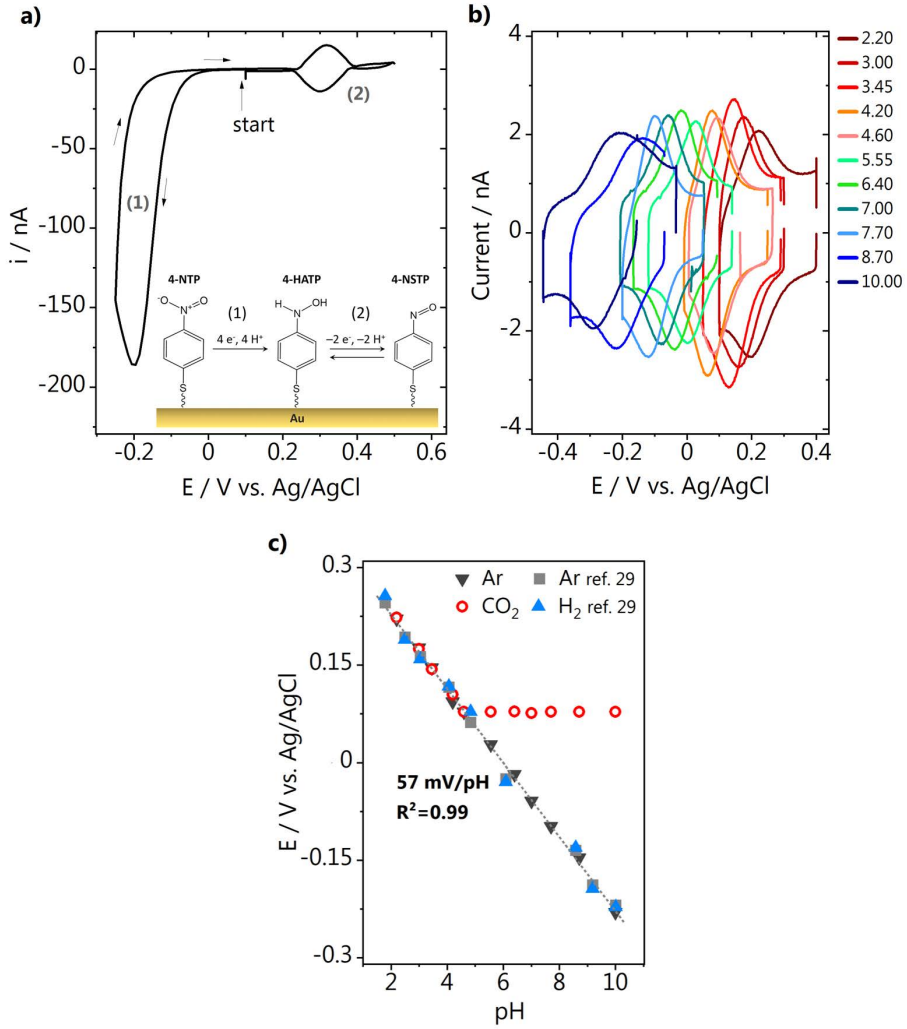

Fig. 4.1. SECM pH sensor synthesis and calibration. **a)** voltammogram of the functionalized Au-UME showing the conversion of 4-nitrothiophenol (4-NTP) to the pH sensitive redox couple 4-hydroxylaminothiophenol (4-HATP)/4-nitrosothiophenol(4-NTP); **b)** pH sensor voltammetry in 0.1 M Li_2SO_4 solutions adjusted to different pH, taken at 200 mV s^{-1}; **c)** calibration curves of the modified Au-UME pH sensor in different gaseous atmospheres. The calibration curves from our previous work (Chapter 3, Ref. 29) are also shown for comparison.

curves presented in Chapter 3[29] in Fig. 4.1c, which show how reproducible the pH sensor response is when comparing different measurements, performed in different gaseous atmospheres.

4.3 SECM measurements

Once the Au-UME is functionalized, the tip is positioned at a certain distance to the sample using a capacitive approach in air, which was introduced in our previous work (Chapter 3).[25,29,31] In short: an AC potential is applied to the sample while the capacitive current generated at the tip is recorded. The capacitance is plotted as a function of distance from the surface (Fig. A.11), and behaves exponentially at small tip-to-surface distances. The fitting of the approach curve (see Chapter 3) is used to determine the absolute surface position. Before performing the SECM pH measurements, the cyclic voltammetry of HER and CO_2RR taking place at the polycrystalline gold sample in 0.1 M Li_2SO_4 (pH_{bulk} = 3) was recorded (Fig. 4.2). In argon atmosphere a large cathodic current is observed at potentials more negative than –0.4 V vs. Ag/AgCl due to the reduction of protons. The reaction becomes diffusion limited due to the depletion of protons at the interface and consequently in the subsequent four cycles a significantly lower proton reduction current is observed. In the presence of CO_2, proton reduction and CO_2 reduction take place in parallel, but a larger current is observed only at potentials more negative than –1 V vs. Ag/AgCl, suggesting that the contribution of CO_2 reduction to the current observed at more positive potentials is minimal. The first cycle overlaps with the CV taken in argon atmosphere, as the starting bulk pH is the same, however larger currents are obtained in the subsequent four cycles in CO_2 atmosphere. The latter indicates that the alkalinity near surface is lower in the presence of CO_2. However, cyclic voltammetry can only provide qualitative information about the proton concentration near the surface.

To quantify the changes in pH in the diffusion layer during these reactions using SECM, the functionalized Au-UME pH sensor is placed at a constant distance of 80 ± 2 µm from the gold surface. Similarly to Chapter 3, the reactions are turned "on" and "off" by stepping the sample potential from –0.5 to –0.9 V vs. Ag/AgCl in 50 mV steps. In between potential steps, the gold substrate is held at 0 V. The tip voltammetry is constantly recorded at 200 mV s^{-1}, which allows capturing the changes in pH with high time resolution (4 seconds/data point). Fig. 4.3a shows the results obtained in argon atmosphere (gray triangles) and then in CO_2 atmosphere (red circles). These data were obtained in two consecutive measurements and are

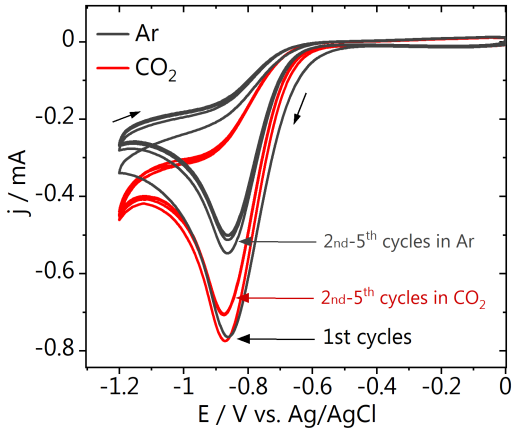

Fig. 4.2. CVs in argon (black) and CO_2 (red) atmosphere taken at the gold sample in 0.1 M Li_2SO_4 (pH = 3, 100 mV s^{-1}).

plotted on top of each other to facilitate comparison. The peak potentials obtained from fitting the 4-HATP/4-NSTP voltammetry (used to extract these pH data) and the current recorded at the sample during the chronoamperometry can be found in Fig. A.12 and Fig. A.13 in Appendix A. From the results in Fig. 4.3a, it can be seen that at low overpotentials and consequently low current densities (between –0.5 and –0.6 V), small pH changes of maximum 1.5 pH unit are observed at the interface, both in argon and CO_2 atmosphere. At these potentials (and pH) proton reduction is the main reaction taking place, and the activity for CO_2RR is still quite low. Although proton reduction is kinetically limited in this narrow potential window, the low proton bulk concentration (pH 3), explains the relatively small effect on the measured pH. The significant pH change we observe even when the reaction appears kinetically limited is related to the presence of the tip, which inhibits local mass transport, as we will later illustrate in the Finite Element modeling section. Between –0.65 and –0.9 V vs. Ag/AgCl, however, the pH recorded in argon atmosphere gradually increases as a function of potential. At these higher interfacial pH values, hydrogen is produced through the reduction of water. As water reduction is a kinetically limited reaction producing OH^-, the alkalinity is expected to increase with the potential. In CO_2 atmosphere, between –0.65 and –0.8 V vs. Ag/AgCl , we observe that the pH does not significantly increase as the potential is scanned more negatively, although we work in an unbuffered electrolyte. When the pH at the interface becomes alkaline, the reversible reaction between CO_2 and

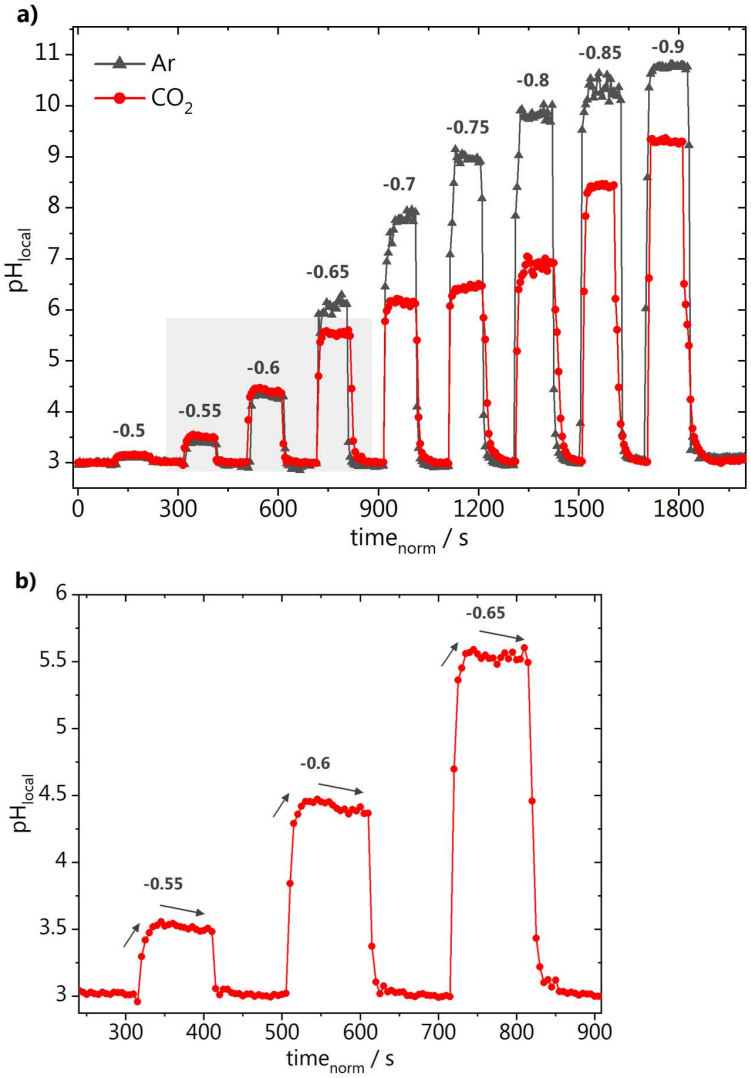

Fig. 4.3. Local pH measured in time. **a)** Comparison of the pH measured at the same distance from the surface in argon and CO_2 atmosphere; **b)** inset of the shaded area of a) showing the pH trend at low overpotentials. The sample potentials are indicated on top of the curves, in V vs. Ag/AgCl.

HCO_3^- (pK_a = 6.4, Eq. 4.6) seems to takes place fast enough, so that the CO_2 supplied is not only a reactant but also acts as a buffer to a certain extent. Once potentials more negative than –0.8 V are applied there is a buffer "breakdown" and the pH increases more than a unit above the pK_a of the CO_2/HCO_3^- reversible reaction. In fact, this buffering can also be observed in CO_2 atmosphere at lower overpotentials, where the maximum pH reached is still below 6. Interestingly, as shown in Fig. 4.3b, once the reaction is turned "on", there is first an increase in pH that reaches a maximum value after 30-35 seconds. Subsequently, the pH decreases as the OH^- produced are neutralized by the forward CO_2/HCO_3^- reaction (Eq. 4.6).

Going one step further here than in Chapter 3[25], the dynamics of the CO_2-derived species in the diffusion layer was investigated by focusing on the relaxation of the pH after the potential is returned to 0 V, in the presence and absence of CO_2. Fig. 4.4a and Fig. 4.4b show the time evolution of the pH measured at the tip once the sample reaction is turned "off", after the different potentials shown in Fig. 4.3a are applied to the sample. It can be seen in Fig. 4.4a that in argon atmosphere, once HER is turned "off", for nearly all sample potentials the pH drops to values below 4.5 within 5 seconds. Only when the reaction is carried out at –0.9 V, it takes slightly longer, but no more than 10 seconds. For low sample overpotentials, the interfacial pH returns to bulk pH within 25 seconds and even at the higher overpotentials this takes only 35 seconds. A very different behaviour is observed in CO_2 atmosphere as a function of sample potential, and consequently local pH, as shown in Fig. 4.4b. Here, the time for returning to the bulk pH value increases gradually with the sample potential applied, which modulates the local pH and consequently the concentration of species in equilibrium in solution. At potentials more positive than –0.65 V, the pH decreases gradually and equals the bulk pH 25 seconds after the reaction is turned "off" (similarly to argon). At intermediate sample potentials (–0.7 to –0.8 V), the initial near-surface pH is above the pK_a of the CO_2/HCO_3^- equilibrium, and therefore the concentration of bicarbonate close to the surface is higher than in the bulk. The curves decay very similarly and for more than 15 seconds the pH stays at around 6. At the more negative sample potentials, in which carbonate is also formed in higher concentrations, the pH drops to 6 within 5 seconds, and then gradually decreases to the bulk value. These observations are a consequence of both how fast the different species formed as a function of pH diffuse in the electrolyte and the rate of the different homogeneous reactions taking place in CO_2 atmosphere. Fig. 4.4c shows a schematic representation of the reactions taking place at the sample surface and in solution. If only HER takes place

(argon atmosphere), even though the interfacial pH reaches relatively higher values, the recovery of the diffusion layer happens fast. This is a consequence of the high diffusion coefficient of the species involved in the reaction ($D_{H^+} = 9.31 \cdot 10^{-5}\,\mathrm{cm^2\,s^{-1}}$ and $D_{OH^-} = 5.27 \cdot 10^{-5}\,\mathrm{cm^2\,s^{-1}}$) and of the absence of any additional buffer system. In contrast, in CO_2 atmosphere, bicarbonate and carbonate are formed, whose concentrations are a function of pH. These are much slower diffusing species ($D_{HCO_3^-} = 1.18 \cdot 10^{-5}\,\mathrm{cm^2\,s^{-1}}$ and $D_{CO_3^{2-}} = 0.95 \cdot 10^{-5}\,\mathrm{cm^2\,s^{-1}}$).

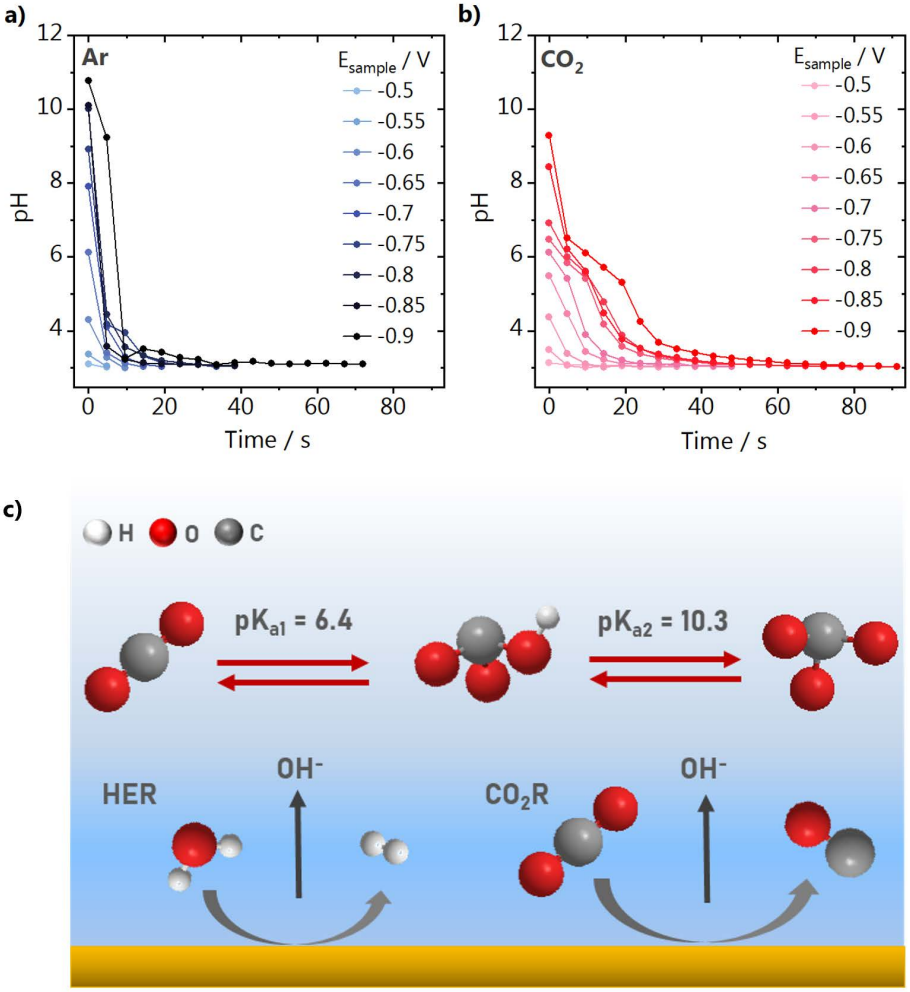

Fig. 4.4. Diffusion layer dynamics: pH recovery in the diffusion layer when **a)** hydrogen evolution and **b)** CO_2 reduction are turned "off". Sample potentials are reported versus Ag/AgCl. **c)** Schematic representation of the homogeneous reactions taking place in solution in parallel to the electrocatalytic reactions.

the reaction of $CO_3^{2-} \rightarrow HCO_3^-$ is fast while the $HCO_3^- \rightarrow CO_2$ reaction is much slower (see values in Table A.3 in Appendix A). As a consequence, the pH decays fast towards the pK_a of the CO_2/HCO_3^- equilibrium, but afterwards takes more than 40 seconds to reach the bulk pH value. These observations have strong implications for experiments in electrocatalysis. For instance, if one wishes to perform several measurements in a row, enough time must be given to the system (without any reaction taking place) in order to restore the bulk pH at the interface. Furthermore, we provide here a tool for probing such equilibrium reactions under operando conditions, which is relevant not only for CO_2 reduction but also for other electrocatalytic systems.

4.4 Tip effect: Finite Element Method (FEM simulations

In SECM it is known that the tip may physically block the diffusion of species and alter their concentrations in the diffusion layer, thus influencing the pH measurement.[32] In order to account for this effect, we have simulated the experimental results presented in Fig. 4.3 (and summarized in Fig. A.14) using Finite Element Method based modelling implemented in COMSOL Multiphysics. Fitted kinetic parameters and the use of a 2D axisymmetric model leads to good agreement between simulated and experimental results. This enables us to quantify the local pH excluding the effect of the SECM tip.

First, we considered the pH response during reactions taking place in argon atmosphere (Fig. 4.3a), namely proton reduction (PR) and water reduction (WR). The governing equations as well as the parameters and the fitting procedure used to obtain these parameters are discussed in detail in Fig. A.15-18 and Table A.1-3 in Appendix A. Here, we only summarize the main points: the PR rate is assumed to be linear in the proton concentration, as is the case if the Volmer step or a large-overpotential Heyrovsky step is rate limiting. This assumption is justified by the Tafel slope obtained from chronoamperometry being 147 mV/dec (see Fig. A.15) [33] The kinetic parameters for proton reduction, as well as the proton diffusion coefficient were obtained by fitting the cyclic voltammetry (Fig. 4.2, argon), the result of which is shown in Fig A.16. Subsequently, the pH-potential relation (Fig. 4.3, argon) after 100 seconds chronoamperometry was fit to obtain kinetic parameters for water reduction. For comparison to experiment, the pH values were thereby averaged over the SECM electrode area. Relevant diffusion coefficients (except the proton diffusion coefficient) and the rate constant for water association were thereby taken from literature (see Table A.3).

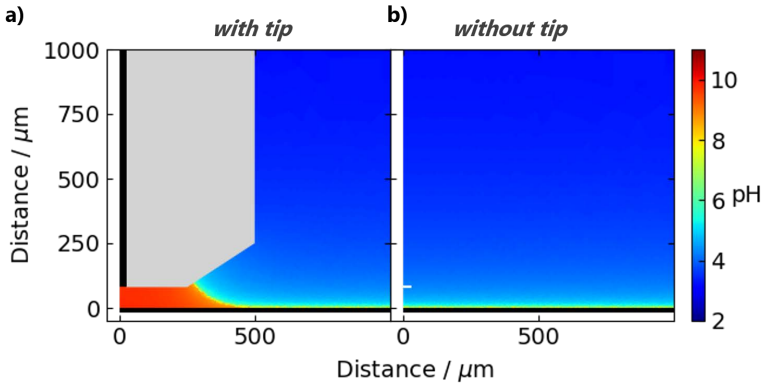

Fig. 4.5. pH profile near the electrode surface during hydrogen evolution reaction **a)** with and **b)** without the SECM tip present. Sample potential applied –0.8 V vs. Ag/AgCl.

The fitted parameters can be used to simulate the pH map during hydrogen evolution after 100 seconds chronoamperometry with and without tip present and hence to investigate the influence of the tip on the pH measurements. As an example, we show the pH map obtained at a substrate potential of –0.8 V vs. Ag/AgCl with and without the probe tip positioned at 80 µm above the surface in Fig. 4.5. The pH maps shown demonstrate that the tip significantly blocks diffusion of species away from the electrode surface. However, this effect is highly localized to the gap below the SECM tip; at horizontal positions far from the tip, the concentration profile approaches the "without tip" conditions.

Similar calculations can also be performed to estimate the influence the tip has on the transient chronoamperometry data. In Fig. 4.6, we simulate the chronoamperometry data at 100 seconds with and without tip present (solid vs. dashed line). The concentration of protons estimated with the tip absent is significantly higher than that obtained with the tip present, especially at potentials between –0.65 and –0.85 V vs. Ag/AgCl. At low overpotentials without the SECM tip present, the pH gradients are minimal. Only at large overpotentials, proton consumption at the surface electrode combined with increased hydroxide production due to the onset of water reduction causes the pH boundary layer to grow to a size comparable to the tip-surface separation (see Fig. A.18 in Appendix A). In the presence of the SECM tip, hindered diffusion directly below the tip causes the pH to rise more gradually already at a much less reducing potential. The sudden raise in pH between overpotentials of –0.6 to –0.7 V vs. Ag/AgCl can be ascribed to

a switch from proton reduction to mainly water reduction, as shown in Fig. A.17 in Appendix A.

A similar analysis was performed for the measurement in CO_2 atmosphere (Fig. 4.6b). See Eq. A.4-9 for the governing electrochemical equations and Eq. A.10-16 in Appendix A for the governing equations of the additional homogeneous reactions. Table A.3 lists the relevant parameters. Although no additional fit was performed, the simulation data (solid line) matches the experimental results (red dots) very well. Comparing Fig. 4.6a and b, it becomes clear that the pH measured in CO_2 atmosphere remains lower than that measured in argon atmosphere over the entire potential range. This is a consequence of the buffering effect of the CO_2 species present, as evidenced by the two plateau regions in the pH-potential relation, which correlate to the pK_a of bicarbonate (Eq. 4.6) and carbonate (Eq. 4.7). Although the buffering effect of the CO_2 species is most striking in the presence of the tip, the buffering of the electrolyte is also relevant in the absence of the tip. This is evidenced by the shift of the sudden increase in pH observed in argon atmosphere at –0.85V to even more negative potentials (not plotted). The presence of CO_2 and its derivatives thus has a significant buffering effect near the electrode at experimentally relevant conditions in both the presence and the absence of the tip.

Hindering the diffusion and inducing a high local alkalinity at the reaction interface allowed us to study the diffusion layer during CO_2RR at relatively low sample potentials (and current densities), which circumvents e.g. bubble issues and allows for gradually modulating the pH below the tip. However, this tip blocking effect could of course be minimized by decreasing the radius of the tip insulating layer or by working at larger distances from the surface. Using calculations similar to those shown in Fig. 4.6a, we have simulated the effect of decreasing the radius of the tip insulation on the pH response. Fig. 4.7 shows the results of the FEM simulations carried out using different insulating radii from $20*R_{tip}$ (the experimental value, R_{tip} from the UME used in this work) down to $1.2*R_{tip,}$ for a constant tip-sample distance. The simulated pH response in the absence of the SECM tip is also plotted for comparison. For an ideal insulation layer radius of $1.2*R_{tip}$ the calculated pH values closely approach those obtained without the tip present. When desired, this situation can be achieved, for example, by using a laser puller to produce the microelectrodes. However, it is important to point out that we find that obtaining a good sealing between the gold and the glass can be challenging, contrary to other metals that have a better adhesion to the insulation

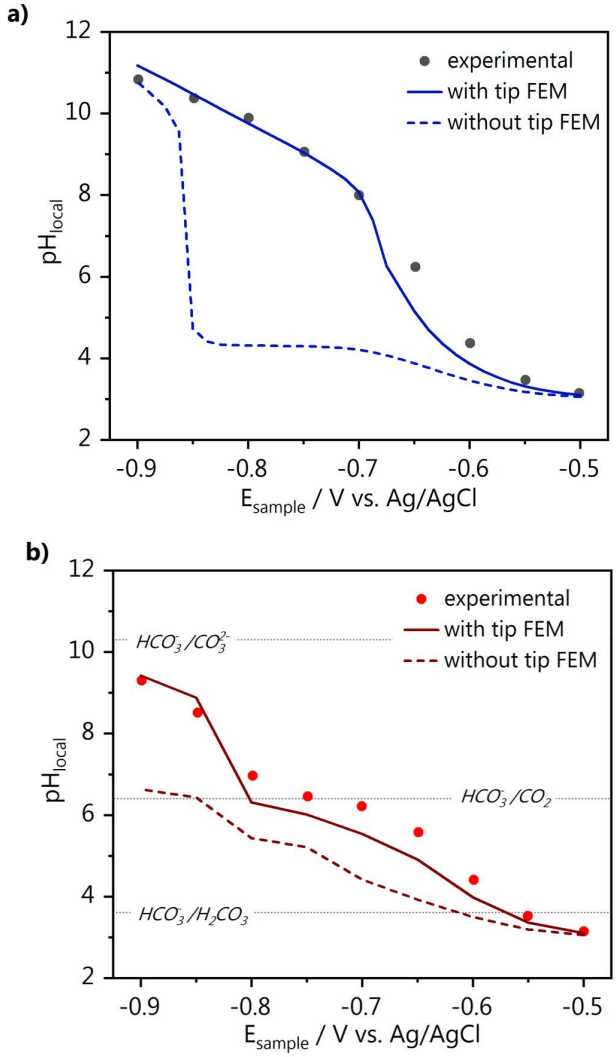

Fig. 4.6. FEM modeling of the pH response measured with SECM. **a)** Hydrogen evolution pH–potential comparison of experimental results in argon (black dots) and FEM simulation results (blue line) for L = 3.4 (close to the surface), compared to the case when the tip is far from the surface (L = 50, blue dashed line). The simulated pH "without tip" is obtained from a cross section at 80 µm from the surface with the tip removed to 1.25 mm from the surface (L = 50); L is the normalized tip-surface separation (see Experimental Section). **b)** Similarly, experimental (red dots) and simulation (dark red line) pH under CO_2 reduction for L = 3.4, is compared to simulated L = 50 (dark red dashed line). Bulk CO_2 concentration was fixed at 10 mM.

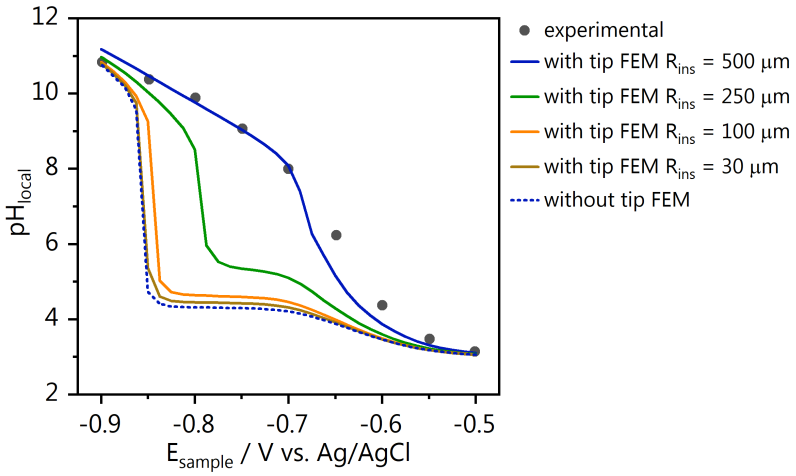

Fig. 4.7. Minimization of tip effects by decreasing the insulation radius. Comparison is made for the experiment in argon, using the results from Fig. 6a, and simulations decreasing the insulation radii, with a constant R_{tip}. The bottom tip insulation radius is maintained at ½ R_{ins} (see Fig. A.8 in Appendix A).

layer, like platinum. Alternatively, decreasing the radius of the tip (R_{tip}) will also decrease the diffusion hindrance and change the profiles shown in Fig. 4.7.

Coupling SECM measurements with FEM simulations is a resourceful way to account for the physical blocking effect that the SECM probe has on interfacial concentration profiles. Our case is concerned with proton concentration, but the approach also applies to the detection of other species in solution, participating or not in a catalytic reaction. On the other hand, this hindrance of diffusion can also be intentionally introduced to induce a high local alkalinity in a controlled fashion, and allow the study of homogeneous and inhomogeneous reactions taking place in the diffusion layer, as shown in this and our other recent work.[25]

4.5 Conclusions

In this Chapter, we have shown that our recently developed SECM pH sensor based on a 4-HATP/4-NSTP functionalized Au-UME is suitable for monitoring the pH in the diffusion layer during CO_2 reduction with high time resolution. We performed experiments using a polycrystalline gold substrate and monitored the pH as a function of potential at a fixed distance from the surface, in both argon and CO_2 atmospheres. Starting from bulk pH 3, we see a gradual increase in pH in argon as the potential applied is more negative, while in the presence of CO_2, a buffering

region is present, keeping the pH around the pK_a of the $CO_2 \rightleftharpoons HCO_3^-$ reversible reaction. By observing the time dependent pH decay once the reaction at the sample is turned "off" as a function of applied potential, we probe how the local pH and the rate of the homogenous reactions involving CO_2, HCO_3^-, CO_3^{2-} influence the time required to bring the diffusion layer pH back to the bulk value. Finally, we have accounted for the effect the SECM tip has on the measured pH by performing FEM simulations. We see how the presence of the tip leads to an overestimation of the local pH, due to the hindered diffusion of species generated by the substrate. Although in this work this hindered diffusion was intentional, we also show with FEM simulations to which extent this effect can be circumvented by, for example, decreasing the radius of the tip insulation layer.

References

(1) Kortlever, R.; Shen, J.; Schouten, K. J. P.; Calle-Vallejo, F.; Koper, M. T. M. *J. Phys. Chem. Lett.* 2015, *6* (20), 4073–4082.
(2) Bagger, A.; Ju, W.; Varela, A. S.; Strasser, P.; Rossmeisl, J. *ChemPhysChem* 2017, *18* (22), 3266–3273.
(3) Yu, F.; Wei, P.; Yang, Y.; Chen, Y.; Guo, L.; Peng, Z. *Nano Mater. Sci.* 2019, *1* (1), 60–69.
(4) Vennekötter, J.-B.; Scheuermann, T.; Sengpiel, R.; Wessling, M. *J. CO2 Util.* 2019, *32*, 202–213.
(5) Moura de Salles Pupo, M.; Kortlever, R. *ChemPhysChem* 2019, *20* (22), 2926–2935.
(6) Kas, R.; Kortlever, R.; Yılmaz, H.; Koper, M. T. M.; Mul, G. *ChemElectroChem* 2015, *2* (3), 354–358.
(7) Varela, A. S.; Kroschel, M.; Reier, T.; Strasser, P. *Catal. Today* 2016, *260*, 8–13.
(8) Marcandalli, G.; Goyal, A.; Koper, M. T. M. *ACS Catal.* 2021, 4936–4945.
(9) Schouten, K. J. P.; Pérez Gallent, E.; Koper, M. T. M. *J. Electroanal. Chem.* 2014, *716*, 53–57.
(10) Varela, A. S.; Kroschel, M.; Leonard, N. D.; Ju, W.; Steinberg, J.; Bagger, A.; Rossmeisl, J.; Strasser, P. *ACS Energy Lett.* 2018, *3* (4), 812–817.
(11) Raciti, D.; Mao, M.; Park, J. H.; Wang, C. *J. Electrochem. Soc.* 2018, *165* (10), F799–F804.
(12) Resasco, J.; Chen, L. D.; Clark, E.; Tsai, C.; Hahn, C.; Jaramillo, T. F.; Chan, K.; Bell, A. T. *J. Am. Chem. Soc.* 2017, *139* (32), 11277–11287.
(13) Thorson, M. R.; Siil, K. I.; Kenis, P. J. A. *J. Electrochem. Soc.* 2012, *160* (1), F69–F74.
(14) Ringe, S.; Clark, E. L.; Resasco, J.; Walton, A.; Seger, B.; Bell, A. T.; Chan, K. *Energy Environ. Sci.* 2019, *12* (10), 3001–3014.
(15) Pérez-Gallent, E.; Marcandalli, G.; Figueiredo, M. C.; Calle-Vallejo, F.; Koper, M. T. M. *J. Am. Chem. Soc.* 2017, *139* (45), 16412–16419.
(16) Hong, S.; Lee, S.; Kim, S.; Lee, J. K.; Lee, J. *Catal. Today* 2017, *295* (July), 82–88.
(17) Resasco, J.; Lum, Y.; Clark, E.; Zeledon, J. Z.; Bell, A. T. *ChemElectroChem* 2018, *5* (7), 1064–1072.
(18) Goyal, A.; Marcandalli, G.; Mints, V. A.; Koper, M. T. M. *J. Am. Chem. Soc.* 2020, *2* (1).
(19) Schulz, K. G.; Riebesell, U.; Rost, B.; Thoms, S.; Zeebe, R. E. *Mar. Chem.* 2006, *100* (1–2), 53–65.
(20) Monteiro, M. C. O.; Koper, M. T. M. *Curr. Opin. Electrochem.* 2021, *25* (November), 100649.
(21) Yang, K.; Kas, R.; Smith, W. A. *J. Am. Chem. Soc.* 2019, *141* (40), 15891–15900.
(22) Ayemoba, O.; Cuesta, A. *ACS Appl. Mater. Interfaces* 2017, *9* (33), 27377–27382.
(23) Zhang, Z.; Melo, L.; Jansonius, R. P.; Habibzadeh, F.; Grant, E. R.; Berlinguette, C. P. *ACS Energy Lett.* 2020, *5* (10), 3101–3107.
(24) Zhang, F.; Co, A. C. *Angew. Chemie Int. Ed.* 2020, *59* (4), 1674–1681.
(25) Monteiro, M. C. O.; Jacobse, L.; Koper, M. T. M. *J. Phys. Chem. Lett.* 2020, *11* (22), 9708–9713.
(26) García, G. *ChemElectroChem* 2017, *4* (3), 459–462.
(27) Gisbert, R.; García, G.; Koper, M. T. M. *Electrochim. Acta* 2011, *56* (5), 2443–2449.
(28) Dieckhöfer, S.; Öhl, D.; Junqueira, J. R. C.; Quast, T.; Turek, T.; Schuhmann, W. *Chem. – A Eur. J.* 2021, *27* (19), 5906–5912.
(29) Monteiro, M. C. O.; Jacobse, L.; Touzalin, T.; Koper, M. T. M. *Anal. Chem.* 2020, *92* (2), 2237–2243.

(30) Touzalin, T. Sorbonne Université, 2018.
(31) Voogd, J. M. De; Spronsen, M. A. Van; Kalff, F. E.; Bryant, B.; Ostoji, O.; Haan, A. M. J. Den; Groot, I. M. N.; Oosterkamp, T. H.; Otte, A. F.; Rost, M. J. *Ultramicroscopy* 2017, *181*, 61–69.
(32) Critelli, R. A. J.; Bertotti, M.; Torresi, R. M. *Electrochim. Acta* 2018, *292*, 511–521.
(33) Shinagawa, T.; Garcia-Esparza, A. T.; Takanabe, K. *Sci. Rep.* 2015, *5* (1), 13801.

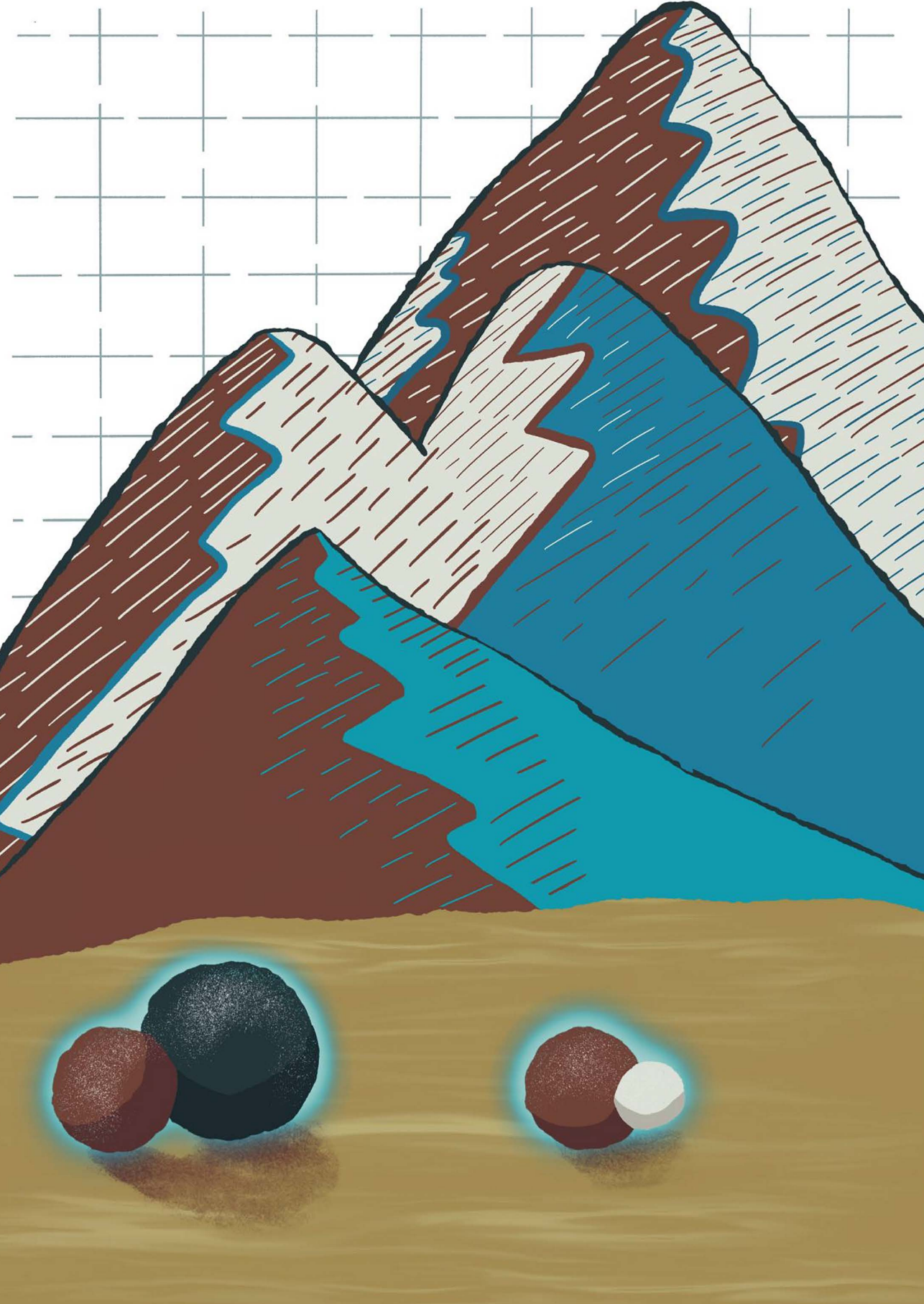

5

Understanding the voltammetry of bulk CO electrooxidation in neutral media through combined SECM measurements

This chapter is based on Monteiro, M. C. O., Jacobse, L., Koper, M. T. M. *J. Phys. Chem. Lett.*, *11 (22)*, 9708–9713 (2020)

Abstract

Recently, the bulk electrooxidation of CO on gold or platinum has been used to detect CO produced during CO_2 reduction in neutral media. The CO bulk oxidation voltammetry may show two distinct peaks depending on the reaction conditions, which up to now have not been understood. We have used Scanning Electrochemical Microscopy (SECM) to probe CO oxidation and pH in the diffusion layer during CO_2 reduction. Our results show that the two different peaks are due to diffusion limitation by two different species, namely CO and OH^-. We find that between pH 7 and 11, CO oxidation by water and OH^- gives rise to the first and second peak observed in the voltammetry, respectively. Additional rotating disc experiments showed that specifically in this pH range the current of the second peak is diffusion limited by the OH^- concentration, since it is lower than the CO concentration.

5.1 Introduction

The electrochemical oxidation of CO on gold[1–4] and platinum[5–9] has been widely studied, especially how pH and surface structure affect the reaction.[10–12] Recently, CO oxidation on these two surfaces has been used in Rotating Ring Disc Electrode (RRDE)[13–15], Scanning Electrochemical Microscopy (SECM)[16,17], and cyclic voltammetry[18] experiments for in-situ probing the products of CO_2 reduction (CO_2RR) or the interfacial pH. In these studies, mostly carried out in neutral media, two distinct or convoluted peaks have been observed in the CO oxidation voltammetry [13,14,16–18], but their assignment is unclear. While the oxidation of a CO adlayer has been extensively studied on mono and polycrystalline platinum at different pH, there are no reports elucidating the mechanism of CO bulk oxidation on platinum in neutral media. These conditions are of special interest as the typical CO_2RR reaction environment.

In general, the electrochemical oxidation of CO is believed to take place through a Langmuir−Hinshelwood mechanism, similar to the gas phase reaction. It is proposed that an adsorbed CO is oxidized by a nearest-neighbor oxygen containing species. The oxygen donor is generally believed to be OH_{ad} from water in acidic (Eq. 5.1) or from OH^- in alkaline (Eq. 5.2) media, respectively.[19]

$$H_2O \rightarrow OH_{ad} + H^+ + e^- \quad \text{Eq. 5.1}$$

$$OH^- \rightarrow OH_{ad} + e^- \quad \text{Eq. 5.2}$$

$$CO_{ad} + OH_{ad} \rightarrow CO_2 + H^+ + e^- \quad \text{Eq. 5.3}$$

Especially on gold electrodes, previous work has shown that CO oxidation takes place at higher overpotentials in acidic than in alkaline media.[3] As studies on bulk CO oxidation have previously been carried out only in strongly acidic or alkaline conditions, there is currently no consistent explanation for the coexistence of two peaks in the bulk CO electrooxidation voltammetry in neutral media.

Using platinum cyclic voltammetry to determine CO_2RR products is a relatively new approach. Narayanaru et al.[16] used a platinum ultramicroelectrode (Pt-UME) in the substrate generation-tip collection (SG-TC) mode of SECM to probe the products of CO_2RR on gold in 0.1 M $KHCO_3$ electrolyte. Two distinct CO oxidation peaks were observed in the Pt-UME voltammetry when the gold sample was held at –1.3 V vs. Ag/AgCl. Although a shift in the CO oxidation peak potential was observed as a function of sample roughness, and attributed to interfacial pH changes, the nature of the two different CO oxidation peaks was not discussed. In the same work, CO oxidation on gold directly after CO_2RR was also performed and

two distinct anodic peaks were observed in the CO oxidation region. The authors attributed the peak at more positive potential to the oxidation of CO and the peak at less positive potential to the oxidation of methanol. Recently, Zhang and Co[13] reported the use of a RRDE with CO_2RR performed on a gold disc while oxidation of the reaction products is carried out on a platinum ring. A broad CO oxidation peak is observed on the platinum ring, which seems actually a convolution of two different peaks. The broadness of the peak was explained by the presence of bubbles and not further discussed. In the same work, CO oxidation was carried out on the polycrystalline Pt ring in CO saturated 0.1 M $KHCO_3$ at pH 6.8 and 9.2. At pH 9.2 two distinct peaks were observed and attributed to CO oxidation taking place at {100} facets and {111} facets of the Pt-UME.

To better understand bulk CO oxidation in the CO_2RR reaction environment, in this chapter, we have used a Pt-UME in the SG-TC mode of SECM while CO_2RR was carried out at a gold substrate. Using the functionalized gold pH sensor from Chapter 3, we have used SECM to also measure the pH in the diffusion layer under the same reaction conditions and approximately same tip-to-surface distance.[20] The correlation of these results and additional Rotating Disc Electrode (RDE) measurements provide a clear understanding on the nature of the two different CO oxidation peaks previously observed[13,14,16–18], and how they are influenced by the interfacial pH. Our measurements show the nature of the oxygen donor as a function of pH, and how in a narrow pH window the diffusion of these species and not (only) the diffusion of CO itself is what limits the current of the oxidation reaction and gives rise to the specific voltammetry. We emphasize that CO diffusion in this chapter refers to CO bulk diffusion, not to CO surface diffusion as it has been studied in CO stripping experiments.[10,11]

5.2 SECM CO oxidation measurements

To probe CO oxidation while CO_2RR and the competing hydrogen evolution (HER) are taking place at the gold sample, a Pt-UME is used. A schematic representation of the experiment is shown in Fig. 5.1a. The blank and CO stripping cyclic voltammetry (CV) of the Pt-UME can be seen in Fig. 5.1c. The Pt-UME used here has a radius of approximately 6.5 ± 0.07 µm, determined with the $Fe(CN)_6^{3-}$/ $Fe(CN)_6^{4-}$ outer sphere reaction (see Fig. B.1 in Appendix B). After characterization of the Pt-UME, a capacitive approach[20,21] is performed in air in order to determine the tip-to-surface distance. Fig. 5.1d shows a measured

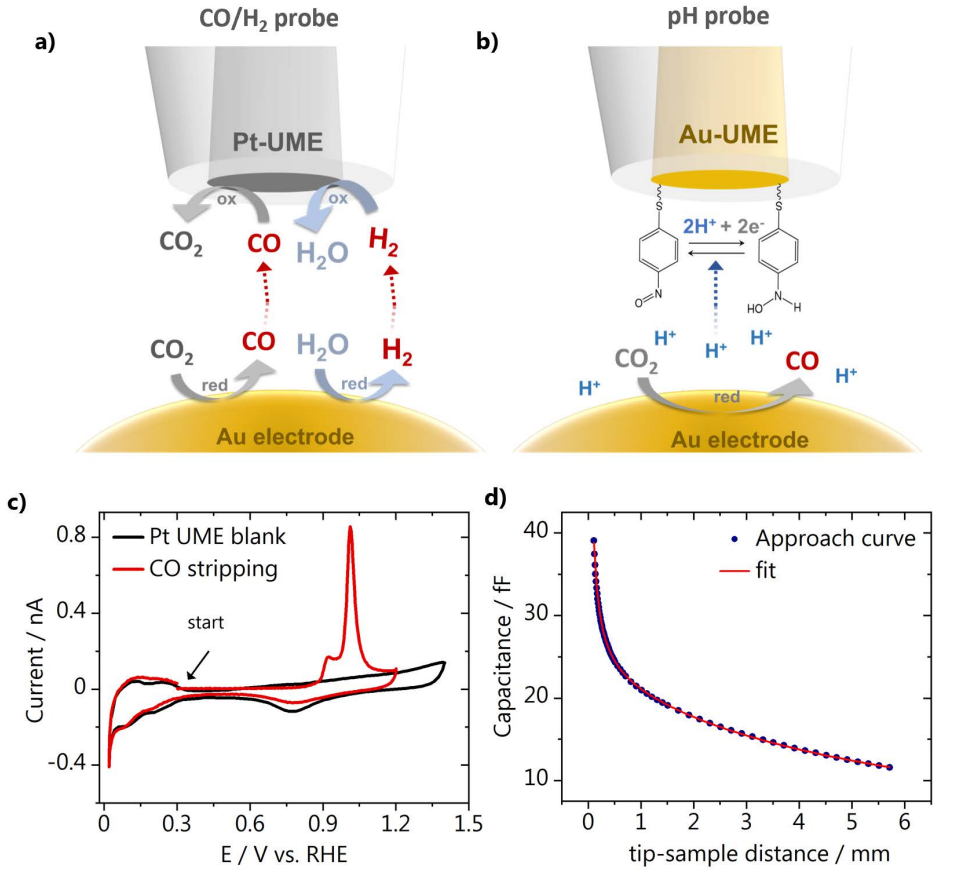

Fig. 5.1. Schematic representation of **a)** the SG-TC collection mode of SECM, where a Pt-UME is used to probe CO and H_2 while CO_2 reduction takes place at the gold sample, **b)** the functionalized Au-UME used to measure pH, **c)** Pt-UME blank voltammetry (black) taken in argon saturated 0.1 M H_2SO_4 and CO stripping voltammetry measured in the same electrolyte after exposing the Pt-UME to a CO atmosphere for 5 minutes. CVs taken at 200 mV s^{-1}. **d)** Capacitive approach curve to determine the absolute tip-to-surface distance.

approach curve (data points) together with its fit (line). Details on the capacitive approach curve measurement and fitting are available in Chapter 3 and Appendix B (Fig. B.2). To minimize the influence of the tip in the diffusion process, it was placed at a relatively large distance of 40 ± 3 µm from the surface.

During CO_2RR, the composition of the reaction interface changes significantly due to OH^- generation. Consequently, the local pH depends on the sample potential. To investigate the nature of the two distinct peaks in the bulk CO oxidation voltammetry, we have created different CO_2RR reaction environments

around the Pt-UME, by using an unbuffered electrolyte (0.1 M Cs_2SO_4, pH = 3) and changing the potential at which the reaction is carried out at the gold substrate.

The Pt-UME voltammetry is constantly recorded while chronoamperometry at the sample is carried out at different potentials. The chronoamperometry data from the gold sample can be found in Fig. B.3 in Appendix B. Fig. 5.2 shows the results obtained at different sample potentials. Ten cycles of the Pt-UME were recorded, and the 10th cycle is displayed. It can be seen that at low sample potentials (Fig. 5.2a) only hydrogen is produced at the gold sample as the tip voltammetry shows features characteristic of hydrogen oxidation (HOR).[22] The HOR current increases when going from –0.1 to –0.3 V but stops increasing between –0.3 and –0.4 V likely due to diffusion limitation of the proton reduction reaction taking place at the surface. At these potentials, no strong pH gradients are expected and bicarbonate is present only in trace amounts, as the pK_a of the $CO_{2(aq)} + H_2O \rightleftharpoons HCO_3^- + H^+$ equilibrium reaction is 6.4. At –0.5 V (sample potential) CO starts being formed. This leads to the poisoning of the Pt-UME for HOR, and a small CO oxidation peak appears in the forward scan (see Fig. 5.2b). This peak gradually increases and shifts slightly positive going from –0.5 to –0.65 V, due to a higher concentration of CO in solution. For simplicity, from now on we will call this "peak I". In the backward scan, a peak due to HOR is still observed at sample potentials –0.5 and –0.55 V, which decreases due to the increase in CO concentration. At –0.6 and –0.65 V only current due to bulk CO oxidation is seen at the Pt-UME voltammetry and a subtle shoulder appears, which we will call "peak II". The shape of the CO oxidation CV with the hysteresis between forward and backward scans is typical for bulk CO oxidation on Pt, and discussed in detail elsewhere.[23]

Fig. 5.2c shows results obtained at sample potentials –0.7 and –0.75 V. At –0.7 V the CO oxidation peak shows a clear shoulder in the Pt-UME voltammetry at 0.45 V vs. Ag/AgCl due to an increase of peak II. At –0.75 V peak II gradually increases while peak I decreases. Here, three subsequent Pt-UME CVs are plotted to show this peak I/peak II transition. This transition suggests a strong change in the reaction environment when –0.75 V is applied to the gold sample. If the rate of OH^- production becomes higher than the rate at which bicarbonate can be formed, the alkalinity near the surface will increase and the concentration of OH^- will become larger than the concentration of HCO_3^-. The coexistence of peak I and peak II strongly suggests that two different mechanisms for CO oxidation are taking place

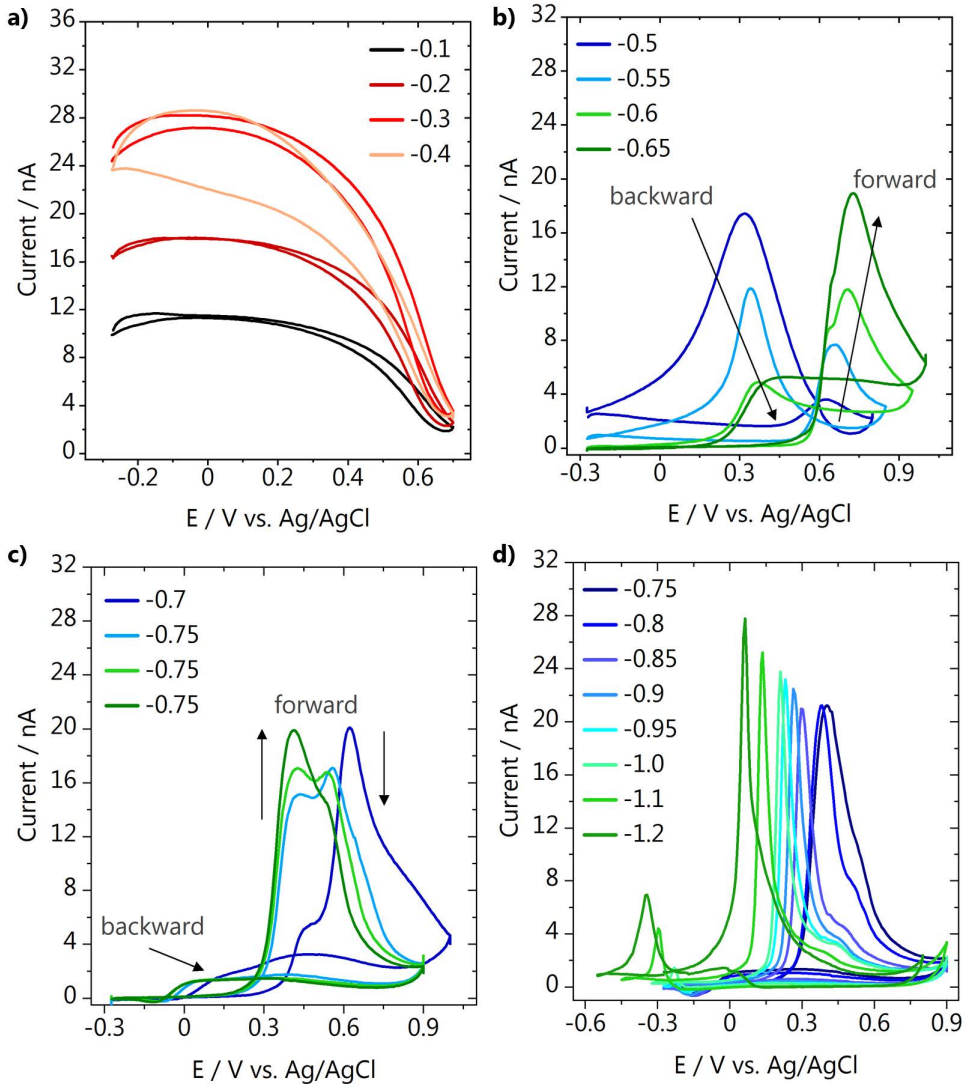

Fig. 5.2. Pt-UME voltammetry recorded in 0.1 M Cs_2SO_4 (200 mV s^{-1}, pH = 3) while CO_2RR and/or HER take place at the gold sample at potentials **a)** from –0.1 to –0.4 V, **b)** from –0.5 to –0.65 V, **c)** from –0.7 to –0.75 V and **d)** from –0.75 to –1.2 V. The gold sample potentials shown in the legend are reported versus the reversible hydrogen electrode.

simultaneously as a function of the reaction environment, i.e. OH^- concentration. At more negative sample potentials, it can be seen in the Pt-UME voltammetry (Fig. 5.2d) that peak I is still present, but gradually becomes less pronounced. Peak II shifts to more negative potentials, likely due to an increase in local alkalinity. At –1 V sample potential, a small peak appears in the backward scan at –0.23 V vs. Ag/AgCl due to hydrogen oxidation.

To better understand the mechanism behind bulk CO oxidation and the diffusion processes taking place, the currents of peak I and peak II are evaluated separately by holding the gold sample at potentials where either peak I or peak II are present (–0.65 and –0.9 V vs. RHE). By varying the scan rate at which the Pt-UME voltammetry is recorded, we can gain insights into the nature of the species participating in the reaction and limiting the current, as the peak current can be calculated following the Randles-Sevcik equation[24]:

$$i_p = 2.69 * 10^5 * n^{3/2} * A * D^{1/2} * C * \nu^{1/2} \qquad \text{Eq. 5.4}$$

where n is the number of electrons transferred, A is the electrode surface area, D is the diffusion coefficient of the reacting species that limits the current and C its concentration, and ν is the scan rate. The peak current plotted as a function of the square root of the scan rate can be seen in Fig. 5.3. The two different slopes

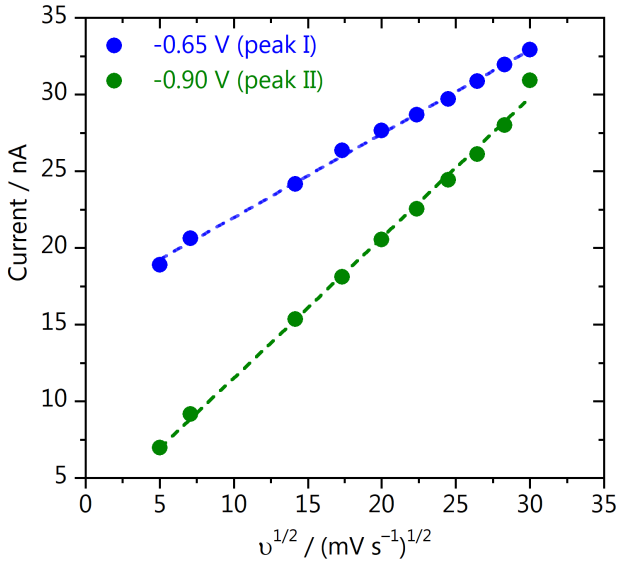

Fig. 5.3. Scan rate dependency of the CO oxidation peak current measured at the Pt-UME. Measurements were performed at two different sample potentials to evaluate separately the CO oxidation peak I (blue) and peak II (green).

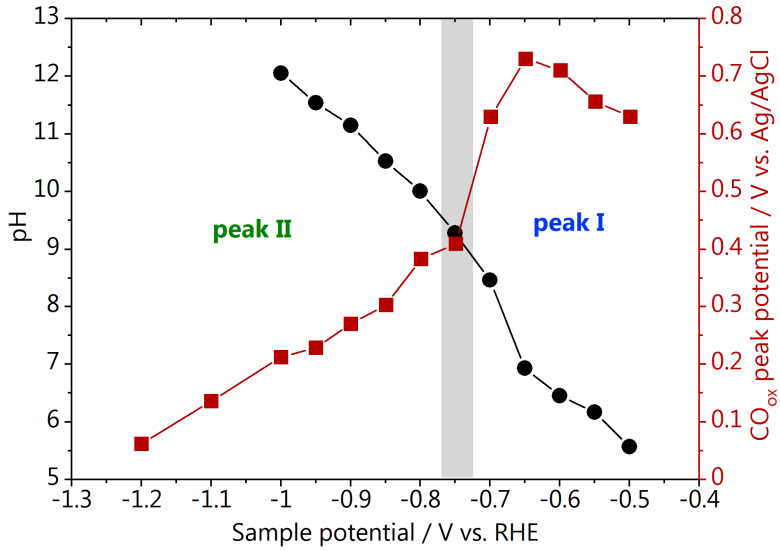

Fig. 5.4. Correlation between the pH measurements performed with a functionalized Au-UME (black circles) with the CO oxidation peak position extracted from the measurements performed with the Pt-UME (red squares) during CO_2 reduction on gold (0.1 M Cs_2SO_4, pH = 3, CO_2 saturated).

found indicate that the reaction is limited by the diffusion of two different species, giving rise to the two observed peaks in the voltammetry. However, derivation of the diffusion coefficient for identification of the species is not possible here, as the exact concentration of the reactants is unknown.

5.3 SECM local pH measurements

To gain better insights into the reaction interface when these two peaks coexist, SECM pH measurements were performed under the same conditions as the previously shown H_2/CO oxidation experiments. Here, the tip is a functionalized gold ultramicroelectrode (Au-UME) pH sensor. The Au-UME used here has a radius of approximately 26.9 ± 0.05 µm, determined with the $Fe(CN)_6^{3-}/Fe(CN)_6^{4-}$ outer sphere reaction (see Fig. B.1 in Appendix B). As can be seen in the scheme in Fig. 5.1b the gold surface is modified with a self-assembled monolayer containing the hydroxylaminothiophenol/4-nitrosothiophenol redox couple. The pH sensing is realized by recording the tip cyclic voltammetry and monitoring the Nernstian shift of the midpeak potential. Details on the sensor fabrication and data processing can be found in Chapter 3, Appendix A and Appendix B.[20] The Au-UME is positioned at

the same distance from the surface as the Pt-UME (40 ± 3 μm) and the tip voltammetry is recorded while changing the sample potential. The pH measurements in time can be found in Fig. B.4 in the Appendix B. The measured pH as a function of sample potential is displayed in Fig. 5.4 together with the peak potential of the CO oxidation peaks from Fig. 5.2. At low sample potentials neither the pH increases, nor the CO oxidation peak I shifts negatively. In this potential range the $CO_{2(aq)} \rightleftharpoons HCO_3^-$ equilibrium buffers the interfacial pH, which value remains near the pK_a of the equilibrium reaction (6.4). At –0.75 V sample potential, where the transition between peak I and peak II is observed (Fig. 5.2c), there is an increase in pH from 7.7 to 9 and the CO oxidation peak also starts to shift negatively. The correlation showed in Fig. 5.4 suggests that peak I exists at neutral pH, and therefore water is the oxygen donor for CO oxidation. As peak II appears when the buffer breaks down and the interface becomes more alkaline, it seems that peak II corresponds to CO being oxidized by OH^-. However, these findings still do not elucidate why different slopes were found in Fig. 5.3, which suggests that the current of peak I and II is limited by two different species, which could be: OH^-, CO, or HCO_3^-.

5.4 Rotating Disc Electrode (RDE) experiments

To assign the species leading to the diffusion limiting current observed for peak I and II, we performed rotating disc electrode (RDE) experiments using a polycrystalline platinum disc The blank voltammetry of the platinum electrode is seen in Fig. B.6 in Appendix B. Fig. 5.5 displays the results obtained in pure 0.1 M Cs_2SO_4 (pH = 7.2) and when 0.03, 0.06 and 1 mM of KOH are added to the electrolyte, leading to pH 9.5, 9.8 and 11, respectively. The electrolyte is saturated with CO during all the measurements, leading to a constant CO concentration of 1 mM. Fig. 5.5a shows the voltammetry of bulk CO oxidation in the different electrolytes taken at 400 rpm. In pure Cs_2SO_4 (neutral pH) only one diffusion limiting plateau is seen between 1.2 and 1.6 V vs. RHE, corresponding to peak I previously observed in the SECM measurements. When 0.03 mM KOH is added to the electrolyte, two plateaus are observed. One with a similar current as before, between 1.2 and 1.6 V vs. RHE, and another with lower diffusion limiting current, between 0.8 and 1.2 V vs. RHE (peak II). Increasing the OH^- concentration leads to an increase in the diffusion limiting current of peak II, confirming the correlation found in the SECM measurements between peak II and pH. At pH 11 (1mM KOH), only one peak is observed at lower overpotentials, with a current matching the one

found at pH 7.2. To elucidate which species cause diffusion limitation in each condition, measurements were also performed at different rotation rates (see Fig. B.7 in Appendix B). The Levich equation describes the relationship between the diffusion limiting current and the rotation rate and can be used to derive the diffusion coefficient of the species leading to the diffusion limitation:[24]

$$j_{lim} = 0.62 * n \quad * F * D^{2/3} * \nu^{-1/6} \ * C * \omega^{1/2} \qquad \text{Eq. 5.5}$$

where n is the number of electrons transferred, F is the Faraday constant, D is the diffusion coefficient of the species, ν is the kinematic viscosity of the solvent, C is

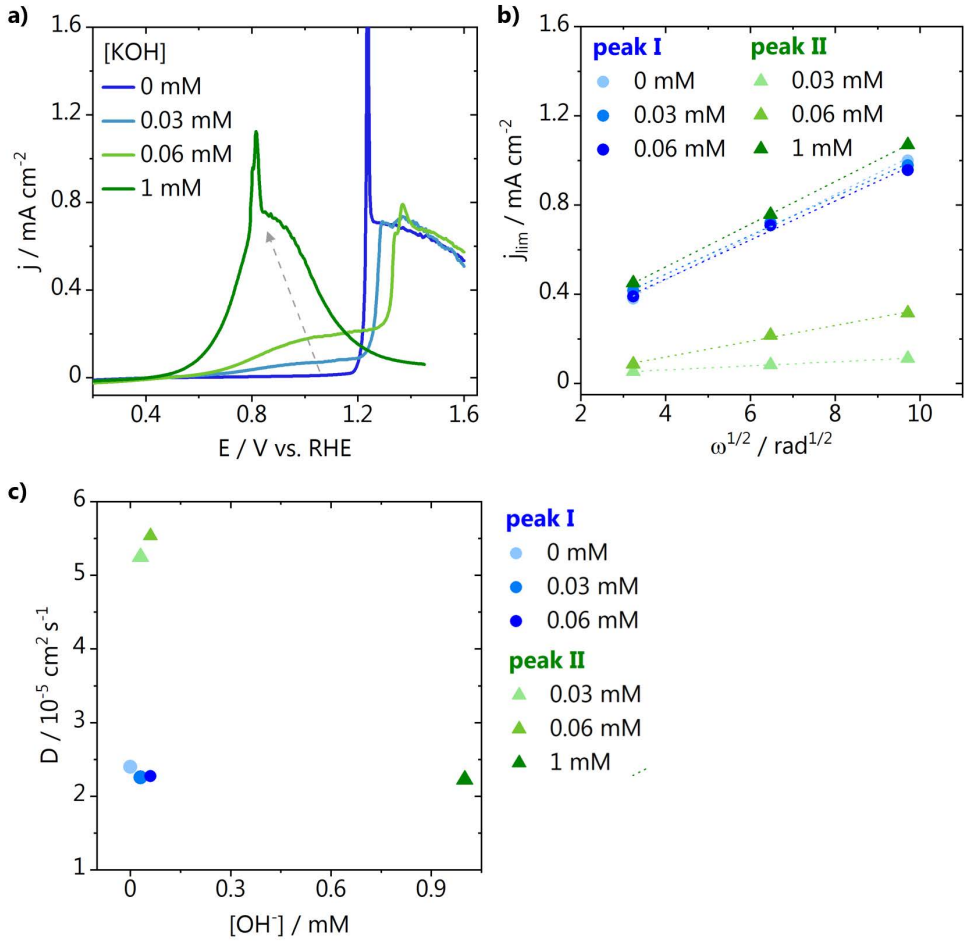

Fig. 5.5. RDE CO oxidation measurements on a polycrystalline Pt disc in Cs_2SO_4 (pH = 7.2) performed at 400 rpm with 25 mV s^{-1} scan rate. **a)** Reaction performed in the presence of different concentrations of KOH, **b)** Levich plot and **c)** derivation of the diffusion coefficients for peak I (blue circles) and peak II (green triangles).

the concentration of the species and ω is the rotation rate. The diffusion limiting currents obtained at the different rotations for the plateaus corresponding to peak I and II are shown in Fig. 5.5b as a function of the square root of the rotation rate. The diffusion coefficients are derived from the slopes obtained in Fig. 5.5b and are displayed in Fig. 5.5c. It can be seen that for peak I, the same slope is found in pure Cs_2SO_4 and in the presence of 0.03 and 0.06 mM of OH^-. The diffusion coefficients calculated all approximate the theoretical value reported for CO which is $2.03 \cdot 10^{-5}$ cm^2 s^{-1}, confirming that the current of peak I is limited by the diffusion of CO.[25] In the case of peak II, interestingly, a different slope is found as a function of the OH^- concentration. When the OH^- concentration is lower than the CO concentration (1 mM), a slope of approximately $5.5 \cdot 10^{-5}$ cm^2 s^{-1} is found based on the OH^- concentration, corresponding to the value reported for OH^- ions ($5.23 \cdot 10^{-5}$ cm^2 s^{-1}).[25] This clearly shows that in this pH range, OH^- is not only the oxygen donor but also the species whose transport limits the reaction. When the $[OH^-]$ = [CO] = 1mM the slope found is similar to the one of peak I and derivation of the diffusion coefficient based on the CO concentration again matches the value reported in literature for CO. The latter implies that at pH 11 or higher, only one peak is present, and the current is limited by the diffusion of CO.

5.5 Discussion and Conclusions

Based on the two different SECM measurements and the RDE results, we can now build a clear understanding of the nature of the two peaks observed during bulk CO electrooxidation in neutral media. As summarized in Table 5.1, at acidic and neutral pH, OH^- is present in small concentrations and CO is oxidized by water. The current is limited by the concentration of CO in solution and only one peak is observed in the voltammetry at high overpotential: peak I. Between pH 7 and 11, two peaks coexist in the CO oxidation voltammetry: peak I and peak II. Peak II appears at lower overpotentials than peak I and is due to CO oxidation by OH^-. The current is limited by the OH^- concentration. Above pH 11, only peak II is present due to CO oxidation by OH^-, and the current is limited again by the concentration of CO, which becomes smaller than the OH^- concentration in this pH range. Even though methanol has been previously observed as a product of CO_2 reduction on roughened gold electrodes[16], we can exclude that methanol oxidation gives rise to peak II. We have analyzed the CO_2RR products formed in the conditions of this study (flat gold electrode, 0.1 M Cs_2SO_4, pH = 3) with online chromatography

Table 5.1. Relationship between pH, j_{lim} species and the bulk CO electrooxidation voltammetry.

pH	O-donor	j_{lim} species	voltammetry
≤ 7	H_2O	CO	peak I
11 > pH > 7	H_2O, OH^-	OH^-	peak I + peak II
≥ 11	OH^-	CO	peak II

(Fig. B.8 in Appendix B). The only products detected are hydrogen and CO, at potentials for which peak I and II are observed.

Summarizing, in the present work we have used SECM in SG-TC mode to probe CO oxidation on a Pt-UME while CO_2RR to CO takes place on a gold sample. By changing the local reaction environment, we could observe the existence of two distinct peaks in the CO oxidation voltammetry as a function of pH. SECM local pH measurements were also performed demonstrating a clear correlation between the OH^- concentration and the coexistence of the two distinct CO oxidation peaks. Additional RDE measurements confirmed that the peaks coexist in a narrow pH range in which the OH^- concentration is smaller than the CO concentration (between pH 7 and 11), which results in two diffusion limited current regimes. It is now clear why these two peaks are mainly observed when probing CO_2 reduction[13,14,16–18], as the pH in the CO_2 reduction reaction environment usually lies in between the CO_2/HCO_3^- pK_a and more alkaline values that develop according to the current density and buffer capacity of the electrolyte used. Considering the increased number of publications where CO oxidation is being used to probe CO_2 reduction, we hope the work presented in this Chapter provides the basis for the correct assignment of the two distinct peaks often observed in the CO oxidation voltammetry.

References

(1) Kita, H.; Nakajima, H.; Hayashi, K. *J. Electroanal. Chem.* 1985, *190* (1–2), 141–156.
(2) Rodriguez, P.; Garcia-Araez, N.; Koper, M. T. M. *Phys. Chem. Chem. Phys.* 2010, *12* (32), 9373–9380.
(3) Rodriguez, P.; Koper, M. T. M. *Phys. Chem. Chem. Phys.* 2014, *16* (27), 13583–13594.
(4) Rodriguez, P.; Plana, D.; Fermin, D. J.; Koper, M. T. M. *J. Catal.* 2014, *311*, 182–189.
(5) Grgur, B. N.; Marković, N. M.; Lucas, C. A.; Ross, P. N. *J. Serbian Chem. Soc.* 2001, *66* (11–12), 785–797.
(6) Kita, H.; Shimazu, K.; Kunimatsu, K. *J. Electroanal. Chem.* 1988, *241* (1–2), 163–179.
(7) Abe, K.; Uchida, H.; Inukai, J. *Surfaces* 2019, *2* (2), 315–325.
(8) Park, I. S.; Chen, D. J.; Atienza, D. O.; Tong, Y. J. *Catal. Today* 2013, *202* (1), 175–182.
(9) Wang, H.; Abruña, H. D. *J. Phys. Chem. Lett.* 2015, *6* (10), 1899–1906.
(10) Lai, S. C. S.; Lebedeva, N. P.; Housmans, T. H. M.; Koper, M. T. M. *Top. Catal.* 2007, *46* (3–4), 320–333.
(11) García, G.; Koper, M. T. M. *ChemPhysChem* 2011, *12* (11), 2064–2072.
(12) Gisbert, R.; García, G.; Koper, M. T. M. *Electrochim. Acta* 2011, *56* (5), 2443–2449.
(13) Zhang, F.; Co, A. C. *Angew. Chemie Int. Ed.* 2020, *59* (4), 1674–1681.
(14) Zhang, F.; Co, A. C. *J. Electrochem. Soc.* 2020, *167* (4), 046517.
(15) Goyal, A.; Marcandalli, G.; Mints, V. A.; Koper, M. T. M. *J. Am. Chem. Soc.* 2020, *2* (1), 4154–4161.
(16) Narayanaru, S.; Chinnaiah, J.; Phani, K. L.; Scholz, F. *Electrochim. Acta* 2018, *264*, 269–274.
(17) Sreekanth, N.; Phani, K. L. *Chem. Commun.* 2014, *50* (76), 11143–11146.
(18) Lee, C. W.; Cho, N. H.; Nam, K. T.; Hwang, Y. J.; Min, B. K. *Nat. Commun.* 2019, *10* (1), 1–8.
(19) McPherson, I. J.; Ash, P. A.; Jones, L.; Varambhia, A.; Jacobs, R. M. J.; Vincent, K. A. *J. Phys. Chem. C* 2017, *121* (32), 17176–17187.
(20) Monteiro, M. C. O.; Jacobse, L.; Touzalin, T.; Koper, M. T. M. *Anal. Chem.* 2020, *92* (2), 2237–2243.
(21) Voogd, J. M. De; Spronsen, M. A. Van; Kalff, F. E.; Bryant, B.; Ostoji, O.; Haan, A. M. J. Den; Groot, I. M. N.; Oosterkamp, T. H.; Otte, A. F.; Rost, M. J. *Ultramicroscopy* 2017, *181*, 61–69.
(22) Sheng, W.; Zhuang, Z.; Gao, M.; Zheng, J.; Chen, J. G.; Yan, Y. *Nat. Commun.* 2015, *6*, 6–11.
(23) Koper, M. T. M.; Schmidt, T. J.; Marković, N. M.; Ross, P. N. *J. Phys. Chem. B* 2001, *105* (35), 8381–8386.
(24) Bard, A. J.; Faulkner, L. R. 2nd ed.; John Wiley & Sons, 2001.
(25) Haynes, W. M. 95th ed.; CRC Press: New York, 2014.

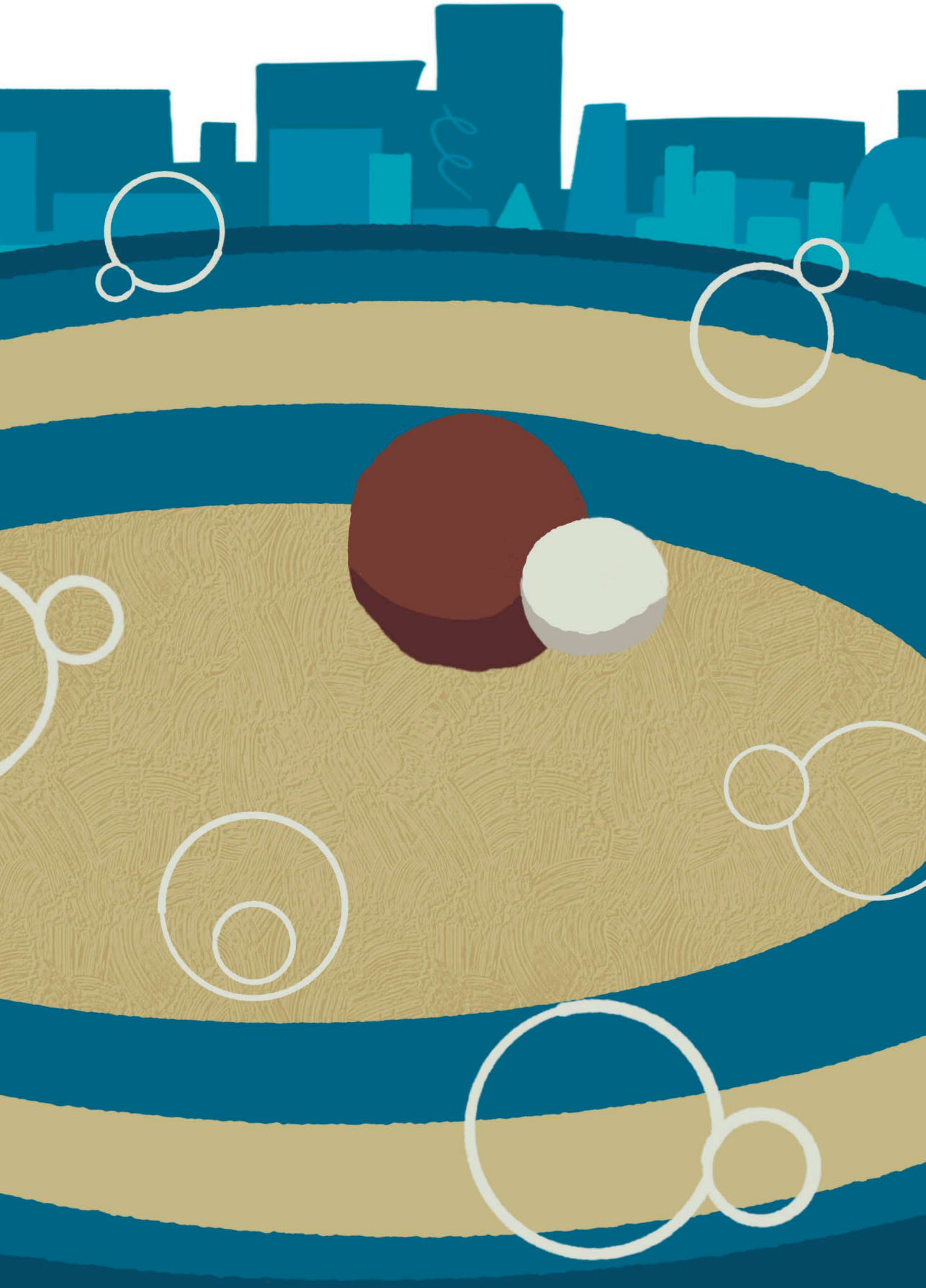

6

Interfacial pH measurements using a Rotating Ring-Disc electrode with a voltammetric pH sensor

This chapter is based on Monteiro, M. C. O., Liu, X., Hagedoorn, B. J. L., Snabilié, D., Koper, M. T. M. *ChemElectroChem*, *8,* DOI: 10.1002/celc.202101223 (2021)

Abstract

Electrochemical reactions in which H^+ or OH^- ions are produced or consumed, affect the pH near the electrode surface. Probing the pH locally is therefore highly desired to understand and model the reaction environment under *operando* conditions. We carried out interfacial pH measurements under mass transport control using a rotating ring-disc electrode (RRDE) coupled with our recently developed voltammetric pH sensor. The interfacial disc pH is detected by functionalizing the gold ring with a hydroxylaminothiophenol (4-HATP)/4-nitrosothiophenol (4-NSTP) redox couple. As protons only have to interact with a monolayer containing the 4-HATP/4-NSTP, the sensitivity and time resolution that can be achieved are superior to potentiometric sensors. We used hydrogen evolution as a model reaction and performed measurements in buffered and unbuffered electrolytes. The effects of the current density, potential, the buffer capacity of the electrolyte and rotation rate on the interfacial pH were investigated. This work shows a reliable and sensitive method for accurately probing the reaction environment under well-defined mass transport conditions, over a wide pH range.

6.1 Introduction

The electrochemical reactions that consume/produce protons or hydroxyl ions can generate a pH gradient between the electrode surface and the bulk of the electrolyte. In general, the value of the local pH developed at the surface is a function of the current drawn, the electrolyte composition, and the mass transport conditions.[1] It has been shown that the (local) electrolyte pH plays a significant role in various reactions, such as hydrogen evolution[2] (HER), CO_2 reduction[3], oxygen evolution[4] and reduction[5], among others. Therefore, it is highly desired to probe the pH gradient near the surface during these electrochemical reactions, with high sensitivity, and with good time and spatial resolution.

In Chapter 2 we review the main techniques available for performing local pH measurements[1], the most frequently used ones being Scanning Electrochemical Microscopy (SECM)[6–8], Scanning Ion Conductance Microscopy (SICM)[9,10], Scanning Ion Selective Electrode (SIET), Rotating Ring-Disc Electrode (RRDE)[11–14], confocal fluorescence scanning microscopy[15], infra-red[16,17] and Raman spectroscopy.[18] Among these, RRDE is the only technique that allows for measurements to be performed under well-defined mass transport conditions, at the expense of the in-plane spatial resolution. Firstly introduced by Albery and Calvo[19–21], pH measurements using RRDE consist of a reaction taking place at the disc electrode and the detection of the proton concentration during the course of this reaction by a pH sensing material at the ring electrode. Due to the electrode geometry and rotation, the flow of species going from the disc to the ring is described by a convective-diffusion equation. This allows the interfacial pH observed at the ring electrode to be directly converted into the pH at the surface of the disc electrode. The advantage is that the detection by the ring electrode does not affect the reactions taking place on the disc electrode. The analytical solution derived by Albery and Calvo[19–21] was recently further developed by Yokoyama et al.[22] by including the autoprotolysis of water in the description, which allows for determining the disc pH more accurately in a wider pH range.

A few works on interfacial pH measurements with RRDE have been reported, however mainly potentiometric pH sensors were employed, the most common being iridium oxide (IrO_x).[11,13,14] The ring electrode is normally modified with an IrO_x film and the pH at the disc is determined based on the Nernstian open circuit potential (OCP) response of the ring. A major drawback of using IrO_x is that the stability and time resolution depend, for example, on the film thickness and pH.[23,24]

Besides IrO_x, certain reactions on bare metal surfaces have also been used to estimate changes in interfacial pH. Figueiredo et al.[12] used shifts in the equilibrium potential of the hydrogen evolution reaction on a Pt ring to estimate the disc pH during ethanol oxidation. Zhang et al. used the CO oxidation reaction on a gold ring to probe the interfacial disc pH during CO_2 reduction to CO on gold.[13] However, it is known that the sensitivity and accuracy of these measurements can be highly compromised by the reaction environment, as both HER and CO oxidation have shown to be affected, i.e. by the cation[25–27], surface structure[28,29] and pH.[30,31] Also, buffering species in the electrolyte are not always taken into account when converting the pH measured at the ring to the interfacial disc pH, which may lead to an overestimation of the local alkalinity. Besides that, based on the analytical description of Yokoyama et al.[22], a small change in pH detected by the ring may correspond to an order of magnitude higher changes of the interfacial disc pH, especially in solutions far from neutral pH. Therefore, a more sensitive pH sensor for RRDE is desired, and in fact necessary, for performing accurate interfacial pH measurements with this technique.

In this Chapter, we have assessed the feasibility of using our recently developed voltammetric pH sensor (Chapter 3) in the RRDE configuration. The sensor consists of a self-assembled monolayer on gold, and in Chapters 3-5 was used for pH measurements in the diffusion layer with SECM.[32,33] The pH response is based on the voltammetry of the hydroxylaminothiophenol (4-HATP)/4-nitrosothiophenol (4-NSTP) redox couple, specifically the Nernstian shift of the oxidation reaction mid-peak potential. We show here that the 4-HATP/4-NSTP voltammetric response is not affected by the electrode rotation, and that this redox couple can be used in a RRDE system. We employed it to probe the interfacial disc pH during hydrogen evolution in buffered and unbuffered electrolytes at mildly acidic pH. With the high sensitivity and time resolution of this voltammetric sensor, we measured the interfacial disc pH during cyclic voltammetry, chronoamperometry and chronopotentiometry experiments, and also determined the rotation rate required to minimize interfacial pH changes in the electrolytes studied. The application of this sensitive and reliable pH sensor for RRDE pH measurements presents an alternative to commonly used potentiometric sensors, and a step forward to more accurately probing the reaction environment under well-defined mass transport conditions.

6.2 Functionalization of the ring electrode

Interfacial pH measurements during hydrogen evolution (HER) using a rotating ring-disc electrode (RRDE) were performed using the electrode assembly schematically represented in Fig. 6.1a. Prior to measurements, the gold ring and disc electrodes are characterized by blank voltammetry, to assure a clean and reproducible surface (see Fig. C.3a in Appendix C). For the pH sensing, the gold ring is modified with a self-assembled monolayer of 4-NTP, which is then electrochemically converted to the 4-HATP/4-NSTP redox couple by cyclic voltammetry, as shown in Fig. 6.1b. The 4-NTP modified gold ring is immersed in the electrolyte under potential control (0.3 V vs. Ag/AgCl) and then a cathodic sweep at 100 mV s^{-1} is performed to partially reduce the monolayer to 4-HATP. The voltammetry of the resulting 4-HATP/4-NSTP redox couple is also shown in Fig. 6.1b recorded at 200 mV s^{-1} (in red), which is the scan rate used during the pH measurements. In principle, even higher scan rates can be used (up to 500 mV s^{-1}), if the process being studied requires better time resolution. Different from our previous work (Chapter 3-5), here the molecule conversion was performed in the same electrolyte as in which HER was carried out. We find that it gives similar results as in the previously used 0.1 M H_2SO_4 if the 60 mV/pH Nernstian shift of the potential window is taken into account. We show here the voltammetry for the conversion in 0.1 M K_2SO_4 at pH = 4 (Fig. 6.1b). In Fig. C.3b in Appendix C, the same is shown in 0.1 KH_2PO_4 and 0.1 M H_2SO_4, for comparison. The molecule conversion has also been successfully performed in, for example, perchlorate and bicarbonate electrolytes, although not shown here.

Before performing the interfacial pH measurements, we have investigated if the rotation of the electrode has any influence on the 4-HATP/4-NSTP response. The ring voltammetry (CV) was constantly recorded while the rotation rate was varied. Results are shown in Fig. 6.1c going from 0 to 2600 rpm. Each data point is the average mid-peak potential (E_{peak}) determined from 10 consecutive cycles together with the standard deviation, and the corresponding CVs are shown in the graph inset. We observe a stable E_{peak} of 0.109 V vs. Ag/AgCl for all rotation rates. There is a slight decrease in the absolute ring current, however this does not affect the peak fitting and extraction of E_{peak}. These results assure that any changes in the ring voltammetry during HER are due to the reaction taking place at the disc, and not affected by the rotation rate or the turbulence of the electrolyte. This is very important, especially when working far from neutral pH. As shown in Fig. 6.1d,

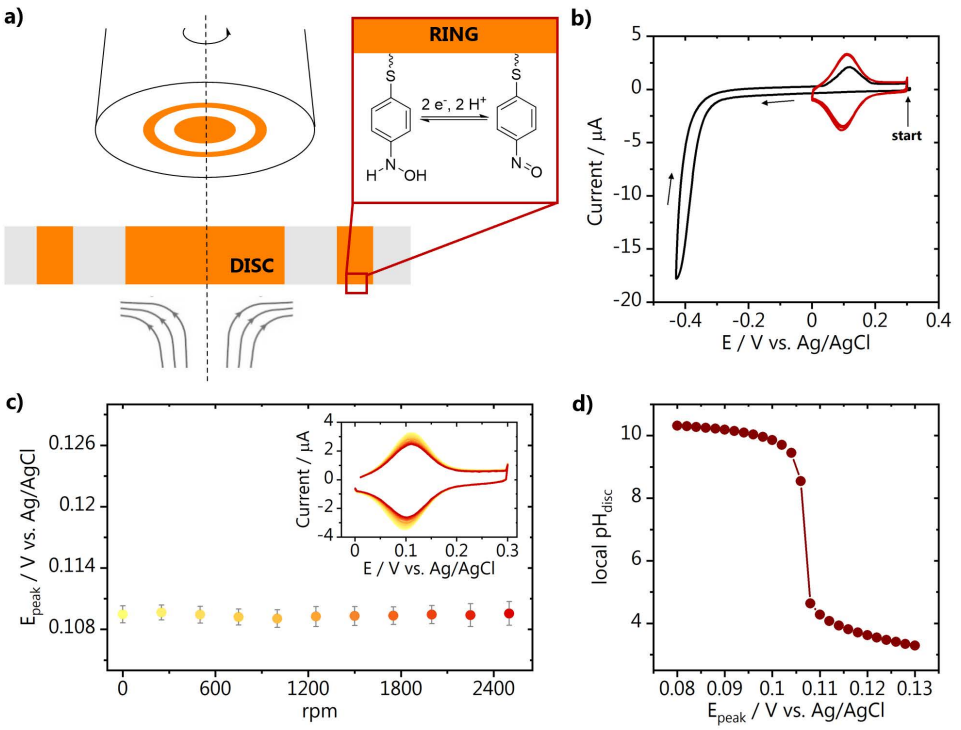

Fig. 6.1. a) Schematic representation of the RRDE with the functionalized ring; **b)** cyclic voltammetry of the 4-NTP to 4-HATP conversion (black, 100 mV s^{-1}) together with a characterization of the 4-HATP/4-NSTP redox couple (red, 200 mV s^{-1}). Both were recorded in 0.1 M K_2SO_4, pH = 4. **c)** Effect of rotation on the pH sensor mid-peak potential, extracted from the voltammograms shown in the inset. **d)** Theoretical relationship between E_{peak} and pH_{disc} using Eq. C.2 for pH_∞ = 4.

considering an unbuffered electrolyte with a bulk pH of 4, a difference of 20 mV in E_{peak} corresponds to a change in pH_{disc} of 7 pH units. The entire E_{peak} range plotted is actually only 50 mV, which corresponds to the detection of a change of less than a unit in the interfacial ring pH. This also indicates how important it is that the pH sensor employed for RRDE measurements is sensitive and stable enough, to measure the interfacial pH accurately. Fig. C.2 in Appendix C shows the theoretical relationships between pH_{Disc} and pH_{Ring} at various pH_∞, comparing Eq. C.2 (Yokoyama) and Eq. C.1 (Albery and Calvo) for an unbuffered electrolyte. The theoretical relationship that can be obtained using the correction we applied for phosphate buffered solutions of different bulk pH is shown in Fig. C.2c. Further experimental details are found in Appendix C.

6.3 Interfacial pH measurements during hydrogen evolution

We employed the modified ring electrode to measure the development of the interfacial pH during a cyclic voltammogram on the gold disc. Hydrogen evolution voltammetry was carried out in phosphate and sulfate electrolyte and the correlation between the current density and the measured interfacial disc pH can be seen in Fig. 6.2a and Fig. 6.2b, respectively. It is important to point out that the conversion from the measured ring pH to the disc pH is done differently for the experiment in unbuffered sulphate electrolyte in comparison to the phosphate

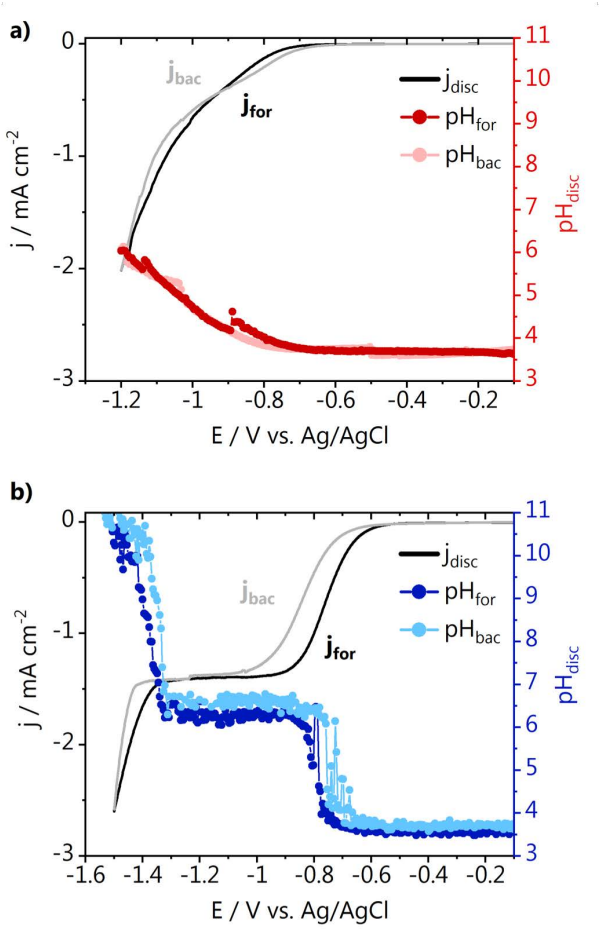

Fig. 6.2. Interfacial pH measurement during the disc cyclic voltammetry in 0.1 M argon saturated at 2000 rpm in **a)** KH_2PO_4 pH_{bulk} = 3.7 and **b)** K_2SO_4 pH_{bulk} = 3.5. CVs were recorded at 2 mV s^{-1} and the 4-HATP/4-NSTP CVs at 200 mV s^{-1}. The forward and backward scans are indicated as j_{for}, pH_{for} and j_{bac}, pH_{bac}.

buffer. For sulphate, the analytical description of Yokoyama et al.[22] is used (Eq. C2 in Appendix C). In the case of phosphate, we have added a correction to account for the homogeneous reactions involving the different phosphate species ($H_2PO_4^-$, HPO_4^-, PO_4^-) that take place upon increase in the local alkalinity (see Eq. C.7-C.29 in the section C.2 "Calculation of the interfacial disc pH" in Appendix C). In Fig. 6.2, we observe that the pH profiles are nearly a mirror image of the current density in both phosphate and sulphate electrolytes. In Fig. 6.2a, we see a gradual increase in current and interfacial pH from 0 to –0.9 V vs. Ag/AgCl. At more negative potentials there is steeper increase in current, likely due to the transition from proton reduction to water and biphosphate reduction as the main branch of HER taking place.[34] Despite the high current, the interfacial disc pH does not go above 6, due to the buffer capacity of the phosphate electrolyte used. In sulphate electrolyte (Fig. 6.2b) a more well-defined plateau is present due to diffusion limited proton reduction ($2H^+ + 2e^- \rightarrow H_2$) followed by a steep increase in current due to water reduction ($2H_2O + 2e^- \rightarrow H_2 + 2OH^-$). The activity for proton reduction starts to increase at about –0.55 V vs. Ag/AgCl and a consequent increase in the interfacial disc pH starts to be observed from –0.57 V vs. Ag/AgCl onwards. This slight delay of 20 mV in the pH response in comparison to the current response is likely because at the very low overpotentials the reaction is only limited by the rate of charge transfer at the electrode-solution interface and there are no pronounced changes in the local proton concentration. At potentials more negative than –0.57 V vs. Ag/AgCl a combination of charge and mass transfer processes control the reaction, and the interfacial pH starts increasing. In the potential window in which the diffusion limited proton reduction plateau is observed, the interfacial disc pH remains around 6.5, until the activity for water reduction increases and consequently the interfacial pH gradually becomes more alkaline. The differences in activity between phosphate and sulphate electrolyte are likely due to the fact that it has been shown that phosphate can outcompete water as a proton donor for hydrogen evolution.[34] We see that due to the high time resolution achieved with the 4-HATP/4-NSTP sensor in combination with the low scan rate of the CV (2 mV s^{-1}), detailed information regarding the correlation between current and pH can be obtained. In principle, the disc voltammetry can also be recorded at higher scan rates, at the expense of the resolution of the pH measurement.

Next, we have performed pH measurements while applying different potentials to the disc electrode. In between potential steps, HER was turned “off”

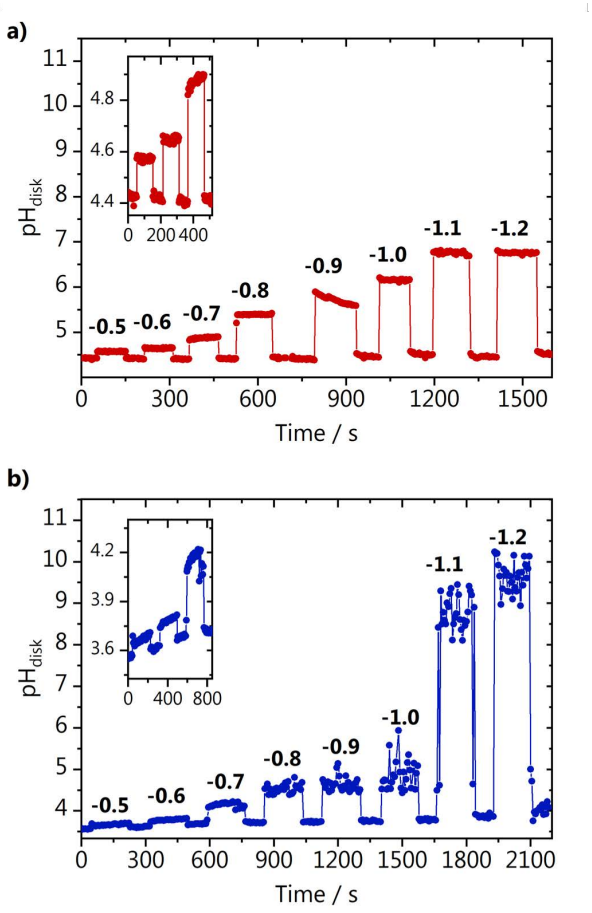

Fig. 6.3. Interfacial pH measurement during chronoamperometry (potentials indicated in the graph in V vs. Ag/AgCl) in 0.1 M argon saturated **a)** KH_2PO_4 pH_{bulk} = 4.4 and **b)** K_2SO_4 pH_{bulk} = 3.6 at 1600 rpm.

by applying 0 V vs. Ag/AgCl to the disc and the ring voltammetry was constantly recorded. The current and potential recorded in time can be seen in Fig. C.4 in Appendix C. Results are shown in Fig. 6.3 for HER carried out in phosphate and sulphate electrolyte. The increase in interfacial pH as a function of potential here is slightly larger than what was observed for the cyclic voltammetry from Fig. 6.2. This is due to the lower rotation rate (1600 rpm) employed during the chronoamperometry, slowing down the transport of species away from the electrode surface. At the low overpotentials, we can accurately detect differences in

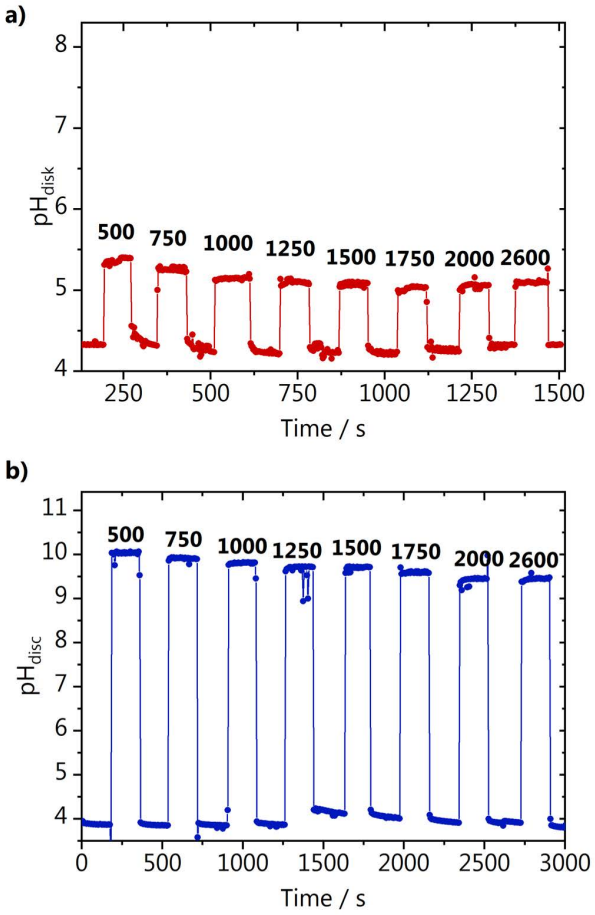

Fig. 6.4. Interfacial pH measurements during chronopotentiometry (constant current density = –0.42 mA cm^{-2}) in 0.1 M argon saturated **a)** KH_2PO_4 pH_{bulk} = 4.4 and **b)** K_2SO_4 pH_{bulk} = 4.0 at the different rotations indicated in the graph in rpm.

interfacial pH as small as 0.1 pH unit, which has not been previously reported for RRDE pH measurements. This is due to the better sensitivity of the 4-HATP/4-NSTP redox couple used in this work compared to the commonly used pH sensors. The insets in Fig. 6.3a and Fig. 6.3b show the pH measured at –0.5, –0.6 and –0.7 V vs. Ag/AgCl, and highlight how the interfacial pH in the phosphate electrolyte always returns to the bulk pH value once the reaction is turned "off". The same does not happen in sulphate, where the baseline keeps increasing due to the lower buffer capacity of the electrolyte. The phosphate electrolyte has different strong buffering regions, namely at pH values around the pK_a of the following reversible reactions:

$H_3PO_4 \rightleftharpoons H_2PO_4^-$ (pK_a = 2.3), $H_2PO_4^- \rightleftharpoons HPO_4^{2-}$ (pK_a = 7.2) and $H_2PO_4^- \rightleftharpoons PO_4^{3-}$ (pK_a = 12.1). In contrast, in the sulfate electrolyte, only one equilibrium reaction is present ($HSO_4^- \rightleftharpoons SO_4^{2-}$) with pK_a = 1.8, considerably lower than the pH developed during HER. It is important to point out that fluctuations of the pH response as observed, for example, at large overpotentials in Fig. 6.3b, occur due to bubbles accumulating near the ring electrode. Even though in this work this did not compromise the measurements, for more challenging systems (or working conditions) this can be circumvented by coating the spacer that separates the ring and the disc electrodes with dopamine.[35]

The buffer capacity of the electrolyte, the current density, and especially the rotation rate, determine the magnitude of the pH gradients developed during RRDE experiments. Therefore, we have also probed to which extent enhancing mass transport affects the interfacial disc pH by performing chronopotentiometry measurements in the same phosphate and sulphate electrolytes. The reaction was turned "on" and "off" by applying a constant current density of –0.4 mA cm^{-2} or –0.001 mA cm^{-2} to the disc, at different rotation rates (see Fig. C.5 in Appendix C for the current and potential recorded). Fig. 6.4 a shows the interfacial disc pH during HER in phosphate electrolyte at different rotation rates. Although the changes in pH are not drastic, we see that between 500 and 1000 rpm, the convective flow of species is not high enough to avoid a larger increase in the local alkalinity, despite the buffer capacity of the electrolyte. Still, the interfacial pH when HER is "on" decreases by increasing the rotation rate. At rotations higher than 1250 rpm, a steady state is reached, i.e. the highest flux of species outwards is achieved and increasing rotation no longer decreases the local alkalinity. This happens because a maximum efficiency at which species move from the disc to the ring is reached, as also discussed in the work of Zimer et al.[11] Due to the buffering species in the phosphate electrolyte, which have easier access to the surface at the higher rotations, the interfacial disc pH in phosphate equilibrates at values around 5.2 at steady state. A different behaviour is observed in the sulphate electrolyte (Fig. 6.4b). Here, although increasing rotation also gradually decreases the interfacial disc pH, a stable pH is never reached at high rotation rates, due to the low buffer capacity of the electrolyte. Additionally, the interfacial disc pH never returns to the bulk value when the reaction is turned "off" (in between different rotations), similarly to what we observed in the chronoamperometry experiment in sulfate (inset of Fig. 6.3b). It is important to point out that even though the calculated interfacial disc pH changes are relatively large, the differences in E_{peak} recorded at the ring electrode

are rather small. Fig. C.6 in Appendix C exemplifies that with the E_{peak} recorded for the experiments shown in Fig. 6.4. The changes in E_{peak} observed during the whole experiment are in the 15-40 mV range, highlighting once more how important it is to employ a sensitive pH sensor for RRDE pH measurements.

6.4 Discussion

The results shown demonstrate that, even though RRDE systems are used to avoid (or minimize) concentration gradients during electrochemical reactions, the effectiveness of the enhancement in mass transport is highly dependent on the electrolyte buffer capacity and on the currents drawn. Assuming "well-defined mass transport conditions" when working with RRDE does therefore not imply absence of concentration gradients, as we see that (in our working conditions) the interfacial disc pH can vary up to 6-7 pH units from the bulk pH. This has important consequences, for example, for measurements performed as a function of rotation rate going from low to high rotations. The interfacial pH values will be significantly different, and their effect is difficult to deconvolute, unless proper quantification of the pH is carried out. In the electrolytes studied, even with a relatively high buffer capacity (phosphate electrolyte) and rotation rates (> 1250 rpm), the interfacial disc pH differed by 1 unit from the bulk. Operating in the steady state regime (strong buffer, high rotations) minimizes convoluted responses due to differences in the interfacial disc pH. However, as evidenced by our results, this regime is strongly dependent on the electrolyte and reaction activity, and has to be identified for each individual system studied. Using the 4-HATP/4-NSTP redox couple as pH sensor on the ring electrode, allows to do so with high temporal resolution and sensitivity. The synthesis of the functionalized gold ring shown in this work is much simpler than what was previously reported for IrO_x[11], highly reproducible, and the system is versatile in terms of disc materials that can be employed, and reactions to be studied.[33] Finally, even though the analytical description from Albery and Calvo[19–21] and Yokoyama et al.[22] is accurate for calculating pH_{disc} for measurements performed in unbuffered electrolytes, here we present a method to correct the description when working in buffered solutions. This is crucial to avoid an overestimation of the interfacial disc pH in buffered systems.

6.5 Conclusions

In this work we have shown that RRDE interfacial pH measurements can be performed with high sensitivity and temporal resolution using a voltammetric pH sensor. A gold ring functionalized with the 4-HATP/4-NSTP redox couple has been used to study pH gradients developing during hydrogen evolution at a gold disc electrode. The interfacial disc pH is measured in phosphate or sulphate electrolyte during different electrochemical experiments: cyclic voltammetry, chronoamperometry and chronopotentiometry. We observed that the changes in interfacial pH at the disc strongly depend on the buffer capacity of the electrolyte and the current drawn (i.e. the activity). By varying the rotation rate at constant current density, we identify the minimum rotation required to achieve the maximum enhancement of mass transport possible and avoid strong concentration gradients during the electrocatalytic measurements. Using HER as a model system, we show that the 4-HATP/4-NSTP voltammetric pH sensor is a powerful tool for accurately measuring interfacial pH with RRDE, with high time resolution.

References

(1) Monteiro, M. C. O.; Koper, M. T. M. *Curr. Opin. Electrochem.* 2021, *25*, 100649.
(2) Goyal, A.; Koper, M. T. M. *Angew. Chemie Int. Ed.* 2021, *60* (24), 13452–13462.
(3) Zhang, Z.; Melo, L.; Jansonius, R. P.; Habibzadeh, F.; Grant, E. R.; Berlinguette, C. P. *ACS Energy Lett.* 2020, *5* (10), 3101–3107.
(4) Giordano, L.; Han, B.; Risch, M.; Hong, W. T.; Rao, R. R.; Stoerzinger, K. A.; Shao-Horn, Y. *Catal. Today* 2016, *262*, 2–10.
(5) Li, M. F.; Liao, L. W.; Yuan, D. F.; Mei, D.; Chen, Y.-X. *Electrochim. Acta* 2013, *110*, 780–789.
(6) Monteiro, M. C. O.; Jacobse, L.; Touzalin, T.; Koper, M. T. M. *Anal. Chem.* 2020, *92* (2), 2237–2243.
(7) Santos, C. S.; Lima, A. S.; Battistel, D.; Daniele, S.; Bertotti, M. *Electroanalysis* 2016, *28* (7), 1441–1447.
(8) Dieckhöfer, S.; Öhl, D.; Junqueira, J. R. C.; Quast, T.; Turek, T.; Schuhmann, W. *Chem. – A Eur. J.* 2021, *27* (19), 5906–5912.
(9) Nadappuram, B. P.; McKelvey, K.; Al Botros, R.; Colburn, A. W.; Unwin, P. R. *Anal. Chem.* 2013, *85* (17), 8070–8074.
(10) Morris, C. A.; Chen, C. C.; Ito, T.; Baker, L. A. *J. Electrochem. Soc.* 2013, *160* (8), H430–H435.
(11) Zimer, A. M.; Medina da Silva, M.; Machado, E. G.; Varela, H.; Mascaro, L. H.; Pereira, E. C. *Anal. Chim. Acta* 2015, *897*, 17–23.
(12) Figueiredo, M. C.; Arán-Ais, R. M.; Climent, V.; Kallio, T.; Feliu, J. M. *ChemElectroChem* 2015, *2* (9), 1254–1258.
(13) Zhang, F.; Co, A. C. *Angew. Chemie - Int. Ed.* 2020, *59* (4), 1674–1681.
(14) Steegstra, P.; Ahlberg, E. *J. Electroanal. Chem.* 2012, *685*, 1–7.
(15) Leenheer, A. J.; Atwater, H. A. *J. Electrochem. Soc.* 2012, *159* (9), H752–H757.
(16) Yang, K.; Kas, R.; Smith, W. A. *J. Am. Chem. Soc.* 2019, *141* (40), 15891–15900.
(17) Ayemoba, O.; Cuesta, A. *ACS Appl. Mater. Interfaces* 2017, *9* (33), 27377–27382.
(18) Henckel, D. A.; Counihan, M. J.; Holmes, H. E.; Chen, X.; Nwabara, U. O.; Verma, S.; Rodríguez-López, J.; Kenis, P. J. A.; Gewirth, A. A. *ACS Catal.* 2021, *11* (1), 255–263.
(19) Albery, W. J.; Calvo, E. J. *J. Chem. Soc. Faraday Trans. 1 Phys. Chem. Condens. Phases* 1983, *79* (11), 2583–2596.
(20) Albery, W. J.; Mount, A. R. *J. Chem. Soc. Faraday Trans. 1 Phys. Chem. Condens. Phases* 1989, *85* (5), 1181.
(21) Albery, W. J.; Mount, A. R. *J. Chem. Soc. Faraday Trans. 1 Phys. Chem. Condens. Phases* 1989, *85* (11), 3717.
(22) Yokoyama, Y.; Miyazaki, K.; Miyahara, Y.; Fukutsuka, T.; Abe, T. *ChemElectroChem* 2019, *6* (18), 4750–4756.
(23) Steegstra, P.; Ahlberg, E. *Electrochim. Acta* 2012, *76*, 26–33.
(24) Bard, A. J.; Mirkin, M. V. Second.; Bard, A. J., Mirkin, M. V., Eds.; CRC Press, 2012.
(25) Chen, X.; McCrum, I. T.; Schwarz, K. A.; Janik, M. J.; Koper, M. T. M. *Angew. Chemie - Int. Ed.* 2017, *56* (47), 15025–15029.
(26) García, G. *ChemElectroChem* 2017, *4* (3), 459–462.
(27) Xue, S.; Garlyyev, B.; Watzele, S.; Liang, Y.; Fichtner, J.; Pohl, M. D.; Bandarenka, A. S. *ChemElectroChem* 2018, *5* (17), 2326–2329.
(28) Rodriguez, P.; Koper, M. T. M. *Phys. Chem. Chem. Phys.* 2014, *16* (27), 13583–13594.

(29) García, G.; Koper, M. T. M. *ChemPhysChem* 2011, *12* (11), 2064–2072.
(30) Kita, H.; Shimazu, K.; Kunimatsu, K. *J. Electroanal. Chem.* 1988, *241* (1–2), 163–179.
(31) Rossmeisl, J.; Chan, K.; Skúlason, E.; Björketun, M. E.; Tripkovic, V. *Catal. Today* 2016, *262*.
(32) Monteiro, M. C. O.; Jacobse, L.; Touzalin, T.; Koper, M. T. M. *Anal. Chem.* 2020, *92* (2), 2237–2243.
(33) Monteiro, M. C. O.; Jacobse, L.; Koper, M. T. M. *J. Phys. Chem. Lett.* 2020, *11* (22), 9708–9713.
(34) Jackson, M. N.; Surendranath, Y. *J. Am. Chem. Soc.* 2016, *138* (9), 3228–3234.
(35) Vos, J. G.; Koper, M. T. M. *J. Electroanal. Chem.* 2019, *850*, 113363.

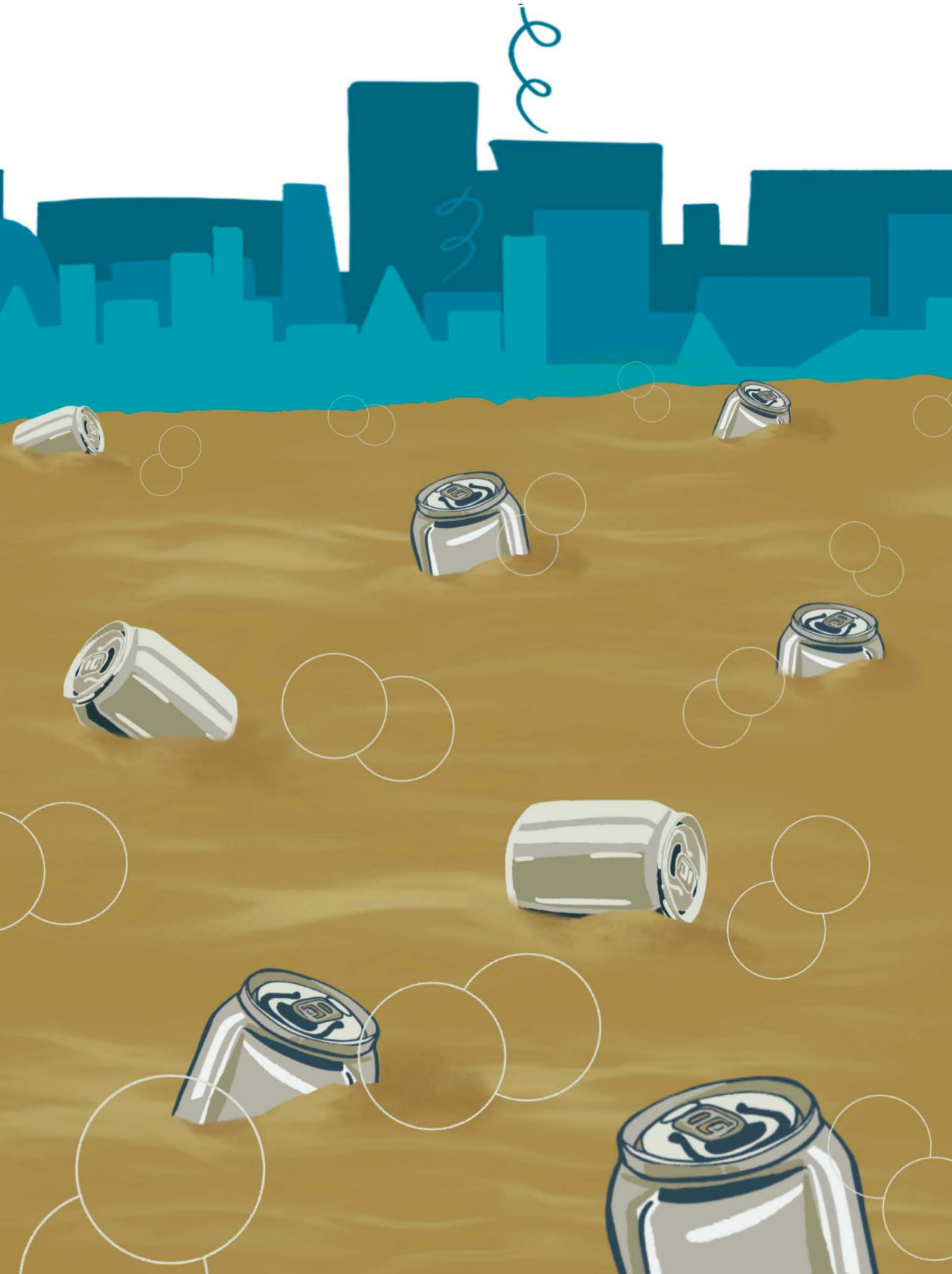

7

Alumina contamination through polishing and its effects on hydrogen evolution on gold electrodes

This chapter is based on Monteiro, M. C. O., Koper, M. T. M. *Electrochimica Acta, 325*, 134915 (2019)

Abstract

In this Chapter we show how the contamination of gold electrodes with alumina particles by electrode polishing leads to an enhancement in activity for hydrogen evolution (HER) in neutral media. Polishing is one of the most used electrode treatments, however, we show that particles from the polishing media cannot be easily removed from the electrode surface by standard cleaning procedures. Comparing the HER activity of gold disc electrodes polished with either diamond suspension or alumina paste, we show that the latter leads to higher current densities, specifically for the water reduction to hydrogen. A similar enhancement in HER activity was observed by the addition of Al^{3+} cations to the electrolyte, demonstrating that the particles are not catalytically active, but that the Al^{3+} species released in solution due to corrosion promote the water reduction reaction. Due to an increase in the local OH^- concentration during HER, the contaminating Al^{3+} cations precipitate and may deposit at the electrode surface as $Al(OH)_3$. In the presence of a high enough Al^{3+} concentration, layered $Al(OH)_3$ plates cover the whole electrode surface. The plates are composed of $Al(OH)_3$ sheets intercalated by sulphate anions. Surprisingly, the $Al(OH)_3$ sheets do not affect the gold blank voltammetry, and therefore remain undetected by simple electrochemical characterization methods.

7.1 Introduction

Gold electrocatalysts are widely studied for several oxidation[1] and reduction reactions[2–9], among which CO_2 reduction and the competing hydrogen evolution have gained a lot of attention recently.[10–12] Understanding these reactions at the atomistic level is key to the design and optimization of larger-scale processes. In fundamental electrocatalysis studies, electrodes are usually pre-treated, in order to obtain a clean, homogeneous and reproducible surface. The most common pre-treatments used for gold electrodes are: mechanical polishing, chemical etching, electropolishing, annealing, or a combination thereof.[13–15] However, the influence of different pre-treatments on the stability, structure, composition, and catalytic activity of gold electrodes is not well documented. Actually, most studies overlook the possibility of such an influence and do not report a detailed characterization of the pre-treated electrodes.

Flame annealing is the most reliable method to prepare electrodes and leads to a clean and (re)ordered surface. It allows, for example, the preparation of single crystals without the need of UHV techniques.[16] Polycrystalline electrodes, on the other hand, are usually cut from metal foils and require mechanical polishing to prepare a smooth, clean and reproducible surface.[17] The quality of the polishing procedure also directly influences the quality of the surface after subsequent flame annealing. In addition, not all kind of electrodes can be flame annealed, such as rotating disc electrodes (when embedded in Teflon holders) or microelectrodes. Metals such as copper cannot be flame annealed in air without avoiding surface oxidation.[18]

Even though electrode polishing is a well-known procedure, it has been reported that even when following standard polishing/cleaning procedures, particle residues from the polishing media can remain on the electrode surface even after rinsing extensively with water or after subjecting to ultra-sonication.[19–22] Polishing pastes and suspensions contain alumina, diamond, silicon carbide or boron carbide powders, depending on the application. The extent of the contamination and how it affects electrochemical and especially electrocatalytic processes is expected to vary depending on the polishing media used.

There are only a few indications in the literature that polishing with alumina influences electrocatalysis, although the effect of trace metal contaminants on hydrogen evolution on gold have been previously reported.[23,24] Jacobse et al. demonstrated that platinum ultra-micro electrodes (UME) polished with alumina have lower catalytic activity than flame annealed UMEs.[25] The effect is attributed to

contamination of the UMEs either due to the preparation method or impurities in the chemicals used. On the other hand, Volpe et al. showed that the mechanical polishing of PtBi catalysts with alumina, instead of diamond, leads to larger activity towards formic acid oxidation.[26] Clark et al. also pointed out that alumina residues could be problematic when studying CO_2 reduction on copper, as metallic aluminium is an active catalyst for the competing hydrogen evolution reaction (HER).[27] However, no further investigations were carried out in this regard. Studies regarding the effect of gold surface pre-treatments have mainly been carried out in the field of biomaterials. It has been demonstrated that the surface preparation method strongly influences the self-assembly of organic molecules due to changes in the surface roughness and cleanliness.[28–31] However, the implications of these treatments on the gold catalytic activity has not been thoroughly investigated.

In this Chapter, we study the effect of the polishing media on the electrocatalytic activity of gold electrodes towards HER. We have chosen this model system, due to its relevance as a competing reaction in different electrocatalytic processes that take place (in aqueous media) at potentials below 0 V vs. RHE. Surprisingly, the presence of alumina particles leads to a significant increase in the gold catalytic activity for HER, even though the presence of alumina remains undetected by standard blank cyclic voltammetry. To investigate this enhancement in reactivity, the electrode structure and composition is studied by using a combination of blank voltammetry, Scanning Electron Microscopy (SEM), and Energy Dispersive X-Ray Spectrometry (EDX) both before and after the electrocatalytic experiments. The results demonstrate that the enhancement is due to the corrosion products from the alumina polishing particles that are released into the electrolyte.

7.2 The effect of the polishing media on HER

Polycrystalline gold electrodes polished with either alumina or diamond paste were subsequently cleaned by ultra-sonication and flame annealing before being characterized by cyclic voltammetry (CV). Recording CVs from 0 to 1.75 V vs. RHE is a standard way to characterize polycrystalline gold electrodes.[32] It provides information about the electrochemical active surface area (ECSA) through the charge associated with the gold reduction peak. Gold is considered an ideal electrode for fundamental studies, due to its extensive double layer region (from 0 to 1.3 vs. V vs. RHE in acid) and weak chemisorption of species in comparison to Pt, for example.[33] As depicted in Fig. 7.1 independent of the polishing media used

(alumina or diamond), the gold displays a similar broad oxidation peak, starting at 1.35 V vs. RHE. During the backward scan, one sharp reduction peak is observed at 1.18 V vs. RHE, related to the reduction of the formed gold oxide layer. The double layer region, between 0.1 and 1.3 V vs. RHE, does not change significantly with the polishing media. Minor differences in ECSA can be observed, although repeated experiments show that these are not related to the polishing media, but to using different electrodes.

Even though the CVs of the gold electrodes polished with diamond or alumina look similar, observation of the electrodes under a Scanning Electron Microscope (SEM) shows that a considerable number of particles remains at the surface even after carrying out the standard cleaning procedures described in the Methods section (Appendix D). As can be seen in the SEM images from Fig. 7.2b, samples polished with alumina get contaminated with particles of various sizes (from 100 nm to 3 μm). Additional SEM images at different magnifications can be found in Fig. D.1a and Fig. D.1b in Appendix D and show that the alumina particles are evenly distributed over the whole surface. In the case of diamond (Fig. 7.2a), mainly large and randomly spaced particles can be found, in much smaller amounts compared to alumina. The line structure observed in Fig. 7.2a on the flat region is believed to be soot, formed during flame annealing. The elemental composition of the particles was investigated by EDX. Line scans through the particles found in the alumina polished sample show that the gold signal intensity decreases when the beam approaches the particles while the aluminium and oxygen signals increase (Fig. 7.2b). This shows that the particles come from the polishing media and are ascribed to Al_2O_3. The Al/O ratio does not agree with the stoichiometry, because of the different interaction depths for different elements (resolution of the technique) and the standardless quantification method used.[34] For a given beam energy, the interaction volume will decrease with increasing atomic number. EDX line scans performed on the diamond polished electrode show that through the particles, the carbon signal increases as the gold signal decreases, whereas no signal for oxygen is observed (Fig. 7.2a). Again, it is confirmed that the particles come from the diamond suspension. It is important to point out that trace amounts of carbon are found in all the samples, due to beam-induced hydrocarbon contamination (both from the instrument and from the sample).[35] The amount of carbon found will depend, for example, on the period of time the beam interacts with the surface and

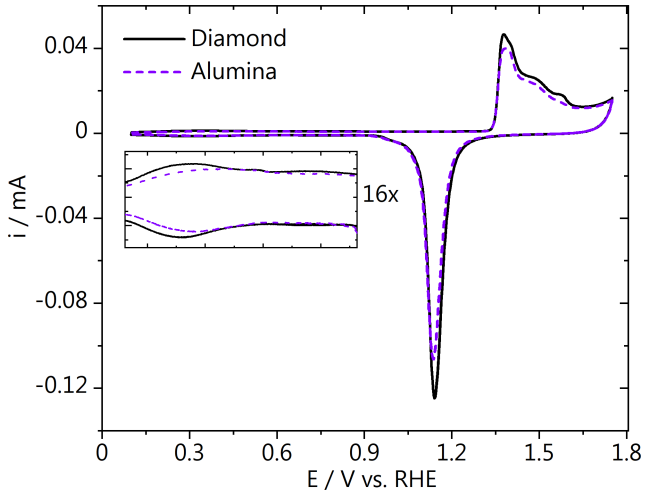

Fig. 7.1. Cyclic voltammetry of polycrystalline gold electrodes polished with either alumina or diamond suspension in 0.1 M H_2SO_4 taken at a scan rate of 50 mV s^{-1}. The inset shows part of the gold double layer region.

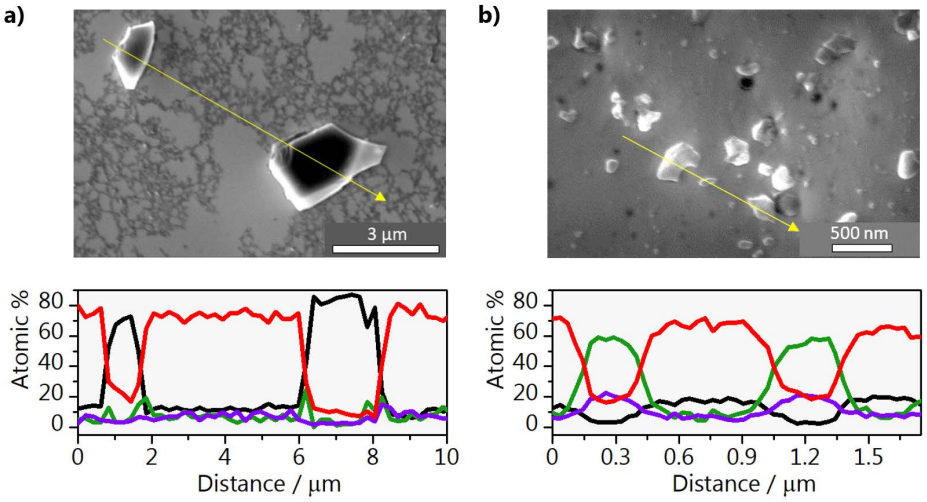

Fig. 7.2. SEM micrographs and EDX line spectra of gold electrodes after polishing with **a)** diamond and **b)** alumina. The lines refer to the following signals: (—) C K, (—) O K, (—) Al K and (—) Au M.

the acceleration voltage. The carbon contamination cannot be detected by cyclic voltammetry characterization.

According to suppliers of polishing media, gold should be polished with diamond suspensions down to 1 µm and the last polishing step should be carried out with alumina paste (0.05 µm).[36] However, they also mention that soft metals like gold are highly prone to diamond embedding. In most work found in literature (including the ones cited in this paper), alumina is the polishing medium of choice for gold electrodes. This is because it is easier to obtain a scratch free, mirror-like finish polishing with alumina than with diamond. It is also important to point out that the surface preparation not only influences the surface morphology but also the reproducibility of electrochemical experiments and the surface cleanliness. In the present work we have only polished and flame annealed the gold electrode, in order to avoid contamination and to have the best reproducibility. A brief explanation on how other treatments, such as chemical etching and electropolishing, affect the surface as well as SEM micrographs can be found in Fig. D.2 in Appendix D, along with a more detailed reasoning of the electrode preparation method chosen for this work.

Considering the large number of polishing particles that remain on the electrode surface even after the standard cleaning procedures, it is surprising that their blank voltammetry is practically identical (see Fig. 7.1). To probe if the particles can influence electrochemical reactions, we have performed HER experiments. Fig. 7.3 shows the curves obtained for HER on gold electrodes polished with either diamond or alumina in the pH = 3 Li_2SO_4 electrolyte. Surprisingly, a significant increase in current density is observed for the alumina polished sample, especially at potentials below –0.8 V vs. RHE. The voltammogram clearly has two different regions. The first cathodic peak observed between 0 and –0.7 V vs. RHE, is attributed to the reduction of protons ($2H^+ + 2e^- \rightarrow H_2$).[37] A peak in the current is observed because the reaction rate is limited by diffusion of protons towards the surface. As the diffusion layer thickness increases and the local pH becomes more alkaline, a proton concentration gradient is built up. The peak current depends on the proton concentration in the electrolyte. In the second region, between –0.8 and –1 V vs. RHE, the reduction of water takes place ($2H_2O + 2e^- \rightarrow H_2 + 2OH^-$).

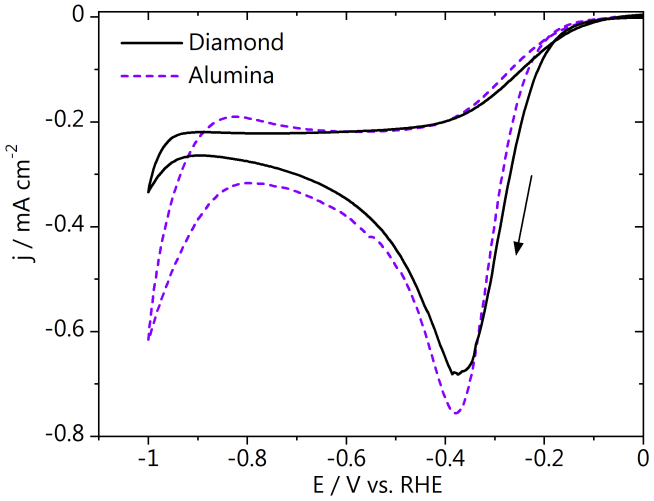

Fig. 7.3. Cyclic voltammogram of hydrogen evolution on gold electrodes polished with alumina or diamond. CVs were recorded in 0.1 M Li_2SO_4 (argon saturated, pH = 3) and taken at a scan rate of 50 mV s^{-1}.

Based on the curves shown in Fig. 7.3, the reduction of H_2O is more affected by the alumina contamination than the reduction of protons. The latter is also confirmed by calculating the Tafel slopes. For proton reduction 101 and 100 mV dec^{-1} were found for the alumina and diamond polished samples, respectively. For water reduction, a lower Tafel slope was found for the alumina polished sample in comparison to the diamond polished sample. The topography and composition of the electrodes was also observed in the SEM directly after the HER experiments. SEM micrographs and EDX spectra can be found in Fig. D.3 in Appendix D. These data show the same situation as shown in Fig. 7.2, i.e. the electrocatalytic experiments have no significant influence on the density, size, and composition of the contaminating polishing particles. In addition, the sulphur signal was also monitored in the EDX line scans after HER, as the reaction was carried out in a sulphate containing electrolyte. However, no significant S signal could be determined.

7.3 Addition of Al^{3+} to the electrolyte

To elucidate why the HER activity increases in the presence of alumina particles, it is necessary to understand how stable these particles are in solution at different pH. According to the Pourbaix diagram of aluminium[38], at pH values below 4 and potentials between –1.69 and 1.9 V vs. RHE, alumina (Al_2O_3) undergoes

corrosion leading to the release of Al^{3+} ions in solution through the following reaction: $Al_2O_3{\cdot}H_2O + 6H^+ \rightarrow 2Al^{3+} + 4H_2O$. It has been shown that alkaline earth cations can strongly influence hydrogen evolution, although the exact mechanism behind it is not yet fully understood.[39] To observe if Al^{3+} has an effect on HER, different amounts of $Al_2(SO_4)_3$ were added to the background electrolyte (0.1 M Li_2SO_4). The gold electrode was polished with diamond, flame annealed and characterized before each addition experiment. The characterization CVs before HER can be found in Fig. D.4 in Appendix D, where a very reproducible surface was obtained by flame annealing prior to each run. Fig. 7.4a shows the HER current densities obtained in the presence of different concentrations of $Al_2(SO_4)_3$ in the electrolyte. An increase in the water reduction current is observed, which strongly indicates that the aluminium ions released in solution (due to corrosion of the alumina particles) are responsible for the enhancement in the HER activity on gold. In addition, it can also be seen in Fig. 7.4a that high concentrations of aluminium cations (above 250 µM Al^{3+}) lead to a second reduction peak at –0.6 V vs. RHE. It is important to point out that the observed current cannot be due to aluminium plating on the gold electrode. The charge associated with the deposition of a full monolayer of aluminium on the electrode would be much lower than obtained, in the order of 600 µC cm^{-2}. In addition, the potential window used is above the equilibrium reduction potential of Al^{3+} at pH = 3 (–1.6934 V). Based on the CVs displayed in Fig. 7.4a, we estimate that the corrosion of the alumina particles during the experiment from Fig. 7.3 leads to an Al^{3+} concentration of less than 50 µM (near the electrode surface). The Tafel slopes were calculated and at high overpotentials, where the activity for water reduction is higher, the Tafel slope decreases 30 mV dec^{-1} in the presence of micro molar concentrations of Al^{3+}. This difference underpins how strongly the Al^{3+} cations affect HER. The gold sample was also characterized after the last HER experiment was performed (with the addition of 500 µM $Al_2(SO_4)_3$). The cyclic voltammograms can be found in Fig. D.5a in Appendix D, showing no apparent changes in the gold blank voltammetry. However, by subsequently analysing the electrode with SEM and EDX (Fig. 7.4b), flakes were found on the surface. Through EDX, it can be seen that these flakes are composed of aluminium and oxygen. A SEM micrograph taken at lower magnification can be found in Appendix D (Fig. D.5b) and shows how homogeneously distributed the deposits are.

Considering the speciation diagram of aluminium (see Fig. D.6a) in Appendix D), at pH above 5 and at high enough Al^{3+} concentration, Al^{3+} precipitates as

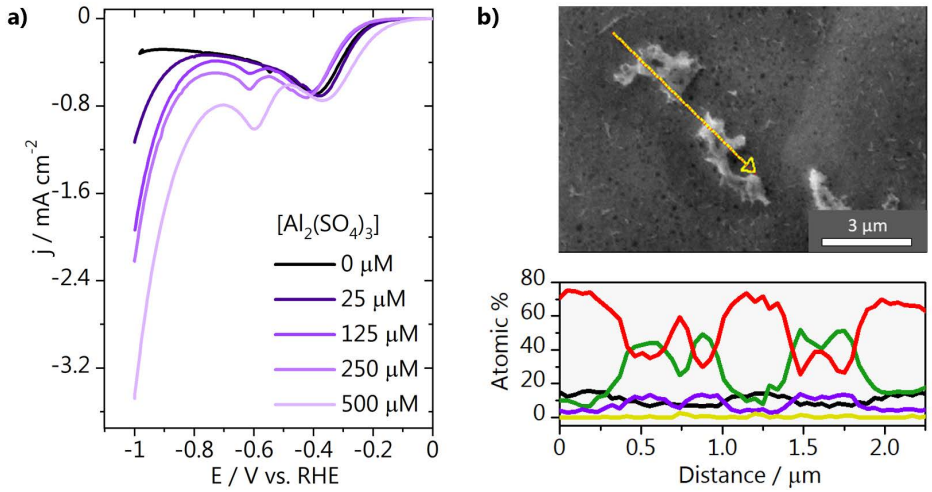

Fig. 7.4. a) Cyclic voltammogram of hydrogen evolution on gold electrodes polished with diamond. CVs were recorded in 0.1 M Li_2SO_4 (argon saturated) at a scan rate of 50 mV s^{-1}. For each curve, different amounts of 0.01 M $Al_2(SO_4)_3$ were added to the electrolyte. Each experiment was done with a fresh electrolyte mixture with a freshly prepared electrode. **b)** SEM micrographs and EDX line spectra of gold electrodes after hydrogen evolution in 0.1 M Li_2SO_4 (argon saturated) with the addition of 500 µM $Al_2(SO_4)_3$. The lines refer to the following signals: (—) C K, (—) O K, (—) Al K, (—) Au M and (—) S K.

$Al(OH)_3$. Even though the bulk pH of our experiments is acidic (pH = 3), during HER, the pH at the electrode surface will be more alkaline. This creates the required environment for $Al(OH)_3$ precipitation. The fact that Al^{3+} can deposit on the surface as hydroxide at increased local pH also means that if an electrode is contaminated with alumina particles and used for experiments during a whole day, the surface composition will not be reproducible throughout all the measurements. As previously shown, these differences will not be apparent in the blank cyclic voltammetry.

To further confirm that Al^{3+} deposits at the electrode surface as aluminium hydroxide during HER, the reaction was also performed on a gold electrode polished with diamond in 0.01 M pure $Al_2(SO_4)_3$. The electrolyte concentration here is lower than in the previous experiments, due to the slow dissolution kinetics of the aluminium salt. Fig. 7.5 shows the CVs for HER in pure $Al_2(SO_4)_3$, together with the curves from Fig. 7.3 for comparison. Larger current densities are obtained in the pure Al^{3+} containing electrolyte, in comparison with HER performed in pure Li_2SO_4. These results are in agreement with Fig. 7.4a, where the addition of small amounts of Al^{3+} to the background electrolyte lead to a 3-fold increase in the HER current

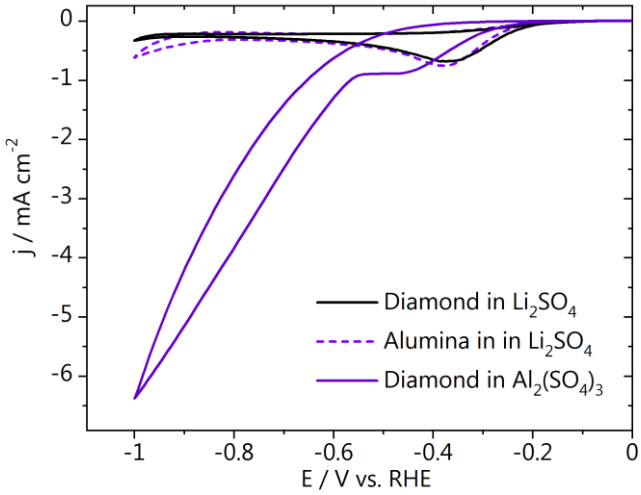

Fig. 7.5. Cyclic voltammogram of hydrogen evolution on gold polished with diamond paste taken at a scan rate of 50 mV s^{-1} in 0.01 M $Al_2(SO_4)_3$ (argon saturated, pH = 2.7). The CVs from Fig. 7.3 are added for comparison.

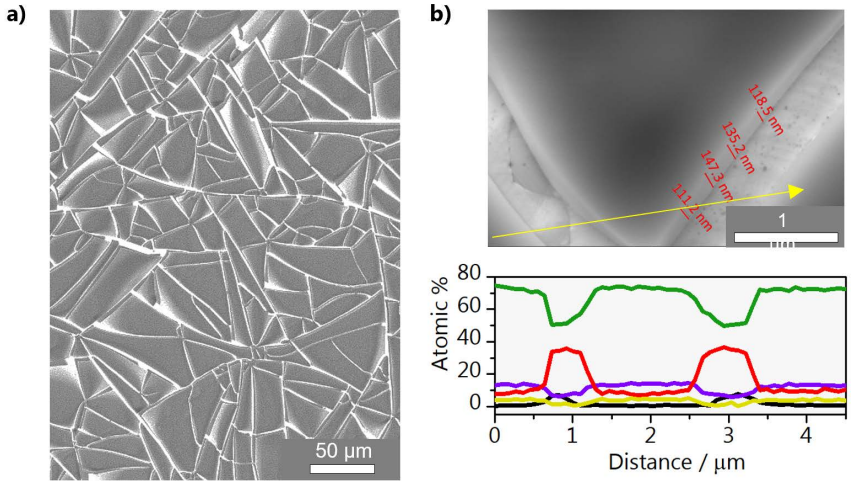

Fig. 7.6. a) SEM micrographs and **b)** EDX line spectra of the gold electrode after hydrogen evolution in 0.01 M $Al_2(SO_4)_3$. The lines refer to the following signals: (—) C K, (—) O K, (—) Al K, (—) Au M and (—) S K.

density. After the HER experiment, SEM and EDX were performed in order to characterize the electrode topography and composition. As shown in Fig. 7.6a, after HER in pure $Al_2(SO_4)_3$, the electrode was fully covered with an aluminium hydroxide layer. Plates, in average 128 ±14 nm thick, are present on the surface with the spacing in between them ranging from 1 to 3 μm. According to EDX (Fig. 7.6b) they are composed of Al, O, and S, but a low signal for gold is still obtained. As previously mentioned, the latter is due to the depth resolution of the technique compared to the hydroxide layer thickness. The region in between the plates is composed of Al, O and again Au, however no sulphur was detected (see Fig. D.7 in Appendix D). The presence of sulphur in the plates as well as their morphology leads to the conclusion that they are layered aluminium hydroxide sheets. The planar sheets are composed by alumina octahedrons, where each aluminium ion shares 3 pairs of OH^- with 3 other Al^{3+}. They are intercalated, in this case, with sulphate ions. See the top and side view of the $Al(OH)_3$ sheets molecular structure in Appendix D (Fig. D.6). Our findings are also supported by comparison with the work of Guo et al.[40] where zinc and aluminium double layered hydroxides were synthesized and the aluminium layer has similar morphology as we obtained (Fig. 7.6a). The gold electrode was also characterized by cyclic voltammetry before and after the hydroxide layer was present on the surface. Surprisingly, the gold CVs nearly overlap (see Fig. D.8 in Appendix D), which not only indicates that the hydroxide plates do not affect the apparent electrochemically active surface area, but are highly porous, so that species in the electrolyte can easily reach the gold surface.

Considering that the voltammetry of the gold was unaltered in the presence of the aluminium hydroxide layer, the activity of this Au-$Al(OH)_3$ modified electrode was also tested for HER. Results can be seen in Fig. 7.7 and show that the HER current for both proton and water reduction obtained during the first cycle is equivalent to that obtained when the electrode is contaminated with alumina particles. During subsequent cycles, two proton reduction peaks are observed and the current due to water reduction increases, indicating that the concentration of Al^{3+} in the vicinity of the electrode surface is also increasing. It is important to notice that during cycles 2 to 5 the proton reduction peak keeps decreasing, likely because of a gradual increase in the local pH. This is expected, as in the presence of the layered hydroxide on the surface, compared to the bare gold, species will take longer to diffuse in and out of the pores. Again, after these HER experiments, the CV of the gold electrode remains unaltered (see Fig. D.8 in Appendix D).

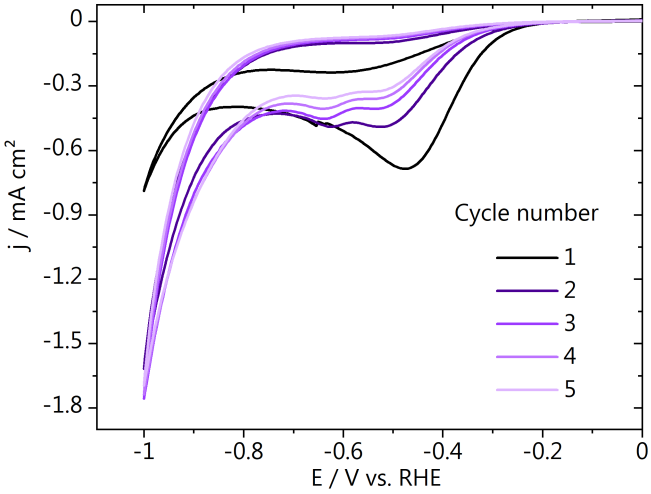

Fig. 7.7. Cyclic voltammogram of hydrogen evolution on gold-$Al(OH)_3$ modified electrode taken at a scan rate of 50 mV s^{-1} in 0.1 M Li_2SO_4 (Argon saturated, pH = 3).

7.4 Alumina removal from the surface

Contaminating alumina particles can of course be removed, by also removing layers of gold. However, for full removal, many electrochemical etching cycles are required. In Fig. D.9 in Appendix D we show that after 2 etching cycles of 1 min in 0.1 M H_2SO_4 (normally 1 etching cycle is performed, for 20 seconds), increased activity for HER is still found. A more detailed discussion on the advantages and disadvantages of prolonged etching is available in Appendix D. Other surface cleaning methods can also be effective for the removal of the polishing contaminants as, for example, sputtering. However, this technique requires ultra-high vacuum (UHV) experiments, which significantly complicates the experimental setup. Thus, mechanical polishing is still the most common surface preparation method in electrochemical studies. Based on the data shown in this work, we believe that a diamond suspension is a safer polishing medium (even though it might lead to a worse surface finish) than alumina, to completely avoid affecting the catalytic activity of electrodes. However, if alumina is employed and only the standard cleaning procedures are performed (mild etching and flame annealing), it is important to be aware that alumina particles on electrode surface corrode in acidic media and release Al^{3+} in the electrolyte. The latter is of extreme importance as cations have shown to influence not only hydrogen evolution but also reactions like CO_2[41] and CO reduction[42], oxygen evolution[43], oxygen reduction, methanol oxidation, among others.[44,45,46] It is also important to highlight that the presence of

surface contaminants cannot be clearly seen by electrochemical characterization of the electrode. Therefore, it is advisable to always use complementary techniques like SEM and EDX to evaluate the surface morphology and composition, no matter which surface pre-treatment was employed.

7.5 Conclusions

Even though polishing is a common electrode preparation method, it may have profound effects on the electrochemical and electrocatalytic reactivity of the electrode. In the present work, we have polished gold samples with either diamond or alumina and evaluated how the polishing medium influences the catalytic activity for hydrogen evolution in mildly acidic electrolyte solutions. Results show that polishing with alumina, despite subsequent electrode cleaning, leads to contamination of the surface with Al_2O_3 particles. Polishing with diamond also leads to contamination, but with significantly fewer particles remaining on the surface. The gold electrodes polished with alumina show higher activity for the water reduction reaction than the ones polished with diamond, due to corrosion of the alumina particles and release of Al^{3+} cations in the electrolyte. The former was confirmed by an increase in HER currents for an electrode polished with diamond, when adding micro molars of Al^{3+} to the background electrolyte. The cations influence water reduction much stronger than proton reduction. Furthermore, we show that by observing the aluminium speciation diagram, it is possible to predict at which pH and applied potentials alumina particles will undergo corrosion or not. We also found that due to an increase in the local pH during HER, even small amounts of Al^{3+} cations deposit on the gold surface as $Al(OH)_3$. At high concentrations (pure Al^{3+} containing electrolyte) layered hydroxides are formed, intercalated with sulphate anions. The alumina contamination can be remediated by the removal of gold layers, which can be achieved by chemical etching, for example. However, several etching cycles are necessary for complete removal and can significantly increase the surface roughness. We hope that our work raises awareness of the potential effects of surface preparation and contamination. This becomes crucial, for example, when studying electrolyte effects on electrochemical reactions. Cations do not only have an effect on hydrogen evolution, but also on many other electrochemical reactions. Therefore, when working in acidic and neutral media, we recommend to polish electrodes with diamond suspensions or other stable polishing media.

References

(1) Burke, L. D.; Nugent, P. F. *Gold Bull.* 1998, *31* (2), 39–50.
(2) Nazemi, M.; Panikkanvalappil, S. R.; El-Sayed, M. A. *Nano Energy* 2018, *49*, 316–323.
(3) Qin, Q.; Heil, T.; Antonietti, M.; Oschatz, M. *Small Methods* 2018, *2* (12), 1800202.
(4) Yao, Y.; Zhu, S.; Wang, H.; Li, H.; Shao, M. *J. Am. Chem. Soc.* 2018, *140* (4), 1496–1501.
(5) El-Deab, M. S.; Okajima, T.; Ohsaka, T. *J. Electrochem. Soc.* 2003, *150* (7), A851.
(6) Sarapuu, A.; Nurmik, M.; Mändar, H.; Rosental, A.; Laaksonen, T.; Kontturi, K.; Schiffrin, D. J.; Tammeveski, K. *J. Electroanal. Chem.* 2008, *612* (1), 78–86.
(7) Laforgue, A.; Addou, T.; Bélanger, D. *Langmuir* 2005, *21* (15), 6855–6865.
(8) Das, J.; Aziz, M. A.; Yang, H. *J. Am. Chem. Soc.* 2006, *128* (50), 16022–16023.
(9) Damian, A.; Omanovic, S. *J. Mol. Catal. A Chem.* 2006, *253* (1–2), 222–233.
(10) Zhao, S.; Jin, R.; Jin, R. *ACS Energy Lett.* 2018, *3* (2), 452–462.
(11) Zhang, B. A.; Ozel, T.; Elias, J. S.; Costentin, C.; Nocera, D. G. *ACS Cent. Sci.* 2019, *5*, acscentsci.9b00302.
(12) Rodriguez, P.; Koper, M. T. M. *Phys. Chem. Chem. Phys.* 2014, *16* (27), 13583–13594.
(13) Ahrens, P.; Zander, M.; Hasse, U.; Wulff, H.; Jeyabharathi, C.; Kruth, A.; Scholz, F. *ChemElectroChem* 2018, *5* (6), 943–957.
(14) Jarosz, M.; Kapusta-Kołodziej, J.; Jaskuła, M.; Sulka, G. D. *J. Nanomater.* 2015, *2015*.
(15) Hamelin, A. *J. Electroanal. Chem.* 1996, *407* (1), 1–11.
(16) Clavilier, J. In *Journal of the American Chemical Society*; Wieckowski, A., Ed.; CRC Press, 2000; Vol. 122, pp 6139–6139.
(17) Samuels, L. E. 4th ed.; ASM International: Ohio, 2003.
(18) Tahir, D.; Tougaard, S. *J. Phys. Condens. Matter* 2012, *24* (17), 175002.
(19) Zhang, L. *J. Electrochem. Soc.* 1999, *146* (4), 1442.
(20) Kiema, G. K.; Aktay, M.; McDermott, M. T. *J. Electroanal. Chem.* 2003, *540*, 7–15.
(21) Kamau, G. N.; Willis, W. S.; Rusling, J. F. *Anal. Chem.* 1985, *57* (2), 545–551.
(22) Kazee, B.; Weisshaar, D. E.; Kuwana, T. *Anal. Chem.* 1985, *53* (13), 2736–2739.
(23) Solla-gullón, J.; Aldaz, A.; Clavilier, J. *J. Electroanal. Chem.* 2017, *793*, 41–47.
(24) Solla-gullón, J.; Aldaz, A.; Clavilier, J. *Electrochim. Acta* 2013, *87*, 669–675.
(25) Jacobse, L.; Raaijman, S. J.; Koper, M. T. M. *Phys. Chem. Chem. Phys.* 2016, *18* (41), 28451–28457.
(26) Volpe, D.; Casado-Rivera, E.; Alden, L.; Lind, C.; Hagerdon, K.; Downie, C.; Korzeniewski, C.; DiSalvo, F. J.; Abruña, H. D. *J. Electrochem. Soc.* 2004, *151* (7), A971.
(27) Clark, E. L.; Resasco, J.; Landers, A.; Lin, J.; Chung, L. T.; Walton, A.; Hahn, C.; Jaramillo, T. F.; Bell, A. T. *ACS Catal.* 2018, *8* (7), 6560–6570.
(28) Ho, L. S. J.; Limson, J. L.; Fogel, R. *ACS Omega* 2019, *4* (3), 5839–5847.
(29) Carvalhal, R. F.; Freire, R. S.; Kubota, L. T. *Electroanalysis* 2005, *17* (14), 1251–1259.
(30) Tkac, J.; Davis, J. J. *J. Electroanal. Chem.* 2008, *621* (1), 117–120.
(31) Hoogvliet, J. C.; Dijksma, M.; Kamp, B.; Van Bennekom, W. P. *Anal. Chem.* 2000, *72* (9), 2016–2021.
(32) Do, U. P.; Seland, F.; Johannessen, E. A. *J. Electrochem. Soc.* 2018, *165* (5), H219–H228.
(33) Xue, S.; Garlyyev, B.; Watzele, S.; Liang, Y.; Fichtner, J.; Pohl, M. D.; Bandarenka, A. S. *ChemElectroChem* 2018, *5* (17), 2326–2329.
(34) Burke, L. D.; Nugent, P. F. *Gold Bull.* 1997, *30* (i), 43–53.
(35) Feliu, J. M.; Herrero, E. *Contrib. Sci.* 2010, *6* (2), 161–172.
(36) Lowe, B. G. In *Introduction to Energy Dispersive X-ray Spectrometry (EDS)*; Goldstein, J., Ed.; Springer Science & Business Media, 2012; p 372.

(37) Vladar, A.; Postek, M. *Microsc. Microanal.* 2005, *11* (S02), 764–765.
(38) Buehler, SUMMET method for gold https://www.buehler.com/sumMet.php?material=Gold (accessed Jul 16, 2019).
(39) Kahyarian, A.; Brown, B.; Nesic, S. *J. Electrochem. Soc.* 2017, *164* (6), H365–H374.
(40) Ashby, M. F.; Jones, D. R. H. 4th ed.; Elsevier Ltd., 2012.
(41) Guo, X.; Xu, S.; Zhao, L.; Lu, W.; Zhang, F.; Evans, D. G.; Duan, X. *Langmuir* 2009, *25* (17), 9894–9897.
(42) Resasco, J.; Chen, L. D.; Clark, E.; Tsai, C.; Hahn, C.; Jaramillo, T. F.; Chan, K.; Bell, A. T. *J. Am. Chem. Soc.* 2017, *139* (32), 11277–11287.
(43) Pérez-Gallent, E.; Marcandalli, G.; Figueiredo, M. C.; Calle-Vallejo, F.; Koper, M. T. M. *J. Am. Chem. Soc.* 2017, *139* (45), 16412–16419.
(44) Zaffran, J.; Stevens, M. B.; Trang, C. D. M.; Nagli, M.; Shehadeh, M.; Boettcher, S. W.; Caspary Toroker, M. *Chem. Mater.* 2017, *29* (11), 4761–4767.
(45) Herranz, J.; Durst, J.; Fabbri, E.; Patru, A.; Cheng, X.; Permyakova, A. A.; Schmidt, T. J. *Nano Energy* 2016, *29*, 4–28.
(46) Strmcnik, D.; Kodama, K.; Van Der Vliet, D.; Greeley, J.; Stamenkovic, V. R.; Marković, N. M. *Nat. Chem.* 2009, *1* (6), 466–472.

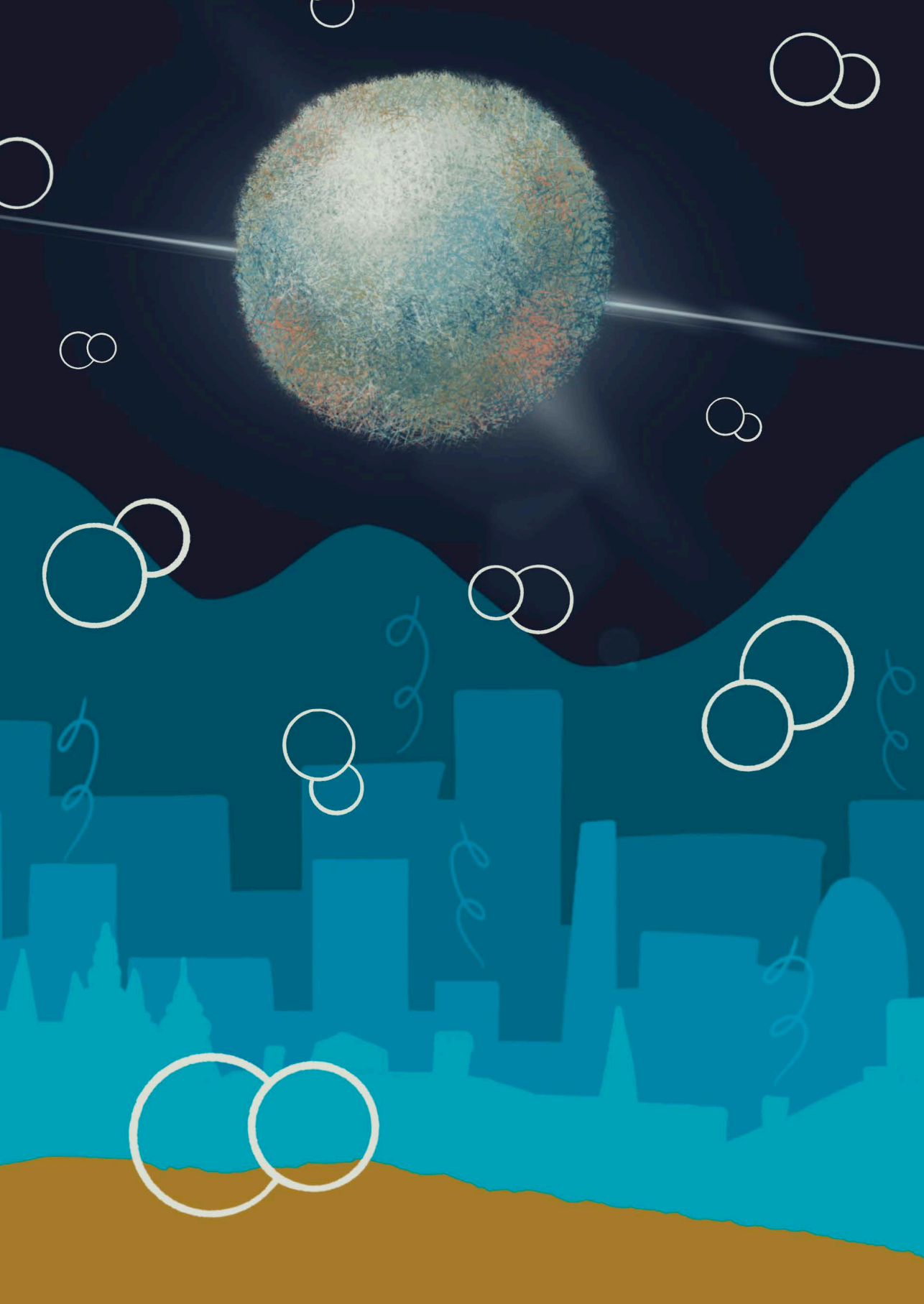

8

Absence of CO_2 electroreduction on copper, gold and silver electrodes without metal cations in solution

This chapter is based on Monteiro, M. C. O., Dattila, F., Hagedoorn, B., García-Muelas, R., López, N., Koper, M. T. M. *Nature Catalysis, 4*, 654–662 (2021)

Abstract

The electrocatalytic reduction of carbon dioxide is widely studied for the sustainable production of fuels and chemicals. Metal ions in the electrolyte influence reaction performance, although their main role is under discussion. Here, we have studied CO_2 reduction on gold electrodes through cyclic voltammetry showing that without a metal cation the reaction does not take place in a pure 1 mM H_2SO_4 electrolyte. We have further investigated CO_2 reduction with and without metal cations in solution using Scanning Electrochemical Microscopy in the surface-generation tip-collection mode with a platinum ultramicroelectrode as a CO and H_2 sensor. CO is only produced on gold, silver or copper if a metal cation is added to the electrolyte. Density Functional Theory simulations confirmed that partially desolvated metal cations stabilize the CO_2^- intermediate *via* a short-range electrostatic interaction, enabling its reduction. Overall, our results redefine the reaction mechanism, providing definitive evidence that positively charged species from the electrolyte are key to stabilize the crucial reaction intermediate.

8.1 Introduction

The electrochemical carbon dioxide reduction reaction (CO_2RR) into fuels and chemicals has recently gained significant attention as a way to close the chemical carbon cycle and to store excess renewable electricity in fuels and chemicals. Good activity and selectivity of the CO_2RR are crucial to make the process industrially viable. In aqueous media, CO_2 reduction on metals such as gold and silver yields almost exclusively carbon monoxide (in addition to hydrogen from the competing proton/water reduction), while on copper C-C bonds are formed.[1] Tailoring the catalyst surface is the most common way of steering activity and selectivity. However, it is well known that the electrolyte composition, especially pH and cation, has a strong impact on the reaction.[2–4] To date, in the majority of the studies, alkali metals have been employed and the activity trend found on different electrodes is $Cs^+ > K^+ > Na^+ > Li^+$.[5–13] Even though this trend is consistent in different research works, diverging theories have been proposed to explain through which molecular mechanism cations affect CO_2 reduction.

There are three main theories which explain how cations at the interface affect the activity and selectivity of electrocatalytic processes, as recently reviewed by Waegele et. al.[14]: modification of the local electric field, buffering of the interfacial pH or stabilization of reaction intermediates. On a negatively charged metal electrode, there is still no agreement if cations adsorb specifically, or if their interaction with the surface is purely electrostatic.[15–17] Especially concerning CO_2RR, Hori and Murata presented one of the first explanations on how metal cations affect the reaction.[18,19] Based on Frumkin`s theory[20], they proposed that cations change the potential profile in the electric double layer through specific adsorption. Weakly hydrated cations lead to steeper potential gradients from the electrode surface towards the outer Helmholtz plane (OHP) compared to strongly hydrated species. More recent studies have ruled out specific adsorption and instead suggested that under CO_2RR conditions cations accumulate near the surface *via* non-covalent interactions giving rise to high electric fields in the vicinity of the ion.[21–23] For instance, Ringe et al. employed a continuum electrolyte model to show that weakly hydrated cations are more concentrated at the OHP and thus induce a higher mean electronic surface charge density, which in turn leads to an enhanced CO_2RR activity and selectivity.[21] A modification of the potential across the plane where the electron transfer happens is proposed to change the apparent activation energy of the

overall reaction, affect the interfacial water energetics, and influence CO_2 adsorption.

In contrast to the Frumkin-type local electric field effect, the second theory was put forward by Singh et al.[24] proposing that cations affect the CO_2RR by buffering the interfacial pH. Even though alkali cations do not undergo hydrolysis in the bulk, near the negatively charged cathode surface the hydration shell of large cations will experience a stronger electrostatic field, which decreases their pK_a of hydrolysis. Ayemoba and Cuesta[25] probed the pH at a gold-electrolyte interface using Attenuated Total Reflection Surface Enhanced Infra-Red Spectroscopy (ATR-SEIRAS) and based on the ratio between the integrated intensity of the CO_2 and HCO_3^- bands, the authors show that larger cations are better buffers and lead to lower pH changes at the interface. Zhang et al.[26] performed similar pH measurements using a Rotating-Ring-Disc Electrode (RRDE) and found that during CO_2 reduction in bicarbonate electrolyte the interfacial pH follows the trend: $Li^+ > Na^+ > K^+ > Cs^+$.

The third theory, introduced by Chen et al.[22] and further developed in the work of Resasco et al.[27], suggests that metal cations stabilize certain CO_2 reduction reaction intermediates through local electrostatic interactions within the electrical double layer. Specifically, the study of Resasco *et al.*[27] focused on the effect of alkali cations on CO_2 reduction over Cu(100) and Cu(111) thin-film electrodes and Ag and Sn polycrystalline electrodes. The formation of CO was suggested to happen through the reaction intermediates shown in Eq. 8.1-8.3:[1]

$$CO_2 + e^- + * \rightarrow *CO_2^- \quad \text{Eq. 8.1}$$

$$*CO_2^- + H^+ \rightarrow *CO_2H \quad \text{Eq. 8.2}$$

$$*CO_2H + H^+ + e^- \rightarrow *CO + H_2O \quad \text{Eq. 8.3}$$

The selectivity trends reported in Ref. 27 are explained through Density Functional Theory (DFT) simulations on a surface/solvated cation interface optimized *via* constrained minima hopping molecular dynamics. Solvated cations with larger ionic radius experience a stronger driving force to accumulate near the surface.[27] As previously demonstrated by Chen et al.,[22] high local electrostatic fields generated by solvated cations can locally stabilize adsorbed intermediates with large dipole moments. Thus, the higher activity observed for CO_2 reduction on copper in the presence of larger cations was attributed to a higher concentration of such cations in the OHP.[27]

To test the above models, in this Chapter, we carry out CO_2 reduction experiments on polycrystalline gold, which is a stable and simple electrocatalytic

system that, under the conditions of this study, yields only CO and H_2. Measurements are performed in the total absence of metal cations (at pH = 3) and in the presence of small amounts of Cs^+. Using Scanning Electrochemical Microscopy in the surface-generation tip-collection mode (SG-TC) as an extremely sensitive technique to detect CO_2 reduction products, we show that without a metal cation in solution, CO_2 reduction does not take place. This remarkable observation is extended to other common catalysts like copper and silver. Of the three models existing in literature, only the model which considers electrostatic interactions between metal cations and key intermediates can explain this observation. We further confirm the role of cations through DFT-based *ab initio* molecular dynamics (AIMD) simulations on a gold/cation/solvent system where we prove the stabilization effect of partially desolvated metal cations on CO_2 adsorption, activation and formation of the CO_2^- intermediate. While our results, in principle, do not exclude the validity of the other two models, they nonetheless clearly show that the main role of the metal cation is to stabilize the key CO_2^- intermediate, to the extent that in its absence, CO_2 reduction does not take place. This conclusion has important implications for CO_2RR modeling and catalyst design.

8.2 Hanging meniscus experiments

In order to elucidate the role of metal cations in the CO_2RR, the reaction was first studied through cyclic voltammetry (CV) using a gold electrode in hanging meniscus configuration. On gold, under the conditions of this study, CO_2 is reduced in the cathodic scan producing only CO. The competing hydrogen evolution reaction (HER) occurs due to the reduction of protons or water, depending on the interfacial proton concentration. As gold is also a very good catalyst for CO oxidation, the CO produced can be probed semi-quantitatively by directly cycling the electrode to positive potentials. The gold electrode used in this study was characterized by blank voltammetry before each measurement (Fig. E.1 in Appendix E), in order to assure cleanliness of the surface, comparability and reproducibility of the experiments, and to allow the determination of the electrochemically active surface area. This consecutive cathodic/anodic cycling was performed first in argon and subsequently in CO_2 atmosphere.

Fig. 8.1a compares the cathodic scans obtained in the absence of a metal cation (in 1 mM H_2SO_4) and in the presence of 280 µM of Cs^+, both solutions at bulk pH = 3. Note that an experiment in the absence of metal cations (which is the focus

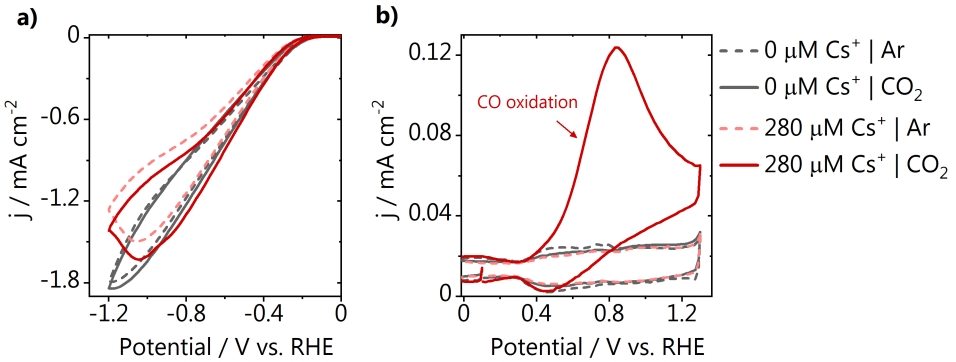

Fig. 8.1. CO_2 reduction on gold with and without 280 µM Cs^+ in solution. **a)** Cathodic scans recorded in argon and CO_2 atmosphere together with **b)** the subsequent recorded anodic scans performed to oxidize any CO produced. All CVs were recorded at 50 mV s^{-1}.

of this work) can only be performed at this or at a lower pH, as for a higher pH without metal cations the electrolyte conductivity would become prohibitively small. Still, due to the local production/consumption of OH^-/H^+, the alkalinity at the interface increases during the course of the reaction. In argon, when only hydrogen evolution is taking place, the proton reduction current is lower and reaches diffusion limitation at lower overpotentials in the presence of Cs^+. This is likely due to migration, which with Cs^+ in solution leads to a lower concentration of protons near the surface. This is further confirmed by the fact that if we increase the Cs^+ concentration (at the same pH = 3), the proton reduction current is even lower (Fig. E.2 in Appendix E). In CO_2 atmosphere, the reduction current increases more significantly in the presence of 280 µM Cs^+ while almost no increase is observed in pure H_2SO_4. In Fig. 8.1b, we show that in the absence of Cs^+ no CO is detected in the anodic scan and the only current observed is due to charging of the electrical double layer, which nearly overlaps for both gaseous atmospheres. With Cs^+ in the electrolyte a large anodic current due to the oxidation of the CO produced is observed. Differently from CO_2 reduction, CO oxidation does take place in the absence of a metal ion in the electrolyte, as is seen in the control experiment (Fig. E.3 in Appendix E). To further confirm that Cs^+ is crucial for enabling the CO_2 reduction reaction, which causes the CO oxidation current observed, we have gradually added different amounts of Cs^+ ions to the electrolyte (Fig. E.4 in Appendix E). The amount of CO produced increases as a function of the Cs^+

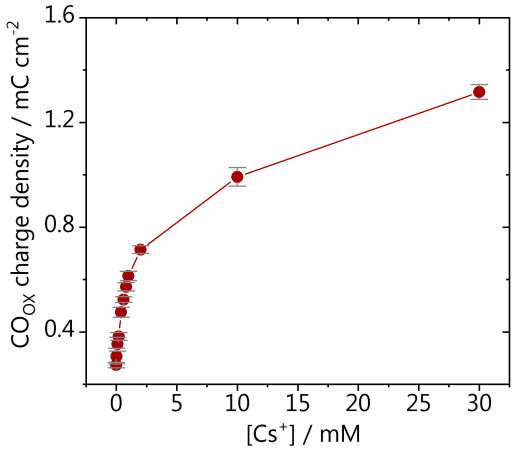

Fig. 8.2. Effect of the Cs^+ concentration. CO produced after polarization to –1 V vs. RHE, in the presence of different concentrations of Cs^+ in a Li_2SO_4 background electrolyte. The total cation concentration in solution was kept 0.1 M and the pH = 3. Error bars are calculated based on three individual measurements.

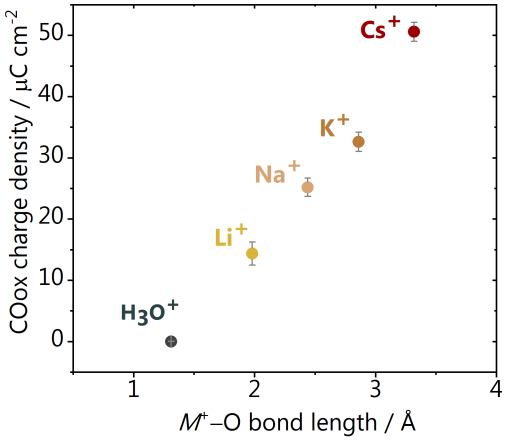

Fig. 8.3. Effect of the cation identity. CO detected on the gold sample directly after CO_2 reduction from 0 to –1.2 V vs. RHE in 1 mM M_2SO_4 with M = H, Li, Na, K, Cs. All solutions, when necessary, were adjusted to pH = 3. The M^+–O bond length is taken as the first peak of the cation-water radial distribution functions calculated from AIMD data, Table E.1 in Appendix E, whilst in the absence of a metal cation we used the proton-oxygen bond length.[28] Error bars are calculated based on three individual measurements**.**

concentration in the electrolyte, as derived from the CO oxidation currents from the CVs. Three subsequent CVs were recorded for every concentration and the trend remains the same over the different cycles.

This enhancement in the CO production by the addition of Cs^+ ions was investigated in a broader concentration range using Li_2SO_4 as background electrolyte at pH = 3. Here, the total cation concentration is kept constant (0.1 M) to avoid contributions of having solutions of different ionic strengths. The gold electrode was cycled from 0 to –1 V vs. RHE in the different electrolytes and the CO produced is oxidized in the positive-going scan, similarly to previous experiments (Fig. 8.1). The cyclic voltammetry is presented in Fig. E.5 in Appendix E and the charge of the CO oxidation peak found for the different concentrations of Cs^+ is depicted in Fig. 8.2. Already with the addition of less than 1 mM of Cs^+ to the electrolyte a steep increase in the CO production is observed. At higher concentrations, a saturation effect appears as the CO production approximates to a plateau.

We have also used the cathodic/anodic voltammetry during CO_2 reduction on gold to evaluate different metal cations in the dilute electrolytes used in this work. The gold electrode was flame annealed and characterized before each measurement and the blank voltammograms can be seen in Fig. E.1 in Appendix E. Experiments were performed in 1 mM M_2SO_4 where M = H, Li, Na, K, Cs. All solutions, if necessary, were adjusted to pH = 3, to exclude pH effects. Fig. 8.3 shows the CO oxidation charge of the first anodic cycle recorded after performing CO_2 reduction from 0 to –1.2 V vs. RHE. The activity for CO formation is correlated with the size of the solvated cation, here represented by the cation-oxygen (M^+–H_2O) bond length. Bond length for each alkali metal is taken as the first peak of cation-water radial distribution functions calculated from AIMD data (Table E.1 in Appendix E) and for the cation-free electrolyte, the proton-oxygen (H^+–H_2O) bond length is used.[28] In agreement with the previous results, no CO_2 reduction product is observed in the absence of a metal cation while in the M_2SO_4 electrolytes the activity for CO production follows the usual trend reported for other metal surfaces: Cs^+ > K^+ > Na^+ > Li^+.[3] We observe a strong correlation between activity and the cation size, which is related to a softer hydration shell, thus favoring the production of CO, in the Computational Model section.

8.3 Scanning Electrochemical Microscopy (SECM)

To confirm that in the absence of a metal cation absolutely no CO is produced on gold and to extend the study to silver and copper, relevant CO_2RR catalysts which are not good for CO oxidation, we have employed Scanning Electrochemical Microscopy (SECM) in the SG-TC mode to detect CO_2 reduction to CO. A schematic representation of the experiments is shown in Fig. 8.4a, where a platinum ultramicroelectrode (Pt-UME) is placed in the diffusion layer above the substrate electrode where CO_2 reduction takes place. The platinum voltammetry is extremely sensitive to trace amounts of CO, as CO strongly chemisorbs on the surface and can be removed by oxidation.[29] Platinum is also a suitable catalyst for hydrogen oxidation, thus we can also detect hydrogen produced due to HER. SECM was used here because of the higher sensitivity that it provides to detect CO, in comparison with other product analysis techniques such as Gas Chromatography (GC) and Differential Electrochemical Mass Spectrometry (DEMS). The procedure used for all measurements is shown in Fig. 8.4b. A negative potential is applied to the sample for 10 seconds and subsequently a cyclic voltammogram of the Pt–UME is recorded. Special care was taken with the samples and electrolytes used in these experiments, to make sure traces of metal impurities would not mislead our conclusions. The Pt-UME was prepared and characterized before each measurement. A blank voltammogram of the Pt-UME can be seen in Fig. 8.4c showing the expected voltammetric features of a clean polycrystalline platinum surface.[30] The polycrystalline gold, copper and silver samples used were also characterized before the measurements as shown in Fig. 8.4d, Fig. 8.4e and Fig. 8.4f, respectively. The voltammetry of copper and silver electrodes used for CO_2RR studies is rarely shown in literature, despite its importance to determine the quality of the surface preparation and consequently reproducibility of the experiments. Here, silver was characterized through the reversible Tl(I) underpotential deposition (UPD), which is used to assess the surface cleanliness and crystallinity.[31] This is seen by the presence and reversibility of the peaks from Fig. 8.4e. To evaluate the copper sample, the electrode was characterized in concentrated hydroxide solution, and the current due to the adsorption and desorption of OH^- can be observed in the region of Cu_2O formation, also indicating the surface crystallinity.[32]

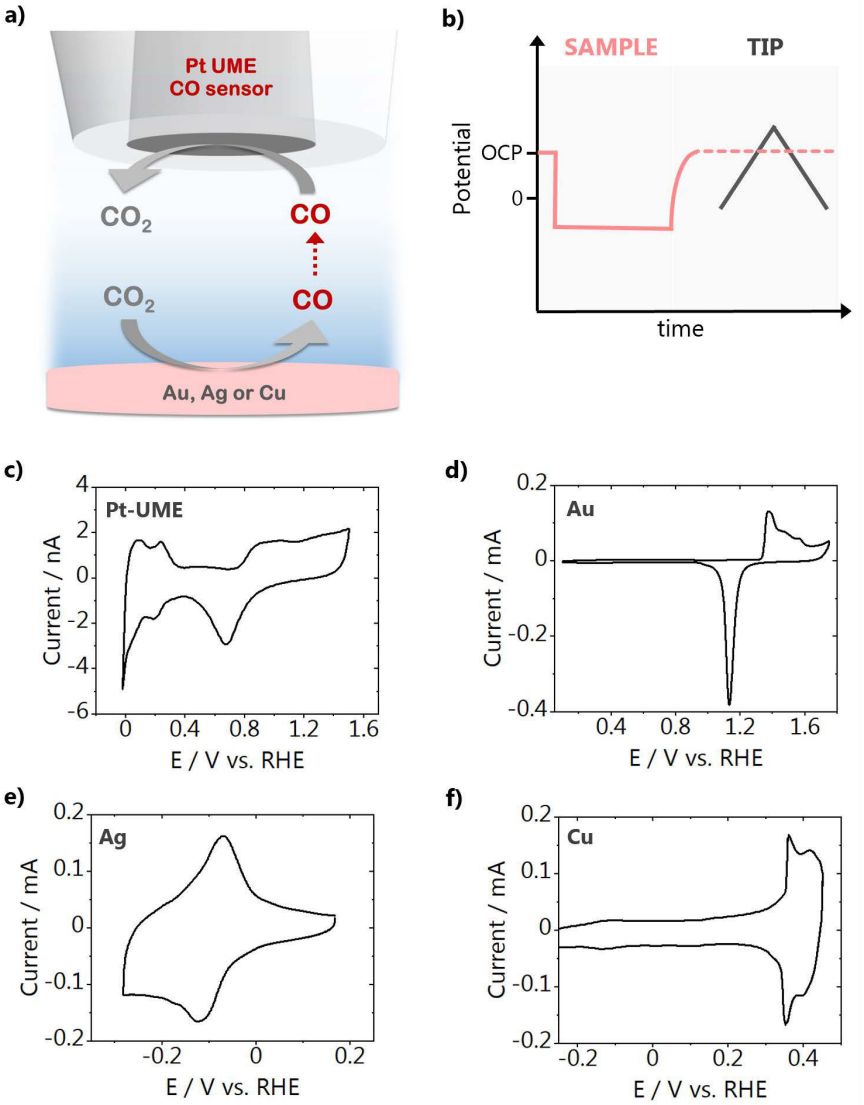

Fig. 8.4. SECM measurement scheme and characterization of the electrodes used. **a)** Schematic representation of the SECM experiment and **b)** method used to perform the measurements; **c)** Blank voltammetry of the Pt–UME used to perform the experiments taken in 0.1 M H_2SO_4; Characterization of: **d)** the gold sample in 0.1 M H_2SO_4; **e)** the silver sample through Tl(I) under potential deposition in 0.5 M Na_2SO_4 + 0.1 M H_2SO_4 + 0.1 M Tl_2SO_4; **f)** the copper sample in 0.5 M NaOH. All sample characterization CVs were recorded at 50 mV s^{-1}.

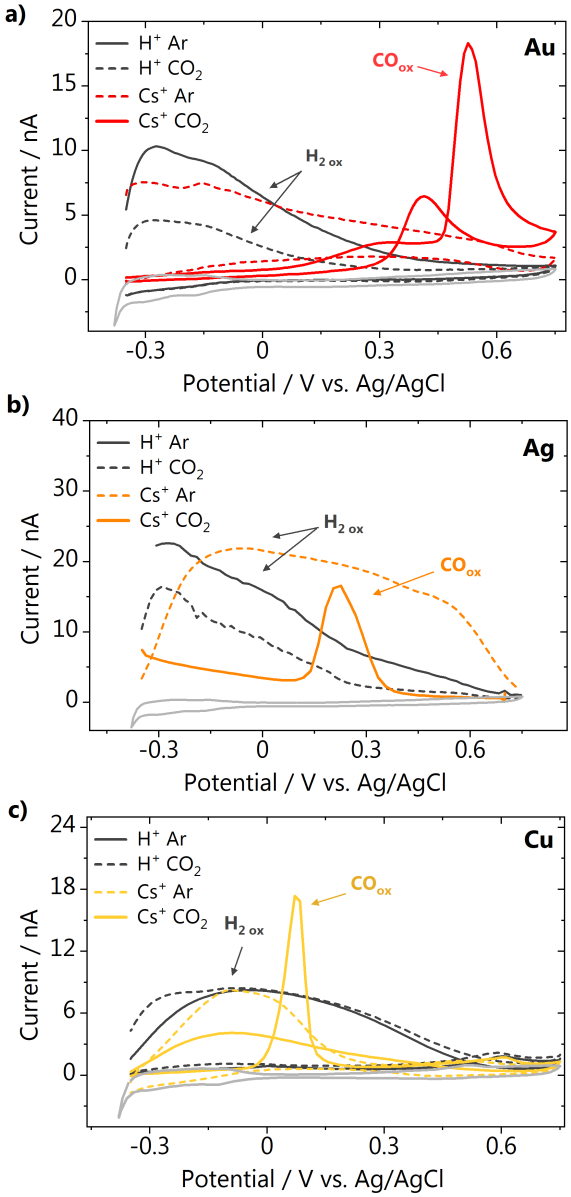

Fig. 8.5. CO detection with SECM. Cyclic voltammetry of the Pt–UME taken directly after CO_2 reduction on **a)** gold, **b)** silver and **c)** copper electrodes. The voltammetry of the Pt–UME before applying any potential to the sample is shown in light gray for reference.

The SECM measurements were carried out in 1 mM H_2SO_4 with and without the addition of 280 μM Cs^+. For each electrolyte, before CO_2 reduction, a control experiment in argon was performed, where only hydrogen is expected as a product. The Pt-UME was always positioned 50 ± 2 μm from the surface by performing a capacitive approach in air, which is essential for keeping the electrolyte free from impurities.[33–35] The uncertainty in the position is the error from the approach curve fits. Approach curves are reported in Fig. E.6 in Appendix E. Fig. 8.5a shows the results obtained for the gold electrode after applying a potential of –0.7 V vs. RHE to the sample. In argon atmosphere, in the absence or presence of Cs^+ only current characteristic to hydrogen oxidation can be seen in the Pt-UME voltammetry. In CO_2 atmosphere, only when Cs^+ is added to the electrolyte a sharp peak due to the oxidation of CO is seen, which confirms that CO_2 reduction on gold does not take place in the absence of a metal cation in solution. Fig. 8.5b shows similar results for the silver electrode at a potential of –0.8 V vs. RHE. As for gold, on silver CO_2 reduction takes place only in the Cs^+ containing electrolyte, as confirmed by the CO oxidation peak in the Pt–UME voltammetry. On copper the same trend is observed when the sample is polarized at –1 V vs. RHE (Fig. 8.5c). In the 1 mM H_2SO_4 electrolyte only hydrogen is detected by the Pt-UME, whilst CO is detected only after addition of Cs^+ to the electrolyte. It must be noted that these individual SECM measurements constitute only a qualitative tool to probe if CO is formed or not. Due to various factors as the different sample potentials applied, bubble formation, diffusion hindrance by the tip, the magnitude of the CO and H_2 oxidation currents measured and their potentials cannot be used for a quantitative comparison between the substrates. For silver and copper, the potential range applicable is limited by the stability of the electrode. At more cathodic potentials, a small amount of metal oxide dissolution is observed and the traces of Ag^+ and Cu^{2+} ions released into the electrolyte lead to the production of CO in 1 mM H_2SO_4 (see Section E.3.2 in Appendix E for details).[36] This happens as during the SECM approach, the electrode surface is exposed to air, which can lead to the formation of (a very small amount) of oxide on the surface. This is confirmed by the Pt-UME voltammetry (Fig. E.7 in Appendix E), which presents voltammetric features characteristic of the under potential deposition of Ag^+ or Cu^{2+} on the Pt-UME surface.[37,38]

8.4 Computational model

To model the experimental system, we carried out DFT-based *ab initio* molecular dynamics on a $3\sqrt{3}\times3\sqrt{3}$–*R*30° Au(111) supercell (4 layers, 15.3 Å × 15.3

Å × 30.0 Å) with 72 explicit water molecules filling 15.0 Å along Z, plus 8 Å vacuum thickness between periodic slabs (see Fig. E.8 in Appendix E, and Videos 1-5 in the online version of the publication).[39] This pristine system (Au–H_2O) is equilibrated for 2 ps at 300 K with a time step of 1 fs, as illustrated in Fig. 8.6a. Then, an alkali metal cation M^+ (M = Li, Na, K, Cs) is inserted close to the gold surface, at an initial cation-surface distance of 3.3 Å. Upon optimization, the cation-surface distances increase for each alkali metal (Fig. E.9 in Appendix E). To specifically investigate the local interactions between cation and CO_2, we kept the cation concentration at the OHP constant, balancing the charge within the unit cell by including an OH^- at the fourth water bilayer (see Methods in Appendix E). Given the volume of the solvation layer and the number of water molecules, the cation surface coverage (0.04 ML) corresponds to a concentration around 0.5–0.8 M. Since the initial position and surface coverage are identical for each cation, any concentration effects are not included in the model. We let the cation solvation shell build up for 2 ps and we classify the final structures as Au-H_2O-M^+ (Fig. 8.6a). The resulting cation-oxygen radial distribution functions $g_{M^+\text{-}H2O}(r)$ (Eq. E.6 and E.7, Fig. E.10) confirmed a proper description of the cation coordination shell, since the estimated cation-oxygen distances $d_{M^+\text{-}O}$ for water molecules in the first solvation shell agree with previous experimental and theoretical results (Table E.1 in Appendix E). Furthermore, the full width at half maximum (FWHM) for the first $g_{M^+\text{-}H2O}(r)$ peak increases following the alkali group, $Li^+ < Na^+ < K^+ < Cs^+$, thus confirming that a larger cation ionic radius implies a softer solvation shell. Finally, we estimate the cation coordination numbers through the structural parameters previously defined (Eq. E8 and E9 in Appendix E). The alkali cations exhibit an average coordination number of 2.8, 3.2, 3.5, and 5.8, with maximum values of 3.9, 4.7, 4.9, and 8.0 for Li^+, Na^+, K^+, and Cs^+ respectively, in line with state-of-the-art reported values (see Table E.2 in Appendix E).[40]

After the equilibration of the Au-H_2O-M^+ systems, we introduce a CO_2 molecule at the electrolyte/surface interface in the proximity of the solvated cation (Fig. 8.6a). Upon AIMD simulations for 2 additional ps, CO_2 adsorbs on the gold surface in a $\eta^2_{C,O}$ conformation (bidentate through the carbon atom and one oxygen) and coordinates to the surrounding cation and water molecules through the second oxygen. Due to its hard solvation shell, Li^+ coordinates to CO_2 for limited periods of the AIMD runs, resulting in an average coordination number $N_{Li^+\text{–}O(CO2)}$ of 0.1 ± 0.3 (Fig. 8.6b, Table E.2 in Appendix E). Instead, other alkali metals continuously bind to the oxygen atom in CO_2, herein called $O(CO_2)$, resulting in the

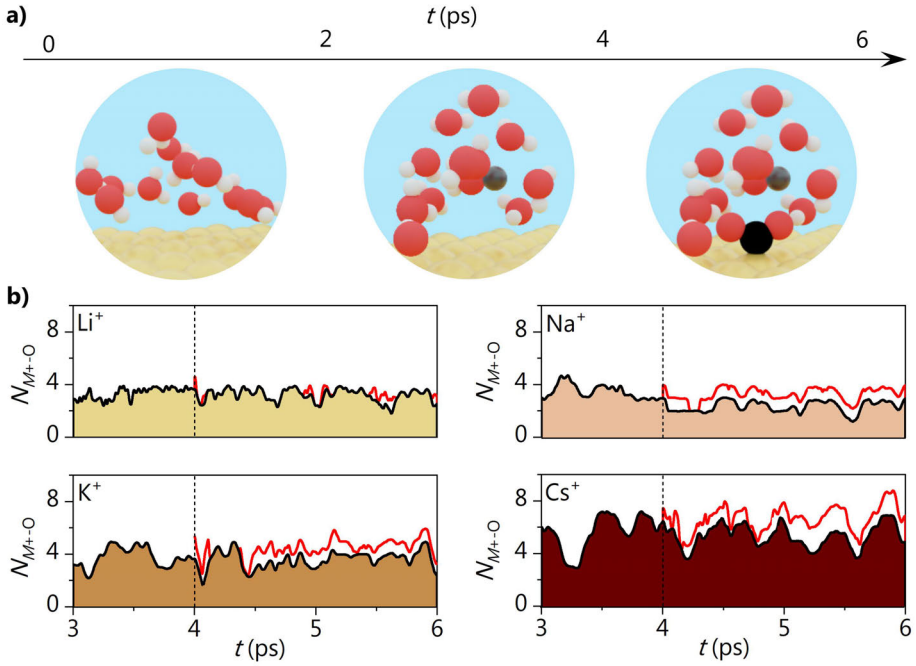

Fig. 8.6. Cation coordination with CO_2. **a)** Timeline for the *ab initio* molecular dynamics simulation at 300 K: 2 ps pre-equilibration for the Au-H_2O system, 2 ps for the Au-H_2O-M^+ system (cation inserted close to the surface, ϑ_{M+} = 0.04 ML), and finally 2 ps for the Au-H_2O-M^+-CO_2 system (CO_2 molecule adsorbed on Au). The portrayed cation is Li^+. **b)** Alkali cation' s coordination number, N_{M+-O}, vs. simulation time for the Au-H_2O-M^+ system. Dashed lines indicate CO_2 insertion in the supercell (t = 4 ps) and red continuous lines indicate the increase in coordination number due to M^+–O(CO_2).

following coordination numbers: $N_{Na+-O(CO2)}$ = 0.9 ±0.2, $N_{K+-O(CO2)}$ = 0.9 ± 0.4, and $N_{Cs+-O(CO2)}$ = 1.3 ± 0.5. Upon coordination to M^+–O(CO_2), the number of water molecules within the cation´s coordination shell remains constant or slightly decreases (Fig. 8.6b).

Partially desolvated cations have three promotional effects which enable CO_2 reduction. The first effect is thermodynamic (Fig. 8.7a). When the cation coordinates to the adsorbate, a short-range M^+–O (CO_2) electrostatic interaction stabilizes CO_2 more strongly than the solvation by water molecules alone by around 0.5 eV (Fig. 8.7a, Table E.3 and Eq. E.8 in Appendix E). Besides, there is a medium-range interaction between the electric dipole of adsorbed $*CO_2^-$ and a cation-induced

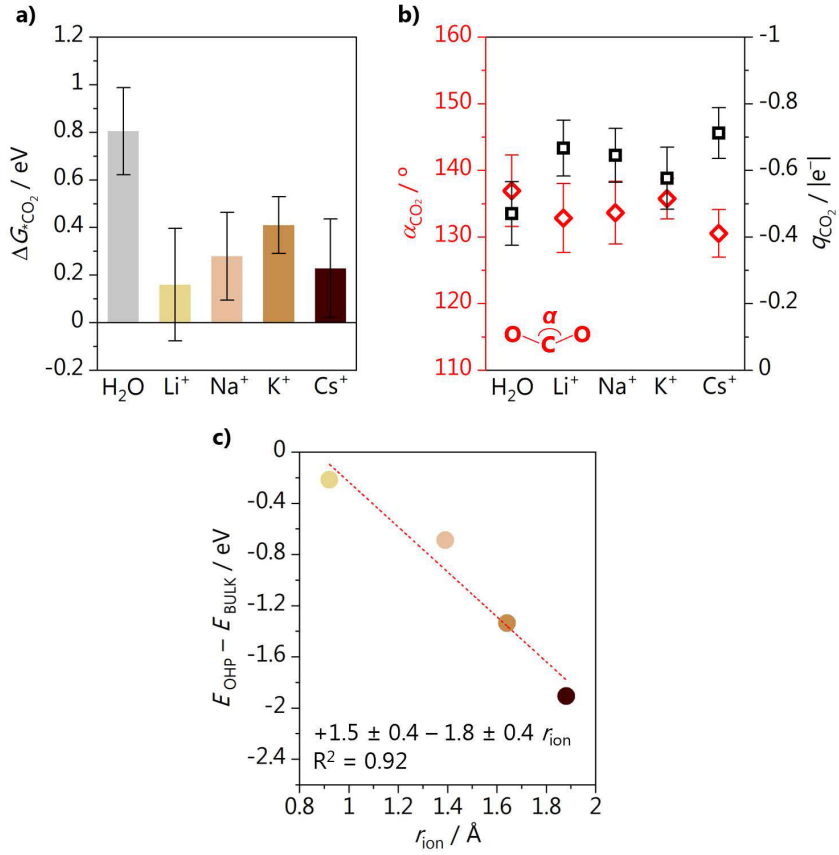

Fig. 8.7. CO_2 activation *via* explicit cation/intermediate interaction, driven by cation concentration at the OHP. **a)** Average CO_2 adsorption Gibbs free energy at U = 0 V vs SHE in absence (gray) or presence of an alkali cation (light to dark brown), with CO_2 and environment (Au-H_2O or Au-H_2O-M^+) as energy references. **b)** CO_2 activation angle, α, and CO_2 Bader charge, q_{CO2}, are shown in red and black, respectively, and reported in Table E.4 in Appendix E. Error bars are calculated as standard deviation of the data (see Methods). **c)** Correlation between thermodynamic driving force at U = 0 V vs SHE for different alkali cations to accumulate at the outer Helmholtz plane (OHP) and their ionic radius (see Methods). Coefficients a = 1.5 ± 0.4 eV; b = 1.5 ± 0.8 eV Å^{-1}.

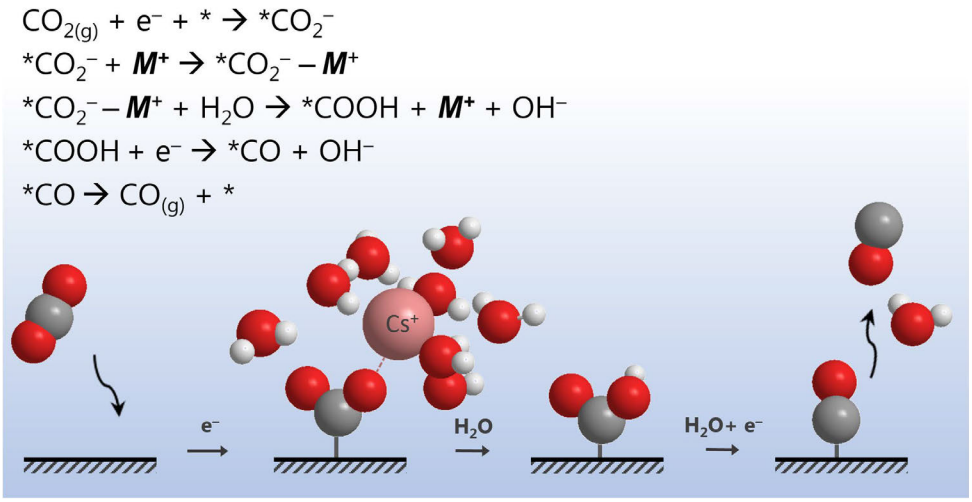

Fig. 8.8. Mechanism of CO_2 reduction to CO. Schematic representation of the interaction of the cation with the negatively charged CO_2^- intermediate together with a proposed reaction mechanism.

electric field, which is irregular and modulated by the electrolyte, solvation and neighboring cations (see Eq. E10 and E11 and Fig. E.11 in Appendix E). [22,27]

Both short and medium-range cation-induced interactions account for an equivalent stabilizing effect. Instead, in the absence of cations, the medium-range $*CO_2^-$-dipole/electric field interaction only accounts for weaker stabilization (–0.2 eV), unable to open the CO_2 reduction pathway (see Eq. E.12 and Fig. E.12 in Appendix E). The second promotional effect is the O–C–O angle α activation, which decreases from linear 180° to below 140° in the presence of a neighboring cation (Fig. 8.7b, red axis, Table E.4 in Appendix E). Thirdly, upon coordination, cations enhance the electron transfer from the catalytic surface to the CO_2 unit, as demonstrated by the CO_2 Bader charges close to –1.0 $|e^-|$ (Fig. 8.7c, Table E.4 in Appendix E). Thus, partially desolvated cations are crucial for the formation of the CO_2^- intermediate, the generally assumed rate-determining step for CO_2 reduction.[41] As a final remark, the activity trends based solely on cation radius (Fig. 8.3) originate both from different cation surface concentrations at the OHP (Fig. 8.7c, Eq. E.8-12 in Appendix E)[27] and their different ability to coordinate to $*CO_2^-$, which ranges from almost no bond for Li^+ to more than a bond for Cs^+, Table E.2.

8.5 Discussion and Conclusions

The results presented here show that without a metal cation in the electrolyte, CO_2 reduction to CO does not take place, neither on gold, silver, or copper electrodes. As discussed earlier, there are currently three major theories regarding the main role of metal cations during CO_2 reduction: modification of the (local) electric field, buffering of the interfacial pH and stabilization of reaction intermediates via local field effects. All theories have been supported with experiments and DFT models, and to some extent they all play a role on the CO_2 reduction reaction. However, based on our experimental and theoretical results, we rule out that the modification of the local electric field or buffering of the local pH are the main reasons for the cation effects observed. These theories suggest that the cation should just affect the CO_2 reduction rate and that this reaction should still take place in cation-free electrolytes. Our results also confirm the view suggested by Chen et al.[22] and Resasco et al.[27], i.e. that a key role of cations on CO_2 reduction is to stabilize negatively charged reaction intermediates, such as $*CO_2^-$ and $*OCCO^-$ via a local electric field effect. Besides the medium-range electric field/electric dipole interaction, we show here an explicit short-range local electrostatic interaction between partially desolvated metal cation and CO_2 accounting for a similar stabilization. Fig. 8.8 shows our proposed reaction mechanism based on the discussed experimental and computational results, together with a pictorial representation. Here, we suggest that the cation is the crucial promoter to enable the reduction process, by forming a complex with CO_2 which allows the formation of the CO_2^- intermediate. Additionally, as shown in Fig. 8.2, the more Cs^+ is added to the electrolyte, the more CO is produced, similarly to ethylene formation on copper, which follows the cation radius trend: $Cs^+ > K^+ > Na^+$ [27]. We propose that the differences in activity observed among the alkali cations for CO_2 reduction are correlated with their different concentrations at the OHP (Fig. 8.7c) and their different capability of interacting with negatively charged adsorbates, as indicated by significantly different cation-CO_2 average coordination numbers over the 2 ps simulation time (Fig. 8.6b). Metal cations with a softer hydration shell have a higher concentration at the interface and they show a stable coordination with CO_2 (Na^+, K^+, Cs^+, Fig. 8.6b), thus they are more likely to stabilize it via a M^+–O(CO_2) local interaction. Instead, hard shell cations as Li^+ coordinate poorly with CO_2, thus they are less effective in enabling this stabilization effect.

The knowledge that CO_2 can only be reduced in the presence of a metal cation interacting with the CO_2^- intermediate, has important implications. From the system design point-of-view, research efforts should focus on finding species that might have an even larger stabilizing effect on CO_2 than Cs^+, such as large multivalent cations[42] or surfactants[7]. Additionally, from the reaction modeling point-of-view, our results highlight that an accurate understanding of the electrochemical activation of CO_2 on copper, silver, and gold must involve cations and water. To simply assume a proton-coupled electron transfer as a first step in DFT-based electrocatalysis fails to account for the stabilization of the key reaction intermediates by electrolyte cations.[43–45] Instead, we here show that the explicit inclusion of cationic species allows the stabilization of the CO_2^- intermediate by around 0.5 eV and is needed to properly estimate its energy. Finally, our mechanism suggests that, at least for a pH of 3 or higher, water is the relevant hydrogen/proton donor, rather than hydronium itself which cannot activate CO_2. As a result, the CO_2 reduction reaction does not consume protons, but it generates OH^-. This statement agrees with, and provides an explanation for, our recent observation that in mildly acidic media, CO_2 reduction can completely suppress the proton reduction to hydrogen, by neutralizing protons through the generated OH^-, rendering the protons no longer available for hydrogen formation.[46]

References

(1) Kortlever, R.; Shen, J.; Schouten, K. J. P.; Calle-Vallejo, F.; Koper, M. T. M. *J. Phys. Chem. Lett.* 2015, *6* (20), 4073–4082.
(2) König, M.; Vaes, J.; Klemm, E.; Pant, D. *iScience* 2019, *19*, 135–160.
(3) Moura de Salles Pupo, M.; Kortlever, R. *ChemPhysChem* 2019, *20* (22), 2926–2935.
(4) Setterfield-Price, B. M.; Dryfe, R. A. W. *J. Electroanal. Chem.* 2014, *730*, 48–58.
(5) Verma, S.; Lu, X.; Ma, S.; Masel, R. I.; Kenis, P. J. A. *Phys. Chem. Chem. Phys.* 2016, *18* (10), 7075–7084.
(6) Thorson, M. R.; Siil, K. I.; Kenis, P. J. A. *J. Electrochem. Soc.* 2012, *160* (1), F69–F74.
(7) Banerjee, S.; Zhang, Z.; Hall, A. S.; Thoi, V. S. *ACS Catal.* 2020, *10* (17), 9907–9914.
(8) Zhang, Q.; Shao, X.; Yi, J.; Liu, Y.; Zhang, J. *Chinese J. Chem. Eng.* 2020, *28* (10), 2549–2554.
(9) Shen, J.; Lan, D.; Yang, T. *Int. J. Electrochem. Sci.* 2018, *13* (10), 9847–9857.
(10) Kyriacou, G. Z.; Anagnostopoulos, A. K. *J. Appl. Electrochem.* 1993, *23*, 483–486.
(11) Kim, H.; Park, H. S.; Hwang, Y. J.; Min, B. K. *J. Phys. Chem. C* 2017, *121* (41), 22637–22643.
(12) Kim, H.-Y.; Choi, I.; Ahn, S. H.; Hwang, S. J.; Yoo, S. J.; Han, J.; Kim, J.; Park, H.; Jang, J. H.; Kim, S.-K. *Int. J. Hydrogen Energy* 2014, *39* (29), 16506–16512.
(13) Gunathunge, C. M.; Ovalle, V. J.; Waegele, M. M. *Phys. Chem. Chem. Phys.* 2017, *19* (44), 30166–30172.
(14) Waegele, M. M.; Gunathunge, C. M.; Li, J.; Li, X. *J. Chem. Phys.* 2019, *151* (16), 160902.
(15) Akhade, S. A.; McCrum, I. T.; Janik, M. J. *J. Electrochem. Soc.* 2016, *163* (6), F477–F484.
(16) Strmcnik, D.; van der Vliet, D. F.; Chang, K.-C.; Komanicky, V.; Kodama, K.; You, H.; Stamenkovic, V. R.; Marković, N. M. *J. Phys. Chem. Lett.* 2011, *2* (21), 2733–2736.
(17) Strmcnik, D.; Kodama, K.; Van Der Vliet, D.; Greeley, J.; Stamenkovic, V. R.; Marković, N. M. *Nat. Chem.* 2009, *1* (6), 466–472.
(18) Murata, A.; Hori, Y. *Bull. Chem. Soc. Jpn.* 1991, *64* (1), 123–127.
(19) Hori, Y.; Suzuki, S. *Bull. Chem. Soc. Jpn.* 1982, *55* (3), 660–665.
(20) Frumkin, A. N. *Trans. Faraday Soc.* 1959, *55* (1), 156–167.
(21) Ringe, S.; Clark, E. L.; Resasco, J.; Walton, A.; Seger, B.; Bell, A. T.; Chan, K. *Energy Environ. Sci.* 2019, *12* (10), 3001–3014.
(22) Chen, L. D.; Urushihara, M.; Chan, K.; Nørskov, J. K. *ACS Catal.* 2016, *6* (10), 7133–7139.
(23) Hussain, G.; Pérez-Martínez, L.; Le, J.-B.; Papasizza, M.; Cabello, G.; Cheng, J.; Cuesta, A. *Electrochim. Acta* 2019, *327*, 135055.
(24) Singh, M. R.; Kwon, Y.; Lum, Y.; Ager, J. W.; Bell, A. T. *J. Am. Chem. Soc.* 2016, *138* (39), 13006–13012.
(25) Ayemoba, O.; Cuesta, A. *ACS Appl. Mater. Interfaces* 2017, *9* (33), 27377–27382.
(26) Zhang, F.; Co, A. C. *Angew. Chemie - Int. Ed.* 2020, *59* (4), 1674–1681.
(27) Resasco, J.; Chen, L. D.; Clark, E.; Tsai, C.; Hahn, C.; Jaramillo, T. F.; Chan, K.; Bell, A. T. *J. Am. Chem. Soc.* 2017, *139* (32), 11277–11287.
(28) Silvestrelli, P. L. *J. Chem. Phys.* 2017, *146* (24), 1–31.
(29) García, G.; Koper, M. T. M. *ChemPhysChem* 2011, *12* (11), 2064–2072.
(30) Jacobse, L.; Raaijman, S. J.; Koper, M. T. M. *Phys. Chem. Chem. Phys.* 2016, *18* (41), 28451–28457.
(31) Bewick, A.; Thomas, B. *J. Electroanal. Chem.* 1975, *65* (2), 911–931.
(32) Schouten, K. J. P.; Pérez-Gallent, E.; Koper, M. T. M. *J. Electroanal. Chem.* 2013, *699*, 6–9.

(33) Monteiro, M. C. O.; Jacobse, L.; Touzalin, T.; Koper, M. T. M. *Anal. Chem.* 2020, *92* (2), 2237–2243.
(34) Voogd, J. M. De; Spronsen, M. A. Van; Kalff, F. E.; Bryant, B.; Ostoji, O.; Haan, A. M. J. Den; Groot, I. M. N.; Oosterkamp, T. H.; Otte, A. F.; Rost, M. J. *Ultramicroscopy* 2017, *181*, 61–69.
(35) Monteiro, M. C. O.; Jacobse, L.; Koper, M. T. M. *J. Phys. Chem. Lett.* 2020, *11* (22), 9708–9713.
(36) Henckel, D. A.; Counihan, M. J.; Holmes, H. E.; Chen, X.; Nwabara, U. O.; Verma, S.; Rodríguez-López, J.; Kenis, P. J. A.; Gewirth, A. A. *ACS Catal.* 2021, *11* (1), 255–263.
(37) Lukaszewski, M.; Soszko, M.; Czerwiński, A. *Int. J. Electrochem. Sci.* 2016, *11* (6), 4442–4469.
(38) Macao, L. H.; Santos, M. C.; Machado, S. A. S.; Avaca, L. A. *J. Chem. Soc. - Faraday Trans.* 1997, *93* (22), 3999–4003.
(39) Bellarosa, L.; García-Muelas, R.; Revilla-López, G.; López, N. *ACS Cent. Sci.* 2016, *2* (2), 109–116.
(40) Marcus, Y. *Chem. Rev.* 2009, *109*, 1346–1370.
(41) Birdja, Y. Y.; Pérez-Gallent, E.; Figueiredo, M. C.; Göttle, A. J.; Calle-Vallejo, F.; Koper, M. T. M. *Nat. Energy* 2019, *4* (9), 732–745.
(42) Schizodimou, A.; Kyriacou, G. *Electrochim. Acta* 2012, *78*, 171–176.
(43) Nørskov, J. K.; Rossmeisl, J.; Logadottir, A.; Lindqvist, L.; Kitchin, J. R.; Bligaard, T.; Jónsson, H. *J. Phys. Chem. B* 2004, *108* (46), 17886–17892.
(44) Peterson, A. A.; Abild-Pedersen, F.; Studt, F.; Rossmeisl, J.; Nørskov, J. K. *Energy Environ. Sci.* 2010, *3*, 1311–1315.
(45) Rossmeisl, J.; Chan, K.; Ahmed, R.; Tripković, V.; Björketun, M. E. *Phys. Chem. Chem. Phys.* 2013, *15*, 10321–10325.
(46) Bondue, C. J.; Graf, M.; Goyal, A.; Koper, M. T. M. *J. Am. Chem. Soc.* 2021, *143* (1), 279–285.

9

The role of cation acidity on the competition between hydrogen evolution and CO_2 reduction on gold electrodes

This chapter is based on Monteiro, M. C. O., Dattila, F., López, N., Koper, M. T. M. *J. Am. Chem. Soc.,* DOI: 10.1021/jacs.1c10171 (2021)

Abstract

The electrochemical CO_2 reduction (CO_2RR) is a sustainable alternative to the exploitation of fossil resources for producing fuels and chemicals. Metal cations in the electrolyte have a strong impact on the reaction activity and selectivity. To date, mainly alkali cations have been studied in detail, although experimental and theoretical works suggest that multivalent species might be even better candidates. Still, little is known regarding how these multivalent ions affect CO_2RR and, more importantly, the competing hydrogen evolution reaction. In this work, we elucidate these phenomena by studying these reactions on polycrystalline gold electrodes in electrolytes containing Li^+, Cs^+, Be^{2+}, Mg^{2+}, Ca^{2+}, Ba^{2+}, Al^{3+}, Nd^{3+} and Ce^{3+} (pH = 3). We observe that cations have no effect on proton reduction at low overpotentials, but at more alkaline surface pH the more acidic cations (Be^{2+}, Al^{3+}, Nd^{3+}, and Ce^{3+}) undergo hydrolysis, generating a second proton reduction regime. We find that the activity and onset for the water reduction reaction correlate with cation acidity, with weakly hydrated trivalent species leading to the highest activity. This has important implications for CO_2RR, as we find that these acidic cations only favor CO_2RR at low overpotentials and in acidic media. At high overpotentials (equivalent to neutral/alkaline pH at the surface), the activity for CO increases in the order Ca^{2+} < Li^+ < Ba^{2+} < Cs^+, showing that to favor this reaction there has to be an interplay between cation stabilization of the CO_2^- intermediate, cation accumulation at the Outer Helmholtz Plane (OHP), and activity for water reduction. *Ab initio* molecular dynamics simulations with explicit electric field confirm that, showing that cation acidity is key to rule cation concentration at the interface and H_2O reduction activity. Non-acidic cations at the metal surface show lower repulsion, so they accumulate more at the OHP and trigger local promoting effects. Water dissociation kinetics is increasingly promoted by strongly acidic cations (Nd^{3+}, Al^{3+}), in agreement with experimental evidence. Larger hydrated radius cations (Cs^+, Ba^{2+}, Nd^{3+}) coordinate to adsorbed CO_2 steadily, thus they enable CO_2^- stabilization and subsequent barrierless protonation to COOH and further reduction products.

9.1 Introduction

The electrochemical reduction of carbon dioxide (CO_2RR) offers a sustainable pathway to produce fuels or base chemicals, without relying on finite and non-renewable resources such as oil and gas.[1–3] During CO_2RR in aqueous electrolyte, the hydrogen evolution reaction (HER) occurs concomitantly, which may significantly lower the faradaic efficiency of CO_2RR.[4–6] Depending on the reaction conditions, specifically the electrolyte pH, the production of hydrogen can either happen through the direct reduction of protons ($2H^+ + e^- \rightarrow H_2$) or the reduction of the solvent itself ($2H_2O + 2e^- \rightarrow H_2 + 2OH^-$). Different strategies have been adopted to favor CO_2RR over HER, such as enhancing mass transport[6], using porous catalysts[7,8] or modifying the catalyst surface.[9] Another approach is to change the electrolyte composition, since the cation identity, for instance, is known to highly influence both the CO_2RR[10–12] reaction and HER[13,14] rates. Up to now, mainly alkali cations have been employed for CO_2RR, but recent theoretical work suggests that multivalent cations may lead to an even larger enhancement of the reaction activity.[11] Still, in order to use that in favor of the CO_2RR in aqueous media, one also has to understand how cation properties affect the competing HER.

Since the work of Hori and co-workers it is known that the species in the electrolyte can influence the product selectivity and faradaic efficiency of the CO_2RR.[15–17] Due to the strong effect that cations have on CO_2RR, mainly alkali metals in neutral or alkaline media have been investigated using copper[11], silver[18] or gold[19,20] electrodes. It has been established that the CO_2RR activity increases in the order: $Li^+ < Na^+ < K^+ < Cs^+$. Three main theories have been suggested to explain this trend, namely: local buffering at the interface[21], changes in the (local) electric field[11,22,23] and electrostatic interactions with reaction intermediates[22,24]. In Chapter 8, we elucidated that the key role of cations on CO_2RR to CO is to stabilize the negatively charged reaction intermediate, CO_2^-.[25] Specifically, we observe that without a metal cation in the electrolyte, CO is not produced on gold, silver, and copper electrodes. Through *ab initio* molecular dynamics simulations, we showed that besides the medium-range electric field/adsorbate dipole interaction at the interface, there is an explicit short-range local electrostatic interaction between the partially desolvated metal cations and CO_2. Additionally, we observe that the activity trend reported for alkali cations originates both from different cation surface concentrations at the Outer Helmholtz Plane (OHP) and their different intrinsic ability to coordinate to adsorbed CO_2^-. In the alkali cations group, these vary from

low concentrations and almost no bond for Li^+, to higher concentrations in the OHP and almost double coordination between cation and CO_2 oxygens for Cs^+.

Considering the previously discussed key role of cations on CO_2RR, it would be attractive to find cationic species that can have an even larger stabilizing effect on CO_2 than Cs^+, and perhaps accumulate at the OHP at higher concentrations, such as large multivalent cations[26] or surfactants[27]. One of the few experimental works on the effect of multivalent cations on CO_2RR was carried out by Schizodimou and Kyriacou[26], who reported that multivalent cations increase the rate of CO_2RR on Cu(88)-Sn(6)-Pb(6) electrodes in highly acidic media (1.5 M HCl) and low overpotentials (–0.65 V vs. Ag/AgCl). The authors observed that at more negative overpotentials, the effect of the cations was less pronounced, and this was attributed to a change in the reaction rate determining step. Although the electrolysis was performed for 2 hours in each electrolyte, no comment was made in terms of salt deposition and/or electrode stability, which are factors that could strongly influence the cation trends observed. For example, in our recent work on polycrystalline gold electrodes, after one HER cyclic voltammogram from 0 to –1.2 V vs. RHE at 50 mV s^{-1} in $Al_2(SO_4)_3$ (argon saturated, pH 3) we observe deposition of a porous aluminium hydroxide layer on the whole surface.[28] Density functional theory (DFT) calculations presented in the work of Ringe et al.[11] also suggest that multivalent cations can have a beneficial effect on the activity of CO_2RR. They predicted the effect of cations on the activity towards CO on Ag(111) electrodes at –1 V vs. RHE (in a nominal 0.1 M electrolyte) and proposed that species such as Be^{2+}, Al^{3+}, Ba^{2+} and La^{3+}, in theory, should exhibit up to two orders of magnitude higher activity for CO than Cs^+, since their larger charge would enhance the interfacial field. In contrast, Bhargava et al.[29] recently reported that multivalent cations hinder the electrochemical reduction of CO_2 to CO on silver gas diffusion electrodes, due to the formation of deposits that block Ag active sites. Despite these interesting predictions and results, in the work of Schizodimou and Kyriacou[26], Ringe et al.[11], and Bhargava et al.[29], the effect of multivalent cations on the competing hydrogen evolution reaction was not discussed. How cations influence the activity of the competing HER on copper surfaces has not been studied in detail. However, on gold and silver electrodes, for instance, the activity for water reduction in alkaline media increases in the order $Li^+ < Na^+ < K^+ < Cs^+$, in solutions of neutral to alkaline pH, and relatively low cation concentration.[14,30] In acidic media, we previously observed that alkali cations have no significant effect on proton reduction[25], while Al^{3+} seems to give rise to an additional proton diffusion limited

regime at more cathodic potentials.[28] However, to fully understand the interplay between CO_2RR and HER activity, and how cation properties (hydration radius, charge, etc.) play a role, a more systematic study is required.

Therefore, in this Chapter we have studied HER and CO_2RR on polycrystalline gold electrodes with the aim to determine how different mono- and multivalent metal cations (Li^+, Cs^+, Be^{2+}, Mg^{2+}, Ca^{2+}, Ba^{2+}, Al^{3+}, $Nd^{3+}$and Ce^{3+}) affect the individual reaction rates. We find that acidic cations with a moderate hydration radius (Nd^{3+}, Ce^{3+}), promote CO_2RR in acidic media/low overpotentials, while the non-acidic, weakly hydrated Cs^+ is the cation that promotes CO_2RR the most in alkaline media/high overpotentials. These differences come from the extreme promotional effects that acidic cations have on water reduction at high overpotentials. We further probed the interaction of the different cations with water and CO_2 using *ab initio* molecular dynamics simulations with an explicit applied electric field and explicit solvation. The simulations highlight three key parameters for CO_2RR performance ruled by cation acidity: cation accumulation at the OHP, water dissociation kinetics, and cation-CO_2 coordination. Overall, in this work, we elucidate through a combination of experiments and simulations which cation properties are important to consider when designing an optimal electrolyte for the CO_2RR system.

9.2 Effect of alkali cations on proton, water, and CO_2 reduction

To better understand how different metal cations (M^{n+}) affect the competition between the CO_2 reduction reaction (CO_2RR) and hydrogen evolution (HER), we studied these reactions through cyclic voltammetry using polycrystalline gold electrodes. First, we studied the effect of alkali cations on HER and CO_2RR in acidic electrolytes (pH 3, 0.1 M M_2SO_4), with M^{n+} = Li^+, Na^+, K^+ and Cs^+. Hydrogen evolution was carried in argon purged solutions as shown in Fig. 9.1a, where a cathodic current due to proton reduction starts at about –0.35 V vs. SHE and a peak due to proton diffusion limitation is observed at –0.66 V vs. SHE. At more negative potentials, the current decreases as the diffusion layer thickness increases. We find that the cation identity does not affect the proton reduction current, both in the kinetic and diffusion limited regimes, in agreement with our previous work where the reaction was carried out in more dilute electrolytes.[25] We also performed cyclic voltammetry (CV) in CO_2 atmosphere (Fig. 9.1b) in order to distinguish the HER current from the CO_2RR current. At potentials more negative than –0.6 V vs. SHE, an increase in the total current is observed in the order Cs^+ > K^+ > Na^+ > Li^+.

Moreover, CO_2 reduction happens in parallel to proton reduction already at low overpotentials, with Cs^+ leading to the highest activity. As the potential is scanned more negatively and the concentration of protons near the surface decreases, a kinetic reduction current appears, which is a contribution from both water and CO_2 reduction and follows the same cation trend. In a consecutively recorded positive-going scan (inset of Fig. 9.1b) a faradaic current is observed due to the oxidation of the CO produced after polarizing the electrode negatively, which in this work we employ as a semi-quantitative analysis of the amount of CO produced. Blank CVs of the gold electrode before the measurements are shown in Fig. F.2 in Appendix F.

This consecutive cathodic/anodic voltammetry is used here as a semi-quantitative tool to selectively probe the amount of CO produced during CO_2RR as a function of potential, *in situ*, and with high sensitivity. Basically, after polarizing the gold electrode at different negative potentials, a positive-going scan is recorded until 1.3 V so the CO produced in the cathodic scan is directly oxidized at the electrode surface. After each measurement, the electrode potential is held for 4 min in the double layer region to restore the diffusion layer and bring the pH near the surface back to the bulk pH at the beginning of each cycle. The voltammetry of these potential opening experiments can be seen in Fig. F.3 in Appendix F, for measurements performed in CO_2 saturated 0.1 M M_2SO_4, pH = 3. The amount of CO produced at every potential was obtained by integrating the CO oxidation CVs and subtracting the double layer charge. We see in Fig. 9.1c that the activity for CO production increases in the order $Li^+ < Na^+ < K^+ < Cs^+$ in the whole potential range. This trend is in agreement with literature and our previous work[25], showing that the consecutive cathodic/anodic voltammetry method presented here is a reliable tool to probe activity for CO with high sensitivity. However, here we see that in the Cs^+ and K^+ electrolyte more CO is produced already at lower potentials than in Na^+ and Li^+ (see the figure inset). This is due to the higher concentration of these weakly hydrated cations near the surface at these potentials, and the higher capability of Cs^+ and K^+ to coordinate with the adsorbed CO_2^- reaction intermediate.[25] Similar experiments as shown in Fig. 9.1a and Fig. 9.1b were carried out in alkaline media (0.1 M $MHCO_3$) and are shown in Fig. F.5a and Fig. F.5b in Appendix F. We find that the activity for water reduction is higher in solutions containing weakly hydrated cations, and increases in the order: $Li^+ < Na^+ < K^+ < Cs^+$, in agreement with what was previously reported by Xue et al. for HER on Au(111) in MOH electrolytes.[30] The activity for CO_2 reduction in bicarbonate electrolyte also follows the same trend with alkali cation identity as water reduction, which means that differently from

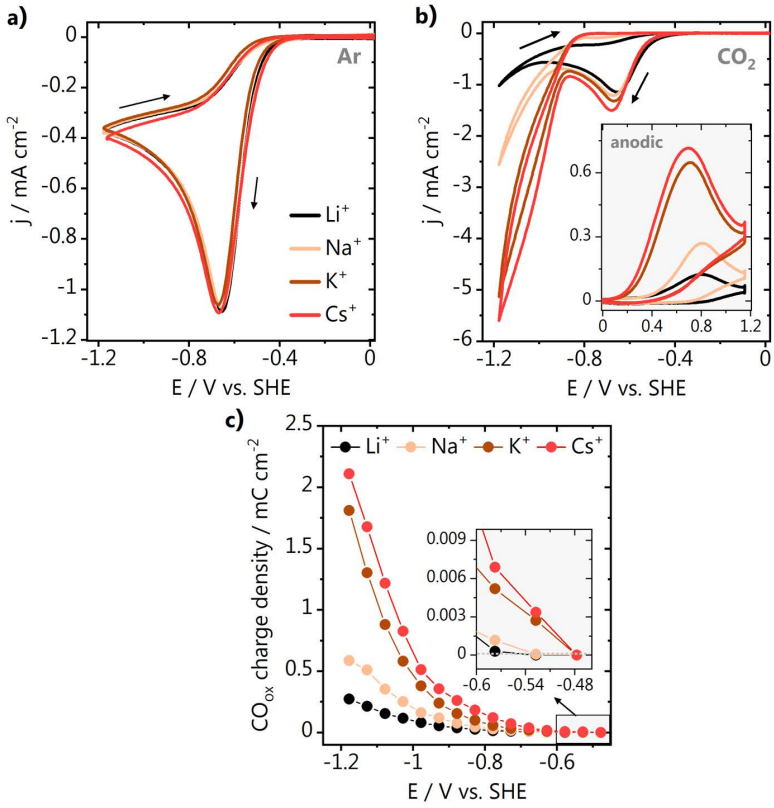

Fig. 9.1. Cyclic voltammetry of **a)** proton reduction and **b)** CO_2 reduction in acidic media (0.1 M M_2SO_4, pH = 3). **c)** Amount of CO produced as a function of potential, obtained by consecutive cathodic/anodic voltammetry.

acidic media, here the alkali cations cannot be used to exclusively favor the CO_2 reduction reaction over HER. Here, we observed that alkali cations do not have any effect on proton reduction, while the activity for CO_2RR to CO and water reduction increases in the order: $Li^+ < Na^+ < K^+ < Cs^+$. We see that the consecutive cathodic/anodic voltammetry method which we present here can be used to reliably probe activity for CO even at low overpotentials, which will be valuable in the next section when we look at multivalent cation species. The advantage is that we are not strongly hindered by detection limits, which is the case for other commonly used product detection techniques, such as gas chromatography. In the next sections we probe the effect of mono- and multivalent cations, first on

hydrogen evolution (proton and water reduction) and then on CO_2 reduction, both experimentally and through simulations.

9.3 Effect of multivalent cations on proton and water reduction

To further elucidate which cation properties determine the activity for HER, we performed cyclic voltammetry on polycrystalline gold at pH 3 in electrolytes containing the following mono- and multivalent metal cations: Li^+, Cs^+, Be^{2+}, Mg^{2+}, Ca^{2+}, Ba^{2+}, Al^{3+}, Nd^{3+}, and Ce^{3+}. In acidic media (pH = 3) all cations investigated are fully soluble, although we have previously reported that acidic cations such as Al^{3+} may reversibly deposit on gold as layered hydroxides during HER, upon an increase in the local alkalinity caused by the surface reaction.[28] To minimize this possible deposition, either 0.1 M Li_2SO_4 or 0.2 M $LiClO_4$ were used here as background electrolytes and only 1% of a given mono- or multivalent cation M^{n+} was added to the solution. 1 mM M^{n+} was added to 0.1 M Li_2SO_4 background, and 2 mM M^{n+} added to the 0.2 M $LiClO_4$, keeping the Li^+ concentration and the M^{n+}/Li^+ ratio constant. Solutions of these two anions were used because not all sulfate/perchlorate salts containing the multivalent cations are available or soluble.

Additionally, using a Li^+ containing electrolyte as background allows us to normalize the data to the results in pure Li^+, and to consequently make a qualitative comparison between sulfates and perchlorates. The following cations were studied in the Li_2SO_4 electrolyte: Cs^+, Be^{2+}, Mg^{2+}, Al^{3+}, Nd^{3+}, and Ce^{3+}; while Ca^{2+} and Ba^{2+} were added to $LiClO_4$. We performed the measurements in argon saturated electrolyte and evaluated how the different cations influence the activity for proton (at low overpotential) and water reduction (at high overpotential). The HER cyclic voltammetry is available in Appendix F together with the blank voltammograms of the gold electrode, recorded before each measurement (Fig. F.8 and Fig. F.9). In the cyclic voltammetry (Fig. F.9), we see that similarly to the alkali cations, the multivalent species do not affect the current of the first regime of proton reduction (cathodic peak at low overpotential). Although the metal cation in solution does not seem to have an effect, comparing the proton reduction current obtained in the sulfate and perchlorate electrolytes (both pH 3), a more negative proton reduction current is found in sulfate. This is due to the stronger buffer capacity of the sulfate electrolyte, which leads to less changes in local pH and consequently a higher proton concentration at the electrode/electrolyte interface.

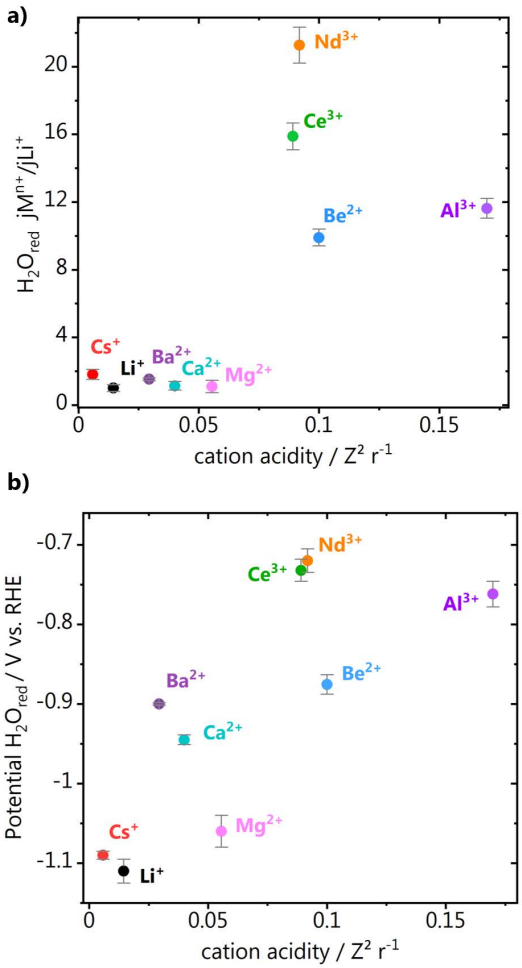

Fig. 9.2. Effect of multivalent cations on HER. **a)** Normalized activity for water reduction extracted from the hydrogen evolution voltammetry performed at pH 3 in 0.1 M Li_2SO_4 + 1 mM M^{n+} electrolytes with M^{n+} = Li^+, Cs^+, Be^{2+}, Mg^{2+}, Al^{3+}, Nd^{3+}, Ce^{3+} and 0.2 M $LiClO_4$ + 2 mM M^{n+} with M^{n+} = Ca^{2+}, Ba^{2+}. The normalization was done by dividing the water reduction current density (at –1.1 V vs. RHE) in 0.1 M Li_2SO_4 + 1 mM M^{n+} by the current density obtained in pure 0.1 M Li_2SO_4. The same was done for the measurements in perchlorate. **b)** Potentials at which the activity for water reduction strongly increases, obtained by taking the derivative of the CVs from Fig. F.7a and the CVs for Ba^{2+} and Ca^{2+} from Fig. F.7b. All electrolytes were saturated with argon prior to the measurements. Error bars (s.d.) were calculated based on three individual measurements.

While the effect of multivalent cations on proton reduction at low overpotential is subtle, we see in Fig. F.9 that they have a strong effect on water reduction, with much more pronounced differences than previously observed for the alkali cations (Fig. F.5, Appendix F). Fig. 9.2a shows a comparison of the activity for water reduction in the presence of the different cations, normalized to the activity obtained in the pure lithium (sulfate or perchlorate) electrolytes. The activity is compared in terms of the water reduction current density obtained at –1.1 V vs. RHE, with the exception of Li^+, Mg^+, and Cs^+ that only show high activity for water reduction at more negative potentials. For these, the current density at –1.2 V vs. RHE was used. We see in Fig. 9.2a the relative activity plotted as a function of the cation acidity, which is defined as the ratio of the cation charge and its ionic radius (derived from the Born equation)[31]. Trivalent cations and Be^{2+} lead to the highest activity for water reduction, whereas the divalent and monovalent species give a much lower (and similar) activity. In fact, within a valence group, we observe that the highest activity is always found for the weaklier hydrated cations: Nd^{3+} and Ce^{3+}, Ba^{2+} and Cs^+. This is likely due to their higher concentration at the OHP at a given potential. In Fig. 9.2b we see the effect of the different cations on the potential at which there is a strong increase in the activity for water reduction. This was determined by taking the derivative of the cyclic voltammograms from Fig. F.7 (Appendix F) and extracting the potential where there is a change in slope. This represents the potentials at which the water reduction current significantly increases, which are shown in Fig. 9.2b for the different cations. We observe that both the activity and water reduction "onset" potential show a strong correlation with the cation acidity. Even though the cations with a smaller ionic radius are more acidic, leading to weaker hydrogen bonds in the water molecules in their hydration shell, their high hydration/ solvation energy hinders their accumulation near the surface. Therefore, the highest activity and earliest onset for water reduction are found for moderately acidic and relatively weakly hydrated cations as Nd^{3+} and Ce^{3+}. We show in Fig. F.8 in Appendix F how the cation acidity is related to the Gibbs free energy of hydration, or in other words, to how strongly water molecules in the cation´s hydration shell interact with the positive charge of the ion.[32] Considering that on gold, the Volmer step ($H_2O + e^- + * \rightarrow *H + OH^-$) is the rate determining step for the water reduction reaction, acidic (trivalent) cations likely lead to a stronger stabilization of the transition state of the water dissociation step (Eq. 9.1).[14]

This will be explored in more detail in the modelling section. It is also important to note that Be^{2+} is an outlier regarding the trends found in Fig. 9.2: in solution, Be^{2+} behaves more like a trivalent species, due to the very high charge density of the beryllium atom, caused by its small size. [33]

$$(H_2O + e^- + * + M^{n+} \rightarrow *H\text{–}OH^{\delta-}\text{–}\ M^{n+} + (1-\delta)e^- \rightarrow *H + OH^- + M^{n+}) \qquad \text{Eq. 9.1}$$

9.4 Cation hydrolysis

As mentioned previously, we do not observe any significant effect of cations on the proton reduction current at low overpotentials, which we call here the first proton reduction regime. However, as shown in Fig. 9.3a, in solutions containing very acidic cations, such as Be^{2+}, Al^{3+}, Nd^{3+}, and Ce^{3+}, a second proton reduction regime (indicated by the black arrows) is observed in the HER cyclic voltammetry at more negative potentials, due to hydrolysis of water molecules from the cation´s hydration shell. This phenomenon had also been observed in our previous work, where micromoles of Al^{3+} were added to the electrolyte, however at the time this was still poorly understood.[28] As shown in the schematics of Fig. 9.3b and the table in Fig. 9.3c, when the pH in the surroundings of a cation reaches the pK_a of hydrolysis of that species, a hydronium ion is released into the electrolyte. The positive charge of the conjugated acid (metal cation) weakens the hydrogen bond of the water molecule by drawing the electron density of the oxygen towards the metal center, thus leading to the release of a proton in solution. The reaction can be expressed as shown in Eq. 9.2, considering water is the only complexing species, where n is the charge of the cation and N is the number of water molecules within its coordination shell.

$$M^{n+}(H_2O)_N \leftrightarrow MOH^{(n-1)+}(H_2O)_{N-1} + H^+ \qquad \text{Eq. 9.2}$$

Once the local pH reaches the pK_a of hydrolysis of the different species, hydronium ions are produced locally and will be readily reduced at the surface, giving rise to the second proton reduction regime from Fig. 9.3a. This happens at more acidic local pH (lower overpotentials) for Al^{3+} cations, in comparison to Be^{2+}, Nd^{3+}, and Ce^{3+}, as typically, the larger the charge and the smaller the radius, the lower the pH at which the metal cation will hydrolyze. Note that for Nd^{3+} and Ce^{3+}, which have the same pKa, the second proton reduction regime indeed starts at nearly the same potential. Be^{2+} is again an exception, as it also forms complexes

with the sulfate ions in the electrolyte, which delays the hydrolysis reaction.[34] Hao et al.[35] argue that Be^{2+} ions are protected from hydrolysis by the formation of $BeSO_4$ ion pairs, and that most of the hydronium ions produced by hydrolysis are initially converted to bisulfate ions. For all cations shown in Fig. 9.3a, as the local pH becomes more alkaline (due to the increase in water reduction current at more cathodic potentials), more water molecules undergo hydrolysis, forming polymeric species of various stoichiometries, depending on the cation charge, size, and coordination number.[36] Eventually, at sufficiently alkaline local pH, a solid hydroxide layer can form on the electrode surface, whose properties will depend on the temperature, anions, ion concentration (Eq. 9.3), where n is the charge of the cation and N is the number of water molecules within its coordination shell.

$$\mathrm{M}^{n+}(\mathrm{H_2O})_N \leftrightarrow \mathrm{MO}_x(\mathrm{OH})_{n-2x}(\mathrm{s}) + n\mathrm{H}^+ + (N - n + x)\mathrm{H_2O} \qquad \text{Eq. 9.3}$$

In Chapter 7, we observed that after recording five HER cyclic voltammograms of a polycrystalline gold electrode in a 0.1 M $Al_2(SO_4)_3$ electrolyte, ~200 nm thick porous hydroxide plates formed on the gold surface, intercalated by sulfate anions.[28] The formation of a thin hydroxide layer upon cycling is also observed here in the consecutive anodic cyclic voltammetry for the various cations (inset of Fig. 9.3a), as evidenced by the shift and suppression in the gold oxide/reduction peaks. Five consecutive CVs can be seen in Fig. F.9 in Appendix F, where this effect is even more pronounced as the proton reduction current decreases from cycle 1 to 5. However, due to the low amount (1%) of acidic cations in the lithium background electrolytes, after the 5 cycles are recorded and the electrode is held at 0.1 V for four minutes, the local pH goes back to the (acidic) bulk value and the hydroxide thin layer formed dissolves; indeed, no deposits are found in SEM/EDX analysis after these experiments (not shown).

We see that the first regime of proton reduction (at low overpotentials) is not influenced by the metal cations in the electrolyte. Still, acidic cations give rise to a second proton reduction regime, due to a local discharge of protons near the surface upon cation hydrolysis. The potential at which this is observed, is a function of the pK_a of hydrolysis. For water reduction, we find that the activity increases going from mono- to di- to trivalent cations due to the effect that acidic cations have on the water dissociation step. Within a valence group, weakly hydrated cations lead to higher activity, as our previous study suggests that these species accumulate more at the OHP. Next, we investigate the consequences of these

trends found for HER on the activity of CO_2 reduction, by carrying out the reaction in CO_2 atmosphere in the same electrolytes from Fig. 9.2.

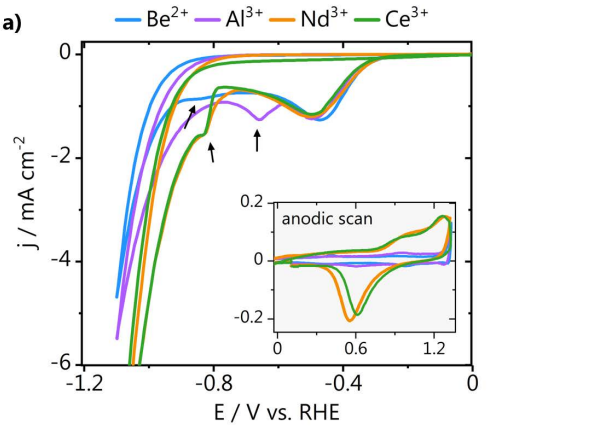

c)

cation	pK_a hydrolysis
Al^{3+}	5.0
Nd^{3+}	8.5
Ce^{3+}	8.5
Be^{2+}	6.2

Fig. 9.3. a) Hydrogen evolution cyclic voltammetry performed at pH 3 in 0.1 M Li_2SO_4 + 1 mM M^{n+} electrolytes with M^{n+} = Be^{2+}, Al^{3+}, Nd^{3+}, Ce^{3+}. An anodic scan recorded directly after HER is shown in the graph inset. **b)** Schematic representation of the mechanism of cation hydrolysis and **c)** pK_a of hydrolysis of the different species, taken from Ref 36.

9.5 Effect of multivalent cations on CO_2 reduction

Fig. 9.4 shows the activity for CO production as a function of potential in electrolytes containing different mono- and multivalent cations. CO_2RR was carried out in the same electrolytes as the measurements shown in Fig. 9.2, and the CO produced as a function of potential was quantified using the consecutive

cathodic/anodic voltammetry method we used for the alkali cations in Fig. 1c. We see in Fig. 9.4a that in sulfate electrolyte at high overpotentials, the highest absolute activity for CO is found in the presence of Cs^+, followed by Li^+, Mg^+, Be^{2+}, Al^{3+}, Nd^{3+}, and Ce^{3+}. In the case of perchlorates, as shown in Fig. 9.4b, more CO is formed at high overpotentials in the Ba^{2+} electrolyte, followed by Ca^{2+} and Li^+. This seems to contradict the predictions made in the work of Ringe et al.[11], in which DFT calculations suggested that higher activity for CO_2RR to CO should be found in electrolytes containing trivalent cations, followed by divalent and monovalent (at –1 V vs. RHE), since the electronic density at the surface is expected to increase accordingly. This is because these simulations disregard the effect of the acidic multivalent cations on the competing water reduction reaction, which is the main branch of HER taking place at high overpotentials. In Fig. 9.2a we see that the activity for water reduction in the presence of species as Be^{2+}, Al^{3+}, Nd^{3+}, and Ce^{3+} is more than ten times higher than for the other cations, which explains why here, despite any promotional effect these cations may have on the CO_2RR, they actually favor even more the production of hydrogen.

Remarkably, looking at the absolute amounts of CO produced at low overpotentials (see inset of Fig. 9.4a and Fig. 9.4b), we see the opposite trend, where more CO is formed in the presence of more acidic cations. To make clearer the differences in activity for CO at low and high overpotentials, and to compare the results in sulfate with perchlorate, we normalized the CO_{ox} charge densities from Fig. 9.4a and Fig. 9.4b to the CO_{ox} charge density obtained in the pure Li_2SO_4 or $LiClO_4$ background electrolytes, respectively. This results in the relative activities depicted in Fig. 9.4c. Values above 1, represent cations that show higher activity for CO than Li^+ at a given potential, and values below 1 represent cations for which the CO_2RR is less active than in pure Li^+ electrolyte. Please note that these are only relative activities, i.e., the higher ratio for Ba^{2+} does not mean CO_2RR is more active in a Ba^{2+} electrolyte than Cs^+, as these were measured with electrolytes of two different anions. We can, however, infer that in both Ba^{2+} and Cs^+ electrolytes the activity for CO is higher at large overpotentials. With that in mind, we see in the results from Fig. 9.4c that at potentials more positive than –0.5 V vs. RHE, the more acidic cations lead to the production of more CO. At these potentials, the main branch of HER competing with CO_2RR is proton reduction, which is a reaction that is not affected by the cation identity, meaning that here the cation can selectively enhance CO_2RR. As proton reduction is here still in the kinetic limited regime (see Fig. 1a), the local pH is not expected to deviate too much from the bulk pH value,

which means that in this regime cations will not rapidly undergo hydrolysis (which would favor proton reduction) but likely can still strongly interact with the reaction interface (enhancing CO_2 reduction). At potentials more negative than –0.6 V vs. RHE, we see that the relative activity found in the presence of acidic cations drops, and higher relative activity for CO is found in the electrolytes containing Cs^+, Li^+, Ba^{2+}, and Ca^{2+}. In fact, this shows that these less acidic, weakly hydrated species

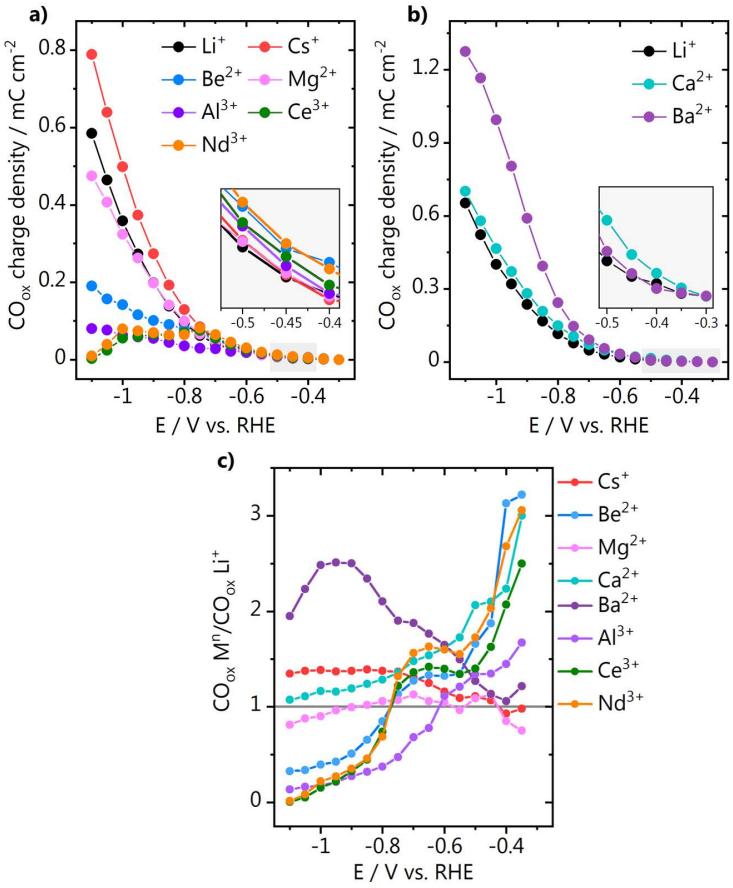

Fig. 9.4. Amount of CO produced probed *via* consecutive cathodic/anodic voltammetry at pH 3 in **a)** 0.1 M Li_2SO_4 + 1 mM M^{n+} electrolytes with M^{n+} = Li^+, Cs^+, Be^{2+}, Mg^{2+} , Al^{3+}, Nd^{3+} , Ce^{3+} and **b)** 0.2 M $LiClO_4$ + 2 mM M^{n+} with M^{n+} = Ca^{2+}, Ba^{2+}; and a **c)** qualitative comparison between the relative activity for CO found in sulfate and perchlorate electrolyte at low and high overpotential, by normalizing the CO_{ox} charge density to the one found in the pure Li_2SO_4 and $LiClO_4$ background electrolytes.

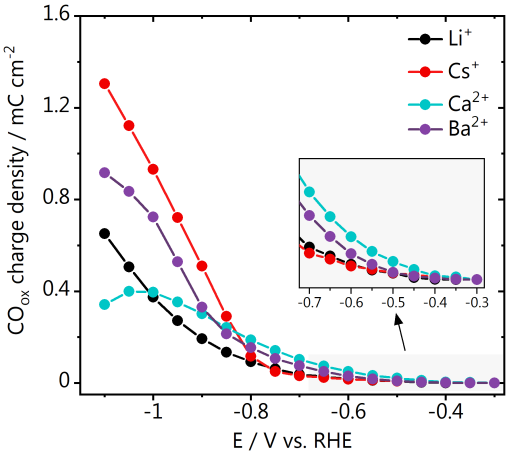

Fig. 9.5. Amount of CO produced probed *via* consecutive cathodic/anodic cycling at pH 3 in 0.2 M_xClO_4 with M^{n+} = Li^+, Cs^+, Ca^{2+}, Ba^{2+}.

lead to a good performance for the CO_2RR, in part, due to their sluggish activity for the water reduction reaction. It seems that multivalent acidic cations enhance the activity for CO, already at low overpotentials, but do not lead to a good performance at high overpotentials due to their extreme promotion of water reduction.

Although Fig. 9.4c provides a qualitative comparison of the relative activity at low and high overpotentials, it does not allow to directly assess which electrolyte leads to the absolute highest activity for CO_2RR to CO. For that, we have compared the CO_2RR activity using pure electrolytes of the most promising species (at high overpotential), namely 0.2 M M_xClO_4 electrolytes, with M^{n+} = Li^+, Cs^+, Ca^{2+}, Ba^{2+}. We see in Fig. 9.5 that at high overpotentials, Cs^+ is the cation that leads to the largest amount of CO produced, due to its weak hydration shell, allowing Cs^+ to accumulate at the reaction interface. Additionally, as Cs^+ is a non-acidic cation, its enhancement on water reduction is not so large, favoring CO_2RR. Interestingly, we find that the activity in Ba^{2+} electrolyte is higher than in Li^+, even though Li^+ has more positive hydration energy and is less acidic (see Fig. F.8 in Appendix F). Here, the activity at low overpotentials (or equivalently in acidic electrolyte) is also found to be higher in the electrolytes containing the more acidic divalent species (Ca^{2+} and Ba^{2+}), in agreement with the results from Fig. 9.4.

9.6 Computational models

To model the competing processes occurring at the electrode/electrolyte interface, we employed *ab initio* molecular dynamics (AIMD) simulations with the PBE+D2 functional.[37–39] We represented the experimental system as a $3\sqrt{3}\times3\sqrt{3}$–*R* 30° Au(111) supercell (4 layers, 15.3 Å × 15.3 Å × 30.0 Å) with 72 water molecules explicitly inserted within a 15 Å solvation layer and an additional 8 Å layer of vacuum. The solvation configuration was retrieved from our recent work,[25,40] where it was optimized for more than 10 ps (time step of 1 fs) at 300 K. Details on the density functional theory setup, as well as AIMD parameters, are available in "Density functional theory modeling" section in Appendix F. We inserted two atoms from six different species (M = Li, Cs, Mg, Ba, Al, Nd) within the solvation layer, at an initial distance from the surface of 3.3 Å. Since each species donates *n* electrons to the simulation cell depending on its valence (M^{n+}), we removed 2*n* hydrogens from the fourth water bilayer to ensure charge balance (–2*n* $|e^-|$ of 2*n* OH^- vs. +2*n* $|e^-|$ of $2M^{n+}$). Thus, these models described six different Au/water/M^{n+} systems (M^{n+} = Li^+, Cs^+, Mg^{2+}, Ba^{2+}, Al^{3+}, Nd^{3+}), with cation coverages of 0.07 ML (2/27) equivalent to 1.0-1.6 molar concentration. The six systems were optimized for 2 ps at 300 K applying an electric field of –0.3 V $Å^{-1}$,[38,53] to mimic local electric field effects.[22,54] The applied electric field roughly corresponds to –0.9 V vs. the potential of zero charge, thus –0.7 V vs. SHE in case of polycrystalline gold (see Appendix F).

To validate our methodology and confirm the convergence of the Au/water/M^{n+} systems despite the short simulation time, we first analyzed the structural properties of multivalent cations during the first 2 ps of equilibration. The cation coordination shell showed excellent agreement with experimental data.[44,45] By fitting the cation-water radial distribution functions (RDF) for all the AIMD snapshots during the 2 ps equilibration, we estimate an average cation-oxygen distance following the trend Al^{3+} < Li^+ < Mg^{2+} < Ba^{2+} < Cs^+, as reported in literature (Fig. F.10, Table F.1).[44,45] Besides, our model shows remarkable accuracy in reproducing cation coordination environment. The coordination shell of Li^+ accounts for 3-4 water molecules, while Cs^+, Ba^{2+}, and Nd^{3+} exhibit higher water-cation coordination numbers, respectively 4-6, 6-8, 4-6 (Fig. F.11 and Table F.2). Finally, cation coordination numbers of 2 and 3 for Mg^{2+} and Al^{3+} are due to $Mg(OH)_2$ and $Al(OH)_3$ compounds which form on the surface, in excellent agreement with experimental observation of the tendency of small radius acidic

cations to form hydroxide layers upon alkalization of the interface (Eq. 9.3). Overall, cation coordination numbers converged to the experimental values after 0.5-0.6 ps of AIMD (Fig. F.11), thus confirming that our model correctly reproduces the cation coordination environment.

9.7 Cation accumulation at the OHP

Looking at the mobility of the different cations across the reaction interface, we see that all the species reach a stable position after 1 ps of initial equilibration (see Fig. F.12). Al^{3+} and Mg^{2+} cations get closer to the surface ($d_{Mn\text{-surface}}$ ~2.1 Å and ~2.5 Å respectively), whilst Li^{+}, Nd^{3+}, Ba^{2+}, and Cs^{+} exhibit larger distances (~2.9 Å, ~3.1 Å, ~3.6 Å, and ~3.7 Å respectively). Interestingly, this effect is seen only for one of the two cations in the cell, while the second one remains at 1-2 Å larger distance from the surface, likely due to steric hindrance or electrostatic repulsion. We find that the average cation-surface distances calculated after 1 ps equilibration correlate well with the cation ionic radius (Fig. 9.6a), indicating that at the low cation concentrations assumed in this study (1.0-1.6 M), cations with a relatively small ionic radius locate closer to the surface due to their small solvation shell. Nevertheless, if we consider the thermodynamics associated to cation accumulation at the OHP, this process becomes increasingly hindered at higher cation concentrations (for acidic cations). To assess such effect, we estimated the energy of a single cation at

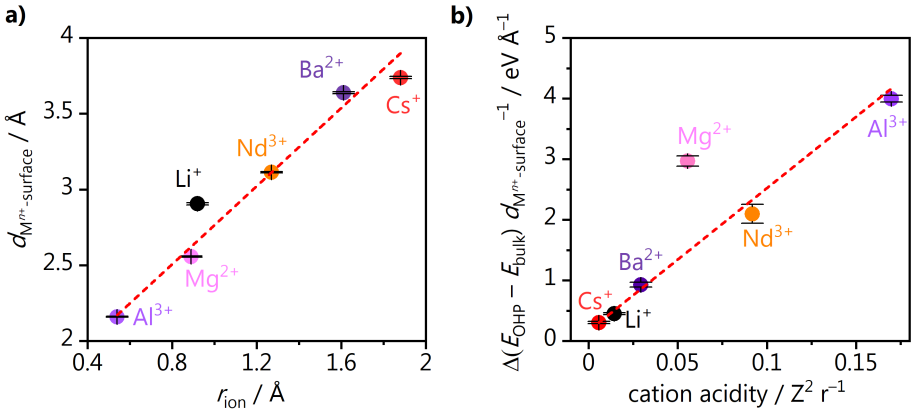

Fig. 9.6. a) Correlation between average cation-surface distance after 1 ps equilibration and cation ionic radius taken from literature values.[32] **b)** Correlation between the calculated thermodynamic driving force for cation accumulation (with respect to cation-surface distance) and cation acidity. Uncertainties are given by the standard deviations of the data points (a) and the fit errors (b) respectively.

different cation-surface distances within the OHP, E_{OHP} ($d_{M\text{-}surface}$), by carrying out single point DFT calculations on 50 AIMD snapshots (every 20 fs after 1 ps equilibration). The reference system was the gold supercell, the solvation layer, and the second cation. Then, we compared the estimated E_{OHP} to the energy of the cation at the bulk electrolyte, E_{bulk}, calculated according to the methodology introduce by Resasco et al.[24,25,46] (see Appendix F for further details). $E_{OHP} - E_{bulk}$ thus gives an estimation of the thermodynamic driving force relative to cation accumulation at a given position within the OHP (Fig. F.13). Even though this process is exothermic for any cation species ($E_{OHP} - E_{bulk} < 0$ eV), it becomes less favorable for shorter cation-surface distances, i.e. for cations closer to the surface. As qualitatively observed during the AIMD, cation-cation repulsion limits cation accumulation and this phenomenon becomes extremely significant for acidic cations, which experience stronger repulsion. The driving force for cation accumulation decreases for Al^{3+}, Nd^{3+}, and Mg^{2+} when these species approach the surface, Fig. F.13, thus this parameter correlates negatively with the cation-surface distance (Table F.3). Instead, non-acidic cations as Li^+ and Cs^+ do not exhibit any strong dependence of $E_{OHP} - E_{bulk}$ vs. cation position, due to their low valence and consequently minimal repulsion. Besides, the variation of driving force for cation accumulation with respect to $d_{M\text{-}surface}$ can be taken as a proxy of the cation-cation repulsion. Such gradient of accumulation driving force correlates with cation acidity (Fig. 9.6b), suggesting that under realistic CO_2 reduction conditions non-acidic cations accumulate more at the OHP. As highlighted in Chapter 8, higher cation concentration due to accumulation at the OHP leads to more significant intrinsic promoting effects, at least in acidic, neutral, or mildly alkaline pH.[25] At high local alkalinity, as we show in Chapter 10, high near-surface cation concentrations are detrimental to HER on gold and platinum, due to blockage of the surface, creating what we call the cation "inhibition regime". In the present work, we are still in the promotion regime, where we see that cation accumulation has different consequences for H_2O reduction and CO_2 reduction performance. Within the valence groups, higher H_2O reduction current densities are found for Cs^+, Ba^{2+}, and Nd^{3+} in contrast to Li^+, Mg^{2+}, and Al^{3+} (Fig. 9.2a). For CO_2 reduction, we see higher activity for Nd^{3+} (low overpotential region) and Cs^+ (high overpotential region) in comparison to Al^{3+} and Li^+ (Fig. 9.4c).

9.8 Mechanism of cation effect on H_2O, H_3O^+ and CO_2 reduction

To study the effect of a neighboring cation on water reduction, we introduced an additional H_2O adsorbed on the surface close to one of the cations, with a surface coverage of 0.04 ML (1 molecule for 27 Au surface atoms), see Fig. 9.7a. We let the resulting systems Au/water/M^{n+}/*H_2O (M^{n+} = Li^+, Cs^+, Mg^{2+}, Ba^{2+}, Al^{3+}, Nd^{3+}) equilibrate during final 2 ps at 300 K with an explicit electric field of –0.3 V $Å^{-1}$.[41,42] Upon introduction of the additional adsorbed water molecule, we see that regardless of the specific coordination between metal cations and adsorbed water, the dissociation of H_2O into OH^- and H^+ occurs (Fig. F.14). Besides this process, no significant change was observed for cation-surface distance and cation coordination shell (Fig. F.15-F.17, Table F.4). The kinetics of water dissociation can be estimated by the AIMD time required for this dissociation to take place, which followed the trend Al^{3+} ~ Nd^{3+} < Cs^+ < Ba^{2+} < Li^+ < Mg^{2+} (Fig. 9.7b). A similar trend was found experimentally for the water reduction activity, Fig. 9.2a, and cation acidity was suggested as a potential descriptor for the performance. Thus, we assessed the potential role of cation acidity in promoting the Volmer step of water reduction, since this reaction is the rate determining step. We estimated the kinetic barrier related to water dissociation on a simplified model accounting for the $3\sqrt{3}\times3\sqrt{3}$–$R30^o$ Au(111) supercell (4 layers, 15.3 Å × 15.3 Å × 30.0 Å), one cation, one adsorbed water molecule, and a cation coordination shell of 2 and 3 water molecules respectively (Fig. 9.7c with 3 H_2O, further details on the model in Appendix F)), and explicit electric field of –0.3 V $Å^{-1}$.[38,54] We chose such simplified coordination shells, since they were previously indicated as the optimal configurations for assessing adsorption energy.[47] n – 1 hydrogens were removed from the solvation layer so that the supercell included only an extra electron, donated from the M^{n+} species. We find that the cation acidity is an accurate descriptor and correlates well with the activation energy for water dissociation, as shown in Fig. 9.7d. Since we considered two different models for the coordination shell, we plot in the figure the average between the activation barriers calculated respectively with 2 and 3 explicit H_2O. In this way, we highlight the case with largest cation stabilization. Water dissociation is close to barrierless in the presence of acidic cations, thus driving the outstanding H_2O reduction performance of, for example, Nd^{3+} and Al^{3+} (Fig. 9.2a).

In the acidic surface pH regime (i.e., H_3O^+ as proton source), the Gibbs free energy for H_3O^+ dissociation correlates with cation acidity as well (Figure F.18 in

Appendix F), although exhibiting a weaker correlation. However, this process is exergonic for every cation species (ΔG < –1.0 eV) and is kinetically barrierless, thus supporting the absence of a cation effect on proton reduction (Fig. 9.1a and Fig. 9.3a). Additionally, we find that the *H adsorption energy is also cation-independent, with ΔG_{*H} ~ +0.3 eV for all the different species studied.

To extend the previous methodology to the case of CO_2 reduction, we introduced a CO_2 molecule to the initial Au/water/M^{n+} system, keeping the same surface coverage as for adsorbed water (0.04 ML, 1/27 ML), and optimizing the system for 2 ps at 300 K (Fig. 9.8a) with an explicit electric field of –0.3 V Å^{-1}.[41,42] After this equilibration, CO_2 adsorbs on the surface *via* a η^1_C conformation (monodentate through the carbon) so that the oxygen atoms coordinate to the alkali cation and to water molecules through hydrogen bonds. The introduction of the adsorbate close to the cation does not affect its position, as suggested by the absence of a significant variation of the cation-surface distance for Au/water/M^{n+} / *CO_2, (Fig. F.19 in Appendix F). Along with alkali cations[25], a cation···O(CO_2) coordination is observed as well for di- and trivalent species. Whilst Li^+ only coordinates with CO_2^- for the first 0.1 ps, Cs^+, Mg^{2+}, Ba^{2+}, Al^{3+}, Nd^{3+} steadily interact with it, accounting for average coordination numbers of 0.7 ± 0.4, 0.6 ± 0.4, 0.9 ± 0.2, 0.5 ± 0.2, 0.9 ± 0.2 (Fig. 9.8b, Table F.5). Cs^+, Ba^{2+}, and Nd^{3+} present more steady coordination, and the duration of the coordination increases according to the cation valence: Cs^+ coordinates for around 1.1 ps, whilst the bi- and trivalent counterpart for 1.3 and 2 ps respectively (Fig. 9.8b). We did not detect any significant variation of the cation coordination shells upon insertion of CO_2 (Fig. F.20, Table F.5 in Appendix F), suggesting that the adsorbate does not promote any dehydration, as in fact only already-dehydrated cations can coordinate with the adsorbate. In our recent work we demonstrated that M···O(CO_2) coordination triggers a short-range stabilization effect on *CO_2^- of around 0.5-0.6 eV,[25] which enables CO_2 electroreduction. Thus, the high CO_2 reduction activity for Nd^{3+} in the low overpotential region, and Ba^{2+} and Cs^+ in the high overpotential region (Fig. 9.4c), can be rationalized through this coordination-driven stabilizing effect.

To investigate if cations have any promoting effect as well on the protonation of the CO_2^- intermediate, we estimated the kinetic barrier related to this process with an analogous computational set up as the water dissociation case ($3\sqrt{3}\times3\sqrt{3}$–*R* 30° Au(111), one cation, *CO_2, 3 explicit water molecules, explicit electric field of –0.3 V Å^{-1}), see Fig. 9.8c. CO_2 protonation is barrierless for every cation species apart from Mg^{2+} and Al^{3+}. In the presence of Mg^{2+} and Al^{3+}, we observed kinetic barriers around 0.7 eV and 1.5 eV, which may be due to

excessive stabilization of the CO_2^- intermediate or repulsion between COOH and the acidic cations.

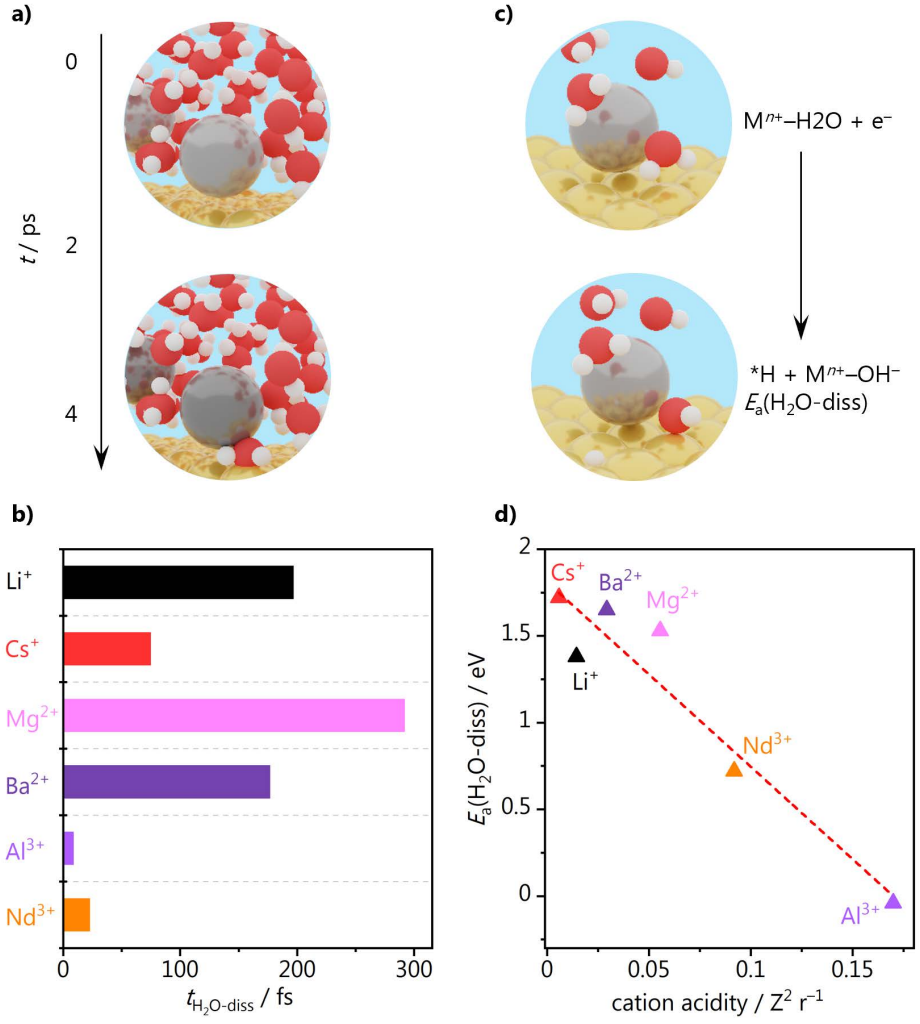

Fig. 9.7. a) Models for AIMD simulation performed at 300 K: equilibration of Au/water/M^{n+} systems (0-2 ps); equilibration of Au/water/M^{n+}/*H_2O (2-4 ps), with M^{n+} = Li^+, Cs^+, Mg^{2+}, Ba^{2+}, Al^{3+}, Nd^{3+}. **b)** Time required for dissociating adsorbed water upon interaction with M^{n+} during AIMD. **c)** Models for initial and final states for water dissociation. **d)** Activation barrier for water dissociation vs. cation acidity, calculated as average of the calculated values for 2 and 3 H_2O molecules in cation solvation shell. This process is barrierless for Al^{3+}. In the panels a) and c), Au, Cs, H, and O atoms are portrayed as yellow, dark yellow, white, and oxygen spheres, respectively.

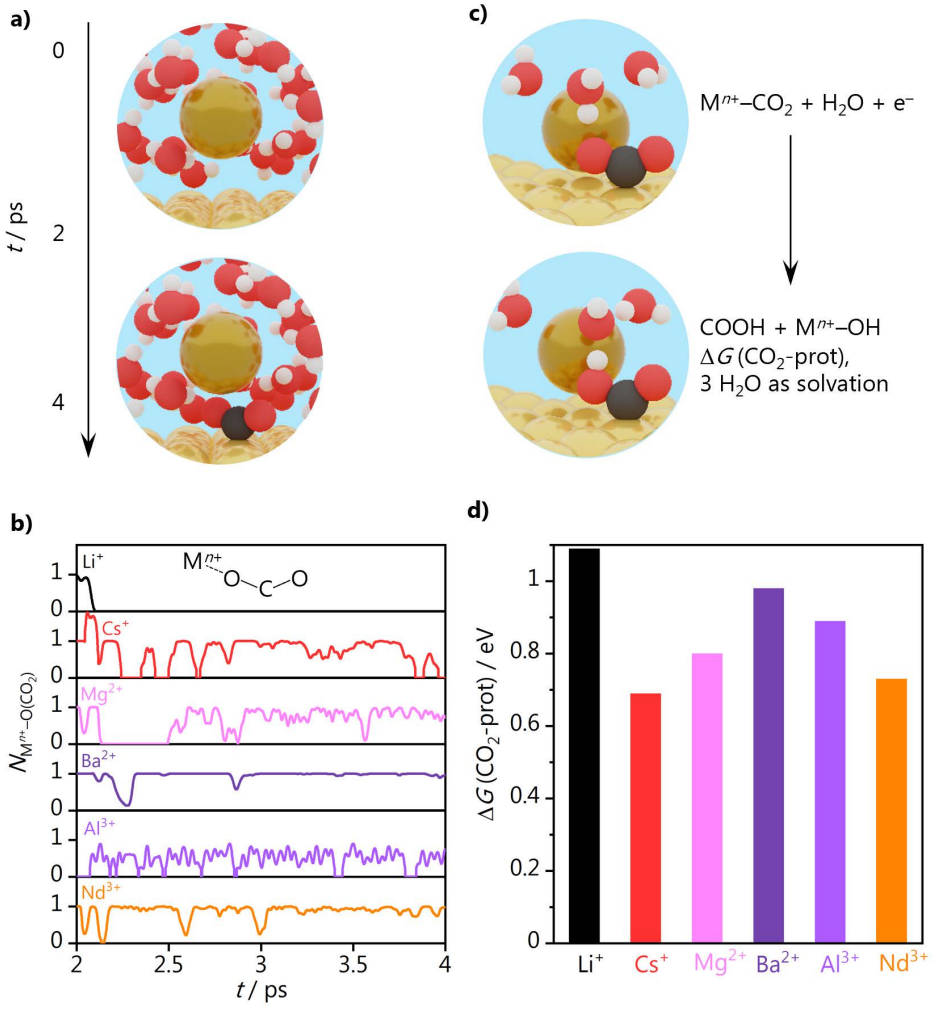

Fig. 9.8. a) Models for AIMD simulation performed at 300 K: equilibration of Au/water/M^{n+} systems (0-2 ps); equilibration of Au/water/M^{n+}/*CO_2 (2-4 ps), with M^{n+} = Li^+, Cs^+, Mg^{2+}, Ba^{2+}, Al^{3+}, Nd^{3+}. **b)** cation-CO_2 coordination ($N_{M^{n+}\text{-}O(CO2)}$) for 2 ps of AIMD simulation. **c)** Model for initial and final state of CO_2 protonation. **d)** Gibbs free energy required for COOH protonation. In the panels a) and c), Au, Cs, C, H, and O atoms are portrayed as yellow, dark yellow, dark grey, white, and oxygen balls, respectively.

This theoretical evidence may explain the low CO_2 reduction performance of Mg^{2+} and Al^{3+} compared to Ba^{2+} and Nd^{3+}respectively, in addition to its lower accumulation. Overall, the thermodynamic energy cost for COOH protonation ranges between 0.4 and 1.0 eV, with Cs^+ and Nd^{3+} accounting for the lowest values (Fig. 9.8d), and it does not depend on the cation species. Since it is just slightly endothermic, this step can occur under CO_2 reduction potentials. To summarize, the differences in CO_2 reduction performance of different cation species at low and high overpotentials can be rationalized considering the competing water reduction, cation accumulation, and coordination-driven stabilization of CO_2^-, while CO_2 protonation is cation independent. As a final remark on the intrinsic cation effect on H_2O and CO_2 reduction, we added a benchmark system where we replaced the two Li^+ atoms with two H^+, to assess the potential role of protons as reaction driving cations. H^+ quickly recombines with solvent molecules to form a H_3O^+ species (Δt < 0.3 ps, Fig. F.21), however neither of these species exhibit any interaction with $*H_2O$ and $*CO_2$ during 2 ps AIMD (Fig. F.14-F.17, F.19 and F.20, Tables F.4-F.5). This insight provides an additional validation of our previous work (Chapter 8),[25] confirming that CO_2 electroreduction needs a metal cation to occur.

9.9 Discussion

Previous work from Schizodimou and Kyriacou[26] and Ringe et al.[11] suggests that multivalent cations promote CO_2 reduction. However, these works did not discuss how the multivalent species affect the hydrogen evolution reaction, while we see that this competition actually determines the reaction selectivity. Our experimental results show that acidic (multivalent) cations only favor CO_2 reduction at low overpotentials (acidic media), whilst at high overpotentials (neutral/alkaline media) such trend overturns, and the activity for CO increases in the order Ca^{2+} < Li^+ < Ba^{2+} < Cs^+. As we proposed in our recent work,[25] an explicit coordination-driven short-range interaction stabilizes the CO_2^- intermediate and enables CO_2 reduction independently from the cation species. In fact, the energy required for CO_2 activation (~0.2-0.4 eV)[25] is significantly lowered in presence of alkali, di-, and trivalent cations (Fig. F.22, Table F.6). Thus, the CO_2 reduction activity solely correlates with the extent of such cation-CO_2 coordination. In general, trivalent cations exhibit more steady $M^{n+}\cdots O(CO_2)$ coordination than di-valent and alkali cations, and this phenomenon is more significant for weakly hydrated cation (Fig. 9.8b). This rationalizes the performances of Nd^{3+} and Al^{3+} vs. Cs^+ and Ba^{2+} for CO_2RR at low and high overpotential regions, respectively. However, it does not explain

the difference between the two potential regions. This difference must be attributed, instead, to the performance of these different cations for water reduction. From the results shown in Fig. 9.2 we clearly see that trivalent species promote water reduction more than di- and monovalent cations. This can be elucidated by the stabilizing effect acidic cations have on the transition state of water dissociation, confirmed by the linear correlation between the water dissociation activation barrier and cation acidity (Fig. 9.7d). Additionally, the reactivity of water molecules surrounding acidic cations comes from the same principle of how cations undergo hydrolysis. The positive charge of the metal cation draws the electron density of the oxygen of a water molecule towards the metal center, weakening the hydrogen bond of the water molecule, thus lowering the barrier for water dissociation. In fact, water molecules adsorbed close to a cation species undergo hydrolysis in less than 200 fs during AIMD, and this effect is faster for more acidic cations (Fig. 9.7c). We show schematically in the top panel of Fig. 9.9a, how with a smaller cation ionic radius and a larger charge, the water molecules surrounding the cation will be more reactive. In the scheme, we show for instance that water dissociation is favored in the presence of Al^{3+} cations in comparison to Li^{+}, and the degree of such promotion is represented here by different intensities of yellow shades on the hydrogen atoms. Besides, the cation acidity dictates the cation hydration energy, which in turn governs how many cations will accumulate at the OHP. This is represented in the lower panel of Fig. 9.9a, where we show that Cs^{+} cations, since they are weakly hydrated, are present at the reaction interface in higher concentrations than more strongly hydrated and more acidic cations such as Li^{+}. This explains why in Fig. 9.2, for the alkaline earth cations the highest activity for water reduction is found for Ba^{2+}, and for the trivalent species for Nd^{3+} and Ce^{3+}. Analogously, for CO_2 reduction, Nd^{3+} outperforms Al^{3+} in the low overpotential region, while the highest activities at high overpotential are observed for Cs^{+} and Ba^{2+}. The loose water structure around these weakly hydrated species prevents effective charge screening, thus allowing these cations to partially lose their hydration shell. By minimizing steric hindrance and electrostatic repulsion effects, Cs^{+}, Ba^{2+}, and Nd^{3+} accumulate more at the interface. Since the extent of cation repulsion correlates with cation acidity (Fig. 9.6a), non-acidic cations are expected to be more concentrated at the OHP.

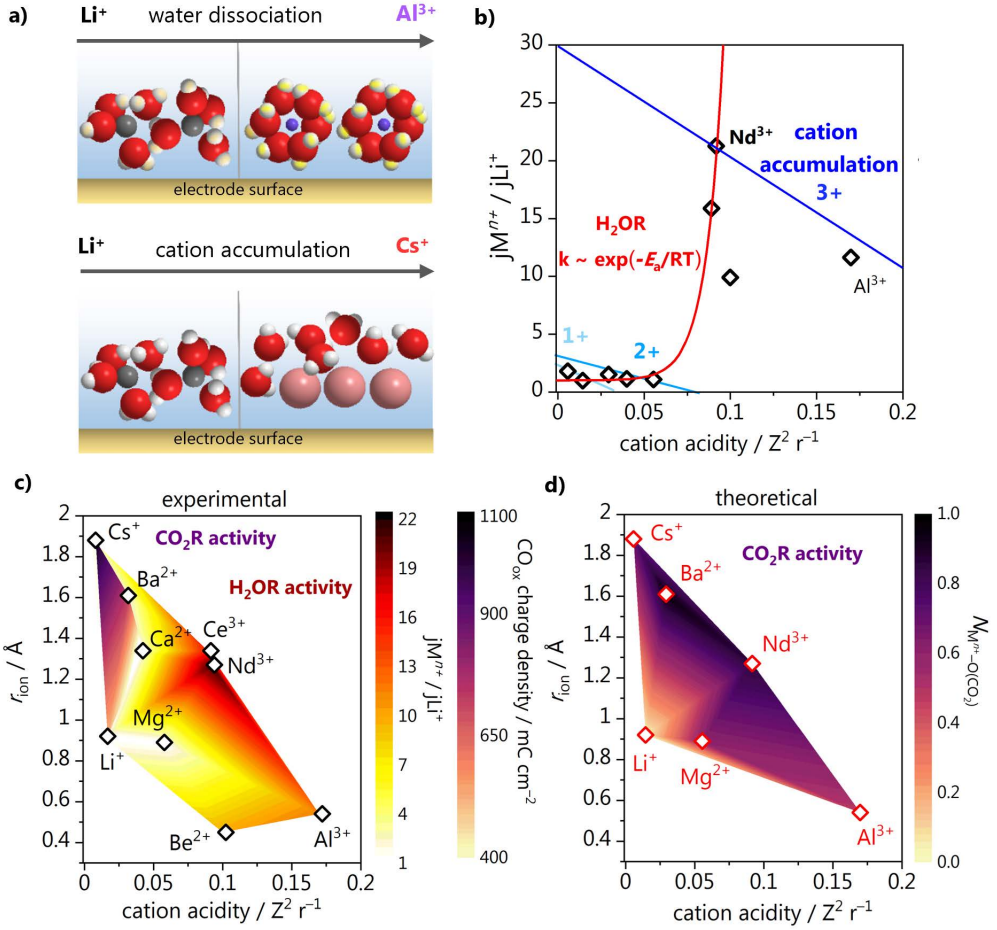

Fig. 9.9. Schematic representation of **a)** the interaction of different cation species with the electrode surface leading to favourable water dissociation and higher accumulation at the OHP. **b)** Normalized activity for water reduction vs. cation acidity and qualitative plot representing the interplay between water dissociation kinetics (red) and cation accumulation (shades of blue) for alkali (1+), di- (2+), and trivalent (3+) species. **c)** Colormap summarizing CO_2 reduction (purple shades, (Fig. 9.5) and H_2O reduction (red shades, Fig. 9.2a) performances at high overpotential vs. cation ionic radius and cation acidity. **d)** CO_2 reduction activity predicted assuming average cation-CO_2 coordination ($N_{M^{n+}\text{-}O(CO2)}$) (Table F.5) as a potential descriptor vs. ionic radius and cation acidity.

In Fig. 9c we summarize the performance of alkali, bi-and trivalent cations for H_2O and CO_2 reduction at high overpotential (Fig. 9.2a, Fig. 9.5). HER activity peaks for mildly acidic cations (red shaded region in Fig. 9.9c), such as Nd^{3+} and Ce^{3+}, and the rationale behind this trend lies in the activity volcano plot due to the interplay of water dissociation kinetics and cation accumulation (Fig. 9.9b). The water dissociation activation barrier decreases for higher cation acidity (Fig. 9.7d), consequently the rate of this step increases exponentially. However, strongly acidic cations such as Be^{2+} and Al^{3+} are limited by their low concentration at the OHP, thus the Nd^{3+} is the optimum, since it accumulates at the OHP and shows high enough reactions rates. As for CO_2 reduction, experimentally, Cs^+ and Ba^{2+} lead to the highest performance at high overpotentials (Fig. 9.5, purple shaded region in Fig. 9.9c), while Nd^{3+} is in the sweet spot for the low overpotential region. Theoretically, this trend can be reproduced assuming the average cation-CO_2 coordination number as the sole descriptor for CO_2 reduction activity in absence of the competing water reduction reaction (Fig. 9.9d). Again, non-acidic, or mildly acidic cations exhibit a steady short-range interaction with the CO_2^- adsorbate, since they can effectively desolvate due to their low dehydration energy.

Finally, both our experimental and computational results demonstrate that water and proton reduction must be taken into account for an accurate prediction of the activity of CO_2RR, since a steady supply of water or protons is key to enable a quick protonation of the CO_2^- intermediate, but also can lead to a high activity for water reduction. When water reduction is not competing with CO_2RR (at low overpotentials or acidic media) acidic and weakly hydrated cations promote CO_2RR, while at high overpotentials (neutral/alkaline media) the commonly used Cs^+ containing electrolyte leads to the highest activity.

9.10 Conclusions

In this work, we assessed the electrocatalytic CO_2 reduction and H_2O reduction activity in mildly acidic electrolytes (bulk pH = 3) containing Li^+, Cs^+, Be^{2+}, Mg^{2+}, Ca^{2+}, Ba^{2+}, Al^{3+}, $Nd^{3+}$and Ce^{3+}. We observed that cations have no effect on proton reduction at low overpotentials. Instead, the activity and onset for the water reduction reaction correlate with cation acidity, so that weakly hydrated trivalent species lead to the highest activity. This observation is rationalized through an activity volcano plot, with one side of the volcano at low cation acidity limited by poor water dissociation kinetics, while the other side is hindered by low cation accumulation (Fig. 9.9c). Consequently, acidic cations only favor CO_2 reduction at

low overpotentials (acidic media), below potentials at which water reduction is active. At high overpotentials (neutral/alkaline media), the activity for CO production increases in the order Ca^{2+} < Li^{+} < Ba^{2+} < Cs^{+}, showing an interplay between concentration at the Outer Helmholtz Plane, with specific cation promoting effects on water dissociation and cation stabilization of CO_2^- determining the CO_2RR versus H_2O reduction competition. *Ab initio* molecular dynamics simulations suggest that cation acidity determines cation accumulation at the OHP and water dissociation kinetics. Softly hydrated cations, such as Cs^{+}, Ba^{2+}, Nd^{3+}, present minimal cation-cation repulsion so they accumulate at the OHP at higher concentrations. Besides, in presence of acidic cations, water dissociation is barrierless, thus explaining their outstanding water reduction performance. As for CO_2 reduction, a short-range interaction driven by coordination between cation and CO_2^- stabilizes this intermediate, thereby activating CO_2 for reduction. Trivalent cations and weakly hydrated species account for a more continuous coordination, thus a higher promoting effect. Hence, Cs^{+}, Ba^{2+}, and Nd^{3+} lead to higher CO_2RR activities than their strongly hydrated counterparts, following the trend Cs^{+} < Ba^{2+} < Nd^{3+}. In summary, H_2O and CO_2 reduction performances are primarily ruled by cation accumulation at the OHP, which lead to higher concentrations and consequently higher rates of intrinsic cation promoting effects. Cation accumulation correlates with cation acidity, so non-acidic cations are expected to have higher near-surface concentrations under CO_2 reduction conditions. As for intrinsic cation effects, trivalent cations promote both CO_2^- stabilization and water dissociation, thus they are active for CO_2 reduction only below potentials which H_2O reduction is highly active. In contrast, Cs^{+} and Ba^{2+} account for high CO_2 reduction activity at high overpotentials, since they can stabilize the CO_2^- intermediate, while they show poor kinetics for water dissociation.

Even though the application of multivalent cations in neutral/alkaline media is not practical, due to hydroxide deposition, they may in principle still be used for CO_2 electrolysis in strong acidic media. In fact, we have recently shown that CO_2RR to CO can be carried out at industrially relevant current densities in acidic media, using gas diffusion electrodes.[48] We obtained faradaic efficiencies for CO close to 90% at lower cell potentials than in neutral media. Future work could therefore focus on trying to improve the energy efficiency even further by adding small amounts of e.g. Nd^{3+} to a Cs^{+} background electrolyte, in a way that hydroxide deposition would not be detrimental to the performance. Pulsed electrolysis also presents an opportunity for the use of multivalent cations for CO_2RR, as possible

hydroxide deposits can dissolve in between cathodic pulses. Besides, theoretical works on CO_2 reduction should also consider the kinetics and thermodynamics of the water dissociation step to accurately model the hydrogen evolution reaction when water is the proton source, instead of using H binding as the sole descriptor.

References

(1) Birdja, Y. Y.; Pérez-Gallent, E.; Figueiredo, M. C.; Göttle, A. J.; Calle-Vallejo, F.; Koper, M. T. M. *Nat. Energy* 2019, *4* (9), 732–745.
(2) Resasco, J.; Bell, A. T. *Trends Chem.* 2020, *2* (9), 825–836.
(3) Smith, W. A.; Burdyny, T.; Vermaas, D. A.; Geerlings, H. *Joule* 2019, *3* (8), 1822–1834.
(4) Zhang, Y. J.; Sethuraman, V.; Michalsky, R.; Peterson, A. A. *ACS Catal.* 2014, *4* (10), 3742–3748.
(5) Ooka, H.; Figueiredo, M. C.; Koper, M. T. M. *Langmuir* 2017, *33* (37), 9307–9313.
(6) Goyal, A.; Marcandalli, G.; Mints, V. A.; Koper, M. T. M. *J. Am. Chem. Soc.* 2020, *142* (9), 4154–4161.
(7) Hall, A. S.; Yoon, Y.; Wuttig, A.; Surendranath, Y. *J. Am. Chem. Soc.* 2015, *137* (47), 14834–14837.
(8) Welch, A. J.; Duchene, J. S.; Tagliabue, G.; Davoyan, A.; Cheng, W. H.; Atwater, H. A. *ACS Appl. Energy Mater.* 2019, *2* (1), 164–170.
(9) Kim, C.; Möller, T.; Schmidt, J.; Thomas, A.; Strasser, P. *ACS Catal.* 2019, *9* (2), 1482–1488.
(10) Moura de Salles Pupo, M.; Kortlever, R. *ChemPhysChem* 2019, *20* (22), 2926–2935.
(11) Ringe, S.; Clark, E. L.; Resasco, J.; Walton, A.; Seger, B.; Bell, A. T.; Chan, K. *Energy Environ. Sci.* 2019, *12* (10), 3001–3014.
(12) König, M.; Vaes, J.; Klemm, E.; Pant, D. *iScience* 2019, *19*, 135–160.
(13) Wang, Y.; Liu, X.; Liu, J.; Al-Mamun, M.; Wee-Chung Liew, A.; Yin, H.; Wen, W.; Zhong, Y. L.; Liu, P.; Zhao, H. *ACS Appl. Energy Mater.* 2018, *1* (4), 1688–1694.
(14) Goyal, A.; Koper, M. T. M. *Angew. Chemie Int. Ed.* 2021, *60* (24), 13452–13462.
(15) Murata, A.; Hori, Y. *Bull. Chem. Soc. Jpn.* 1991, *64* (1), 123–127.
(16) Hori, Y.; Suzuki, S. *Bull. Chem. Soc. Jpn.* 1982, *55* (3), 660–665.
(17) Hori, Y.; Murata, A.; Takahashi, R. *J. Chem. Soc. Faraday Trans. 1 Phys. Chem. Condens. Phases* 1989, *85* (8), 2309.
(18) Thorson, M. R.; Siil, K. I.; Kenis, P. J. A. *J. Electrochem. Soc.* 2013, *160* (1), F69–F74.
(19) Kim, H.; Park, H. S.; Hwang, Y. J.; Min, B. K. *J. Phys. Chem. C* 2017, *121* (41), 22637–22643.
(20) Zhang, B. A.; Costentin, C.; Nocera, D. G. *J. Chem. Phys.* 2020, *153* (9), 094701.
(21) Ayemoba, O.; Cuesta, A. *ACS Appl. Mater. Interfaces* 2017, *9* (33), 27377–27382.
(22) Chen, L. D.; Urushihara, M.; Chan, K.; Nørskov, J. K. *ACS Catal.* 2016, *6* (10), 7133–7139.
(23) Hussain, G.; Pérez-Martínez, L.; Le, J.-B.; Papasizza, M.; Cabello, G.; Cheng, J.; Cuesta, A. *Electrochim. Acta* 2019, *327*, 135055.
(24) Resasco, J.; Chen, L. D.; Clark, E.; Tsai, C.; Hahn, C.; Jaramillo, T. F.; Chan, K.; Bell, A. T. *J. Am. Chem. Soc.* 2017, *139* (32), 11277–11287.
(25) Monteiro, M. C. O.; Dattila, F.; Hagedoorn, B.; García-Muelas, R.; López, N.; Koper, M. T. M. *Nat. Catal.* 2021, *4* (8), 654–662.
(26) Schizodimou, A.; Kyriacou, G. *Electrochim. Acta* 2012, *78*, 171–176.
(27) Banerjee, S.; Zhang, Z.; Hall, A. S.; Thoi, V. S. *ACS Catal.* 2020, *10* (17), 9907–9914.
(28) Monteiro, M. C. O.; Koper, M. T. M. *Electrochim. Acta* 2019, *325*, 134915.
(29) Bhargava, S. S.; Cofell, E. R.; Chumble, P.; Azmoodeh, D.; Someshwar, S.; Kenis, P. J. A. *Electrochim. Acta* 2021, 139055.
(30) Xue, S.; Garlyyev, B.; Watzele, S.; Liang, Y.; Fichtner, J.; Pohl, M. D.; Bandarenka, A. S. *ChemElectroChem* 2018, *5* (17), 2326–2329.
(31) Born, M. *Zeitschrift für Phys.* 1920, *1* (1), 45–48.
(32) Lide, D. R. 84th ed.; Lide, D. R., Ed.; CRC Press, 2003; Vol. 85.

(33) Alderighi, L.; Gans, P.; Midollini, S.; Vacca, A. In *Advances in Inorganic Chemistry*; 2000; Vol. 50, pp 109–172.
(34) Rudolph, W. W. *J. Solution Chem.* 2010, *39* (7), 1039–1059.
(35) Hao, L.; Lu, R.; Leaist, D. G. *J. Solution Chem.* 1996, *25* (3), 231–242.
(36) Ekberg, C.; Brown, P. L. Vol 1.; Wiley-VCH Verlag GmbH & Co. KGaA: Germany, 2016.
(37) Perdew, J. P.; Burke, K.; Ernzerhof, M. *Phys. Rev. Lett.* 1996, *77*, 3865–3868.
(38) Grimme, S. *J. Comput. Chem.* 2006, *27*, 1787–1799.
(39) Bucko, T.; Hafner, J.; Lebègue, S.; Ángyán, J. G. *J. Phys. Chem. A* 2010, *114*, 11814–11824.
(40) Dattila, F. Cation-effect-CO2-reduction *ioChem-BD* 2021, DOI: 10.1038/s41929-021-00655-5.
(41) Almora-Barrios, N.; Carchini, G.; Błoński, P.; López, N. *J. Chem. Theory Comput.* 2014, *10*, 5002–5009.
(42) Feibelman, P. J. *Phys. Rev. B* 2001, *64* (12), 125403.
(43) McCrum, I. T.; Bondue, C. J.; Koper, M. T. M. *J. Phys. Chem. Lett.* 2019, *10* (21), 6842–6849.
(44) Waegele, M. M.; Gunathunge, C. M.; Li, J.; Li, X. *J. Chem. Phys.* 2019, *151* (16), 160902.
(45) Marcus, Y. *Chem. Rev.* 1988, *88* (8), 1475–1498.
(46) Nørskov, J. K.; Rossmeisl, J.; Logadottir, A.; Lindqvist, L.; Kitchin, J. R.; Bligaard, T.; Jónsson, H. *J. Phys. Chem. B* 2004, *108* (46), 17886–17892.
(47) Garcia-Ratés, M.; García-Muelas, R.; López, N. *J. Phys. Chem. C* 2017, *121* (25), 13803–13809.
(48) Monteiro, M. C. O.; Philips, M. F.; Schouten, K. J. P.; Koper, M. T. M. *Nat. Commun.* 2021, *12* (1), 4943.

10

Understanding cation trends for hydrogen evolution on platinum and gold electrodes in alkaline media

This chapter is based on Monteiro, M. C. O., Goyal, A., Moerland, P., Koper, M. T. M. *ACS Catalysis, 11*, 14328–14335 (2021)

Abstract

In this Chapter we study how the cation identity and concentration alter the kinetics of hydrogen evolution (HER) on platinum and gold electrodes. Previous work suggested an inverted activity trend as a function of alkali metal cation when comparing the performance of platinum and gold catalysts in alkaline media. We show that weakly hydrated cations (K^+) favor HER on gold only at low overpotentials (or lower alkalinity), whereas in more alkaline pH (or high overpotentials) the higher activity is found using electrolytes containing strongly hydrated cations (Li^+). We find a similar trend for platinum, however the inhibition of HER by weakly hydrated cations on platinum is observed already at lower alkalinity and lower cation concentrations, suggesting that platinum interacts stronger with metal cations than gold. We propose that weakly hydrated cations stabilize the transition state of the water dissociation step more favorably due to their higher near-surface concentration in comparison to a strongly hydrated cation such as Li^+. However, at high pH and consequently higher cation concentrations, the accumulation of these species at the Outer Helmholtz Plane inhibits HER. This is especially pronounced on platinum, where a change in the rate determining step is observed at pH 13 when using a Li^+ or K^+ containing electrolyte.

10.1 Introduction

Efficient water electrolysis is an important technology towards a more sustainable society.[1] While water electrolysis in acidic media leads to the highest activity, it utilizes scarce and expensive materials (platinum, iridium); in alkaline media, more abundant materials can be used, but at the expense of a lower activity. To understand this difference in activity between the two media, the cathode reaction, i.e. hydrogen evolution (HER), has been studied extensively both in acidic and alkaline media. The focus of most works has been on tailoring the catalyst surface.[2,3] However, metal cations in the electrolyte have been shown to have a significant effect on the activity of HER, although usually not taken into account in reaction mechanisms.[4–7] In fact, the underlying mechanisms of the non-covalent interactions between cations and HER intermediates remain incompletely understood. Therefore, systematically studying electrolyte-related phenomena on different metal surfaces is desired, to improve our understanding of the underlying phenomena and to assist in further optimization of alkaline and proton exchange membrane (PEM) electrolysers.

Platinum and gold are two model catalysts for understanding electrocatalytic reactions, including hydrogen evolution. Although two noble metals, it has been shown that the interaction of these surfaces with adsorbed species (reaction intermediates) and water is very different.[8,9] Platinum is considered an optimal catalyst for HER (in acidic media), a consequence of the optimal hydrogen binding energy ($\Delta G_{Hads} \approx 0$). On the other hand, on gold electrodes, hydrogen binds weakly and the activity for HER at low overpotentials is significantly inferior to the activity found on Pt. Very recently, efforts have been dedicated to the effect that metal cations have on the activity of HER on different metal surfaces. A main contribution has been made by Xue et al.[7] who studied the HER activity of Pt, Ir, Au, and Ag in alkaline media, as a function of the cation identity (Li^+, Na^+, K^+, Rb^+, Cs^+). They report that weakly hydrated cations such as Cs^+ favour HER on Au and Ag while they are detrimental to the reaction activity on Pt and Ir. The authors explain this "inverted" trend based on the binding energy of hydrogen to the metal, which weakens as a function of the alkali metal cation: $Cs^+ > Rb^+ > K^+ > Na^+ > Li^+$. They propose that weakly hydrated cations as Cs^+ are beneficial to HER on Au and Ag electrodes, which lie on the weak binding side of the activity volcano, while being detrimental to HER on Pt and Ir, due to an over stabilization of the adsorbed intermediates.

The hydrogen adsorption energy is generally considered to be an accurate descriptor for HER activity in acidic media, where the adsorbed hydrogen is formed from proton/hydronium (H_3O^+) reduction. However, in alkaline media, where water dissociation has to occur in order for hydrogen to adsorb, other descriptors appear to be needed to describe activity trends.[8] On platinum, the hydrogen binding energy (HBE) is derived from the underpotential hydrogen region (H_{upd}) in the blank voltammetry.[10,11] A positive shift of the H_{upd} peak, for example as a function of pH, has been ascribed to an increase in the hydrogen binding energy and an associated lower activity for HER. However, it has been shown that this positive shift is actually associated with a weakening of the OH adsorption on Pt {100} and {110} steps and facets due to the presence of alkali metal cations at the reaction interface.[12] The so-called H_{upd} region is therefore a hydrogen-cation-hydroxyl region, and therefore it cannot serve as a simple activity descriptor. The nature of the rate-determining step for HER in alkaline media is still under debate. The work of Markovic et al. suggests that on platinum, in alkaline media, water dissociation is the rate determining step.[5] However, Liu et al.[4] suggests that for a similar system, the driving force for OH desorption weakens in the order $Li^+ > Na^+ > K^+$, and this trend gives rise to the HER activity trend of LiOH > NaOH > KOH at pH 13. Gold is a much less investigated catalyst for HER, but of interest as a catalyst for the electrocatalytic reduction of carbon dioxide, for which HER is a competing reaction.[13] As discussed above, an inverted activity trend ($K^+ > Na^+ > Li^+$), compared to platinum, has been reported for gold electrodes in 0.1 M *M*OH.[7] Our recent work on polycrystalline gold and Au(111) in alkaline media (NaOH), shows that up to pH 11, increasing the Na^+ concentration significantly enhances the HER activity.[14] At higher pH (>12) and consequently high (near-surface) cation concentrations, the activity for HER decreases, likely due to a blockage effect. However, this phenomenon has not yet been investigated for other metal surfaces, as a function of the cation identity.

Taking the hydrogen binding energy as a descriptor, cannot explain the different cation trends for HER on Pt and Au as a function of the cation identity. This is especially relevant in alkaline media, where our recent work has shown that the local pH and cation concentration are two interrelated variables.[13–15] Therefore, in this Chapter, we have systematically investigated the effect of pH and cation concentration on the activity for HER on polycrystalline Pt and Au, comparing electrolytes containing weakly (K^+) and strongly (Li^+) hydrated cations. In alkaline media, on gold, we see that the surface blockage phenomena (previously observed at pH 13 in Na^+ containing electrolyte) is not present in a Li^+ containing electrolyte,

due to the less pronounced accumulation of Li^+ ions near the surface, even at high pH. In contrast, K^+ ions are detrimental to the reaction activity above pH 13. Similar behavior is observed on platinum, however already at pH 11, and at low cation concentrations, suggesting that cations interact stronger with Pt than with Au electrodes. These results show that on Pt in alkaline media, cations typically act as inhibitors, whereas on gold in alkaline media, cations can act as either a promotor or an inhibitor, depending on their local accumulation in the double layer.

10.2 Hydrogen evolution in alkaline media

We initially studied how cations affect the hydrogen evolution reaction (HER) on polycrystalline platinum and gold electrodes using stationary cyclic voltammetry, and the results are shown in Fig. 10.1a-c. We carried out the experiments in alkaline media (pH 13) and we find that K^+ cations promote water reduction on gold, while they are detrimental to the reaction on platinum, in agreement with the results found by Xue et al. for Au(111) and polycrystalline Pt at the same pH and similar overpotentials.[7] We have also recorded the blank voltammetry of the polycrystalline platinum electrode in alkaline media and a positive shift of the H_{upd} peak in K^+ containing electrolyte is also found at pH 13 (Fig. 10.1c). Similar measurements were performed in acidic media (see Fig. G.1a-c and discussion in Appendix G). There, water reduction is promoted by weakly hydrated cations on both gold and platinum, and a similar (but less pronounced) positive shift in the H_{upd} of the platinum electrode is found in K^+ electrolyte. Although the effect of the different cations on water reduction on platinum is inverted for acidic and alkaline media, it seems that at both pH weakly hydrated cations interact with the adsorbed H/OH in a similar fashion, suggesting that the mechanism behind this inverted trend goes beyond just an effect on the hydrogen binding energy, as proposed by Xue et al.[7] A more pronounced positive shift in the H_{upd} at pH 13, in comparison to pH 3 was also observed by Chen et al.[12] In the same work, DFT calculations suggest that higher coverages of alkali metal cation adsorbed along the steps of Pt(553) becomes more favourable by increasing electrolyte pH (at the same potential on an RHE scale). Therefore, we expect that the larger shift we observe on polycrystalline platinum for the experiment carried out at pH 13 is due to an increase in the cation–OH_{ads}–H_{ads} interactions, at higher cation coverages. The blank voltammetry of the polycrystalline gold and platinum electrode, taken before the measurements shown in , can be seen in Fig. G.2 in Appendix G.

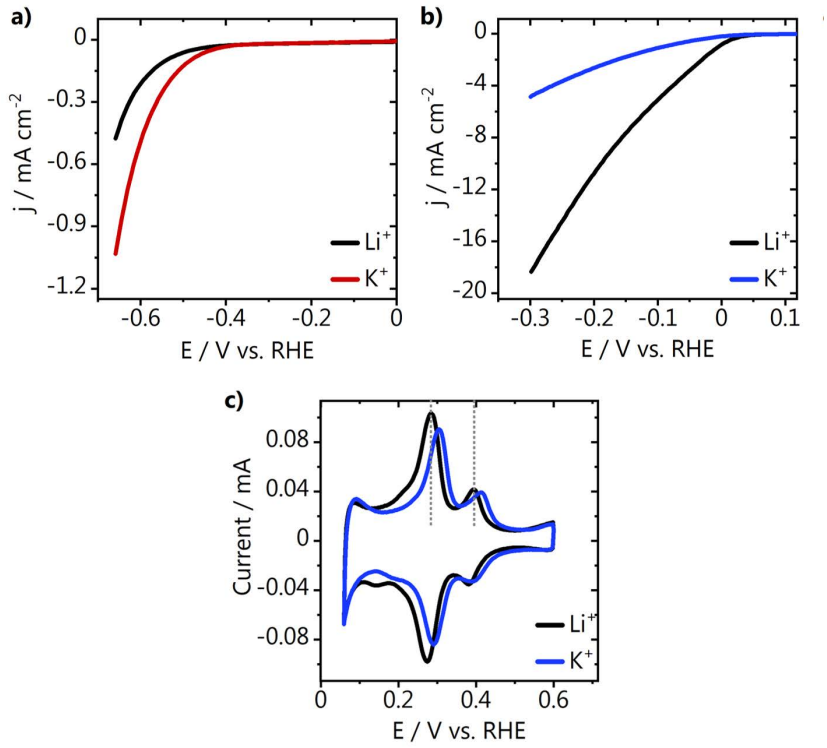

Fig. 10.1. Stationary hydrogen evolution on **a)** gold and **b)** platinum in alkaline media (0.1 M *M*OH, pH = 13), together with **c)** the blank voltammetry of the platinum electrode. *M* = Li^+ or K^+. The voltammetry was recorded at 50 mV s^{-1}.

In Fig. 10.2 we show the Tafel slopes, derived from the cyclic voltammograms from Fig. 10.1 and Fig. G.1 (Appendix G), as a function of the applied potential. Eq. 10.1-10.5 display the three accepted reaction steps during proton (H_3O^+) or water reduction, with the rate-determining step in the mechanism that can be derived from Tafel slope analysis in parenthesis.[16] Here * represent a free surface adsorption site. Tafel slopes of around 120 mV dec^{-1} are obtained for the gold electrode in the Li^+ and K^+ electrolytes, in both acidic and alkaline media. This indicates that at the potentials studied, in both cases the activity for HER is controlled by the first electron transfer step (Volmer step, Eq. 10.1), which in alkaline media is in fact governed by the barrier of the electrochemical water dissociation (Eq. 10.2). The latter is in agreement with our previous studies in Na^+ containing electrolyte.[14] For platinum, in acidic media, Tafel slopes of around 40 mV dec^{-1} imply that the second electron transfer Heyrovsky step (Eq. 10.3) is the rate determining step, in both Li^+ and K^+ electrolyte.[17] In contrast, in alkaline media, where we see higher HER activity

in Li^+ than K^+, the Tafel slopes indicate that in Li^+ the Heyrovsky step is still rate determining while there seems to be a change in the reaction mechanism in K^+ electrolyte. A Tafel slope of 112 mV dec^{-1} suggests either the Volmer step or a Heyrovsky step at high coverage of adsorbed hydrogen (at high overpotentials) as the rate limiting step. Considering the Tafel analysis was performed using the current response at low overpotentials, the Volmer step is more likely to be the rate determining step here. This change in the reaction mechanism on platinum suggests that the cation identity plays an important role on how accessible the surface is for hydrogen adsorption.

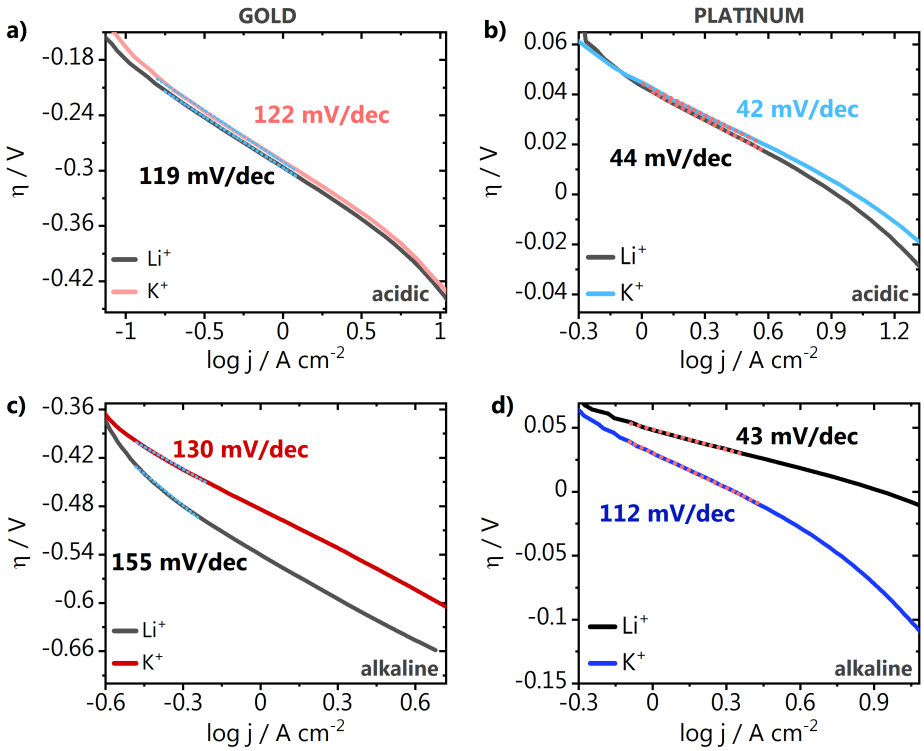

Fig. 10.2. Tafel slopes derived from the stationary cyclic voltammetry, recorded on **a)** gold and **b)** platinum in acidic media (0.1 M M_2SO_4, pH = 3), as well as for **c)** gold **d)** platinum in alkaline media (0.1 M *M*OH, pH = 13). *M* = Li^+ or K^+. The range used for the curve fitting is indicated in all plots with a dotted line.

$H_3O^+ + e^- + * \rightarrow H^* + H_2O$	(Volmer, acidic media)	Eq. 10.1
$H_2O + e^- + * \rightarrow H^* + OH$	(Volmer, alkaline media)	Eq. 10.2
$H^* + H_3O^+ + e^- \rightarrow H_2 + H_2O + *$	(Heyrovsky, acidic media)	Eq. 10.3
$H^* + H_2O + e^- \rightarrow H_2 + OH^- + *$	(Heyrovsky, alkaline media)	Eq. 10.4
$2H^* \rightarrow H_2 + 2*$	(Tafel)	Eq. 10.5

Previous work reported higher HER activity for gold in electrolytes containing weakly hydrated cations, in the order $Cs^+ > K^+ > Na^+ > Li^+$, and the opposite trend was observed for platinum electrodes in alkaline media.[7] However, experiments on gold have usually been carried out in a limited potential range, as at large overpotentials currents become impractical, i.e. due to bubble formation and a consequent loss of potential control. To further elucidate the nature of this "inverted" trend, we have performed HER on gold at pH 11 and 13 over a wide potential range in electrolytes containing Li^+, Na^+ and K^+ cations (Fig. 10.3). As shown in Fig. 10.3a, at pH 13 and low overpotentials, indeed the activity trend is found to be $K^+ > Na^+ > Li^+$. Remarkably, at more negative overpotentials (–0.8 V vs. RHE) the trend inverts, and a higher current is obtained in the Li^+ electrolyte. This strongly suggests that on gold, upon an increase in the local alkalinity at high overpotentials, and consequent increase in the near-surface cation concentration, weakly hydrated cations are actually detrimental to water reduction. This is likely due to an accumulation at the reaction interface and blockage of the surface, as proposed in our previous work.[14] This blockage effect is less pronounced in Na^+ and even less in the Li^+ electrolyte, as the stronger binding of water molecules in the hydration shell of these cations prohibit their accumulation at the Outer Helmholtz Plane (OHP), as we have also shown in Chapter 8 through DFT based *Ab Initio* Molecular Dynamics (AIMD) simulations on the interaction of alkali cations with Au(111).[18]

To further support these observations, we have performed the same experiment at pH 11, where there is in principle a lower driving force for cations to accumulate near the surface than at pH 13, due to the lower interfacial electric field strength. As shown in Fig. 10.3b, at pH 11 the inversion of the HER activity trend as a function of the cation identity happens at ca. 0.25 V more negative potential than at pH 13. This confirms that the local alkalinity defines the concentration of cations near the surface, and that weakly hydrated cations hinder HER on gold if their local concentration is high enough. This behaviour is similar to platinum, although on

platinum this effect is already observed at lower overpotentials, whereas on gold more driving force is required. At pH 11, more current is required to reach high local alkalinity, while at pH 13 this happens at lower overpotentials.

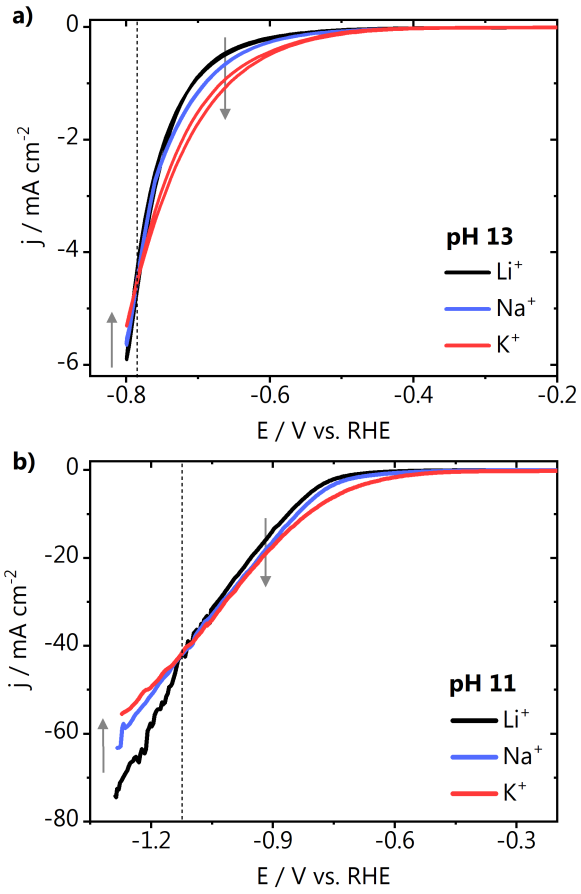

Fig. 10.3. Stationary hydrogen evolution cyclic voltammetry on gold at pH **a)** 13 and **b)** 11 recorded in 0.1 M *M*OH and 0.001 M *M*OH, with *M* = Li^+, Na^+ or K^+ at 50 mV s^{-1}. The dotted gray lines indicate the potential in which the CVs cross and the arrows point going from the strongly to the weakly hydrated metal cation species.

10.3 Cation concentration dependence

The results shown in Fig. 10.3a and Fig. 10.3b suggest that the cation trends for HER on platinum and gold are not actually "inverted" as previously stated[7], but just depend on the reaction conditions, such as bulk/local pH, near-surface cation concentration and cation identity. In order to further elucidate that, we have performed HER under well-defined mass transport conditions, using rotating disc electrodes (RDE) of gold and platinum. We changed the cation concentration in electrolytes having different bulk pH, and observed the effect of those variables on the HER kinetics. The HER cyclic voltammetry on gold is shown in Fig. G.4 in Appendix G, and the correspondent reaction order plots in Fig. 10.4. In the Li^+ containing electrolyte, a positive reaction order is found both at pH 11 and 13, differently from what we observed for instance for Na^+ in our previous work.[14] In the case of K^+, at pH 11 a higher cation concentration promotes HER, as shown by the higher reaction order than found in Li^+. However, at pH 13 we see a negative reaction order, with HER being inhibited as the concentration of K^+ increases.

The HER inhibition in alkaline pH seems to be more pronounced for weakly hydrated cations and need less driving force to be observed on platinum than on gold, as we show in Fig. 10.1. To better define the experimental conditions in which this phenomenon takes place, we performed similar experiments as shown in Fig. 10.4 on platinum, also using a rotating disc electrode. The cyclic voltammetry is shown in Fig. G.5 (Appendix G) and the correspondent reaction order plots are depicted in Fig. 10.5. It is important to point out that although the electrolytes in this work were used as received, no metal contaminants are expected to affect our measurements, as evidenced by the overlapping consecutive CVs shown in Fig. G.6 in Appendix G.[19] We see in in Fig. 10.5a and Fig. 10.5b that, similarly to gold, on platinum, increasing the concentration of Li^+ cations promotes HER both at pH 11 and 13. In contrast, for the K^+ electrolyte, at pH 9 and 10 we observe at low K^+ concentration a positive reaction order, and that at the highest concentrations HER starts to be inhibited, confirming the relationship between local alkalinity and concentration of weakly hydrated cations at the reaction interface. At pH 11, while on gold we see a promotion of HER by increasing the K^+ concentration, for platinum we observe a negative reaction order, with even more negative values at pH 12. This indicates that weakly hydrated metal cations in the electrolyte interact stronger with platinum than with gold electrodes, under the same experimental conditions.

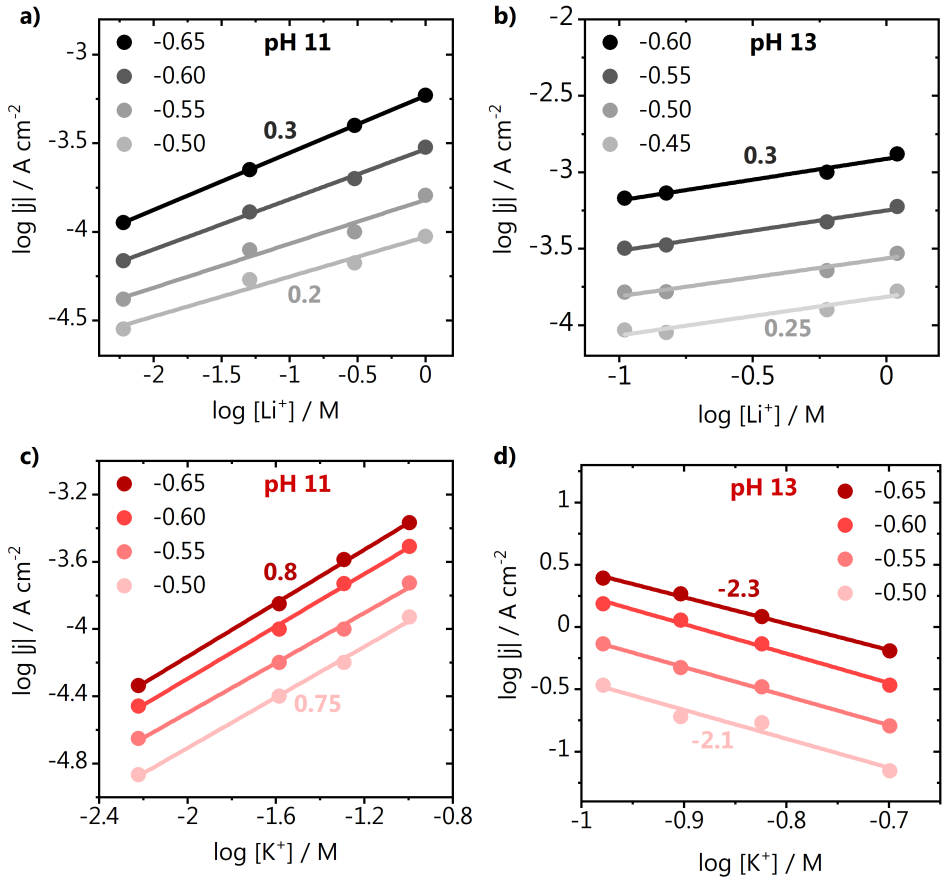

Fig. 10.4. Reaction order plot of HER on polycrystalline gold in the cation concentration at pH 11 and 13 in **a)-b)** Li^+ and **c)-d)** K^+ containing electrolyte. The current is reported for 50 mV potential steps (vs. RHE) plotted as a function of the logarithm of the current density on the y-axis and logarithm of the cation concentration on the x-axis. The slopes extracted from the linear fit of the current response (reaction orders) are shown next to the plots. The slope at the top corresponds to the most negative potential applied and the slope at the bottom to the most positive, as indicated also by the colors. CVs are shown in Fig. G4 and were recorded using a rotating disc electrode, at 25 mV s^{-1} and 2500 rpm.

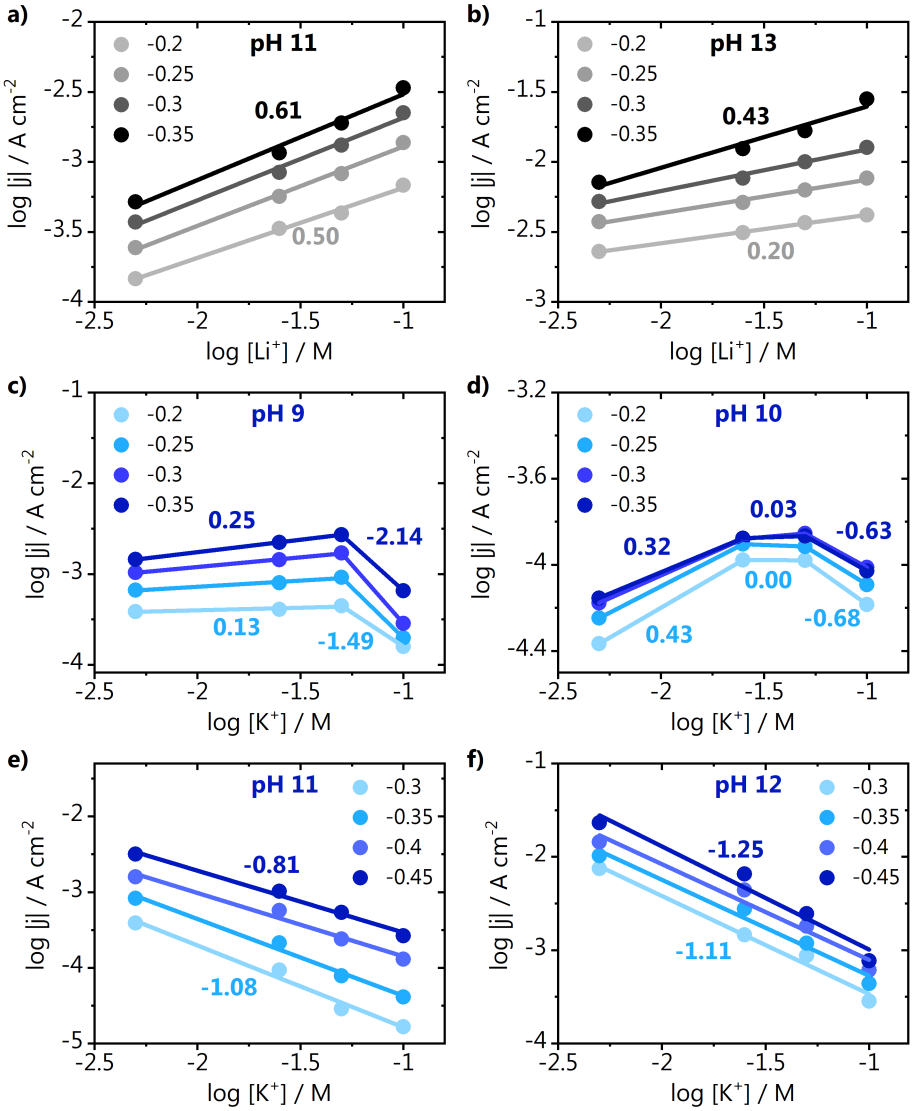

Fig. 10.5. Reaction order plot of HER on polycrystalline platinum in the cation concentration at pH 11 and 13 in **a)-b)** Li^+ and pH 9-12 in **c)-d)** K^+ containing electrolyte. The current is reported for 50 mV potential steps (vs. RHE) plotted as a function of the logarithm of the current density on the y-axis and logarithm of the cation concentration on the x-axis. The slopes extracted from the linear fit of the current response (reaction orders) are shown next to the plots. The slope at the top corresponds to the most negative potential applied and the slope at the bottom to the most positive, as indicated also by the colors. CVs are shown in Fig. G5 and were recorded using a rotating disc electrode, at 25 mV s^{-1} and 2500 rpm.

10.4 Discussion

The opposite cation trends for HER on platinum and gold electrodes in alkaline media have previously been explained using the hydrogen binding energy as a descriptor for HER.[20] However, our recent work has shown that although this might be a suitable descriptor for HER in acidic media, on gold, in alkaline media, the rate of this reaction depends on the near-surface pH and near-surface cation concentration.[14] In our present work we elucidate that the inverted cation trend between platinum and gold strongly depends on the cation identity, the electrolyte bulk pH and the local alkalinity. We see that on gold, HER is promoted by weakly hydrated cations only at low current densities and moderately alkaline pH, as shown in Fig. 10.3. This is confirmed by the different cation reaction orders on polycrystalline Pt and Au as a function of pH, potential, and cation identity. For gold, we find a positive reaction order in a Li^+ electrolyte at pH 13, while in K^+ electrolyte there is an inhibition of HER at the same pH. The same is observed for platinum, however on this electrode HER starts to be inhibited already at lower pH and lower cation concentrations, indicating that metal cations interact stronger with platinum than with gold electrodes. Additionally, on platinum we see a change in the reaction mechanism as a function of the electrolyte cation: in Li^+ electrolyte the Heyrovsky step is the rate determining step and in K^+ the Volmer step seems to be rate determining. These differences of cation interaction with gold and platinum have also been suggested by other studies. For instance, DFT calculations presented in the work of Hersbach et al.[21] indicate that cation adsorption is more energetically favourable on platinum {111} and {100} facets than on gold. Additionally, work from our group has reported an anomalously large diffuse-layer Gouy-Chapman capacitance for the Pt(111)-aqueous electrolyte interface in comparison to Au(111) and Hg.[22] It shows that the double layer of Pt(111) (and to some extent also of Au(111)) is more compact than predicted by Gouy-Chapman theory, because the electrolyte interacts stronger with Pt than with Au and Hg. Therefore, we suggest that at the cathodic potentials in which HER takes place, the driving force for cations to accumulate near the platinum surface is higher.

Site blocking by metal cations has been previously proposed in various works. An early report by Herasymenko and Šlendyk assumed a simple competitive Langmuir adsorption model to rationalize cation trends for HER, which was later further rationalized in the work of Frumkin considering the effect of cation adsorption on reaction rates.[23,24] The specific adsorption of cations on catalytic sites

for HER has been extensively discussed in the recent review of Waegele at al.[25], showing that despite various theoretical and experimental evidences, it is still unclear under which specific conditions (potential, pH, concentration, electrode surface) cations specifically adsorb, if they do at all. Another site-blocking theory has been put forward by Markovic and co-workers, in which they propose that non-covalent interactions between hydrated alkali metal cations $M^+(H_2O)_x$ and adsorbed OH (OH_{ad}) give rise to OH_{ad}–$M^+(H_2O)_x$ clusters at the interface. They propose the concentration of these clusters increases in the same order as the hydration energies of the corresponding cations ($Li^+ >> Na^+ > K^+ > Cs^+$). However, we can rule out this being the reason for the inhibition of HER that we observe in our experiments, as we find positive reaction orders in Li^+ electrolyte both on gold and platinum (see Fig. 10.4 and Fig. 10.5), and the inhibition effect is only seen in K^+ electrolyte (and in our previous work in Na^+).[14]

Based on our results and the work discussed above, we propose that the model that we recently formulated for cation effects in HER on gold in alkaline media, is more broadly applicable. That model has two regimes, depending on local cation concentration: a promotion regime, and an inhibition regime (see Fig. 10.6). In the promotion regime (low cation concentration, low pH), both strongly and weakly hydrated cations stabilize the transition state of the first electron transfer step, the water dissociation (Eq. 10.6).[14]

$$H_2O + e^- + * + M^+ \rightarrow *H–OH^{\delta-}–M^+ + (1 - \delta)e^- \rightarrow *H + OH^- + M^+ \qquad \text{Eq. 10.6}$$

Weakly hydrated cations lead then to higher activity due to their stronger driving force to accumulate at the OHP and consequently higher concentration at the interface, as we have shown in Chapters 8 and 9 both through experiments and simulations.[18] We see that this promotion regime is more limited for platinum than for gold, due to stronger interaction of metal cations with platinum, already pronounced in weakly alkaline conditions and moderate cation concentrations. In case of such a very strong interaction, the promotion regime develops into the inhibition regime, in weakly hydrated cations accumulate near the surface to such an extent that they hinder the access of water to the reaction interface or lower the availability of free surface sites. In this regime, the HER has a negative reaction order on cation concentration. Experiments with Pt electrodes are typically in this inhibition regime, whereas experiments with Au are typically in the promotion

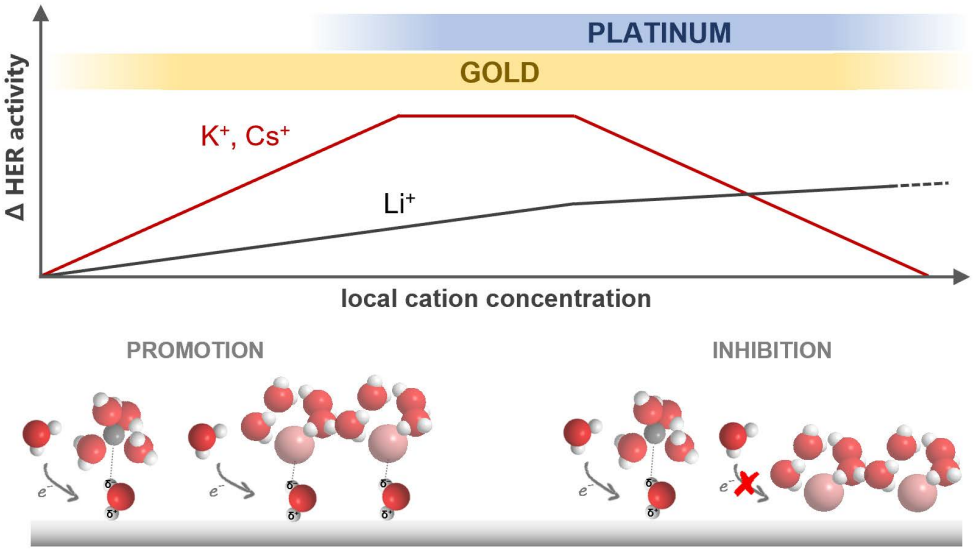

Fig. 10.6. Schematic representation of the effect of cation concentration on the activity of HER comparing platinum and gold, together with a pictorial description of the mechanism through which weakly (K^+, Cs^+) and strongly (Li^+) hydrated cations promote and/or inhibit HER.

regime. This model explains the inverted cation dependence between Pt and Au, observed here as well as in previous work.[20]

Our findings may have important implications for electrolysers in which HER is the cathode reaction. Due to the high current densities of operation, a high local alkalinity can develop near the cathode surface. As our work shows, depending on the electrolyte cation identity, the activity for HER can be compromised upon local alkalization of the reaction interface. Tuning the cathode geometry and consequently enhancing the transport of species, or selecting a specific cation, can help to mitigate these negative effects.

10.5 Conclusions

In this work we have elucidated the cation effects on HER on gold and platinum electrodes in alkaline media. Through cyclic voltammetry and rotating disc electrode experiments we investigated HER in alkaline media in electrolytes containing strongly and weakly hydrated cations, namely Li^+, Na^+, and K^+. In agreement with the model that we recently formulated for HER on gold, we show here that for platinum there are also two distinct regimes for how cations affect

HER, according to the cation concentration. At low cation concentration and mildly alkaline media, both weakly and strongly hydrated cations promote HER on gold and platinum. At more alkaline pH and consequently higher near-surface cation concentrations, HER is inhibited by weakly hydrated cations. This inhibition regime is observed for platinum at lower alkalinity and cation concentration than for gold electrodes, as platinum interacts stronger with cations in the electrolyte. On platinum, based on Tafel slopes, we find a change in the reaction mechanism at pH 13 from the Heyrovsky to the Volmer step, when the reaction is carried out in Li^+ or K^+ electrolyte, respectively. This can be understood as an inhibition of the Volmer step in K^+ electrolyte, whereas Li^+ actually promotes the Volmer step. The observation that HER on gold is mostly in the promotion regime, whereas HER on platinum is mostly in the inhibition regime, explains the previously observed inverted cation dependence of HER on gold and platinum. Our work shows the complexity of the electrode-electrolyte interface during hydrogen evolution on platinum and gold, and that to achieve high activity, cation identity and near-surface cation concentration are crucial activity descriptors, with the latter depending on the electrolyte pH and metal surface employed.

.

References

(1) Shiva Kumar, S.; Himabindu, V. *Mater. Sci. Energy Technol.* 2019, *2* (3), 442–454.

(2) Strmcnik, D.; Lopes, P. P.; Genorio, B.; Stamenkovic, V. R.; Markovic, N. M. *Nano Energy* 2016, *29*, 29–36.

(3) Zhou, Z.; Pei, Z.; Wei, L.; Zhao, S.; Jian, X.; Chen, Y. *Energy Environ. Sci.* 2020, *13* (10), 3185–3206.

(4) Liu, E.; Li, J.; Jiao, L.; Doan, H. T. T.; Liu, Z.; Zhao, Z.; Huang, Y.; Abraham, K. M.; Mukerjee, S.; Jia, Q. *J. Am. Chem. Soc.* 2019, *141* (7), 3232–3239.

(5) Subbaraman, R.; Tripkovic, D.; Chang, K.-C.; Strmcnik, D.; Paulikas, A. P.; Hirunsit, P.; Chan, M.; Greeley, J.; Stamenkovic, V.; Markovic, N. M. *Nat. Mater.* 2012, *11* (6), 550–557.

(6) Huang, B.; Muy, S.; Feng, S.; Katayama, Y.; Lu, Y. C.; Chen, G.; Shao-Horn, Y. *Phys. Chem. Chem. Phys.* 2018, *20* (23), 15680–15686.

(7) Xue, S.; Garlyyev, B.; Watzele, S.; Liang, Y.; Fichtner, J.; Pohl, M. D.; Bandarenka, A. S. *ChemElectroChem* 2018, *5* (17), 2326–2329.

(8) Dubouis, N.; Grimaud, A. *Chem. Sci.* 2019, *10* (40), 9165–9181.

(9) Huang, B.; Myint, K. H.; Wang, Y.; Zhang, Y.; Rao, R. R.; Sun, J.; Muy, S.; Katayama, Y.; Corchado Garcia, J.; Fraggedakis, D.; Grossman, J. C.; Bazant, M. Z.; Xu, K.; Willard, A. P.; Shao-Horn, Y. *J. Phys. Chem. C* 2021, *125* (8), 4397–4411.

(10) Jiao, L.; Liu, E.; Mukerjee, S.; Jia, Q. *ACS Catal.* 2020, *10* (19), 11099–11109.

(11) Weber, D. J.; Janssen, M.; Oezaslan, M. *J. Electrochem. Soc.* 2019, *166* (2), F66–F73.

(12) Chen, X.; McCrum, I. T.; Schwarz, K. A.; Janik, M. J.; Koper, M. T. M. *Angew. Chemie - Int. Ed.* 2017, *56* (47), 15025–15029.

(13) Goyal, A.; Marcandalli, G.; Mints, V. A.; Koper, M. T. M. *J. Am. Chem. Soc.* 2020, *142* (9), 4154–4161.

(14) Goyal, A.; Koper, M. T. M. *Angew. Chemie Int. Ed.* 2021, *60* (24), 13452–13462.

(15) Goyal, A.; Koper, M. T. M. *J. Chem. Phys.* 2021, *155* (13), 134705.

(16) Shinagawa, T.; Garcia-Esparza, A. T.; Takanabe, K. *Sci. Rep.* 2015, *5* (1), 13801.

(17) Ledezma-Yanez, I.; Wallace, W. D. Z.; Sebastián-Pascual, P.; Climent, V.; Feliu, J. M.; Koper, M. T. M. *Nat. Energy* 2017, *2* (4), 1–7.

(18) Monteiro, M. C. O.; Dattila, F.; Hagedoorn, B.; García-Muelas, R.; López, N.; Koper, M. T. M. *Nat. Catal.* 2021, *4* (8), 654–662.

(19) Li, X.; Gunathunge, C. M.; Agrawal, N.; Montalvo-Castro, H.; Jin, J.; Janik, M. J.; Waegele, M. M. *J. Electrochem. Soc.* 2020, *167* (10), 106505.

(20) Xue, S.; Garlyyev, B.; Watzele, S.; Liang, Y.; Fichtner, J.; Pohl, M. D.; Bandarenka, A. S. *ChemElectroChem* 2018, *5* (17), 2326–2329.

(21) Hersbach, T. J. P.; McCrum, I. T.; Anastasiadou, D.; Wever, R.; Calle-Vallejo, F.; Koper, M. T. M. *ACS Appl. Mater. Interfaces* 2018, *10* (45), 39363–39379.

(22) Ojha, K.; Arulmozhi, N.; Aranzales, D.; Koper, M. T. M. *Angew. Chemie Int. Ed.* 2020, *59* (2), 711–715.

(23) Herasymenko, P.; Šlendyk, I. *Z Phys Chem A* 1930, No. 149, 123–139.

(24) Frumkin, A. N. *Trans. Faraday Soc.* 1959, *55* (1), 156–167.

(25) Waegele, M. M.; Gunathunge, C. M.; Li, J.; Li, X. *J. Chem. Phys.* 2019, *151* (16), 160902.

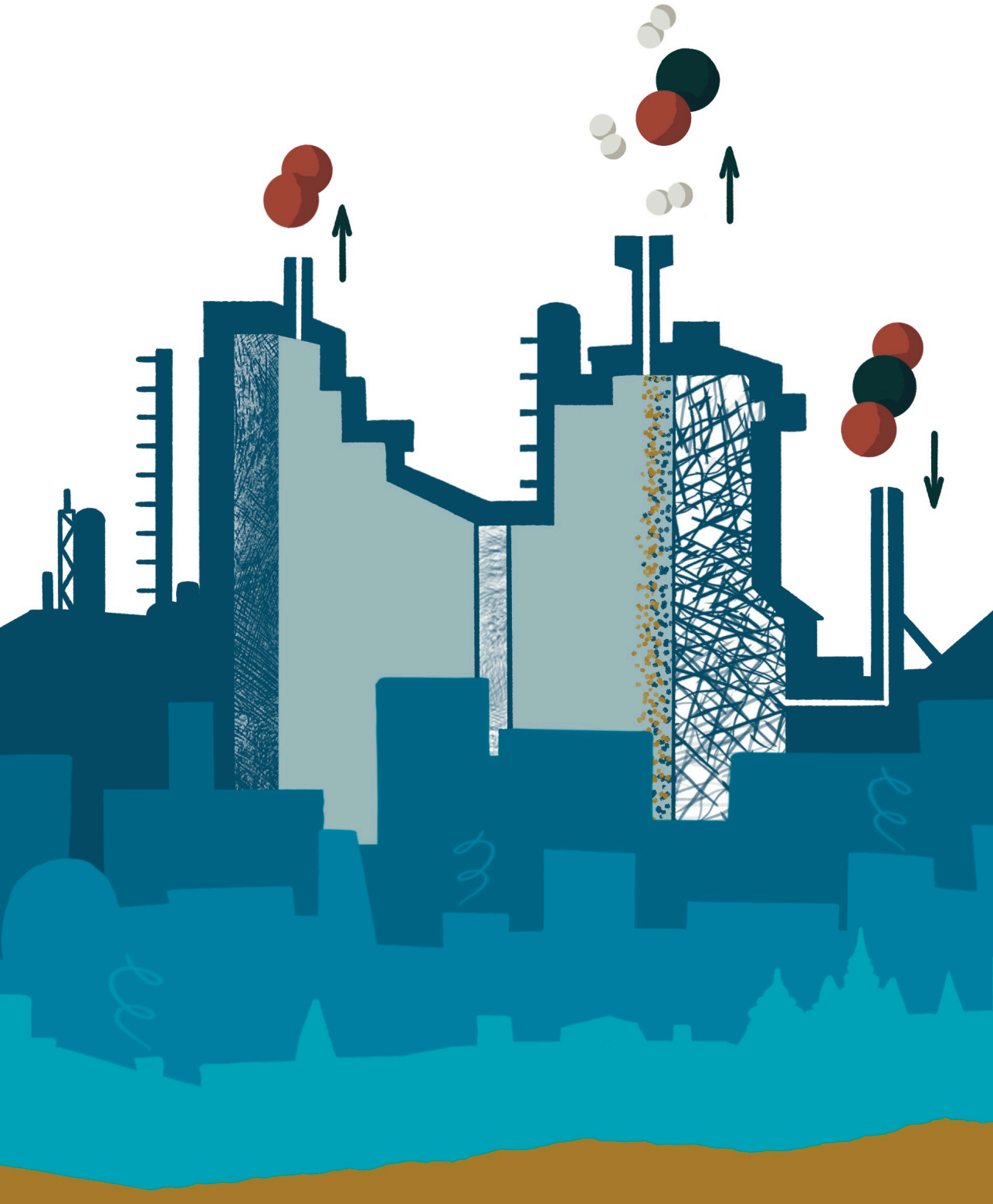

11

Efficiency and selectivity of CO_2 reduction to CO on gold gas diffusion electrodes in acidic media

This chapter is based on Monteiro, M. C. O., Philips, M. F., Schouten, K. J. P., Koper, M. T. M. *Nature Communications, 12*, 4943 (2021)

Abstract

The electrochemical reduction of CO_2 to CO is a promising technology for replacing production processes employing fossil fuels. Still, low energy efficiencies hinder the production of CO at commercial scale. CO_2 electrolysis has mainly been performed in neutral or alkaline media, but recent fundamental work shows that high selectivity for CO can also be achieved in acidic media. Therefore, we investigate the feasibility of CO_2 electrolysis at pH 2-4 at industrially relevant conditions, using 10 cm^2 gold gas diffusion electrodes. Operating at current densities up to 200 mA cm^{-2}, we obtain CO faradaic efficiencies between 80-90% in sulfate electrolyte, with a 30% improvement of the overall process energy efficiency, in comparison with neutral media. Additionally, we find that weakly hydrated cations are crucial for accomplishing high reaction rates and enabling CO_2 electrolysis in acidic media. This study represents a step towards the application of acidic electrolysers for CO_2 electroreduction.

11.1 Introduction

The finiteness of fossil fuel resources and the attempt to minimize the world´s CO_2 footprint drive research towards alternative technologies for the production of fuels and chemicals. An important building block employed in large scale for the production of commodity and specialty chemicals is carbon monoxide (CO).[1] It can be produced via the electrochemical reduction of CO_2 (CO_2RR), and, provided the electricity comes from zero emission technologies, the carbon cycle can be closed.[2] CO is among the most economically viable products that can be obtained through the electrocatalytic reduction of CO_2 as it has a high ratio of molecular weight per electron transferred.[3–5] Generating CO electrochemically can enable a less centralized CO production chain by allowing for on-site CO production on demand and eliminate transportation hazards and costs. Nevertheless, in order to achieve CO_2 electrolysis to CO at a commercial scale, three main key figures of merit are desired: high current efficiency and current density, low cell potential, and no dependency of these variables on the electrode size.[4]

A known limitation of the electrocatalytic CO_2RR is the low solubility of CO_2 in aqueous media (33 mM at 1 atm and 25 °C) and consequently the poor transport of CO_2 to the catalyst surface.[6] This limitation can be overcome with the use of gas diffusion electrodes (GDEs), which are porous structures that contain a gas diffusion layer and a catalyst layer.[7] The electrocatalytic reaction happens at the solid-liquid-gaseous interface and the transport of reactants to the catalyst surface is highly enhanced, which allows for achieving higher reaction rates than in conventional systems. Besides the high reaction rates, in order to achieve high current efficiencies for CO, the competing hydrogen evolution (HER) reaction must be suppressed, either by engineering the catalyst/electrode[7] or the reaction environment (electrolyte).[8,9]

The development of CO_2 to CO electrolysers at relatively large scale (GDE area > 5 cm^2) is recent, and in most work reported so far the reaction is performed in neutral to alkaline media. In general, the local concentration of various species (such as CO_2, HCO_3^-, CO_3^{2-} OH^-, and H^+) has shown to play a crucial role on the competition between CO_2 reduction and hydrogen evolution, through proton[10,11] , bicarbonate[12], or water[13] reduction. This is relevant as, for instance, the activity of the water reduction reaction at high overpotentials may limit the window in which high current densities can be achieved while sustaining high CO current efficiencies. Industrially relevant current densities have been accomplished at GDEs with a

geometrical area larger than 5 cm^2, however, often at the expense of relatively high cell potentials.[14–18] An additional disadvantage of using neutral or alkaline media is carbonate formation, leading to significant energy and carbon losses.[19]

Because of the high activity of proton reduction at low overpotentials, the current efficiencies found for CO in acidic media are usually low, especially on electrodes with low roughness. In fact, only in a few works in the literature, CO_2RR has been investigated (at small scale) in acidic media.[10,11,20,21] Recent work from Bondue et al.[10] has indicated that proton reduction can be fully suppressed in acidic media, as long as the rate of CO/OH^- formation from CO_2RR is high enough to compensate the mass transfer of protons to the electrode surface. Differential electrochemical mass spectrometry (DEMS) was used to quantify the formation of CO/H_2 and consumption of CO_2. The results show that with a high surface area rough gold electrode (R = 20.3), higher CO_2 pressures (high local concentration of CO_2) allow approaching a faradaic efficiency of nearly 100% for CO in mildly acidic electrolyte. A key conclusion from that work was also that CO_2 is reduced primarily by H_2O, not by protons, even in acidic media, hence leading to the formation of OH^-. However, it remains to be seen if the results from this small-scale idealized DEMS study can be translated to high-surface-area gas diffusion electrode systems. Furthermore, our recent work has shown that tailoring the electrolyte cation identity offers an opportunity to favor the water-mediated CO_2 reduction over proton-mediated hydrogen evolution in acidic media.[21] Studies carried out in sulfate electrolytes (pH 3) using a flat gold electrode, showed that cations have no effect on the rate of proton reduction, which is only a function of the (local) proton concentration. Meanwhile, the activity for CO_2RR to CO increases as a function of the cation identity in the order $Li^+ < Na^+ < K^+ < Cs^+$. Additionally, performing CO_2RR in acidic media presents several advantages to a large-scale process in terms, for example, of the electrolyte conductivity, HCO_3^- crossover, anode reaction kinetics (in case of oxygen evolution) and electrolyser design.

In this Chapter we have assessed the feasibility of acidic CO_2 electrolysis with practical electrode geometries. Using a 10 cm^2 gold gas diffusion electrode, we performed CO_2RR in sulfate electrolytes at different current densities (10-200 mA cm^{-2}). Our results show that high CO selectivity (~ 90%) can be achieved at 100-200 mA cm^{-2} in mildly acidic media, as long as weakly hydrated cations are present in the electrolyte (Cs^+, K^+). Through a direct comparison with neutral media (1 M $KHCO_3$) we find that in 1 M Cs_2SO_4 electrolyte, CO_2RR can be carried out at considerably lower cell potentials, leading to a reduction of up to 30% in process

energy costs. Our work represents an important step towards acidic CO_2 electrolysis at industrial conditions, with improved energy efficiency.

11.2 CO_2 electrolysis in acidic media

CO_2 reduction was carried out on gold gas diffusion electrodes, whose schematic structure is depicted in Fig. 11.1. At the gold-based cathode, CO_2 is fed through the back of the electrode and reduced to CO ($CO_2 + H_2O + 2e^- \rightarrow CO + 2OH^-$) at a three-phase boundary between the catalyst, the catholyte and $CO_{2(g)}$. At the DSA® anode, water is oxidized to O_2 ($H_2O \rightarrow ½O_2 + 2H^+ + 2e^-$). Depending on the reaction conditions, not all the CO_2 supplied to the cathode is converted to CO. Hydrogen (H_2) can competitively form either through proton reduction or water reduction, depending on the acidity of the local reaction environment. The local pH near the cathode surface can change significantly as a function of the current density and reaction selectivity. However, the OH^- produced during CO_2 reduction can be neutralized by protons (if the catholyte is acidic) or by the reactant itself, succesively forming bicarbonate and carbonate ($CO_2 + OH^- \rightarrow HCO_3^-$; $HCO_3^- + OH^- \rightarrow CO_3^{2-} + H_2O$). Because of these homogeneous reactions, it is important to supply

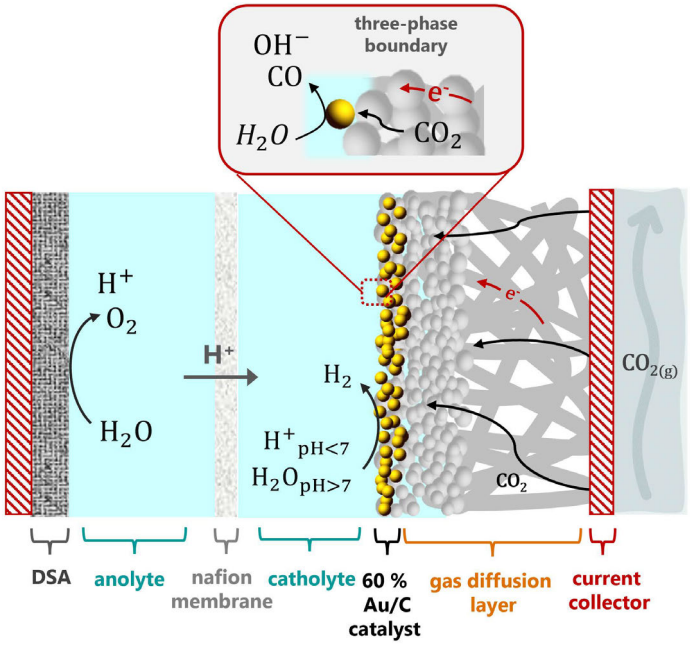

Fig. 11.1. Schematic representation of the gold gas diffusion electrode system studied in this work.

an excess of CO_2 in order to achieve high current densities and CO faradaic efficiencies. For all the measurements described in this work, the flow of CO_2 (50 mL min^{-1}) and electrolyte (30 mL min^{-1}) were kept constant, and the anolyte was always 0.5 M H_2SO_4. The setup did not allow the introduction of a reference electrode, but all system parameters were kept constant to allow a comparison of the effect of electrolyte pH on the cathodic reaction. That is: the only parameters varied were on the cathode side, where different electrolytes were investigated and two different loadings of gold nanoparticles were applied to 10 cm^2 GDEs, namely 2 and 1 mg cm^{-2}.

We have first investigated the feasibility of carrying out CO_2 electrolysis on GDEs in acidic media, by performing bulk electrolysis in 1 M Cs_2SO_4 solutions of pH 2, 3 and 4. The faradaic efficiencies (FE) for CO as a function of the total applied current density can be seen in Fig. 11.2a. The only products formed were CO and H_2, evidenced by the CO and H_2 FEs adding up to 100% (see Fig. H.1 in Appendix H). Even though formate has been reported as a possible product from CO_2RR on gold electrodes[22], it was not detected under our working conditions (if it was formed it was below our detection limit). At low current densities, we see that the selectivity for CO is lower at the more acidic electrolyte than at pH 4. However, at 200 mA cm^{-2} more than 70% FE for CO is obtained, regardless of the bulk pH. A FE of 90% is achieved at pH 4, at 100 mA cm^{-2}. In terms of selectivity, these results not only show that large scale CO_2RR to CO can be accomplished in acidic media, but are also in agreement with the model recently proposed by Bondue et al. based on small-scale DEMS measurements.[10] However, in our case, at low current densities, and low pH, due to the lower mass transport limitation in the GDE configuration, the activity for CO (and corresponding production of OH^-) is not high enough to neutralize the protons diffusing towards the catalyst surface, favouring hydrogen production. On the other hand, at current densities above 50 mA cm^{-2}, especially for bulk pH 3 or 4, the local acidic environment can be rapidly neutralized[23,24], enabling FEs for CO above 80%. We see that when starting from bulk pH 2, higher current densities are required to achieve this suppression of proton reduction. The slight decrease in selectivity for CO going from 150 to 200 mA cm^{-2} is likely due to the strong alkalinity developing around the catalyst (depletion of CO_2 due to the formation of carbonate) and the onset potential of the water reduction reaction. When operating electrolysers at high (> 100 mA cm^{-2}) current densities, low energy costs are crucial to make the process feasible. The cell potentials obtained at pH

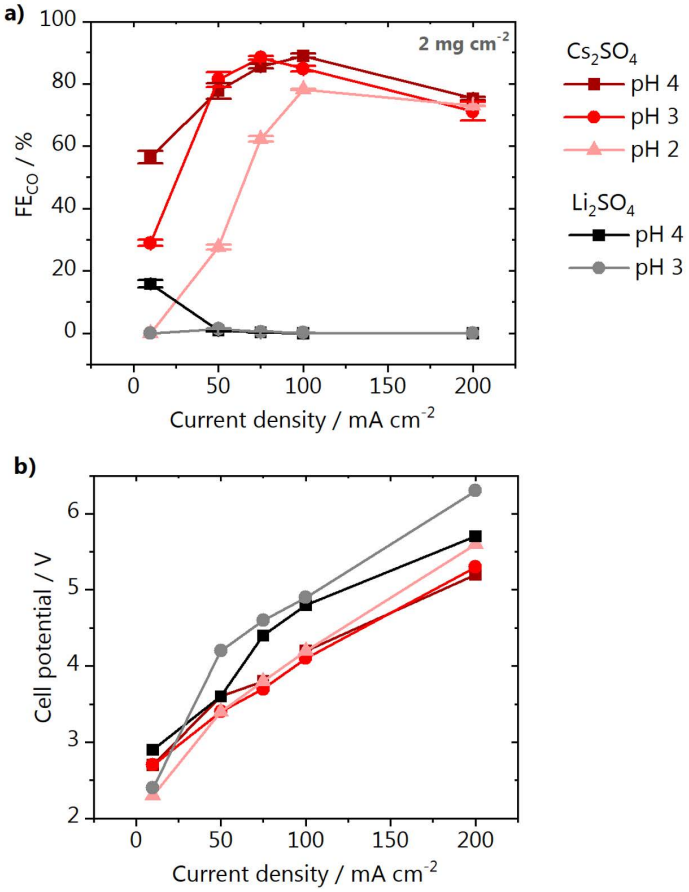

Fig. 11.2. Effect of pH and cation identity on CO_2 electrolyis: **a)** faradaic efficiency for CO and **b)** cell potential. Electrolysis performed in either 1 M Cs_2SO_4 (red) or 1 M Li_2SO_4 (gray scale), catalyst loading 2 mg cm^{-2}. Error bars are calculated based on three individual measurements.

2-4 are shown in Fig. 11.2b, and no significant differences are observed as a function of pH at intermediate current densities, where the selectivities for CO are high. However, at 10 mA cm^{-2}, a lower cell potential is found at pH 2, as mainly proton reduction is taking place. The inverse happens at 200 mA cm^{-2}, likely due to the lower activity of water reduction. We point out that the measurements at different current densities were performed sequentially, and the GDEs were stable throughout the experiments, i.e. no problems with flooding were encountered.

11.3 Cation identity and catalyst loading effects

The cation identity has also been shown to play an important role on the selectivity and activity of CO_2 reduction. In neutral and alkaline media, Bhargava et al.[25] have recently reported FEs for CO on silver GDEs increasing from 40 up to nearly 100% depending on the cation used, in the order $Na^+ < K^+ < Cs^+$ at 50 mA cm^{-2}. In acidic media, we have recently shown that the cation identity does not affect the activity for proton reduction, while weakly hydrated cations lead to a drastic increase in the activity for CO.[21] We showed that the cation acts as a necessary promotor for the reaction and that the cation trend for CO is related to the higher ability that weakly hydrated cations, such as Cs^+, have to coordinate with the adsorbed CO_2^- intermediate, and their high concentration near the electrode surface. In contrast, cations having a strong hydration shell such as Li^+, do not strongly coordinate with the oxygen of the adsorbed CO_2, and accumulate less near the surface, leading to their inferior promoting activity for CO production.[21] Therefore, we have also investigated to which extent the electrolyte cation identity plays a role when carrying out CO_2RR in acidic media in the GDE geometry. The results obtained in 1 M Li_2SO_4 at pH 3 and 4 are compared to Cs_2SO_4 in Fig. 11.2a and the total FEs for CO and H_2 are available in Appendix H, Fig. H.2. Surprisingly, we observe that in Li_2SO_4 nearly no CO is produced at all applied current densities, regardless of the bulk pH. The low activity for CO_2RR to CO in Li_2SO_4 does not allow for reaching high enough CO_2RR currents at low overpotentials and to hinder the access of protons to the catalytic active sites, yielding near 100% FEs for H_2 at these current densities. This is confirmed by the higher cell potentials are observed in nearly the whole current range investigated (Fig. 11.2b). These findings underscore that differently from neutral and alkaline media, the choice of a cation that favors the production of CO is crucial to enable CO_2 electrolysis in acidic media.

We have also prepared a GDE with half the loading of gold nanoparticles than the one used in the experiments shown in Fig. 11.2. CO_2 electrolysis was carried out at the gold GDE with 1 mg cm^{-2} loading in the same conditions as before (1 M Cs_2SO_4, pH 2-4) and the FEs for CO and cell voltages are displayed in Fig. 11.3. The total faradaic efficiencies for CO and H_2 are shown in Fig. H.3, in Appendix H. Fig. 11.3a shows the same FE trend observed for the 2 mg cm^{-2} GDE as a function of pH. However, the overall values are slightly higher for the lower loading GDE, independent of the bulk pH (see a direct comparison in Fig. H.4 in Appendix H). There are several structural factors of the GDE that could lead to the observed

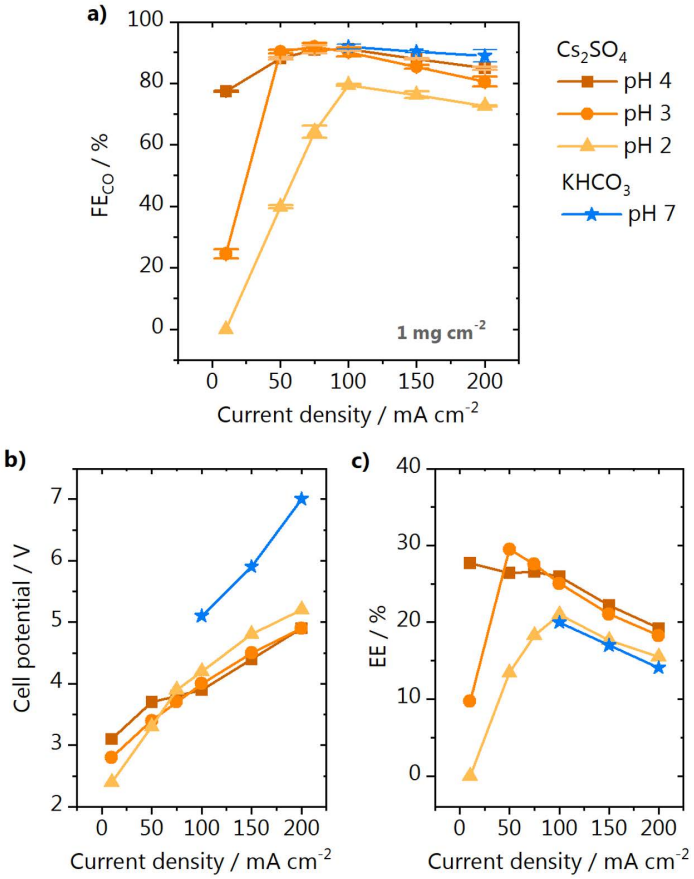

Fig. 11.3. Comparison between acidic and neutral media. **a)** faradaic efficiency for CO; **b)** cell potential and **c)** energy efficiency for CO_2 electrolysis performed in either 1 M Cs_2SO_4 (orange) or 1 M $KHCO_3$ (blue stars), catalyst loading 1 mg cm^{-2}. Error bars are calculated based on three individual measurements.

differences. The dispersion of the nanoparticles, for instance, could affect how accessible the catalytic sites are for the buildup of the three-phase reaction boundary. Significant differences in thickness of the GDE could also alter the potential drop across the layer and consequently the activity/selectivity. In the literature, there is no consensus about the exact effect that changing the catalyst loading has on the reaction. The work of Bhargava et al.[25] with Ag-based 1 cm^2 GDEs suggests that no significant differences are found in terms of CO faradaic efficiency for loadings above 1 g cm^{-2}. In the work of Duarte et al.[17], on the other hand, using 10 cm^2 Ag-based GDEs, a higher activity for CO was found in

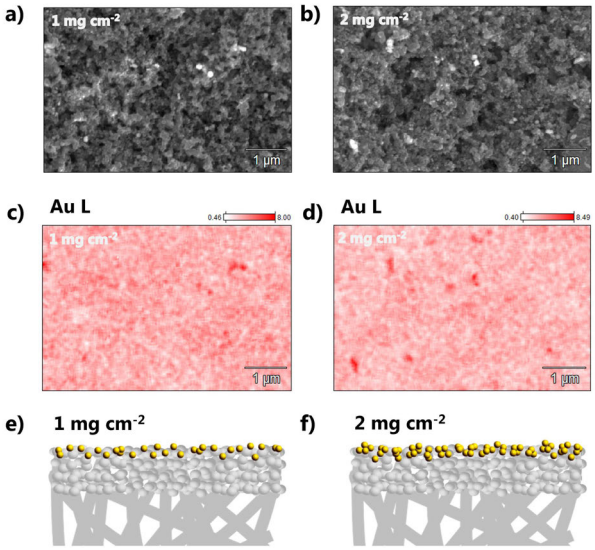

Fig. 11.4. Characterization of the GDEs with different catalyst loadings. **a)-b)** SEM micrographs, **c)-d)** EDX elemental map and **e)-f)** schematic representation of the gold GDEs with 1 mg cm^{-2} and 1 mg cm^{-2} loading, respectively.

potentiostatic measurements when increasing the catalyst loading from 0.5 to 2 g cm^{-2}. Nevertheless, no significant changes in selectivity were observed.

The differences in GDE dimensions and production procedures, in addition to the complex morphologies of these electrodes, currently do not allow drawing a general rule in terms of the effect of the catalyst loading. In view of that, we have analyzed our specific case, by characterizing the morphology and composition of the GDEs used in this work using Scanning Electron Microscopy (SEM) and Energy Dispersive X-Ray Spectroscopy (EDX). The SEM micrographs for the GDEs with 1 and 2 mg cm^{-2} loading can be seen in Fig. 11.4a and Fig. 11.4b, respectively. There are no clear differences between the overall morphology of the two GDEs, which can be also seen in the additional micrographs from Fig. H.5 in Appendix H. However, looking at the dispersion of the gold nanoparticles, it becomes clear that more particle agglomerates are present at the surface of the GDE with the higher catalyst loading. This is further confirmed by elemental analysis (Fig. 11.4c and Fig. 11.4d), implying that at the GDE with a lower loading, the nanoparticles are better dispersed on the PTFE matrix. Even though more nanoparticles are present in the GDE with higher loading, these particles are likely less accessible for the reactants, hindering the formation of the three-phase reaction boundary. A schematic

representation of these differences is depicted in Fig. 11.4e and Fig. 11.4f. It is important to point out that although only one micrograph is shown here, several areas of the GDEs were imaged in order to draw these conclusions. The images shown here are representative of the trend found throughout the whole surface. The complete EDX elemental analysis of the GDEs is shown in Fig. H.6 and H.7 in Appendix H. The two GDEs have nearly the same composition, in which carbon and fluorine are present in large amounts, due to the PTFE-based gas diffusion layer. Additionally, as the analysis was performed after the catalysts were used for the CO_2 electrolysis (for obtaining a more realistic picture of the GDE during/after operation) cesium and potassium hydroxide deposits are also found homogeneously distributed in the GDE structure, due to the extreme alkalinity developed at high current densities.

11.4 Comparison with neutral media

The performance of the 1 mg cm^{-2} GDE in acidic media was compared with its performance in neutral media, by carrying out the electrolysis in 1 M $KHCO_3$, a commonly used electrolyte for CO_2RR. The total FEs for CO and H_2 in $KHCO_3$ are shown in Fig. H.8 in Appendix H. The FEs for CO are compared in Fig. 11.3a, where we see that the selectivity in sulfate, especially at pH 3 and 4, is nearly the same as in $KHCO_3$ for current densities between 100-200 mA cm^{-2}. However, by comparing the respective cell potentials (Fig. 11.3b), we find remarkably lower values in acidic media. This is likely a consequence of the much higher conductivity of the 1 M Cs_2SO_4 (234.4 10^{-4} S m^2 mol^{-1}) electrolyte in comparison to 1 M $KHCO_3$ (117.9 10^{-4} S m^2 mol^{-1}), which decreases the ohmic losses. Considering that the electricity is the main operating cost of CO_2 electrolysis,[5] it is crucial that the energy efficiency is optimized in order to make the technology industrially viable. It can be seen in Fig. 11.3c, that operating the cathode in acidic media, in sulfate electrolyte, leads to a considerable improvement of the process energy efficiency compared to $KHCO_3$ (see Eq. H.1 in Appendix H). A similar comparison in terms of the energy consumption per ton of CO produced can be made (Fig. H.9) and shows that running CO_2 electrolysis in Cs_2SO_4 at pH 4 instead of $KHCO_3$ (both 1 M) leads to an energy saving of 24, 25 and 30% at 100, 150, and 200 mA cm^{-2}, respectively Considering, for example, an electricity price of 0.03 dollars per kWh[5], running the reaction in Cs_2SO_4 at pH 4 instead of $KHCO_3$ (at 200 mA cm^{-2}) could lead to saving 1343 dollars per ton of CO produced. The process energetics in sulfate could of

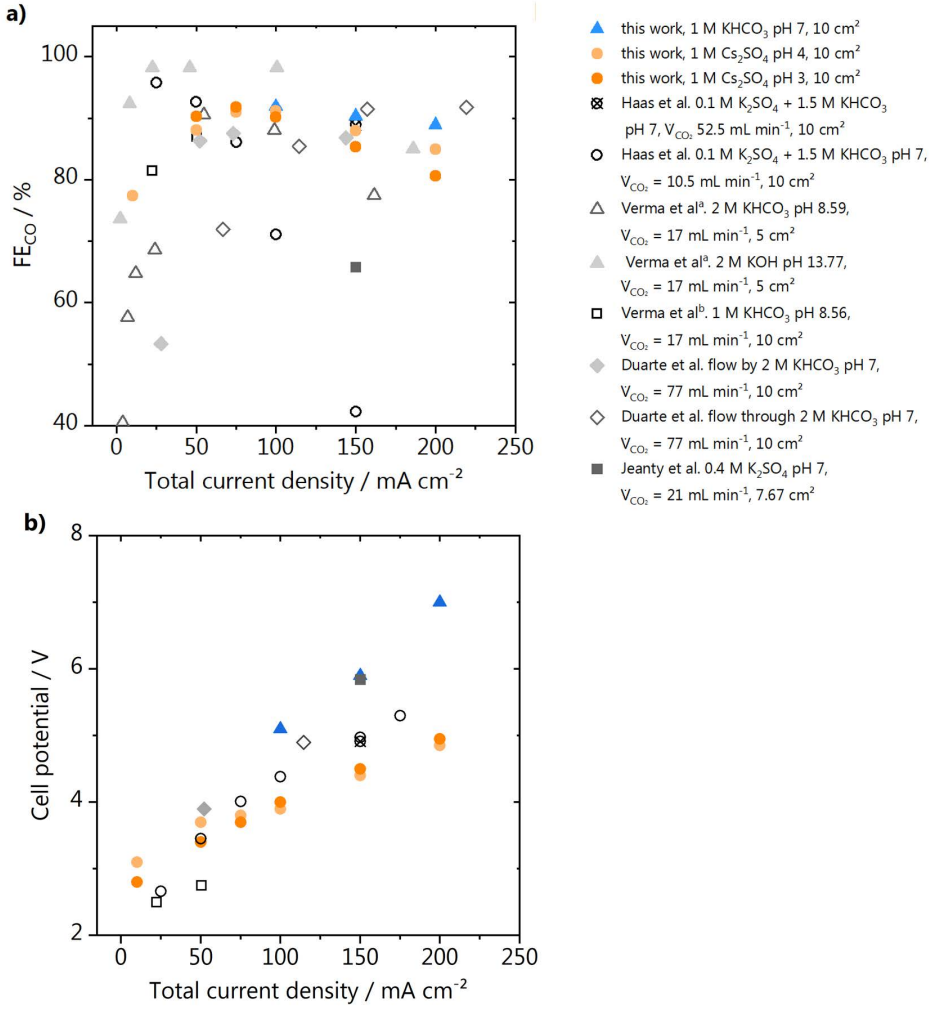

Fig. 11.5. Comparison of our results in acidic media with literature values. **a)** faradaic efficiencies and **b)** cell potentials reported in different work from literature, in which CO_2 electrolysis was performed in neutral to alkaline media, using GDEs equal or larger than 5 cm^2. Results from this work shown in orange circles (acidic media) and blue triangles (neutral media). Data points extracted from the work of Haas et al.[16], Verma et al.[a] [14], Verma at al.[b] [15], Duarte et al.[17] and Jeanty at al.[18] shown in gray.

course be improved even further, by increasing the ionic strength of the electrolyte in order to reduce ohmic losses, and by refining the cell design.

We have also compared the results of our work, performed in acidic media, with recently reported literature values, for CO_2RR to CO in neutral/alkaline media

performed in gas diffusion electrodes having a geometrical area ≥ 5 cm^2. It must be noted that although CO_2RR is intensively studied, mainly potentiostatic experiments are carried out, which are not representative of an electrocatalytic industrial process. Often, only partial current densities for CO are reported, and no information regarding the cell potential is given. This creates a gap in terms of determining the economic feasibility of the process, and for comparing different reaction conditions and catalysts. Therefore, we have only compared here results obtained in (fairly) similar systems to the one of this work. The main difference is that, in all work reported so far, CO_2RR has been carried out in catholytes of pH 7 or higher. We have only compared measurements performed at similar scale (5-10 cm^2 GDEs) and in electrolytes with moderate to high ionic strength (0.5-2 M). The collection of data points is shown in Fig. 11.5, for the CO faradaic efficiencies and cell potentials as a function of the total current density. We see in Fig. 11.5a that in terms of selectivity, the performance of our GDEs at acidic pH is quite comparable to results obtained in neutral and alkaline media, especially at the higher current densities. On the other hand, in Fig. 11.5b it can be seen that the cell potentials we obtained in acidic media are considerably lower than the literature values, supporting what we have also concluded based on our own comparison with $KHCO_3$.

11.5 Discussion and Conclusions

Based on our results in acidic media, the system design rules for CO_2 electrolysers, recently presented by Bhagarva et al.[25], should be reconsidered. In their work, pH 14 is pointed out as nearly the sole condition that can yield optimum CO_2RR to CO performance. However, their comparison is based only on experiments carried out in 1 cm^2 GDEs in electrolytes with pH higher than 6. Our work shows that operating in acidic media, specifically in sulfate electrolyte, can considerably decrease the energy costs without harming other important figures of merit such as current density and FE. Table 11.1 gives an overview of the molar conductivities of different anions and cations that have been used/considered to carry out CO_2RR. It can be seen that an acidic electrolyte (of a given cation) will always have higher conductivity than an alkaline one. Additionally, the less bicarbonate formed during the course of the reaction, the better it is in terms of carbon and efficiency losses.

In acidic media, the protons can to some extent neutralize the OH^- produced upon reduction of CO_2 while in alkaline media these species will be neutralized by

Table 11.1. Electrolyte compositions for CO_2 electrolysis. Equivalent ionic conductivity[26] ($\Lambda°$) of commonly used electrolyte ions, and feasible molality based on the solubility[27] of potassium salts containing different anions.

Conductivity			
cation	**Λ_+ $10^4 \cdot S \cdot m^2 \cdot mol^{-1}$**	**anion**	**Λ_- $10^4 \cdot S \cdot m^2 \cdot mol^{-1}$**
H^+	349.6	OH^-	198
Rb^+	77.8	SO_4^{2-}	160
Cs^+	77.2	CO_3^{2-}	138.6
K^+	73.4	HPO_4^{2-}	114
Na^+	50.1	Br^-	78.1
Li^+	38.7	I^-	76.8
		Cl^-	76.3
		NO_3^-	71.4
		ClO_4^-	67.3
		F^-	55.4
		HCO_3^-	44.5
		$H_2PO_4^-$	36
Solubility			
salt	**molal***	**salt**	**molal***
KOH	21.6	K_2HPO_4	8.6
K_2SO_4	6.9	KBr	45.0
K_2CO_3	8.0	KNO_3	31.3
$KHCO_3$	2.2	$KClO_4$	0.1

*Molality (mol kg^{-1}) calculated assuming the maximum concentrations feasible according to the solubility values at 20 ºC.[27]

CO_2 itself, lowering the reactant´s concentration at the reaction interface. Although pH 14 or larger has been proposed as the optimum condition to carry out CO_2 electrolysis[25], it has been recently emphasized that a series of difficulties can arise from operating in hydroxide-based electrolytes at large scale. The work from Nesbit and Smith[28] shows that at high current densities (> 1 A cm^{-2}) there is a local increase in the electrolyte concentration, which consequently increases its viscosity, slows down diffusion, lowers the electrolyte conductivity (e.g. for KOH concentration > 5 M) and CO_2 solubility, increases the rate of HCO_3^- production, increases the solute activity and lowers the activity of water. According to the authors, these factors slow

down the rate of CO_2R and shift the reaction equilibrium potentials. These contributions would be much less significant if operating in an acidic electrolyte.

Additionally, it is important to point out a few considerations that must be made in terms of the choice of anion for carrying out CO_2 electrolysis in acidic media. As shown in Table 11.1, sulfate anions not only have the highest conductivity (after OH^-) but also allow for working in highly concentrated electrolyte. A potassium sulfate solution, for example, can be prepared in concentrations up to 6.8 M. This is not the case for perchlorate, for example, which despite its use in many fundamental electrochemical studies, is poorly soluble and could never be employed in a large-scale process. Analyzing Table 11.1 further, halide anions would be an option considering their high solubility, however it has been shown that specific adsorption is detrimental for the activity for CO_2 reduction. Finally, although hydrogenphosphate has relatively good conductivity and solubility, it has been proposed to act as a proton donor for hydrogen evolution.[29]

In summary, here we have shown that, while most of the efforts in the CO_2R field have been on developing better cathode catalysts, the electrolyte design, specifically operating in acidic media, can considerably lower the cell potential and consequently improve the energy efficiency, without compromising the FE for CO. Based on the recent observation in idealized small-scale DEMS measurements that under suitable conditions proton reduction can be suppressed during CO_2R, our results show that FEs between 80-90% for CO can be achieved at a gold gas-diffusion electrode at current densities up to 200 mA cm^{-2}, demonstrating the feasibility of running CO_2 electrolysis in acidic media. Under these industrially relevant conditions, the high rate of CO_2 reduction (i.e. high current density) leads to the production of sufficient OH^- to neutralize the protons before they reach the catalyst layer. This hinders proton reduction and enables a high selectivity for CO even at bulk pH 2, at 200 mA cm^{-2}. Furthermore, we observe that employing weakly hydrated cations in the electrolyte, such as Cs^+ and K^+, is crucial for assuring a high CO_2 reduction activity in acidic media. Considering operation at industrially relevant scales, there must be a tradeoff between performance and cost, which means K^+ sulfate salts are likely more suitable. Finally, by comparing results in acidic and neutral media, we show that considerably lower cell potentials can be achieved at low pH in sulfate electrolyte, which result in energy savings up to 30 % operating at 200 mA cm^{-2}. Further research is of course necessary to lower energy costs even more, achieve higher current densities and

fully optimize the process. Our work, however, lays down a new path towards the development of acidic CO_2 electrolysers.

References

(1) Bierhals, J. In *Ullmann´ s Encyclopedia of Industrial Chemistry*; Wiley-VCH Verlag GmbH & Co. KGaA: Weinheim, Germany, 2001.
(2) Küngas, R. *J. Electrochem. Soc.* 2020, *167* (4), 044508.
(3) Verma, S.; Kim, B.; Jhong, H. R. M.; Ma, S.; Kenis, P. J. A. *ChemSusChem* 2016, *9* (15), 1972–1979.
(4) Philips, M. F.; Gruter, G. J. M.; Koper, M. T. M.; Schouten, K. J. P. *ACS Sustain. Chem. Eng.* 2020, *8* (41), 15430–15444.
(5) Jouny, M.; Luc, W.; Jiao, F. *Ind. Eng. Chem. Res.* 2018, *57* (6), 2165–2177.
(6) Dodds, W. S.; Stutzman, L. F.; Sollami, B. J. *Ind. Eng. Chem. Chem. Eng. Data Ser.* 1956, *1* (1), 92–95.
(7) Vennekoetter, J. B.; Sengpiel, R.; Wessling, M. *Chem. Eng. J.* 2019, *364*, 89–101.
(8) Vennekötter, J.-B.; Scheuermann, T.; Sengpiel, R.; Wessling, M. *J. CO2 Util.* 2019, *32*, 202–213.
(9) Moura de Salles Pupo, M.; Kortlever, R. *ChemPhysChem* 2019, *20* (22), 2926–2935.
(10) Bondue, C. J.; Graf, M.; Goyal, A.; Koper, M. T. M. *J. Am. Chem. Soc.* 2021, *143* (1), 279–285.
(11) Ooka, H.; Figueiredo, M. C.; Koper, M. T. M. *Langmuir* 2017, *33* (37), 9307–9313.
(12) Marcandalli, G.; Goyal, A.; Koper, M. T. M. *ACS Catal.* 2021, 4936–4945.
(13) Goyal, A.; Marcandalli, G.; Mints, V. A.; Koper, M. T. M. *J. Am. Chem. Soc.* 2020, *142* (9), 4154–4161.
(14) Verma, S.; Hamasaki, Y.; Kim, C.; Huang, W.; Lu, S.; Jhong, H. R. M.; Gewirth, A. A.; Fujigaya, T.; Nakashima, N.; Kenis, P. J. A. *ACS Energy Lett.* 2018, *3* (1), 193–198.
(15) Verma, S.; Lu, X.; Ma, S.; Masel, R. I.; Kenis, P. J. A. *Phys. Chem. Chem. Phys.* 2016, *18* (10), 7075–7084.
(16) Haas, T.; Krause, R.; Weber, R.; Demler, M.; Schmid, G. *Nat. Catal.* 2018, *1* (1), 32–39.
(17) Duarte, M.; De Mot, B.; Hereijgers, J.; Breugelmans, T. *ChemElectroChem* 2019, *6* (22), 5596–5602.
(18) Jeanty, P.; Scherer, C.; Magori, E.; Wiesner-Fleischer, K.; Hinrichsen, O.; Fleischer, M. *J. CO2 Util.* 2018, *24* (3), 454–462.
(19) Rabinowitz, J. A.; Kanan, M. W. *Nat. Commun.* 2020, *11* (1), 5231.
(20) Moreno-Garciá, P.; Kovács, N.; Grozovski, V.; Gálvez-Vázquez, M. D. J.; Vesztergom, S.; Broekmann, P. *Anal. Chem.* 2020, *92* (6), 4301–4308.
(21) Monteiro, M. C. O.; Dattila, F.; Hagedoorn, B.; García-Muelas, R.; López, N.; Koper, M. T. M. *Nat. Catal.* 2021, *4*, 654–662.
(22) Cave, E. R.; Montoya, J. H.; Kuhl, K. P.; Abram, D. N.; Hatsukade, T.; Shi, C.; Hahn, C.; Nørskov, J. K.; Jaramillo, T. F. *Phys. Chem. Chem. Phys.* 2017, *19* (24), 15856–15863.
(23) Dieckhöfer, S.; Öhl, D.; Junqueira, J. R. C.; Quast, T.; Turek, T.; Schuhmann, W. *Chem. –A Eur. J.* 2021, *27* (19), 5906–5912.
(24) Monteiro, M. C. O.; Jacobse, L.; Koper, M. T. M. *J. Phys. Chem. Lett.* 2020, *11* (22), 9708–9713.
(25) Bhargava, S. S.; Proietto, F.; Azmoodeh, D.; Cofell, E. R.; Henckel, D. A.; Verma, S.; Brooks, C. J.; Gewirth, A. A.; Kenis, P. J. A. *ChemElectroChem* 2020, *7* (9), 2001–2011.
(26) Vanýsek, P. In *Handbook of Chemistry and Physics*; CRC Press: Boca Raton, 1992; pp 76–78.
(27) Hansen, C. M. 2013; Vol. 53.
(28) Nesbitt, N. T.; Smith, W. A. *J. Phys. Chem. C* 2021, *125* (24), 13085–13095.

(29) Jackson, M. N.; Jung, O.; Lamotte, H. C.; Surendranath, Y. *ACS Catal.* 2019, *9* (4), 3737–3743.

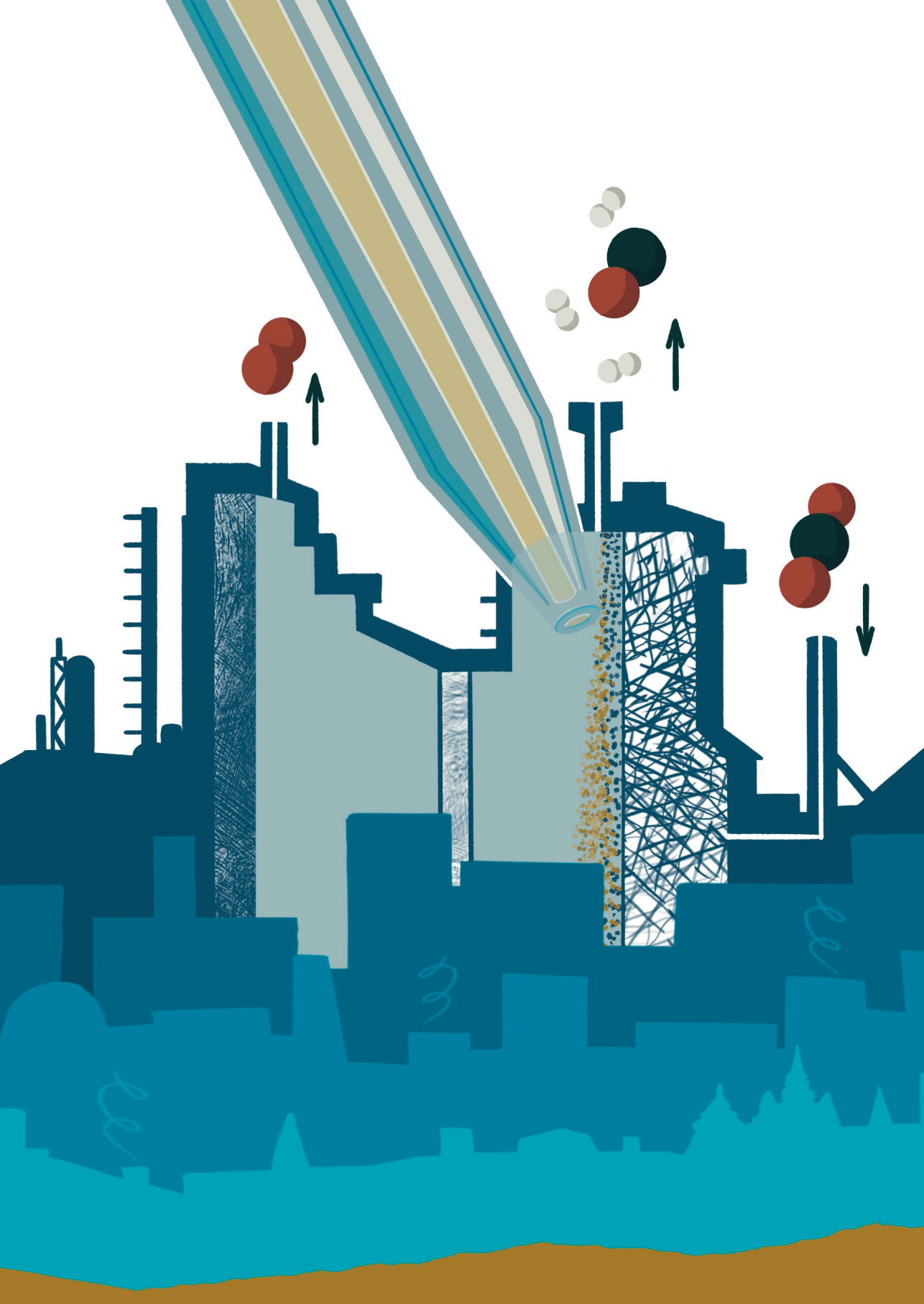

12

Probing the local activity of CO_2 reduction on gold gas diffusion electrodes: effect of the catalyst loading and CO_2 pressure

This chapter is based on Monteiro, M. C. O., Dieckhöfer, S., Bobrowski, T., Quast, T., Pavesi, D., Koper, M. T. M., Schuhmann, W. *Chem. Sci. 12*, 15682–15690 (2021)

Abstract

Large scale CO_2 electrolysis can be achieved using gas diffusion electrodes (GDEs), and is an essential step towards broader implementation of carbon capture and utilization strategies. Different variables are known to affect the performance of GDEs. Especially regarding the catalyst loading, there are diverging trends reported in terms of activity and selectivity, e.g. for CO_2 reduction to CO. We have used shear-force based Au nanoelectrode positioning and scanning electrochemical microscopy (SECM) in the surface-generation tip collection mode to evaluate the activity of Au GDEs for CO_2 reduction as a function of catalyst loading and CO_2 back-pressure. Using a Au nanoelectrode, we have locally measured the amount of CO produced along a catalyst loading gradient under operando conditions. We observed that an optimum local loading of catalyst is necessary to achieve high activities. However, this optimum is directly dependent on the CO_2 back-pressure. Our work does not only present a tool to evaluate the activity of GDEs locally, it also allows drawing a more precise picture regarding the effect of catalyst loading and CO_2 back-pressure on their performance.

12.1 Introduction

The electrochemical reduction of CO_2 (CO_2RR) has the potential to replace processes involving fossil fuels for the production of fuels and chemicals. Several studies have been performed to determine how to tune the activity and selectivity towards the various gaseous and liquid products (e.g. CO, $HCOO^-$, C_2H_4, CH_4, CH_3CH_2OH) on different catalyst surfaces.[1,2] However, these studies are often performed at a small scale, using idealized systems. Due to the poor solubility of CO_2 in water, achieving high current densities at conventional electrodes is, among other factors, hindered by CO_2 mass transport.[3,4] To realize CO_2 electrolysis at more industrially relevant currents, gas diffusion electrodes (GDEs) have been used. GDEs are hence promising, considering potential industrial applications of the CO_2RR.[5–9] However, due to the complexity of the reaction itself,[10] the substrate,[11] and the electrolyser stack,[12] there is still a lack of understanding on how the GDE performance is affected by different system parameters. Gas diffusion electrodes consist of a porous conducting material with the electrocatalyst being deposited on the surface, which is immersed into the catholyte, while the reactant (CO_2) is fed from the backside, either in a flow-through or flow-by configuration. The reaction happens at 3-phase boundaries formed by the catalyst, the electrolyte, and the gaseous CO_2. This configuration minimizes the depletion of CO_2 at the reaction interface, allowing to operate at higher current densities. Additionally, the porous structure of the GDE needs to be of hydrophobic nature to allow gas transport while preventing electrolyte flooding. Various parameters have been shown to influence the activity of GDEs, such as the catalyst loading, pressure, electrolyte flow rate, reactor geometry, electric resistance, conductivity, wettability of the substrate, among others, and deconvolution of their interrelated effects can be challenging.[13]

For a conventional system in which CO_2 is bubbled into the electrolyte phase, an increased electrochemically active surface area in contact with the electrolyte, would in principle, lead to higher activity assuming sufficient CO_2 mass transport. However, in the case of GDEs, this does not necessarily apply, as not only the catalyst has to be present, but it also has to be simultaneously reached by the CO_2 feed and wetted by the electrolyte. Previous studies on CO_2RR to CO on GDEs have been performed to assess the effect of the catalyst loading on the activity and faradaic efficiency (FE) for CO. Duarte et al. investigated the reaction on 10 cm^2 Ag-GDEs with catalyst loadings between 0.5 and 2 mg cm^{-2}.[6] Their results show little effect of the loading on the reaction selectivity, but an increase in activity was

observed with higher loading. On the other hand, Bhargava et al.[7] conducted CO_2 electrolysis on 1 cm^2 Ag-GDEs with catalyst loadings ranging from 0.3 to 3 mg cm^{-2}. They observed an increase in the CO partial current density with increasing loading up to 1 mg cm^{-2}, with the highest mass activity as a function of potential being obtained with a loading of 0.3 mg cm^{-2}. Along the same line, we recently reported on the selectivity and efficiency of CO_2 reduction to CO in acidic media on 10 cm^2 Au-GDEs with different loadings (Chapter 11).[14] In galvanostatic measurements, we observed slightly improved selectivity for CO with the GDE having lower catalyst loading (1 mg cm^{-2}) than the one with higher loading (2 mg cm^{-2}). Through scanning electron microscopy (SEM) analysis of the two GDEs, we attributed those differences to agglomerates within the catalyst layer at a loading of 2 mg cm^{-2}, which prevents access of the reactants to the catalyst nanoparticle surface. These contradicting results show that in-depth knowledge concerning the parameters determining an optimal catalyst loading is not available. Additionally, a systematic comparison becomes difficult as the experimental conditions and fabrication procedures vary from one work to another.

Another approach to improve the activity of GDEs, is to increase the CO_2 pressure at the back of the GDE or the CO_2 flow rate in a flow-through electrolyzer.[15–17] However, operating at too high CO_2 pressures, with the aim to supply sufficient CO_2 to the whole catalyst surface, can be detrimental to the GDE stability and may lead to flooding.[18] It is important to point out that even though activity and selectivity values are reported as a function of the CO_2 flow rate or pressure and catalyst loading, a comparison between different studies is nearly impossible due to differences of at least some of the experimental conditions. Electrolyzers and GDEs have different sizes, the substrates have different compositions, and there is always limited information about the actual flux of CO_2 reaching the electrocatalyst surface/electrolyte interface. The ability to probe the activity of GDEs *in situ* may contribute to the understanding of the interplay between these parameters as well as the impact of the surface topography, the formation of the 3-phase boundary, and ultimately provide the basis for the optimization of the performance of CO_2RR electrolyzers. Such information cannot be obtained using conventional product detection techniques such as gas/liquid chromatography, mass spectrometry, rotating-ring-disc electrodes (RRDE), due to their lack of spatial resolution and sensitivity. In contrast, scanning probe techniques are powerful tools for investigating activity locally with high resolution.[19–26] Mayer et al.[22] used a Pt ultramicroelectrode (Pt-UME) to detect formate, CO and H_2 during CO_2RR on

Sn/SnO_x arrays. However, here, the tip-to-surface distance was determined using O_2 reduction diffusion limitation, which may mainly practical for probing flat electrodes. Similarly, in Chapter 5 of this thesis, we have used a Pt-UME in the surface-generation tip-collection (SG-TC) mode to detect CO produced during CO_2RR on Au, Cu and Ag electrodes.[25,26] Although these previous measurements were performed on non-permeable substrates, it has also been demonstrated that probing the local pH during the oxygen reduction reaction (ORR) and CO_2RR on GDEs can be achieved with SECM by shear-force positioning of Pt nanoelectrodes at ~100 nm above the GDE surface.[23,24] This experimental approach allows for simultaneously deriving modulations of the local pH value in correlation with the current density, and the topography *in situ* and with high resolution.

In this Chapter, we have developed a method using SECM and shear-force positioning to probe the local activity of gas diffusion electrodes under *operando* conditions. We investigate how the catalyst loading and CO_2 back-pressure affect the local activity of Au-GDEs under different applied potentials. For that, we prepared 3 cm^2 Au-nanoparticles modified GDEs containing different catalyst gradients ranging from low to high loading regions, and we used SECM in the SG-TC mode to probe the activity during CO_2RR to CO. By approaching the surface using shear-force positioning, we are able to map the local CO product fluxes along these Au-catalyst loading gradients at a very short distance of about 100 nm above the GDE surface. The diffusion-limited CO oxidation current is constantly recorded at the positioned Au nanoelectrode while the SECM tip is scanned across the loading gradient. Simultaneously, the applied sample potential and the CO_2 back-pressure are varied, and the interplay between catalyst loading and CO_2 back-pressure is evaluated for optimum operation of GDEs. These measurements and the obtained information opens up pathways towards investigating these systems on a deeper level. This should eventually help to better design and optimize GDEs for CO_2 electrolysis.

12.2 Characterization of the gas diffusion electrodes

To investigate the effect of the catalyst loading on the CO_2RR activity of gas diffusion electrodes (GDEs), we prepared two different GDEs containing loading gradients of 60% Au/C nanoparticles. The Au nanoparticles, with an average diameter of 20 nm (inset Fig. 12.1a), were sprayed on a porous gas diffusion layer using an automated air-brush type spray-coater.[27,28] Different volumes of the catalyst ink were sprayed along 2 cm of carbon/PTFE GDE surfaces (Fig. 12.2a),

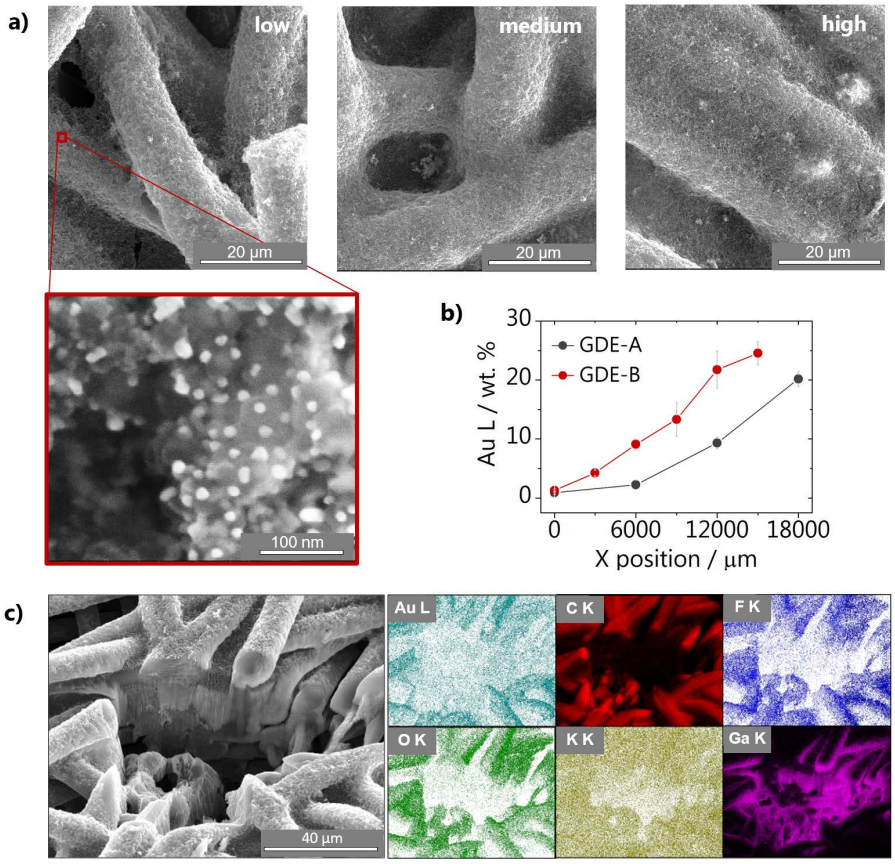

Fig. 12.1. Characterization of the gas diffusion electrodes. **a)** SEM micrographs taken in the low, medium and high loading regions of a Au/C catalyst gradient sprayed on the gas diffusion layer. The zoomed-in image (red box) shows the shape and distribution of the 20 nm particles on the GDE. **b)** Gold weight percentage measured with EDX along the loading gradient showing a shallow (GDE-A) and steep (GDE-B) gradient. Each data point is an average of three measurements around the same X-position, and error bars are the respective standard deviation. **c)** SEM micrograph of the cross-section of GDE-B exposed after milling with a focused ion beam, together with the EDX elemental maps recorded in the same area.

leading to GDE-A, exhibiting a shallow Au/C gradient, and GDE-B, having a steep increase in the amount of Au nanoparticles along the length of the sample. It is important to point out that the substrate used for this work does not contain a microporous layer, so the catalyst ink was applied directly onto the gas diffusion layer. Fig. 12.1a shows SEM images, representative of the different loading regions of the resulting GDEs. At the low loading area, the carbon fibers are not entirely covered by the Au/C nanoparticles. As moving to regions of higher loading, the coverage increases as the shape of the fibers becomes less evident and the gaps between the fibers are filled with the catalyst ink. The volume of catalyst ink dispensed at each spray increment along the length of GDEs A and B indicates the steepness of the two different catalyst gradients (see Fig. I.3; Appendix I). In addition, we characterized the different loading regions using energy dispersive X-rays (EDX) mapping for comparing the amount of Au along the length of the GDEs. The percentage of Au found along GDE-A and GDE-B is displayed in Fig. 12.1b, showing that, as expected, for GDE-B, a higher loading and a faster increase along the gradient is achieved compared with GDE-A. The values are an average of three measurements around a given position. The EDX results are exemplarily shown in Fig. I.4 and Fig. I.5 in Appendix I, together with SEM micrographs of GDE-A and GDE-B at the corresponding positions. Due to the complex morphology of the GDEs, we used focused ion beam (FIB) milling in combination with EDX to evaluate the composition of the GDEs through a cross-sectional cut perpendicular to the surface. Results for GDE-B are shown in Fig. 12.1c, and the SEM image suggests that the GDE exhibits dense areas together with a few long pore-type channels connected throughout the fibers. EDX elemental analysis shows the presence of Au, C, F, O, K, and Ga (which originates from the ion source of the FIB). The majority of the Au/C nanoparticles are located on top of the fibers. As EDX characterization was performed after CO_2 electrolysis in $KHCO_3$, K is found throughout the whole imaged area. As recently shown by Cofell et al.[29], this is due to $KHCO_3$ deposition due to concentration gradients and increased local alkalinity developed during electrolysis.

12.3 SECM and shear-force positioning

The activity of the GDEs was evaluated in the SG-TC mode of SECM, as schematically shown in Fig. 12.2a. The GDEs were mounted on a specifically designed cell (see experimental details in Appendix I) so that the whole catalyst gradient was in contact with the electrolyte, while CO_2 was constantly fed through the gas channel at the backside of the GDE. A Au nanoelectrode was used to detect

the local amount of CO produced while CO_2RR roccurred at the GDE. The Au wire was platinized before it was inserted into the laser puller to improve the adhesion between the Au wire and the insulating quartz capillary to fabricate a well-sealed Au nanoelectrode. SEM micrographs of a Au nanoelectrode with a tip radius of 1.0 ± 0.02 µm are shown in Fig. 12.2b. During the SECM measurements, the tip was brought as close as about 100 nm to the GDE surface at every XY position by performing a shear-force based approach.[30] A frequency spectrum and an example of an approach curve, can be seen in Fig. I.6 (Appendix I). A blank voltammogram of the Au nanoelectrode was recorded in the shear-force interaction region before each experiment (Fig. I.7a, Appendix I), showing that at the chosen experimental conditions in CO_2 saturated 1 M $KHCO_3$ only voltammetric features characteristic of the Au oxide formation, reduction and double layer charging are present.[31] To assure that applying different potentials to the GDE does not affect the nanoelectrode current and that the catalyst-free GDE is inert, we have also consecutively recorded voltammograms of the Au nanoelectrode in the shear-force interaction distance while stepping the potential at the catalyst-free GDE from –0.6 to –1.4 V vs. Ag/AgCl (Fig. I.7b, Appendix I). We did not observe any CO formation at the catalyst-free GDE, evidenced by the stable double layer charging current in the potential range between –0.25 and 0.6 V vs. Ag/AgCl. To demonstrate that the Au nanoelectrode responds to CO, a calibration gas contai-ning 1 vol. % CO was fed through the back of the GDE for 10 s while a potential of –0.6 V vs. Ag/AgCl was applied to the GDE (Fig. I.6a, Appendix I). Two characteristic anodic current plateaus become visible due to diffusion-limited CO oxidation to CO_2. These two plateaus appear only in a specific alkaline pH range, as shown previously, confirming that they are due to CO oxidation limited by the diffusion of two different species.[26,32] At more positive potentials, more specifically at 1.2 V vs. Ag/AgCl, the anodic current is due to oxygen evolution. The two voltammetric cycles recorded before the gas mixture was introduced show the difference in magnitude between the double-layer charging and the faradaic current due to CO oxidation. In the next step, we evaluated the voltammetric response of the Au nanoelectrode, which was positioned in the shear-force interaction distance above the GDE, at potentials of –0.6 and –1.2 V vs. Ag/AgCl applied to GDE-A (shallow catalyst gradient) in 1 M $KHCO_3$ under a CO_2 back pressure of 2 mbar. The voltammograms for the two GDE potentials are shown in Fig. I.8b in Appendix I. At –0.6 V vs. Ag/AgCl applied at the GDE only current

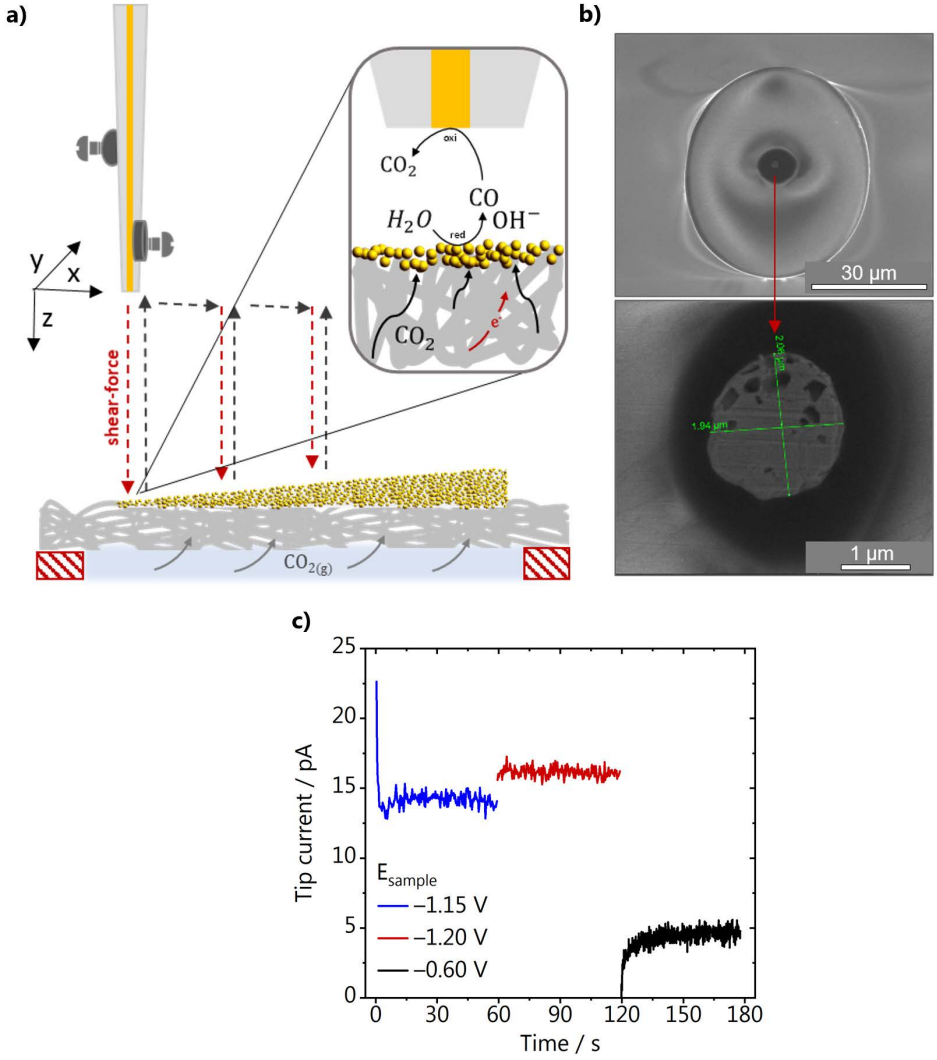

Fig. 12.2. a) Schematic representation of the SECM experimental setup, with piezo elements mounted at the Au nanoelectrode tip, approaching a catalyst loading gradient in hopping mode. The SECM is operated in SG-TC mode, as shown in the inset; **b)** SEM micrographs of the gold nanoelectrode; **c)** tip current recorded at a constant potential of 0.19 V vs. Ag/AgCl, upon applying different potentials to the GDE in 1 M CO_2 saturated $KHCO_3$.

due to double layer charging is observed at the Au nanoelectrode, whereas at –1.2 V vs. Ag/AgCl a diffusion limited plateau arises. Although the voltammetric features are very similar to the ones observed when using the calibration gas (Fig. I.8a), a distinct shift of the CO oxidation current plateau to more negative potentials is observed due to the concurrent formation of OH^- and an increase in the local alkalinity. The Au nanoelectrode current was recorded at a fixed potential of 0.190 V vs Ag/AgCl during the SECM scans to account for these possible shifts, a potential which is located in the middle of the diffusion-limited CO oxidation plateau. An example of the current that is recorded at the Au nanoelectrode in the shear-force interaction distance during a SECM scan is shown in Fig. 12.2c. Stable diffusion-limited currents increasing from GDE potentials of –1.15 to –1.2 V vs. Ag/AgCl due to the concomitantly increasing amount of CO produced at the GDE are observed. In contrast, when the GDE potential is –0.6 V, the current drops and is only due to the charging of the Au nanoelectrode double layer.

12.4 Effect of the catalyst loading

We have evaluated the amount of CO produced along the catalyst gradients of GDE-A and GDE-B using the diffusion-limited CO oxidation current recorded at the Au nanoelectrode. All SECM experiments were performed in the hopping mode, where at each XY-position, a shear-force approach curve was performed. The Au nanoelectrode current at different GDE potentials was recorded in the shear-force interaction distance (~100 nm above the GDE surface), and then the Au nanoelectrode was retracted and moved to a new XY-coordinate (Fig. 12.2a). The average diffusion-limited CO oxidation current recorded at the Au nanoelectrode during 60 s at every X-position and constant Y-position along the GDE is shown for different GDE potentials. Results for GDE-A, at a CO_2 back pressure of 2 mbar, are shown in Fig. 12.3a. We observe that the increase in catalyst loading along the X-direction leads to a nearly linear increase in the amount of CO produced, as the tip current rises from 4 pA (at X = 0 μm) to almost 6 pA (at X = 17000 μm). However, surprisingly, most of the activity comes from localized hot spots, which are present both in the low and high loading regions of GDE-A. CO hotspots and CO_2 pockets (marked with a yellow and red shade in the SECM array scan, respectively; Fig. 12.3) were detected at certain X-positions where not only relatively higher CO oxidation currents were measured at the Au nanoelectrode, but also constant bubble formation was disturbing the Au nanoelectrode signal. Bubbles were identified due to the signature of the noise they

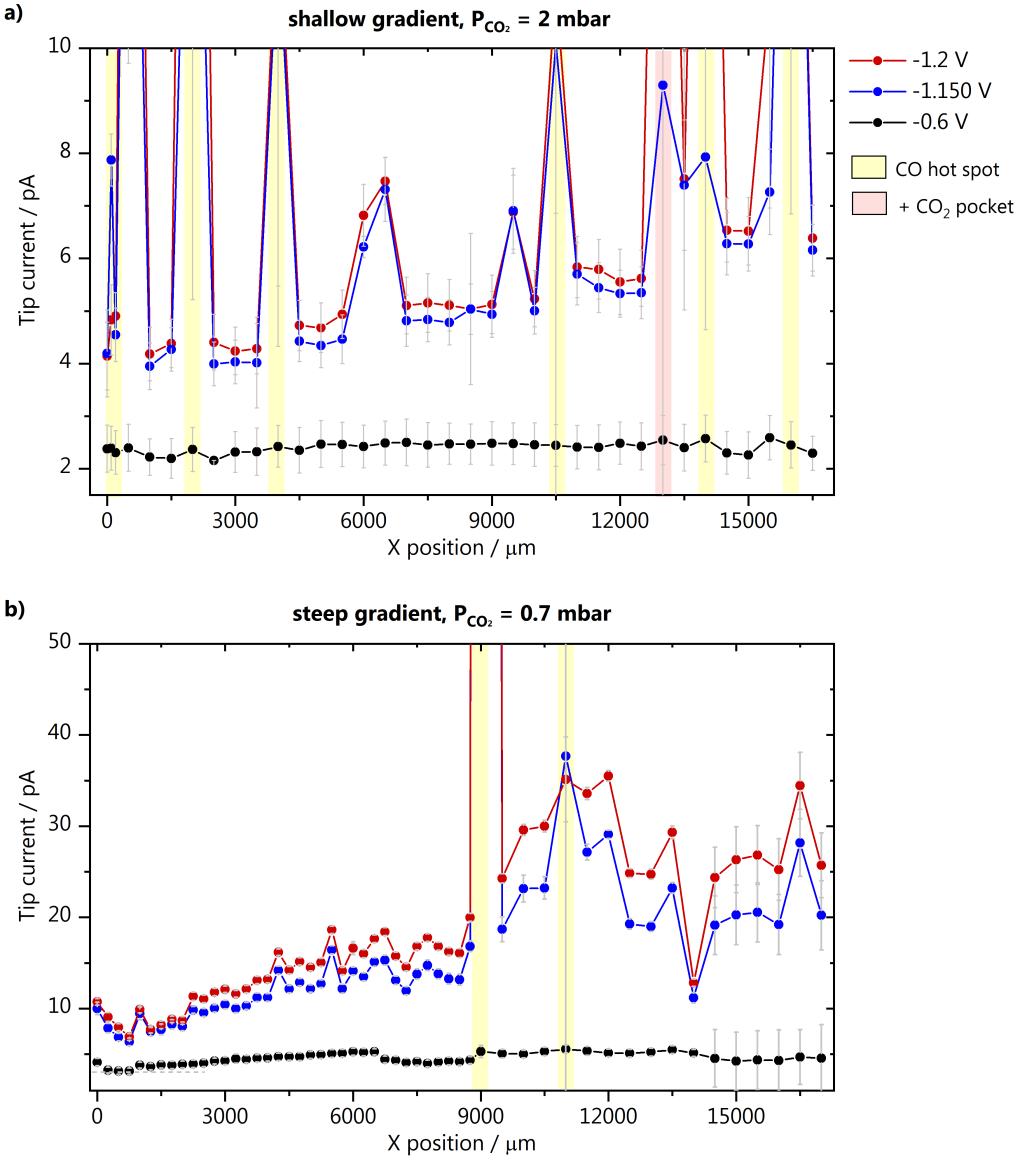

Fig. 12.3. SECM array scans along **a)** the catalyst gradient of GDE-A at a CO_2 back-pressure of 2 mbar, and **b)** the steep gradient of GDE-B at a CO_2 pressure of 0.7 mbar. The potentials applied to the GDEs were –1.2 V (red), –1.15 V (blue) and –0.6 V (black) vs. Ag/AgCl in 1 M $KHCO_3$ as electrolyte. CO hot spots and CO_2 pockets are marked with a yellow and red shade, respectively.

cause in the Au nanoelectrode current response (see Fig. I.9 in Appendix I). CO hot spots (marked with a yellow shade in the SECM array scan; Fig. 12.3) were identified at positions where the noise in the Au nanoelectrode current was detected upon applying potentials of –1.20 or –1.15 V vs. Ag/AgCl to the GDE. CO_2 pockets are found at positions where even at a potential of –0.6 V vs Ag/AgCl (no CO produced at the GDE), the Au nanoelectrode current was showing the characteristic noise due to bubbles. We observed that every CO_2 pocket was also a CO hot spot, but not every CO hot spot was a CO_2 pocket. The bubble-associated noise was not considered for calculating the average diffusion-limited currents as it is not representative of the CO concentration. Fig. 12.3a zooms in the low current range, and a plot displaying the complete current range is shown in Fig. I.10 in Appendix I. The current at the hotspot locations is up to 5-6 times higher than the maximum current obtained at the other measurement areas of the catalyst gradient. This suggests that at the relatively low catalyst loading along the gradient, the formation of the three-phase boundary within the GDE is more critical to assure high activity than the amount of catalyst on the GDE surface. Additionally, it is important to point out that the pore network and transport properties of the gas diffusion layer may play an important role on the formation of these hot spots. For example, CO can accumulate in the pores near highly active areas of the GDE. These gas-filled pores find the optimal pore system for breaking through and therefore the surface of the GDE where the gas-filed pore network opens to the bulk electrolyte is detected as a hot spot. An example of such a pore system can actually be seen in the FIB cross section depicted in Fig. 12.1c. Despite the complexity of these processes, our measurements show how inhomogeneous the activity is along the gradient and that a higher catalyst loading alone, does not assure high activity.

The activity along GDE-B with a steeper catalyst gradient was also evaluated, however, at a lower CO_2 back pressure of 0.7 mbar (Fig. 12.3b). In general, higher activity is observed in comparison to GDE-A, despite the lower CO_2 pressure. Up to X = 11000 µm, a steeper increase in the amount of formed CO is seen, which is in good agreement with the EDX characterization (Fig. 12.1b). In contrast to the results obtained from GDE-A, the activity starts to decrease for GDE-B at X > 11000 µm. Due to the lower CO_2 availability and the higher density and thickness of the catalyst layer, it seems that at higher loading, a part of the Au/C nanoparticles is less accessible to the CO_2. At lower backpressure, no CO_2 pockets and nearly no CO hot spots along GDE-B are detected. We have also investigated the relationship between activity and GDE topography to better understand the effect of the CO_2

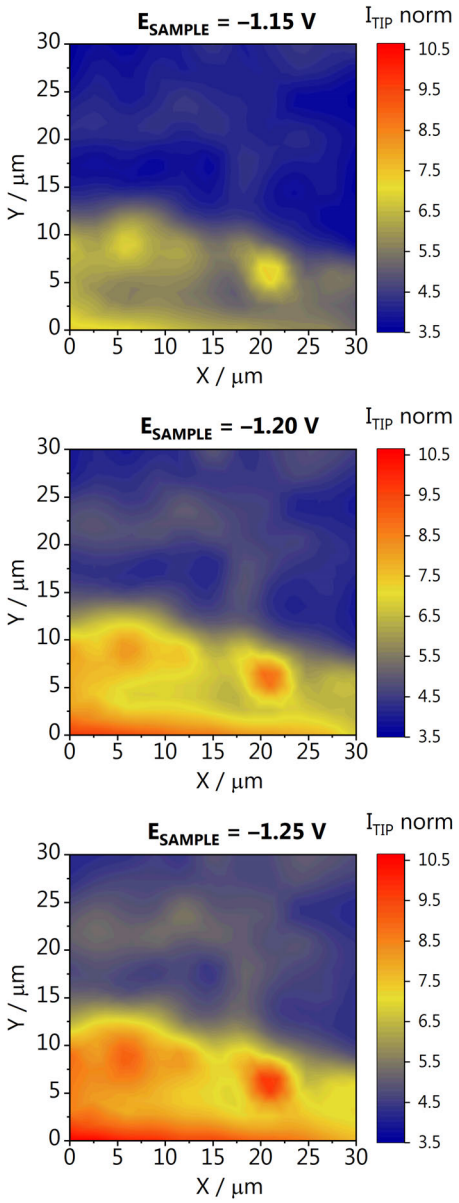

Fig. 12.4. Activity map recorded for GDE-B at a CO_2 back-pressure of 0.7 mbar. The different GDE potentials are reported versus Ag/AgCl in 1 M $KHCO_3$. The tip current (I_{TIP} norm) is normalized to the double-layer charging current recorded at –0.6 V.

gradient through the gas diffusion layer. A height profile was derived from the absolute Z-position of the shear-force interaction distance of the closest approach of the Au nanoelectrode above the GDE surface. This topography profile is plotted together with the Au nanoelectrode current from Fig. 12.3b at –1.2 V vs. Ag/AgCl (Fig. I.11 in Appendix I). Interestingly, locations where more CO is detected (indicated by red arrows) coincide with lower absolute Z-positions of the Au nanoelectrode. This suggests a CO_2 concentration gradient from the back towards the surface of the GDE, and hence at these lower Z-positions, e.g. above a pore, the local concentration of CO_2 is likely higher, yielding more CO. The same analysis cannot be done for the measurement from Fig. 12.3a (GDE-A), as the large amount of bubbles leads to an uncertainty in the positioning of the Au nanoelectrode over CO_2 pockets and CO hotspots.

12.5 High-resolution activity map

To better understand how localized the hot spots are, and how much the activity can vary within a small area of the GDE, we have recorded activity maps on a 30 x 30 µm area of GDE-B. The origin of the map (X,Y = 0,0) corresponds to position X = 10000 µm in Fig. 12.3b within the high activity region along the catalyst concentration gradient. For constructing the activity maps, at each XY position a Z-approach was carried out and the CO oxidation current was recorded at the tip while four different potentials were applied to the GDE (–1.15, –1.20, –1.25 and –0.60 V vs. Ag/AgCl). The current determined at each position was normalized to the double-layer charging current recorded at –0.6 V, to account for slight changes of the tip response, which can occur during these long-term measurements (~ 14 h). The activity maps at different GDE potentials are shown in Fig. 12.4, and the data processing in Fig. I.12 in Appendix I. We observe a similar activity trend as for the array scans in Fig. 12.3a and Fig. 12.3b, where more CO is formed at more negative potentials. Interestingly, large differences in activity are observed, demonstrating the inhomogeneity of the lateral response over the GDEs. For example, at position (X,Y = 0,0), the activity is seven times higher than at the center of the mapped area (X,Y = 15,15). As the catalyst gradient was formed over a much wider length of the GDE (1.7 cm) than the one visualized in the array scan in Fig. 12.4 (30 µm), we hypothesize that the detected differences are not due to a difference in the catalyst loading. These differences highlight that apart from a high catalyst loading, it is imperative to supply enough CO_2 and to provide a homogeneous distribution of pores of the GDE accessible for CO_2, in order to form

a three-phase reaction boundary. The used experimental SECM-based strategy allows to spatially resolve inhomogeneous CO_2RR activity, which is a direct result of inhomogeneous three-phase boundary properties within the GDE pore system. Thus, different CO fluxes detected at the Au nanoelectrode are not only a function of catalyst quantity at a given location, but are additionally related to the gas transport of CO_2 through channels below the actual accessible GDE surface as well as the local reaction rate and the concomitant local change in the pH value.

We have marked the region where the activity maps were measured to analyze the morphology-activity relationship of the GDE. After the experiments, GDE-B was marked with a 1.2 mm tip, at two known and safe distances from the area that was mapped (Fig. I.13 in Appendix I). SEM images of the marked GDE area were obtained, and although we cannot assure the location of the specific area of the SECM activity map with a sufficiently small confidence interval, a quite high number of larger pores can be seen in this region. From Fig. I.11 in Appendix I we are confident that the area is very similar to the area selected as shown in Fig. I.13b (Fig. I.13c). Above and in the pores, the concentration of CO_2, and consequently the formed CO, is significantly higher than above the topmost fibers of the GDE. These deeper pores and differences in the pore network are most likely responsible for the significant activity differences shown in Fig. 12.4.

12.6 Effect of the CO_2 pressure

As most results so far point out the importance of CO_2 reaching the wetted catalyst layer, we have also performed an array scan along GDE-B, but now at a CO_2 back-pressure of 4.2 mbar (Fig. 12.3b). This is the highest possible CO_2 pressure at which we could perform SECM measurements without gas bubbles disturbing the electrolyte. Surprisingly, compared to Fig. 12.3b, we see that upon increasing the CO_2 pressure, the activity in the low loading region ($0 < X < 7000$) increases by an order of magnitude (Fig. 12.5). However, here the effect of the catalyst gradient is much less pronounced. Due to the higher back-pressure, more hot spots and CO_2 pockets are formed along the catalyst loading gradient. In contrast to the low loading region, above X = 7500 µm (compare Fig. 12.3b), a large increase in the Au nanoelectrode current is seen reaching a maximum at a higher catalyst loading than at a CO_2 back-pressure of 0.7 mbar. This suggests that a large portion of the catalyst layer is not utilized at lower back-pressure because it is not reached by the reactant. Once the CO_2 pressure is increased, the maximum activity is shifted to a higher

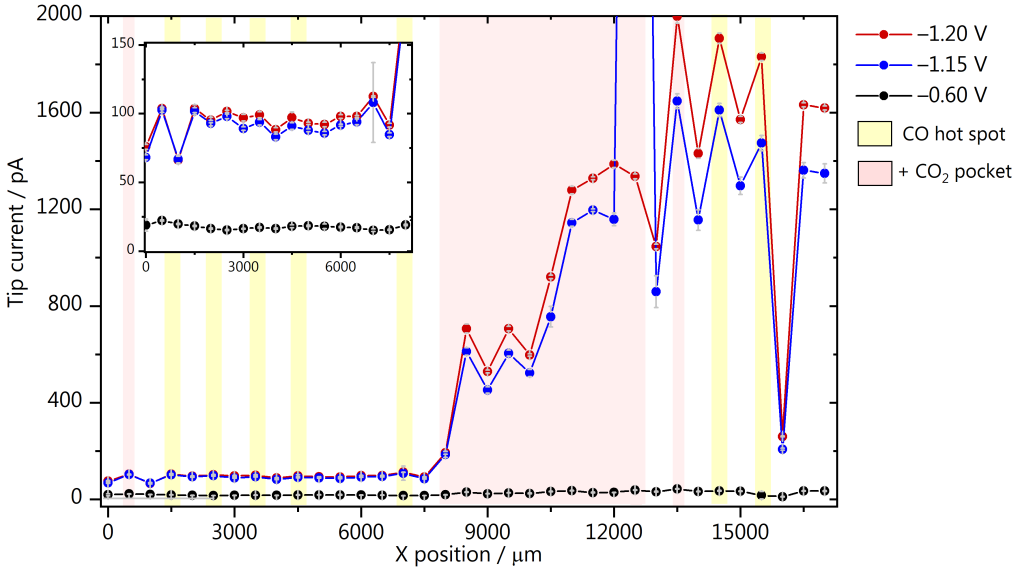

Fig. 12.5. SECM array scans through the catalyst gradient of GDE-B at a CO_2 back-pressure of 4.2 mbar. The applied GDE potentials were –1.2 V (red), –1.15 V (blue) and –0.6 V (black), reported versus Ag/AgCl and measurements were performed in 1 M $KHCO_3$. CO hot spots and CO_2 pockets are marked with a yellow and red shade, respectively.

catalyst loading area. If the loading is too high, the surface will be blocked and it will be more difficult for CO_2 to reach the active sites at the catalyst surface.

12.7 Discussion

These results have implications for the design and optimization of GDE-based CO_2 electrolysis systems. We see that overall, higher catalyst loadings lead to higher activity for CO, provided enough CO_2 is supplied. However, we can now also better understand why results in literature show opposing dependencies regarding the relation between local CO_2R activity and catalyst loading in GDEs. The optimal loading to achieve the highest activity is strongly dependent on the CO_2 back-pressure and the permeability of the gas diffusion substrate (Fig. 12.3b and Fig. 12.5). For example, we previously performed experiments with a large excess of CO_2, and the GDE with lower catalyst loading exhibited a higher faradaic efficiency for CO.[14] On the other hand, Duarte et al.[6] observed an increase in CO partial current density with increasing loading but with no effect on the faradaic efficiency. This also points out to the fact that different gas diffusion layers highly differ in terms of how the pore channels are distributed and how permeable and hydrophobic the layer is. All these parameters will play a role and should be tested for and taken into

account when establishing optimum operation conditions for GDEs. Despite the complexity of GDE-based CO_2 electrolyser systems, we have now a tool at hand to go one step further in finding the optimal operation parameters based on the local information which can be attained using the experiments we show here. Even though we could already obtain valuable insights into the effect of catalyst loading on the activity of GDEs, a more systematic study would allow to establish more quantitative system design rules. Additionally, we propose that spray-coating, the currently most used production process for GDEs, may not be ideal in the sense that most of the catalyst particles are located only at the topmost layer of the GDE, where the CO_2 concentration is lowest in a flow-through or flow-by configuration. This suggests that the catalyst particles should be dispersed within the GDE matrix and homogeneously distributed along the electrode cross-section, while still, of course, allowing for electrolyte to percolate. In that way, most of the catalyst will be utilized, and the CO_2 back-pressure can be moderate.

12.8 Conclusions

We have assessed the effect of catalyst loading and CO_2 pressure on the activity of Au GDEs. We used shear-force based Au nanoelectrode positioning, and the SG-TC SECM mode in combination with catalyst loading gradients on the GDE. CO_2 reduction to CO was carried out and the formed CO was detected using the Au nanoelectrode. Our results show that higher catalyst loadings lead to higher activity for CO, provided that enough CO_2 is supplied. We confirm experimentally, that an optimum balance between the available amount of catalyst and the supplied CO_2 is necessary to achieve high activity for CO_2 reduction. Evidently, employing a large amount of catalyst without providing enough CO_2 does not sufficiently utilize the catalyst. The proposed methodology opens up opportunities for probing the activity of GDEs locally in a more controlled manner than using conventional product detection techniques. On top of that, the shear-force positioning used here, allows to directly correlate the activity data with the electrode topography. With that, the influence of other variables on the activity of GDEs can be investigated, such as gas diffusion layer composition and GDE porosity.

.

References

(1) Kortlever, R.; Shen, J.; Schouten, K. J. P.; Calle-Vallejo, F.; Koper, M. T. M. *J. Phys. Chem. Lett.* 2015, *6* (20), 4073–4082.

(2) Birdja, Y. Y.; Pérez-Gallent, E.; Figueiredo, M. C.; Göttle, A. J.; Calle-Vallejo, F.; Koper, M. T. M. *Nat. Energy* 2019, *4* (9), 732–745.

(3) Zhang, B. A.; Ozel, T.; Elias, J. S.; Costentin, C.; Nocera, D. G. *ACS Cent. Sci.* 2019, *5* (6), 1097–1105.

(4) Goyal, A.; Marcandalli, G.; Mints, V. A.; Koper, M. T. M. *J. Am. Chem. Soc.* 2020, *142* (9), 4154–4161.

(5) Vennekötter, J.-B.; Scheuermann, T.; Sengpiel, R.; Wessling, M. *J. CO2 Util.* 2019, *32*, 202–213.

(6) Duarte, M.; De Mot, B.; Hereijgers, J.; Breugelmans, T. *ChemElectroChem* 2019, *6* (22), 5596–5602.

(7) Bhargava, S. S.; Proietto, F.; Azmoodeh, D.; Cofell, E. R.; Henckel, D. A.; Verma, S.; Brooks, C. J.; Gewirth, A. A.; Kenis, P. J. A. *ChemElectroChem* 2020, *7* (9), 2001–2011.

(8) Jeanty, P.; Scherer, C.; Magori, E.; Wiesner-Fleischer, K.; Hinrichsen, O.; Fleischer, M. *J. CO2 Util.* 2018, *24* (March), 454–462.

(9) Burdyny, T.; Smith, W. A. *Energy Environ. Sci.* 2019, *12* (5), 1442–1453.

(10) Dunwell, M.; Luc, W.; Yan, Y.; Jiao, F.; Xu, B. *ACS Catal.* 2018, *8* (9), 8121–8129.

(11) Junge Puring, K.; Siegmund, D.; Timm, J.; Möllenbruck, F.; Schemme, S.; Marschall, R.; Apfel, U. P. *Adv. Sustain. Syst.* 2021, *5* (1), 1–13.

(12) Vennekoetter, J. B.; Sengpiel, R.; Wessling, M. *Chem. Eng. J.* 2019, *364* (12), 89–101.

(13) Weng, L.; Bell, A. T.; Weber, A. Z. *Phys. Chem. Chem. Phys.* 2018, *20* (1), 16973–16984.

(14) Monteiro, M. C. O.; Philips, M. F.; Schouten, K. J. P.; Koper, M. T. M. *Nat. Commun.* 2021, *12* (1), 4943.

(15) De Mot, B.; Hereijgers, J.; Duarte, M.; Breugelmans, T. *Chem. Eng. J.* 2019, *378*, 122224.

(16) Endrődi, B.; Bencsik, G.; Darvas, F.; Jones, R.; Rajeshwar, K.; Janáky, C. *Prog. Energy Combust. Sci.* 2017, *62*, 133–154.

(17) Lu, X.; Leung, D. Y. C.; Wang, H.; Xuan, J. *Appl. Energy* 2017, *194*, 549–559.

(18) Leonard, M. E.; Clarke, L. E.; Forner-Cuenca, A.; Brown, S. M.; Brushett, F. R. *ChemSusChem* 2020, *13* (2), 400–411.

(19) Kai, T.; Zhou, M.; Duan, Z.; Henkelman, G. A.; Bard, A. J. *J. Am. Chem. Soc.* 2017, *139* (51), 18552–18557.

(20) Mariano, R. G.; McKelvey, K.; White, H. S.; Kanan, M. W. *Science* 2017, *358* (6367), 1187–1192.

(21) Mariano, R. G.; Kang, M.; Wahab, O. J.; McPherson, I. J.; Rabinowitz, J. A.; Unwin, P. R.; Kanan, M. W. *Nat. Mater.* 2021, *20*, 1000–1006.

(22) Mayer, F. D.; Hosseini-Benhangi, P.; Sánchez-Sánchez, C. M.; Asselin, E.; Gyenge, E. L. *Commun. Chem.* 2020, *3* (1), 1–9.

(23) Botz, A.; Clausmeyer, J.; Öhl, D.; Tarnev, T.; Franzen, D.; Turek, T.; Schuhmann, W. *Angew. Chemie - Int. Ed.* 2018, *57* (38), 12285–12289.

(24) Dieckhöfer, S.; Öhl, D.; Junqueira, J. R. C.; Quast, T.; Turek, T.; Schuhmann, W. *Chem. –A Eur. J.* 2021, *27* (19), 5906–5912.

(25) Monteiro, M. C. O.; Dattila, F.; Hagedoorn, B.; García-Muelas, R.; López, N.; Koper, M. T. M. *Nat. Catal.* 2021, *4* (8), 654–662.

(26) Monteiro, M. C. O.; Jacobse, L.; Koper, M. T. M. *J. Phys. Chem. Lett.* 2020, *11* (22), 9708–9713.

(27) Junqueira, J. R. C.; Bobrowski, T.; Krysiak, O. A.; Gutkowski, R.; Schuhmann, W. *ChemCatChem* 2019, *11* (24), 6417–6424.
(28) Elumeeva, K.; Masa, J.; Medina, D.; Ventosa, E.; Seisel, S.; Kayran, Y. U.; Genç, A.; Bobrowski, T.; Weide, P.; Arbiol, J.; Muhler, M.; Schuhmann, W. *J. Mater. Chem. A* 2017, *5* (40), 21122–21129.
(29) Cofell, E. R.; Nwabara, U. O.; Bhargava, S. S.; Henckel, D. E.; Kenis, P. J. A. *ACS Appl. Mater. Interfaces* 2021, *13* (13), 15132–15142.
(30) Hengstenberg, A.; Kranz, C.; Schuhmann, W. *Chem. - A Eur. J.* 2000, *6* (9), 1547–1554.
(31) Monteiro, M. C. O.; Koper, M. T. M. *Electrochim. Acta* 2019, *325*, 134915.
(32) Marcandalli, G.; Villalba, M.; Koper, M. T. M. *Langmuir* 2021, *37* (18), 5707–5716.

A

Scanning Electrochemical Microscopy (SECM):

setup, methods, and supporting information to Chapters 3 and 4

A.1 Scanning Electrochemical Microscopy (SECM) setup

SECM experiments were performed in a home-built system equipped with x-y-z stepper motors (C-863 Mercury, PI) and piezo positioners (E-665, PI). A schematic representation of the cell and the configuration of the electrodes can be seen in Fig. A.1. A glass cell (5 ml capacity) with a 0.8 mm diameter opening at the bottom is pressed against a base plate with the help of 4 screws. An O-ring (Viton) is placed between the sample and the glass to assure a good sealing. A copper plate (0.5 mm thick, MaTeck) is used to make the electrical contact to the sample. As depicted in the figure, the system is operated by two distinct potentiostat channels. All the SECM measurements reported in this work were performed using a Bio-Logic 2-channel potentiostat/galvanostat/EIS (SP-300). The sample counter electrode is a ring carefully positioned around the sample in order to assure a homogeneous electric field and the tip reference electrode is placed as close as possible to the tip. Prior to experiments the glass SECM cell and gas bubblers are cleaned by immersion in potassium permanganate solution for 24 h (1 g L^{-1} $KMnO_4$ dissolved in 0.5 M H_2SO_4) followed by immersion in dilute piranha in order to remove residues of manganese oxide and permanganate anions. The glassware is further cleaned by boiling at least five times in ultrapure water. The cell and positioning system are mounted on a steady base plate and enclosed in a Faradaic cage to minimize the noise and vibration interference in the measurements.

A.2 Capacitive approach system

The mediator-free approach of the modified gold microelectrode to the gold working electrode was performed in air by applying a 10 kHz AC voltage with an amplitude of 4 V_{pp} (1.41 V_{RMS}) to the sample using a function generator (33210A, Keysight). The gold microelectrode was connected to a low noise current preamplifier (SR570, Stanford Research) operated at high-bandwidth with a gain of $2{\cdot}10^8$ V A^{-1}. The capacitive tip current was obtained using a virtual lock-in amplifier (LabView).

A.3 SECM pH sensor fabrication

Gold ultramicroelectrodes (Au-UMEs) were fabricated by sealing a gold wire (50 µm diameter, H. Drijfhout en Zoon's Edelmetaalbedrijven B.V.) in a glass capillary (0.4 mm i.d., Drummond Scientific Co.) and exposing a cross section by grinding the electrode with a silicon carbide paper (grit size 600, MaTeck). The

surface was prepared by polishing with a 1, 0.25 and 0.05 µm diamond suspension (MetaDi, Buehler) for 2 min. In between each polishing step the electrode was sonicated (Bandelin SONOREX RK 52H) in ultrapure water (>18.2 MΩ cm, Millipore Milli-Q) for 5 minutes and after the last step 5 minutes in ethanol followed by 15 minutes in water. After surface preparation the electrode was characterized by cyclic voltammetry in 0.1 M H_2SO_4, recorded in a one compartment cell (20 ml) using a gold wire (0.5 mm diameter, MaTeck, 99.9%) as counter electrode and a Ag/AgCl (LowProfile, Pine Research Instrumentation) reference electrode. The gold ultramicroelectrode (Au-UME) blank voltammetry shows a broad oxide peak starting at 1.0 V vs. Ag/AgCl and a sharp reduction peak in the cathodic scan. The low double layer charging current demonstrates that the electrode preparation leads to a smooth surface. This, and the surface cleanliness are very important for the subsequent functionalization of the Au-UME with a self-assembled monolayer. The Au-UMEs were modified with 4-nitrothiophenol (4-NTP, Merck, 80%) by immersion in a 1 mM 4-NTP/ethanol solution. After 20 min the electrode was thoroughly rinsed with ethanol and ultrapure water in order to remove weakly adsorbed species. The functionalized electrode was transferred back to a 0.1 M H_2SO_4 solution in order to convert the organic molecule by polarization from 0.1 to -0.25 V vs. Ag/AgCl (100 mV s^{-1}). Calibrations of the pH sensor was performed by cyclic voltammetry in 0.1 M Li_2SO_4 (Alfa Aesar, anhydrous, 99.99% metal basis) solutions saturated with different gases at various pH. The pH was adjusted by the addition of appropriate amounts of 1 M H_2SO_4 (Merck, Suprapur, 96%) or 1 M LiOH (Merck, monohydrate, 99.995% trace metals basis). The pH of the calibration solutions was determined with a glass-electrode pH meter (Lab 855, SI Analytics) calibrated with standard buffer solutions (Radiometer Analytical). The functionalized gold UME was calibrated in 0.1 M Li_2SO_4 solutions of various pH as this is the electrolyte used for the hydrogen evolution experiments shown in this work. The calibration was performed with the electrolyte saturated with either argon or hydrogen, as these are also the gases present during the experiments. The tip voltammetry can be seen in Fig. A.3 and clearly the different gases do not have any influence thereof.

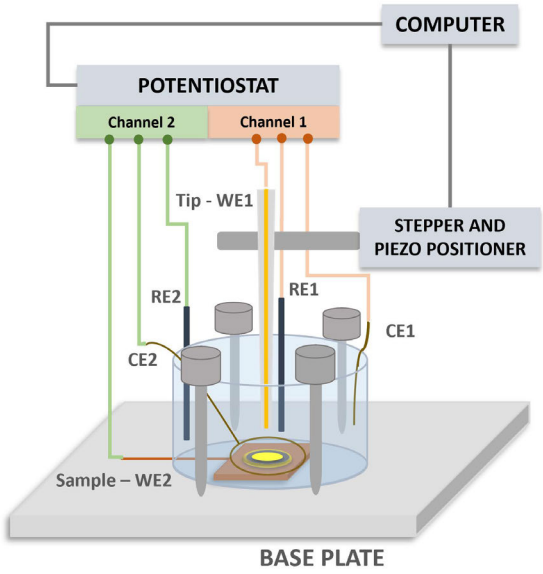

Fig. A.1. Schematic representation of the home built SECM setup.

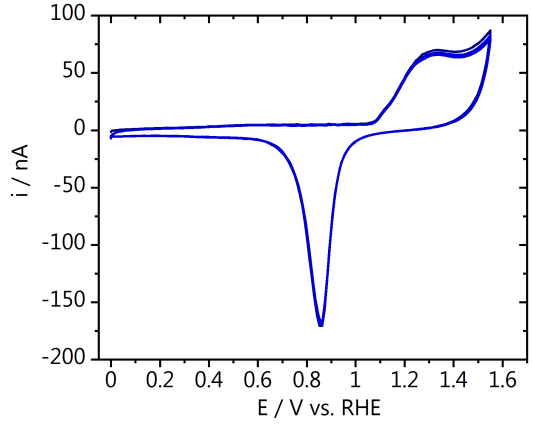

Fig. A.2. Blank voltammetry of the Au-UME in 0.1 M H_2SO_4 taken at 100 mV s^{-1}. The figure shows 5 subsequent cycles.

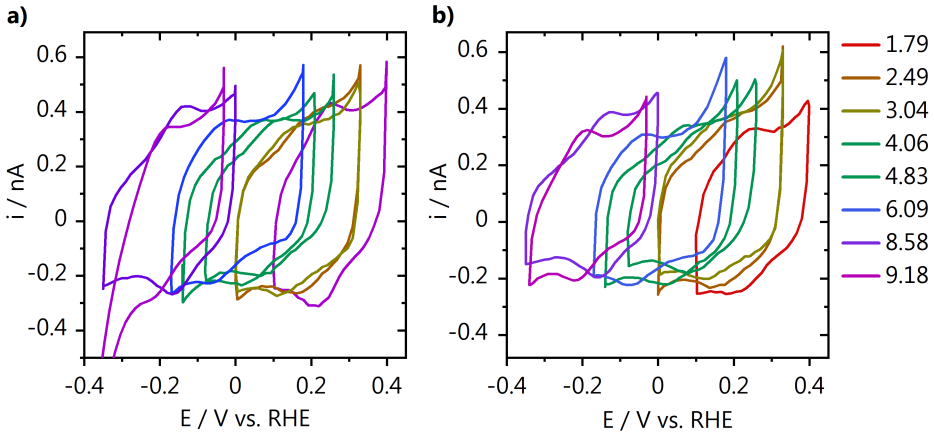

Fig. A.3. Calibration of the functionalized Au-UME in 0.1M Li_2SO_4 saturated with **a)** argon or **b)** hydrogen at various pH. The CVs were taken at 100 mV s^{-1}.

A.4 pH measurements

To perform the pH measurements, the SECM electrochemical cell is filled with 4 ml of electrolyte. For the measurements described in Chapter 3 and Chapter 4 the sample is a gold disc (0.5 mm thick, MaTeck, 99.995%) cleaned and polished with diamond suspension using the protocol described in Chapter 7. Two gold wires and two Ag/AgCl electrodes are used as counter and reference electrodes, respectively. Gases (argon or CO_2) are purged through and above the solution throughout the whole experiment to avoid oxygen diffusion into the electrolyte. Measurements are performed with the pH sensor at a constant distance from the surface and the tip voltammetry is constantly recorded at a scan rate of 200 mV s^{-1} (5 seconds per cycle) while the sample potential is varied.

A.5 Local pH during hydrogen evolution (Chapter 3)

The sample chronoamperometry is recorded and can be seen in Fig. A.4. Initially the sample is held at 0 V vs. Ag/AgCl and subsequently different negative potentials where hydrogen evolution is taking place are applied. In between measurements the sample potential is again set to 0 V for long enough that the measured pH is equal to the bulk pH, demonstrating the recovery of the diffusion

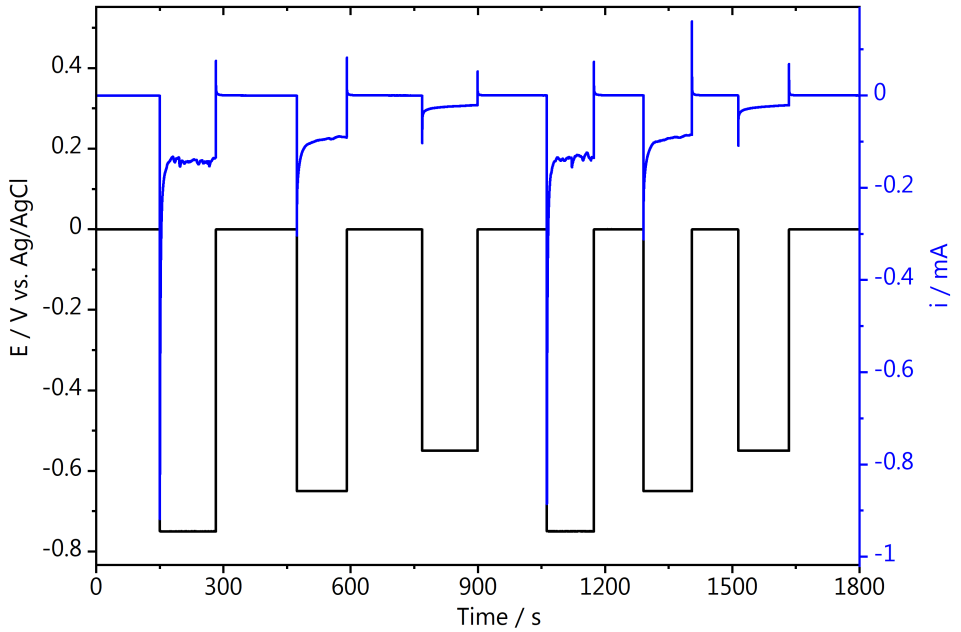

Fig. A.4. Chronoamperometry recorded at the gold sample during the pH measurements (0.1 M Li_2SO_4, pH = 3.2).

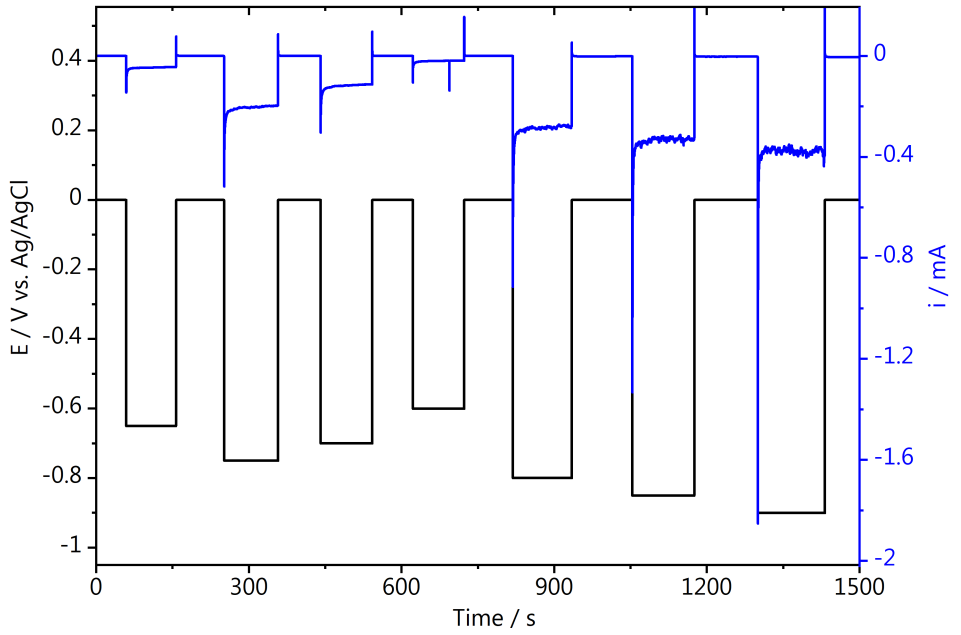

Fig. A.5. Chronoamperometry recorded at the gold sample during the pH measurements (0.1 M Li_2SO_4, pH = 3).

layer gradient. A second set of experiments was performed changing the sample potential in smaller steps to show not only the sensitivity of the pH sensor but also that it can be used in a wide pH range. The chronoamperometry can be found in Fig. A.5.

A.6 Data processing from pH measurements

The pH probe is positioned at a constant distance from the surface with the sample potential held at 0 V vs. Ag/AgCl. In Chapter 3 for example, hydrogen evolution reaction (HER) is turned "on" and "off" at the substrate and the tip voltammetry is measured in time. An example of the peak shift monitored at the tip can be found in Fig. A.6, for HER turned "on" at the sample at –0.75 V vs. Ag/AgCl. The data processing is performed by fitting the tip voltammetry with a Gaussian function with a linear background (Eq. A.1) to extract the anodic mid-peak position. The fitted data for –0.75 , –0.65 and –0.55 V vs. Ag/AgCl (two runs) can be found in Fig. A.7.

$$f(x) = y_0 + a_1 * x + a_2 * exp(-((x - x_0)/width)^2) \qquad \text{Eq. A.1}$$

The mid-peak potential for each cycle was obtained by fitting the tip voltammetry (see SI) and converted to pH using the calibration curve.

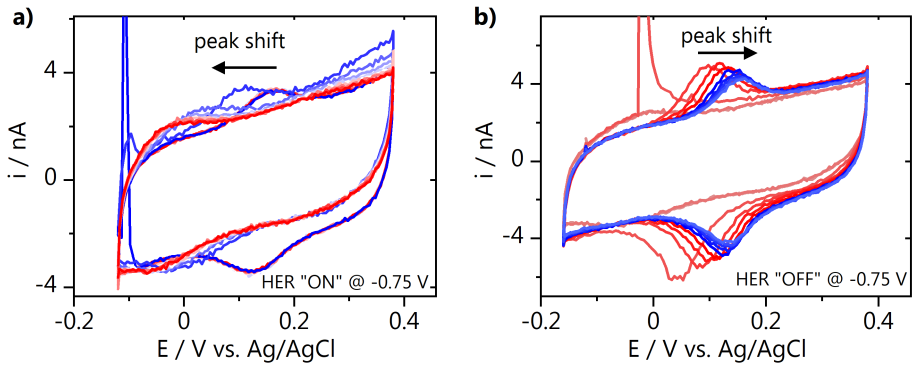

Fig. A.6. Mid-peak potential shift of the pH probe when hydrogen evolution is turned **a)**"on" and **b)**"off" at the gold sample at –0.75 V vs. Ag/AgCl.

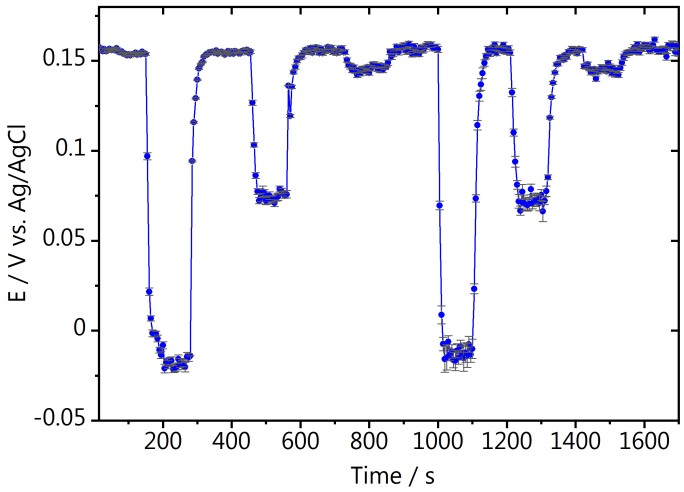

Fig. A.7. Data points obtained by fitting the tip voltammetry.

A.7 Finite Element Method (FEM) simulation methods (Chapter 4)

The experimental system from Chapter 4 is represented by a 2D axisymmetric cylindrical SECM tip and a planar working electrode at the bottom of a cylindrical cell. Geometric parameters[1] are listed in Table A.1 with a graphical depiction of the geometry in Fig. A.8.

Table A.1. Geometric parameters

Parameter	Value
Tip Radius (R_{tip}, µm)	25
Insulation Radius (R_{ins}, µm)	500
Working Electrode Radius (R_{sub}, mm)	5
Boundary Radius (R_{bound}, mm)	8
Normalized tip-surface separation (L)	3.4
Tip electrode height (h_{ins}, mm)	7.4

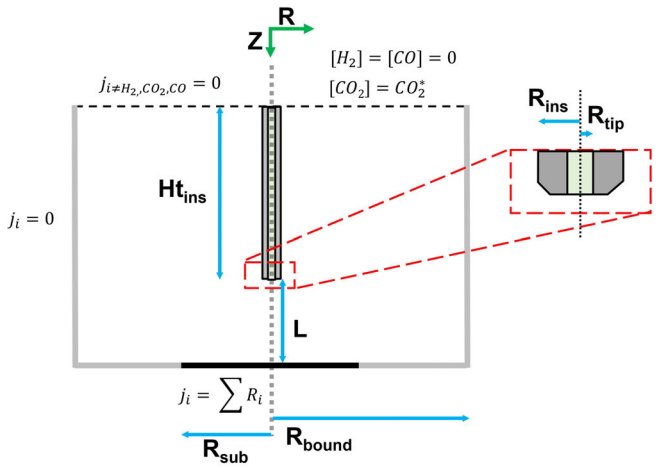

Fig. A.8. Geometric description of the experimental system with simulation boundary conditions used for hydrogen evolution and CO_2 reduction.

Migration is neglected and transport is governed by Fick´s second law of diffusion. Proton-hydroxide ion recombination is included as a homogeneous reaction along with the carbon dioxide reversible reactions (Eq. 4.4-4.7 in Chapter 4). The governing equations are:

$$\frac{dC_i}{dt} = D_i \nabla^2 C_i + \sum R_{ij} \qquad \text{Eq. A.2}$$

where C_i is the concentration of each species in solution (H^+, OH^-, H_2O, H_2, Li^+, and SO_4^{2-}), D_i is the species diffusion coefficient, and the reversible reaction rates, R_{ij}, for each species, i, are summed for each reversible reaction , j.

The boundary conditions, visually represented in Fig. A.8, are as follows: at the WE surface ($z = 0$), a flux balance is applied using the electrode reaction:

$$-D \nabla C_i \cdot \bar{n} = \sum_j r_{ij} \qquad \text{Eq. A.3}$$

where $\bar{n}$ is the surface normal. The summation is over all surface reactions, j, and r_{ij} is the rate of production of species i due to reaction j; $\sum r_{ij}$ is the summation of the reactions involving a given species, i. Proton reduction (PR), water reduction (WR) and carbon dioxide reduction (CO_2RR, Eq. A.6) are considered at the substrate. Proton reduction and water reduction rates are assumed to be limited by Volmer adsorption of hydrogen (Eq. A.4 and A.5, respectively, E_{app} is an arbitrary reference potential for the first reaction step).[2,3]

PR, Volmer step: $H^+ + \mathrm{S} + e^- \overset{k_{0,\mathrm{PR}}}{\leftrightarrow} H_{\mathrm{ads}}$ Eq. A.4

$$E_{app} = 0\ V\ vs.\ SHE\ at\ pH = 0$$

WR, Volmer step: $H_2O + e^- \overset{k_{0,\mathrm{WR}}}{\leftrightarrow} OH^- + H_{ads}$ Eq. A.5

$$E_{app} = 0\ V\ vs\ SHE\ at\ pH = 0$$

CO_2RR: $CO_2 + \mathrm{H_2O} + 2e^- \overset{k_{0,\mathrm{CO_2R}}}{\leftrightarrow} 2\mathrm{OH^-} + CO$ Eq. A.6

$$E_0 = -0.52\ V\ vs\ SHE$$

The rates of PR and WR, due to the large overpotentials, were expressed by Tafel kinetics. CO_2RR was expressed in Butler-Volmer form:

$$r_{\mathrm{PR}} = k_{0,\mathrm{PR}}(C_{H^+} \exp(-\alpha_{\mathrm{PR}} n_{\mathrm{PR}} f \eta_{\mathrm{PR}}))$$ Eq. A.7

$$r_{\mathrm{WR}} = k_{0,\mathrm{WR}}\left(C_{H_2O} \exp(-\alpha_{\mathrm{WR}} n_{\mathrm{WR}} f \eta_{\mathrm{WR}})\right)$$ Eq. A.8

$$r_{\mathrm{CO_2RR}} = k_{0,\mathrm{CO_2RR}}\left(C_{CO_2RR}\mathrm{C}_{H^+}^2 \exp(-\alpha_{\mathrm{CO_2RR}} n_{\mathrm{CO_2RR}} f \eta_{\mathrm{CO_2RR}}) - \mathrm{C}_{H_2O} C_{CO} \exp\left(\left(1 - \alpha_{\mathrm{CO_2RR}}\right) n_{\mathrm{CO_2RR}} f \eta_{\mathrm{CO_2RR}}\right)\right)$$ Eq. A.9

where $k_{0,j}$ are the rate constants, the number of electrons is n_j, the charge transfer coefficient is α_j, and $\eta_j = E - E_{0,j}$, where the $E_{0,j}$ are the formal potentials are and E is the applied surface potential. Finally, $f = \frac{F}{RT}$ where F is Faraday´s constant, R is the gas constant and T is the temperature.

Three surface reactions occur simultaneously at the gold surface electrode. At the liquid-atmosphere boundary($z = L + ht_{ins}$), the concentration of molecular hydrogen, H_2, is zero (Fig. A.8), the bulk concentration of CO_2 is set to 0 (under Ar) or 10 mM (under CO_2), and flux is set to zero for all other species. This bulk CO_2 concentration, which is roughly half of the estimated saturation concentration (23 mM, for 1 atm CO_2 in 0.1 M Li_2SO_4 at pH 3 and 25 °C), is set to avoid numerical convergence issues encountered at higher concentrations. At all other boundaries, a zero-flux condition is imposed for all species. Diffusivities used in the simulation are listed in Table A.3 with the equilibrium and dissociation constants for the reversible reactions. Kinetic rate constants for the homogeneous dissociation reactions were obtained from Wuttig et al.[4] and Bohra et al.[5] The tip electrode proton adsorption is assumed to have negligible effects on the pH.

A.8 pH measurements during HER and CO_2 reduction (Chapter 4)

A.8.1 Calibration functionalized Au-UME in CO_2 atmosphere

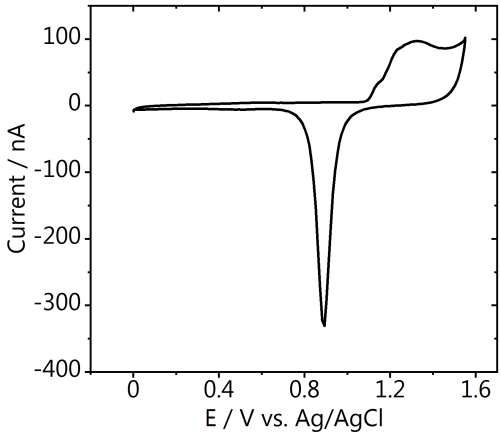

Fig. A.9. Blank voltammetry of the Au-UME used for the pH measurements taken in argon saturated 0.1 M H_2SO_4 at 50 mV s^{-1}.

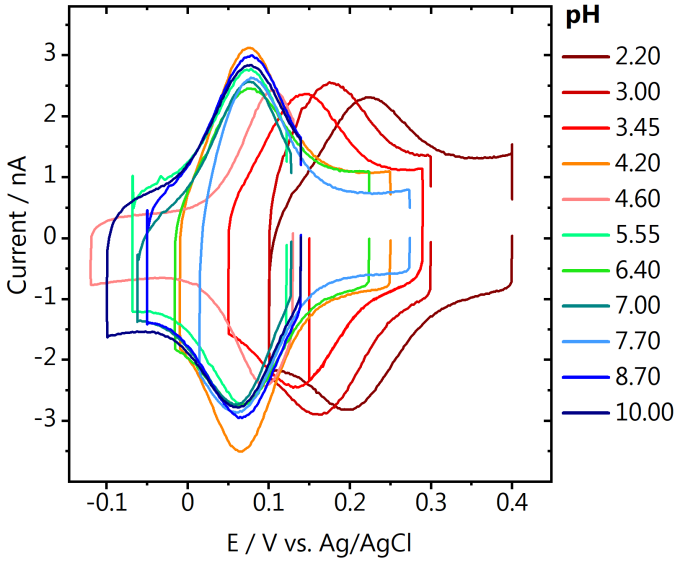

Fig. A.10. Voltammetric response of the Au-UME functionalized with the 4-HATP/4-NSTP redox couple in 0.1 M Li_2SO_4 solutions of different bulk pH after saturation with CO_2 for 5 minutes.

A.8.2 Capacitive approach curve

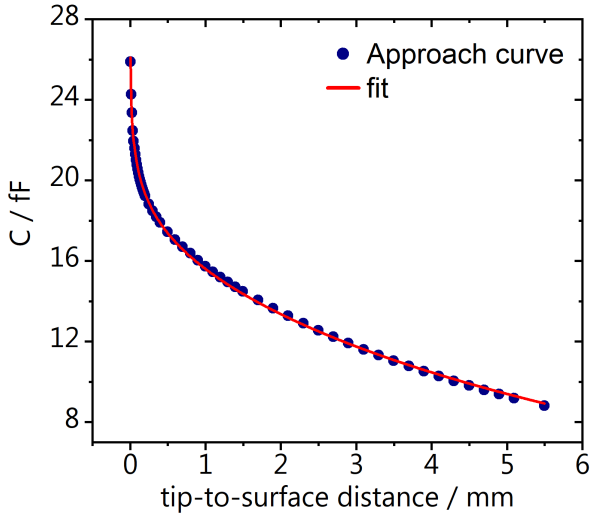

Fig. A.11. Capacitive approach curve recorded before the pH measurements, in order to define the surface position.

A.8.3 pH measurements

SECM pH measurements were performed in 0.1 M Li_2SO_4, pH = 3. The sample potential was stepped from –0.5 to –0.9 V vs. Ag/AgCl in 50 mV steps. Chronoamperometry at the sample was carried out for about 3 minutes at each potential while the pH was measured with the tip. The pH response as a function of potential shown in Fig. 4.3 in Chapter 4 is summarized in the figure below, where each value displayed is the pH measured after 100 seconds of chronoamperometry at the sample.

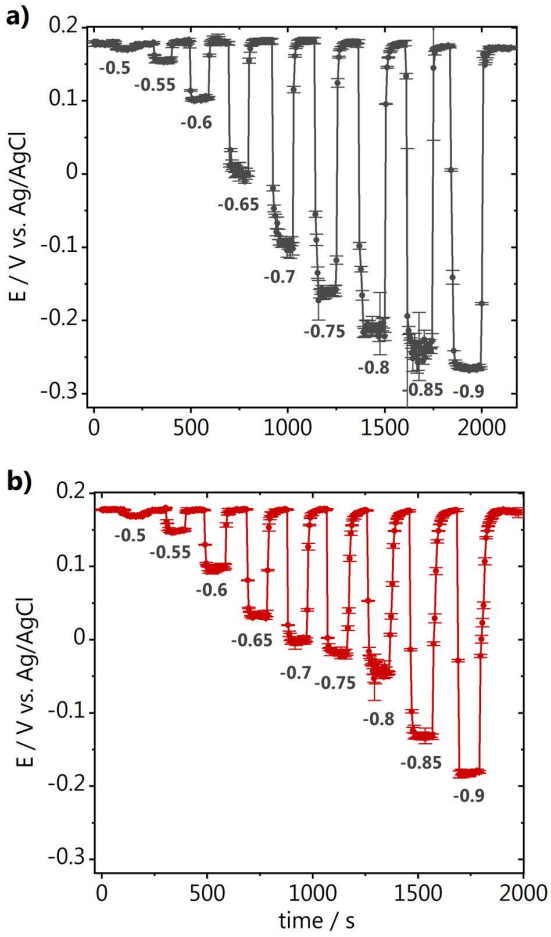

Fig. A.12. Mid-peak potential obtained by fitting the voltammetry of the 4-HATP/4-NSTP functionalized Au-UME recorded while the sample potential was stepped in 0.1 M Li_2SO_4 either in **a)** argon or **b)** CO_2 atmosphere. The sample potentials are indicated below the curves, in V vs. Ag/AgCl.

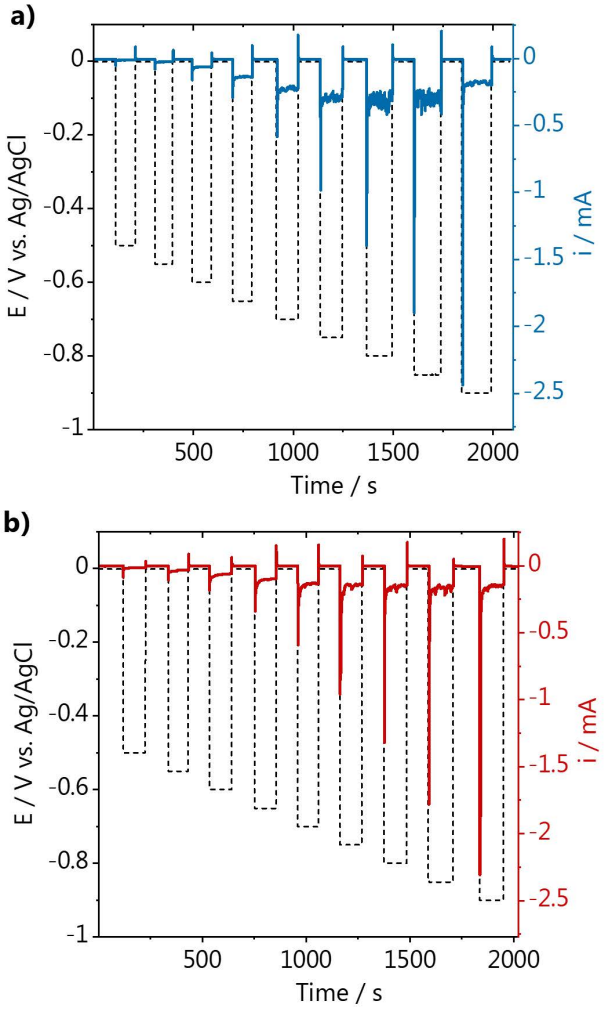

Fig. A.13. Chronoamperometry recorded at the polycrystalline gold sample in **a)** argon and **b)** CO_2 atmosphere in 0.1 M Li_2SO_4, pH 3.

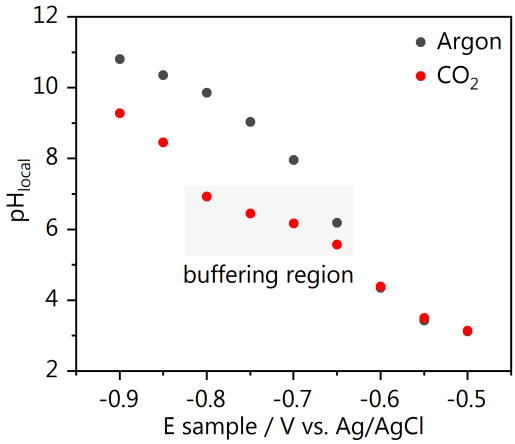

Fig. A.14. Comparison of the pH measured at the same distance from the surface in argon and CO_2 atmosphere. Values taken from Fig. 4.3 in the main text, after each potential was applied for 100 s.

A.9 Finite Element Method (FEM) simulation

Simulations were completed using COMSOL Multiphysics with transport of dilute species. A triangular mesh was used with an increased resolution surrounding the surface and tip electrodes. All species were included in the simulation and the properties defined below were used to describe the transport and reactivity of each species.

A.9.1 Hydrogen evolution reaction kinetics

The hydrogen evolution reaction is simulated by solving Eq. A.2 and A.3 shown in Section A.8. The use of Eq. A.7 to calculate initial proton reduction kinetic rate parameters is justified by the Tafel slope of 147 mV dec^{-1} (Fig. A.15), indicating that a Volmer or large overpotential Heyrovsky steps are likely the rate limiting step.[2] When the reduction reaction is largely irreversible, the Heyrovsky response approaches that of the Volmer. Initial guesses of α_p and $k_{0,PR}$ were determined from the Tafel plot (see Fig. A.15) and $E_0 = 0$ V vs. SHE at pH = 0. Subsequently, kinetic parameters for proton reduction (PR) appearing in Eq. A.7 in the main text, were obtained from fitting to cyclic voltammetric data, specifically the reductive peak of the third cathodic sweep under argon (Fig. A.16) over a potential range from 0 to 0.9 V vs. Ag/AgCl. We expect this CV current to be mainly due to proton reduction

and not water reduction, because of the fast potential sweep rate (100 mV s^{-1}) and low bulk pH. During a CV cycle, the surface pH remains below 6.5, supporting this

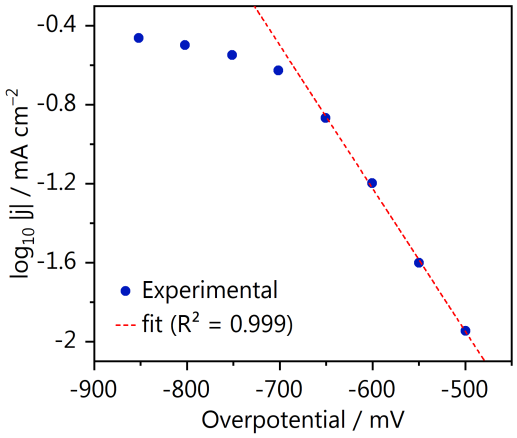

Fig. A.15. Tafel slope for HER at pH 3 extracted from the chronoamperometry (Fig. A.13a) experiment.

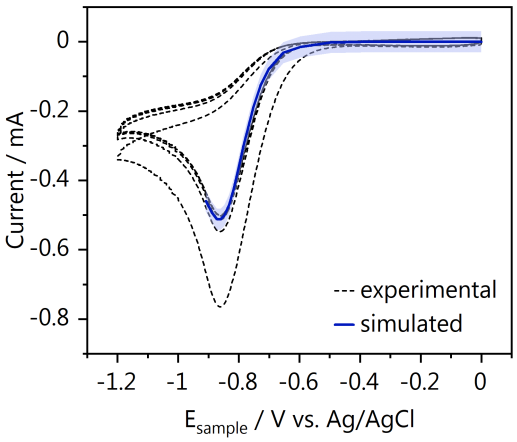

Fig. A.16. Cyclic voltammogram of proton and water reduction in argon. Experimental results (black) are compared to FEM simulation results (blue line) with a 95% confidence interval.

Table A.2. Kinetic parameters estimated by fit to the Tafel plot (Fig. A.15), the cyclic voltammogram (Fig. A.16), or the pH-V relation (see Fig. 4.6a in Chapter 4). Values that were fixed and not fitted are marked with a star (*).

Parameter	Tafel (Fig. A.15)	CV fit (Fig.A.16)	pH-Vfit (Fig. A.14)	Literature	Ref.
$k_{0,\mathrm{PR}}$ [cm/s]	4.2E-8 ± 1.8E-8	3.8E-8 ± 1.8E-8	-	1E-6–1E-10	6–9
α_{PR}	0.41 ± 0.01	0.43 ± 0.03	-	-	-
n_{PR}	-	1.3 ± 0.01	-	-	-
$E_{0,\mathrm{PR}}$ [V vs. SHE]	0*	0*	0*		
D_{H^+}[cm^2/s]	-	1.4E-5 ± 5.5E-6	-	9.3E-5	4
$k_{0,\mathrm{WR}}$ [cm/s]	-	-	3E-14±2E-14	-	-
α_{WR}	-	-	0.5*		
n_{WR}	-	-	1*		
$E_{0,\mathrm{PR}}$ [V vs. SHE]	-	-	0*		
D_{OH^-}[cm^2/s]	-	-	5.3E-5*		10
R^2	0.999	0.993	0.976	-	-

assumption. The resulting parameters for α_P, $k_{0,\mathrm{PR}}$, D_{H^+} and n_P are listed in Table A.2, where the calculated charge transfer coefficient ($\alpha_p = 0.41$) agrees with the result obtained from the Tafel slope in Fig. A.15.

After having fit the cyclic voltammogram, the rate constant for the water reduction reaction, $k_{0,\mathrm{WR}}$, described by Eq. A.8 was obtained by fitting the pH–voltage relation shown in Fig. 4.6 of Chapter 4. All other parameters appearing in Eq. A.8, were set to the values given in Table A.3. For comparison to experiment, the pH values were averaged over the SECM electrode area. During the optimization of $k_{0,\mathrm{WR}}$, the parameters obtained for the hydrogen evolution reaction were kept constant. As the pH response is largely dominated by the water reduction reaction at potentials more negative than –0.65 V vs. Ag/AgCl (Fig. A.17), keeping the hydrogen evolution reaction parameters fixed, is a reasonable approach. Because of this, only the water reduction rate constant ($k_{0,w}$ = 3E–14 ± 2E–14 cm s^{-1}) was fit for this data set. With an R^2 value of 0.976, the simulation results shown in Fig. 4.6a of Chapter 4 match reasonably well with the experimental results, except at the potential of –0.65 V vs. Ag/AgCl, where the simulation underestimates the pH change. The water reduction current at the portion of the surface electrode directly below the surface (r = 0 – $\mathrm{R_{tip}}$, z = 0) reaches a local maximum at –0.65 V vs. RHE due to the large pH increase (OH^- accumulation) directly below the tip. This

hydroxide accumulation drives a decrease in the water reduction rate directly below the SECM tip.

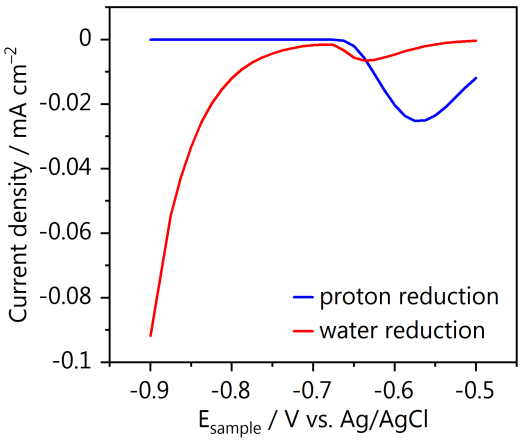

Fig. A.17. Calculated contributions of the local chronoamperometric current density at the gold electrode and beneath the SECM tip, due to proton (blue) and water (red) reduction. Current density is calculated from average flux of each species over 25 µm (R_{Tip}) from the center of the surface electrode, which is below the SECM tip electrode.

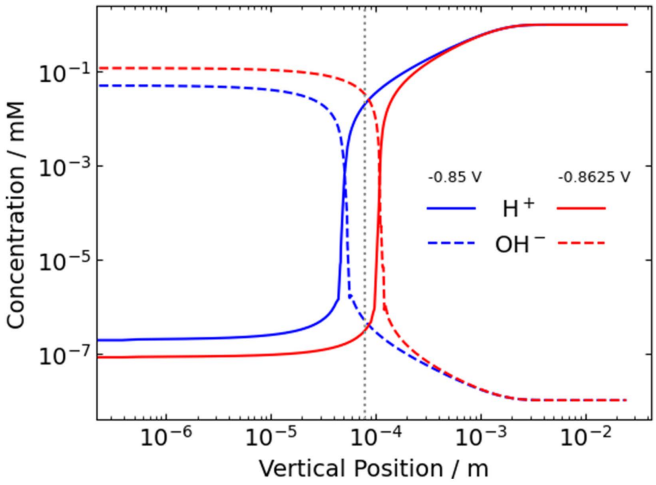

Fig. A.18. Vertical concentration profiles during HER in the absence of CO_2 for H^+ (solid) and OH^- (dashed) as the boundary layer approaches the tip position (dotted grey line). Surface electrode potentials of –0.850 V (blue) and –0.8625 V (red) vs. Ag/AgCl are shown.

A.9.2 CO_2 reduction reaction kinetics

The electrochemical reduction of CO_2 is described by Eq. A.9. The relevant parameters, which are listed in Table A.2, are either set to the theoretical values or taken from literature. Homogeneous reactions are represented by the below rate laws (Eq. A10-A16). The values for the equilibrium, K_i, and dissociation rate constants, k_{-i}, are listed in table A.3.

$$-r_{s1*\mathrm{H_2O}} = K_1 * k_{-1} C_{CO_2} C_{H_2O} - k_{-1} C_{H_2CO_3} \quad \text{Eq. A.10}$$

$$-r_{s2*\mathrm{H_2CO_3}} = K_2 * k_{-2} C_{H_2CO_3} - k_{-2} C_{HCO_3^-} C_{H^+} \quad \text{Eq. A.11}$$

$$-r_{s3*\mathrm{OH^-}} = K_3 * k_{-3} C_{CO_2} C_{\mathrm{OH^-}} - k_{-3} C_{HCO_3^-} \quad \text{Eq. A.12}$$

$$-r_{s4*\mathrm{OH^-}} = K_4 * k_{-4} C_{HCO_3^-} C_{\mathrm{OH^-}} - k_{-4} C_{CO_3^{2-}} \quad \text{Eq. A.13}$$

$$-r_{s5*\mathrm{H^+}} = K_5 * k_{-5} C_{H^+} C_{\mathrm{OH^-}} - k_{-5} C_{\mathrm{H_2O}} \quad \text{Eq. A.14}$$

$$-r_{s6*\mathrm{HCO_3^-}} = K_6 * k_{-6} C_{HCO_3^-} - k_{-6} C_{CO_3^{2-}} C_{H^+} \quad \text{Eq. A.15}$$

$$-r_{s7*\mathrm{H_2O}} = K_7 * k_{-7} C_{CO_2} C_{H_2O} - k_{-7} C_H C_{HCO_3^-} \quad \text{Eq. A.16}$$

Table A.3. FEM system parameters. Values for proton reduction and water reduction are given in Table A.2.

Variable	Value	Reference
$\boldsymbol{D_{\mathrm{H_2}}}$, $cm^2\ s^{-1}$	5.5E-5	11
$\boldsymbol{D_{\mathrm{H_2O}}}$, $cm^2\ s^{-1}$	2.2E-5	12
$\boldsymbol{D_{\mathrm{Li^+}}}$, $cm^2\ s^{-1}$	1.0E-5	13
$\boldsymbol{D_{\mathrm{SO_4^{2-}}}}$, $cm^2\ s^{-1}$	2.0E-5	11
$*\boldsymbol{D_{\mathrm{H^+}}}$, $cm^2\ s^{-1}$	9.3E-5	4
$\boldsymbol{D_{\mathrm{OH^-}}}$, $cm^2\ s^{-1}$	5.3E-5	10
$\boldsymbol{D_{\mathrm{HSO_4^-}}}$, $cm^2\ s^{-1}$	2.3E-5	4
$\boldsymbol{D_{\mathrm{CO_2}}}$, $cm^2\ s^{-1}$	1.7E-5	4
$\boldsymbol{D_{\mathrm{CO}}}$, $cm^2\ s^{-1}$	1.6E-5	4
$\boldsymbol{D_{\mathrm{HCO_3^-}}}$, $cm^2\ s^{-1}$	1.0E-5	4
$\boldsymbol{D_{\mathrm{CO_3^{2-}}}}$, $cm^2\ s^{-1}$	8.0E-6	4
$\boldsymbol{D_{\mathrm{H_2CO_3}}}$, $cm^2\ s^{-1}$	3.5E-5	4
$\boldsymbol{K_1}$	2.6E-3	4,14,15
$\boldsymbol{k_{-1}}$, s^{-1}	2E4	4
$\boldsymbol{K_2}$, M	1.7E-4	4,14

k_{-2} , $M^{-1}\ s^{-1}$	1E12	[4]
K_3 , M^{-1}	4E7	[5,14,15]
k_{-3} , s^{-1}	5E-5	[5]
K_4 , M^{-1}	1.7E3	[5,15]
k_{-4} , $M^{-1}\ s^{-1}$	1E6	[5]
K_5 , M^2	1E-14	[5,16]
k_{-5} , $M^{-1}\ s^{-1}$	2E9	[5,16]
K_6 , M	5E-11	[4,5,16]
k_{-6} , $M^{-1}\ s^{-1}$	1E12	[4,16,17]
K_7 , M	4.4E-7	[15,16]
k_{-7} , $M^{-1}\ s^{-1}$	9E4	[15]
k_{0,CO_2RR}	1E-15	
α_{CO_2RR}	0.5	
n_{CO_2RR}	2	
E_{0,CO_2R} [V vs. SHE]	–0.52	

*see Table A.2 for fitted value used in FEM simulations

References

(1) Monteiro, M. C. O.; Jacobse, L.; Touzalin, T.; Koper, M. T. M. *Anal. Chem.* 2020, *92* (2), 2237–2243.
(2) Shinagawa, T.; Garcia-Esparza, A. T.; Takanabe, K. *Sci. Rep.* 2015, *5* (1), 13801.
(3) Carneiro-Neto, E. B.; Lopes, M. C.; Pereira, E. C. *J. Electroanal. Chem.* 2016, *765*, 92–99.
(4) Wuttig, A.; Yoon, Y.; Ryu, J.; Surendranath, Y. *J. Am. Chem. Soc.* 2017, *139* (47), 17109–17113.
(5) Bohra, D.; Chaudhry, J. H.; Burdyny, T.; Pidko, E. A.; Smith, W. A. *Energy Environ. Sci.* 2019, *12* (11), 3380–3389.
(6) Hamelin, A.; Weaver, M. J. *J. Electroanal. Chem. Interfacial Electrochem.* 1987, *223* (1), 171–184.
(7) Brug, G. J.; Sluyters-Rehbach, M.; Sluyters, J. H.; Hemelin, A. *J. Electroanal. Chem. Interfacial Electrochem.* 1984, *181* (1), 245–266.
(8) Perez, J.; Gonzalez, E. R.; Villullas, H. M. *J. Phys. Chem. B* 1998, *102* (52), 10931–10935.
(9) Dubouis, N.; Grimaud, A. *Chem. Sci.* 2019, *10* (40), 9165–9181.
(10) Lee, S. H.; Rasaiah, J. C. *J. Chem. Phys.* 2011, *135* (12), 124505.
(11) Green, D. W.; Perry, R. H. 8th ed.; McGraw Hill Professional, 2007.
(12) Mills, R. *J. Phys. Chem.* 1973, *77* (5), 685–688.
(13) Banerjee, P.; Bagchi, B. *J. Chem. Phys.* 2019, *150* (19), 190901.
(14) Keene, R. F.; Sullivan, B. P.; Krist, K.; Guard, H. E. 1st ed.; Elsevier, 1993.
(15) Gupta, N.; Gattrell, M.; MacDougall, B. *J. Appl. Electrochem.* 2006, *36* (2), 161–172.
(16) Singh, M. R.; Goodpaster, J. D.; Weber, A. Z.; Head-Gordon, M.; Bell, A. T. *Proc. Natl. Acad. Sci.* 2017, *114* (42), E8812--E8821.
(17) Schulz, K. G.; Riebesell, U.; Rost, B.; Thoms, S.; Zeebe, R. E. *Mar. Chem.* 2006, *100* (1–2), 53–65.

B

Methods and supporting information to Chapter 5

B.1 Microelectrode and pH sensor fabrication

The platinum ultramicroelectrode (Pt-UME) was made by etching and sealing a platinum wire (50 µm diameter, Goodfellow, 99.99%) into a soda lime glass capillary using a butane torch. Details can be found elsewhere.[1] The gold ultramicroelectrode (Au-UME) was fabricated also by sealing a gold wire (50 µm diameter, H. Drijfhout en Zoon's Edelmetaalbedrijven B.V.) in a soda lime glass capillary, however without the etching step. A cross section of the wires was exposed by grinding the UMEs with a silicon carbide paper (grit size 600, MaTeck). The surface preparation was done by polishing with a 1, 0.25 and 0.05 µm diamond suspension (MetaDi, Buehler) for 2 min. To remove as much as possible polishing particle residues, the electrode was sonicated (Bandelin SONOREX RK 52H) in ultrapure water (>18.2 MΩ cm, Millipore Milli-Q) for 5 minutes in between each polishing step and after the last step sonicated for 5 minutes in ethanol and 15 minutes in water. The resulting Pt-UME and Au-UME used in Chapter 5 have a radius of approximately 6.5 ± 0.07 µm and 26.9 ± 0.05 µm, respectively, determined with the $Fe(CN)_6^{3-}/Fe(CN)_6^{4-}$ outer sphere reaction. Prior to experiments, the Pt-UME was cycled 200 times between 0.06 and 1.60 V vs. RHE in 0.1 M H_2SO_4 (Merck, Suprapur, 96%) at 1 V s^{-1}, yielding a reproducible blank voltammogram. The Au-UME was also characterized by cyclic voltammetry in 0.1 M H_2SO_4, to assure that there is no leakage between the wire and the sealing. The blank voltammetry of the Pt and Au UMEs and the voltammetry in $Fe(CN)_6^{3-}/Fe(CN)_6^{4-}$ can be found in Fig. B.1. The Au-UME pH sensor synthesis is done as described in Chapter 3 and Appendix A.

B.2 Scanning Electrochemical Microscopy (SECM) methods

SECM experiments were carried out in our home-built SECM setup, which was described in detail in Appendix A.[2] All the equipment and cleaning procedures used here, are exactly the same as also reported in Appendix A. The sample used is a gold disc (0.5 mm thick, MaTeck, 99.995%) cleaned and polished with diamond suspension using the protocol described in Chapter 7 and Appendix D.[3] Measurements were performed in 5 ml of 0.1 M Cs_2SO_4 (Alfa Aesar, Puratronic™, 99.997%, metals basis) which was constantly purged with CO_2. The electrolyte choice was made based on the high activity for CO_2 reduction achieved in Cs^+ containing electrolytes. Measurements were performed at a constant distance from the surface and the tip voltammetry was constantly recorded at a scan rate of 200 mV s^{-1} while the sample potential was varied.

B.3 RDE methods

RDE experiments were performed using a MSR Electrode Rotator (Pine Research Instrumentation) equipped with an AFE6M shaft. The RDE measurements were carried out in a three-electrode glass cell in which the reference was a reversible hydrogen electrode (RHE) separated from the work compartment by a Luggin capillary. The working electrode was a polycrystalline platinum disc (5.0 mm OD x 4.0 mm thick, Pine Research and Instrumentation) and the counter electrode a platinum mesh. Prior to experiments, the Pt working electrode was cycled 200 times between 0.06 and 1.65 V vs. RHE in 0.1 M H_2SO_4 (Merck, Suprapur, 96%) at 1 V s^{-1}, yielding a reproducible blank voltammogram. Measurements were performed in 50 ml of 0.1 M Cs_2SO_4 (Alfa Aesar, Puratronic™, 99.997%, metals basis) while constantly saturating the electrolyte with CO. To change the OH^- concentration, appropriate amounts of KOH (Alfa Aesar, 99.99%, metals basis) were added and the pH of the CO saturated solution was determined using a glass-electrode pH meter (Lab 855, SI Analytics) calibrated with standard buffer solutions (Radiometer Analytical).

B.4 Characterization of the ultramicroelectrodes

Characterization of the platinum and gold ultramicroelectrodes (UMEs) was performed before the SECM experiments. The blank voltammetry can be seen in Fig. B.1 below, together with the voltammetry of the outer sphere reaction $Fe(CN)_6^{3-}$/ $Fe(CN)_6^{4-}$. The diffusion limiting currents from Fig. B.1b and d were used to calculate the radius of the platinum and gold UMEs, respectively, using Eq. B.1:

$$r_{UME} = i_{lim}/4nFDc \qquad \text{Eq. B.1}$$

where i_{lim} is the diffusion limited current in A, n is the number of electrons transferred, F is the Faraday constant in s A mol^{-1}, D is the diffusion coefficient of $Fe(CN)_6^{3-}$ in cm^2 s^{-1} and c is the concentration in mol cm^{-3}.

B.5 Capacitive approach

The tip-to-surface distance was determined by performing a capacitive approach[2,4] in air before all SECM measurements as described in Appendix A. The absolute surface position is determined by fitting the approach curve with Eq. B.2.

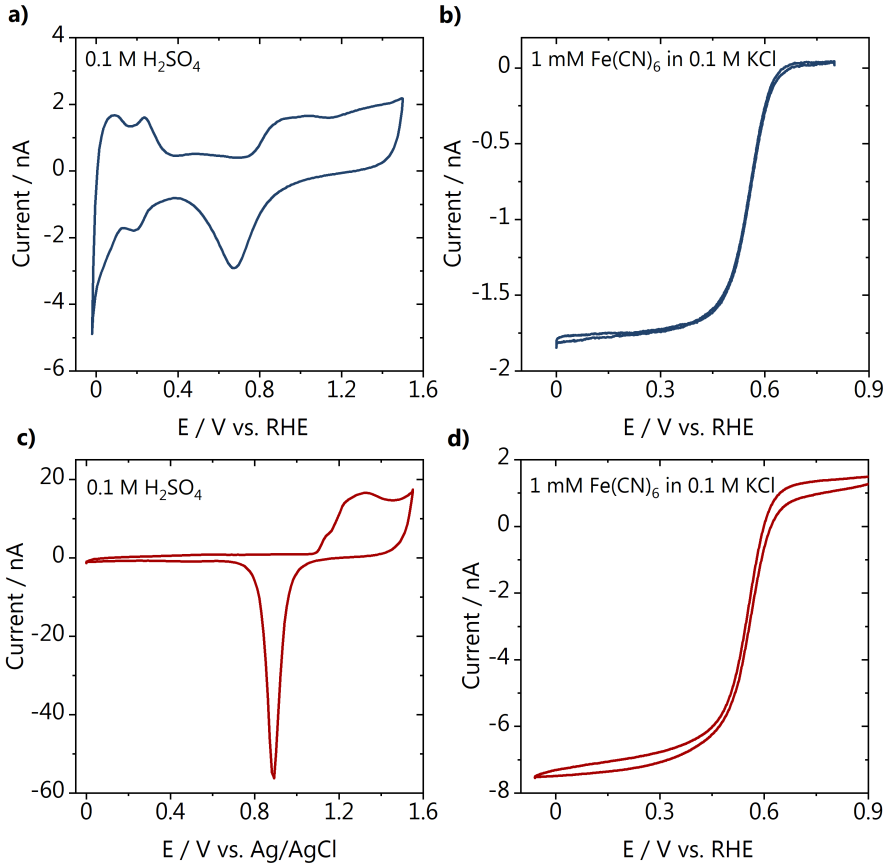

Fig. B.1. Blank voltammetry of **a)** the Pt-UME and **c)** the Au-UME taken in 0.1 M H_2SO_4 at 200 mV s^{-1}. Voltammetry of the outer sphere reaction recorded in argon saturated $K_3Fe(CN)_6^3$ + 0.1 M KCl at 10 mV s^{-1} with the **b)** Pt-UME and **d)** Au-UME.

$$\boldsymbol{C_{tot}(Z) = -A_1 * \ln(d_0 - Z) + B + \left(\frac{A_2}{L_{par} + d_0 - Z} \right)} \qquad \text{Eq. B.2}$$

The approach curves measured before the different SECM experiments from Chapter 5 can be seen in Fig. B.2 together with their fit. Fig. B.2a and b show the approach curve for the experiments performed with the Pt-UME, changing sample potential and changing scan rate, respectively. Fig. B.2c displays the approach curve performed with the functionalized Au-UME for the pH measurements.

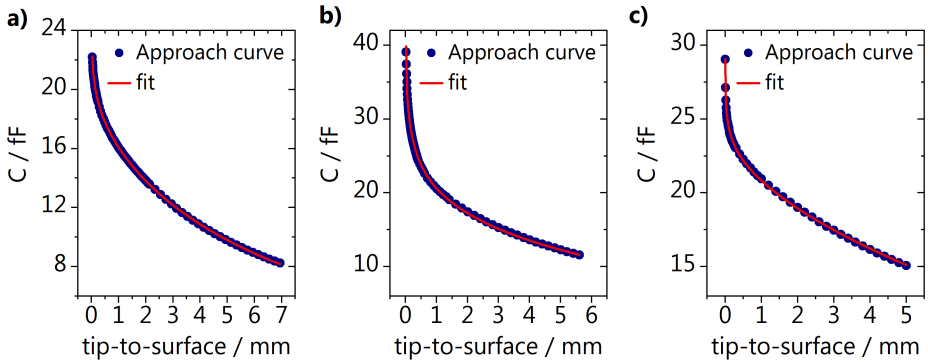

Fig. B.2. Approach curves recorded before the different SECM experiments: **a)** Pt-UME in SG-TC mode with potential steps applied to the sample; **b)** Pt-UME in SG-TC mode constant potential applied to the sample, changing the scan rate of the tip voltammetry; **c)** pH measurements with the functionalized Au-UME.

B.6 CO oxidation measurements with the Pt-UME

During the experiments, the Pt-UME voltammetry was recorded (shown in the manuscript) while the gold sample potential was varied. The chronoamperometry data recorded at the gold sample can be seen in Fig. B.3.

B.7 pH measurements with the functionalized Au-UME

pH measurements were performed by turning CO_2 reduction "on" and "off" at the gold sample and simultaneously recording the functionalized Au-UME voltammetry. The CO_2 reduction reaction was carried out at sample potentials from –0.5 to –1.0 V vs. RHE, in 50 mV steps. Fig. B.4 shows the results, where each data point corresponds to the value extracted from one tip cyclic voltammogram. The pH values displayed in Fig. 5.4 in the main text, correspond to the average of three pH values recorded in 15 seconds. The three data points chosen are the ones acquired at the same time scale the Pt-UME CVs shown in Fig. 5.2 were recorded, after each sample potential step.

B.8 RDE measurements

Before the RDE experiments, the platinum disc electrode was characterized in 0.1 M H_2SO_4 and the blank voltammetry can be found in Fig. B.5.

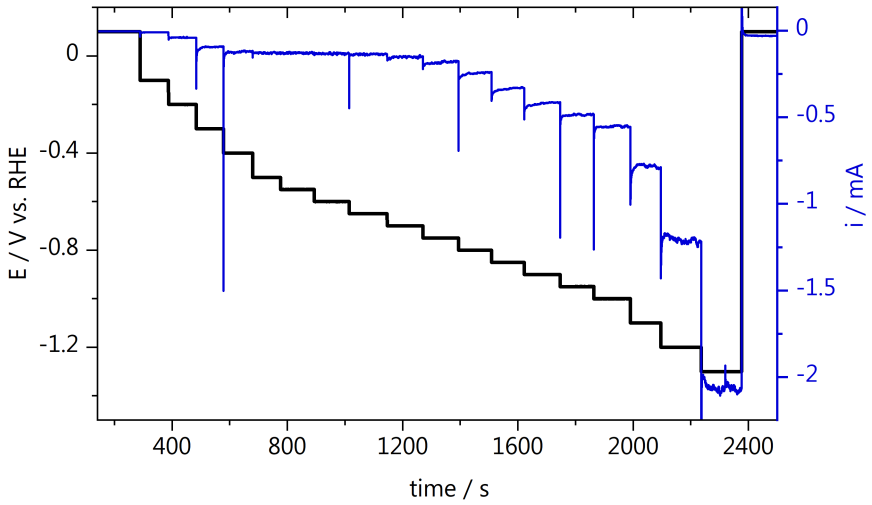

Fig. B.3. Chronoamperometry recorded at the gold sample during CO_2 reduction in 0.1 M Cs_2SO_4, pH = 3.

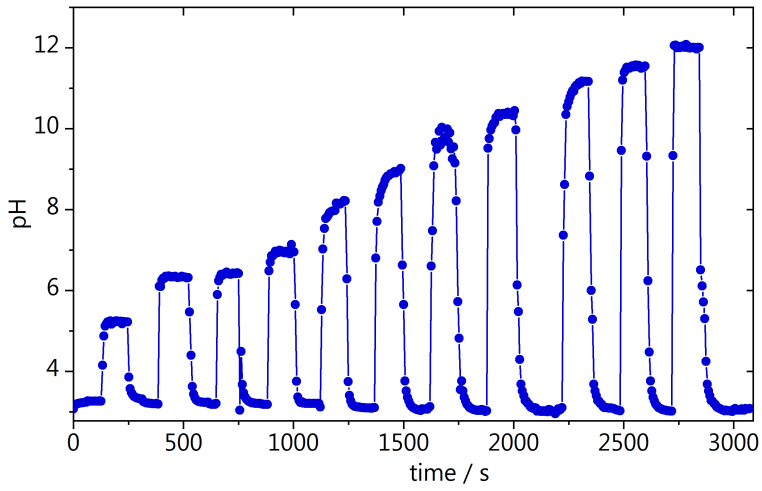

Fig. B.4. pH measured with the Au-UME when the sample potential was varied from -0.5 to -1 V vs. RHE in 50 mV steps.

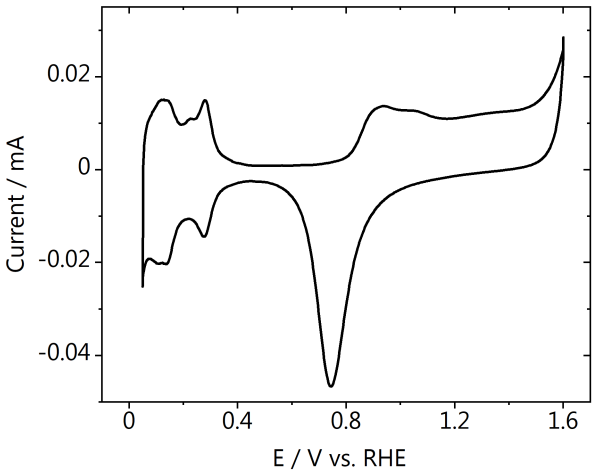

Fig. B.5. Blank voltammetry of the platinum disc taken at 50 mV s^{-1} in argon saturated 0.1 M H_2SO_4.

The voltammetry of bulk CO electrooxidation on the platinum RDE was recorded at different rotation rates (100, 400 and 900 rpm) in pure Cs_2SO_4 electrolyte and with the addition of different amounts of KOH. The results can be seen in Fig. B.6, and the diffusion limiting currents from peak I and peak II obtained for each electrolyte were used to derive the diffusion coefficients shown in Chapter 5.

B.9 CO_2 reduction products

To exclude that methanol formation at the gold sample is what gives rise to peak II observed in the Pt-UME voltammetry, we performed product analysis in the same electrolyte used in this work (0.1 M Cs_2SO_4, pH 3) using gas chromatography (GC) and high-pressure liquid chromatography (HPLC). We used a two-compartment electrochemical cell and liquid and gas samples were taken during electrolysis every 20 minutes. As it can be seen in Fig. B.7, only CO and hydrogen were detected by GC and no liquid products were detected by HPLC.

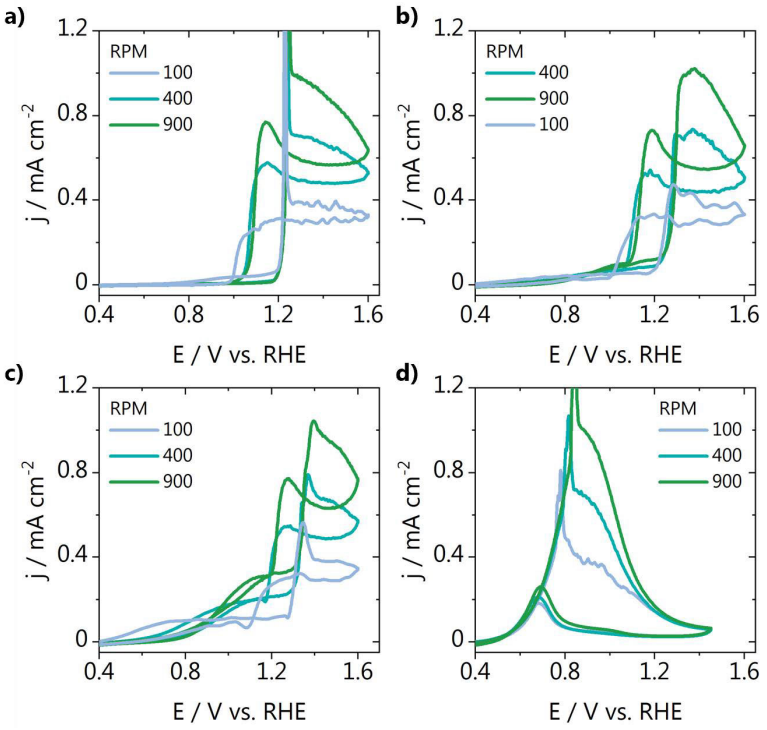

Fig. B.6. CO oxidation voltammetry take at different rotation rates in **a)** Cs_2SO_4 and with the addition of **b)** 0.03 mM, **c)** 0.06 mM, and **d)** 1 mM KOH.

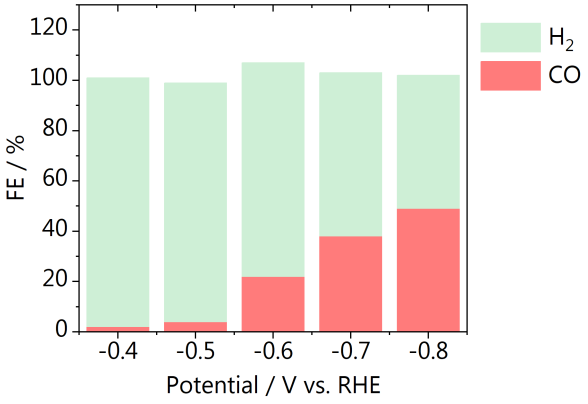

Fig. B.7. Faradaic efficiency for CO_2 reduction on a flat gold electrode, carried out in 0.1 M Cs_2SO_4, pH = 3.

References

(1) Jacobse, L.; Raaijman, S. J.; Koper, M. T. M. *Phys. Chem. Chem. Phys.* 2016, *18* (41), 28451–28457.
(2) Monteiro, M. C. O.; Jacobse, L.; Touzalin, T.; Koper, M. T. M. *Anal. Chem.* 2020, *92* (2), 2237–2243.
(3) Monteiro, M. C. O.; Koper, M. T. M. *Electrochim. Acta* 2019, *325*, 134915.
(4) Voogd, J. M. De; Spronsen, M. A. Van; Kalff, F. E.; Bryant, B.; Ostoji, O.; Haan, A. M. J. Den; Groot, I. M. N.; Oosterkamp, T. H.; Otte, A. F.; Rost, M. J. *Ultramicroscopy* 2017, *181*, 61–69.

C

Methods and supporting information to Chapter 6

C.1 Methods

C.1.1 Materials

All glassware used was cleaned by immersion in a potassium permanganate solution overnight (1 g/L $KMnO_4$ dissolved in 0.5 M H_2SO_4), followed by immersion in dilute piranha. The glassware was further boiled in ultrapure water at least five times. The electrolytes used in this work, KH_2PO_4 (Alfa Aesar, dried, 99.99 %) and K_2SO_4 (Alfa Aesar, Puratronic, 99.997 %, metals basis), were adjusted to pH 3-5 by addition of appropriate amounts of H_2SO_4 (Merck, Suprapur, 96%) or H_3PO_4 (ortho-Phosphoric acid 85%, Suprapur®, Merck).

C.1.2 pH sensor fabrication and characterization

A gold ring electrode (E6R1PK tip, Pine Research Instrumentation) was used in this work, together with a gold disc (diameter = 5 mm, Pine Research Instrumentation). Prior to experiments, the ring and the disc (Pine Research Instrumentation) were polished with a polycrystalline diamond suspension of 0.25 µm (MetaDi, Buehler) and then sonicated (Bandelin Sonorex RK 52H) in ultrapure water (>18.2 MΩ cm, Millipore Milli-Q) for 10 minutes.[1] Before functionalization of the ring with the pH sensing monolayer, the ring and disc were characterized by recording the blank voltammetry between 0.1 and 1.75 V vs. RHE in argon saturated (6.0 purity, Linde) 0.1 M H_2SO_4 (Merck, Suprapur, 96%) in a one compartment electrochemical cell. A gold wire (0.5 mm diameter, MaTeck, 99.9%) was used as counter electrode and a reversible hydrogen electrode (RHE) as reference. The electrochemically active surface area (ECSA) of the disc was calculated based on the charge corresponding to the gold oxide reduction and a surface charge of 386 µC cm^{-2}.[2] The gold ring electrode is modified by immersing it (without the disc inserted) into a 1 mM solution of 4-NTP (Merck, 80%) in ethanol for 15 minutes. The ring is then thoroughly rinsed with ethanol and water, and dried. The disc electrode is carefully inserted in the shaft, avoiding too much friction (which could damage the 4-NTP monolayer). The 4-NTP is then electrochemically reduced to 4-HATP in the working electrolyte (pH ≈ 4) by cycling the ring from 0.3 to -0.43 V vs. Ag/AgCl (argon saturated, 100 mV s^{-1}). It is important to point out that the monolayer can be easily removed from the gold ring by polishing it with a polycrystalline diamond suspension of 0.25 µm. This can be done whenever necessary i.e. when the 4-HATP/4-NSTP signal is for some reason compromised. A decrease in signal can be caused e.g., by bubbles and loss of potential control

during measurements. Considering how simple and fast the pH sensor synthesis is, it is advised to always have a fresh monolayer adsorbed onto the surface at the start of new experiments.

C.1.3 RRDE pH measurements

All electrochemical measurements were carried out using a BioLogic 2-channel potentiostat/galvanostat/EIS (SP-300). The ring and disc electrodes were controlled simultaneously, by two different potentiostat channels. Two gold wires (0.5 mm diameter, MaTeck, 99.9%) were used as counter electrodes and a Ag/AgCl (low profile, BioLogic) as reference. Argon (6.0 purity, Linde) was purged through the solution for 20 minutes prior to the experiments. The argon flow was kept also during the experiments in order to avoid oxygen diffusing into the electrolyte. The ring cyclic voltammetry (CV) was constantly recorded at 200 mV s^{-1} while hydrogen evolution took place at the disc.

C.2 Calculation of the interfacial disc pH

The mid-peak potential (E_{peak}) of the 4-HATP oxidation to 4-NSTP was determined by fitting the forward scans with a Gaussian function containing a linear background (see details in Chapter 3 and Appendix A). E_{peak} was then converted to the ring pH (pH_{ring}) using the calibration curve of the 4-HATP/4-NSTP from our previous work: $pH_{ring} = (0.341 - E_{peak})/0.057$ (Chapter 3).[3] To calculate the interfacial disc pH (pH_{disc}), for an unbuffered electrolyte, we use Eq. C.2, from Yokoyama et al.[4], which is an extension of the analytical solution of Albery and Calvo[5,6] (Eq. C.1), taking the autoprotolysis of water (Eq. C.3) into account.

$$c_r = c_\infty + N_D(c_d - c_\infty) \qquad \text{Eq. C.1}$$

$$c_{r,H^+} - c_{r,OH^-} = N_D\left(c_{d,H^+} - c_{d,OH^-}\right) + (1 - N_D)\left(c_{\infty,H^+} - c_{\infty,OH^-}\right) \qquad \text{Eq. C.2}$$

$$K_W = c_{rt,H^+}c_{rt,OH^-} \qquad \text{Eq. C.3}$$

where c_∞ represents the proton or OH^- concentration in the bulk and $c_{d,}$ and $c_{r,}$ the same at the disc and ring, respectively. The detection efficiency N_D is given by Eq. C.4 and C.5 and is only dependent on the geometrical parameters of the ring and disc electrode (see Fig. C.1). For the electrode used in this work $N_D = 0.23$.

$$N_D = 1 - \frac{1}{6}F\left[\left(\frac{r_2}{r_1}\right)^3 - 1\right] - \frac{2}{3}F\left[\left(\frac{r_2+r_3}{2r_1}\right)^3 - 1\right] - \frac{1}{6}F\left[\left(\frac{r_3}{r_1}\right)^3 - 1\right] \qquad \text{Eq. C.4}$$

where *F*[x] is:

$$F[x] = \frac{3^{\frac{1}{2}}}{4\pi}\ln\left(\frac{\left(1+x^{\frac{1}{3}}\right)^3}{1+x}\right) + \frac{3}{2}\tan^{-1}\left(\frac{2x^{\frac{1}{3}}-1}{3^{\frac{1}{2}}}\right) + \frac{1}{4} \qquad \text{Eq. C.5}$$

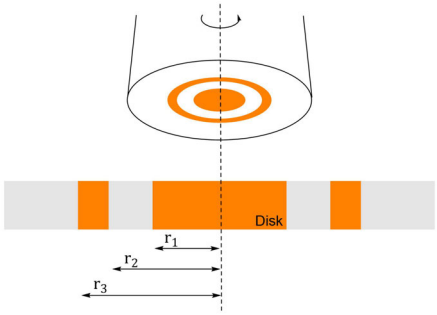

Fig. C.1. Schematic representation of the rotating ring-disc electrode with the geometrical parameters from Eq. C.4 indicated.

Fig. C.2 shows the theoretical relationships between pH_{Disc} and pH_{Ring} at various pH_{∞}, comparing Eq. C.2 (Yokoyama) and Eq. C.1 (Albery and Calvo) for an unbuffered electrolyte. It can be observed that not taking the autoprotolysis of water into account can lead to over/underestimating the disc pH, depending on the bulk pH. Eq. C.2 is rewritten as follows and used to convert pH_{ring} to pH_{disc} for unbuffered electrolytes:

$$pH_{disk} = -\log\left(\frac{c_{r,H^+} - c_{rt,OH^-}}{N_D} - \frac{c_{\infty,H^+} - c_{\infty,OH^-}}{N_D} + c_{\infty,H^+} - c_{\infty,OH^-}\right) \qquad \text{Eq. C.6}$$

For buffered systems, as the phosphate electrolyte used in this work, a correction must be applied to Eq. C.6, to consider the homogeneous reactions taking place involving the phosphate species. In this case, the OH^- concentration is given by Eq. C.7 and is applied to Eq. C.8 to obtain the interfacial disc pH.

$$c'_{OH^-} = c_{OH^-} + [H_2PO_4^-] + 2\,[HPO_4^{2-}] + 3\,[PO_4^{3-}] \qquad \text{Eq. C.7}$$

$$N_D = \frac{c'_{r,OH^-} - c'_{\infty}}{c'_{d,OH^-} - c'_{\infty}} \qquad \text{Eq. C.8}$$

The following equilibrium constants and equations were used to calculate the concentration of phosphate species[7]:

$$H_3PO_4 \rightleftharpoons H_2PO_4^- + H^+ \qquad K_{a1} = 7.5 \times 10^{-3} \qquad \text{Eq. C.9}$$

$$H_2PO_4^- \rightleftharpoons HPO_4^{2-} + H^+ \qquad K_{a2} = 6.2 \times 10^{-8} \qquad \text{Eq. C.10}$$

$$HPO_4^{2-} \rightleftharpoons PO_4^{3-} + H^+ \qquad K_{a3} = 2.14 \times 10^{-13} \qquad \text{Eq. C.11}$$

The total concentration of species is given by TC and the concentration of each species to be used in Eq. C.7 is determined based on Eq. C.12-C.16:

C

$$TC = [H_3PO_4] + [H_2PO_4^-] + [HPO_4^{2-}] + [PO_4^{3-}] \qquad \text{Eq. C.12}$$

$$[H_3PO_4] = \frac{TC[H^+]^3}{[H^+]^3+K_{a1}[H^+]^2+K_{a1}K_{a2}[H^+]+K_{a1}K_{a2}K_{a3}} \qquad \text{Eq. C.13}$$

$$[H_2PO_4^-] = \frac{TCK_{a1}[H^+]^2}{[H^+]^3+K_{a1}[H^+]^2+K_{a1}K_{a2}[H^+]+K_{a1}K_{a2}K_{a3}} \qquad \text{Eq. C.14}$$

$$[HPO_4^{2-}] = \frac{TCK_{a1}K_{a2}[H^+]}{[H^+]^3+K_{a1}[H^+]^2+K_{a1}K_{a2}[H^+]+K_{a1}K_{a2}K_{a3}} \qquad \text{Eq. C.15}$$

$$[PO_4^{3-}] = \frac{TCK_{a1}K_{a2}K_{a3}}{[H^+]^3+K_{a1}[H^+]^2+K_{a1}K_{a2}[H^+]+K_{a1}K_{a2}K_{a3}} \qquad \text{Eq. C.16}$$

Finally, expanding Eq. C.7 and C.8, the relationship between pH_{ring} and pH_{disc} for a phosphate buffered electrolyte is given by Eq. C.17:

$$N_D = \frac{c_{r,OH^-}+[H_2PO_4^-]_r+2\,[HPO_4^{2-}]_r+3\,[PO_4^{3-}]_r- c_{\infty,OH^-}-[H_2PO_4^-]_\infty- 2\,[HPO_4^{2-}]_\infty- 3\,[PO_4^{3-}]_\infty}{c_{d,OH^-}+[H_2PO_4^-]_d+2\,[HPO_4^{2-}]_d+3\,[PO_4^{3-}]_d- c_{\infty,OH^-}-[H_2PO_4^-]_\infty-2\,[HPO_4^{2-}]_\infty- 3\,[PO_4^{3-}]_\infty} \qquad \text{Eq. C.17}$$

A quartic equation can be derived from Eq. C.7-C.17, where *a*, *b*, *c*, *d*, and *e* are parameters of C_{r,OH^-}, and *x* stands for C_{d,H^+}.

$$ax^4 + bx^3 + cx^2 + dx + e = 0 \qquad \text{Eq. C.18}$$

Solving the equation, four roots can be obtained and the nature of which can be inferred from the sign of the discriminants Δ, P and D. In our cases, all the roots are real and distinct roots since the $\Delta>0$, $P<0$ and $D<0$.

$$\Delta = 256a^3e^3 - 192a^2bde^2 - 128a^2c^2e^2 + 144a^2cd^2e - 27a^2d^4 + 144ab^2ce^2 - 6ab^2d^2e - 80abc^2de + 18abcd^3 + 16ac^4e - 4ac^3d^2 - 27b^4e^2 + 18b^3cde - 4b^3d^3 - 4b^2c^3e + b^2c^2d^2 \quad \text{Eq. C.19}$$

$$\mathrm{P} = 8ac - 3b^2 \quad \text{Eq. C.20}$$

$$\mathrm{D} = 64a^3e - 16a^2c^2 + 16ab^2c - 16a^2bd - 3b^4 \quad \text{Eq. C.21}$$

So that:

$$x_{1,2} = -\frac{b}{4a} - S \pm \frac{1}{2}\sqrt{-4S^2 - 2p + \frac{q}{S}} \quad \text{Eq. C.22}$$

$$x_{3,4} = -\frac{b}{4a} + S \pm \frac{1}{2}\sqrt{-4S^2 - 2p - \frac{q}{S}} \quad \text{Eq. C.23}$$

where:

$$p = \frac{8ac - 3b^2}{8a^2} \quad \text{Eq. C.24}$$

$$q = \frac{b^3 - 4abc + 8a^2d}{8a^3} \quad \text{Eq. C.25}$$

$$S = -\frac{1}{2}\sqrt{-\frac{2}{3}p + \frac{2}{3a}\sqrt{\Delta_0}\cos\frac{\varphi}{3}} \quad \text{Eq. C.26}$$

$$\varphi = \cos^{-1}\left(\frac{\Delta_1}{2\sqrt{\Delta_0^3}}\right) \quad \text{Eq. C.27}$$

with:

$$\Delta_0 = c^2 - 3bd + 12ae \quad \text{Eq. C.28}$$

$$\Delta_1 = 2c^3 - 9bcd + 27b^2e + 27ad^2 - 72ace \quad \text{Eq. C.29}$$

The Eq. C.22 and C.23 are solved and C_{d,H^+} can be determined out of the four solutions by limiting x (C_{d,H^+}) to be positive and relatively smaller than the corresponding C_{r,H^+}. The theoretical relationship that can be obtained using this description between the interfacial ring (pH_{ring}) and disc (pH_{disc}) pH for phosphate buffered solutions of different bulk pH is shown in Fig. C.2c.

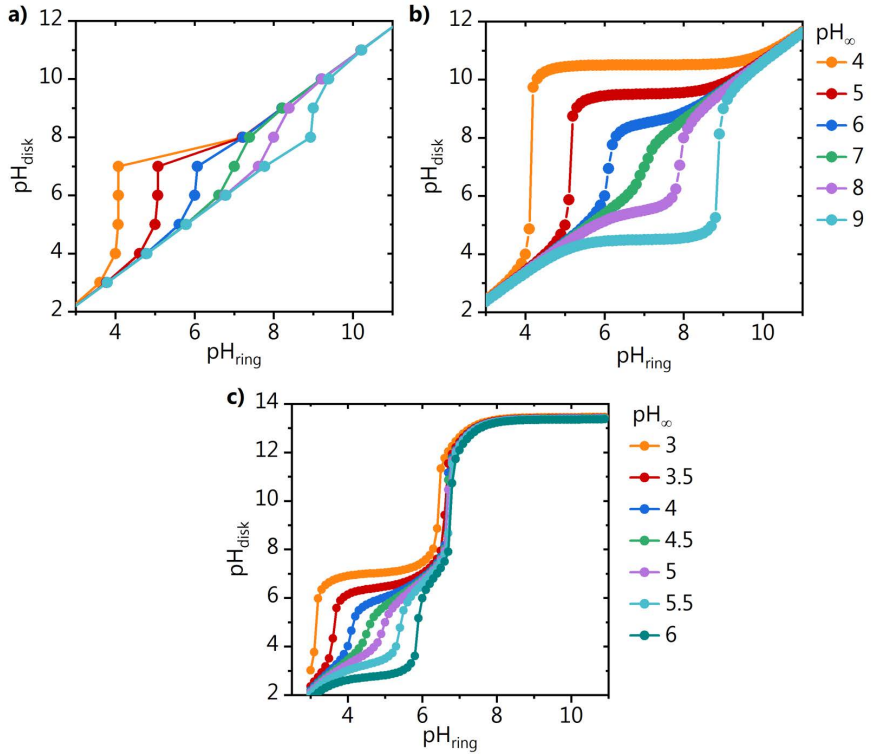

Fig. C.2. Theoretical relationship between pH_{ring} and pH_{disk} for different bulk pH (pH_∞) using **a)** the analytical equation reported by Albery and Calvo[8] and **b)** the extended theory, reported by Yokoyama et al.[4] (both for unbuffered systems), and **c)** the correction presented in this work for a phosphate buffered electrolyte.

C.3 RRDE pH measurements additional data

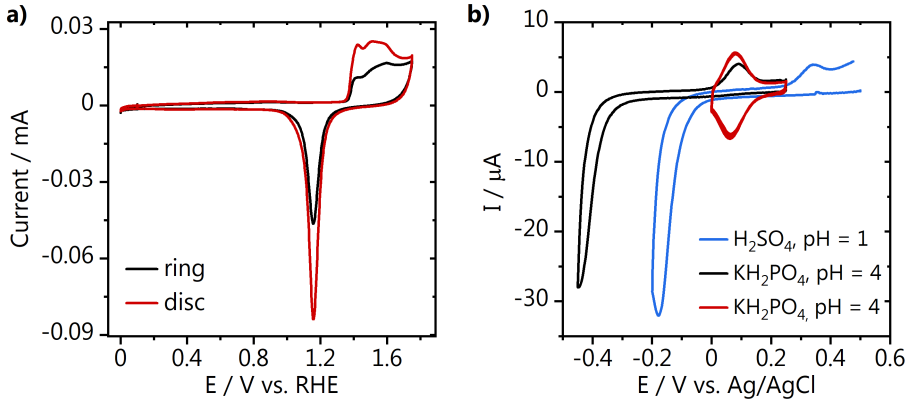

Fig. C.3. a) Blank voltammetry of the ring (black) and disc (red) electrodes taken in 0.1 M H_2SO_4 at 50 mV s^{-1} . **b)** cyclic voltammetry of the 4-NTP to 4-HATP conversion in 0.1 M KH_2PO_4 (black, 100 mV s^{-1}) and 0.1 M H_2SO_4 (blue), together with a characterization of the 4-HATP/4-NSTP redox couple (red, 200 mV s^{-1}) in phosphate.

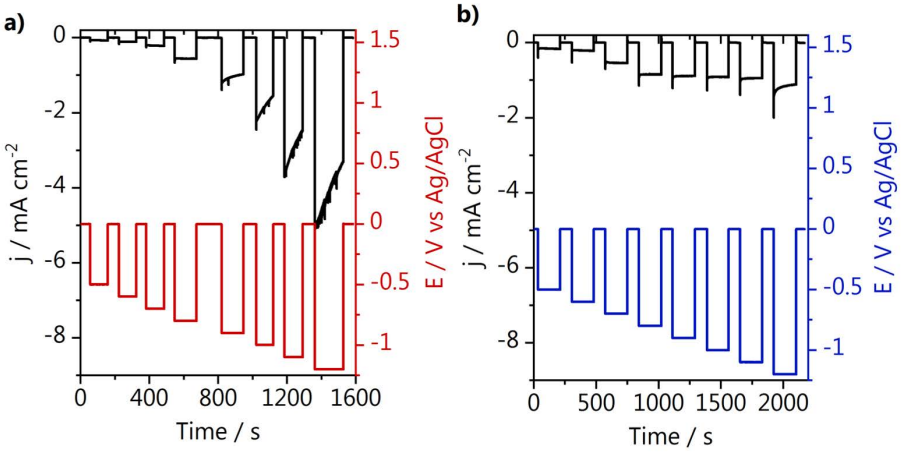

Fig. C.4. Chronoamperometry from pH measurements at different potentials in 0.1 M argon saturated **a)** KH_2PO_4 pH_{bulk} = 4.4 and **b)** K_2SO_4 pH_{bulk} = 3.6 at 1600 rpm.

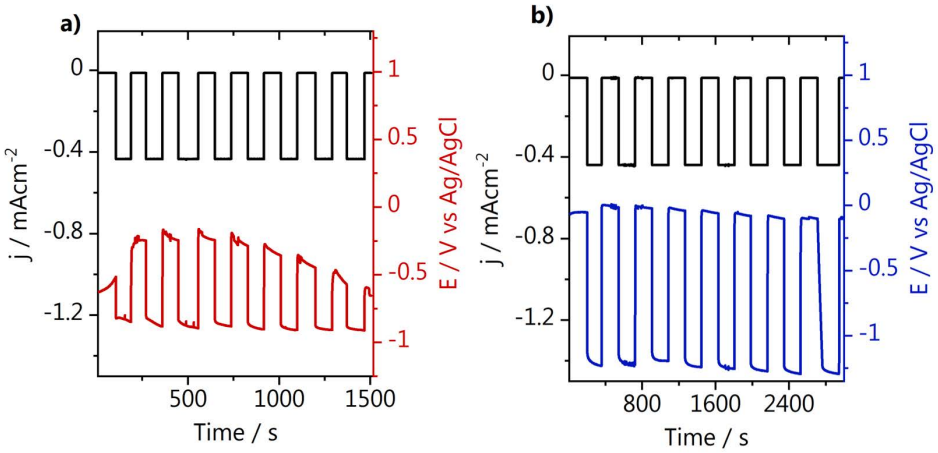

Fig. C.5. Chronopotentiometry from pH measurements in 0.1 M argon saturated **a)** KH_2PO_4 pH_{bulk} = 4.4 and **b)** K_2SO_4 pH_{bulk} = 4.0 at different rotations (500, 750, 1000, 1250, 1500, 1750, 2000, 2600 rpm).

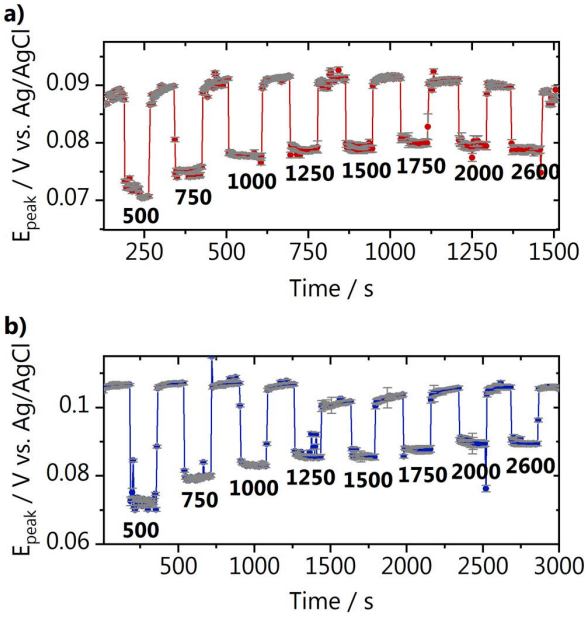

Fig. C.6. Mid-peak potential extracted from the 4-HATP/4-NSTP voltammetry for the experiment in 0.1 M argon saturated **a)** KH_2PO_4 pH_{bulk} = 4.4 and **b)** K_2SO_4 pH_{bulk} = 4.0 at different rotations (500, 750, 1000, 1250, 1500, 1750, 2000, 2600 rpm).

References

(1) Monteiro, M. C. O.; Koper, M. T. M. *Electrochim. Acta* 2019, *325*, 134915.
(2) Do, U. P.; Seland, F.; Johannessen, E. A. *J. Electrochem. Soc.* 2018, *165* (5), 219–228.
(3) Monteiro, M. C. O.; Jacobse, L.; Touzalin, T.; Koper, M. T. M. *Anal. Chem.* 2020, *92* (2), 2237–2243.
(4) Yokoyama, Y.; Miyazaki, K.; Miyahara, Y.; Fukutsuka, T.; Abe, T. *ChemElectroChem* 2019, *6* (18) 4750–4756.
(5) Albery, W. J.; Mount, A. R. *J. Chem. Soc. Faraday Trans. 1 Phys. Chem. Condens. Phases* 1989, *85* (5), 1181.
(6) Albery, W. J.; Calvo, E. J. *J. Chem. Soc. Faraday Trans. 1 Phys. Chem. Condens. Phases* 1983, *79* (11), 2583–2596.
(7) Powell, K. J.; Brown, P. L.; Byrne, R. H.; Gajda, T.; Hefter, G.; Sjöberg, S.; Wanner, H. *Pure Appl. Chem.* 2005, *77* (4), 739–800.
(8) Calvo, E. J.; Albery, W. J. *J. Chem. Soc. Faraday Trans. 1* 1983, *79*, 2583–2596.

D

Methods and supporting information to Chapter 7

D.1. Methods

Gold disc electrodes of 5 mm in diameter were cut from a polycrystalline gold foil (0.5 mm thick, MaTecK, 99.995%) and prepared by first grinding with a silicon carbide paper (grit size 600, MaTecK) to level and clean the sample, so that a mirror-like surface can be obtained by polishing for the shortest possible time. Subsequently, the electrodes were polished on a microcloth (Buehler) with either diamond suspension (MetaDi 3, 1, 0.25 and 0.05 µm, Buehler) or alumina (3, 1, 0.3 and 0.05 µm, Buehler) for 1 minute with each size. In between polishing steps, the electrodes were cleaned in an ultrasonic bath (Bandelin SONOREX RK 52 H) in ultrapure (>18.2 MΩ cm, Millipore Milli-Q) water for 3 minutes. After the last step, the electrodes were sonicated in ethanol for 3 minutes. and subsequently in ultrapure water for 10 minutes. Different commonly reported gold pre-treatments were also performed: chemical etching in 0.1 M H_2SO_4 (Merck, Suprapur, 96%) by applying a potential of 10 V vs. a graphite counter electrode for 20 seconds and removing the gold oxide layer formed by dipping the electrode in 6 M HCl (Merck, EMSURE® ACS, 37%); electrochemical roughening by cycling the electrode 200 times between 0 and 1.75 V vs. RHE (0.1 M H_2SO_4, 1 V s^{-1}); flame annealing the electrode until it glows and then three subsequent times for 5 seconds using a butane torch held about 1 cm away from the surface. In this study, polishing and (subsequent) flame annealing were performed before each experiment.

All glassware was stored in potassium permanganate solution (1 g L^{-1} $KMnO_4$ dissolved in 0.5 M H_2SO_4) and cleaned prior to each experiment by immersion in dilute piranha in order to remove residues of manganese oxide and permanganate anions. After, the glassware was further cleaned by boiling at least five times in ultrapure water. The electrochemical experiments were performed in a one-compartment cell (Duran, 25 ml) with the gold working electrode in the hanging meniscus configuration. Measurements were carried out using a Bio-Logic potentiostat/galvanostat/EIS (SP-300). A gold wire (0.8 mm thick, Mateck, 99.9%) was used as counter electrode and a reversible hydrogen electrode (RHE) as reference. The gold electrodes were characterized before each experiment by recording a cyclic voltammogram between 0 and 1.75 V vs. RHE (0.1 M H_2SO_4, 0.05 V s^{-1}). The gold electrochemical surface area (ECSA) was determined by calculating the charge corresponding to the gold oxide reduction. The obtained value was normalized to the charge density associated with the reduction of a monolayer of gold oxide (386 µC cm^{-2}).[1] Hydrogen evolution reaction was carried out in 0.1 M

Li_2SO_4 (Alfa Aesar, anhydrous, 99.99% (metal basis)), unless stated otherwise. Lithium is the alkaline earth cation that promotes HER on gold the least and therefore was chosen for these studies.[2] The solution was brought to pH = 3 by the addition of adequate amounts of H_2SO_4. The electrolyte was always purged from oxygen by bubbling argon (Linde, 6.0 purity) for 5 minutes prior to the experiments. During the experiments, an argon flow was kept above the electrolyte, to avoid oxygen diffusion into the solution. Appropriate amounts of a 0.01 M $Al_2(SO_4)_3$ (Acros Organics, 99.999%, trace metal basis) solution were added to the electrolyte in order to perform experiments in the presence of different concentrations of Al^{3+}. The dissolution kinetics of $Al_2(SO_4)_{3(s)}$ is very slow, therefore the solution was stirred for 48 h at 60 ºC until the salt fully dissolved. The 0.01 M $Al_2(SO_4)_3$ solution pH is 2.7 (due to the cation acidity) and adding it to the background electrolyte (0.1 M Li_2SO_4) did not lead to changes in the pH. Before each HER experiment, the solution resistance was determined by Electrochemical Impedance Spectroscopy (EIS) and the electrode potential was compensated for 85% of the ohmic drop. All the voltammograms in this work show the first cycle recorded, unless stated otherwise.

The gold electrode topography and composition were characterized by Scanning Electron Microscopy (SEM) in an Apreo SEM (ThermoFisher Scientific). Micrographs were obtained using an acceleration voltage of 10 kV and an electron beam current of 0.4 nA. Energy Dispersive X-Ray Spectrometry (EDX) was used for elemental analysis (Oxford Instruments X-Max^N 150 Silicon Drift detector). EDX data processing was done with the Pathfinder™ X-ray Microanalysis software v1.3. The data is displayed in atomic percentage for easier visualization however the quantification was performed in automatic mode (without providing external standards).

D.2. Micrographs of polished gold electrodes

This section contains additional scanning electron (SEM) micrographs of the gold electrodes after polishing with diamond or alumina and flame annealing three times using a butane torch. As can be seen in Fig. D.1a, polishing with diamond leads to a clean electrode, with a few large contaminating diamond particles on the surface. Opposite, polishing with alumina (Fig. D.1b) leads to contaminating alumina particles of various sizes (from 100 nm to 3 µm) distributed over the whole surface. Higher magnification images also show the presence of small corrosion pits from polishing, and carbonaceous deposits due to flame annealing.

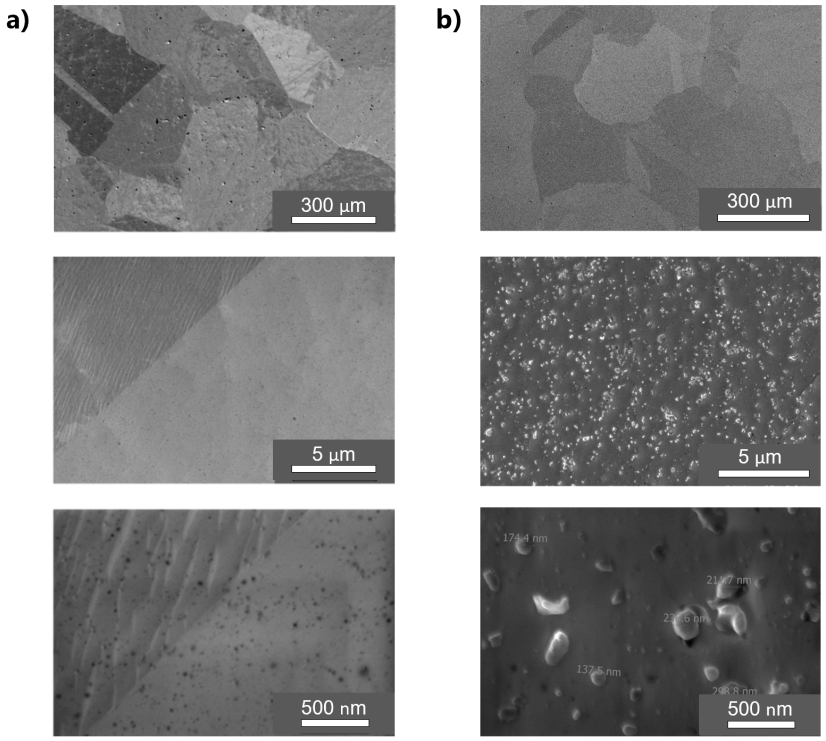

Fig. D.1. SEM micrographs of gold polished with **a)** diamond or **b)** alumina and flame annealed.

D.3. Gold surface preparation

This section contains additional SEM micrographs of the gold electrodes after polishing with diamond and applying different surface preparation methods for gold electrodes. Diamond was chosen here as polishing media, because the alumina particles are detrimental to the proper visualization of the surface topography. Only polishing (Fig. D.2a) leads to a surface that contains scratches and pits of different sizes. During our studies we observed that the gold voltammetry of electrodes that are only polished is not very reproducible. Polishing followed by flame annealing, on the other hand, smoothens the surface and brings it to its most stable state, where defined grains and grain boundaries are observed (Fig. D.2b). The flame annealing procedure reported in this work (1x until glowing + 3x for 5 seconds at 1 cm distance of the electrode), when systematically performed, leads to a very clean and reproducible surface (see the cyclic voltammograms displayed in the following section). It is important to notice that the quality of the flame annealed surface is

directly related to the quality of the mechanical polishing procedure. Chemically etching the gold electrode after polishing (Fig. D.2c), leads to partial removal of polishing contaminants by the removal of gold layers. To remove enough gold layers, etching has to be performed for long enough periods, although this significantly increases the surface roughness. If a smooth, reproducible, and highly crystalline surface is desired, prolonged chemical etching is therefore not recommended. Roughening the polished electrode by repeated cycling at high scan rate, leads to the formation of nanoparticles that are more homogeneously distributed in the polished (Fig. D.2d) than in the polished and flame annealed electrode (Fig. D.2e). The reactivity of nanoparticles is different than of flat surfaces, and not much is known about their stability during electrochemical experiments. Based on this evaluation, we concluded that polishing with diamond and flame annealing gold (following a strict protocol) is the best way to obtain a clean and reproducible surface for fundamental cyclic voltammetry studies.

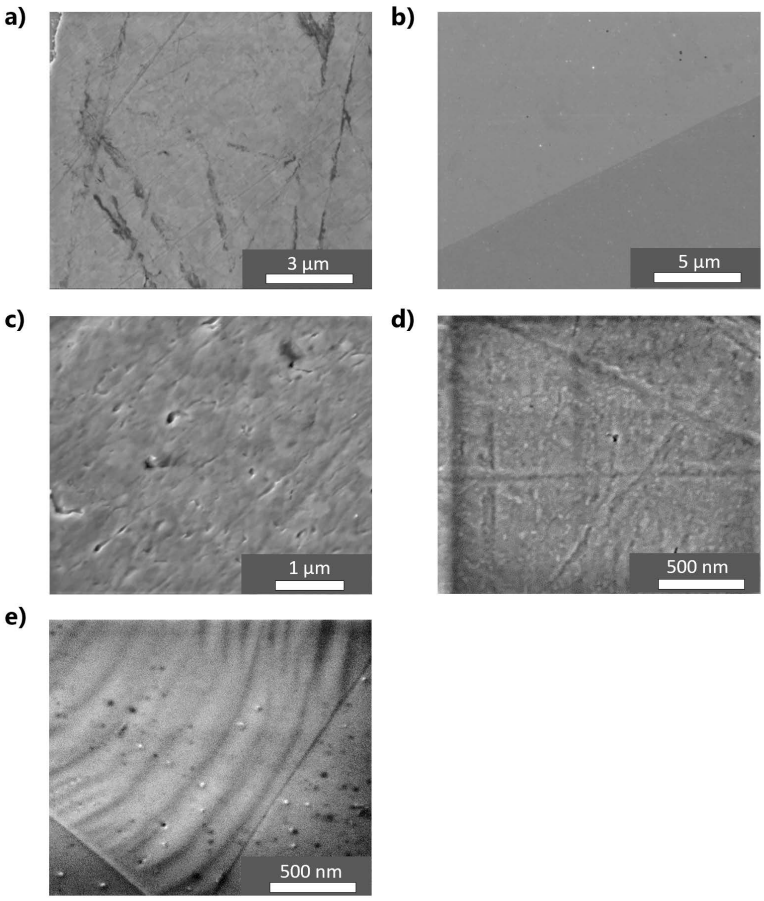

Fig. D.2. SEM micrographs of gold electrodes **a)** polished with diamond and additionally **b)** flame annealed 1x until glowing and subsequently 3x for 5 s, **c)** chemically etched in 0.1 M H_2SO_4 at 10 V vs. OCP for 20 seconds, **d)** electropolished by 200 cycles from 0 to 1.75 V vs. RHE in 0.1 M H_2SO_4 at 1 V s^{-1}, **e)** flame annealed and electropolished.

D.4. Surface characterization after hydrogen evolution

The topography and composition of the gold electrodes polished with diamond (Fig. D.3a) or alumina (Fig. D.3b) was evaluated after the hydrogen evolution reaction. Fig. D.3 shows that for both cases the contaminating particles remain on the surface after the reaction is carried out. In addition, by comparison with the EDX spectra obtained before the experiments (see Chapter 7), the surface composition remains unchanged. No sulphur is detected by EDX, even though HER was performed in a sulphate containing electrolyte.

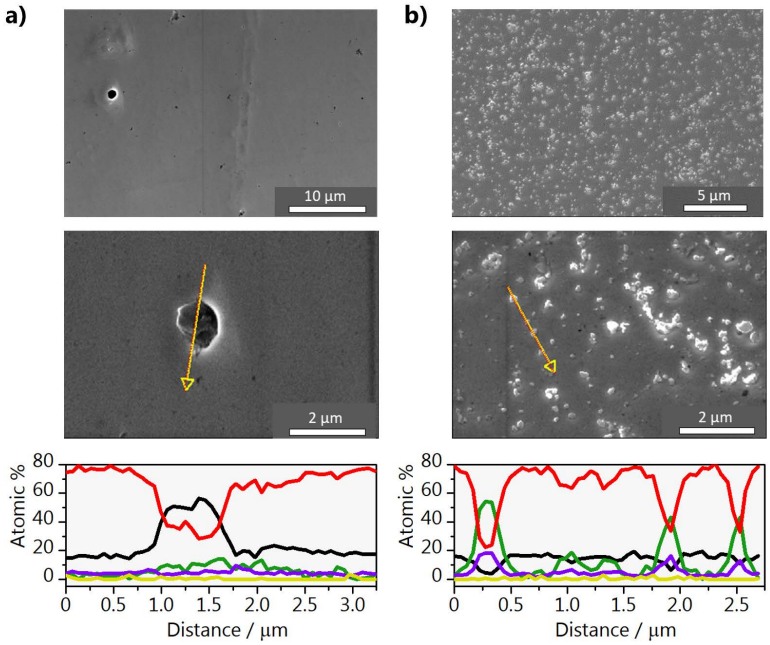

Fig. D.3. SEM micrographs and EDX line spectra of the gold electrodes polished with **a)** diamond or **b)** alumina after hydrogen evolution. The lines refer to the following signals: (—) C K, (—) O K, (—) Al K, (—) Au M and (—) S K.

D.5. HER in the presence of different Al^{3+} concentrations

Experiments adding micro molars of Al^{3+} to the background electrolyte were carried out in order to confirm that the enhancement in HER activity by the presence of alumina particles is actually due to the release of Al^{3+} cations in the electrolyte. Before each experiment, gold electrodes were polished with diamond, flame annealed and characterized. The resulting cyclic voltammograms (CVs) from Fig. D.4 show that the preparation method chosen leads to a reproducible surface, which is very important when performing voltammetry studies. The electrode was also characterized after the HER experiments. The CV of gold before and after HER is shown in Fig. D.5a and no significant changes are observed in the blank voltammetry. SEM characterization, on the other hand, shows that deposits form on the surface during HER, in the form of flakes. The micrograph shown in Fig. D.5b displays how these deposits are homogeneously distributed throughout the surface. An image at higher magnification and EDX line spectra are presented in Chapter 7. The elemental composition found by EDX together with the speciation diagram from Fig. D.6a indicate that these flakes are $Al(OH)_3$. The deposition can happen, as during hydrogen evolution the local pH is more alkaline than the bulk.

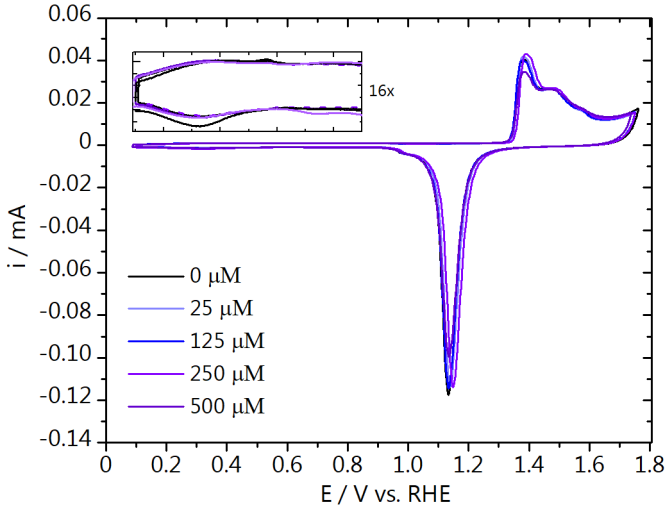

Fig. D.4. Cyclic voltammogram of gold electrodes polished with diamond paste taken at a scan rate of 50 mV s^{-1} in 0.1 M H_2SO_4 before the Al^{3+} addition experiments.

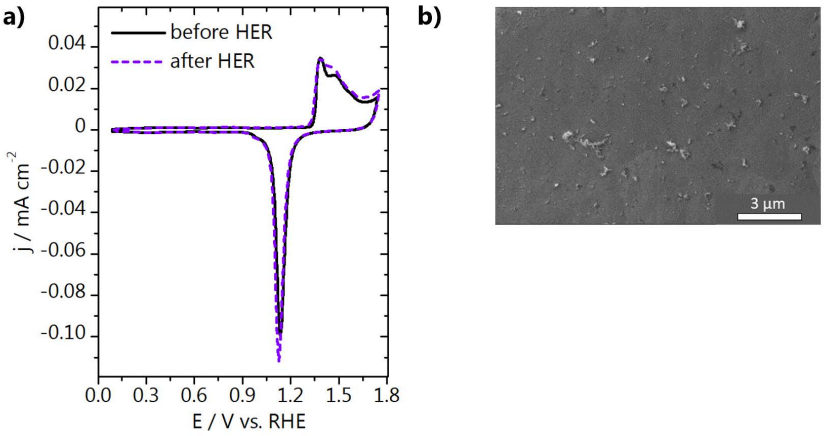

Fig. D.5. a) Comparison of the cyclic voltammogram of gold before and after the HER experiment with 500 µM $Al_2(SO_4)_3$ added to the electrolyte. CV taken at a scan rate of 50 mV s^{-1} in 0.1 M H_2SO_4. **b)** SEM micrograph after HER.

D.6. Speciation of Al^{3+} and aluminium hydroxide deposition

A speciation diagram of Al^{3+} was constructed with the Hydra-Medusa software[3], in order to support that the flakes found on the surface after HER in the presence of Al^{3+} are $Al(OH)_3$. The diagram can be seen in Fig. D.6a, where the molar fraction of aluminium containing species present in the electrolyte is shown as a function of pH. Even though the diagram is plotted as a function of the aluminium containing species, the real concentrations and solubility products of all the different ionic species present in the working electrolyte (H^+, OH^-, H_3O^+, SO_4^{2-}, Li^+, and Al^{3+}) are taken into account for the calculations. It can be seen that below pH 3.7, aluminium is octahedrally coordinated by water molecules (as Al^{3+}) or complexed with SO_4^{2-}. At higher OH^- concentrations, starting at pH 4.2, the number of OH^- bound to each Al^{3+} increases and polymerization of the octahedrons starts to take place through sharing of edge atoms. Above pH 5.2, the polymerization process leads to the formation of planar $Al(OH)_3$ sheets, where each aluminium ion shares 3 pairs of OH^- with 3 other aluminium ions.[4] See the top and side view of the $Al(OH)_3$ sheets structure in Fig. D.6b. Experiments in 0.01 M $Al_2(SO_4)_3$ electrolyte were performed in order to confirm that aluminium cations deposit on the gold electrode surface due to an increase in local pH during HER. Below, additional SEM images of the layer formed and an EDX line scan are presented. Fig. D.7a shows that $Al(OH)_3$ plates are formed during HER, with a spacing of 1-3 µm in between them.

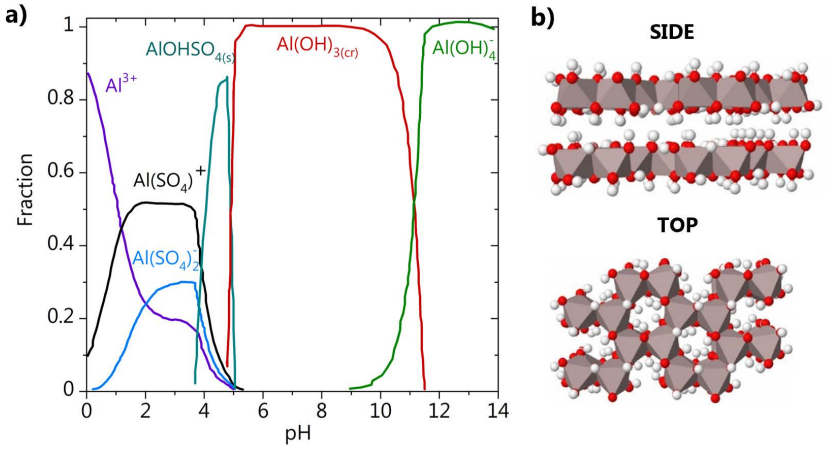

Fig. D.6. a) Speciation diagram of Al^{3+} in the experimental conditions used in this work (HER in 0.1 M Li_2SO_4 + 500 μM $Al_2(SO_4)_3$). This diagram was constructed with the software Hydra-Medusa and is presented as provided. **b)** Molecular structure of $Al(OH)_3$ sheets. Figure adapted from reference.[5]

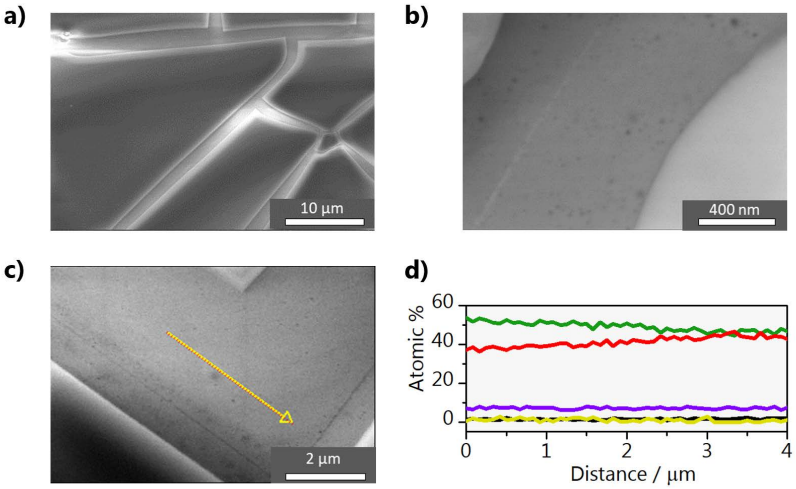

Fig. D.7. SEM micrographs characterizing **a)** the aluminium hydroxide layer deposited on gold, **b)** the region in between the aluminium hydroxide sheets, **c)** and **d)** EDX line spectra determining the composition in the region between the hydroxide sheets. The lines refer to the following signals: (—) C K, (—) O K, (—) Al K, (—) Au M and (—) S K.

Table D.1. Layer composition measured by EDX in 3 different spots of the Au-$Al(OH)_3$ modified electrode.

	Atomic %				
	C	O	Al	Au	S
1	1	74.89	12.07	6.13	5.04
2	0	75.86	12.89	4.26	5.46
3	0	76.26	12.91	5.06	5.57

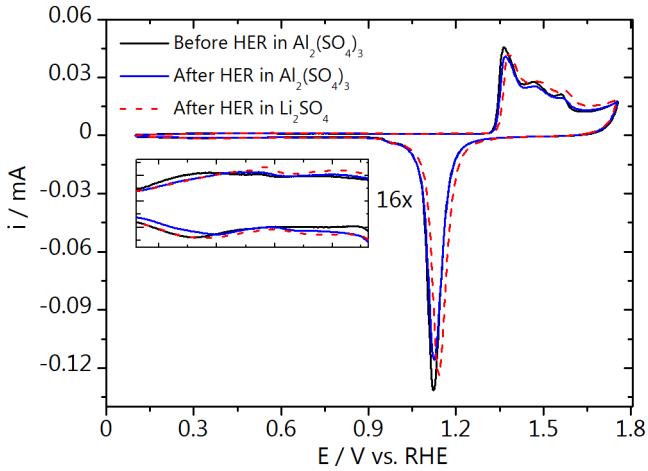

Fig. D.8. Cyclic voltammogram of gold in 0.1 M H_2SO_4 taken at a scan rate of 50 mV s^{-1} before and after HER experiment in 0.01 M $Al_2(SO_4)_3$.

The EDX line scan (Fig. D.7d) from the region showed in Fig. D.7c, demonstrates that the gold is not fully exposed in the region in between the plates, and a thin layer containing Al and O can be found. The thickness of this layer is probably only a few nanometres, as the EDX line scan going through the 128 ± 14 nm thick plate, shows a much lower Au signal. The fact that no sulphur is found in this region (but it is present in the plates) also suggests that this is a thin initiation layer, instead of the highly crystalline hydroxide sheets intercalated with sulphate anions. In order to assure the composition of the surface deposits, EDX scans were also performed in 3 different spots of the sample. Table D.1 shows that the layer composition is nearly the same for the 3 different measurements, which is expected considering the high crystallinity of the $Al(OH)_3$ sheets.

Fig. D.8 shows the CVs of the gold electrodes before HER in 0.01 M $Al_2(SO_4)_3$ (black), directly after HER with the $Al(OH)_3$ sheets on the surface (blue) and after

this Au-$Al(OH)_3$ modified electrode was used for HER in 0.1 M Li_2SO_4 (red dotted line). Surprisingly, the gold CV remains nearly unchanged, with only a small decrease in the gold oxidation and reduction peaks when the hydroxide sheets are present on the surface. This indicates that the deposited layer is highly porous and does not hinder access of the electrolyte to the gold.

D.7. Removal of alumina from the surface

Prolonged etching after polishing the electrode with alumina was performed (2x 60 seconds), as an attempt to fully remove the alumina particles of the surface. The sample was subsequently flame annealed. SEM micrographs from Fig. D.9b show that prolonged etching does not lead to full removal of the alumina particles. Fig. D.9a shows the comparison of the HER curves obtained for the gold electrode polished with diamond, alumina, and alumina with subsequent prolonged etching. Results show that 2 minutes are not enough to fully remove the particles and that their corrosion still leads to larger HER currents than obtained on gold polished with diamond. It is important to point out that the time scale of these experiments is very short, and certainly in longer experiments, an increasing amount of Al^{3+} cations will be present in the electrolyte and this effect will be even more pronounced.

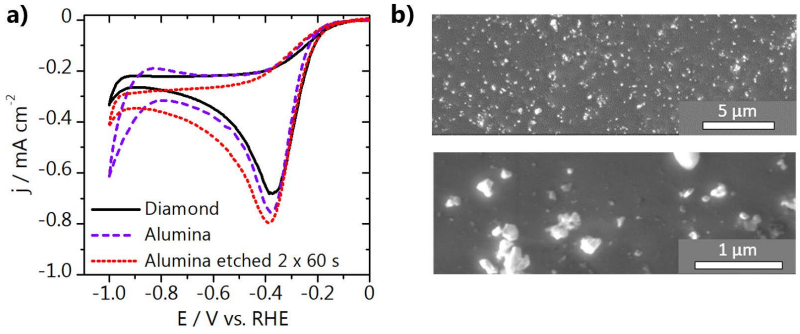

Fig. D.9. a) Cyclic voltammogram of HER on gold electrodes polished with alumina (with and without 2 etching cycles of 1 min) and polished with diamond in argon saturated 0.1 M Li_2SO_4 taken at a scan rate of 50 mV s^{-1} (pH = 3) and **b)** SEM micrographs after etching.

References

(1) Do, U. P.; Seland, F.; Johannessen, E. A. *J. Electrochem. Soc.* 2018, *165* (5), H219–H228.
(2) Xue, S.; Garlyyev, B.; Watzele, S.; Liang, Y.; Fichtner, J.; Pohl, M. D.; Bandarenka, A. S. *ChemElectroChem* 2018, *5* (17), 2326–2329.
(3) Puigdomenech, I. KTH Royal Institute of Technology: Stockholm 2015.
(4) Hem, J. D.; Roberson, C. E. *USGPO* 1967, No. 1827-A.
(5) Lisensky, G. Solid State Structures https://archive.education.mrsec.wisc.edu/pmk/pages/AlOExample.html (accessed Jul 9, 2019).

E

Methods and supporting information to Chapter 8

E.1. Methods

E.1.1 Cyclic voltammetry experiments

CO_2 reduction measurements were performed in a three-electrode glass cell in which the reference was a reversible hydrogen electrode (RHE) separated from the work compartment by a Luggin capillary and the counter electrode was a gold wire (0.8 mm thick, Mateck, 99.9%). Polycrystalline gold (0.5 mm thick, MaTecK, 99.995%) discs of 5 mm in diameter were used as working electrode in the hanging meniscus configuration. The surface was first prepared using the procedure reported in Chapter 7.[1] After each flame annealing, the electrode was characterized by cyclic voltammetry in 0.1 M H_2SO_4 (Merck, Suprapur, 96%). The electrochemical surface area (ECSA) was determined using the charge corresponding to the gold oxide reduction peak. The charge was converted to surface area using the charge density associated with the reduction of a monolayer of gold oxide (386 μC cm^{-2}).[2] Prior to the experiments, the glassware was stored in potassium permanganate solution (1 g L^{-1} $KMnO_4$ dissolved in 0.5 M H_2SO_4), and afterwards cleaned by immersion in dilute piranha and boiled at least five times in ultrapure water. Measurements were performed in 50 ml of electrolyte, using a Bio-Logic potentiostat/galvanostat/EIS (SP-300). The experiments in the absence of metal cations were performed in 1 mM H_2SO_4 (Merck, Suprapur, 96%). Other measurements were performed using different high purity sulfate electrolytes: 1 mM Li_2SO_4 (Alfa Aesar, anhydrous, 99.99%, metal basis), 1 mM Na_2SO_4 (Alfa Aesar, Puratronic™, 99.9955%, metals basis), 1 mM K_2SO_4 (Alfa Aesar, Puratronic™, 99.997%, metals basis) and 1 mM Cs_2SO_4 (Alfa Aesar, Puratronic™, 99.997%, metals basis). During the measurements the electrolyte was constantly purged with argon or CO_2 and the pH was always adjusted to 3 using H_2SO_4. The solution resistance was determined by performing Potentiometric Electrochemical Impedance Spectroscopy (PEIS) prior to every measurement and the electrode potential was always automatically compensated for 85% of the ohmic drop.

E.1.2 SECM measurements

The SECM measurements were performed in our home-built SECM setup, previously described in Chapter 3.[3] The SECM cell cleaning and all equipment used are the same as previously reported.[3] The SECM samples were prepared and characterized prior to every measurement. The polycrystalline gold, silver and copper samples were mechanically polished exactly like described for the gold disc

used in the hanging meniscus experiments. The copper sample was further electropolished in 66% H_3PO_4 at 3 V vs. a Cu counter electrode for 10 seconds. The SECM gold sample was characterized by cyclic voltammetry in 0.1 M H_2SO_4 (Merck, Suprapur, 96%). The silver sample was characterized by thallium under potential deposition (UPD) carried out in a mixture of 0.1 M Tl_2SO_4 (ACROS Organics™, 99.9%, trace metal basis) + 0.1 M H_2SO_4 (Merck, Suprapur, 96%) + 0.5 M Na_2SO_4 (Alfa Aesar, Puratronic™, 99.9955%, metals basis). The copper sample was characterized by cyclic voltammetry in 0.1 M NaOH (Merck, EMPLURA®, 32%). All electrolytes were purged with argon prior to the characterization. For both the characterization and SECM measurements a gold wire was used as counter electrode when using the gold sample, and a platinum wire used for the silver and copper electrodes. A platinum ultramicroelectrode (Pt-UME) was fabricated by etching and sealing a platinum wire (50 µm diameter, Goodfellow, 99.99%) into a soda lime glass capillary using a butane torch. The detailed procedure is reported elsewhere.[4] The Pt-UME was polished before every set of SECM measurements and further cleaned by cycling 200 times between 0.06 and 1.60 V vs. RHE in 0.1 M H_2SO_4 at 1 V s^{-1}, always resulting in a reproducible blank voltammogram. The Pt-UME used in this work has a radius of approximately 6.4 ± 0.05 µm determined using the $Fe(CN)_6^{3-}/Fe(CN)_6^{4-}$ outer sphere reaction. Before the measurements the tip-to-surface distance was determined using a capacitive approach performed in air. The details can be found in Chapter 3.[3] All SECM measurements were performed with the Pt–UME at a fixed distance (50 ± 2µm) from the surface. A 2–channel Bio-Logic potentiostat/galvanostat/EIS (SP-300) was used to control the sample and the tip individually. Chronoamperometry was performed at the sample for 10 seconds and subsequently the tip cyclic voltammetry was recorded at 200 mV s^{-1}. During the experiments, the electrolyte was constantly purged with CO_2 or argon and an argon flow was kept above the solution to avoid oxygen diffusing into the solution. The electrolyte used was 1 mM H_2SO_4 (pH = 3) with the addition of 140 µM Cs_2SO_4 when necessary (Alfa Aesar, Puratronic™, 99.997%, metals basis).

E.1.3 Density Functional Theory parameters

Density Functional Theory (DFT) simulations were performed with the VASP code.[5,6] We choose the PBE density functional[7] including dispersion through the DFT-D2 method,[8,9] with our reparametrized C_6 coefficients.[10] Inner electrons were represented by PAW pseudopotentials[11,12] and the monoelectronic states for the

valence electrons were expanded as plane waves with a kinetic energy cutoff of 450 eV.

E.1.4 Computational model

Polycrystalline Au was modeled by a $3\sqrt{3}\times3\sqrt{3}$–*R*30° Au(111) (4 layers, 15.3 Å × 15.3 Å × 30.0 Å, 8 Å vacuum thickness), which was geometrically optimized (2 outermost layers relaxed, bulk fixed). The Brillouin zone was sampled at the Γ–point. Since Pt and Au have similar lattice constants, we inherited the solvent configuration (72 H_2O molecules, 15 Å thick) optimized by AIMD for 11 ps at 300 K from our previous study regarding water-metal interface for $3\sqrt{3}\times3\sqrt{3}$–*R*30° Pt(111).[13] We inserted the pre-equilibrated water molecules on top of the Au surface and we carried out AIMD simulations for a total of 6 ps (1 ps of equilibration + 5 production, 1 fs time step), in a canonical NVT ensemble at 300 K regulated by a Nosé-Hoover thermostat.[14–16] First, we optimized the hydrogen bond network between the water molecules for 2 ps on the Au–H_2O system (Fig. E.8). Then, we inserted an alkali metal cation M^+ (Li^+, Na^+, K^+, Cs^+) in a cavity of the first solvation layer close to the surface, whilst we removed a hydrogen from a water molecule in the fourth water bilayer to keep charge balance. The cation coverage was set to 0.04 ML (1/27), which corresponded to a surface concentration of 0.5–0.8 M. The resulting four systems were named Au-H_2O-M^+ and underwent AIMD for 2 additional ps. Finally, we added a CO_2 (0.04 ML, 1/27) to the Au-H_2O and 4 Au-H_2O-M^+ proximal to the catalytic surface and the cation. The resulting 4 Au-H_2O-M^+-CO_2 and 1 Au-H_2O-CO_2 systems underwent AIMD for 2ps and 1 ps, respectively, and were used to investigate the activation of CO_2 in the presence and absence of an alkali cation (Fig. E.8). As the cation, CO_2, and the explicit water molecules were placed only on one side of the slab, we applied a dipole correction to remove spurious contributions arising from the asymmetric slab model.[17]

E.1.5 Data analysis

Cation-water radial distribution functions were obtained for the 2 ps equilibration of the Au-H_2O-M^+ systems. From these parameters, we determined the cation coordination number to water or CO_2 oxygens. Finally, the CO_2 binding energy at U = 0.0 V vs. RHE in the presence and absence of a cation was averaged from static DFT single point calculations from AIMD configurations taken every 20 fs during the last 0.5 ps with standard deviation taken as uncertainty. Gibbs free energies were calculated at 298.15 K by correcting DFT energies for entropic

contributions. The energy references were chosen as CO_2(g) and single point calculations of the previously described Au–H_2O–CO_2 and Au–H_2O–M^+–CO_2 configurations upon removal of the CO_2 molecule (Eq. E.1).

$$* + M^+(H_2O)_N + CO_2 + e^- \rightleftharpoons * CO_2^- + M^+(H_2O)_N;\ \Delta G_{CO_2} \quad \text{Eq. E.1}$$

E.1.6 Cation accumulation at the outer Helmholtz plane

To assess the thermodynamics of cation accumulation at outer Helmholtz plan (OHP), we applied the methodology introduced by Resasco et al.[18] The energy of a solvated cation at the bulk electrolyte can be referenced to the energy of the bulk alkali metal following the principles of the Computational Hydrogen Electrode.[19] At the standard reduction potential U_0,[20] a cation M^+ is in equilibrium with its reduced state M, Eq. E.2. Thus, we can derive the energy of the cation/electron pair at a given potential U vs SHE from the DFT energy of the bulk alkali metal, Eq. E.3.

$$M^+ + e^- \leftrightarrow M,\ U = U_0 \quad \text{Eq. E.2}$$

$$E_{M^+ + e^-} = E_M - |e^-|\,(U - U_0) \quad \text{Eq. E.3}$$

We can instead estimate the energy of a cation at the OHP at U = 0 V vs SHE from our *ab initio* molecular dynamics simulations, since we specifically inserted an alkali metal at the OHP, which donates its valence electron to the solvation layer, Eq. E.4. The gold surface is represented by the symbol *, whilst the solvation layer is indicated by solv. Thus, we can calculate the thermodynamic driving force for each cation to accumulate at the OHP as in Eq. E.5. Considering the lowest energy configurations for Li^+, Na^+, K^+, Cs^+ during the last 2 ps of AIMD simulation, E(OHP) – E(bulk electrolyte) correlates with cation ionic radius.[21] Cations with larger radius are thermodynamically more prone to accumulate at the OHP, thus they exhibit higher concentration across the surface/electrolyte interface.[18]

$$* + \text{solv} + M \rightarrow * + \text{solv} + M^+ + e^-, E_{M^+ + e^-}(\text{OHP}) \quad \text{Eq. E.4}$$

$$\Delta E = E_{M^+ + e^-}(\text{OHP}) - E_{M^+ + e^-}(\text{bulk}) \quad \text{Eq. E.5}$$

E.1.7 Data availability

The datasets generated though Density Functional Theory simulation and analysed during the current study are available in the ioChem-BD database[22] at DOI: 10.19061/iochem-bd-1-194.[23]

E.2. Hanging meniscus experiments

E.2.1 Characterization of the gold electrode

Before all the CO_2 reduction experiments in hanging meniscus configuration were performed, the gold electrode was flame annealed using the protocol previously described[1] and the electrode was characterized in 0.1 M H_2SO_4. The characterization by cyclic voltammetry (CV) was done in between all measurements, to assure a reproducible surface which allows for comparison of the CO_2 reduction results and determination of the electrochemical active surface area. The characterization CVs recorded during the hanging meniscus experiments presented in the main text can be found in Fig. E.1.

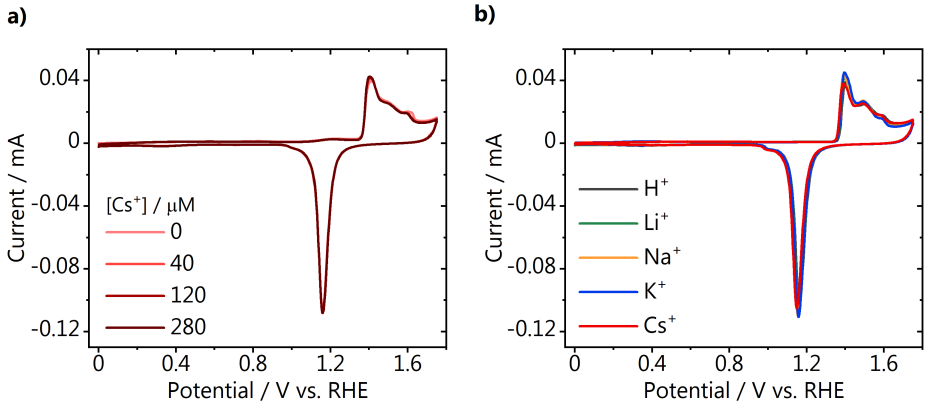

Fig. E.1. Blank voltammetry of the gold electrode used in the hanging meniscus experiments after surface preparation through polishing and flame annealing. **a)** CVs recorded before the measurements in 1 mM H_2SO_4 with the addition of different amounts of Cs^+, **b)** CVs recorded before the measurements in 1 mM M_2SO_4 (M = H, Li, Na, K, Cs).

E.2.2 Hydrogen evolution and CO_2 reduction in 1mM M_2SO_4 (M = H, Li, Na, K, Cs)

Hydrogen evolution and CO_2 reduction were also carried out in 1 mM sulfate solutions of different cations, all adjusted to pH = 3 when necessary. The cyclic voltammetry can be seen in the figure below, together with the results obtained in 1 mM H_2SO_4, for comparison. To calculate the CO oxidation charge density shown in the main text, the double layer charge recorded in Argon was subtracted from the total charge found in CO_2 atmosphere.

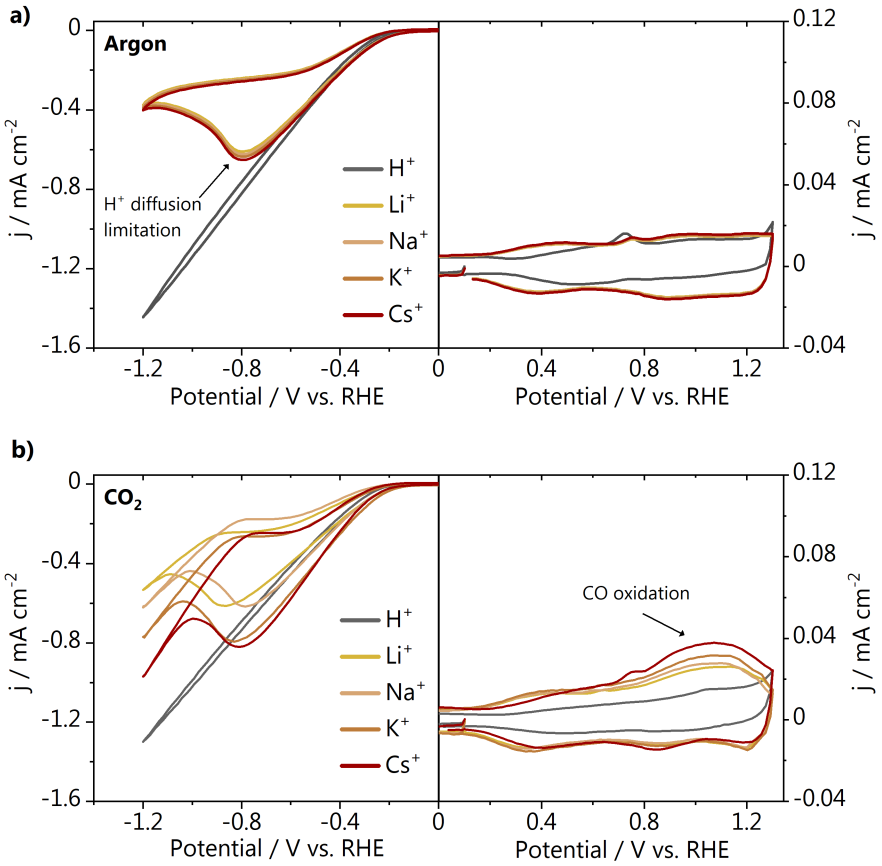

Fig. E.2. Cyclic voltammetry recorded in **a)** argon and **b)** CO_2 atmosphere on gold in 1 mM M_2SO_4 (M = H, Li, Na, K, Cs) at pH = 3 (50 mV s^{-1}).

E.2.3 CO oxidation control experiment

A control experiment was performed to show that CO can be oxidized on the gold electrode in the absence of a metal cation in the electrolyte. Before the measurement the gold electrode was characterized in argon saturated 0.1 M H_2SO_4 electrolyte. The 0.1 M H_2SO_4 electrolyte was saturated with CO for 5 minutes and subsequently a cyclic voltammogram was recorded. Fig. E.3 displays both CVs, in which the large anodic current (red curve) starting at 0.8 V vs. RHE shows that CO can be oxidized without a metal ion in solution.

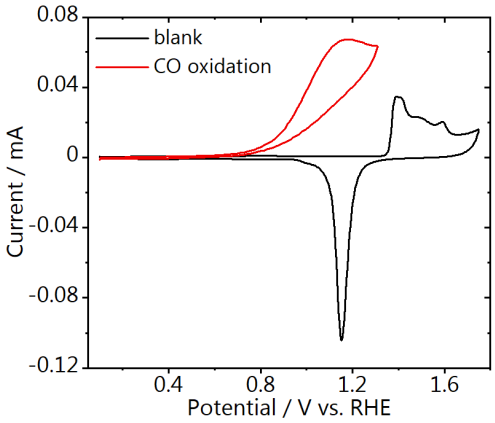

Fig. E.3. CO oxidation voltammetry on gold recorded in 0.1 M H_2SO_4 after saturation the electrolyte with CO (50 mV s^{-1}).

E.2.4 CO_2 reduction in 1mM H_2SO_4 + µM Cs^+

CVs were recorded directly after the CO_2 reduction cathodic scan from 0 to –1.2 V vs. RHE in 1 mM H_2SO_4 in order to semi-quantitatively determine the amount of CO produced with and without the addition of different amounts of Cs^+. The three subsequently cycles recorded are shown in Fig. E.4a-c and the first cycles are shown in the main text. The increase in the amount of CO produced over the 3 cycles for each concentration is likely due to an accumulation of CO_2 near the surface after CO oxidation. Additionally, considering a direct competition between proton and CO_2 reduction, an increase of the interfacial pH and consequent suppression of proton reduction, could lead to more CO produced.

E.2.5 CO_2 reduction in Li_2SO_4 + µM Cs^+

Li_2SO_4 was used as background electrolyte to investigate the effect of the Cs^+ concentration in the CO production. The cathodic and subsequently anodic cyclic voltammetry recorded can be seen in Fig. E.5.

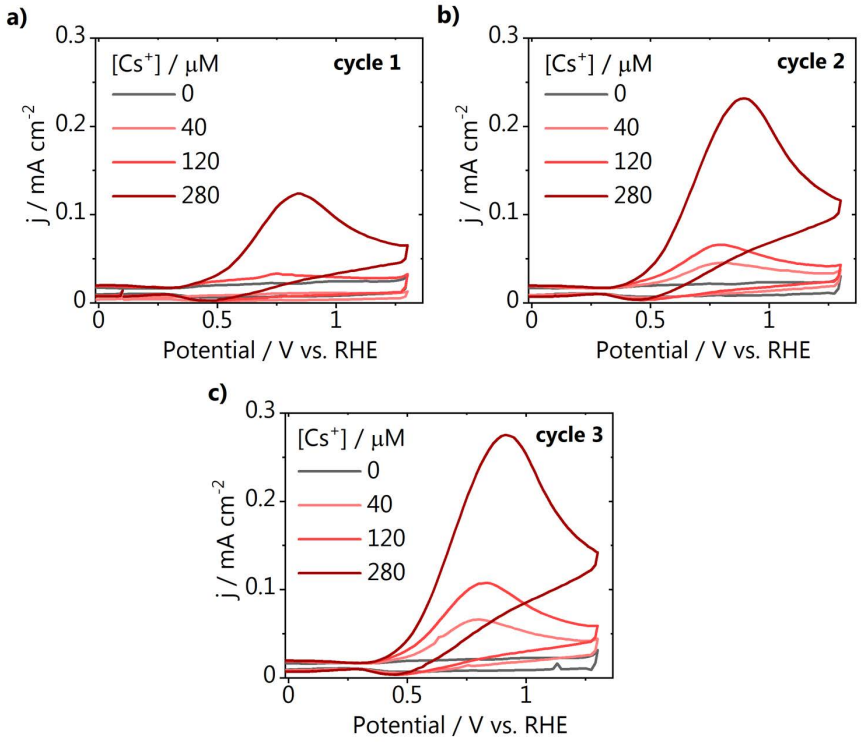

Fig. E.4. a) First, **b)** second and **c)** third cycles recorded at 50 mV s^{-1} on a gold electrode directly after a cathodic scan in CO_2 atmosphere when different amounts of Cs^+ were added to the 1 mM H_2SO_4 electrolyte.

E.3. SECM experiments

E.3.1 Capacitive approach curve fitting

A capacitive approach in air is performed before the SECM measurements in order to determine the tip-to-surface distance. Fig. E.6 shows the Pt-UME approach curves recorded before the SECM experiments performed using the gold, silver and copper samples. The fit is shown in red.

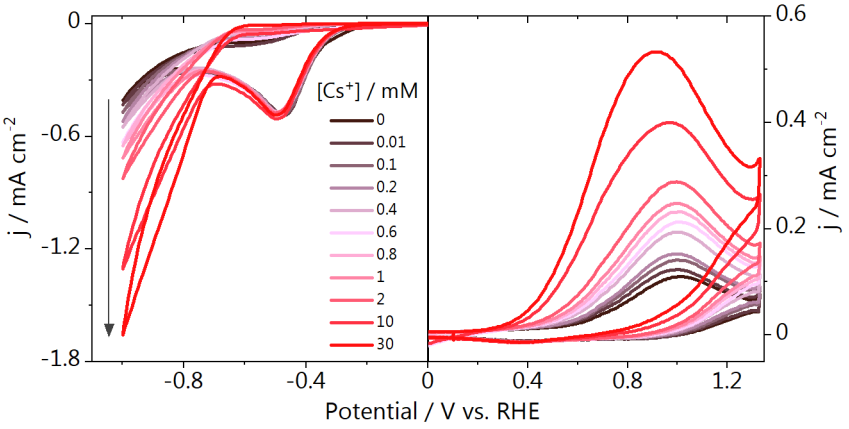

Fig. E.5. Cyclic voltammetry recorded at 50 mV s^{-1} during CO_2 reduction on gold in Li_2SO_4 electrolyte contaning different concentrations of Cs^+. The total cation concentration in solution was kept 0.1 M and the pH = 3.

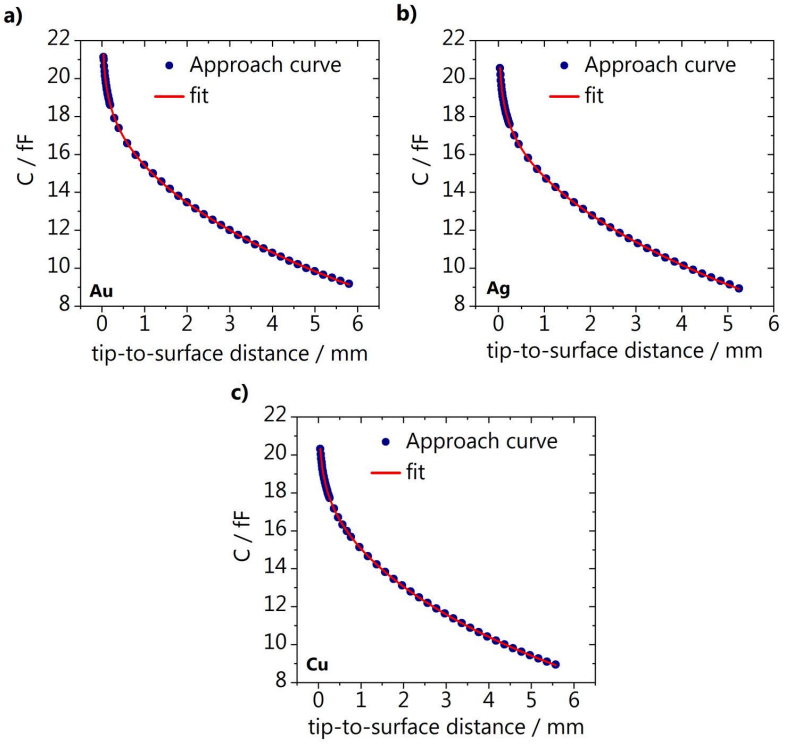

Fig. E.6. Capacitive approach curves recorded before the SECM experiments on **a)** gold, **b)** silver and **c)** copper.

E.3.2 Stability of the silver and copper electrodes

Fig. E.7 shows the instability of the silver and copper electrodes when potentials more cathodic than –0.8 and –1 V vs. RHE are applied to the sample, respectively. It shows different cycles of the Pt-UME voltammetry recorded subsequently, either after hydrogen evolution or CO_2 reduction are carried out at the sample. As can be seen in Fig. E.7a when CO_2 reduction is performed on silver in 1 mM H_2SO_4 at –1 V vs. RHE, CO is produced, at small amounts. This goes against what was observed in all the other experiments shown in the main text, in which CO_2 reduction does not take place at all without a metal ion in solution. The difference here, is that under this cathodic potential Ag^+ ions go into solution, enabling the CO_2 reduction reaction.[25] This happens as due to the SECM capacitive approach, the sample is exposed to air for a relatively long period of time, which likely leads to the formation of a very small amount of oxide. The presence of Ag^+ ions in the electrolyte can be confirmed looking at the 5th cycle recorded from the Pt-UME shown in Fig. E.7b, which presents voltammetric features characteristic of the underpotential deposition of Ag^+ on polycrystalline platinum.[26] The same happens with the copper sample when polarized more negatively than –1 V vs. RHE. Copper deposition is observed in the Pt-UME voltammetry and can be seen in Fig. E.7c.[27] These observations were made when either HER or CO_2 reduction were performed at the sample and are crucial for the correct execution and judgment of the experimental results. In between measurements, the SECM cell was always fully disassembled and thoroughly cleaned as here we observed that trace amounts of metal ions can already lead to the production of CO.

E.4. Model

An accurate density functional theory (DFT) modeling of the interaction between ions and water molecules close to the catalytic surface requires *ab initio* molecular dynamics (AIMD) simulations with a suitable number of explicit solvent molecules and a proper choice of the equilibration time. Generally, at least 4 water bilayers are required, as well as at least 10 ps of equilibration time.[13] Since platinum and gold present similar structural properties, we inherited an explicit solvation configuration equilibrated for 11 ps of AIMD on $(3\sqrt{3}\times3\sqrt{3})R30^{o}$ Pt(111) at 300 K (4 water bilayers, 72 water molecules).[13] The pre-equilibrated water molecules were inserted on top of a $(3\sqrt{3}\times3\sqrt{3})$ $R30^{o}$ Au(111) (4 layers, 15.3 Å × 15.3 Å × 30.0 Å, 8 Å vacuum thickness) and let further equilibrate for 2 ps with time steps of 1 fs at 300 K on the gold supercell (Fig. E.8a). This system was named Au-H_2O, since it

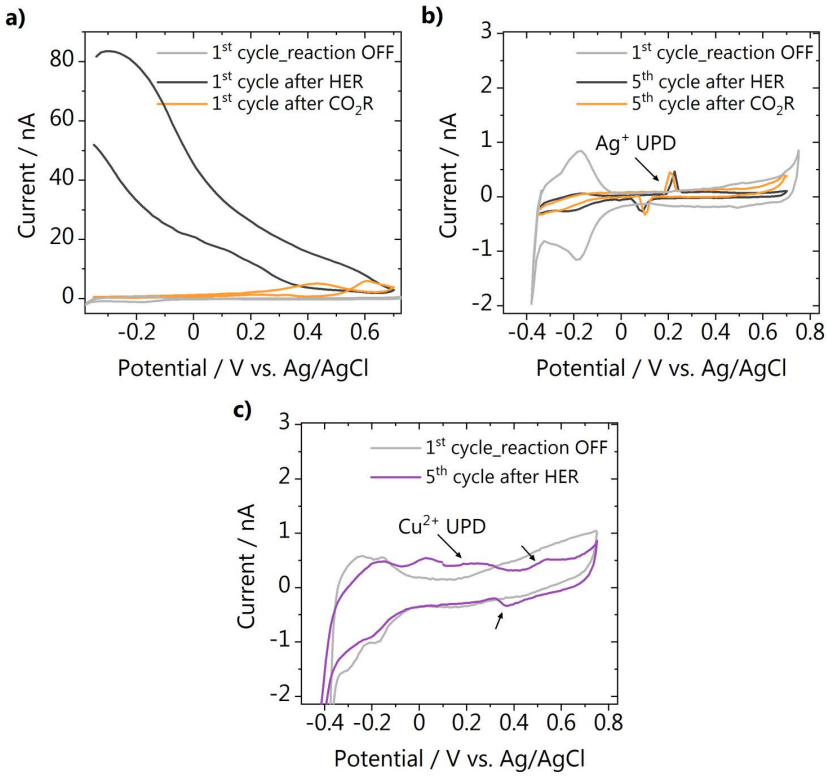

Fig. E.7. Pt-UME voltammetry **a)** after HER or CO_2 reduction are performed on silver in 1 mM H_2SO_4 and **b)** subsequent cycles from the same experiment showing the presence of Ag^+ ions in the electrolyte and **c)** similar observations on the copper electrode.

reproduces the cation-free experimental sample. After this equilibration, an alkali atom (Li, Na, K, or Cs) was inserted in a solvation cavity close to the surface (initial $d_{M\text{-surface}}$ = 3.3 Å, Fig. E.9) and the four systems were equilibrated for 2 ps at 300 K (Fig. E.8b). A hydrogen was removed from a water molecule in the fourth water bilayer, so that the +1 $|e^-|$ charge of the cation was balanced by the –1 $|e^-|$ charge of the resulting OH^-. These systems were classified as Au-H_2O-M^+ where M^+ stands for Li^+, Na^+, K^+, and Cs^+. Given the thickness of the solvation layer, around 1.4 nm, Au geometrical area, 2.0 nm^2, and the number of water molecules, 72, the cation surface concentration is between 0.5 ($1/N_A$ mol of cation within V = 3.29 nm^3) and 0.8 M (1/72 of water molar concentration, 55.5 M). Finally, a CO_2 molecule was inserted close to the surface for both Au-H_2O and Au-H_2O-M^+ systems, with a surface coverage of 0.04 ML (1 molecule for 27 Au surface atoms), as shown in Fig. E.8c. Upon interaction with solvation molecules and cation during 2 additional ps

at 300 K, CO_2 adsorbed on the surface *via* a $\eta^2_{C,O}$ conformation (bidentate through carbon and one oxygen) and the second oxygen coordinated to the alkali cation or to water molecules through H-bonds. These final systems were labelled Au-H_2O-CO_2 and Au-H_2O-M^+-CO_2.

E.4.1 Cation-water radial distribution functions

Cation-water radial distribution functions, $g_{M^+\text{-}H2O}(r)$ were obtained for the 2 ps equilibration of the Au-H_2O-M^+ systems to account for the density of water molecules around the alkali metal center, M^+. We first calculated the distribution of distances, $\eta(r)$, defined as the number of H_2O oxygens at a distance between r and $r + \Delta r$ for all the molecular dynamics steps, where r is the position vector from the central cation and Δr is its differential. We then normalized $\eta(r)$ for the expected surface density of cations ρ corresponding to 2D annulus formed by the solvation layer, Eq. E.6:

$$g(r)_{2D} = \frac{\eta(r)}{2\pi r \cdot \Delta r \cdot \rho} \qquad \text{Eq. E.6}$$

where $g(r)$ is the radial distribution function (dimensionless), $\eta(r)$ the distribution of distances (dimensionless), r the position vector, Δr its differential (both in Å), and ρ the cation surface density (Å^{-2}). Cation-water radial distribution functions are reported in Fig. E.10 and the parameters of the Lorentzian fit on the first solvation shell peaks are shown in Table E.1. A Lorentzian fit was applied through Eq. E.7 and it was preferred to a Gaussian fit since it was numerically more stable:

$$g(r) = g(r)_0 + \left(\frac{2A}{\pi}\right) \cdot \left(\frac{w}{4(r - d_{M^+\text{-}O})^2 + w^2}\right) \qquad \text{Eq. E.7}$$

where $g(r)$ is the radial distribution function, r the position vector (Å), w the full width at half maximum (Å), $d_{M^+\text{-}O}$ the cation-oxygen bond length (Å), whilst $g(r)_0$ (dimensionless) and A (Å) are fit parameters.

For larger alkali cations, the first solvation shell becomes softer as indicated by the broadening of the first $g_{M^+\text{-}H2O}(r)$ peak and the increase of w (Table E.1). For Cs^+ the transition between first, second, and third solvation shell is continuous, therefore this alkali metal can easily modify its coordination. The parameters of the Lorentzian fit (dashed lines) and the consequent estimation of the cation-oxygen distances in the first solvation shell are reported in Table E.1 and agree with previous experimental and theoretical reports.[28,29] The cation-oxygen bond length ($d_{M^+\text{-}O}$) and its associated uncertainty are obtained from the fit parameters on the $g(r)$ first

peaks. The term $d_{M^+\text{-O(S.A.)}}$ stands for averages of state-of-the-art values for cation-water distances.[28,29]

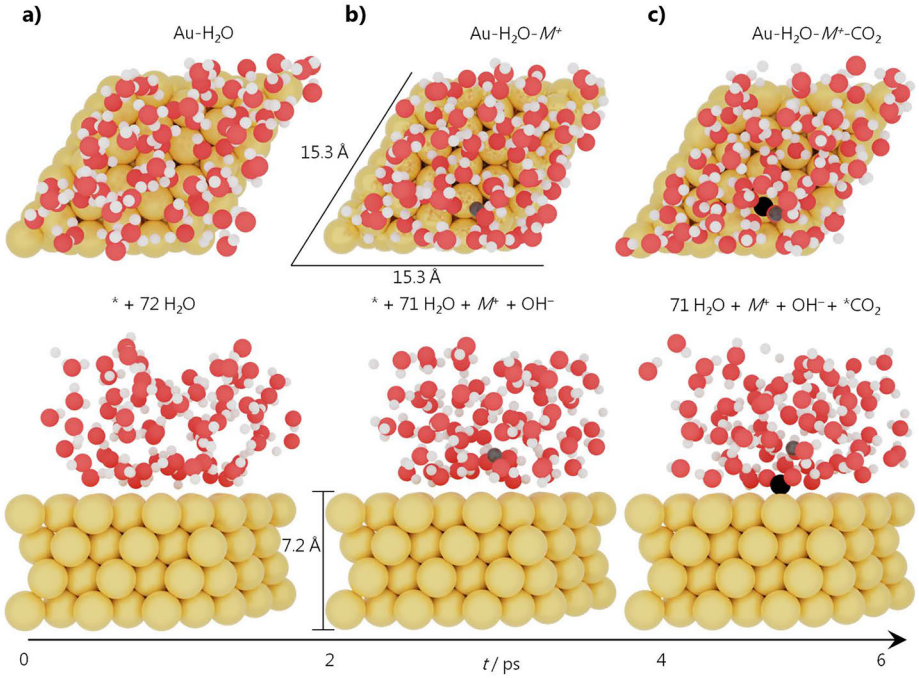

Fig. E.8. Input models for *ab initio* molecular dynamics simulation carried out on a $(3\sqrt{3}x3\sqrt{3})R30^{o}$ Au(111) supercell (15.3 Å x 15.3 Å x 30.0 Å) with 72 water molecules. **a)** The Au-H_2O system equilibrated for 2 ps (1 fs time step) at 300 K. **b)** Insertion of an alkali cation (Li^+, Na^+, K^+, Cs^+) close to the surface and equilibration for another 2 ps at 300 K. **c)** Addition of a CO_2 molecule to the system, that interacts with the gold surface *via* a $\eta^2_{C,O}$ conformation with one oxygen coordinated to the alkali cation, and AIMD further carried out for 2 ps at 300 K. The portrayed cation is Li^+.

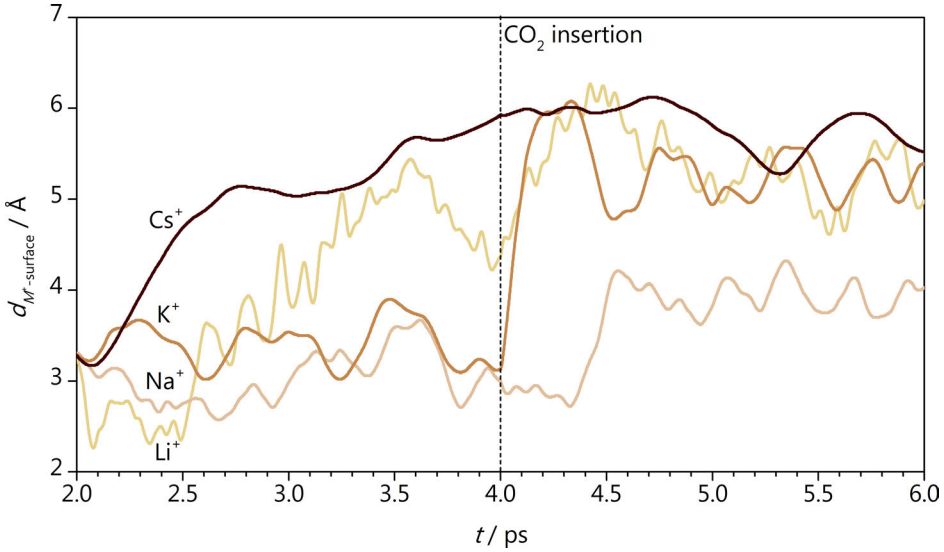

Fig. E.9. Distance between cation (M^+) and surface calculated during equilibration of the Au-H_2O-M^+ system (from 2 to 4 ps) and upon insertion of CO_2 in the vicinity of the cation (from 4 to 6 ps).

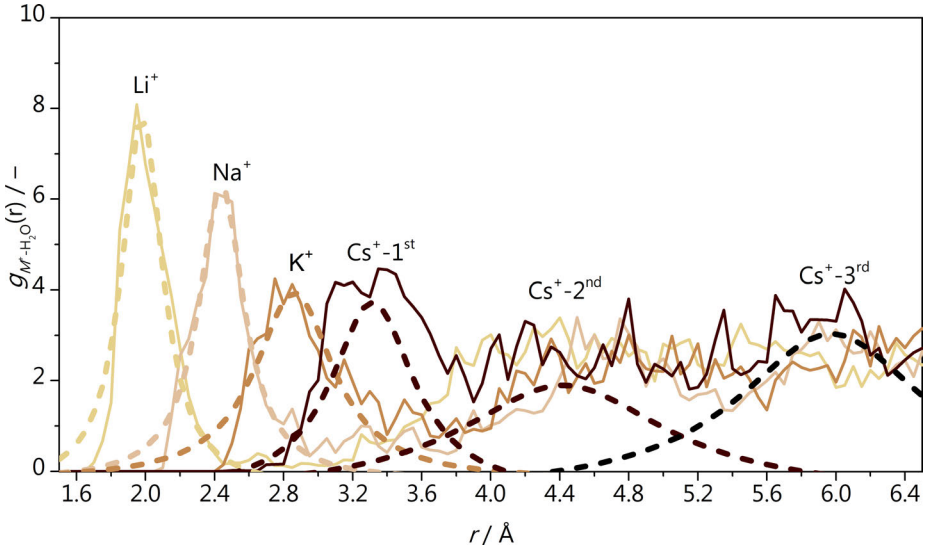

Fig. E.10. Cation solvation shells during 2 ps equilibration of the Au-H_2O-M^+, described by the cation-water radial distribution functions.

Table E.1. Parameters of the Lorentzian fit and distances between cation and water molecules in the first solvation shell, estimated from the position of the first peak of cation-water radial distribution functions, Fig. E.10. $g(r)_0$, A, w(Å), χ^2_ν and $d_{M^+\text{-O}}$ (Å) are fit parameters with the associated fit uncertainties. The state-of-the-art values for cation-water distances, $d_{M^+\text{-O(S.A.)}}$ (Å), and associated uncertainties are taken from Ref. 9.

M^+	$g(r)_0$ / –	A / Å	w / Å	χ^2_ν / –	$d_{M^+\text{-O}}$ / Å	$d_{M^+\text{-O(S.A.)}}$ / Å
Li^+	–0.39 ± 0.16	3.7 ± 0.3	0.28 ± 0.02	0.34	1.981 ± 0.007	2.08 ± 0.07
Na^+	–0.22 ± 0.08	3.3 ± 0.2	0.32 ± 0.02	0.12	2.440 ± 0.005	2.36 ± 0.06
K^+	–0.22 ± 0.12	3.6 ± 0.4	0.55 ± 0.06	0.22	2.86 ± 0.02	2.80 ± 0.08
Cs^+-1st	–0.53 ± 0.12	3.9 ± 0.6	0.58 ± 0.07	0.21	3.32 ± 0.02	3.14 ± 0.08
Cs^+-2nd	–0.53 ± 0.12	6 ± 2	1.5 ± 0.4	0.21	4.42 ± 0.08	–
Cs^+-3rd	–0.53 ± 0.12	7 ± 2	1.3 ± 0.4	0.21	5.97 ± 0.06	–

E.4.2 Cation coordination number

To obtain the coordination number $N_{M^+\text{-O}}$ of the alkali cations M^+, we assigned a bond value equal to one if the cation-oxygen distance $r_{M^+\text{-O}}$ was equal or lower than the cation-oxygen bond length $d_{M^+\text{-O}}$, Table E.1. Otherwise, the bond value was set to zero if $r_{M^+\text{-O}}$ was larger than a certain threshold $th_{M^+\text{-O}}$: 2.5, 3.0, 3.5, 4.0 Å for Li^+, Na^+, K^+, and Cs^+, respectively (Fig. E.10). Between these extremes, $N_{M^+\text{-O}}$ was calculated through Eq. E.8 following a decay controlled by the error function (erf), Eq. E.9.[30] In Eq. E.8, $N_{M^+\text{-O}}$ is the cation coordination number (dimensionless), $r_{M^+\text{-O}}$ is the cation-oxygen distance (Å), $d_{M^+\text{-O}}$ the cation-oxygen bond length (Å), $th_{M^+\text{-O}}$ the cation-oxygen threshold (Å) and avg stands for average. In Eq. E.9, t (dimensionless) is the variable of integration and 0 and z represent the integration limits.

$$N_{M^+\text{-O}} = \frac{1}{2} - \frac{1}{2}\,\mathrm{erf}\left(\frac{r_{M^+\text{-O}} - \mathrm{avg}(d_{M^+\text{-O}}, th_{M^+\text{-O}})}{0.2\ \text{Å}}\right) \qquad \text{Eq. E.8}$$

$$\mathrm{erf}\,(z) = \frac{2}{\sqrt{\pi}}\int_0^z \exp(-t^2)\,dt \qquad \text{Eq. E.9}$$

E.4.3 Cation-induced electric field

We estimated the cation-induced electric field following a similar procedure as introduced by Chen et al.[31] First, we calculated the electrostatic potential induced by the cation upon removal of the CO_2 intermediate through Eq. E.10, where $U_{\text{surf+solv+ion}}$, $U_{\text{surf+solv}}$, U_{ion} indicate the electrostatic potential for the overall system (surface, solvation and ion), the environment (surface and solvation), and the ion alone respectively. Then, assuming the cation as a point charge, we define the local electric field E_{el} through Eq. E.11, where $U(r)$ is the cation-induced electrostatic

potential difference at a given coordinate $\vec{r}$. $\vec{r}_{\mathrm{ads}}$ and $\vec{r}_{M+}$ represent the adsorbate and cation positions, respectively. The additional negative sign is introduced to assess the electric field induced on a negatively charged adsorbate, such as $*CO_2^-$.

$$U(\vec{r}) = U_{\mathrm{surf+solv+ion}} - U_{\mathrm{surf+solv}} - U_{\mathrm{ion}} \quad \text{Eq. E.10}$$

$$-\vec{E}_{\mathrm{el}} = -\left(-\frac{U(\vec{r}_{\mathrm{ads}})-U(\vec{r}_{M+})}{\|\vec{r}_{\mathrm{ads}}-\vec{r}_{M+}\|}\right)\hat{r} \quad \text{Eq. E.11}$$

We calculated the local electric field around the $*CO_2^-$ adsorbate for different cation configurations over the last 1 ps of AIMD simulation. We applied Eq. E.10 to estimate $\vec{E}_{\mathrm{el}}$ at the position of C, O_1, and O_2 and then we plotted the averaged value versus the average between cation-(C, O_1, O_2) distances and cation-water coordination numbers. The electric field distribution is affected by both d(M^+,{C,O_1,O_2}) and the instantaneous coordination number $N(M^+–O(H_2O))$ and highest intensities are reported for low cation-water coordination numbers and short distances, in agreement with a recent theoretical characterization for electrochemical CO_2 reduction on gold.[32]

Table E.2. Cation coordination numbers to oxygen atoms in water ($N_{M+\text{-}O(H2O)}$) and CO_2 ($N_{M+\text{-}O(CO2)}$) in presence and absence of adsorbed CO_2 as calculated through Eq. E.8. Cation coordination to water molecules or CO_2 was calculated for Au-H_2O-M^+ and Au-H_2O-M^+-CO_2 during 2 ps AIMD at 300 K. Coordination numbers are reported as averages with their associated standard deviation $\sigma(N_{M^+\text{-}O})$, median, maximum, and minimum values.

	$N_{M+\text{-}O(H2O)}$ (Au-H_2O-M^+)				$N_{M+\text{-}O(H2O)}$ (Au-H_2O-M^+-CO_2)				$N_{M+\text{-}O(CO2)}$ (Au-H_2O-M^+-CO_2)			
M^+	Mean	Median	Max	Min	Mean	Median	Max	Min	Mean	Median	Max	Min
Li^+	2.8 ± 0.8	2.9	3.9	0.3	3.2 ± 0.5	3.3	3.9	1.8	0.1 ± 0.3	0.0	1.0	0.0
Na^+	3.2 ± 0.5	3.0	4.7	2.1	2.3 ± 0.4	2.3	3.0	1.2	0.9 ± 0.2	1.0	1.0	0.0
K^+	3.5 ± 0.9	3.4	4.9	1.1	3.6 ± 0.6	3.7	4.9	1.7	0.9 ± 0.4	1.0	2.0	0.0
Cs^+	5.8 ± 1.2	5.9	8.0	2.9	5.4 ± 0.9	5.4	6.9	3.6	1.3 ± 0.5	1.1	2.0	0.0

Table E.3. Average CO_2 adsorption Gibbs free energy ΔG_{*CO2} (eV) and cation induced stabilization, $\Delta\Delta G_{*CO2}$ (eV). ΔG_{*CO2} are reported with their associated standard deviations $\sigma(\Delta G_{*CO2})$. The systems under study were Au-H_2O-CO_2 and Au-H_2O-CO_2-M^+ equilibrated for 1 and 2 ps AIMD respectively. The explicit solvent layer includes 72 H_2O molecules. Those containing cations have a water molecule replaced by M^+OH.

System	ΔG_{*CO2} / eV	$\Delta\Delta G_{*CO2}$ / eV
H_2O	+0.80 ± 0.18	–
Li^+	+0.16 ± 0.24	–0.64
Na^+	+0.28 ± 0.18	–0.53
K^+	+0.41 ± 0.12	–0.39
Cs^+	+0.23 ± 0.21	–0.58

Table E.4. Average CO_2 adsorption Gibbs free energy ΔG_{*CO2} (eV), CO_2 activation angle α (degrees), Bader charges for CO_2 intermediate and cation M^+, either coordinated to CO_2 or in the reference system (CO_2 removed), reported in elementary charge ($|e^-|$) and net CO_2 surface normal electric dipole moment $\vec{p}$ reported in $|e^-|$Å. Uncertainties are given as the standard deviation of the data. For cation Bader charges, $\Delta q \leq 0.01\ |e^-|$.

System	ΔG_{*CO2} / eV	α / °	q_{CO2} / $\|e^-\|$	$q_{M+(CO2)}$ / $\|e^-\|$	$q_{M+(ref)}$ / $\|e^-\|$	$\vec{p}_{CO2}$ / $\|e^-\|$Å
H_2O	+0.80 ± 0.18	137 ± 5	–0.47 ± 0.10	–	–	+0.40 ± 0.09
Li^+	+0.16 ± 0.24	133 ± 5	–0.67 ± 0.08	–0.91	–0.90	+0.66 ± 0.11
Na^+	+0.28 ± 0.18	134 ± 5	–0.65 ± 0.08	–0.91	–0.90	+0.54 ± 0.08
K^+	+0.41 ± 0.12	136 ± 3	–0.58 ± 0.09	–0.91	–0.90	+0.54 ± 0.09
Cs^+	+0.23 ± 0.21	131 ± 4	–0.71 ± 0.08	–0.91	–0.91	+0.65 ± 0.13

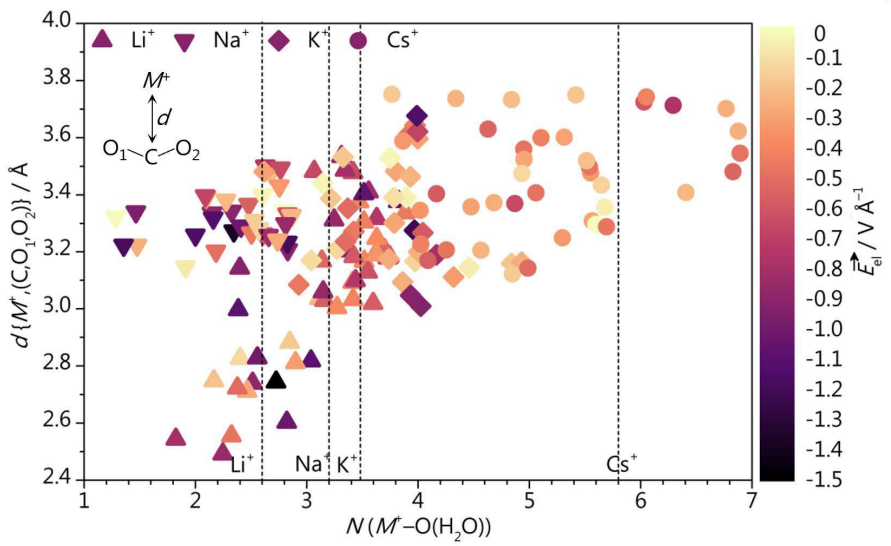

Fig. E.11. Cation-induced electric field as a function of the cation-water coordination number, $N(M^+–O(H_2O))$, (horizontal axis) and the average between cation-(C,O_1,O_2) distances (vertical axis) for different AIMD configurations. ▲, ▼, ◆, and ● represent Li^+, Na^+, K^+, and Cs^+ respectively. Dashed lines represent average cation-water coordination numbers and are taken from Table E.2.

E.4.4 Electric dipole effects

Intermediates with large electric dipole moments are affected by electrostatic fields across the electrical double layer (EDL), and their Gibbs free energy of adsorption changes according to Eq. E.12.[33] Thus, the stabilization (or destabilization) of adsorbates depends on their net electric dipole moment $\vec{p}$ and their relative orientation with respect to the electric field $\vec{E}_{\mathrm{el}}$ within the EDL. The electric field is caused by the electric potential U applied to the electrode with respect to its potential of zero charge U_{pzc} (+0.2 V vs. SHE for polycrystalline gold[34]), and the contribution of neighboring ions, $\vec{E}_{\mathrm{el-ion}}$, which is in the order of 1 V Å^{-1}.[18,31] In Eq. E.12 d stands for the thickness of the EDL, which is usually assumed around 3 Å.[19,31,33]

$$\Delta G = +\vec{p}\cdot\vec{E}_{\mathrm{el}} = +\vec{p}\cdot\left(\frac{U-U_{\mathrm{pzc}}}{d}\hat{z}+\vec{E}_{\mathrm{el-ion}}\right) \qquad \text{Eq. E.12}$$

Given the electric dipole moments calculated for adsorbed CO_2 (Table E.4), we estimated that the stabilization for CO_2^- adsorption due to dipole/electric field interactions adds up to 0.6 eV in the presence of a partially desolvated neighboring

cation ($\vec{E}_{el}$ = 1 V Å^{-1}, Fig. E.12). These values agree with the change in the Gibbs free energy of adsorption for CO_2^- due to cation-CO_2 interaction (Fig. 8.7 in Chapter 8). In the absence of a cation, a cathodic potential as negative as –3.0 V vs. RHE is required to induce an equivalent electric field. Therefore, under standard CO_2 reduction conditions the cation is key to open the reduction reaction pathway *via* explicit ionic bond with negatively charged intermediate and explicit, short-range dipole/cation-induced electric field effect.

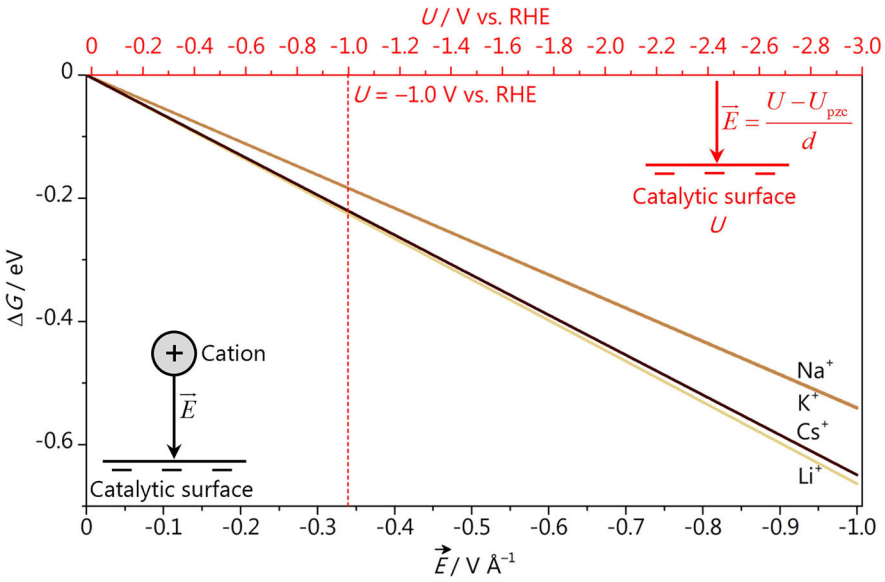

Fig. E.12. Stabilization of CO_2 adsorption due to the interaction between CO_2 dipole moment and local electric field generated by the cation (bottom axis, inset on the left). Top *x*-axis (red, inset on the right) reports the cathodic potential needed to achieve an equivalent electric field in absence of cation, according to Eq. E.12 and assuming an EDL thickness, *d*, of 3 Å.[19,31,33] Red dashed line indicates the potential applied during the study of CO production vs. Cs^+ concentration on gold (Fig. 8.2 in Chapter 8).

References

(1) Monteiro, M. C. O.; Koper, M. T. M. *Electrochim. Acta* 2019, *325*, 134915.
(2) Do, U. P.; Seland, F.; Johannessen, E. A. *J. Electrochem. Soc.* 2018, *165* (5), H219–H228.
(3) Monteiro, M. C. O.; Jacobse, L.; Touzalin, T.; Koper, M. T. M. *Anal. Chem.* 2020, *92* (2), 2237–2243.
(4) Jacobse, L.; Raaijman, S. J.; Koper, M. T. M. *Phys. Chem. Chem. Phys.* 2016, *18* (41), 28451–28457.
(5) Kresse, G.; Furthmüller, J. *Phys. Rev. B* 1996, *54*, 11169–11186.
(6) Kresse, G.; Furthmüller, J. *Comput. Mater. Sci.* 1996, *6*, 15–50.
(7) Perdew, J. P.; Burke, K.; Ernzerhof, M. *Phys. Rev. Lett.* 1996, *77*, 3865–3868.
(8) Grimme, S. *J. Comput. Chem.* 2006, *27*, 1787–1799.
(9) Bucko, T.; Hafner, J.; Lebègue, S.; Ángyán, J. G. *J. Phys. Chem. A* 2010, *114*, 11814–11824.
(10) Almora-Barrios, N.; Carchini, G.; Błoński, P.; López, N. *J. Chem. Theory Comput.* 2014, *10* , 5002–5009.
(11) Blöchl, P. E. *Phys. Rev. B* 1994, *50*, 17953–17979.
(12) Kresse, G.; Joubert, D. *Phys. Rev. B* 1999, *59*, 1758–1775.
(13) Bellarosa, L.; García-Muelas, R.; Revilla-López, G.; López, N. *ACS Cent. Sci.* 2016, *2* (2), 109–116.
(14) Marx, D.; Hutter, J. Cambridge University Press, 2009.
(15) Nosé, S. *J. Chem. Phys.* 1984, *81*, 511–519.
(16) Hoover, W. G. *Phys. Rev. A* 1985, *31*, 1695–1697.
(17) Makov, G.; Payne, M. *Phys. Rev. B* 1995, *51*, 4014–4022.
(18) Resasco, J.; Chen, L. D.; Clark, E.; Tsai, C.; Hahn, C.; Jaramillo, T. F.; Chan, K.; Bell, A. T. *J. Am. Chem. Soc.* 2017, *139* (32), 11277–11287.
(19) Nørskov, J. K.; Rossmeisl, J.; Logadottir, A.; Lindqvist, L.; Kitchin, J. R.; Bligaard, T.; Jónsson, H. *J. Phys. Chem. B* 2004, *108* (46), 17886–17892.
(20) Haynes, W. M. 95th ed.; CRC Press: New York, 2014.
(21) Lide, D. R. 84th ed.; Lide, D. R., Ed.; CRC Press, 2003; Vol. 85.
(22) Álvarez-Moreno, M.; de Graaf, C.; López, N.; Maseras, F.; Poblet, J. M.; Bo, C. *J. Chem. Inf. Model.* 2015, *55* (1), 95–103.
(23) Dattila, F. *ioChem-BD* 2021, DOI 10.19061/iochem-bd-1-194.
(24) Monteiro, M. C. O.; Jacobse, L.; Koper, M. T. M. *J. Phys. Chem. Lett.* 2020, *11* (22), 9708–9713.
(25) Henckel, D. A.; Counihan, M. J.; Holmes, H. E.; Chen, X.; Nwabara, U. O.; Verma, S.; Rodríguez-López, J.; Kenis, P. J. A.; Gewirth, A. A. *ACS Catal.* 2021, *11* (1), 255–263.
(26) Macao, L. H.; Santos, M. C.; Machado, S. A. S.; Avaca, L. A. *J. Chem. Soc. - Faraday Trans.* 1997, *93* (22), 3999–4003.
(27) Lukaszewski, M.; Soszko, M.; Czerwiński, A. *Int. J. Electrochem. Sci.* 2016, *11* (6), 4442
(28) Waegele, M. M.; Gunathunge, C. M.; Li, J.; Li, X. *J. Chem. Phys.* 2019, *151* (16), 160902.
(29) Marcus, Y. *Chem. Rev.* 1988, *88* (8), 1475–1498.
(30) Dattila, F.; García-Muelas, R.; López, N. *ACS Energy Lett.* 2020, *5*, 3176–3184.
(31) Chen, L. D.; Urushihara, M.; Chan, K.; Nørskov, J. K. *ACS Catal.* 2016, *6* (10), 7133–7139.
(32) Zhu, Q.; Wallentine, S.; Deng, G.; Baker, L. R. 2021, DOI: 10.26434/chemrxiv.14410655
(33) McCrum, I. T.; Bondue, C. J.; Koper, M. T. M. *J. Phys. Chem. Lett.* 2019, *10* (21), 6842–6849.
(34) White, R. E.; Bockris, J. O.; Conway, B. E. Kluwer Academic Publishers, 2002.

F

Methods and supporting information to Chapter 9

F.1 Methods

F.1.1 Electrode preparation

Gold disc electrodes were cut from a polycrystalline gold foil (0.5 mm thick, MaTecK, 99.995%) and prepared by polishing and flame annealing according to the procedure we have previously described.[1] The gold electrode cleanliness was assured by Scanning Electron Microscopy (SEM) performed using an Apreo SEM (ThermoFisher Scientific). Micrographs were obtained using an acceleration voltage of 10 kV and an electron beam current of 0.4 nA. Additionally, elemental analysis of the surface composition was performed using Energy Dispersive X-Ray Spectrometry (EDX) (Oxford Instruments X-Max^N 150 Silicon Drift detector). The EDX data was processed using the Pathfinder™ X-ray Microanalysis software v1.3. The SEM micrographs and EDX spectra are shown in Fig. F.1. Establishing surface cleanliness is crucial when studying cation effects on CO_2RR and HER as we have previously shown that, for instance, polishing alumina particles can contaminate the gold surface and promote water reduction by the release of Al^{3+} ions in an acidic electrolyte.[1]

F.1.2 Materials

Appropriate amounts of the following salts were employed to prepare the electrolytes used in this work: Li_2SO_4 (Alfa Aesar, anhydrous, 99.99%, metal basis), Na_2SO_4 (Alfa Aesar, anhydrous, 99.99%, metal basis), K_2SO_4 (Sigma Aldrich, anhydrous, 99.99%, metal basis), Cs_2SO_4 (Alfa Aesar, Puratronic®, 99.997%, metals basis), $BeSO_4$ (Alfa Aesar, tetrahydrated, 99.99%, metal basis), $MgSO_4$ (Sigma Aldrich, ≥ 99.99%, trace metal basis), $Al_2(SO_4)_3$ (Sigma Aldrich, 99.99%, trace metal basis), $Nd_2(SO_4)_3$ (Sigma Aldrich, 99.99%, trace metal basis), $Ce_2(SO_4)_3$ (Sigma Aldrich, ≥ 99.99%, trace metal basis), $LiClO_4$ (Sigma Aldrich, 99.99%, trace metal basis), $CsClO_4$ (Sigma Aldrich, 99.99%, trace metal basis), $Mg(ClO_4)_2$ (American Elements, 99.99%), $Ca(ClO_4)_2$ (American Elements, tetrahydrated, 99.99%), $Ba(ClO_4)_2$ (Sigma Aldrich, 99.999%), Li_2CO_3 (Merck, 99.99%, trace metal basis), $NaHCO_3$ (Sigma Aldrich, ≥99.7%, ACS reagent), $KHCO_3$ (Sigma Aldrich, ≥99.95%, trace metal basis), Cs_2CO_3 (Merck, 99.9%, trace metal basis), H_2SO_4 (Merck, Suprapur, 96%). The carbonate and bicarbonate electrolytes were purified by long term electrolysis prior to the experiments. Two large surface area gold electrodes were used and a potential of –2 V was applied for 12 hours, similarly to the procedure reported elsewhere.[2] The pH of the electrolytes prepared was certified using a glass-

electrode pH meter (Lab 855, SI Analytics) calibrated with standard buffer solutions (Radiometer Analytical). The experiments were performed in a one-compartment, three-electrode cell with the gold working electrode in hanging meniscus configuration. The glassware used in this work was stored in potassium permanganate solution (1 g L^{-1} $KMnO_4$ dissolved in 0.5 M H_2SO_4) overnight and cleaned by immersion in dilute piranha. Subsequently, the glassware was boiled at least five times in ultrapure water (>18.2 MΩ cm, Millipore Milli-Q). A gold wire (0.8 mm thick, Mateck, 99.9%) was used as counter electrode and a reversible hydrogen electrode (RHE) or a Hydroflex (Gaskatel) as reference, connected to the cell via a Luggin capillary.

F.1.3 Electrochemical measurements

Experiments were carried out using a Bio-Logic potentiostat/galvanostat/EIS (SP-300). The gold electrode was characterized before each experiment by recording a cyclic voltammogram between 0 and 1.75 V vs. RHE in 0.1 M H_2SO_4 at 50 mV s^{-1}. The gold electrochemical surface area (ECSA) was determined by calculating the charge corresponding to the gold oxide reduction. This value was converted to ECSA using the charge density associated with the reduction of a monolayer of gold oxide (386 µC cm^{-2}).[3] Hydrogen evolution or CO_2 reduction were conducted after purging the electrolyte with either argon or CO_2 for at least 20 minutes. During the experiments, the respective gas flow was kept above the electrolyte, to avoid oxygen diffusion into the solution. Before each measurement, the solution resistance was determined by Electrochemical Impedance Spectroscopy (EIS) and the electrode potential was compensated for 85% of the ohmic drop. The potential opening CO_2 reduction experiments were performed by cycling the gold electrode from 0.1 V vs. RHE to different negative potentials and in the reverse scan up to 1.3 V vs. RHE. In between two different potential steps the electrode potential was held at 0.1 V vs. RHE for four minutes to recover from the concentration (pH) gradients developed in the diffusion layer during the cathodic scan.

F.1.4 Density functional theory modeling

Density functional theory (DFT) simulations were performed using the Vienna Ab Initio Simulation Package(VASP),[4,5] with the PBE density functional.[6] To properly account for dispersion, we applied the DFT-D2 method,[7,8] with the C_6 coefficients reparametrized from one of our groups.[9] Inner electrons were represented by PAW

pseudopotentials[10,11] and the monoelectronic states for valence electrons were expanded as plane waves with a kinetic energy cutoff of 450 eV. *Ab initio* molecular dynamics were applied on the Au/water/cation system (see Computational model) for 4 ps (1 fs time step) in a canonical NVT ensemble at 300 K regulated by a Nosé-Hoover thermostat.[12–15]. To account for the self-interaction error due to the localized *f* electrons of Nd^{3+}, we applied a Hubbard correction U_{eff} = 6.76 eV – 0.76 eV following the Dudarev´s approach,[16] taken from a study of electronic and magnetic properties of a Nd adatom.[17]

F.2 Experimental

F.2.1 Gold electrode characterization

Scanning Electron Microscopy (SEM) and Energy Dispersive X-Ray Spectroscopy (EDX) of the gold electrode used in this study.

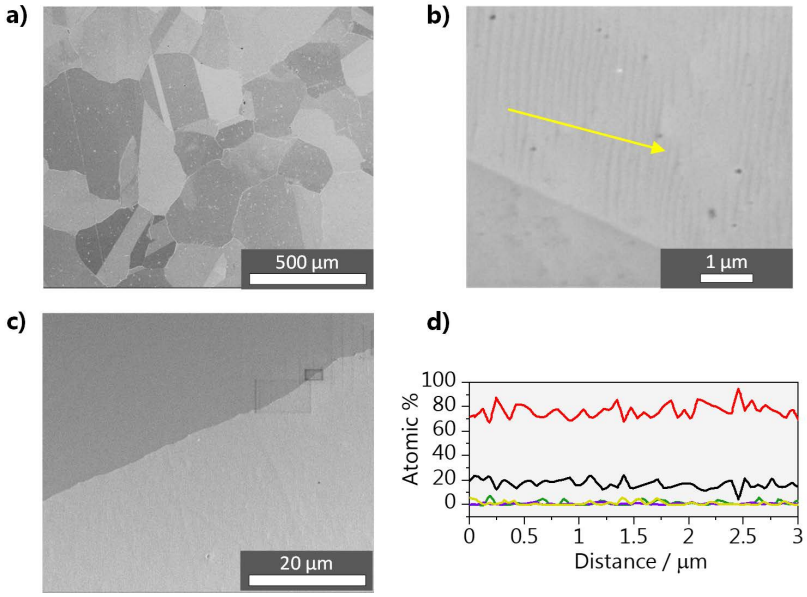

Fig. F.1. a)-c) SEM micrographs and **d)** EDX line spectra of the gold electrode (region marked with a yellow arrow) used for the experiments after polishing with diamond suspension and flame annealing. The lines refer to the following signals: — (black) C K, — (green) O K, — (purple) Al K and — (red) Au M.

F.2.2 Potential opening experiments at pH 3 (0.1 M M_2SO_4)

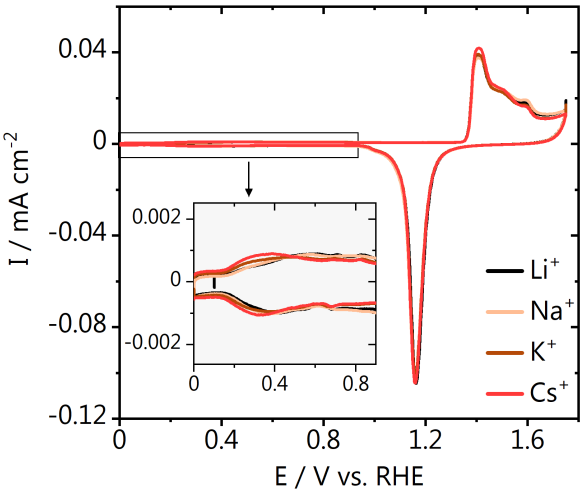

Fig. F.2. Blank voltammetry of the gold electrode after flame annealing taken at 50 mV s^{-1} in 0.1 H_2SO_4.

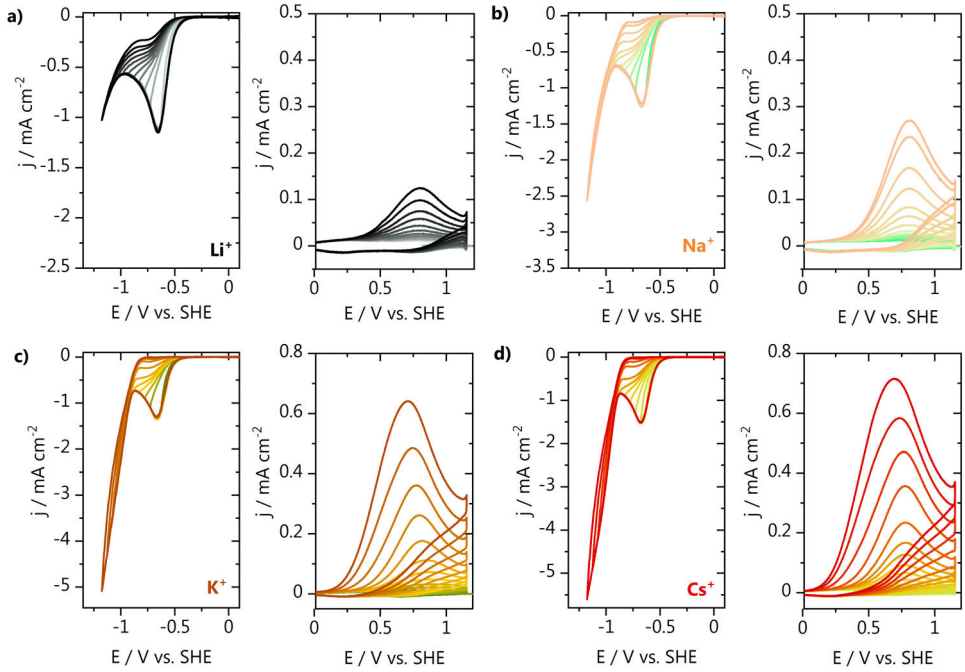

Fig. F.3. a)-d) Consecutive cathodic/anodic voltammetry of the CO_2 reduction potential opening experiments in 0.1 M M_2SO_4 with M^{n+} = Li^+, Na^+, K^+, Cs^+ at pH = 3.

F.2.3 HER and CO_2RR experiments at pH 6.8 (0.1 M MHCO$_3$)

Blank voltammetry of the gold electrode taken before the experiments performed at pH 6.8 in 0.1 M MHCO$_3$ electrolytes with M^{n+} = Li^+, Na^+, K^+ and Cs^+.

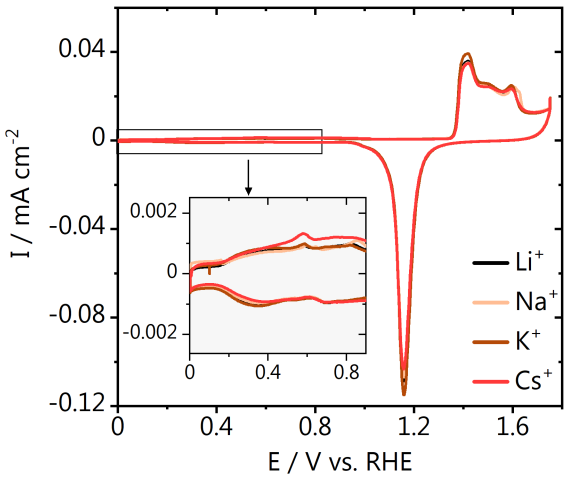

Fig. F.4. Blank voltammetry of the gold electrode after flame annealing taken at 50 mV s^{-1} in 0.1 H_2SO_4.

Similarly to our experiments in acidic media, in bicarbonate the CO produced in the cathodic scan can also be detected in the positive-going scan. The inset of Fig. F.5b, shows the CO produced after the gold electrode is polarized negatively and that the highest amount of CO is produced in the Cs^+ and K^+ electrolytes. The two peaks observed in the CO oxidation voltammetry in bicarbonate are due to diffusion limitation by two different species, namely, CO and OH^-, as a function of the local pH. In our previous work, we find that between pH 7 and 11, CO oxidation by water and OH^- gives rise to the first and second peak observed in the voltammetry, respectively, and that the current of the second peak is diffusion limited by the OH^- concentration, since it is lower than the CO concentration at this pH.[18]

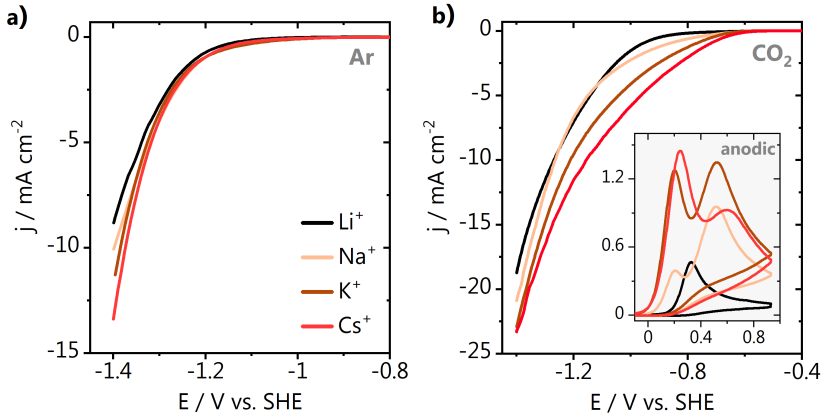

Fig. F.5. Cyclic voltammetry of **a)** water reduction and **b)** CO_2 reduction in 0.1 M MHCO$_3$, pH 9 (argon atmosphere) and pH 7 (CO_2 atmosphere).

F.2.4 Hydrogen evolution in electrolytes containing multivalent cations

Blank voltammetry of the gold electrode before the experiments performed at pH 3 in 0.1 M Li_2SO_4 + 1 mM M^{n+} electrolytes with M^{n+} = Li^+, Cs^+, Be^{2+}, Mg^{2+} , Al^{3+} , Nd^{3+} , Ce^{3+} and 0.2 M $LiClO_4$ + 2 mM M^{n+} with M = Ca^{2+}, Ba^{2+}.

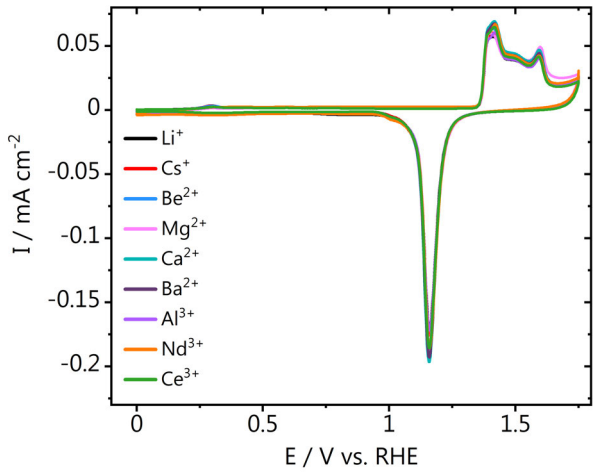

Fig. F.6. Blank voltammetry of the gold electrode after flame annealing taken at 50 mV s^{-1} in 0.1 H_2SO_4. The blank CVs were taken before the HER experiments performed in the presence of the different cations.

CVs of the gold electrode during hydrogen evolution performed at pH 3 in 0.1 M Li_2SO_4 + 1 mM M^{n+} electrolytes with M^{n+} = Li^+, Cs^+, Be^{2+}, Mg^{2+}, Al^{3+}, Nd^{3+}, Ce^{3+} and 0.2 M $LiClO_4$ + 2 mM M^{n+} with M^{n+} = Ca^{2+}, Ba^{2+}. All electrolytes were saturated with Argon prior to the measurements.

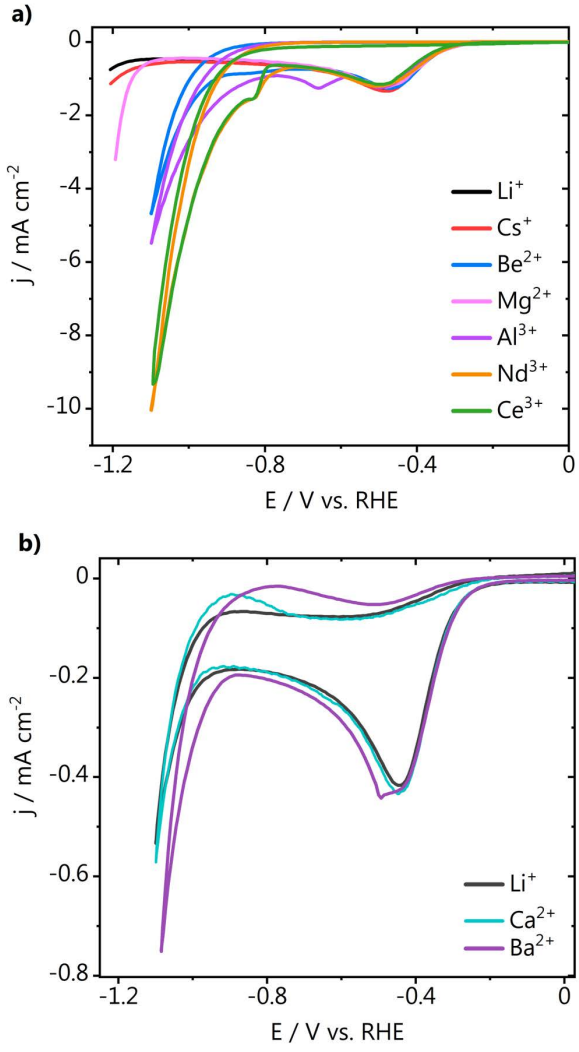

Fig. F.7. Cyclic voltammetry of HER in **a)** 0.1 M Li_2SO_4 or **b)** 0.1 M $LiClO_4$ electrolyte solutions containing different cations.

Relationship between cation acidity and Gibbs free energy of hydration.[19]

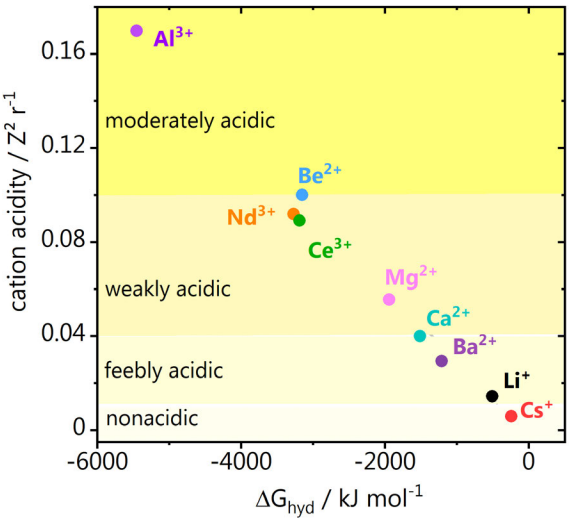

Fig. F.8. Cation acidity and Gibbs free energy of hydration for the different multivalent cations used in this work.

Fig. F.9 shows the CVs of HER and the effect of cation hydrolysis on the first and second regimes of proton reduction and on hydroxide deposition.

F.3 Density functional theory modeling

We carried out density functional theory (DFT) simulations through the Vienna Ab Initio Package (VASP).[4,5] We chose the PBE density functional[6] including dispersion through the DFT-D2 method,[7,8] with our reparametrized C_6 coefficients.[9] Inner electrons were represented by PAW pseudopotentials[10,11] and the monoelectronic states for the valence electrons were expanded as plane waves with a kinetic energy cutoff of 450 eV. Since Nd presents a localized *f* electron, which leads to self-interaction error, we applied a Hubbard correction U_{eff} = 6.76 eV – 0.76 eV to the Nd atom following the Dudarev's approach.[16] This value was taken from a previous computational work, where the authors assessed electronic and magnetic properties for a Nd adatom.[17]

We modeled the experimental system as in Chapter 8.[15] We employed a $3\sqrt{3}\times3\sqrt{3}$–*R*30° Au(111) supercell, which included 4 layers with 15.3 Å × 15.3 Å lateral dimensions and overall thickness 30.0 Å (8 Å vacuum). The solvation layer accounted for 72 H_2O molecules within 15 Å and it was retrieved from our work mentioned above.[15] During that study,[15,20] the system was optimized for more than

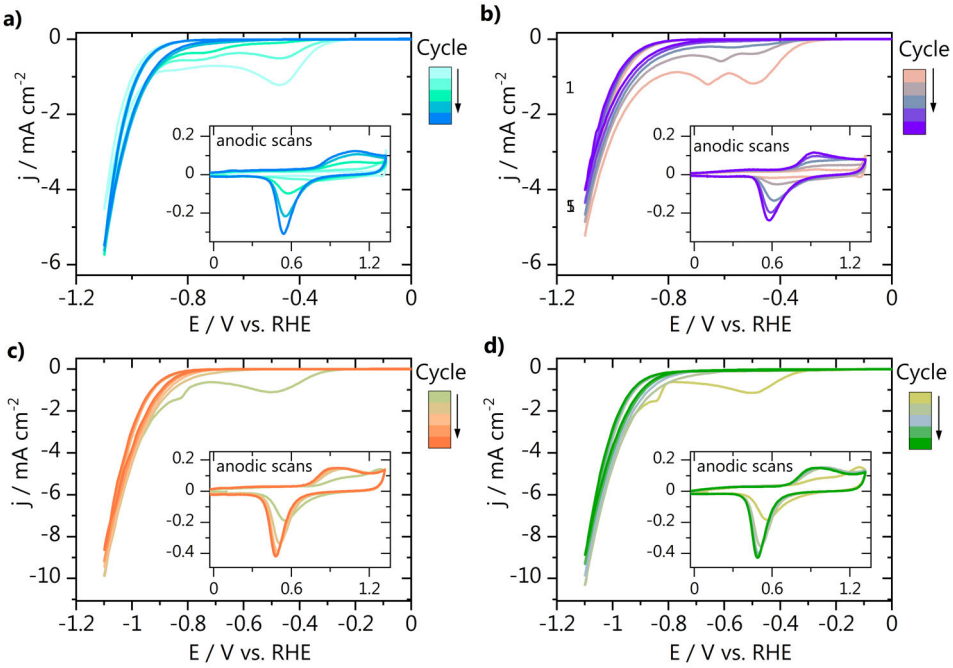

Fig. F.9. Hydrogen evolution cyclic voltammetry performed at pH 3 in 0.1 M Li_2SO_4 + 1 mM M^{n+} electrolytes with M^{n+} being **a)** Be^{2+}, **b)** Al^{3+}, **c)** Nd^{3+}, **d)** Ce^{3+}. An anodic scan recorded directly after HER is shown in the graph inset.

10 ps via AIMD simulation in a canonical NVT ensemble at 300 K regulated by a Nosé-Hoover thermostat.[12–15]. We introduced two cations M^{n+} (Li^+, Cs^+, Mg^{2+}, Ba^{2+}, Al^{3+}, Nd^{3+}) within the first solvation layer, whilst we removed $2n$ hydrogens from water molecules in the fourth water bilayer to keep charge balance (n = cation charge). Considering the thickness of the solvation layer (1.4 nm), the geometrical area (2.0 nm^2) and the overall number of solvent molecules (72), a cation surface coverage of 0.08 ML (2/27) is equivalent to a surface concentration between 1.0 ($2/N_A$ mol within a volume of 3.29 nm^3) and 1.6 M (2/72 of water molar concentration, 55.5 M). Besides, to better mimic explicit electrostatic effects, we applied an electric field of –0.3 V $Å^{-1}$,[9,21] equivalent to a potential of –0.9 V vs. potential of zero charge (U_{PZC}), assuming an electrical double layer thickness of 3 Å.[22,23] Since the U_{PZC} for polycrystalline gold is reported as +0.2 V vs SHE,[24] the applied electric field is equivalent to an electric potential of –0.7 V vs. SHE, Eq. F.1.

$$U\,(\mathrm{vs.\,SHE}) = U_{\mathrm{PZC}} + \vec{E}_{\mathrm{EDL}} \cdot d_{\mathrm{EDL}} \qquad \text{Eq. F.1}$$

The Au/water/cation systems underwent 2 ps of AIMD simulations. Finally, we added either a CO_2 or an additional water molecule (0.04 ML, 1/27) to the equilibrated Au/water and Au/water/cations model, which adsorbed on the surface close to one of the cations. Besides, to check a reference case with proton as the cation, we replaced the 2 optimized Li^+ atoms in the Au/H_2O/Li^+ systems with H^+. The resulting 6 Au/water/M^{n+}/*ads* and 1 Au/water/H^+/*ads* systems (*ads* = *CO_2, *H_2O) were further optimized for 2 ps to assess the activation of CO_2 and H_2O in the presence and absence of a metal cation. Since cations, adsorbates CO_2, and the explicit solvation later were placed only on one side of the slab, we applied an additional dipole correction to remove spurious contributions arising from the asymmetric slab model.[25]

F.3.1 Cation-water radial distribution functions

We obtained the cation-water radial distribution functions, $g_{M^{n+}\text{-}H2O}(r)$ from the 2 ps equilibration of the Au/water/M^{n+} systems to estimate the density of water molecules around the two M^{n+} centers introduced in the supercell. First, we calculated the distribution of distances of H_2O oxygens from the cation, $\eta(r)$, defined for all the molecular dynamics steps within an interval (r, $r + \Delta r$), where r is the position vector from M^{n+} and Δr is its differential. We then normalized $\eta(r)$ for the surface density of cations ρ corresponding to 2D annulus formed by the solvation layer, Eq. F.2.

$$g(r)_{2D} = \frac{\eta(r)}{2\pi r \cdot \Delta r \cdot \rho} \qquad \text{Eq. F.2}$$

In Eq. F.2, $g(r)$ is the radial distribution function (dimensionless), $\eta(r)$ the distribution of distances (dimensionless), r the position vector, Δr its differential (both in Å), and ρ the cation surface density (Å^{-2}). Cation-water radial distribution functions are reported in Fig. F.10 and the parameters of the Lorentzian fit on the first solvation shell peaks are shown in Table F.1. A Lorentzian fit was applied through Eq. F.3, as in Ref. 15.

$$g(r) = g(r)_0 + \left(\frac{2A}{\pi}\right) \cdot \left(\frac{w}{4(r - d_{M-O})^2 + w^2}\right) \qquad \text{Eq. F.3}$$

where $g(r)$ is the radial distribution function, r the position vector (Å), w the full width at half maximum (Å), $d_{M+\text{-}O}$ the cation-oxygen bond length (Å), whilst $g(r)_0$ (dimensionless) and A (Å) are fit parameters. The parameters of the Lorentzian fit

and the resulting estimation of the cation-oxygen distances in the first solvation shell are reported in Table F.1 and agree with previous experimental and theoretical reports.[26,27] The cation-oxygen bond length ($d_{M\text{-}O}$) and its associated uncertainty are obtained from the fit parameters on the $g(r)$ first peaks. The term $d_{M\text{-}O(S.A.)}$ stands for averages of state-of-the-art values for cation-water distances.[26,27]

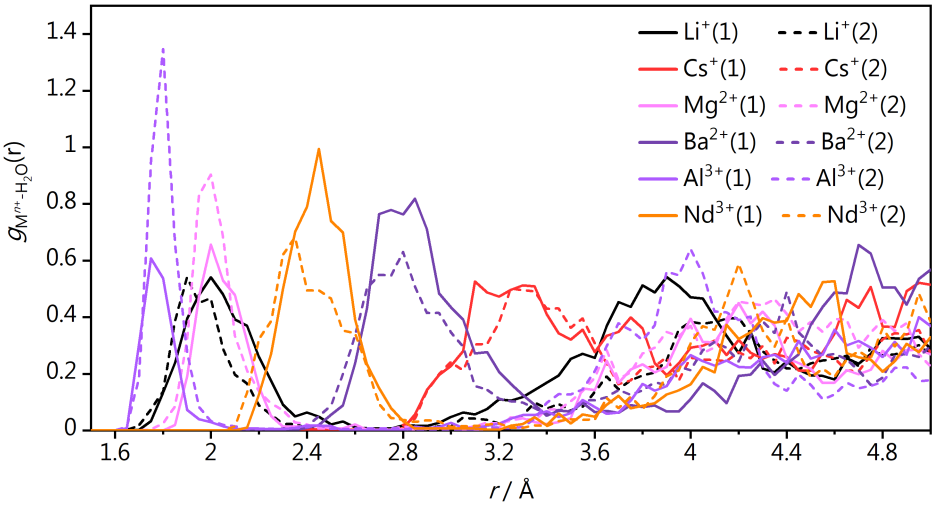

Fig. F.10. Cation solvation shells during 2 ps equilibration (0-2 ps) of the Au/water/M^{n+}, described by the cation-water radial distribution functions.

Table F.1. Parameters of the Lorentzian fit and distances between cation and water molecules in the first solvation shell, estimated from the position of the first peak of cation-water radial distribution functions, Fig. F.10, for an AIMD equilibration of 2 ps. $g(r)_0$, A, w (Å) and χ^2_v are fit parameters. Uncertainty associated with fit parameters is given as standard deviation of the data, whilst uncertainty related to averages of state-of-the-art values for cation-water distances, $d_{M\text{-}O(S.A.)}$, is taken from Ref. 26 and 27.

M^{n+}	$g(r)_0$	A / Å	w / Å	χ^2_v	$d_{M\text{-}O}$ / Å	$d_{M\text{-}O(S.A.)}$ / Å
Li^+(1)	–0.030 ± 0.009	0.281 ± 0.018	0.31 ± 0.02	1.1E–03	2.021 ± 0.006	2.08 ± 0.07
Li^+(2)	–0.022 ± 0.008	0.206 ± 0.013	0.233 ± 0.018	1.1E–03	1.945 ± 0.005	
Cs^+(1)	–0.09 ± 0.02	0.35 ± 0.05	0.48 ± 0.07	3.5E–03	3.275 ± 0.017	3.14 ± 0.08
Cs^+(2)	–0.057 ± 0.013	0.34 ± 0.04	0.46 ± 0.05	2.7E–03	3.326 ± 0.015	
Mg^{2+}(1)	–0.031 ± 0.012	0.214 ± 0.017	0.196 ± 0.018	2.1E–03	2.028 ± 0.005	2.09 ± 0.04
Mg^{2+}(2)	–0.023 ± 0.011	0.241 ± 0.013	0.154 ± 0.010	2.0E–03	1.996 ± 0.003	
Ba^{2+}(1)	–0.028 ± 0.013	0.49 ± 0.03	0.36 ± 0.03	3.6E–03	2.826 ± 0.007	2.81
Ba^{2+}(2)	–0.025 ± 0.010	0.40 ± 0.02	0.40 ± 0.03	1.8E–03	2.798 ± 0.008	
Al^{3+}(1)	–0.012 ± 0.007	0.124 ± 0.008	0.110 ± 0.10	9.6E–04	1.772 ± 0.002	1.887 ± 0.015
Al^{3+}(2)	–0.026 ± 0.011	0.232 ± 0.011	0.102 ± 0.006	2.4E–03	1.791 ± 0.002	
Nd^{3+}(1)	–0.042 ± 0.011	0.41 ± 0.02	0.259 ± 0.015	2.4E–03	2.445 ± 0.004	2.472 ± 0.033
Nd^{3+}(2)	–0.039 ± 0.015	0.37± 0.03	0.34 ± 0.03	3.1E–03	2.384 ± 0.009	

F.3.2 Cation coordination number

To obtain the coordination number $N_{M\text{-}O}$ of the multivalent cations M^{n+}, we assigned a bond value equal to one if the cation-oxygen distance $r_{M\text{-}O}$ was equal or lower than the cation-oxygen bond length $d_{M\text{-}O}$, Table F.1. Otherwise, the bond value was set to zero if $r_{M\text{-}O}$ was larger than a certain threshold $th_{M\text{-}O}$: 2.5, 3.5, 2.4, 3.5, 2.0, 2.8 Å for Li^+, Cs^+, Mg^{2+}, Ba^{2+}, Al^{3+}, Nd^{3+} respectively (Fig. F.10). Between these extremes, $N_{M\text{-}O}$ was calculated through Eq. F.4 following a decay controlled by the error function (erf), Eq. F.5.[28] In Eq. F.4, $N_{M\text{-}O}$ is the cation coordination number (dimensionless), $r_{M\text{-}O}$ is the cation-oxygen distance (Å), $d_{M\text{-}O}$ the cation-oxygen bond length (Å), $th_{M\text{-}O}$ the cation-oxygen threshold (Å) and avg stands for average. In Eq. F.5, t (dimensionless) is the variable of integration and 0 and z represent the integration limits.

$$N_{M-O} = \frac{1}{2} - \frac{1}{2}\,\mathrm{erf}\left(\frac{r_{M-O} - \mathrm{avg}(d_{M-O}, th_{M-O})}{0.2\ \text{Å}}\right) \qquad \text{Eq. F.4}$$

$$\mathrm{erf}\,(z) = \frac{2}{\sqrt{\pi}} \int_0^z \exp(-t^2)\,dt \qquad \text{Eq. F.5}$$

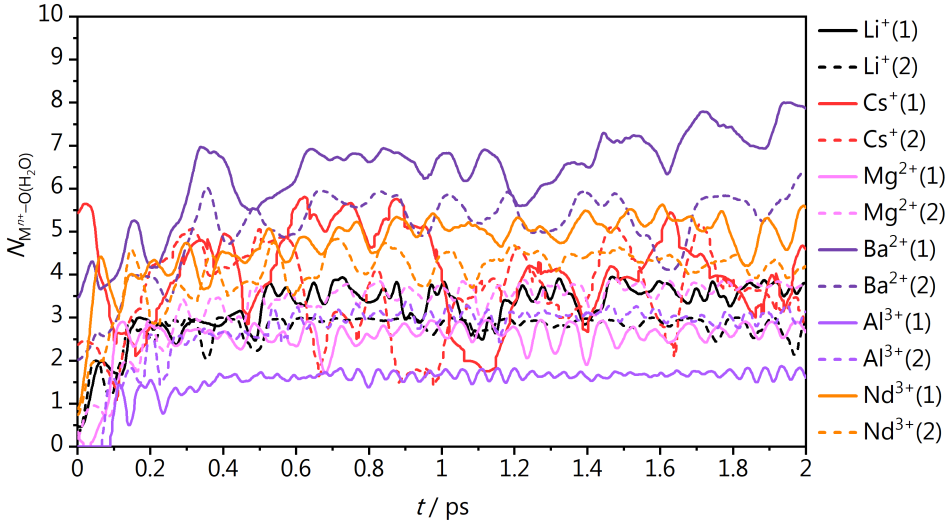

Fig. SF.11. Cation coordination numbers to oxygen atoms in water ($N_{M\text{-}O(H2O)}$) during equilibration of the Au/water/M^{n+} system (from 0 to 2 ps).

Table F.2. Cation coordination numbers to oxygen atoms in water ($N_{M\text{-}O(H2O)}$) as calculated through Eq. F.4 for Au/water/M^{n+} during 2 ps AIMD at 300 K (Fig. F.11). Coordination numbers are reported as averages with their associated standard deviation $\sigma(N_{M\text{-}O})$, median, maximum, and minimum values.

	$N_{M\text{-}O(H2O)}$ (Au/water/M^{n+})			
M^{n+}	Mean	Median	Max	Min
$Li^{+}(1)$	3.5 ± 0.3	3.6	3.9	2.5
$Li^{+}(2)$	2.8 ± 0.2	2.9	3.0	2.1
$Cs^{+}(1)$	3.7 ± 0.9	3.9	5.4	1.7
$Cs^{+}(2)$	3.7 ± 0.7	3.7	5.2	2.0
$Mg^{2+}(1)$	2.6 ± 0.2	2.7	2.9	1.9
$Mg^{2+}(2)$	3.6 ± 0.2	3.7	3.9	3.0
$Ba^{2+}(1)$	6.9 ± 0.6	6.9	8.0	5.6
$Ba^{2+}(2)$	5.4 ± 0.5	5.6	6.5	4.1
$Al^{3+}(1)$	1.68 ± 0.08	1.7	1.9	1.5
$Al^{3+}(2)$	3.03 ± 0.14	3.1	3.3	2.4
$Nd^{3+}(1)$	5.1 ± 0.3	5.1	5.6	4.2
$Nd^{3+}(2)$	4.3 ± 0.2	4.3	4.7	3.7

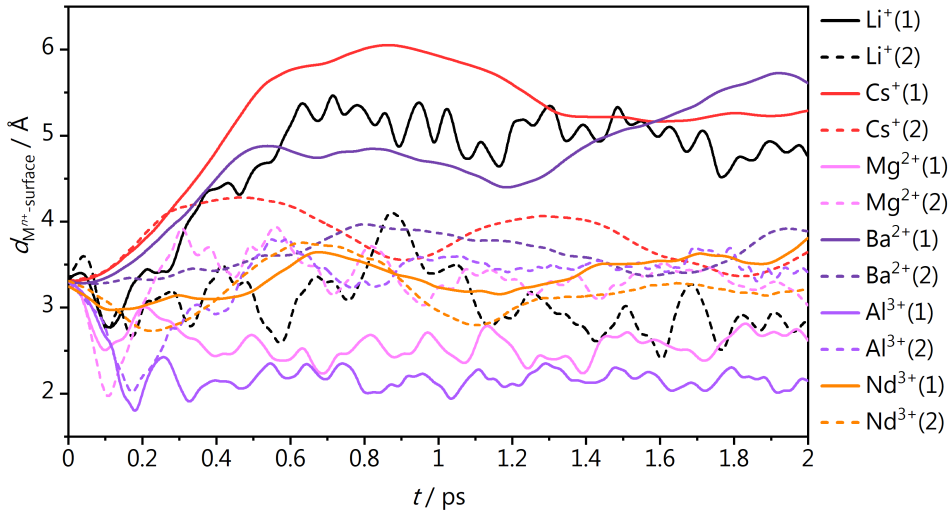

Fig. F.12. Distance between cation (M^{n+}) and surface calculated during equilibration of the Au/water/M^{n+} system (from 2 to 4 ps).

F

F.3.3 Cation accumulation at the Outer Helmholtz layer

To assess the thermodynamics of cation accumulation at outer Helmholtz plan (OHP), we applied the methodology introduced by Resasco et al.[29] The energy of a solvated cation at the bulk electrolyte can be referenced to the energy of the bulk metal following the principles of the Computational Hydrogen Electrode.[30] In the following lines, we define such methodology for the case of alkali cations, which can be easily generalized to multivalent species. At the standard reduction potential U^0,[31] a cation M^+ is in equilibrium with its reduced state M, Eq. F.6. Thus, we can derive the energy of the cation/electron pair at a given potential U vs SHE from the DFT energy of the bulk alkali metal, Eq. F.7.

$$\mathrm{M^+ + e^- \leftrightarrow M},\ U = U^0 \qquad \text{Eq. F.6}$$

$$E_{\mathrm{M^+ + e^-}} = E_{\mathrm{M}} - |\mathrm{e^-}|\ (U - U^0) \qquad \text{Eq. F.7}$$

We can instead estimate the energy of a cation at the OHP at U = 0 V vs SHE from our *ab initio* molecular dynamics simulations, since we specifically inserted two metals at the OHP, which donate their valence electron to the solvation layer,

Eq. F.8. * accounts for the gold surface and the label env for the environment, i.e. the solvation layer and the second cation. Thus, we can calculate the thermodynamic driving force for one of the two cations to accumulate at the OHP as in Eq. F.9 for 50 AIMD snapshots after 1 ps equilibration (every 20 fs from 1 ps to 2 ps).

$$* + \mathrm{env} + \mathrm{M} \rightarrow * + \mathrm{env} + \mathrm{M}^{+} + \mathrm{e}^{-}, E_{\mathrm{M}^{+}+\mathrm{e}^{-}}(\mathrm{OHP}) \qquad \text{Eq. F.8}$$

$$\Delta E = E_{\mathrm{M}^{+}+\mathrm{e}^{-}}(\mathrm{OHP}) - E_{\mathrm{M}^{+}+\mathrm{e}^{-}}(\mathrm{bulk}) \qquad \text{Eq. F.9}$$

Table F.3. Fit parameters for linear correlations shown in Fig. F.13.

$$E_{\mathrm{OHP}} - E_{\mathrm{bulk}} = a + b * d_{\mathrm{M}^{n+}-\mathrm{surface}}$$

M^{n+}	a / eV	b / eV Å^{-1}	R^2
Li^+	+2.61 ± 0.07	–0.45 ± 0.02	0.87
Cs^+	+2.05 ± 0.09	–0.30 ± 0.02	0.70
Mg^{2+}	+10.5 ± 0.3	–2.97 ± 0.08	0.93
Ba^{2+}	+5.5 ± 0.2	–0.93 ± 0.04	0.84
Al^{3+}	+14.5 ± 0.2	–4.00 ± 0.06	0.98
Nd^{3+}	+8.0 ± 0.5	–2.1 ± 0.2	0.65

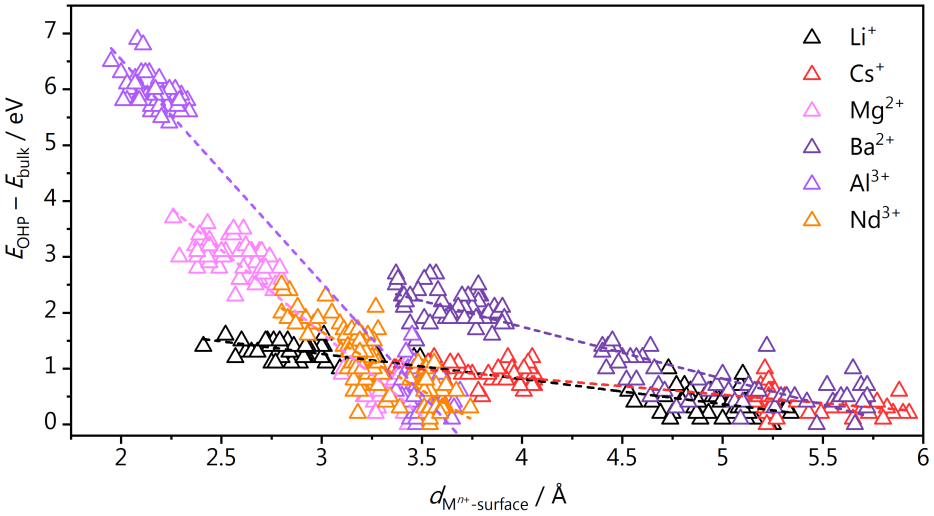

Fig. F.13. Correlation between the thermodynamic driving force for cation accumulation at the OHP estimated at U = 0 V versus SHE and cation-surface distance. The data points have been referenced to the minimum for each cation, respectively –2.4, –2.2, –6.7, –8.1, –11.4, –8.5 eV for Li^+, Cs^+, Mg^{2+}, Ba^{2+}, Al^{3+}, and Nd^{3+}. All the data points are therefore negative, confirming that cation accumulation at the OHP is an exothermic process.

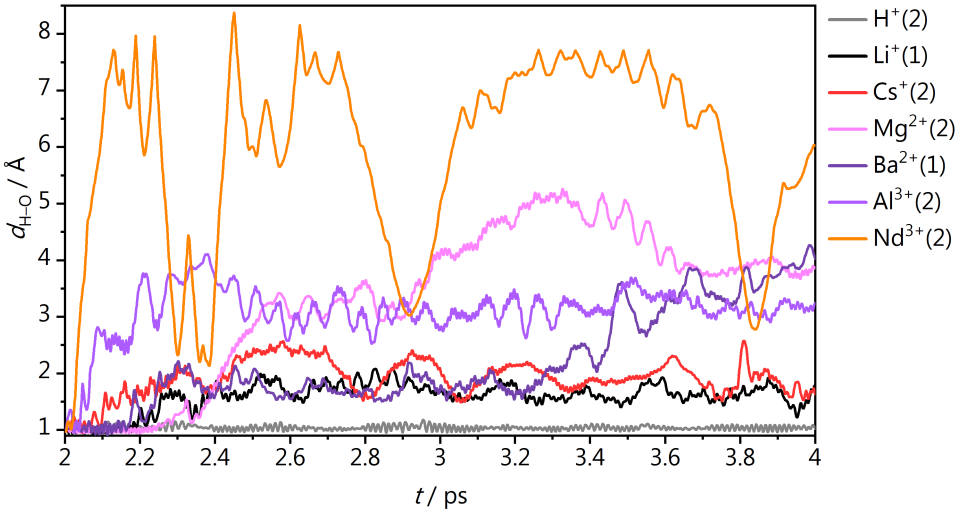

Fig. F.14. H-O Distances in the adsorbed water molecule for the Au/water/M^{n+}/*H_2O system (from 2 to 4 ps). For all the metal cations *H_2O dissociates into OH^- and H^+ after less than 0.3 ps.

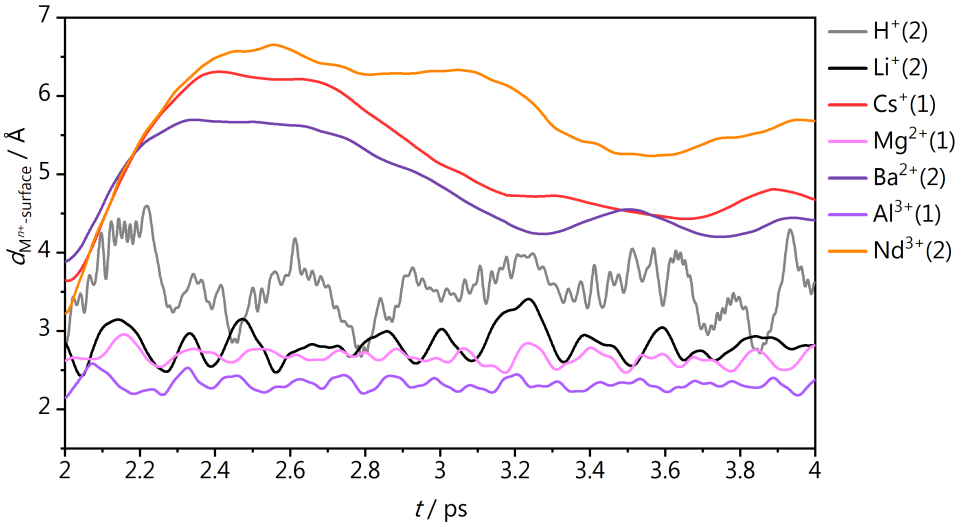

Fig. F.15. Distance between cation (M^{n+}) and surface calculated for the Au/water/M^{n+}/*H_2O system (from 2 to 4 ps).

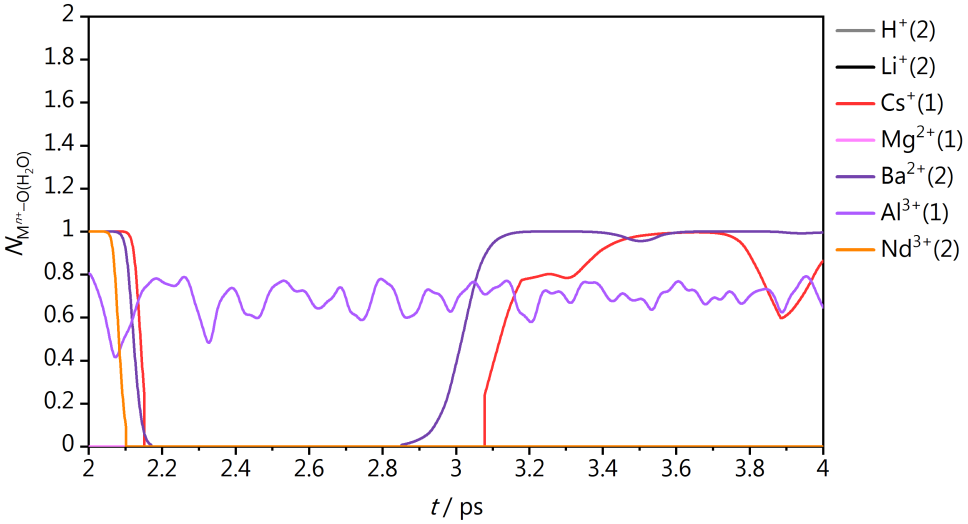

Fig. F.16. Cation coordination numbers to oxygen atoms in adsorbed H_2O ($N_{M\text{-}O(H2O)}$) for the Au/water/M^{n+}/*H_2O system (from 2 to 4 ps).

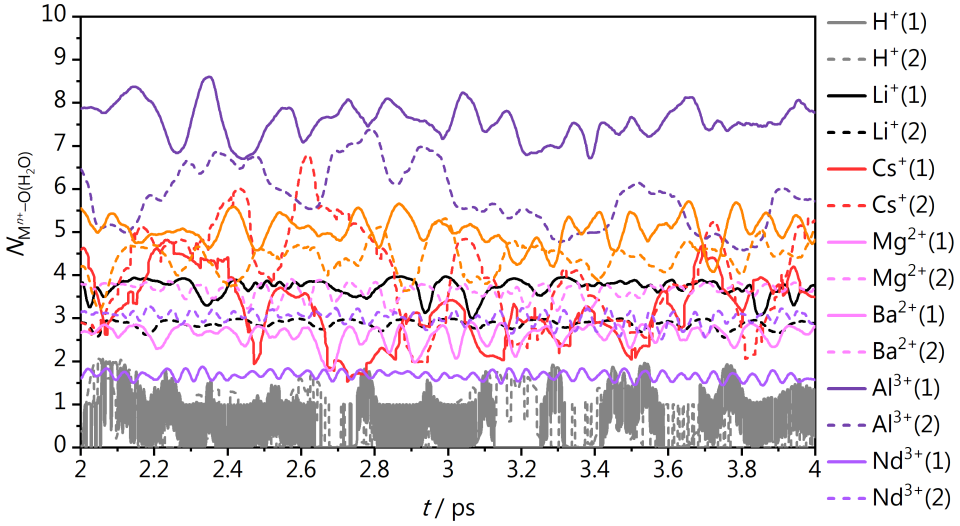

Fig. F.17. Cation coordination numbers to oxygen atoms in solvent molecules ($N_{M\text{-}O(H2O)}$) for the Au/water/M^{n+}/*H_2O system (from 2 to 4 ps).

Table F.4. Cation coordination numbers to oxygen atoms in adsorbed H_2O ($N_{M\text{-}O(H2O)}$) as calculated through Eq. F.4 for Au/water/M^{n+}/H_2O during 2 ps AIMD at 300 K (Fig. F.16-F.17). Coordination numbers are reported as averages with their associated standard deviation $\sigma(N_{cat\text{-}O})$, median, maximum, and minimum values.

	$N_{M\text{-}O(H2O)}$ (Au/water/M^{n+}/*H_2O)				$N_{M\text{-}O(CO2)}$ (Au/water/M^{n+}/*H_2O)			
M^{n+}	Mean	Median	Max	Min	Mean	Median	Max	Min
H^+	0.6 ± 0.6	0.2	2.1	0.0	0.0 ± 0.0	0.0	0.0	0.0
Li+	2.87 ± 0.09	2.9	3.0	2.6	0.0 ± 0.0	0.0	0.0	0.0
Cs^+	4.0 ± 1.1	4.0	6.8	2.0	0.5 ± 0.4	0.6	1.0	0.0
Mg^{2+}	2.6 ± 0.2	2.7	2.9	1.8	0.0 ± 0.0	0.0	0.0	0.0
Ba^{2+}	5.8 ± 0.7	5.8	7.4	4.6	0.6 ± 0.5	0.9	1.0	0.0
Al^{3+}	1.67 ± 0.09	1.7	1.9	1.4	0.7 ± 0.1	0.7	0.8	0.4
Nd^{3+}	4.4 ± 0.4	4.4	5.3	3.2	0.0 ± 0.2	0	1.0	0

F.3.4 Determination of the activation barriers.

To estimate the activation energies for H_2O and H_3O^+ dissociation and CO_2 protonation, we considered an Au/2-3H_2O/M^{n+}/*ads* system, with simplified cation solvation shell with 2-3 water molecules. Eq. F10-12 define the processes for 3 water molecules in the solvation shell. We then removed $n - 1$ protons (n for H_3O^+ dissociation) from the system to keep an extra electron in the system (n = 1, 2, 3 for proton and alkali, divalent and trivalent cations respectively). Then, we let *CO_2, H, *H_3O^+, *H_2O, H_2O + *H and OH^- + *H adsorb close to the cation, and we further optimized the overall system Au/2-3H_2O/M^{n+}/*ads* (*ads* = *CO_2, *COOH, H_3O^+, *H_2O, H_2O + *H and OH^- + *H). Activation energies were calculated trough the Nudged Elastic Band (NEB) method and all of them exhibit a single imaginary vibrational frequency.[29] Gibbs free energies were calculated at 298.15 K by correcting DFT energies for entropic contributions. The energy references were chosen as CO_2(g), H_2(g) and H_2O(g) and single point calculations for the Au/2-3H_2O/M^{n+} system.

$$* CO_2^- \cdots M^{n+}(H_2O)_{(3-n)} + (n-1)OH^- \rightleftharpoons * COOH + M^{n+}(H_2O)_{(3-n-1)} + nOH^- \quad \text{Eq. F.10}$$

$$* H_2O + e^- + M^{n+}(H_2O)_{(3-n)} + (n-1)OH^- \rightleftharpoons * H + OH^- \cdots M^{n+}(H_2O)_{(3-n)} + (n-1)OH^- \quad .11$$

$$* H_3O^+ + e^- + M^{n+}(H_2O)_{(3-n)} + nOH^- \rightleftharpoons * H + H_2O \cdots M^{n+}(H_2O)_{(3-n)} + nOH^- \quad \text{Eq. F.12}$$

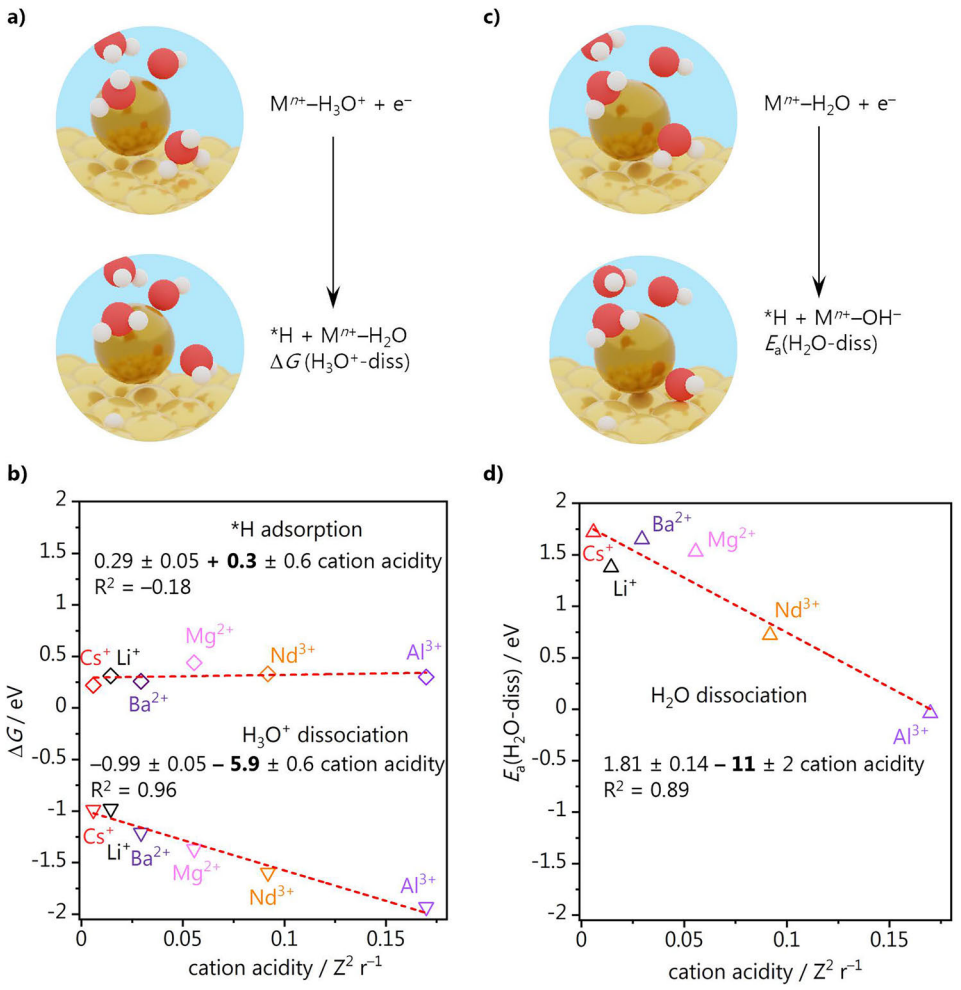

Fig. F.18. a)-b) Gibbs free energy for *H adsorption (diamonds) and H_3O^+ dissociation (down-pointing triangles, Eq. F.12) vs. cation acidity, calculated with 3 H_2O molecules in cation solvation shell. **c)-d)** Activation barrier for water dissociation (up-pointing triangles, Eq. F.11) vs. cation acidity, calculated as average of the calculated values for 2 and 3 H_2O molecules in cation solvation shell. In the schemes, Au, Cs, H, and O atoms are portrayed as yellow, dark yellow, white, and oxygen spheres, respectively.

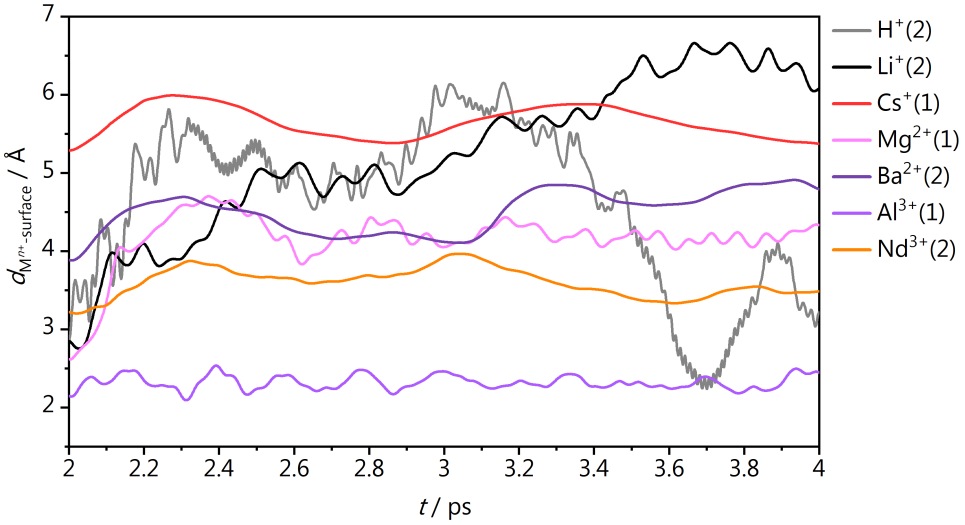

Fig. F.19. Distance between multivalent cation (M^{n+}) and surface calculated for the Au/water/M^{n+}/*CO_2 system (from 2 to 4 ps).

F

Table F.5. Cation coordination numbers to oxygen atoms in solvent molecules ($N_{M\text{-}O(H2O)}$) and adsorbed CO_2 ($N_{M\text{-}O(CO2)}$) as calculated through Eq. F.3 for Au/water/M^{n+}/*CO_2 during 2 ps AIMD at 300 K (Fig. F.16-F.17). Coordination numbers are reported as averages with their associated standard deviation $\sigma(N_{M\text{-}O})$, median, maximum, and minimum values.

	$N_{M\text{-}O(H2O)}$ (Au/water/M^{n+}/*CO_2)				$N_{M\text{-}O(H2O)}$ (Au/water/M^{n+}/*CO_2)			
M^{n+}	Mean	Median	Max	Min	Mean	Median	Max	Min
H^+	0.5 ± 0.6	0.1	1.9	0.0	0 ± 3E–4	0.0	0.01	0.0
Li+	3.1 ± 0.5	3.0	3.9	2.0	0.0 ± 0.2	0.0	1.0	0.0
Cs^+	3.5 ± 0.6	3.5	4.8	2.0	0.7 ± 0.4	0.8	1.8	0.0
Mg^{2+}	3.0 ± 0.4	3.0	3.8	2.0	0.6 ± 0.4	0.7	1.0	0.0
Ba^{2+}	5.6 ± 0.7	5.5	7.1	3.8	0.9 ± 0.2	1.0	1.0	0.1
Al^{3+}	1.63 ± 0.12	1.6	1.9	1.2	0.5 ± 0.2	0.5	0.9	0.0
Nd^{3+}	3.9 ± 0.4	3.9	4.7	2.8	0.9 ± 0.2	0.9	1.0	0

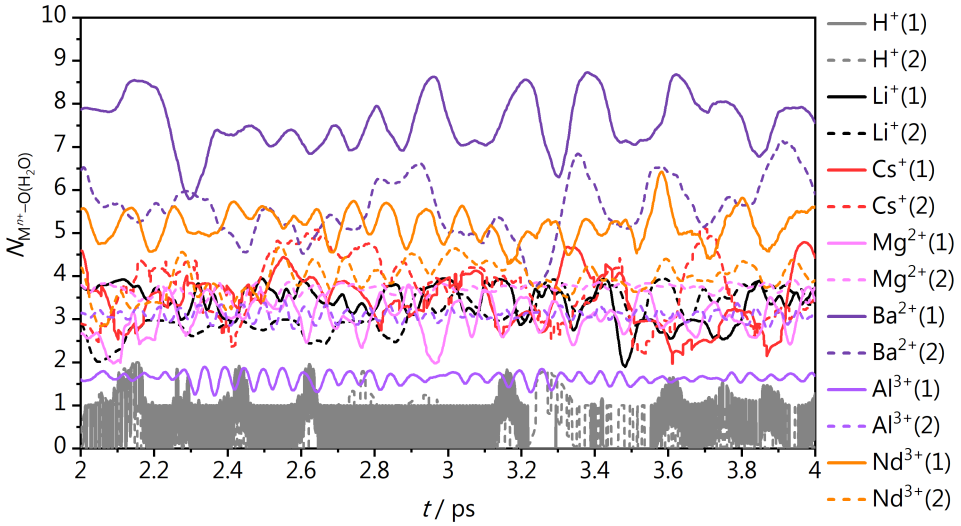

Fig. F.20. Cation coordination numbers to oxygen atoms in solvent molecules ($N_{M\text{-}O(H2O)}$) for the Au/water/M^{n+}/*CO_2 system (from 2 to 4 ps).

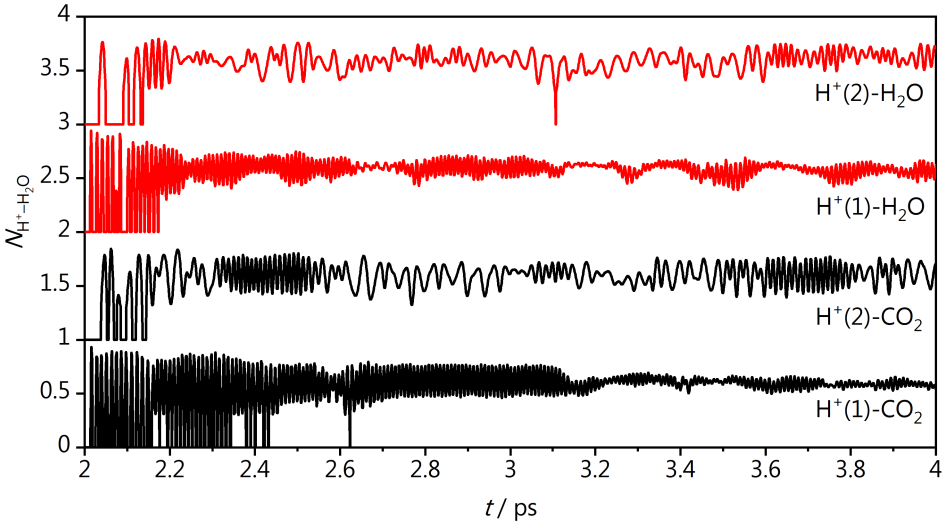

Fig. F.21. Bond formation between H^+ and neighboring water molecule for Au/water/H^+/*CO_2 system and Au/water/H^+/*H_2O system (from 2 to 4 ps). Proton is not effective as a CO_2 reduction promoter, since it combined with a neighboring water molecule to form a H_3O^+ after less than 0.2 ps.

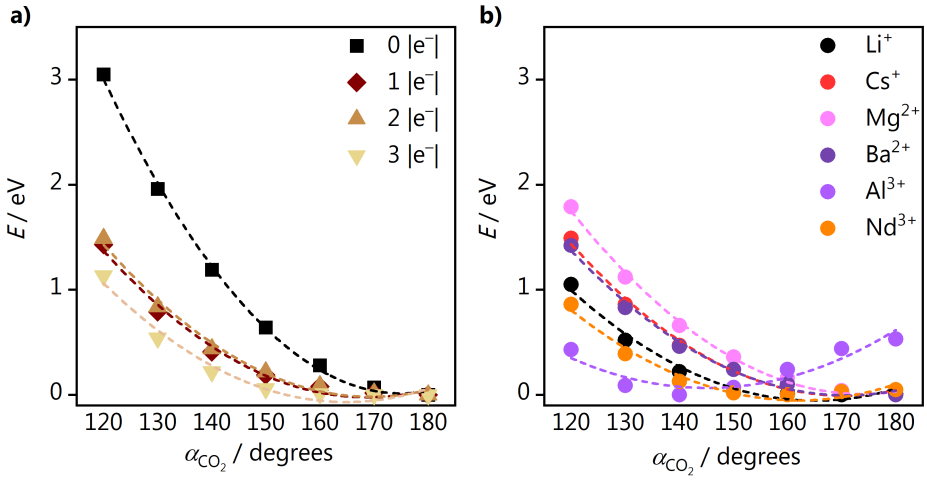

Fig. F.22. DFT energy of **a)** a free CO_2 and **b)** a CO_2 coordinated to a multivalent cation as a function of the CO_2 activation angle, α. Lower α values indicate CO_2 activation. $M^{n+}\cdots O(CO_2)$ distances have been set according to AIMD results (Table F.1). Different colors highlight **a)** additional electrons in the simulation cell (from 1 to 3) and **b)** different cation species. Dashed lines represent a quadratic fit over the data points.

F

Table F.6. Fit parameters for quadratic correlations shown in Fig. F.21:

$$E = \mathrm{a} + \mathrm{b} * \alpha_{\mathrm{CO_2}} + \mathrm{c} * {\alpha_{\mathrm{CO_2}}}^2$$

System	a / eV	b / eV degrees^{-1}	c / eV degrees^{-2}	R^2
CO_2 (0 |e$^-$|)	+30 ± 1	–0.35 ± 0.02	+9.9E-04 ± 6E-05	0.998
CO_2 (1 |e$^-$|)	+17 ± 2	–0.20 ± 0.02	+5.9E-04 ± 7E-05	0.98
CO_2 (2 |e$^-$|)	+17 ± 2	–0.20 ± 0.02	+5.9E-04 ± 7E-05	0.985
CO_2 (3 |e$^-$|)	+15 ± 2	–0.19 ± 0.03	+5.6E-04 ± 9E-05	0.97
$Li^+\cdots CO_2$ (1 |e$^-$|)	+14 ± 2	–0.17 ± 0.02	+5.2E-04 ± 7E-05	0.97
$Cs^+\cdots CO_2$ (1 |e$^-$|)	+17 ± 1	–0.19 ± 0.02	+5.7E-04 ± 7E-05	0.988
$Mg^{2+}\cdots CO_2$ (2 |e$^-$|)	+18 ± 1	–0.209 ± 0.014	+6.0E-04 ± 5E-05	0.996
$Ba^{2+}\cdots CO_2$ (2 |e$^-$|)	+16 ± 1	–0.18 ± 0.02±	+5.3E-04 ± 6E-05	0.989
$Al^{3+}\cdots CO_2$ (3 |e$^-$|)	+10 ± 2	–0.13 ± 0.03	+4.52E-04 ± 1.1E-04	0.77
$Nd^{3+}\cdots CO_2$ (3 |e$^-$|)	+13 ±2	–0.16 ± 0.02	+4.9E-04 ± 7E-05	0.96

References

(1) Monteiro, M. C. O.; Koper, M. T. M. *Electrochim. Acta* 2019, *325*, 134915.
(2) Li, X.; Gunathunge, C. M.; Agrawal, N.; Montalvo-Castro, H.; Jin, J.; Janik, M. J.; Waegele, M. M. *J. Electrochem. Soc.* 2020, *167* (10), 106505.
(3) Do, U. P.; Seland, F.; Johannessen, E. A. *J. Electrochem. Soc.* 2018, *165* (5), H219–H228.
(4) Kresse, G.; Furthmüller, J. *Phys. Rev. B* 1996, *54*, 11169–11186.
(5) Kresse, G.; Furthmüller, J. *Comput. Mater. Sci.* 1996, *6*, 15–50.
(6) Perdew, J. P.; Burke, K.; Ernzerhof, M. *Phys. Rev. Lett.* 1996, *77*, 3865–3868.
(7) Grimme, S. *J. Comput. Chem.* 2006, *27*, 1787–1799.
(8) Bucko, T.; Hafner, J.; Lebègue, S.; Ángyán, J. G. *J. Phys. Chem. A* 2010, *114*, 11814–11824.
(9) Almora-Barrios, N.; Carchini, G.; Błoński, P.; López, N. *J. Chem. Theory Comput.* 2014, *10*, 5002–5009.
(10) Blöchl, P. E. *Phys. Rev. B* 1994, *50*, 17953–17979.
(11) Kresse, G.; Joubert, D. *Phys. Rev. B* 1999, *59*, 1758–1775.
(12) Marx, D.; Hutter, J. Cambridge University Press, 2009.
(13) Nosé, S. *J. Chem. Phys.* 1984, *81*, 511–519.
(14) Hoover, W. G. *Phys. Rev. A* 1985, *31*, 1695–1697.
(15) Monteiro, M. C. O.; Dattila, F.; Hagedoorn, B.; García-Muelas, R.; López, N.; Koper, M. T. M. *Nat. Catal.* 2021, *4* (8), 654–662.
(16) Dudarev, S. L.; Botton, G. A.; Savrasov, S. Y.; Humphreys, C. J.; Sutton, A. P. *Phys. Rev. B* 1998, *57* (3), 1505–1509.
(17) Kozub, A. L.; Shick, A. B.; Máca, F.; Kolorenč, J.; Lichtenstein, A. I. *Phys. Rev. B* 2016, *94* (12), 125113.
(18) Monteiro, M. C. O.; Jacobse, L.; Koper, M. T. M. *J. Phys. Chem. Lett.* 2020, *11* (22), 9708–9713.
(19) Lide, D. R. 84th ed.; Lide, D. R., Ed.; CRC Press, 2003; Vol. 85.
(20) Bellarosa, L.; García-Muelas, R.; Revilla-López, G.; López, N. *ACS Cent. Sci.* 2016, *2* (2), 109–116.
(21) Feibelman, P. J. *Phys. Rev. B* 2001, *64* (12), 125403.
(22) McCrum, I. T.; Bondue, C. J.; Koper, M. T. M. *J. Phys. Chem. Lett.* 2019, *10* (21), 6842–6849.
(23) Chen, L. D.; Urushihara, M.; Chan, K.; Nørskov, J. K. *ACS Catal.* 2016, *6* (10), 7133–7139.
(24) White, R. E.; Bockris, J. O.; Conway, B. E. Kluwer Academic Publishers, 2002.
(25) Makov, G.; Payne, M. *Phys. Rev. B* 1995, *51*, 4014–4022.
(26) Waegele, M. M.; Gunathunge, C. M.; Li, J.; Li, X. *J. Chem. Phys.* 2019, *151* (16), 160902.
(27) Marcus, Y. *Chem. Rev.* 1988, *88* (8), 1475–1498.
(28) Dattila, F.; García-Muelas, R.; López, N. *ACS Energy Lett.* 2020, *5*, 3176–3184.
(29) Resasco, J.; Chen, L. D.; Clark, E.; Tsai, C.; Hahn, C.; Jaramillo, T. F.; Chan, K.; Bell, A. T. *J. Am. Chem. Soc.* 2017, *139* (32), 11277–11287.
(30) Nørskov, J. K.; Rossmeisl, J.; Logadottir, A.; Lindqvist, L.; Kitchin, J. R.; Bligaard, T.; Jónsson, H. *J. Phys. Chem. B* 2004, *108* (46), 17886–17892.
(31) Haynes, W. M. 95th ed.; CRC Press: New York, 2014.
(32) Henkelman, G.; Jónsson, H. *J. Chem. Phys.* 2000, *113* (22), 9978–9985.

G

Methods and supporting information to Chapter 10

G.1 Methods

G.1.1 Materials

The following chemicals were used to prepare the electrolytes used in this work: Li_2SO_4 (Sigma Aldrich, 99.99 % metal basis), K_2SO_4 (Alfa Aesar, Puratronic, 99.997 %, metals basis), H_2SO_4 (Merck, Suprapur, 96%), $LiClO_4$ (Sigma Aldrich, 99.99%, trace metal basis), $KClO_4$ (Sigma Aldrich, ≥99.99%, trace metal basis), LiOH (Sigma Aldrich, 99.995%, monohydrate), NaOH (Merck, 30% solution, Suprapur®), KOH (Merck, 99.995%, Suprapur®). The sulfate salts were used for the experiments in acidic media and the hydroxides for the experiments in alkaline media. For the measurements in alkaline media in which the cation concentration is varied, appropriate amounts of perchlorate salts were added to the electrolyte. Gold and platinum disc electrodes were cut from a polycrystalline gold (0.5 mm thick, MaTecK, 99.995%) and platinum (0.5 mm thick, MaTecK, 99.99%) foil and prepared according to the method described in Chapter 7. All glassware used was cleaned by immersion in a potassium permanganate solution overnight (1 g/L $KMnO_4$ dissolved in 0.5 M H_2SO_4), followed by immersion in dilute piranha. The glassware was further boiled in ultrapure water at least five times before use.

G.1.2 Electrochemical measurements

All electrochemical measurements were carried out using a BioLogic two-channel potentiostat/galvanostat/ EIS (SP-300). The hanging meniscus and rotating disc electrode (RDE) experiments were carried out in a one compartment glass cell. A gold (0.5 mm diameter, MaTeck, 99.9%) or a platinum (0.5 mm diameter, MaTeck, 99.9%) wire was used as counter electrode (depending on the working electrode) and a reversible hydrogen electrode (Gaskatel, HydroFlex) as reference. Argon (6.0 purity, Linde) was purged through the solution for 20 minutes prior to the experiments. The argon flow was kept also during the experiments in order to avoid oxygen diffusing into the electrolyte. Before the measurements, the gold electrode was prepared by flame annealing, using the procedure described in our previous work.[1] The platinum electrode was also flame annealed and subsequently cycled 200 times between 0.06 and 1.65 V vs. RHE in 0.1 M H_2SO_4 at 1 V s^{-1}, in order to yield a reproducible blank voltammogram. Blank CVs were recorded in argon saturated 0.1 M H_2SO_4 prior to every measurement. The electrochemically active surface area (ECSA) of gold was calculated based on the charge corresponding to the gold oxide reduction and a surface charge density of 386 µC cm^{-2}.[2] For platinum, the integral of the hydrogen desorption region 0.06 < E < 0.6 V was used

(after subtraction of the double layer charge), and the ECSA was calculated based on the specific charge of 230 μC cm^{-2} reported for a polycrystalline Pt surface in sulfuric acid.[3] RDE experiments were performed using a MSR Electrode Rotator (Pine Research Instrumentation) equipped with a AFE6M shaft, and a gold and a platinum disk (diameter = 5 mm, Pine Research Instrumentation). The rotating disc electrodes were polished with a polycrystalline diamond suspension of 0.25 μm (MetaDi, Buehler) and then sonicated (Bandelin Sonorex RK 52H) in ethanol and ultrapure water (>18.2 MΩ cm, Millipore Milli-Q) for 10 minutes before the measurements. For all hydrogen evolution experiments, the solution resistance was determined by performing Potentiometric Electrochemical Impedance Spectroscopy (PEIS) and the electrode potential was always automatically compensated for 85% of the ohmic drop.

G.2 Hydrogen evolution in acidic media

In mildly acidic media (pH = 3), we see first a cathodic current due to proton reduction ($2H^+ + 2e^- \rightarrow H_2$) on both gold (Fig. G.1a) and platinum (Fig. G.1b) followed by a peak due to diffusion limitation. On gold, the reaction kinetics is not affected by the cation identity, and is only dependent on the proton concentration at the reaction interface, as we also observed in our recent work.[4] On platinum, we see that K^+ slightly increases the rate of the reaction, as higher currents are obtained at low overpotentials, where the reaction is only kinetically limited. In acidic media, an often used descriptor for HER on platinum is the hydrogen binding energy and the free energy of hydrogen adsorption ($\Delta G_{H,ads}$), which on platinum is close to zero. A way to probe the hydrogen binding energy on Pt is by recording the blank voltammetry, as we show in Fig. G.1c in Li^+ and K^+ containing electrolyte. We see a positive shift of 10 mV in the underpotential hydrogen (H_{upd}) peak (between 0.2 and 0.3 V vs. RHE) in K^+ electrolyte, which has been previously ascribed to an increase in the hydrogen binding energy.[5] However, work from our group on Pt(553) shows that there is a cation dependence of the potential of the {110}-step related H_{upd} peak. It shows through experiments and Density Functional Theory (DFT) that alkali-metal cations adsorbed near the step, weaken low coverage hydroxide adsorption, shifting the step associated peak to more positive potentials.[6] Therefore, we cannot ascribe the shift we observe in Fig. G.1c to changes in the hydrogen binding energy, but actually to a cation–OH_{ads}–H_{ads} interaction.[6] In Fig. G.1a and Fig. G.1b, at more negative potentials, as proton reduction reaches diffusion limitation and the interfacial pH becomes more alkaline, water reduction starts to takes place ($2H_2O$

+ $2e^- \rightarrow H_2 + 2OH^-$). We see that on both metal surfaces the water reduction reaction (in neutral to mildly alkaline media) is still promoted by K^+ cations, although the differences are more pronounced for gold than for platinum.

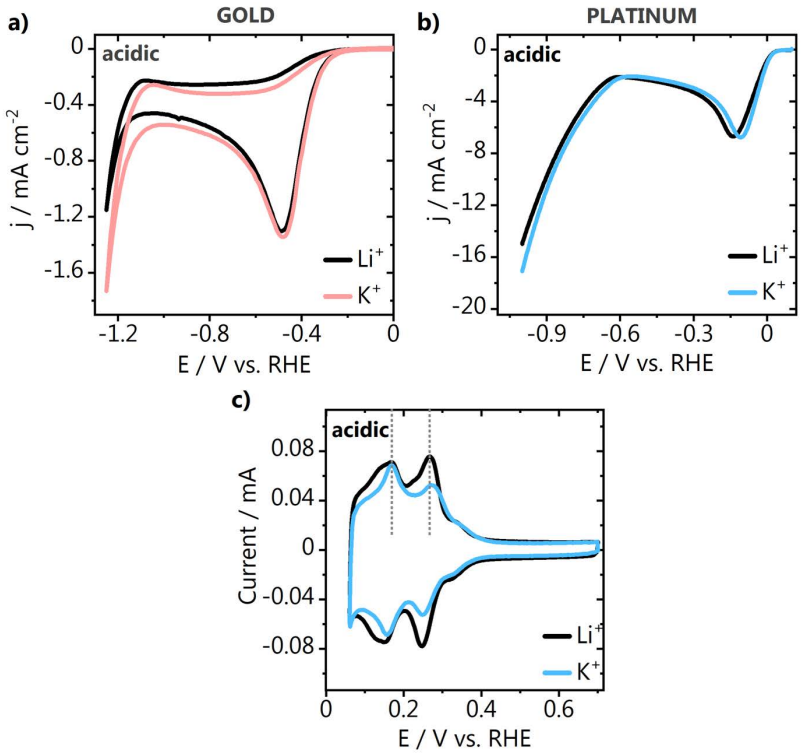

Fig. G.1. Stationary hydrogen evolution on **a)** gold and **b)** platinum in acidic media (0.1 M M_2SO_4, pH = 3), together with **c)** the blank voltammetry of the platinum electrode.

G.3 Blank voltammetry: stationary experiments

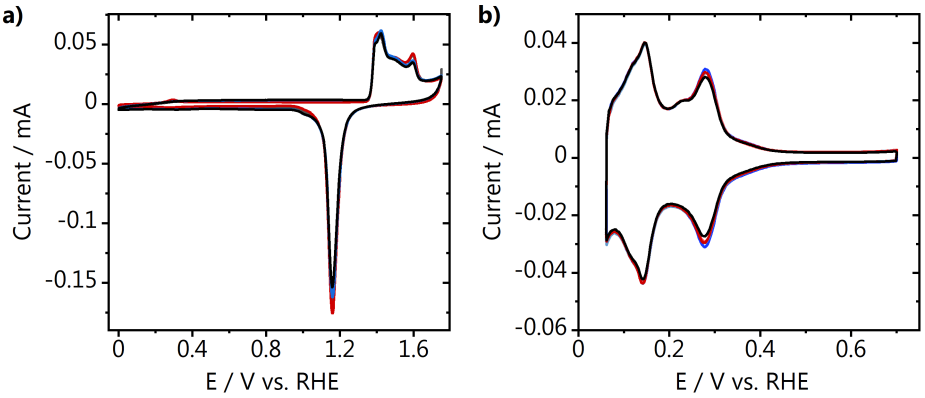

Fig. G.2. Blank voltammetry of the polycrystalline **a)** gold and **b)** platinum electrodes used for the stationary experiments in this work, recorded in 0.1 M H_2SO_4 at 50 mV s^{-1}. Several CVs are overlapped, which were recorded before the HER experiments carried out in different electrolytes, pH.

G.4 Blank voltammetry: rotating disc experiments

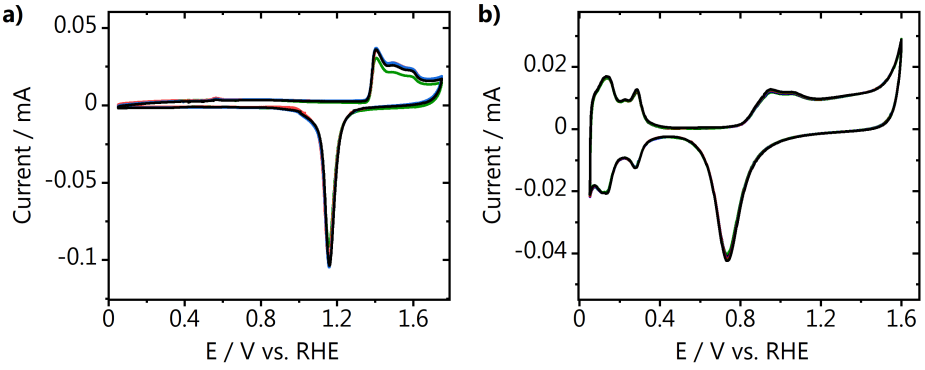

Fig. G.3. Blank voltammetry of the polycrystalline **a)** gold and **b)** platinum electrodes used for the rotating disc experiments in this work, recorded in 0.1 M H_2SO_4 at 50 mV s^{-1}. Several CVs are overlapped, which were recorded before the HER experiments carried out in different electrolytes, pH.

G.5 Cation concentration: cyclic voltammetry on gold

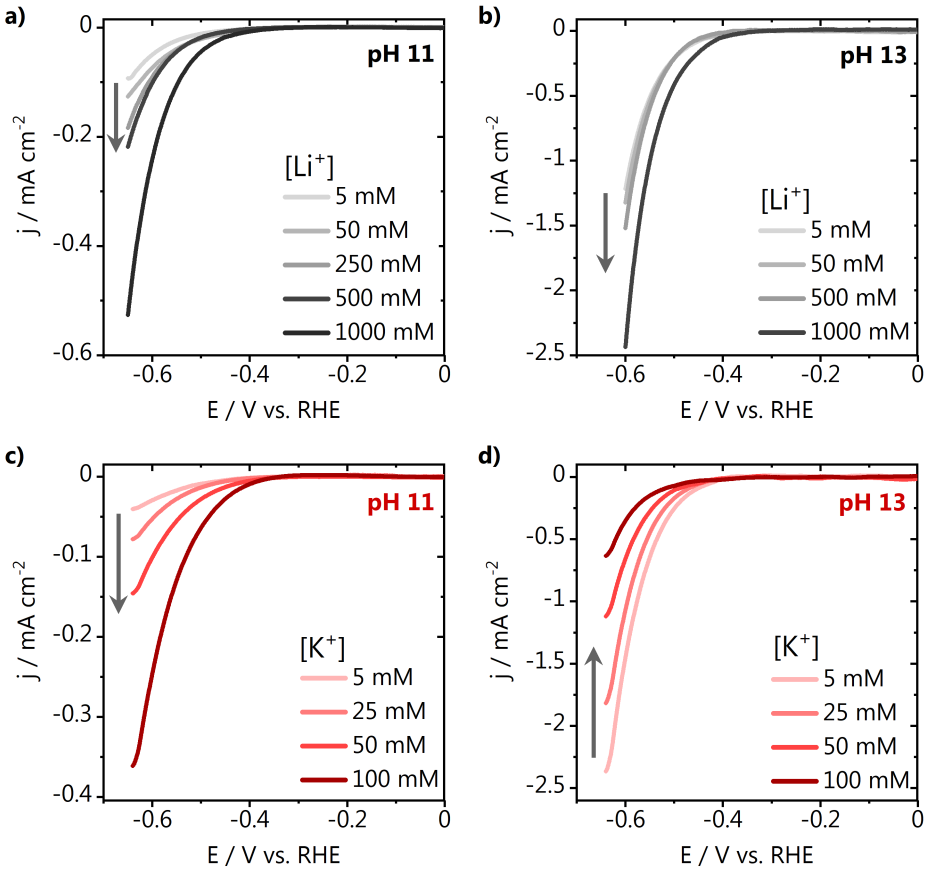

Fig. G.4. a)-d) Hydrogen evolution cyclic voltammograms recorded on polycrystalline gold in *M*OH + *X* mM *M*ClO_4, at different pH, with *M* = Li^+ or K^+ and *X* = 5, 25, 50 and 100, using a rotating disc electrode, at 25 mV s^{-1} and 2500 rpm.

G.6 Cation concentration: cyclic voltammetry on platinum

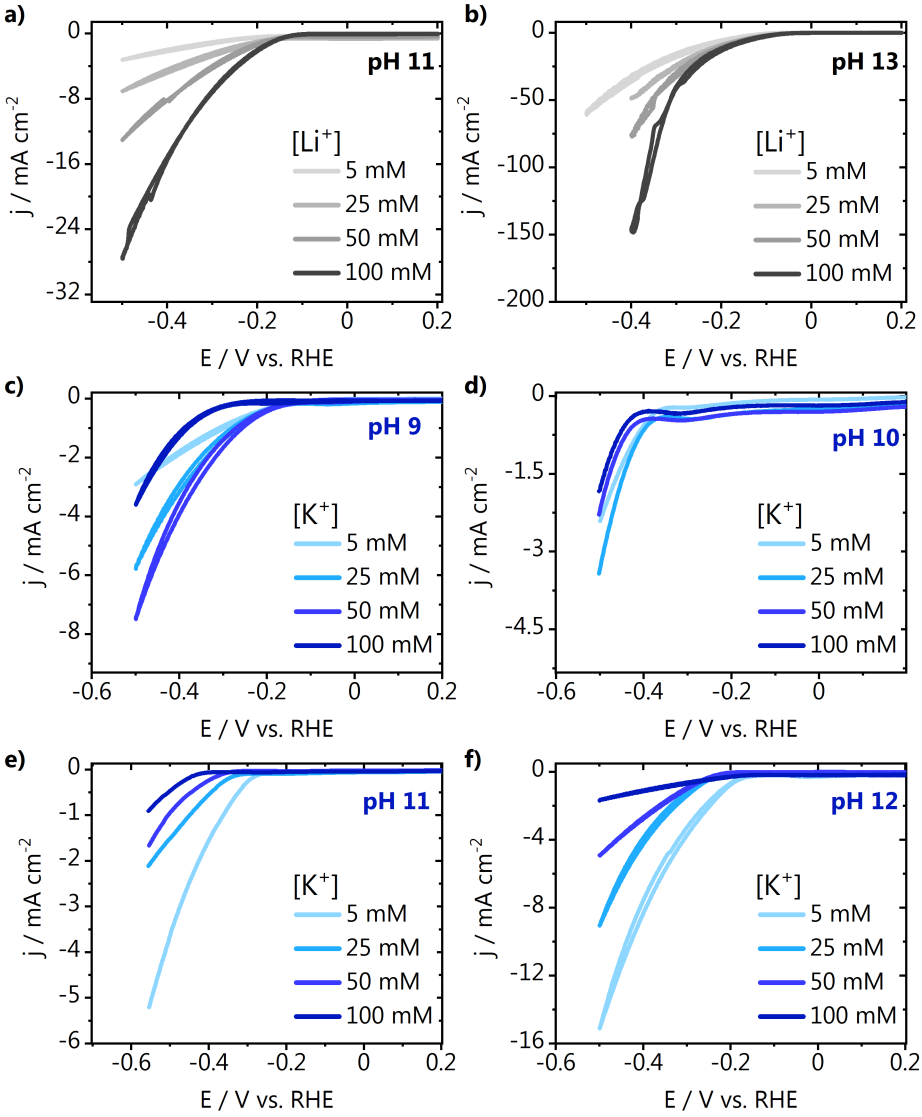

Fig. G.5. a)-f) Hydrogen evolution cyclic voltammograms recorded on polycrystalline platinum in *M*OH + *X* mM *M*ClO_4, at different pH, with *M* = Li^+ or K^+ and *X* = 5, 25, 50 and 100, using a rotating disc electrode, at 25 mV s^{-1} and 2500 rpm.

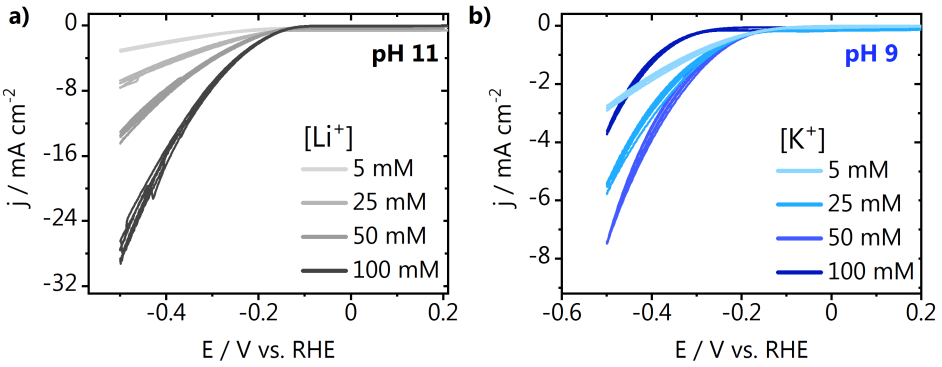

Fig. G.6. Five consecutive hydrogen evolution cyclic voltammograms recorded on polycrystalline platinum in *M*OH + *X* mM *M*ClO_4, at different pH, with *M* as **a)** Li^+ or **b)** K^+ and *X* = 5, 25, 50 and 100, using a rotating disc electrode, at 25 mV s^{-1} and 2500 rpm.

References

(1) Monteiro, M. C. O.; Koper, M. T. M. *Electrochim. Acta* 2019, *325*, 134915.
(2) Do, U. P.; Seland, F.; Johannessen, E. A. *J. Electrochem. Soc.* 2018, *165* (5), 219–228.
(3) Chen, Q.-S.; Solla-Gullón, J.; Sun, S.-G.; Feliu, J. M. *Electrochim. Acta* 2010, *55* (27), 7982–7994.
(4) Monteiro, M. C. O.; Dattila, F.; Hagedoorn, B.; García-Muelas, R.; López, N.; Koper, M. T. M. *Nat. Catal.* 2021, *4* (8), 654–662.
(5) Sheng, W.; Zhuang, Z.; Gao, M.; Zheng, J.; Chen, J. G.; Yan, Y. *Nat. Commun.* 2015, *6*, 6–11.
(6) Chen, X.; McCrum, I. T.; Schwarz, K. A.; Janik, M. J.; Koper, M. T. M. *Angew. Chemie - Int. Ed.* 2017, *56* (47), 15025–15029.

H

Methods and supporting information to Chapter 11

H.1 Synthesis and characterization of gas diffusion electrodes

The synthesis method for the gas diffusion layer (GDL) was adjusted from a patented method.[1] First, 15 g of acetylene black (Soltex, 75%-03) was mixed with 8.91 mL PTFE (FuelCellStore, Teflon™ PTFE DISP 30) and 60 mL of a 1:1 volume water/isopropyl alcohol (IPA). After mixing, a dough was obtained and rolled with a marble rolling pin before using a cross rolling technique to obtain the desired thickness. The PTFE dispersion was diluted by 50% with 1:1 volume water/IPA, applied to the back of the dough, and graphitized carbon was placed on top. A Carver heated press (Model number 4533) was used to press the structure at 140 °C and 10.25 Ton for 32.5 min. Then the temperature was raised to 308 °C at the same pressure and held for 32.5 minutes. Finally the temperature was raised to 317.5 °C at 13 ton and held for 32.5 min before removing the structure from the press. GDLs of 17.16 cm^2 were cut from the resulting structure. Commercial gold nanoparticles were used as catalyst (60% gold supported on vulcan XC-72 (carbon), FuelCellStore). The catalyst ink was prepared by suspending the particles in ethanol and adding 250 µL of a Nafion© solution under constant stirring. The inks were additionally sonicated for 30 minutes. The obtained ink was airbrushed on a 17 cm^2 GDL and let dry. The catalysts metal loading was calculated by weighing the electrodes before and after the spraying.

The gold GDEs topography and composition were characterized by Scanning Electron Microscopy (SEM) in an Apreo SEM (ThermoFisher Scientific). Micrographs were obtained using an acceleration voltage of 10 kV and an electron beam current of 0.8 nA. Energy Dispersive X-Ray Spectroscopy (EDX) was used for elemental analysis (Oxford Instruments X-MaxN 150 Silicon Drift detector). EDX data processing was done with the Pathfinder™ X-ray Microanalysis software v1.3. The data is displayed in atomic percentage for easier visualization, however the quantification was performed in automatic mode, without providing external standards.

H.2 Electrolysis measurements

The gas diffusion electrodes were mounted in a commercial two-compartment 10 cm^2 GDE flow cell (ElectroCell, Micro Flow Cell) for the bulk electrolysis. The anolyte and the catholyte were separated by a reinforced Nafion™ membrane N324. For all measurements the anolyte was a 0.5 M H_2SO_4 solution and the anode a dimensionally stable anode (DSA®, ElectroCell). The electrolyte flow rate was 30 mL min^{-1}, achieved with a peristaltic pump. A CO_2 flow of 50 mL min^{-1}

was employed for all the measurements. The following chemicals were used to prepare the electrolytes for bulk CO_2 electrolysis: Cs_2SO_4 (Sigma Aldrich, 98%), Li_2SO_4 (Sigma Aldrich, 98%), $KHCO_3$ (Acros Organics, 99.5%), H_2SO_4 (Acros Organics, for analysis ACS, 95% solution in water). Either 1 M Cs_2SO_4, Li_2SO_4, or $KHCO_3$ were used as catholyte. The pH of the solutions was adjusted with H_2SO_4 when necessary using a pH meter. Galvanostatic bulk electrolysis measurements were controlled using a power supply and each different current density was applied for one hour. The product analysis was performed using a gas chromatograph (Varian 4900 micro GC) equipped with four modules: COx module, MS5 (mol. sieve) module, PPQ (poraplotQ) module and 52C WAX module. Gaseous samples were taken from the headspace every 3 minutes. The current efficiencies shown throughout this work represent the average values obtained during 1 hour of electrolysis, with the corresponding standard deviation.

H.3 Faradaic efficiency for CO and H_2

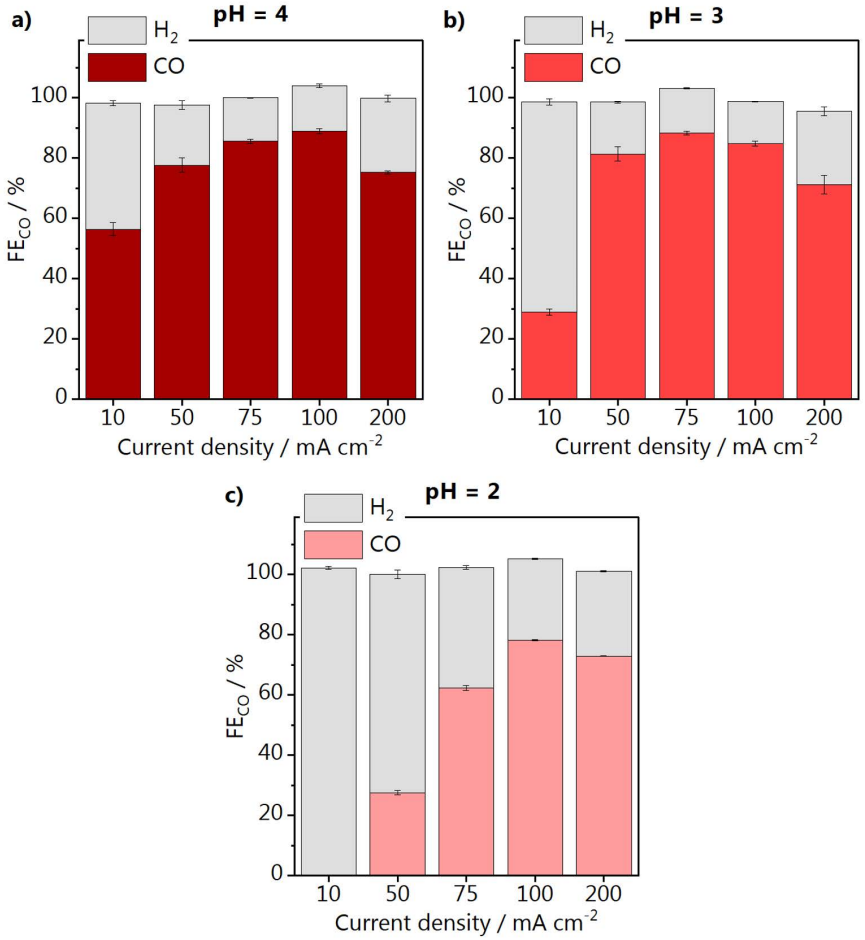

Fig. H.1. Faradaic efficiencies for CO and H_2 obtained during one hour electrolysis at each current density displayed. The catholyte was 1 M Cs_2SO_4, **a)** pH 4, **b)** pH 3 and **c)** pH 2. Catalyst loading 2 mg cm^{-2}. Error bars are calculated based on three individual measurements.

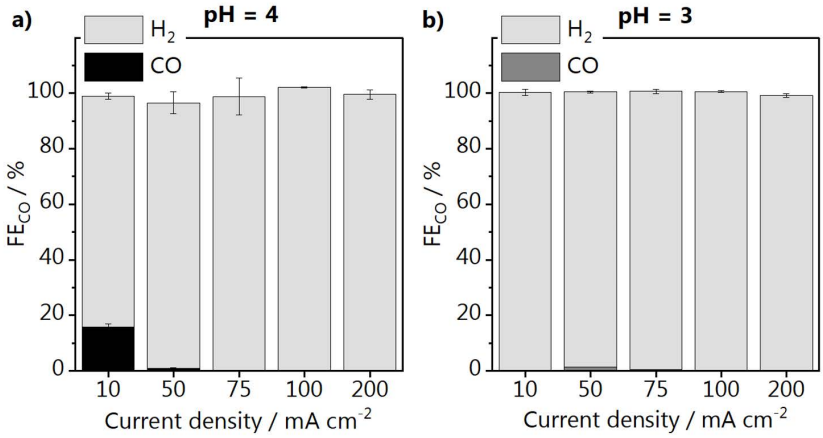

Fig. H.2. Faradaic efficiencies for CO and H_2 obtained during one hour electrolysis at each current density displayed. The catholyte was 1 M Li_2SO_4, **a)** pH 4 and **b)** pH 3. Catalyst loading 2 mg cm^{-2}. Error bars are calculated based on three individual measurements.

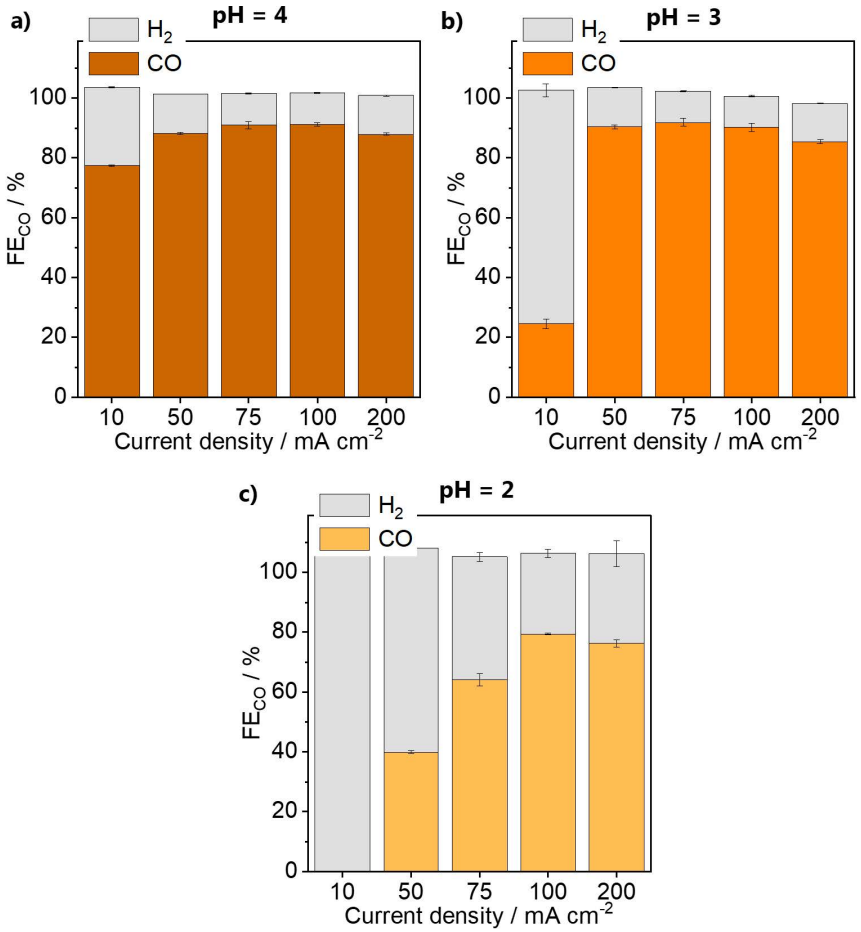

Fig. H.3. Faradaic efficiencies for CO and H_2 obtained during one hour electrolysis at each current density displayed. The catholyte was 1 M Cs_2SO_4; **a)** pH 4, **b)** pH 3 and **c)** pH 2. Catalyst loading 1 mg cm^{-2}. Error bars are calculated based on three individual measurements.

H.4 Effect of the catalyst loading

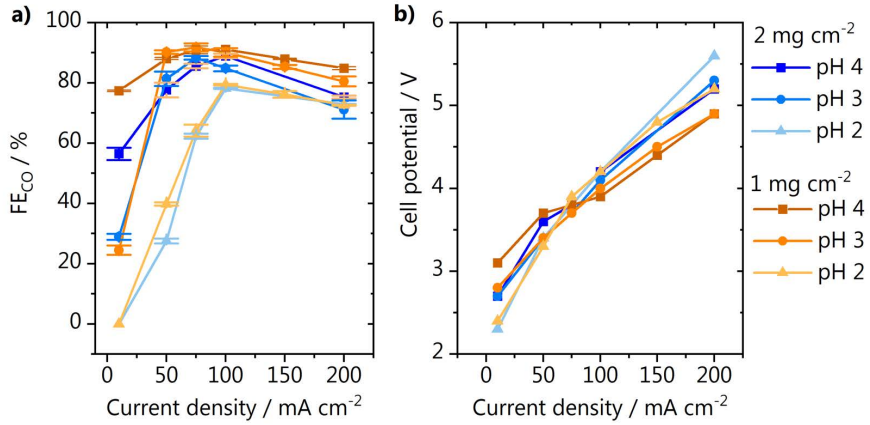

Fig. H.4. Electrolysis performed in 1 M Cs_2SO_4, catalyst loading 1 mg cm^{-2} or 2 mg cm^{-2}, **a)** faradaic efficiency for CO and **b)** cell potential. The data points displayed are an average obtained during 1 hour electrolysis. Error bars are calculated based on three individual measurements.

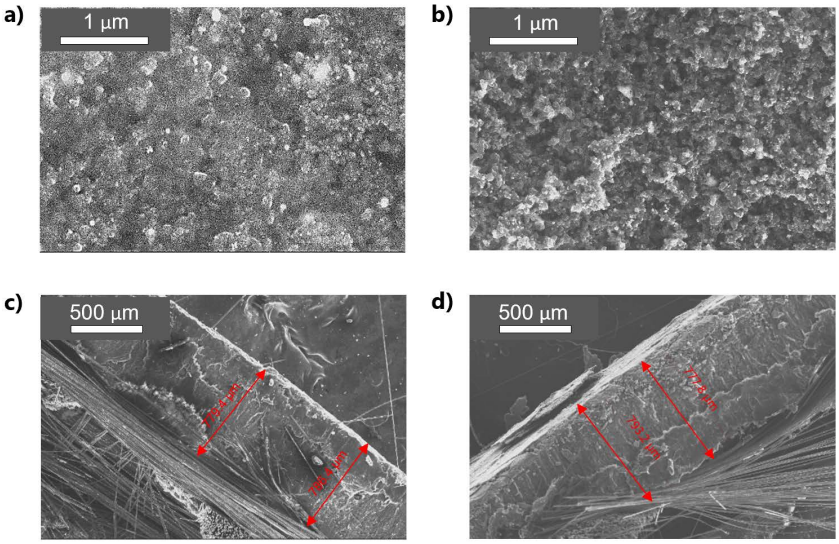

Fig. H.5. SEM micrograph of the gold GDEs. Top view of the **a)** 1 mg cm^{-2} and **b)** 2 mg cm^{-2} catalyst, and cross-section of the **c)** 1 mg cm^{-2} and **d)** 2 mg cm^{-2} catalyst.

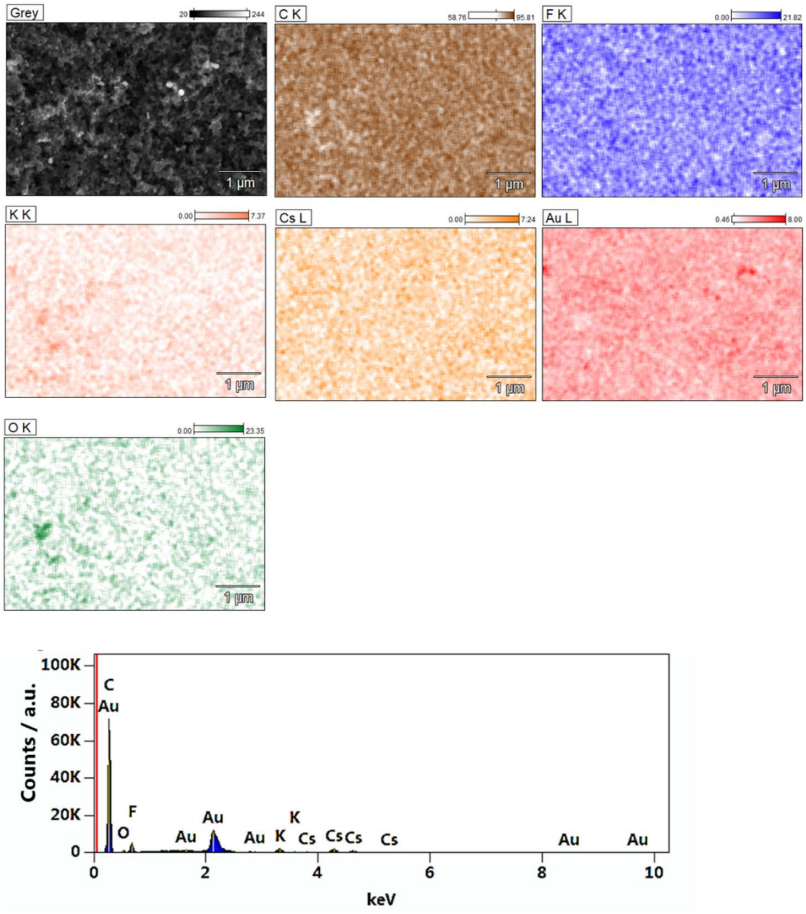

Fig. H.6. SEM micrograph, EDX elemental map and spectrum of the gold GDE with 1 mg cm^{-2} loading.

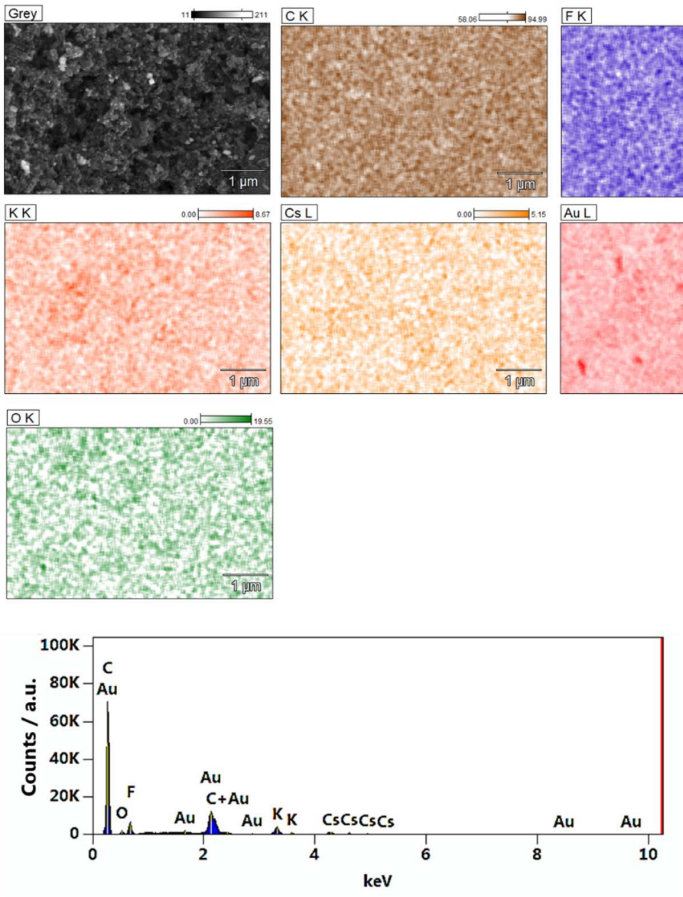

Fig. H.7. SEM micrograph, EDX elemental map and spectrum of the gold GDE with 2 mg cm^{-2} loading.

H.5 Comparison with neutral media

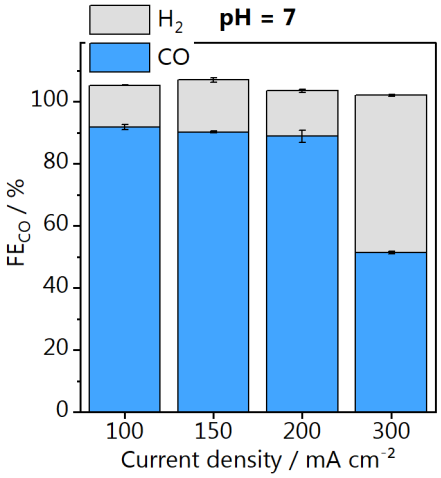

Fig. H.8. Faradaic efficiencies for CO and H_2 obtained during one hour electrolysis at each current density displayed. The catholyte was 1 M $KHCO_3$ (pH 7) and the catalyst loading 1 mg cm^{-2}. Error bars are calculated based on three individual measurements.

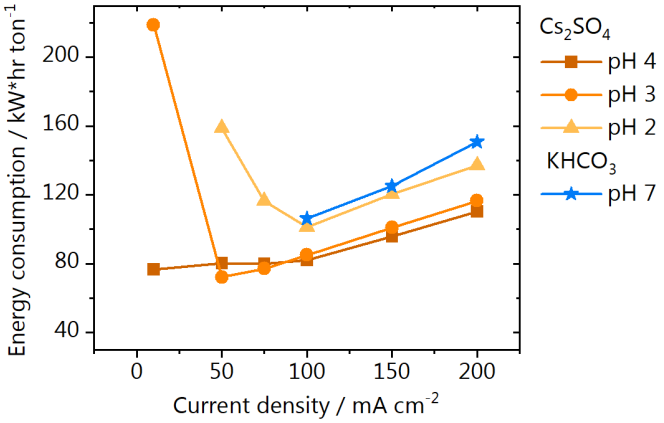

Fig. H.9. Energy consumption per ton of CO produced, based on the faradaic efficiencies and cell potentials obtained for electrolysis in 1 M Cs_2SO_4 or 1 M $KHCO_3$ at different current densities (catalyst loading 2 mg cm^{-2}).

Energy consumption per ton of CO produced, based on the faradaic efficiencies and cell potentials obtained for electrolysis in 1 M Cs_2SO_4 or 1 M $KHCO_3$ at different current densities (catalyst loading 2 mg cm^{-2}).

Energy efficiency calculation:

$$\varepsilon_{energy} = \frac{\left(E^0_{CO_2} + E^0_{O_2}\right) * FE_{CO}}{E_{Cell}} \qquad \text{Eq. H.1}$$

where E^0 are the standard potentials of the cathode and anode reactions, *FE* is the faradaic efficiency as percentage, and *Ecell* is the cell potential in V.

Energy consumption calculation:

$$\frac{kW*h}{ton} = \frac{E_{cell}*n*F}{MW*FE_{CO}*3.6} \qquad \text{Eq. H.2}$$

where *n* is the number of electrons transferred (dimensionless), *F* is Faraday´s constant in C mol^{-1}, *MW* is the molecular weight of CO in g mol^{-1}.

H.6 Comparison with literature

Table H.1. Experimental details of the different work from literature, used for the comparison made in Figure 5 in the main text. Only GDEs with geometrical surface area equal or larger than 5 cm^2 were considered.

	Cathode (GDE)	Anode	Electrolyte	CO_2 flow ($mL\ min^{-1}$)	Load ($mg\ cm^{-2}$)	Cathode area (cm^2)	Ref
this work	Au nanoparticles	DSA®	1 M Cs_2SO_4	50	1	10	this work
Haas 2018	Ag GDE Covestro	Ir-MMO/Ti sheet	0.1 M K_2SO_4 + 1.5 M $KHCO_3$	52 and 10.5	n.a.	10	[1]
Verma 2018	MWNT/PyPBI/Au on Sigracet® 35 BC	IrO_2	2 M $KHCO_3$ or 2 M KOH	17	1	5	[2]
Verma 2016	Ag NP on Sigracet® 35 BC	IrO_2	1 M $KHCO_3$	17	2	10	[3]
Duarte 2019	Ag NP on Sigracet® 39 BC	platinized Ti	2 M $KHCO_3$	77	0.75	10	[4]
Jeanty 2018	Ag GDE Covestro	n.a.	0.4 M K_2SO_4	21	n.a.	7.67	[5]

References

(1) Philips, M. F.; Davide, A.; Figueiredo, M. C.; Krasovic, J. WO2020165074A1, 2020.

(2) Haas, T.; Krause, R.; Weber, R.; Demler, M.; Schmid, G. *Nat. Catal.* 2018, *1* (1), 32–39.

(3) Verma, S.; Hamasaki, Y.; Kim, C.; Huang, W.; Lu, S.; Jhong, H. R. M.; Gewirth, A. A.; Fujigaya, T.; Nakashima, N.; Kenis, P. J. A. *ACS Energy Lett.* 2018, *3* (1), 193–198.

(4) Verma, S.; Lu, X.; Ma, S.; Masel, R. I.; Kenis, P. J. A. *Phys. Chem. Chem. Phys.* 2016, *18* (10), 7075–7084.

(5) Duarte, M.; De Mot, B.; Hereijgers, J.; Breugelmans, T. *ChemElectroChem* 2019, *6* (22), 5596–5602.

(6) Jeanty, P.; Scherer, C.; Magori, E.; Wiesner-Fleischer, K.; Hinrichsen, O.; Fleischer, M. *J. CO2 Util.* 2018, *24* (March), 454–462.

I

Methods and supporting information to Chapter 12

I.1 Synthesis and characterization of gas diffusion electrodes

I.1.1 Nanoparticle synthesis

The procedure for preparing the gold nanoparticles was adapted from Kimling et al.[1] Gold nanoparticles supported on carbon were synthesized by dissolving 0.034 g of $HAuCl_4$ trihydrate (>49% Au, Fisher Scientific) in 95 mL of water and 0.097 g of trisodium citrate dihydrate (≥99%, Sigma-Aldrich) in 5 mL of water. The Au solution was brought to a boil under vigorous stirring, and the citrate solution was pre-heated. As soon as the gold solution boiled, the pre-heated 5 mL of citrate solution was added. Upon addition, the solution, which was initially yellow, turns transparent, then black and finally, after 15 min dark red. After the solution cooled down, still under vigorous stirring, an amount of VXC72 Vulcan carbon (Cabot) was added to yield a metal loading of 60% Au on the carbon support. The solution was then tip sonicated for 20 min at 31% amplitude with a MS73 ultrasonic probe (Bandelin) and kept stirring overnight. Once all the Au nanoparticles were supported on the carbon, the solution became transparent. The Au/C particles were filtered and rinsed several times with water.

I.1.2 Gas diffusion electrodes spraying

A catalyst ink stock solution was prepared by first adding 28.9 mg of Au/C nanoparticles to a solution containing 2.43 ml water and 2.43 ml ethanol to spray the 60% Au/C gold nanoparticles on carbon-based gas diffusion electrodes (GDEs). This mixture was tip sonicated for 5 min with a MS73 ultrasonic probe. Then 139 µL Nafion 5% solution (Sigma Aldrich) was added, and the ink was sonicated for another 5 min. For spraying, the ink was diluted 100 times with water. A gas diffusion layer (H23C2, Freudenberg) was cut to 4 x 10 cm sheets and used as substrate. The ink was deposited on the substrate using the spray-coating apparatus previously described.[2,3] The H23C2 substrates were placed on a heating block at 100 °C for quickly evaporating the solvent, hence reducing the possible formation of agglomerates. A template was used in order to limit the sprayed area to 1 x 3 cm. The spraying parameters were controlled with software written in Microsoft Visual Basic 6.0. The Au/C catalyst gradients were realized by adjusting the volume of ink dispensed along the substrate stepwise, using a defined array as a function of the XY position of the spray-tip. The total loading was determined by the number of times the procedure was repeated over the entire area of the

substrate. Fig. I.1 shows a photograph of one of the gas diffusion electrodes after spraying, indicating the Au/C nanoparticle gradient deposited in the exposed area.

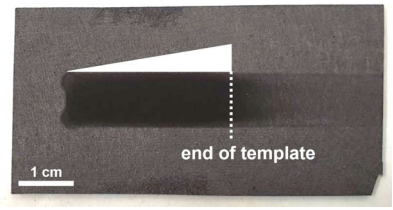

Fig. I.1. Photograph of the gas diffusion electrode after spraying showing a 1 x 3 cm^2 catalyst loading gradient.

I.1.3 Characterization of the gas diffusion electrodes

Scanning electron microscopy (SEM) and energy-dispersive X-ray spectroscopy (EDX) characterization of the GDEs and Au-nanoelectrode was performed using a Quanta 3D ESEM (FEI) at 20 kV acceleration voltage in high-vacuum mode. The Au-nanoelectrode was mounted on a customized metallic holder, and electric contact between the different samples and the metallic holder was established using a conductive carbon tape to minimize electrostatic charging. Focused ion beam (FIB) milling of the GDE substrate was performed for GDE-B to obtain a cross-sectional analysis of the pore structure. In the first step, the FIB milling process was used to mill a hole into the substrate from the top to create a ramp with a slope of approximately 45° using a FIB current of 65 nA for 2 h. This is a prerequisite for EDX analysis of the cross-sectional view later. In a 90° angle to this cut, another ramp with a 45° slope was milled into the substrate using the same parameters. The sample was then tilted by 2°, and a FIB cross-section polishing procedure was applied for about 10 min to obtain the shown cross-sectional view inside the substrate. EDX of the exposed cross-section after FIB milling was conducted at an acceleration voltage of 30 kV.

I.1.4 Au-nanoelectrode preparation

Au-nanoelectrodes suitable for the approach via shear-force based distance feedback were fabricated with a laser puller (Model 2000, Sutter Instruments). As already mentioned in the main text, the adhesion properties of untreated gold wires to the capillary glass walls are not sufficient for the reliable production of well-sealed Au SECM tips. Therefore, we modified the adhesion characteristics of the gold wire (50 µm diameter, >99.99 %, Goodfellow) by electrochemically coating it

with a thin layer of platinum. Platinum deposition was performed in a 3-electrode electrochemical setup with the Au wire as working electrode, a Pt mesh as counter electrode, and a Ag/AgCl/3 M KCl as reference electrode. A commercial Pt plating solution (Met-Pt 209, Metalor) was used as electrolyte. Contact with the electrolyte was made with the gold wire at 0 V, and then three potential pulses of 100 ms to –1 V and 500 ms to 0 V were performed. The coated Au-wire was further immersed into the plating solution for 2 h without any applied bias voltage, and then thoroughly rinsed with water. Once dried at ambient atmosphere, 1 cm long pieces of Pt-plated gold wire were positioned in the centre of soda-lime glass capillaries (Hilgenberg) with an inner diameter of 0.5 mm and an outer diameter of 1 mm. Next, the filled glass capillaries were fixed in a laser puller. Both capillary inlets were connected to a vacuum pump (Laboport, KNF Neuberger) to avoid the inclusion of air bubbles during the subsequent sealing step. During sealing of the Au wire in 7-9 heating/cooling cycles (20 s and 40 s, laser ON/OFF), the puller bars were fixed with a metal clamp to prevent a continuous pulling force on the capillary. The following laser puller parameters were used during the sealing step: heat: 260; filament: 5; velocity: 90; delay: 140; pull: 0. After confirming a visually complete Au/glass seal with the help of an optical microscope, the capillary was reinserted into the laser puller for the hard pull step. In this step, the Au/glass composite was liquified by laser heating and pulled into two parts using the following parameter set: heat: 300; filament: 5; velocity: 90; delay: 140; pull: 90-110. The resulting long-tapered glass/Au tips were electrically contacted by conductive 2-component epoxy glue (Polytec EC 151-L, Polytec PT). The glue was filled into the glass capillary using the tip of a Cu-wire (outer diameter of 0.3 mm) up to the non-sealed section of the Au wire. One end of the Cu wire was left inside the filled capillary while curing the glue at 90 °C for 1 h. The tip was polished in a homemade polishing setup which individually rotates the electrode and a hard disc covered with an abrasive film to expose the cross-section of the gold wire. The tip was also subsequently polished on the following abrasive layers: P2000 sandpaper (Starcke), 0.5 µm and 0.1 µm diamond lapping film (661X, 3M Deutschland). Prior to polishing on each lapping film, the Au tip was ultrasonicated in EtOH/water for 10 min.

I.1.5 Shear-force based approach

The local detection of CO during CO_2 reduction over gold GDEs requires approaching the Au-nanoelectrodes to a sub-µm distance from the substrate. Such precise positioning is done by shear-force distance-controlled scanning

electrochemical microscopy (SECM). Its approach feedback mechanism is based on short-range hydrodynamic forces, which occur in the order of a few 100 nm away from solid surfaces.[4] During the approach of a resonantly oscillating SECM tip towards a solid surface, those forces modulate the tip´s oscillation characteristics, which serve as feedback for determining the absolute surface position. To assure a successful approach, all setup components are located inside of a homemade faraday cage to allow for shielding of electrical noise, with the exception of the lock-in amplifier and the potentiostat. Vacuumed polystyrene panels (Vaku-Isotherm) are used to cover the inner walls of the faraday cage to maintain a constant temperature around the measurement cell. Vibrational noise during SECM measurements was minimized by mounting the faraday cage on an actively damped table (Newport RS 2000). The precise approach of the Au-nanoelectrode towards different spots of the GDE surface was facilitated by a positioning system combining both a stepper motor and a piezo positioning unit. A coarse alignment of the SECM tip in the X, Y and Z coordinates was established via stepper motor (OWIS) controlled µm-screws. The pre-approach in the Z-direction was visually controlled with the help of a video microscope (monochrome USB camera, The ImagingSource). After the pre-approach, a piezo positioning unit (PI) enabled further approach in nanometer increments. In parallel to the approach, the oscillation magnitude of the resonantly vibrating Au tip was recorded as feedback signal. Such shear-force-based distance control loops require mounting two piezo elements (Piezomechanik Pickelmann) to the Au tip glass body. Both piezo elements were connected to a lock-in amplifier (Ametek 7280) via BNC connectors. One of those piezo elements served as the detection element for the magnitude of the oscillation at the tip apex and was mounted as close as possible to the tip´s taper. The second piezo unit had the function to generate a tip oscillation at a defined frequency by applying an AC voltage via the lock-in amplifier. This excitation piezo was mounted in a distance of 1-1.5 cm above the detection piezo and was displaced by an angle of around 45°. To establish a reliable distance control, it is crucial to identify a tip resonance frequency with high sensitivity towards the tip-to-surface distance. For that purpose, before every experiment, a frequency spectrum in the range from 200-500 kHz (linear ramp over 300 s, 200 mV magnitude) was recorded while the tip was kept in the pre-approach position above the GDE substrate. Subsequently, electrolyte (1 M $KHCO_3$) was filled into the electrochemical cell, so that the Au tip got immersed into this differently oscillating medium. Another frequency spectrum was then recorded and compared to the one

in air. Resonant frequencies with significantly different oscillation magnitudes in both scans indicate possible tip frequencies for the shear-force based approach, since only resonant frequencies originating from the tip, and not from other system components such as the electrode holder, are altered by a change of the oscillation medium. Once a stable tip resonance frequency is identified, it is constantly set at the excitation piezo. During that defined oscillation, the tip is approached in nanometer increments towards the surface while continually monitoring the oscillation magnitude. The approach is automatically terminated once a magnitude change of 3 % of the lock-in value is detected by the software. This rapid change in magnitude is a characteristic feature in the approach curve, demonstrating that the tip reached a distance within the shear-force interaction region (in the order of 100 nm from the sample surface).

I.2 SECM experiments

SECM experiments using the shear-force approach method were performed in an electrochemical cell made of polyetheretherketon (PEEK) as shown in Fig. I.2. The GDE substrate was mounted between the electrolyte compartment (upper part of the cell) and a gas compartment with the help of an O-ring. The GDE was electrically contacted using Cu tape which was fixed along all GDE edges to minimize the electrical resistance. The gas compartment was connected to gas inlet and outlet Swagelok connectors allowing for a flow of gaseous CO_2 towards the GDE backside during the experiment. The flow rate of CO_2 into the gas compartment was controlled via a GFC17 mass flow controller (Aalborg). The gas outlet was fed via a tube into a water-filled glass column in order to adjust the GDE backpressure (overpressure with respect to atmosphere) via the immersion depth of that tube. Electrochemical measurements were conducted using an analogue bi-potentiostat (IPS PG 100, IPS Peter Schrems) which was controlled by an in-house software. The GDE substrate and SECM tip were connected as working electrodes 1 and 2, as indicated in Fig. I.2 by WE1 and WE2, respectively. The counter electrode (CE) was constructed from two dimensionally stable anodes (48 x 10 x 1 mm, MMO Type 197, Umicore), which were placed at two opposite edges of the electrolyte reservoir by means of a Au wire ring. The reference electrode (RE) was a homemade Ag/AgCl/3 M KCl with the filling solution reservoir separated from the electrolyte via a ceramic frit. The Ag-wire (99.995 %, ChemPur) was electrochemically coated with AgCl from a 3 M KCl solution (VWR Chemicals) containing 0.1 M HCl (Sigma

Aldrich) solution applying 5 V for 1 min and 10 V for 10 min vs. a Pt counter electrode. A fresh 1 M $KHCO_3$ electrolyte solution (99.7 %, Sigma-Aldrich) was used for each measurement, and was cleaned from metal cation impurities prior to use with the help of a Chelex-100 (Bio-Rad) resin as reported elsewhere.[5] For each SECM experiment, the CO_2 flow was switched on after filling the electrolyte (prior to the frequency scan in liquid) to prevent gas from breaking through dry GDE pores. After finding a suitable tip resonance frequency, the tip was positioned in the low loading region of the GDE (next to the left edge of the spraying template, Fig. I.1). After ensuring the tip functionality within the shear-force interaction region by cyclic voltammetry (example in Fig. I.7), an array scan along the first 1.7 cm of the sprayed Au/C loading gradient was performed in hopping mode. At each X-Y coordinate of that scan, a shear-force based approach was performed to account for topological differences along the gradient towards higher catalyst loadings, with the substrate held at –0.6 V. Once the distance feedback criterion was met, different potentials were subsequently applied to the GDE for 60 s while recording both the GDE and Au tip current. After the final potential was applied, the GDE was held again at –0.6 V, and the Au tip was retracted by 100 µm before moving to the next X-Y position of the GDE to avoid collision with surface features.

I.3 Characterization of the gas diffusion electrodes

The volume of ink dispensed using the spray-coater along the substrate is shown in Fig. I.3 for GDE-A (shallow catalyst gradient) and GDE-B (steep catalyst gradient). SECM measurements were performed along 1.7 cm of the substrates, corresponding approximately to the area highlighted in yellow in Fig. I.3. The two GDEs were characterized by SEM and EDX at different X-positions along the Au/C catalyst gradient. Results are shown in Fig. I.4 and Fig. I.5, for GDE-A and GDE-B, respectively.

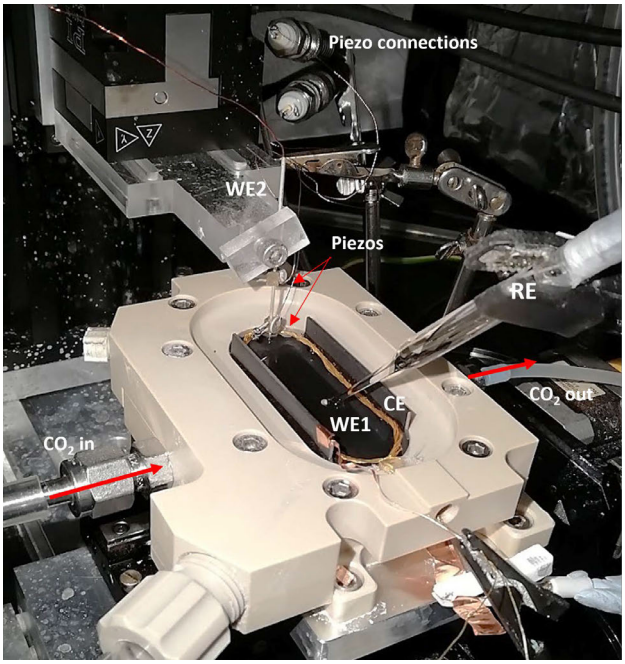

Fig. I.2. Electrochemical cell mounted in the SECM setup. The GDE substrate and the Au nanoelectrode are indicated as WE1 and WE2, together with the Ag/AgCl reference electrode (RE) and the DSA counter electrode (CE). The piezo elements and connectors are also indicated in the image, as well as the CO_2 gas inlet and outlet.

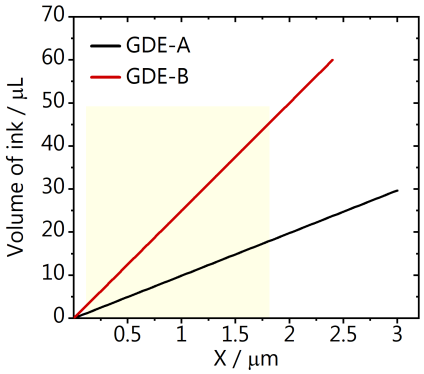

Fig. I.3. Volume of ink dispensed along the gas diffusion layer creating a more (GDE-B) or less (GDE-A) steep catalyst gradient.

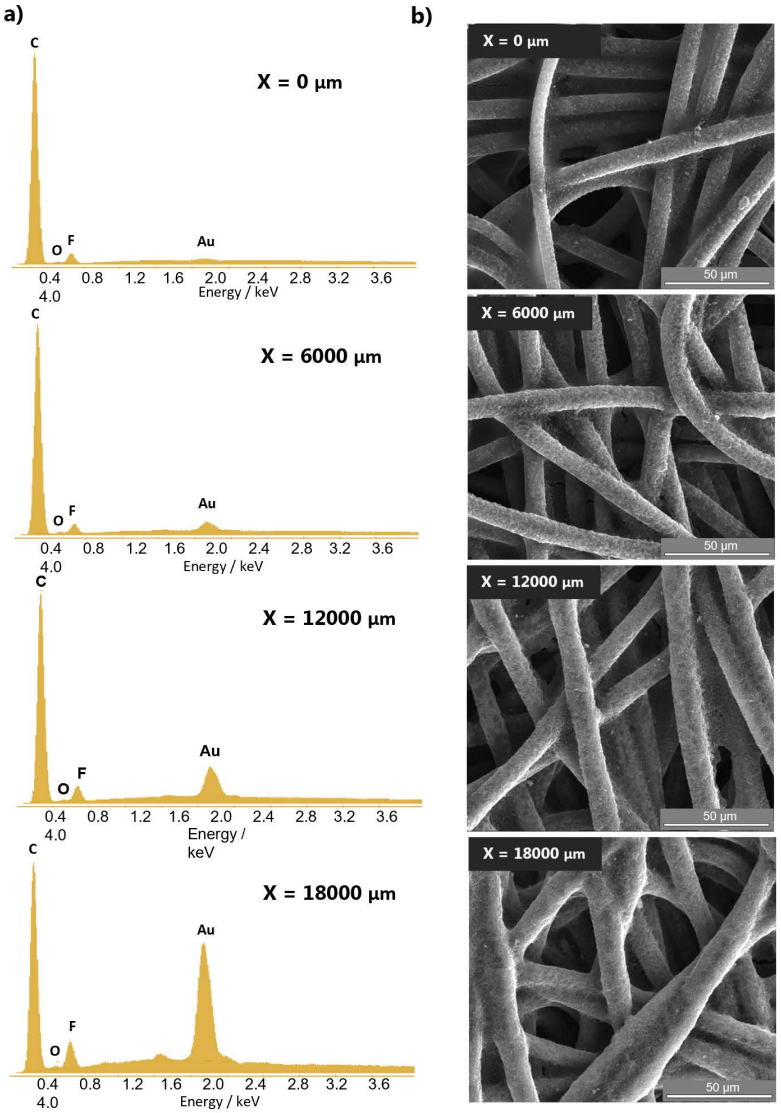

Fig. I.4. a) EDX spectra and **b)** SEM micrographs obtained at different X-positions along the catalyst gradient of GDE-A.

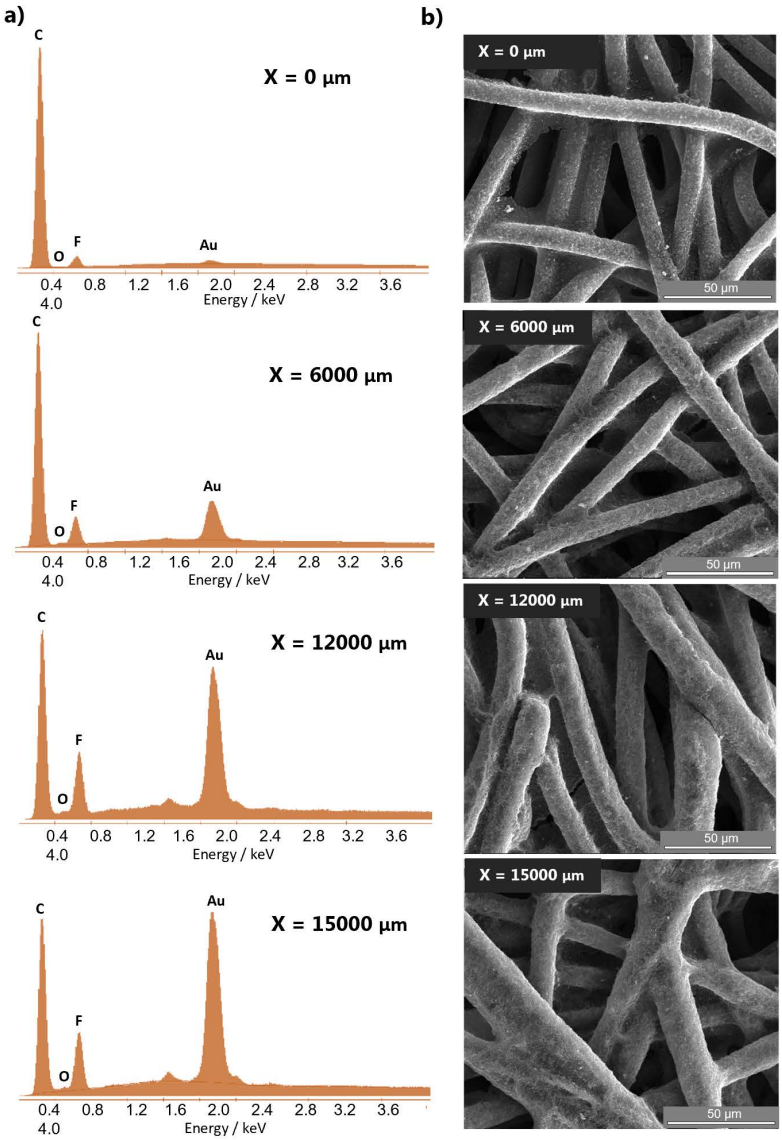

Fig. I.5. a) EDX spectra and **b)** SEM micrographs obtained at different X-positions along the catalyst gradient of GDE-B.

I.4 Shear-force approach

For positioning of the tip above the gas diffusion electrodes, first, a frequency spectrum of the gold nanoelectrode (Fig. I.6a) is recorded in air and then in electrolyte in order to determine the resonance frequencies characteristic from the tip. Using one of these frequencies, e.g. shown in Fig. I.6b (and marked in yellow in Fig. I.6a), an approach curve (Fig. I.6c) is performed to place the tip ~100 nm from the surface. Approach curves were performed at every XY position of the substrates before the measurements.

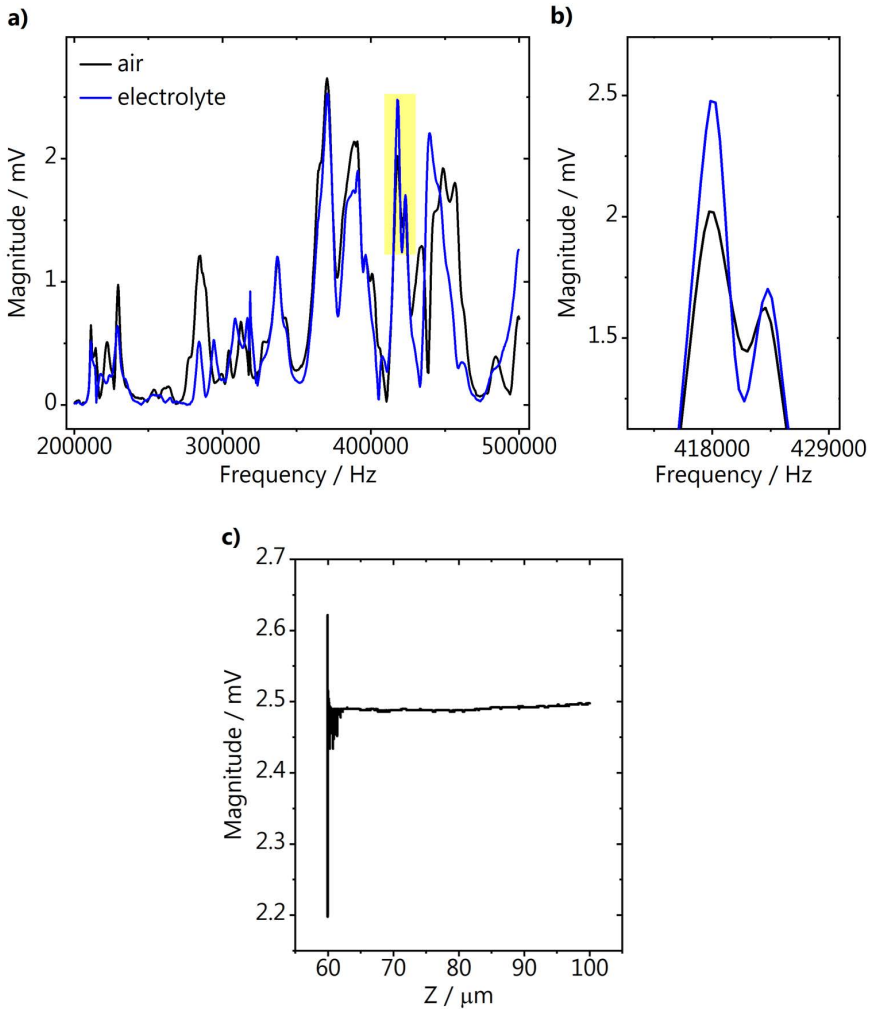

Fig. I.6. a) Frequency spectra recorded in air and electrolyte, **b)** zoom in of the tip resonance frequency used for the approach curve (yellow area from a)), **c)** approach curve.

I.5 Gold nanoelectrode response

The blank voltammetry of the gold nanoelectrode was recorded in the shear-force interaction region (~100 nm from the surface) before each measurement to assure a clean and reproducible Au surface. An example of a blank CV is shown in Fig. I.7a. CVs were also recorded while applying different potentials to the bare gas diffusion layer (without catalyst) in CO_2 saturated electrolyte (Fig. I.7b). No CO is produced by the bare substrate, and a reproducible double layer charging current is observed between 0 and 0.55 V vs Ag/AgCl.

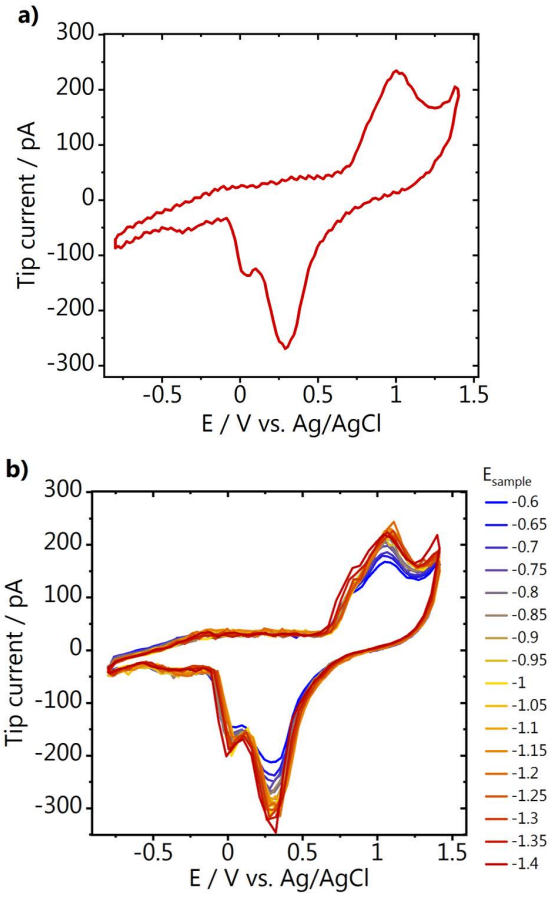

Fig. I.7. a) Blank CV of the gold nanoelectrode and b) voltammetry recorded in the shear-force interaction region while stepping the GDE potential. The sample potentials reported (E_{sample}) are versus Ag/AgCl, and the CVs were recorded in 1 M $KHCO_3$, CO_2 saturated, at 200 mV s^{-1}.

The gold nanoelectrode CVs were also recorded after flowing a calibration gas containing 1% CO for 10 seconds through the cell (Fig. I.8a). Two characteristic plateaus show the diffusion-limited oxidation of CO.[6] Additionally, voltammetric features of the gold oxidation and the overpotential of the oxygen evolution reaction (OER) can be observed. In Fig. I.8b, the voltammetric response of the Au nanoelectrode is shown while different potentials were applied to the gas diffusion electrode.

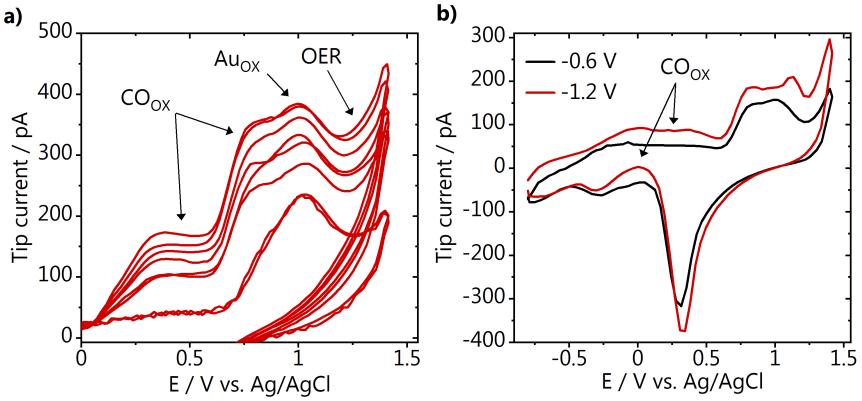

Fig. I.8. CVs of the gold nanoelectrode **a)** after feeding a calibration gas containing 1 % CO though the substrate for 10 s and **b)** upon applying different potentials to the GDE. The sample potentials reported are versus Ag/AgCl, and the CVs were recorded in 1 M $KHCO_3$, CO_2 saturated, at 200 mV s^{-1}.

I.6 SECM array scans

An example of how bubbles affect the current measured at the gold nanoelectrode is shown in Fig. I.9, where the sample (GDE-A) was held at –1.15 V vs. Ag/AgCl.

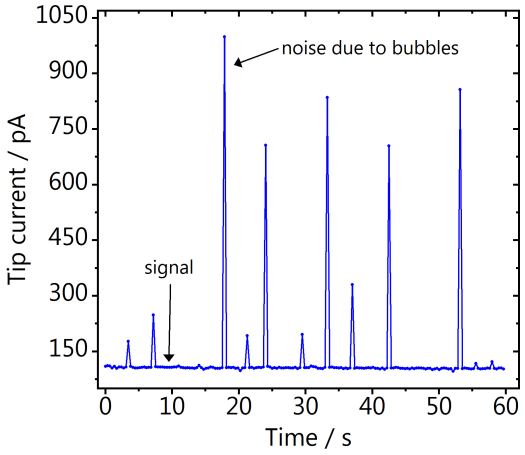

Fig. I.9. Raw tip current data recorded during a measurement where GDE-A was held at –1.15 V vs. Ag/AgCl.

The activity of GDE-A along the catalyst gradient is shown in Fig. I.10. The experiment was performed in 1 M $KHCO_3$ with a CO_2 pressure of 2 mbar.

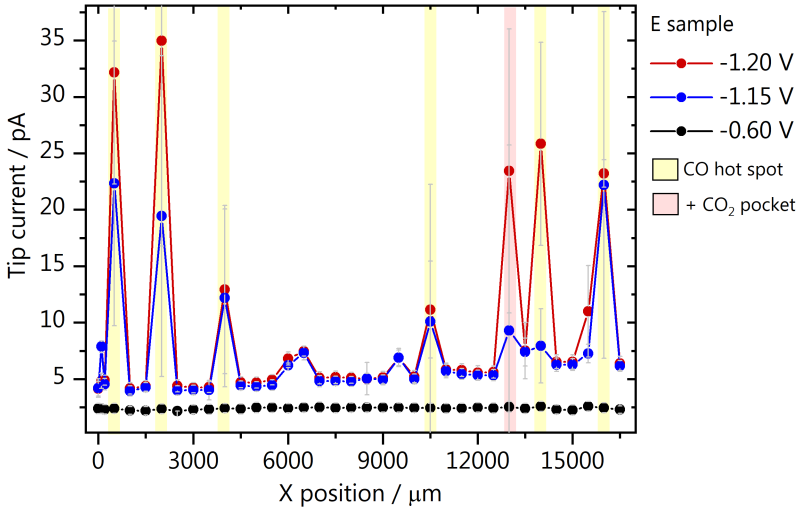

Fig. I.10. SECM array scan of GDE-A in 1 M $KHCO_3$ at a CO_2 pressure of 2 mbar. Potentials are reported versus Ag/AgCl.

Fig. I.11 shows the correlation between the sample height profile and the amount of CO detected along the gradient of GDE-B, at a CO_2 pressure of 0.7 mbar.

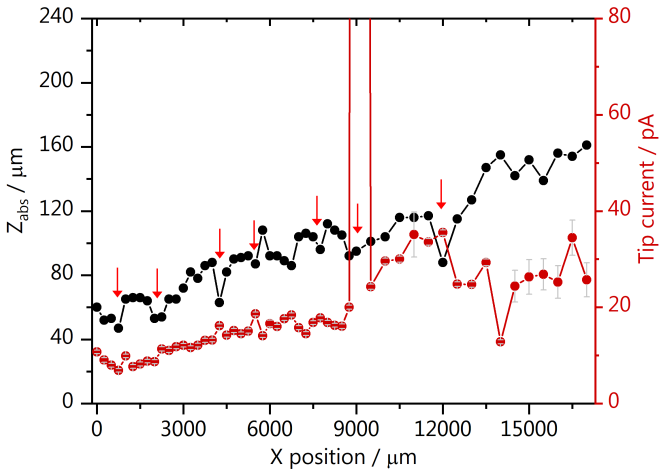

Fig. I.11. Absolute position of the shear force interaction region along the catalyst gradient of GDE-B, together with the CO activity.

Fig. I.12 presents the activity maps recorded in a 30 x 30 µm area of GDE-B (CO_2 pressure 0.7 mbar). Here, three different ways of visualizing the same data are presented for the three different substrate potentials applied. The top panel shows a realistic representation of the data measured, considering the diameter of the Au nanoelectrode, and the middle panel the same data but with the space filled. The interpolated data (using nearest neighbours) are shown in the lowest panel and allows for easier visualization and interpretation of the activity trends and is therefore shown in the main text.

After recording the activity maps, we have marked the substrate using a 1.2 mm probe at a distance of 1 mm of the scanned area, as shown in the SEM micrograph in Fig. I.13a. Although there is an uncertainty in the exact location of the map, Fig. I.13b shows that the mapped region likely has large variations in topography, i.e. deep pores and fibres at different levels. Taking this into consideration together with the results shown in Fig. I.11, we are confident that the mapped area is likely the region shown in Fig. I.13c.

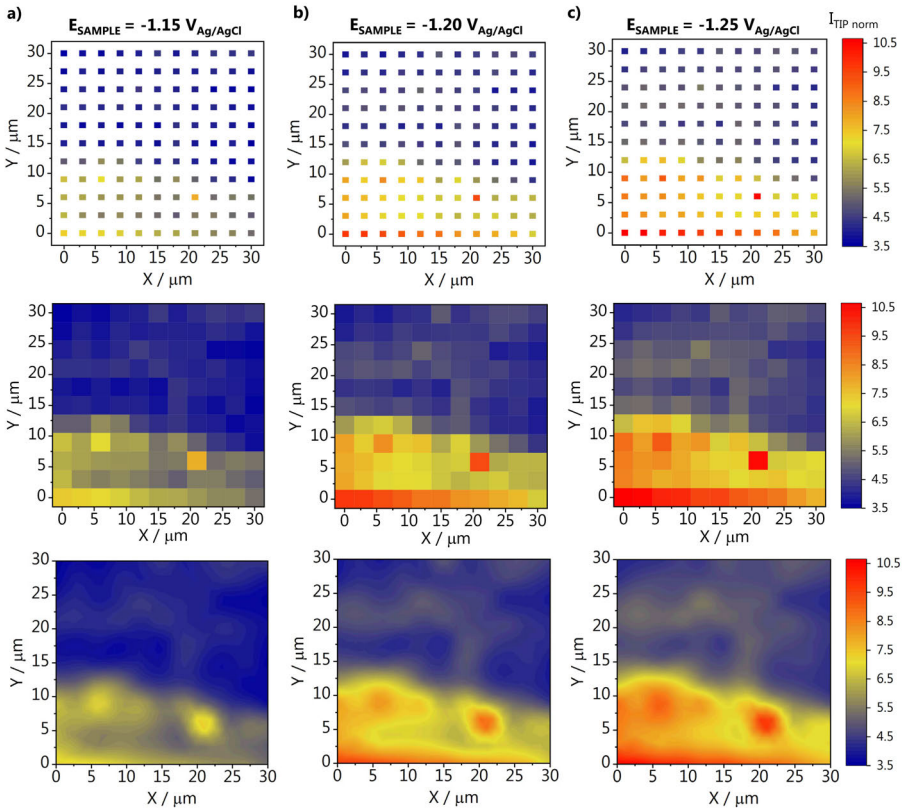

Fig. I.12. Activity map of GDE-B recorded at sample potential **a)** -1.15 V, **b)** -1.2 V and **c)** -1.25 V. Three different ways of visualizing the data are presented, namely by plotting the individual data points with and without space filling, and the interpolated data shown in the main text. Potentials are reported versus Ag/AgCl.

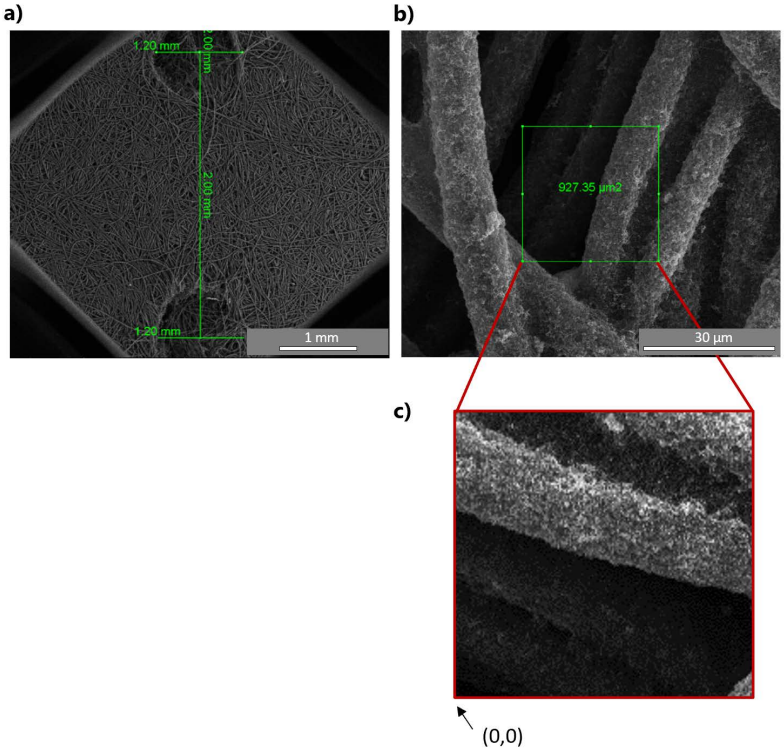

Fig. I.13. SEM micrographs of **a)** the marks made in GDE-B after the activity maps were recorded, **b)** the mapped region, within a confidence interval and **c)** a suggested topography of the mapped area.

References

(1) Kimling, J.; Maier, M.; Okenve, B.; Kotaidis, V.; Ballot, H.; Plech, A. *J. Phys. Chem. B* 2006, *110* (32), 15700–15707.
(2) Junqueira, J. R. C.; Bobrowski, T.; Krysiak, O. A.; Gutkowski, R.; Schuhmann, W. *ChemCatChem* 2019, *11* (24), 6417–6424.
(3) Bobrowski, T.; Conzuelo, F.; Ruff, A.; Hartmann, V.; Frank, A.; Erichsen, T.; Nowaczyk, M. M.; Schuhmann, W. *Chempluschem* 2020, *85* (7), 1396–1400.
(4) Nebel, M.; Eckhard, K.; Erichsen, T.; Schulte, A.; Schuhmann, W. *Anal. Chem.* 2010, *82* (18), 7842–7848.
(5) Wuttig, A.; Surendranath, Y. *ACS Catal.* 2015, *5* (7), 4479–4484.
(6) Monteiro, M. C. O.; Jacobse, L.; Koper, M. T. M. *J. Phys. Chem. Lett.* 2020, *11* (22), 9708–9713.

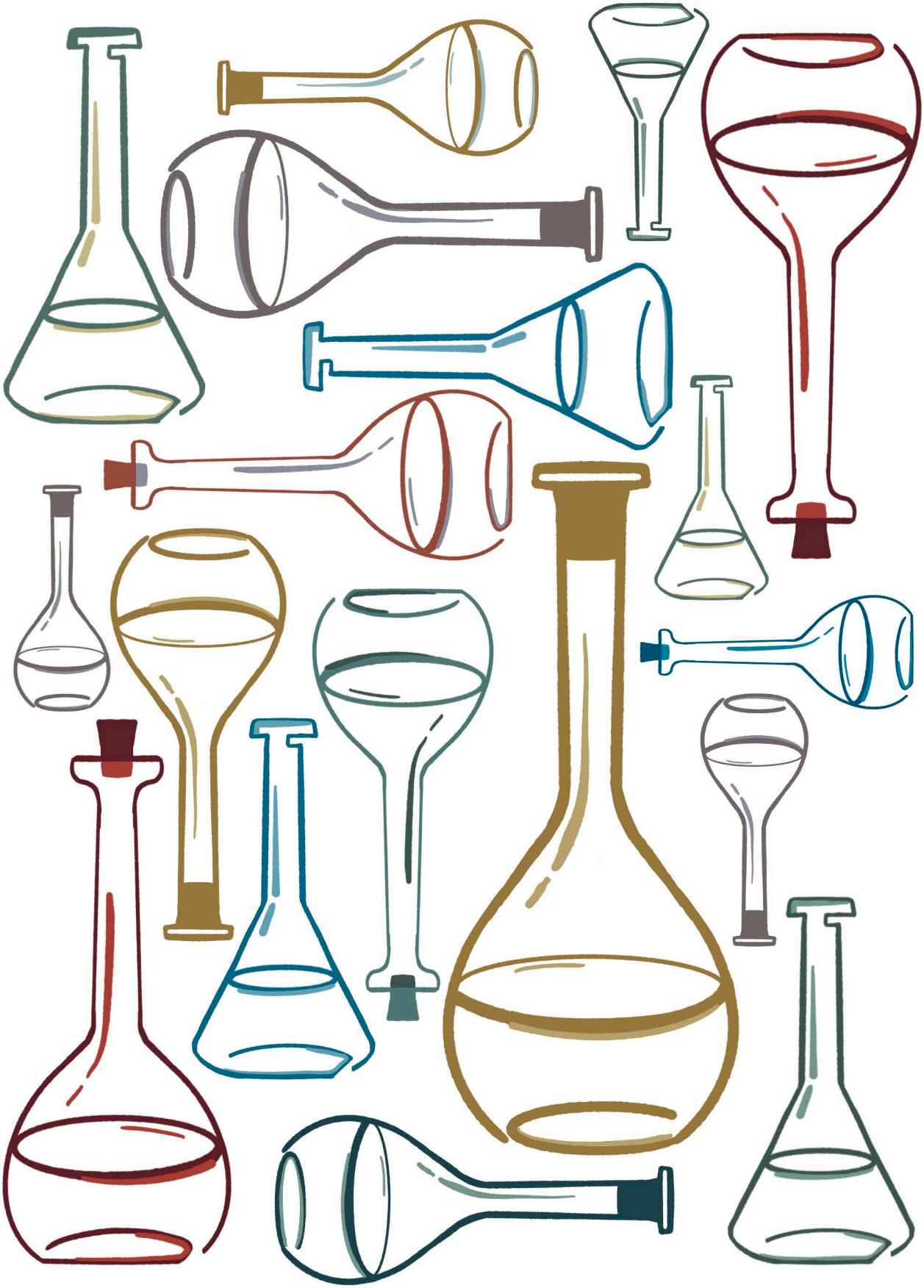

Summary and Outlook

Summary

Electrocatalysis allows for storing electricity or converting it into chemical bonds, producing chemical building blocks and fuels using renewable resources. Therefore, it plays an important role in the transition towards a more sustainable future for our society through electrification. Still, to bring electrochemical technologies to industrial scale and make them competitive, optimization of various aspects of electrocatalytic reactions are needed. To improve a system, one must first (at least roughly) understand it. Many fundamental studies focus on understanding the catalyst surface, however, different components of the electrolyte, as pH and cations, have also shown to significantly affect the reaction activity and selectivity. In view of that, in this thesis, various aspects of the electrode-electrolyte interface are studied at different scales, using Scanning Electrochemical Microscopy (SECM), stationary and rotating-disc electrode voltammetry techniques, and bulk electrolysis.

During electrocatalytic reactions that consume or produce protons or OH^-, the pH at the electrode surface may differ drastically from the pH in the bulk of the electrolyte. These pH gradients may affect the reaction taking place at the surface and homogeneous reactions taking place in the electrolyte, therefore quantifying them is desired. **Chapter 2** presents a review on different methods to probe pH locally in electrochemistry and highlights SECM as a powerful and versatile technique. In **Chapter 3**, we describe the development of a voltammetric pH sensor based on the 4-hydroxiaminothiophenol/4-nitrosothiophenol (4-HATP/4-NSTP) voltammetry. We apply this sensor to study the local pH developed during hydrogen evolution on gold at different potentials, using SECM. These proof-of-concept experiments show that the 4-HATP/4-NSTP pH sensor is highly selective and sensitive, allowing to measure differences as small as 0.1 pH unit with high time resolution. Thereby, in **Chapter 4** we employed the same pH sensor to also perform SECM local pH measurements during CO_2 reduction. Here, we investigate the diffusion layer dynamics and how the different homogeneous reactions involving CO_2 modulate the local pH. Beyond that, we show through Finite Element Method (FEM) simulations how the SECM tip affects the diffusion of species leading to an additional alkalinization of the local reaction environment and discuss ways to avoid that.

In **Chapter 5**, we use SECM to understand the voltammetric features of CO electrooxidation on gold as a function of pH. We probe CO oxidation using a

platinum ultramicroelectrode positioned above an electrode that is reducing CO_2 (therefore locally producing CO). We also perform local pH measurements at the same tip-to-surface position, and the correlation of these two experiments allow to draw a better understanding on the nature of the distinct CO oxidation voltammetric features. Different peaks in the voltammetry appear as a function of the local pH, and are related to CO being oxidized by H_2O or OH^- and the reaction being limited by the diffusion of different species, namely CO or OH^-.

Among the techniques reviewed in Chapter 2, rotating ring-disc electrode (RRDE) is the only one that currently enables local pH measurements to be performed under well-defined mass transport control conditions. However, pH sensors used in combination with RRDE, so far, lacked in temporal resolution, sensitivity, and selectivity. Considering the potential of the 4-HATP/4-NSTP voltammetric pH sensor, in **Chapter 6** we assessed the feasibility of its application to a RRDE system. We show that the 4-HATP/4-NSTP redox couple can be successfully incorporated to a gold ring electrode and we use it to measure the local pH at a gold disc evolving hydrogen. This is successfully done during cyclic voltammetry, chronopotentiometry and chronoamperometry under different rotation rates and potentials, in buffered and unbuffered electrolytes.

In Chapter 7 we investigate a different aspect of the electrochemical interface, namely how surface contamination can affect electrocatalysis. Electrodes must be prepared before they are used for an experiment, and the simplest and most used surface preparation method is polishing. In **Chapter 7**, we show how polishing gold electrodes with alumina paste leads to an enhancement in the hydrogen evolution reaction in acidic media. This is due to the release of Al^{3+} ions in the electrolyte, which promote the water reduction reaction. This should in many cases be avoided, as water reduction competes with various reactions taking place in aqueous media at cathodic potentials, as CO_2 and nitrate reduction.

Apart from the local pH and contamination, ions dissolved in the supporting electrolyte can also strongly affect electrocatalytic reactions. However, the mechanism describing this phenomenon is in many cases still under debate. In **Chapter 8**, we elucidate how metal cations in the electrolyte affect the CO_2 reduction reaction. Through cyclic voltammetry and SECM experiments, we make the remarkable observation that CO_2 reduction to CO happens on gold, copper, and silver electrodes only if a metal cation is added to the electrolyte. By combining the experimental results with density functional theory (DFT) and *ab initio* molecular dynamics simulations, we suggest a new mechanism for the reaction, in which metal cations favor CO_2 adsorption,

and explicitly interact with the CO_2^- reaction intermediate. Furthermore, we see that differences in activity for CO formation among alkali cation species come from the different driving force cations with different hydration energies have to accumulate near the surface. Owing to the complexity of the cation-electrode-reactants interactions, in **Chapter 9** we have extended the study from Chapter 8 to multivalent cationic species. Here, we define which cation properties dictate the activity for CO_2 reduction and for the competing hydrogen evolution reaction at different potentials. We see that electrolytes containing acidic and weakly hydrated cations favor the water reduction reaction, and are therefore detrimental to the activity of CO_2 reduction at high overpotentials. Again, in combination with *ab initio* molecular dynamics, we see that this happens because these species lower the barrier for water dissociation and accumulate more near the surface. Simulations and experiments show that cation acidity is an appropriate activity descriptor and dictates the competition between CO_2 reduction and water reduction. In **Chapter 10**, we look further into the effect alkali cations have on water reduction, as opposite trends as a function of alkali cation identity have been reported for platinum and gold electrodes. We find that weakly hydrated cations (K^+) favor water reduction on gold at low overpotentials (lower alkalinity) while at high overpotentials (more alkaline pH) these are detrimental to the reaction, and higher activity is found using electrolytes containing strongly hydrated cations (Li^+). A similar trend is found for platinum, however this inhibition effect on platinum is already pronounced at lower alkalinity and lower cation concentrations, suggesting that platinum interacts stronger with metal cations in the electrolyte than gold.

The knowledge obtained in the fundamental studies from Chapters 8-10 and in the work of Bondue et al.[1], is transferred to a larger scale device in **Chapter 11**. Normally, CO_2 reduction is performed in neutral to alkaline media, as it is believed CO_2 cannot outcompete proton reduction in acidic media. Nevertheless, in Chapter 11, we show that CO_2 electrolysis can be carried out in acidic media using 10 cm^2 gold gas diffusion electrodes (GDEs). Up to 90% selectivity for CO is obtained at industrially relevant current densities (50-200 mA cm^{-2}) using a Cs_2SO_4 electrolyte, at pH 2-4. We show that this is comparable to results obtained in similar systems operating in neutral to alkaline conditions, with the advantage that in acidic media we can improve the process energy efficiency by 30%. Additionally, we observe that weakly hydrated cations like Cs^+ or K^+ are essential to run the reaction in acidic

media, as in Li_2SO_4 electrolytes at pH 2-4 nearly no CO is produced, in agreement with the findings from Chapters 8 and 9.

In Chapter 11, we also study the effect of the amount of catalyst applied to the GDE on the activity for CO, by running the reaction in gold GDEs with 1 and 2 mg cm^{-2} catalyst loading. The GDE with 1 mg cm^{-2} shows slightly better performance, but no clear trends can be observed, also not when comparing with similar work in the literature. To address that, in **Chapter 12** we used a system to locally probe the activity of GDEs using SECM with a shear-force based positioning, which also allows to a certain extent, to obtain information about the surface topography. We prepared GDEs having a gradient of gold nanoparticles going from a low to a high loading region. A gold nanoelectrode is used to detect the amount of CO produced along the GDE catalyst gradient. We see that more CO is produced as the loading increases. However, hot spots are found throughout the whole gradient, showing that more important than the amount of catalyst, is how accessible the catalyst particles are to the reactants. We confirm that by measurements at different CO_2 pressures which show that at the highest pressures there is an optimum loading necessary to achieve high activity. Finally, this system opens up a new path for locally probing the activity and topography of GDEs under *operando* conditions and with high spatial resolution.

Outlook

The work presented in this thesis addresses a number of research questions, especially concerning CO_2 reduction and hydrogen evolution, using a multiscale approach. With that, we believe the tools developed to probe local pH and local activity, and the findings on how cations interact at the reaction interface, contribute not only to the existing research in these fields, but to the field of electrocatalysis in general. The following sections present ongoing and future directions for the different topics discussed in this thesis.

Local pH measurements

The pH sensor developed in Chapter 3 and used in Chapters 4-6 showed to be robust enough and its applications can be numerous. Both in the SECM and RRDE configurations, the 4-HATP/4-NSTP functionalized gold electrode can be used to probe local pH during other electrocatalytic reactions as nitrate reduction, oxygen reduction, CO oxidation. It can also be applied, for instance, to monitor the

pH during electrodeposition or corrosion processes. In fact, testing its functionality in these various systems would be beneficial for finding out its limitations. The main advantage of this sensor is the fact that it is just formed by a monolayer of molecules on the gold surface, therefore the response time upon changes in proton concentration is fast. On the other hand, currently, the main drawback of using the 4-HATP/4-NSTP sensor is the instability of the redox couple under current or potential overloads, caused e.g. by bubble formation. This is especially relevant in the RRDE system, and overcoming it should still be addressed, i.e. by applying a hydrophobic coating to the ring-disc spacer.[2]

Mono- and multivalent cation effects on CO_2 reduction and H_2 evolution

In Chapter 7, we see that layered hydroxides can be deposited on gold upon cycling into hydrogen evolution in a 0.1 M $Al_2(SO_4)_3$ electrolyte. These materials have various applications, e.g. for: energy storage, dye degradation, organic pollutant degradation, water treatment, photoelectrochemical water splitting and carbon dioxide reduction.[3] Conventionally, the synthesis of layered (double) hydroxides is done via co-precipitation (followed by calcination), sol-gel or hydrothermal methods, which are sometimes time consuming and may involve high temperatures and various steps.[3] Additionally, the synthesis products may have to be filtered and re-deposited on a support, if the layered hydroxides are to be used as water splitting or CO_2 reduction catalysts. The electrosynthesis of these materials has been reported, but has not yet been well-investigated and understood in detail.[4] It can present a few advantages for the synthesis of catalysts in comparison to the commonly used methods, as the electrochemically synthesized layered hydroxides can be directly deposited on a conductive support and the synthesis can be done at room temperature.

In Chapter 8 we find that CO_2 reduction to CO does not take place without a metal cation in the electrolyte. We rationalize this with the fact that metal cations explicitly interact with the CO_2^- intermediate, thereby stabilizing it. To draw a larger picture on how cations interact with reaction intermediates, it would be interesting to do similar measurements involving other reactions or other CO_2 reduction intermediates. For example, CO_2 or CO reduction to ethylene on copper is proposed to proceed through a CO dimer (negatively charged) intermediate ($OCCO^-$).[5] It is therefore desired to check if ethylene forms from CO/CO_2 reduction in the absence of a metal cation in the electrolyte. As a next step, extending this study to other

reactions, could allow to draw a more general understanding on which reactions/surfaces need a cation to proceed, which do not, and why is that.

Moving on to Chapter 9, we see that 1 mM of multivalent cations as Nd^{3+} added to a Li^{+}-containing background electrolyte have an up to 25-fold enhancement effect on the activity for water reduction on gold. Even though these species may deposit on the electrode surface as hydroxides/oxides, the surface is still active and accessible to reactants. It would be interesting to see how this applies to other metal surfaces, as platinum. Also, it will be interesting to test if this strategy can be used to improve the performance of CO_2 or water electrolysers at larger scale.

Probing cation-surface interactions: Surface X-Ray Diffraction (SXRD)

In Chapter 10, we investigate the effect of alkali cations on the water reduction reaction in alkaline media on platinum and gold electrodes. Previous work from our group has shown that cations and pH play a role in the kinetics of water reduction.[6,7] The proposed model suggests that increasing the (local) electrolyte pH also increases the concentration of cations near the surface, which promotes water reduction. However, it was also observed that cations start to inhibit H_2 production on gold at too high near-surface cation concentrations (or analogously bulk pH $\geq$ 13), likely by blocking the surface. Despite the many insights gained through cyclic voltammetry experiments, both in Chapter 10 and in the studies of Goyal et al.[6,7], we still miss direct experimental evidence on the pH dependence of the cation-surface interactions.

To resolve the structure of the electrochemical interface, we performed *in situ* Surface X-Ray Diffraction (SXRD) experiments at the German Electron Synchrotron (DESY). Several SXRD studies have been performed previously, to determine the electrode-cation distance, as well as cation coverage from specular crystal truncation rod (CTR) measurements.[8–10] In general, these studies indicate that cations are present at the interface, without being specifically adsorbed. However, the data is far too sparse to obtain a general understanding. Moreover, most measurements were performed at potentials close to the electrode potential of zero charge (PZC). At more negative potentials, the electrode-cation interaction is expected to be stronger, and this potential region is also much more relevant for the electrocatalytic reactions studied in this thesis, and to experimentally confirm the model suggested in the works of Goyal et al.[6,7] and in Chapter 10. Therefore, we

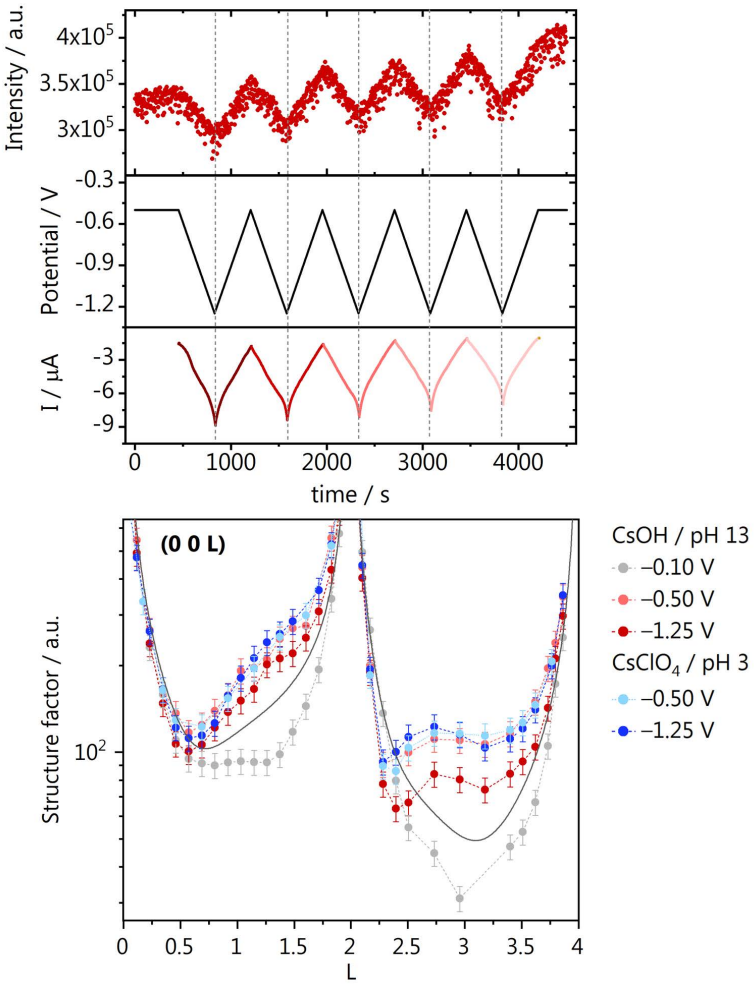

Fig. 1. Specular Crystal Truncation Rods (CTRs) of Au(100) in Cs^+ containing electrolyte: **a)** signal intensity (L = 0.54) during a cyclic voltammogram (2 mV s^{-1}) at pH 13; **b)** CTRs measured at different constant potentials (V vs. Ag/AgCl) at pH 3 and 13. The gray line overlapped in the plot represents the simulated CTR of the hexagonally reconstructed Au(100) surface in the absence of cations.

probed the interaction of Cs^+ ions with Au(100) at different negative potentials, both in acidic ($CsClO_4$, pH = 3) and alkaline media (CsOH, pH = 13).

From specular CTR measurements during cyclic voltammetry, we see reversible changes in the signal intensity as a function of potential for the hexagonally reconstructed Au(100) in 0.1 M CsOH (pH 13). Such behavior as a function of potential is not present in the absence of cations in the electrolyte, for both the unreconstructed and hexagonally reconstructed Au(100) surface, as

previously shown in the work of Ocko et al. and our own simulations (not shown).[11] Furthermore, we observe that Cs^+ interacts stronger with the surface in alkaline than in acidic media (Fig 1b). This is especially visible by the surface-sensitive, low intensity features of the CTRs (at –1.2 V) at L = 0.5, 1.5, 2.39. This confirms the model that has been recently proposed[6], and represents a direct experimental evidence of its validity. We are currently further fitting and analyzing the data, in order to determine the electrode-cation distance as well as cation coverage at the different conditions.

Owing to the success of the SXRD measurements using Au(100), we will soon extend this study to platinum surfaces and other cationic species. Our experimental work shown in Chapter 10 suggests that Pt and Au interact very differently with metal cations in the electrolyte.[12] For both surfaces, weakly hydrated cations (K^+) promote water reduction only at low overpotentials (lower alkalinity) whereas at high overpotentials (higher alkalinity) the higher activity is found using electrolytes containing strongly hydrated cations (Li^+). The difference between Pt and Au is that the inhibition of water reduction on platinum is observed at lower overpotentials and lower pH, suggesting that platinum interacts stronger with metal cations in the electrolyte than gold. The same is also suggested by Density Functional Theory (DFT) calculations, which show that the adsorption potential of alkali cations on Pt(111) and Pt(100) is less negative than on Au(111) and Au(100).[13] In view of these experimental and theoretical results, we will perform SXRD measurements of Pt(111) and Au(111) in Cs^+ electrolyte, to also compare surface structures (as we previously measured Cs^+ on Au(100), Fig. 1. By systematically defining the experimental conditions, these measurements will enable a direct comparison between the interaction of cations with Au and Pt regarding the electrode-cation distance and cation coverage as a function of cation identity, pH and potential. With these data, we hope to explain the catalytic activity trends from Chapter 10 in more detail and formulate a more general understanding of the role of cations on the electrochemical reactivity of different metal surfaces.

Bridging the gap: assessing the performance of gas diffusion electrodes using scanning probe microscopy techniques

Finally, in Chapter 11, we find that CO_2 reduction to CO can be carried out in acidic media using gold gas diffusion electrodes, with better energy efficiency than in neutral media. It is desired to optimize this process further, by working in more

concentrated electrolytes, and trying to operate at even more acidic pH and higher current densities. Also, assessing the performance of silver catalysts instead of gold, can further help reducing the capital costs. Still regarding gas diffusion electrodes, in Chapter 12 we present a system that allows for systematically probing their local activity using SECM with shear-force positioning. We only looked at the effect of the catalyst loading, but it is desired to also use such a setup to investigate how other parameters define the local GDE performance, by varying for example, the binder composition, and the thickness of the microporous layer. On another hand, shear-forced based SECM alone does not provide accurate topographical resolution, which prevents understanding local GDE structure-activity relationships in detail. This is because the shear-force positioning is very sensitive to disturbances in the reaction environment under technologically relevant operating conditions, such as bubble evolution. Therefore, inspired by the work of Nadappuram et al.[14] it would be interesting to develop a dual-barrel scanning probe microscopy system, combining Scanning Electrochemical Microscopy (SECM) and Scanning Ion Conductance Microscopy (SICM) to simultaneously measure the local GDE activity *in situ*, under *operando* conditions, and obtain the electrode topography with high spatial resolution.

References

(1) Bondue, C. J.; Graf, M.; Goyal, A.; Koper, M. T. M. *J. Am. Chem. Soc.* 2021, *143* (1), 279–285.

(2) Vos, J. G.; Koper, M. T. M. *J. Electroanal. Chem.* 2019, *850*, 113363.

(3) Jijoe, P. S.; Yashas, S. R.; Shivaraju, H. P. *Environ. Chem. Lett.* 2021, *19* (3), 2643–2661.

(4) Mignani, A.; Ballarin, B.; Giorgetti, M.; Scavetta, E.; Tonelli, D.; Boanini, E.; Prevot, V.; Mousty, C.; Iadecola, A. *J. Phys. Chem. C* 2013, *117* (31), 16221–16230.

(5) Pérez-Gallent, E.; Marcandalli, G.; Figueiredo, M. C.; Calle-Vallejo, F.; Koper, M. T. M. *J. Am. Chem. Soc.* 2017, *139* (45), 16412–16419.

(6) Goyal, A.; Koper, M. T. M. *Angew. Chemie Int. Ed.* 2021, *60* (24), 13452–13462.

(7) Goyal, A.; Koper, M. T. M. *J. Chem. Phys.* 2021, *155* (13), 134705.

(8) Nakamura, M.; Nakajima, Y.; Hoshi, N.; Tajiri, H.; Sakata, O. *ChemPhysChem* 2013, *14* (11), 2426–2431.

(9) Nakamura, M.; Nakajima, Y.; Kato, K.; Sakata, O.; Hoshi, N. *J. Phys. Chem. C* 2015, *119* (41), 23586–23591.

(10) Liu, Y.; Kawaguchi, T.; Pierce, M. S.; Komanicky, V.; You, H. *J. Phys. Chem. Lett.* 2018, *9* (6), 1265–1271.

(11) Ocko, B. M.; Wang, J.; Davenport, A.; Isaacs, H. *Phys. Rev. Lett.* 1990, *65* (12), 1466–1469.

(12) Monteiro, M. C. O.; Goyal, A.; Moerland, P.; Koper, M. T. M. *ACS Catal.* 2021, 14328–14335.

(13) Hersbach, T. J. P.; McCrum, I. T.; Anastasiadou, D.; Wever, R.; Calle-Vallejo, F.; Koper, M. T. M. *ACS Appl. Mater. Interfaces* 2018, *10* (45), 39363–39379.

(14) Nadappuram, B. P.; McKelvey, K.; Al Botros, R.; Colburn, A. W.; Unwin, P. R. *Anal. Chem.* 2013, *85* (17), 8070–8074.

Samenvatting

Elektrokatalyse kan gebruikt worden om elektriciteit, bij voorkeur geproduceerd uit hernieuwbare bronnen, op te slaan of te gebruiken om chemische bouwstenen of synthetische brandstoffen te maken. Door deze mogelijkheden speelt elektrokatalyse een belangrijke rol in de transitie naar een duurzamere samenleving door middel van elektrificatie. Desondanks moeten elektrokatalytische reacties nog op verschillende vlakken verbeterd worden om ze op een industriële schaal economisch competitief te maken. Die verbeteringen kunnen alleen gerealiseerd worden als (tenminste globaal) bekend is hoe deze reacties plaatsvinden. In fundamenteel onderzoek ligt de focus vaak op het oppervlak van de (elektro)katalysator, terwijl de eigenschappen van de elektrolietoplossing, bijvoorbeeld pH en de soort kationen ook een significant effect kunnen hebben op de activiteit en selectiviteit van de reactie. In dit proefschrift wordt het grensvlak tussen het oppervlak van de elektrode en het elektroliet onderzocht. Verschillende experimentele technieken, zoals raster-elektrochemische-microscopie (Scanning Electrochemical Microscopy, SECM), voltammetrie onder stationaire en dynamische (roterende schijfelektrode, rotating disc electrode, RDE) omstandigheden, en bulk elektrolyse leveren inzichten op verschillende lengteschalen.

Tijdens elektrokatalytische reacties die protonen of OH^- verbruiken of produceren, kan de pH dicht bij het elektrodeoppervlak significant afwijken van de pH in de bulk elektrolietoplossing. Omdat deze pH gradiënten een effect kunnen hebben op zowel de reactie(s) aan het oppervlak als op homogene reacties die plaatsvinden dicht bij het oppervlak, wil men ze graag in kaart brengen. **Hoofdstuk 2** geeft een overzicht van allerlei experimentele technieken die gebruikt worden in dit soort lokale pH metingen. Specifieke aandacht is er daarbij voor SECM, de meest veelzijdige techniek. In **Hoofdstuk 3** beschrijven we de ontwikkeling van een nieuwe, voltammetrische, pH sensor gebaseerd op het 4-hydroxiaminothiofenol/4-nitrosothiofenol (4-HATP/4-NSTP) redox koppel. Deze sensor hebben we gebruikt om, met behulp van SECM metingen, de lokale pH te meten als gevolg van de vorming van waterstofgas aan een goudelektrode bij verschillende potentialen. Onze proof-of-concept experimenten tonen aan dat deze 4-HATP/4-NSTP pH sensor niet alleen heel selectief is, maar ook heel gevoelig, waardoor verschillen van slechts 0.1 pH eenheid met hoge snelheid gemeten kunnen worden. Vervolgens gebruiken we, in **Hoofdstuk 4**, dezelfde pH sensor om de lokale pH tijdens de reductie van CO_2 te bepalen. Daarbij onderzoeken we ook de dynamiek van de

diffuse laag als gevolg van potentiaalveranderingen en het effect van de verschillende homogene reacties waarbij CO_2 betrokken is. Met behulp van eindige elementenmethode (Finite Element Method, FEM) simulaties beschrijven we ook in hoeverre de SECM tip zelf leidt tot extra pH veranderingen en hoe dit te voorkomen is.

In **Hoofdstuk 5** gebruiken we SECM om de voltammetrie van CO elektro oxidatie te bestuderen als functie van de pH. Daarvoor meten we CO oxidatie met behulp van een platina ultramicroelektrode (UME) vlak boven een andere elektrode waaraan CO_2 reductie plaatsvindt (waarbij lokaal CO gevormd wordt). Op dezelfde positie meten we ook de lokale pH en de correlatie tussen deze twee experimenten helpt de verschillende pieken in de CO oxidatie voltammetrie te begrijpen. Die verschillende pieken ontstaan doordat CO geoxideerd kan worden door H_2O of OH^- en doordat de reacties gelimiteerd worden door de diffusie van verschillende moleculen/ionen, namelijk CO of OH^-.

Een roterende ring-schijfelektrode (rotating ring-disc electrode, RRDE) experiment is, van de methodes beschreven in Hoofdstuk 2, als enige te gebruiken voor lokale pH metingen onder goed gedefinieerde massa transport condities. Helaas hebben de RRDE pH sensoren die tot nu gebruikt werden een relatief lange responstijd en een gelimiteerde gevoeligheid en selectiviteit. Gezien de veelbelovende resultaten van de 4-HATP/4-NSTP pH sensor, onderzoeken we in **Hoofdstuk 6** of deze metingen ook gebruikt kunnen worden in een RRDE experiment. Door de pH sensor te adsorberen aan een goud(ring)elektrode is het mogelijk om de lokale pH tijdens waterstofevolutie aan de andere goud(schijf)elektrode te meten. Deze metingen zijn op allerlei manieren succesvol uitgevoerd: bij constante potentiaal of stroom, tijdens een scan van de potentiaal, bij verschillende rotatiesnelheden, en in (on)gebufferde elektrolietoplossingen.

In **Hoofdstuk 7** onderzoeken we een ander aspect van elektrochemische grensvlakken, namelijk het effect dat vervuiling van het oppervlak heeft op de katalytische activiteit. Voor een experiment, moeten elektroden altijd geprepareerd worden, en de eenvoudigste en meest gebruikte methode daarvoor is polijsten. In Hoofdstuk 7 laten we zien hoe de reactiviteit van goudelektrodes voor waterstofevolutie toeneemt door alumina polijstpasta te gebruiken. Dit wordt veroorzaakt doordat niet alle aluminadeeltjes weer van het oppervlak verwijderd kunnen worden, wat leidt tot Al^{3+} ionen, die de reductie van water bevorderen, in het elektroliet. In veel gevallen moet dit vermeden worden, omdat water reductie

concurreert met andere reacties die plaatsvinden in waterige oplossingen bij kathodische potentialen, zoals de reductie van CO_2 en nitraat.

Elektrokatalytische reacties kunnen ook sterk beïnvloed worden door ionen die, in tegenstelling tot vervuilingen, wél bewust aan het elektroliet toegevoegd worden. Het onderliggende mechanisme, is echter in veel gevallen niet goed bekend. In **Hoofdstuk 8** beschrijven we de invloed van metaal kationen in het elektroliet op de elektroreductie van CO_2. Met behulp van voltammetrie en SECM tonen we aan dat, verrassend genoeg dat de reductie van CO_2 naar CO aan goud, koper, en zilver elektroden alleen plaatsvindt als zo een kation aan het elektroliet wordt toegevoegd. Door de experimentele resultaten te combineren met dichtheidsfunctionaaltheorie (density functional theory, DFT) berekeningen en *ab initio* moleculaire dynamica (AIMD) simulaties, kunnen we een nieuw reactiemechanisme ophelderen waarin de kationen de adsorptie van CO_2 aan het oppervlak bevorderen en expliciet interacteren met het CO_2^- tussenproduct. Verder zien we dat het verschil in effect tussen de soorten kationen onderling, veroorzaakt wordt doordat kationen met verschillende hydratatie energieën een andere drijvende kracht ondervinden om zich op te hopen aan het oppervlak.

In **Hoofdstuk 9** breiden we het onderzoek uit Hoofdstuk 8 uit naar meervoudig geladen kationen. Hier beschrijven in meer detail welke eigenschappen van de kationen, bij verschillende potentialen, bepalend zijn voor CO_2 reductie activiteit en de daarmee concurrerende waterstofevolutie. Het blijkt dat elektrolietoplossingen met daarin relatief zure en zwak gehydrateerde kationen de waterstofevolutie het meest bevorderen en daarmee nadelig zijn voor de CO_2 reductie bij grote overpotentialen. Door opnieuw gebruik te maken van AIMD simulaties tonen we aan dat dit soort kationen zich in grotere mate aan het oppervlak ophoopt en de energie barrière voor de dissociatie van water verlaagt. Uit zowel de simulaties als de experimenten blijkt dat de zuurtegraad van een kation een goede maatstaf is voor de activiteit en doorslaggevend is in de competitie tussen de reductie van CO_2 en water.

In **Hoofdstuk 10** gaan we dieper in op het effect van alkali kationen op de reductie van water, omdat voor goud en platina tegenovergestelde trends (als functie van het soort kation) zijn beschreven. Hier vinden we voor goudelektroden dat zwak gehydrateerde kationen (K^+) water reductie bevorderen bij lage overpotentialen (lagere pH) terwijl deze bij hogere overpotentialen (hogere pH) de reactie juist hinderen. In dat laatste geval zorgen elektrolieten met sterk gehydrateerde kationen (Li+) voor de hoogste activiteit. Voor platina elektroden

vinden we een vergelijkbare trend, maar het blokkerende effect is hier verschoven naar lagere pH en lagere kation concentraties. Dit is een indicatie dat platina een sterkere interactie aangaat met de metaal kationen in het elektroliet dan goud.

In **Hoofdstuk 11** passe we de kennis uit de fundamentele experimenten in Hoofdstuk 8-10 toe op een grotere schaal, in een apparaat. In het algemeen worden neutrale of basische oplossingen gebruikt voor CO_2 reductie, vanwege de overtuiging dat in zure oplossingen, CO_2 reductie het aflegt tegen proton reductie. Wij tonen echter aan dat CO_2 reductie wel degelijk plaatsvindt in zure oplossingen door gebruik te maken van 10 cm^2 goud gasdiffusie-elektrodes (GDEs). Wij halen een selectiviteit tot 90% voor de vorming van CO bij stroomdichtheden die relevant zijn voor industriële toepassingen (50-200 mA cm^{-2}) in een Cs_2SO_4 oplossing met een pH van 2-4. Deze resultaten zijn vergelijkbaar met experimenten in neutrale of basische oplossen, maar het voordeel van de zure oplossing is dat het totale energieverbruik met 30% afneemt. Tot slot zien we, in overeenstemming met Hoofdstuk 8 en 9, dat dit alleen werkt door gebruik te maken van zwak gehydrateerde kationen, zoals Cs^+ of K^+, terwijl in zure oplossingen met $LiSO_4$ praktisch geen CO gevormd wordt.

In Hoofdstuk 11 onderzoeken we ook het effect van de hoeveelheid katalysator in de GDE op de activiteit voor de vorming van CO door gebruik te maken van GDEs met 1 en 2 mg cm^{-2} katalysator. Om dit beter in kaart te brengen, meten we in **Hoofdstuk 12** de lokale GDE activiteit met behulp van SECM en een positioneringsmethode gebaseerd op de schuifkracht tussen de UME en het GDE oppervlak. Tot op zekere hoogte levert dit experiment tegelijkertijd ook informatie op over de topografie van de GDE. Op de GDEs is een gradiënt van goud nanodeeltjes aangebracht, waardoor metingen bij verschillende hoeveelheden katalysator uitgevoerd kunnen worden. Een goud nanoelektrode wordt vervolgens gebruikt om de hoeveelheid gevormd CO te detecteren langs de katalysator gradiënt. In het algemeen zien we dat er een grotere hoeveelheid katalysator leidt tot een grotere CO productie. Echter, langs de hele gradient vinden we ook hotspots, wat aantoont dat de toegankelijkheid van de katalysatordeeltjes voor de reactanten belangrijker is dan de hoeveelheid katalysator. We bevestigen dit door metingen te doen bij verschillende CO2 drukken, waarbij we zien dat bij de hoogste drukken er een optimale hoeveelheid katalysator is die leidt tot de hoogste activiteit. Tot slot levert deze benadering een nieuwe methode op om, met hoge resolutie, de lokale activiteit en topografie van GDEs te meten onder *operando* condities.

Resumo

A eletrocatálise permite armazenar eletricidade ou convertê-la em ligações químicas, o que resulta na produção, por exemplo, de componentes químicos de base e combustíveis através do uso de recursos renováveis. Portanto, ela desempenha um papel importante na transição para um futuro mais sustentável para nossa sociedade por meio da eletrificação. A fim de implementar as tecnologias eletroquímicas em escala industrial e torná-las competitivas, faz-se necessária a otimização de vários aspectos das reações eletrocatalíticas.

Para atingir a melhoraria de um sistema, deve-se, primeiramente, ter um mínimo entendimento dele. Atualmente, muitos estudos fundamentais focam na compreensão dos processos que acontecem na superfície do catalisador. Entretanto, diferentes características do eletrólito, como o pH e a presença de cátions, também podem afetar significativamente a atividade e a seletividade da reação. Tendo isto em vista, nesta tese, vários aspectos da interface eletrodo-eletrólito são investigados em diferentes escalas, utilizando-se a Microscopia Eletroquímica de Varredura (MEqV), as técnicas de voltametria com eletrodo de disco(-anel) rotativo e eletrodo estacionário, e a eletrólise em batelada.

Durante as reações eletrocatalíticas que consomem ou produzem prótons (ou OH^-), o pH na superfície do eletrodo pode diferir significativamente do pH das demais partes do eletrólito. Esses gradientes de pH podem afetar a reação na superfície do eletrodo e as reações homogêneas que ocorrem no eletrólito. Portanto, almejamos a quantificação dessas mudanças no pH local. O **Capítulo 2** desta tese apresenta uma revisão bibliográfica sobre diferentes métodos aplicados para medir o pH local na eletroquímica e destaca a MEqV como uma técnica eficaz e versátil.

O **Capítulo 3** descreve o desenvolvimento de um sensor de pH baseado na voltametria de óxido-redução do 4-hidroxiaminothiofenol (4-HATP) e 4-nitrosothiophenol (4-NSTP). Aplicamos esse sensor para estudar o pH local desenvolvido durante a evolução do hidrogênio em eletrodos de ouro, sob diferentes potenciais eletroquímicos, usando a MEqV. Esses experimentos demonstram que o sensor de pH 4-HATP/4-NSTP é altamente seletivo e sensível, permitindo a medição de diferenças tão pequenas quanto 0,1 unidade de pH, com alta resolução temporal. O **Capítulo 4** relata a utilização do mesmo sensor de pH para medições de pH local com a MEqV durante a redução do dióxido de carbono (CO_2). Investigamos a dinâmica da camada de difusão e como as diferentes reações

homogêneas envolvendo CO_2 modulam o pH local. Além disso, mostramos, através de simulações usando o Método dos Elementos Finitos (MEF), como o ultramicroeletrodo da MeqV afeta a difusão das espécies no eletrólito, levando a uma alcalinização adicional do pH local. Finalmente, discutimos estratégias para evitar esse fenômeno.

O **Capítulo 5** relata a utilização da MEqV para compreender as características voltamétricas da eletrooxidação do monóxio de carbono (CO) em eletrodos de ouro em função do pH. Investigamos a oxidação do CO usando um ultramicroeletrodo de platina, posicionado acima de um eletrodo que está reduzindo CO_2, ou seja; que produz CO de forma localizada. Adicionalmente, realizamos medições de pH local na mesma posição no eletrólito e a correlação desses dois experimentos nos permite interpretar a natureza das distintas características voltamétricas da oxidação de CO. Diferentes picos na voltametria aparecem em função do pH local, os quais estão relacionados ao CO sendo oxidado por uma molecula de água ou OH^- e a corrente sendo limitada pela difusão de diferentes espécies, CO ou OH^-.

Entre as técnicas revisadas no Capítulo 2, o eletrodo de disco-anel rotativo (RRDE) é a única que atualmente permite que as medições de pH local sejam realizadas sob condições de transporte de massa controladas. No entanto, os sensores de pH usados em combinação com o RRDE, até agora, não possuíam resolução temporal, sensibilidade e seletividade satisfatórias o suficiente. Considerando o potencial do sensor de pH 4-HATP/4-NSTP desenvolvido no Capítulo 3, no **Capítulo 6** avaliamos a viabilidade de sua aplicação em um sistema de RRDE. Mostramos que o par de óxido-redução 4-HATP/4-NSTP pode ser incorporado com sucesso a um eletrodo de anel de ouro. Sendo assim, ele foi utilizado para medir o pH local em um disco de ouro durante a evolução de hidrogênio. O mesmo foi realizado com êxito durante experimentos de voltametria cíclica, cronopotenciometria e cronoamperometria sob diferentes taxas de rotação e potenciais eletroquímicos, em eletrólitos tamponados e não tamponados.

No **Capítulo 7** investigamos um outro aspecto da interface eletroquímica, avaliando como a contaminação da superfície do eletrodo pode afetar a eletrocatálise. Antes de um experimento a superfície do eletrodo deve ser preparada e o método de preparação mais simples e utilizado é o polimento. Portanto, no Capítulo 7 mostramos como o polimento de eletrodos de ouro com pasta de alumina leva a um aumento na atividade da reação de evolução do hidrogênio em meio ácido devido à liberação de íons Al^{3+} no eletrólito, que promovem a reação de redução da água. Isso deve, em muitos casos, ser evitado,

uma vez que a redução da água compete com várias reações, ocorrendo em potenciais catódicos em meio aquoso, como a redução do CO_2 e de nitrato.

Além do pH local e da contaminação, íons dissolvidos no eletrólito de suporte também podem afetar significativamente as reações eletrocatalíticas. No entanto, os mecanismos que descrevem essas interações, em muitos casos, ainda estão em debate. No **Capítulo 8** elucidamos como os cátions metálicos dissolvidos no eletrólito afetam a reação de redução do CO_2. Através de experimentos de voltametria cíclica e MEqV, observamos, pela primeira vez, que a redução do CO_2 para CO acontece em eletrodos de ouro, cobre e prata apenas se um cátion metálico é adicionado ao eletrólito. Combinando os resultados experimentais com a Teoria do Funcional da Densidade (Density Functional Theory, DFT) e as simulações de Dinâmica Molecular *ab initio,* sugerimos um novo mecanismo para a reação, no qual as espécies catiônicas metálicas favorecem a adsorção do CO_2 e interagem explicitamente com o CO_2^- adsorvido na superfície (um intermediário da reação). Além disso, notamos que as diferenças de atividade para a formação de CO em eletrólitos contendo diversos metais alcalinos vêm das distintas energias de hidratação destes cátions e, consequentemente, da tendência que eles têm em se acumular próximo à superfície. Devido à complexidade das interações entre cátions e o eletrodo, no **Capítulo 9** estendemos o estudo do Capítulo 8 para espécies catiônicas multivalentes. Neste estudo,definimos quais propriedades dos cátions ditam a atividade para a redução do CO_2 e para a concomitante reação de evolução do hidrogênio em diferentes potenciais eletroquímicos. Observamos que eletrólitos contendo cátions ácidos e fracamente hidratados favorecem a reação de redução da água e, portanto, são prejudiciais à atividade da redução do CO_2 em altos potenciais negativos. Novamente, em conjunto com a DFT e a Dinâmica Molecular *ab initio,* observamos que isso acontece porque essas espécies diminuem a barreira termodinâmica para a dissociação da água e se acumulam em maior quantidade perto da superfície. As simulações e dados experimentais mostram que a acidez do cátion é um descritor de atividade apropriado e é o que determina a competição entre a redução do CO_2 e a redução da água.

No **Capítulo 10** prosseguimos com uma análise sobre o efeito que os cátions alcalinos têm na reação de redução da água, uma vez que tendências opostas em função da identidade do cátion foram relatadas ao comparar eletrodos de platina e ouro. Mostramos que os cátions fracamente hidratados, como o K^+, favorecem a redução da água em eletrodos de ouro em baixos potenciais (alcalinidade local baixa), enquanto em altos potenciais (pH mais alcalino) estes são prejudiciais à

reação, e maior atividade é encontrada usando eletrólitos com cátions fortemente hidratados (como o Li^+). Uma tendência semelhante é encontrada para a platina, porém o efeito de inibição da produção de hidrogênio na platina ocorre em eletrólitos de menor alcalinidade e sob concentrações de cátion mais baixas, sugerindo que a platina interage fortemente com os cátions no eletrólito em comparação ao ouro.

O conhecimento obtido nos estudos fundamentais dos Capítulos 8-10 é transferido no **Capítulo 11** para um dispositivo de maior escala. Normalmente a redução do CO_2 é realizada em meio neutro para alcalino, pois acredita-se que a atividade da redução do CO_2 não consegue superar a atividade da redução de prótons em meio ácido. No Capítulo 11 mostramos, contrariamente, que a eletrólise do CO_2 pode ser feita em meio ácido aplicando eletrodos de difusão de gás de ouro de 10 cm^2 (gas diffusion electrodes, GDEs). Seletividades de até 90% para CO são obtidas com densidades de corrente relevantes industrialmente (50-200 mA cm^{-2}) utilizando um eletrólito composto de Cs_2SO_4, em pH 2-4. Mostramos que esses resultados são comparáveis àqueles obtidos em sistemas similares que operam em meio neutro ou alcalino, com a vantagem de que em meio ácido melhoramos a eficiência energética do processo em 30%. Além disso, observamos que cátions fracamente hidratados, como o Cs^+ ou o K^+, são essenciais para executar a reação em meio ácido, de acordo com os resultados apresentados nos Capítulos 8 e 9.

No Capítulo 11 também estudamos o efeito da quantidade de catalisador aplicado aos GDEs na atividade para CO, executando a reação em GDEs de ouro com carregamentos de catalisador de 1 e 2 mg cm^{-2}. O GDE com 1 mg cm^{-2} apresentou um desempenho ligeiramente melhor em termos de seletividade, mas não observamos tendências claras, mesmo quando comparamos com trabalhos semelhantes na literatura. Para entender melhor essas diferenças, no **Capítulo 12** utilizamos um sistema para investigar a atividade dos GDEs *in situ* usando a MEqV com um posicionamento baseado na força de cisalhamento, que também permite, até certo ponto, obter informações sobre a topografia da superficie. Preparamos os GDEs com um gradiente de nanopartículas de ouro, de uma região de baixa para outra de alta carga. Um nanoeletrodo de ouro é usado para detectar a quantidade de CO produzida ao longo do gradiente de catalisador no GDE. Observamos que mais CO é produzido à medida que a carga de catalisador aumenta. No entanto, "hot-spots" são encontrados ao longo de todo o gradiente, mostrando que mais importante do que a quantidade é o quão acessíveis as partículas de

catalisador estão para os reagentes. Confirmamos isso através de medidas em diferentes pressões de CO_2, as quais mostram que em pressões mais altas há um carregamento de catalisador ideal necessário para alcançar alta atividade. Finalmente, esse sistema abre um novo caminho para investigar a atividade e a topografia dos GDEs *in situ* em condições de operação, com alta resolução espacial.

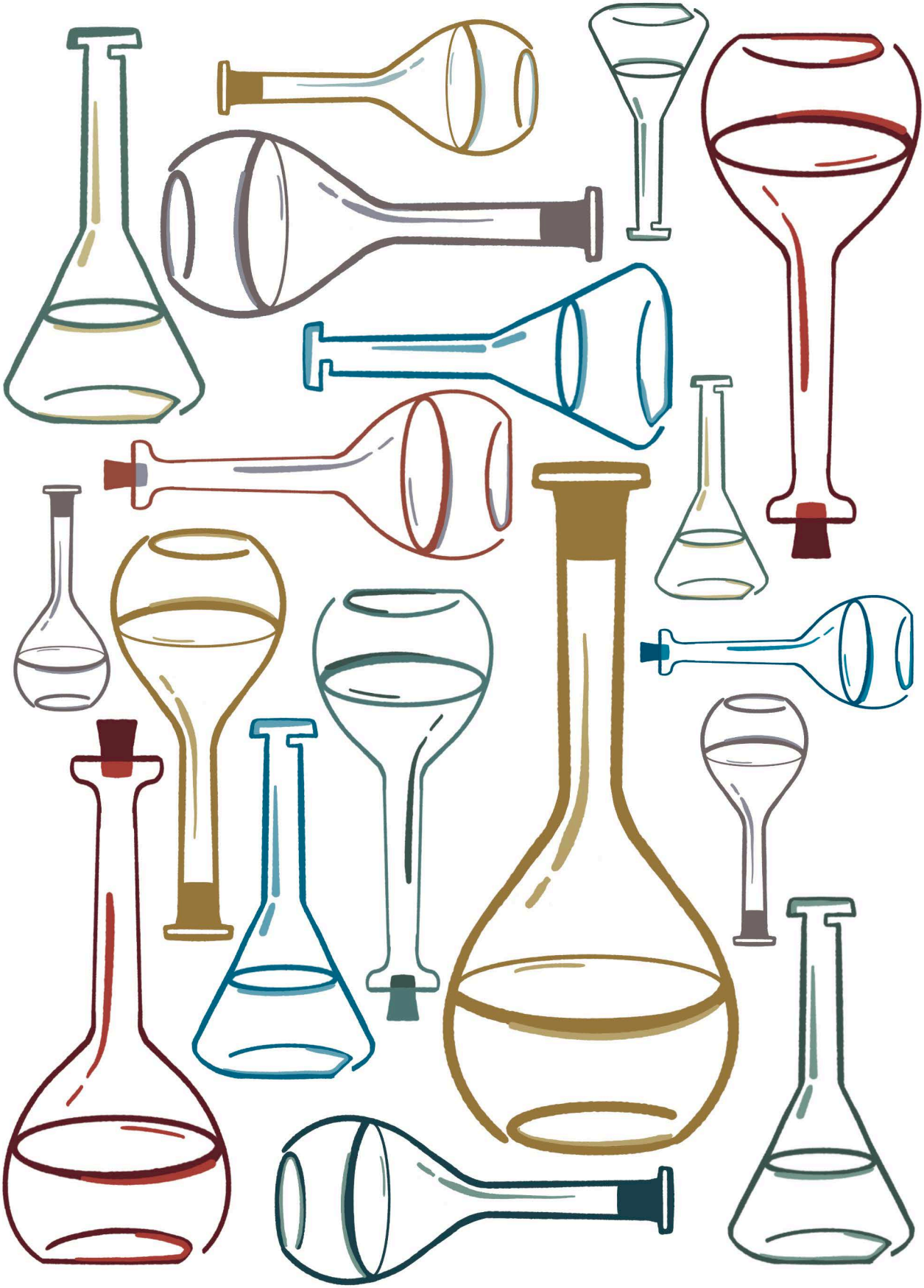

List of publications

Chapter 2

Measuring local pH in electrochemistry

Monteiro, M. C. O., Koper, M. T. M. *Curr. Opin. Electrochem.* 25, 100649. (2021)

Chapter 3

Mediator-free SECM for probing the diffusion layer pH with functionalized gold ultramicroelectrodes.

Monteiro, M. C. O., Jacobse, L., Touzalin, T., Koper, M. T. M. *Anal. Chem.* 92 (2), 2237–2243. (2020)

Chapter 4

Time-resolved local pH measurements during CO_2 reduction using Scanning Electrochemical Microscopy: buffering and tip effects.

Monteiro, M. C. O., Mirabal, A., Jacobse, L., Doblhoff-Dier, K., Barton, S. C., Koper, M. T. M. *JACS Au*, 1 (11), 1915–1924. (2021)

Chapter 5

Understanding the voltammetry of bulk CO electrooxidation in neutral media through combined SECM measurements.

Monteiro, M. C. O., Jacobse, L., Koper, M. T. M. *J. Phys. Chem. Lett.* 11 (22), 9708–9713. (2020)

Chapter 6

Interfacial pH measurements using a Rotating Ring-Disc electrode with a voltammetric pH sensor.

Monteiro, M. C. O., Liu, X., Hagedoorn, B., Snablié, D., Koper, M. T. M. *ChemElectroChem* 8, DOI: 10.1002/celc.202101223 (2021)

Chapter 7

Alumina contamination through polishing and its effect on hydrogen evolution on gold electrodes.

Monteiro, M. C. O., Koper, M. T. M. *Electrochim. Acta* 325, 134915. (2019)

Chapter 8

Absence of CO_2 electroreduction on copper, gold and silver electrodes without cations in solution.

Monteiro, M. C. O., Datilla, F., Hagedoorn, B., Garćia-Muelas, R., López, N., Koper, M. T. M. *Nat. Catal.* 4 (8), 654–662 (2021)

- Cations play an essential role in CO_2 reduction. Chen, L. D. *Nat. Catal.,* News and Views 4 (8), 641–642 (2021)
- Insight into the effect of metal cations in the electrolyte on performance for electrocatalytic CO_2 reduction reaction. Li, J. J., Zhang, Z. C., & Hu, W. P. *EEM,* Highlight, DOI: 10.1002/eem2.12294 (2021)
- Leiden chemists improve electrochemical production of sustainable chemical building blocks. Moezelaar, R. *Leiden University News*, 16th August (2021)
- Metal cations drive carbon dioxide´s chemical reduction. Lopatka, A. *Physics Today online*, 27th August, DOI: 10.1063/PT.6.1.20210827a (2021)
- Metal cations drive carbon dioxide´s chemical reduction. Lopatka, A. *Physics Today 74*, 10, 20, DOI: 10.1063/PT.3.4852 (2021)

Chapter 9

The role of cation acidity on the competition between CO_2 reduction and hydrogen evolution on gold electrodes

Monteiro, M. C. O., Datilla, F., López, N., Koper, M. T. M. *J. Am. Chem. Soc.,* DOI: 10.1021/jacs.1c10171 (2022)

Chapter 10

Understanding cation trends for hydrogen evolution on platinum and gold electrodes in alkaline media.

Monteiro, M. C. O., Goyal, A., Moerland, P., Koper, M. T. M.*ACS Catalysis,* 11, 14328–14335 (2021)

Chapter 11

Efficiency and selectivity of CO_2 reduction to CO on gold gas diffusion electrodes in acidic media.

Monteiro, M. C. O., Philips, M. F., Schouten, K. J. P., Koper, M. T. M.*Nat. Commun.* 12 (1), 4943 (2021)

- pH dependence of CO_2 reduction to CO. *Dioxide Materials News*, November (2021)

Chapter 12

Probing the local activity of CO_2 reduction on gold gas diffusion electrodes: effect of the catalyst loading and CO_2 pressure.
Monteiro, M. C. O., Dieckhöfer, S., Bobrowski, T., Quast, T., Pavesi, D., Koper, M. T. M.; Schuhmann, W.*Chem. Sci.* 12, 15682–15690 (2021)

Other publications

Electrolyte buffering species as oxygen donor shuttles in CO electrooxidation.
Marcandalli, G., Monteiro, M. C. O., Koper, M. T. M.*Phys. Chem. Chem. Phys.,* DOI: 10.1039/D1CP05030C (2022)

In situ observation of the Cs^+-Au(100) interactions at acidic and alkaline pH using Surface X-Ray Difraction.
Monteiro, M. C. O., Jacobse, L., Vonk, V., Deng, X., Koper, M. T. M., Stierle, A., in preparation

Electrolyte Effects on CO_2 Electrochemical Reduction to CO.
Marcandalli, G., Monteiro, M. C. O., Goyal, A., Koper, M. T. M*. Acc. Chem. Res.* , in preparation

Best Practices for Experimentation, Analysis, and Benchmarking of Electrochemical Water Splitting
Shih, A., Ojha, K., Monteiro, M. C. O., Park, S., Vos, R., Marques da Silva, A., Pavesi, D., Philips, M., McCrum, I., Dattila, F., Mom, R., López, N., Koper, M. T. M. *Nat. Rev. Methods Primers,* in preparation

From waste to valuable resource: lignin as a sustainable anti-corrosion coating.
Dastpak, A., Yliniemi, K., Monteiro, M. C. O., Höhn, S., Virtanen, S., Lundström, M., Wilson, B. *Coatings* 8 (12), 454 (2018)

Metal–phosphate bilayers for anatase surface modification.
Monteiro, M. C. O., Cha, G., Schmuki, P., Killian, M. S. *ACS Appl. Mater. Interfaces* 10 (7), 6661–6672 (2018)

Tuning anatase surface reactivity toward carboxylic acid anchor groups. Monteiro, M. C. O., Schmuki, P., Killian, M. S. *Langmuir* 33 (49), 13913–13922 (2017)

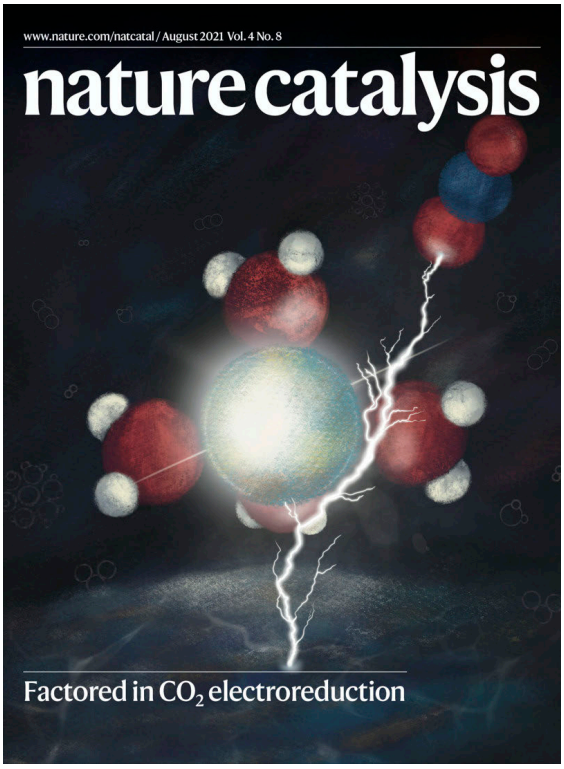
www.nature.com/natcatal / August 2021 Vol. 4 No. 8
nature catalysis
Factored in CO_2 electroreduction

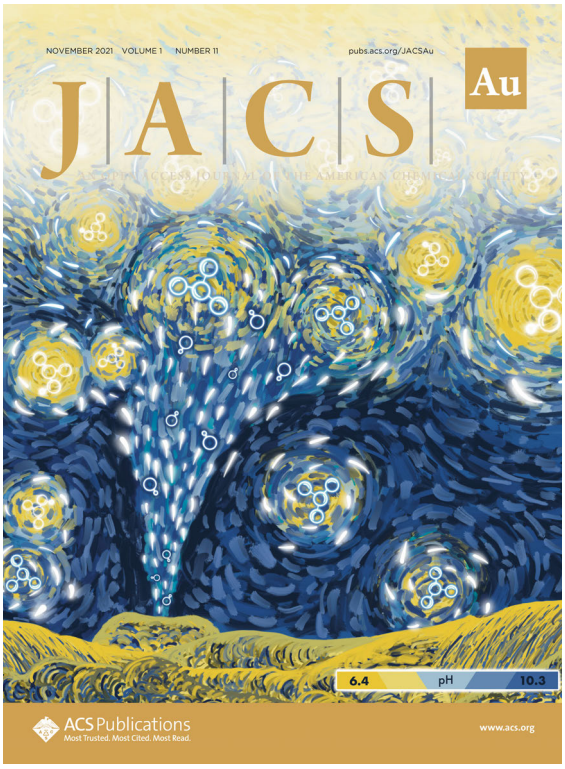
NOVEMBER 2021 VOLUME 1 NUMBER 11
pubs.acs.org/JACSAu
JACS Au
6.4
pH
10.3
ACS Publications
Most Trusted. Most Cited. Most Read.
www.acs.org

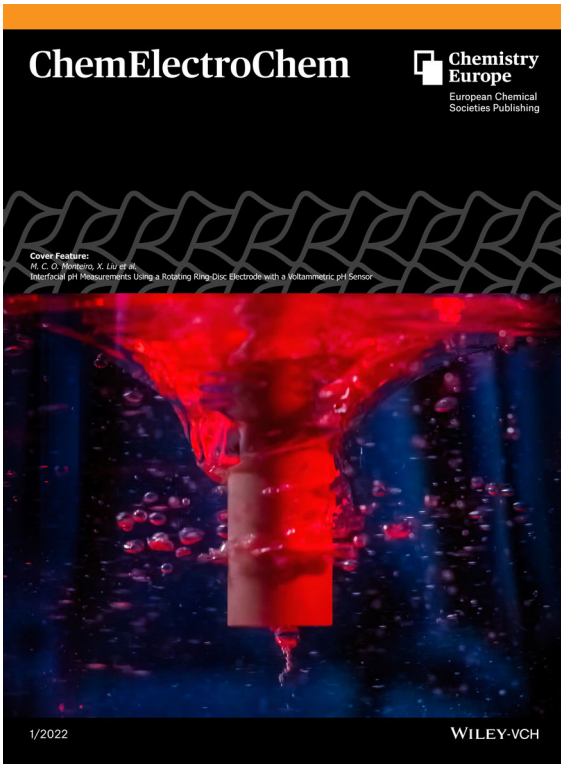
ChemElectroChem
Chemistry Europe
European Chemical Societies Publishing
Cover Feature:
M. C. O. Monteiro, X. Liu et al.
Interfacial pH Measurements Using a Rotating Ring-Disc Electrode with a Voltammetric pH Sensor
1/2022
WILEY-VCH


Xxxxx XX, XXXX
Volume XX
Number XX
pubs.acs.org/JACS
JACS
JOURNAL OF THE AMERICAN CHEMICAL SOCIETY
ACS Publications
Most Trusted. Most Cited. Most Read.
www.acs.org

Curriculum vitae

Mariana Cecílio de Oliveira Monteiro was born on the 21st of February 1991 in Belo Horizonte, Minas Gerais, Brazil. During high school (2006-2009) she developed a strong interest for chemistry, while having many extracurricular activities as a Classical Ballet and Jazz dancer and teacher. In 2009 Mariana decided to further explore her interest in chemistry and started her bachelor studies in Chemical Engineering at the Federal University of São Joao Del-Rei, in Ouro Branco, Brazil. In parallel to her studies, she still worked as a teacher at a local dance school. During her bachelors, Mariana had her first contact with the scientific research world thanks to Prof. Dr. Jorge D. A. Bellido, with whom she worked for 2 years with as an undergraduate research assistant investigating heterogeneous catalysts for the ethanol steam reforming.

In 2012 Mariana was awarded a full scholarship from the Brazilian National Council for Scientific and Technological Development (CNPQ) under the "Science Without Borders" program, which gave her the unique opportunity to study in The Netherlands. Mariana did part of her bachelor studies in the University of Groningen and during her stay, worked as an undergraduate research assistant in the group of Prof. Dr. Francesco Picchioni, investigating the synthesis of polyketones. This led to her master thesis research, which was carried out in the same group, entitled "Polymeric amines by chemical modifications of alternating aliphatic polyketones for arsenic removal of wastewater". To expand her experiences beyond academic research, Mariana also worked for 6 months as an R&D intern in the paper department of the Dutch starch industry Avebe, optimizing paper surface sizing solutions.

Mariana continued her education in 2015, following the Elite Master´s Programme in Advanced Materials and Processes at the Friedrich-Alexander University Erlangen-Nürnberg (FAU), Germany, with specialization in Nanomaterials and Advanced Processes. Beyond the master curriculum, Mariana followed several soft-skill courses, was a member of the Elite Network of Bavaria, and class representative in the program board. In the interest of pursuing a career in research, during her masters Mariana worked as a graduate research assistant in various groups. At the Institute of Chemical Reaction Engineering, Mariana worked in the group of Prof. Dr. Peter Wasserscheid on projects regarding the decomposition of formic acid and catalyst synthesis via electrophoretic deposition. At the Institute of Biomaterials, Mariana worked in the group of Prof. Dr. Aldo Boccacini on the synthesis of Bioglass® and Bioglass®-chitosan coatings. At the Institute of Surface Science and Corrosion, Mariana worked for 1.5 years on projects for Siemens regarding the corrosion behavior of pipeline materials. Mariana developed her master thesis at the same institute, under the supervision of Prof. Dr. Manuela S. Killian in the group of Prof. Dr. Patrick Schmuki. She graduated *cum laude* with a master thesis entitled "Boosting anatase surface reactivity towards carboxylic acid anchor groups", which also resulted in her first two scientific publications. Besides the publications, in 2017 Mariana was awarded the FAU Deutschlandstipendium prize, and in 2018 Mariana´s master thesis was awarded the Luise Prell Prize.

Mariana moved back to the Netherlands in 2017 to pursue a PhD in electrocatalysis under the guidance of Prof. Marc Koper, at Leiden University. The project was part of the Marie Curie ITN ELCOREL and involved seven partner institutions, creating a very dynamic and exciting research atmosphere. Mariana`s initial task was to unveil electrolyte effects on the electrochemical CO_2 reduction reaction. However, Mariana dedicated the first years of her PhD to building a dedicated Scanning Electrochemical Microscope (SECM) from scratch, together with miniaturized (pH, H_2, CO) sensors. This and many other techniques were used during her PhD to answer questions related to CO_2 and H_2 electrocatalysis and the interaction between the electrolyte and metal electrodes. Mariana also had the chance to transfer the fundamental insights obtained in Leiden into a larger-scale CO_2 electrolysis system, while being a visiting researcher at the company Avantium, in Amsterdam, under the supervision of Dr. Klaas Jan Schouten and Matthew Philips. Mariana continued bridging fundamental and applied research also in a collaboration with the group of Prof. Dr. Wolfgang Schuhmann at the University of Bochum, Germany. During a month stay, she used shear-force-based SECM to probe the local activity of technologically relevant gas diffusion electrodes. During her PhD, Mariana also established collaborations with theoreticians from the group of Prof. Dr. Núria López from the Institute of Chemical Research of Catalunya (Spain), and Prof. Dr. Scott Calabrese Barton from the Michigan State University (USA). Finally, Mariana also performed Surface X-Ray Diffraction measurements at the German Electron Synchrotron DESY as part of a (still ongoing) collaboration with the group of Prof. Dr. Andreas Stierle, to investigate cation-surface interactions at the molecular/atomic level.

During her PhD, Mariana supervised 3 master and 4 bachelor students, and taught instrumental analysis in the “Organic Chemistry” practical course. She was a member of the Holland Research School of Molecular Chemistry (HRSMC) PhD platform. Mariana gave invited oral presentations at the FunCOS seminar (Erlangen, Germany), Bernoulli Symposium (Groningen, The Netherlands), Vlaamse Instelling voor Technologisch Onderzoek (VITO, Mol, Belgium) and at the University of Copenhagen (Copenhagen, Denmark). Mariana also presented her research work in various (inter)national conferences. She was awarded poster prizes at the SurfCat Summer School (2018, Denmark), and at the 71th and 72th meetings of the ISE - International Society of Electrochemistry (2020, Belgrade and 2021, Jeju). Mariana gave contributed talks in the 72nd ISE (2021, Jeju), nanoGE Conference (2021, online), Electrochemical Society Fall meeting (2021, Chicago/online), HRSMC Symposium (2022, Amsterdam) and at the Netherlands' Catalysis and Chemistry Conference (NCCC) in 2020, where she was also appointed a lecture award. Mariana´s work has been highlighted in the cover of Vol. 4 Issue 8 of *Nature Catalysis*, Vol. 1 Issue 11 of *JACS Au* and the *Journal of The American Chemical Society* (in press) through the beautiful artwork from Katrina Goretskaya; and *ChemElectroChem 1/2022* with a cover picture developed by her.

Starting from April 2022, Mariana will continue her scientific career as a postdoc fellow in the Interface Science Department of the Fritz-Haber-Institute of the Max-Planck-Society in Berlin with Prof. Dr. Beatriz Roldán Cuenya and Dr. Sebastian Oener. Mariana will keep bridging fundamental and applied electrochemistry using SECM and Scanning Ion Conductance Microscopy (SICM) to study bipolar membranes and gas diffusion electrodes.

Acknowledgments

First, I want to thank Prof. Marc Koper for providing me with the opportunity to join the Catalysis and Surface Chemistry (CASC) group four years ago. Marc, thank you for giving me the freedom to develop my own ideas and for the subtle yet impactful advises you gave me throughout the way. Beyond all the scientific knowledge, you thought me a lot about scientific conduct, which I will always carry with me in my career. Thank you for encouraging me to pursue my curiosities and develop new projects, but also for saying "enough is enough" in the right moments. I also want to express my gratitude to my former mentors, Prof. Jorge Alguiar Bellido and Prof. Manuela Killian, who contributed to my PhD, years ago, by helping to shape who I am as a researcher.

Secondly, after these four years, I am certain that one cannot do science alone. This thesis only came to be due to the valuable contributions of several people along the way. I want to express my gratitude to all former and current members of CASC with whom I had the chance to work with. You created a healthy and stimulating work environment, thank you for all the valuable inputs on my research. I also want to thank José Dijkzeul for the care and Wen Tian Fu for the funny conversations while sharing the X-Ray/SECM lab. Some colleagues became good friends and made these four years go by in a light and fun way. My dear paranymph Thomas, thank you for introducing me to the 4-NTP molecule, for helping me with the SECM struggles, for celebrating with me every step of the way, and for the scientific and non-scientific conversations over a glass of bubbles. Sabine, thank you for being such a good friend, and for all the support. Elena, Richard, Stefan, Giulia and Akansha, thank you for your friendship, the discussions, the relaxing and happy moments. To my Master students: Max, Bellenod and Demi; I hope I contributed to your scientific formation at least as much as you contributed to this thesis.

Besides CASC, I was lucky to be part of the Marie Curie ITN ELCoREL, which provided me with an exciting research and learning environment and also brought me good friends. I want to thank all ELCoREL members, especially Federico and Rebecca, for the nice moments we shared during (and outside) project meetings. Also, my gratitude to the friends Vlad and Katrina, for all the efforts to make my thesis artwork. Katrina, I have no words to describe how talented you are.

Furthermore, the large body of work of my thesis was, in part, only possible due to the successful collaborations I established along the way. I want to thank Prof. Scott Calabrese Barton and Alex Mirabal for taking up the challenge of simulating my local pH experiments, which led to the contributions to Chapter 4. Also, I thank my co-promotor Prof. Núria López and Federico Dattila, for educating me in the world of theoretical electrocatalysis, and for the contributions to Chapters 8 and 9. I also thank Dr. Klaas Jan Schouten for giving me the opportunity to be at Avantium, and Matthew Philips for the guidance in the lab work, which resulted in Chapter 11. I want to also thank Prof. Wolfgang Schuhmann for warmly welcoming me in his group in Bochum during weird pandemic times, and Stefan Dieckhöfer for the intense but exciting three weeks we shared by the SECM, which

resulted in Chapter 12. Finally, I want to thank Prof. Andreas Stierle for the nice collaboration we developed for performing synchrotron-based X-Ray Diffraction measurements, which I am sure will still lead to many interesting results as we continue.

My last words of gratitude go to those who not always fully understood my work but were always enthusiasts and supporters. I have an amazing family, thank you for being inspiring, for all your support and cheering. Tia Bú *(in memoriam)*, you left us when I was halfway this journey, but your love and support I carry with me forever. A special thanks to Tia Rosa and to Tati, for the care and advises; and to Manu and Mumu, for bringing joy to my life. To my childhood friends, in special Isis, Ana, Paula, Lívia, Bárbara, Ligia; to my friends from República Só Benzeno; Bel, Loreny, to the friends from Groningen, and everyone else that somehow is in my life, thank you for, from close or far away, being with me at every step. A special thanks to Mari and Gui for being my rock in The Netherlands, and always being there for me.

My dear Leon, all my love and gratitude for how you helped shaping my PhD, for your care, for letting me be me, but also for driving me to be a better person. Thanks for inspiring and challenging me, and for all the "never boring days". We started this journey as colleagues who were also good friends, and we now continue as partners in life and in science. I could not have wished for more. Many thanks also to your family, for being there for me, their love and care.

Finally, and most important, I would like to thank my parents, Marcelo and Elvira, for their unconditional support and for always being so close to me, no matter how physically far we actually have been from each other for the past years. We came a long way, that none of us thought was possible… this is "our" thesis. You keep reminding me that even the small victories should not be taken for granted and are my biggest examples. I love you, your kindness, and your funny advises. Thank you and let´s see what next adventures wait for us.

Agradecimentos

Em primeiro lugar, quero agradecer o Prof. Marc Koper pela oportunidade de ingressar no grupo de Catálise e Química de Superfície (CASC), em Leiden. Marc, obrigado por me dar liberdade para desenvolver minhas próprias ideias e por seus conselhos sutis, mas impactantes, ao longo do caminho. Além de todo conhecimento científico, você me ensinou muito sobre conduta científica, ensinamentos que levarei para minha carreira. Obrigado por me encorajar na exploraração de minhas curiosidades e desenvolvimento de novos projetos, e por ter dito "basta" nos momentos certos. Minha gratidão também aos meus ex-mentores, Prof. Jorge Alguiar Bellido e Prof. Manuela Killian, que contribuíram para o meu doutorado, quando há anos atrás, incentivaram a minha formação como pesquisadora.

Após esses quatro anos, estou certa de que a ciencia é um trabalho de equipe. Esta tese só é possível devido às pessoas que me rodeavam nesta caminhada. Quero expressar minha gratidão a todos os membros do CASC, antigos e atuais, com quem tive a oportunidade de trabalhar. Vocês criaram um ambiente de trabalho saudável e estimulante. Obrigado por todas as contribuições valiosas para minha pesquisa. Quero agradecer também a José Dijkzeul pelo cuidado e a Wen Tian Fu pelas conversas engraçadas no laboratório que compartilhavamos. Algumas pessoas, além de colegas tornaram-se bons amigos e fizeram esses quatro anos leves e divertidos. Meu querido paraninfo Thomas, obrigado por me apresentar à molécula 4-NTP, por me ajudar com os problemas do SECM, por comemorar comigo cada passo do caminho e pelas conversas científicas e não científicas durante uma taça de espumante. Sabine, obrigada por ser uma amiga extraordinária e pelo suporte. Elena, Richard, Stefan, Giulia e Akansha, obrigado pela amizade, pelas discussões, e pelos momentos relaxantes. Aos meus alunos de mestrado: Max, Bellenod e Demi; espero ter contribuído para a sua formação científica tanto quanto vocês contribuiram para esta tese.

Além do CASC, tive a sorte de fazer parte do projeto Marie Curie ELCoREL, que me proporcionou um ambiente estimulante de pesquisa e aprendizado e me trouxe bons amigos. Gostaria de agradecer a todos os membros do ELCoREL, em especial Federico e Rebecca pelos bons momentos que compartilhamos durante (e fora) das reuniões do projeto. Minha gratidão aos amigos Vlad e Katrina, por todos os esforços para a arte da minha tese. Katrina, não tenho palavras para descrever a dimensão do seu talento.

O grande volume de trabalho da minha tese, em parte, só foi possível, devido às colaborações bem-sucedidas que foram estabelecidas ao longo do caminho. Quero agradecer o Prof. Scott Calabrese Barton e Alex Mirabal por aceitarem o desafio de simular meus experimentos de pH local, o que resultou em contribuições para o Capítulo 4. Agradeço também a minha co-promotora, Prof. Núria López e a Federico Dattila, por me educar no mundo da eletrocatálise teórica e pelas contribuições aos Capítulos 8 e 9. Agradeço ao Dr. Klaas Jan Schouten pela oportunidade de estagiar na Avantium, e a Matthew Philips pela orientação no laboratório, o que resultou no Capítulo 11. Quero também agradecer o Prof.

Wolfgang Schuhmann, por me receber em seu grupo, em Bochum, durante tempos estranhos de pandemia, e ao Stefan Dieckhöfer pelas intensas, mas divertidas três semanas que compartilhamos ao lado do SECM, resultando no Capítulo 12. Finalmente, devo agradecer ao Prof. Andreas Stierle pela colaboração que desenvolvemos para realizar medições de Difração de Raios-X no síncrotron, as quais espero que ainda nos levem a muitos resultados interessantes, a medida que continuarmos.

Minhas últimas palavras de agradecimento vão para aqueles que nem sempre compreenderam totalmente o meu trabalho, mas sempre foram entusiastas e me apoiaram. Tenho uma família e amigos incríveis, obrigada por serem inspiradores, e pela torcida. Tia Bú *(in memoriam)*, você nos deixou quando eu estava na metade dessa jornada, mas seu amor e apoio levo comigo para sempre. Um agradecimento especial à Tia Rosa e à Tati, pelo carinho e conselhos; e a Manu e o Mumu, por trazerem alegria à minha vida. Minhas amigas de infância, em especial Isis, Ana, Paula, Lívia, Bárbara, Ligia; às amigas da República Só Benzeno; Bel, Loreny; amigas e amigos de Groningen, e todos aqueles que de algum forma se fazem presentes na minha vida; obrigado por, de perto ou de longe, estarem comigo a cada passo dessa caminhada. Um agradecimento especial a Mari e ao Gui, por serem meu porto seguro na Holanda, e por estarmos sempre juntos.

Meu querido Leon, todo meu amor e gratidão por tudo; pela sua ajuda no desenvolvimento do meu doutorado, pelo seu cuidado, por me deixar ser eu, mas também por me levar a ser uma pessoa melhor. Obrigado por me inspirar e desafiar, e por todos os "dias nada entediantes". Começamos esta jornada como colegas e também bons amigos, e agora seguimos como parceiros na vida e na ciência. Eu não poderia ter desejado mais. Muito obrigado à sua família, por estar ao meu lado, pelo amor e carinho.

Por fim, e mais importante, quero agradecer meus pais, Marcelo e Elvira, pelo apoio incondicional e por sempre estarem tão próximos de mim, por mais distantes que estivemos fisicamente nos últimos anos. Percorremos um longo caminho, que nenhum de nós pensava ser possível... essa é a "nossa" tese. Vocês me lembram constantemente que as pequenas vitórias devem ser celebradas, e são meus maiores exemplos. Amo vocês, sua bondade e seus conselhos engraçados. Obrigado, e vamos ver quais próximas aventuras nos esperam.